Author:
Swankie, Troy Dennis

Title:
The role of shear and constraint in mixed mode fracture.

THE ROLE OF SHEAR AND CONSTRAINT

IN

MIXED MODE FRACTURE

BY

Troy Dennis Swankie

December 1999

A dissertation submitted to the University of Bristol

in accordance with the requirements of

the degree of Doctor of Philosophy

in the Department of Mechanical Engineering

in the Faculty of Engineering

Word count: 64833

ABSTRACT

In this thesis, two steels; BS1501-224 Grade 490B and A508 Class 3 are studied using single edge notch, SEN specimens under mixed mode I/II loading conditions.

The first steel, BS1501 was used to investigate the influence of prior loading on the low temperature mixed mode I/II fracture. A prior Mode I proof load at room temperature resulted in an increase in the Mode I low temperature fracture toughness and load bearing capacity. This benefit reduced with increasing shear (Mode II) until for pure Mode II loading where there was no change in toughness. A prior Mode II proof load at room temperature resulted in a decrease in low temperature fracture toughness and load bearing capacity. With increasing shear this reduction was not so great. For pure Mode II loading there was no change in toughness or load bearing capacity at low temperature. Fractographic studies revealed that there was a change in failure mechanism from cleavage to ductile tearing with increasing Mode II loading.

The second steel, A508 was used to assess the role of shear (Mode II) and constraint in mixed mode ductile fracture. Constraint was addressed in terms of a variation in specimen thickness (B=10mm, 20mm and 40mm), width (W=20mm, 40mm and 80mm) and crack depth to specimen width ratio (a_o/W=0.1, 0.5 and 0.7). A new testing fixture was designed and successfully used to apply combinations of tension (Mode I) and shear (Mode II) loading through the crack tip of each specimen, regardless of specimen size and crack depth. For each combination of B, W and a_o/W, a series of multiple specimen crack growth resistance curves (R-curves) which provide a measure of the relative toughness required to initiate a crack (J_{init}) and its resistance to further tearing (defined by the slope of the R-curve, dJ/da) for the complete range of mixed mode loading. Finite element analysis was used to determine specific elastic and plastic parameters used to determine mixed mode I/II J-integrals. In addition, finite element analyses has been used been used to give a qualitative prediction of the crack propagation path during mixed mode loading.

The A508 results demonstrate that the effect of B on the size and shape of the R-curve is negligible regardless of mode of loading. Conversely, the experiments show that W has a significant effect on the magnitude of the R-curve, since W=80mm is less than 40mm which is less than 20mm. For mode I loading this is consistent with data presented in the open literature. However, contrary to the literature, the effect of increasing Mode II is to reduce the value of J_{init} and dJ/da until the limiting condition of pure Mode II is reached. Moreover, Mode II loading produced lower bound R-curves for each crack depth studied. With the exception of Mode II loading the magnitude of the R-curves is dependent on W. The Mode II R-curves are independent of specimen size and can be described by a single 'Master Curve'.

The R-curves are dependent on crack depth. Essentially, the deeper the crack, the higher the constraint, the lower the R-curve. For Mode I loading, dJ/da for a_o/W=0.5 is greater than dJ/da for a_o/W=0.7. Similarly, for Mode II loading, dJ/da for a_o/W=0.1 is greater than for a_o/W=0.5 which is greater than for a_o/W=0.7. For Mode I loading, an R-curve for a_o/W=0.1 could not be generated since gross yielding occurred throughout the entire length of the specimen prior to crack initiation. Mixed mode studies for a_o/W were also unsuccessful due to gross yielding.

R-curves have also been used to assess the relative contributions from crack opening (Mode I, J_{Icn}) and crack sliding (Mode II, J_{Icp}) for each combination of mixed mode loading. For pure Mode I loading J_{Icn} was greater than J_{Icp}. For pure Mode II loading J_{Icp} was greater than J_{Icn}. In between Mode I and Mode II loading a change in failure mechanism from dimple rupture (tensile dominant) to shear decohesion (shear dominant) occurs and the relationship between J_{Icn} and J_{Icp} has been shown to predict this change well.

ACKNOWLEDGEMENTS

There are a number of people who have contributed significantly to the completion of this research. In particular, my colleagues and good friends, Professor David Smith and Dr Majid Reza Ayatollahi have given me much encouragement and technical input throughout the course of this research.

My thanks also go to my many friends in the Mechanical Engineering workshop who encouraged me every step of the way and helped by manufacturing the many specimens that were tested in this research. In particular, Ian Milnes who took over from me as technician to Professor Smith's research group, who has provided invaluable advice and assistance in maintaining the testing facilities to ensure my time throughout this research was 'stress' free!

I would also like to mention my late colleague, Mr David Ogden. David and I worked together as technicians in Professor Smith's research group. It is he who I have to thank for nurturing me in the field of materials testing and for guiding me to study for a higher degree. Unfortunately he was unable to see me complete my research but I'm sure he would have been satisfied with the result and moreover, proud of what I have achieved during my thirteen years at Bristol University.

Penultimately, I would like to acknowledge the financial support given by the Engineering and Physical Science Research Council (EPSRC) and British Energy plc., without whom this research would not have been possible.

Finally, I must apologise to my fiancée, Nikki for dragging the writing of this thesis on and on. Although she has given me strength and encouragement throughout, I do acknowledge that my enthusiasm to finish writing this thesis has put our lives on hold for a while. Perhaps now we can finally set a date for our wedding!

AUTHOR'S DECLARATION

I declare that this dissertation, submitted for the degree of Doctor of Philosophy at the University of Bristol, is entirely the work of the author and in no way represents the views of the University of Bristol.

All of the work in this dissertation was carried out in accordance with the Regulations of the University of Bristol. This work is original, except where indicated by special reference in the text, and no part of the dissertation has been submitted for any other degree.

This dissertation has not been presented to any other University for examination either in the United Kingdom or overseas.

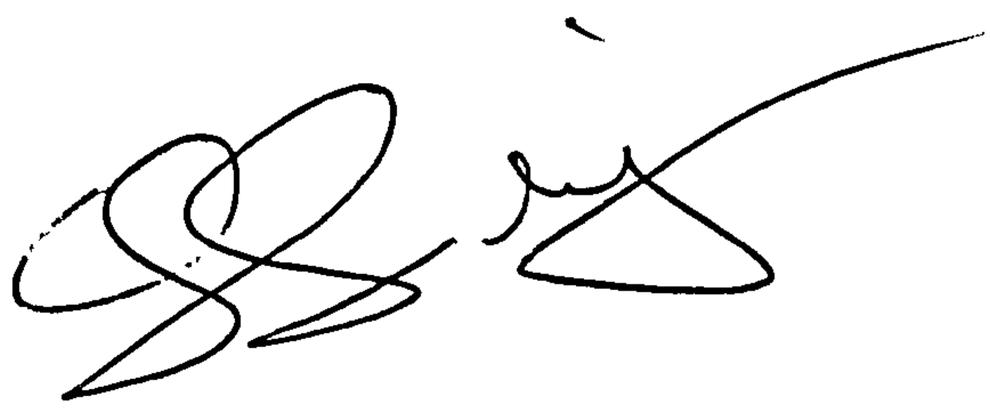

Troy Dennis Swankie

December 1999

PUBLICATIONS

The following publications have resulted from this research:

a. Journal Publications

D.J. Smith, J.C.W. Davenport and T.D. Swankie, 1998, 'Mixed Mode Brittle and Ductile Fracture of a High Strength Rotor Steel at Room Temperature', International Journal of Fracture

T.D. Swankie and D.J. Smith, 1998, 'Low Temperature Mixed Mode Fracture of a Pressure Vessel Steel Subject to Prior Loading', Engineering Fracture Mechanics

b. Conference Proceedings

T.D. Swankie, M.R. Ayatollahi, D.J. Smith and M.J. Pavier, 1998, 'Brittle and Ductile Fracture Under Mixed Mode Loading', Proceedings of the 12th European Conference on Fracture (ECF12), Sheffield, UK, Vol. 2

T.D. Swankie, J.C.W. Davenport and D.J. Smith, 1997, 'Brittle and Ductile Fracture Transition in Steels Subjected to Mixed Mode Loading', The 9th International Congress on Fracture (ICF9), Sydney, Australia, Vol. 1

TABLE OF CONTENTS

LIST OF TABLES

Tables in Chapter 4

LIST OF FIGURES

Figures in Chapter 1.

Figures in Chapter 2

Figures in Chapter 3

Figures in Chapter 4

Figures in Chapter 5

ACRONYMS

C(T)	Compact tension specimen
CDS	Compact double shear specimen
DE(T)	Double edge tension specimen
DPS	Double punch shear specimen
G	Maximum Energy Release Rate Criterion
HRR	Hutchinson, Rice and Rosengren
LBC	Load bearing capacity
LCF	Load-cool-fracture
LCUF	Load-cool-unload-fracture
LUCF	Load-unload-cool-fracture
M(T)	Middle tension specimen
MIIP	Mode II proof load
MIP	Mode I proof load
MTS	Maximum Tangential Stress Criterion
NP	Non proof load
PS	Plain sided
S	Strain Energy Density Criterion
SE(B)	Single edge bend specimen
SE(T)	single edge tension specimen
SEN	Single edge notch specimen
SG	Side grooved
SZW	Stretch zone width
WPS	Warm prestress

INTRODUCTION

In engineering structures crack like flaws or defects are always present. This is in-spite of rigorous quality control that is employed to reduce their quantity during fabrication of the structure, since inspection techniques in themselves can not always resolve flaws of certain orientations and size.

Fracture mechanics is concerned with the performance of the structural component when flaws are present within the material. It is an engineering tool that can be used in design, inspection and failure analysis. At the design stage fracture mechanics can be used to assess the limiting conditions that would cause a component to fail in service when subject to specified loading conditions. Alternatively, fracture mechanics can be used to make a remaining life assessment of a component that is already in service. Moreover, if a component has failed, fracture mechanics can be used to assess the cause of failure.

The material from which a component is made can fail in either a brittle or ductile manner depending on a number of factors which include environmental conditions, the applied loads and the general condition of the material. A brittle failure is where a crack propagates rapidly through a component and requires little driving force once initiated. The deformation of the material prior to fracture is small and the relationship between load and displacement is linear. Conversely, the global deformation of a material that fails in a ductile manner is significant and the relationship between load and displacement is non-linear. Moreover, a ductile material is highly resistant to crack growth and requires a much higher driving force for the crack to propagate and continue to grow.

Due to the inhomogenous nature of structural materials a crack can be subject to three different types of loading, usually simultaneously, rarely unique. They are denoted Modes I, II and III. Mode I loading refers to tensile loading where the crack flanks tend to open. Modes II and III are concerned with shear loading where the crack faces slide over one another. When one crack face slides over the other in a direction which is parallel to the plane of the initial crack the applied loading

conditions are termed Mode II. When the crack faces slide over one another, out of the plane of the initial crack, the loading conditions are termed Mode III.

Preferably, the best method of assessing the integrity of a cracked structural component is to test the component itself. However the inherent costs of testing a full size component invariably precludes such an approach. As a consequence it is often more convenient to perform experiments in the laboratory, on smaller, less expensive specimens, and then translate the laboratory results to the performance of the real component.

The majority of models and analytical techniques are for Mode I loading situations. However, structural components are usually subject to complex loading situations, resulting in combinations of Mode I, Mode II and Mode III loading. At present the methods of inferring the integrity of the real component from mixed mode loading laboratory tests is uncertain. There are additional problems associated with the behaviour of laboratory test specimens. For example, when the specimen dimensions or geometry are varied, but the length of the crack remains the same, the value of fracture toughness is known to vary considerably, particularly for Mode I (Garwood, 1982; Gibson et al., 1987; Joyce and Link, 1995).

The general approach to considering the influence of specimen dimensions and geometry is to consider the effects as due to varying constraint. There has been considerable effort in addressing such problems of constraint, although principally for Mode I loading conditions only. A single parameter characterisation of fracture, using parameters such as, Stress Intensity (Irwin, 1957), J-Integral (Rice, 1968) or Crack Opening Displacement (Wells, 1961), has limited success when there are different levels of constraint. Instead two-parameter methodologies such as, K-T (Betegón and Hancock, 1991) and J-Q (O'Dowd and Shih, 1991; 1992) have been developed, where the second term provides a measure of constraint. Garwood et al., (1975) proposed a three-parameter technique to correct J for a growing crack, replacing the actual load versus displacement curve by a fictitious non-linear elastic loading curve, which can match the load, displacement and crack length to real test pieces at any load or displacement point. Ernst et al., (1983) proposed a similar

procedure, although based on just two-parameters, where the load can be expressed as a function of crack length and displacement.

Although a number of approaches to the problems of constraint have been proposed, no one approach has been shown to be universally applicable and therefore theoretical and experimental work in this area is continuing.

The aim of this research was to obtain a fundamental understanding of the role of shear and constraint in ductile fracture for combinations of tension (Mode I) and shear (Mode II) loading of a candidate power generation material using experimental techniques under controlled laboratory conditions. The effect of constraint has been studied in terms of specimen size (combinations of thickness, B where $10 \leq B \leq 40$mm and width, W where $20 \leq W \leq 80$mm) and crack depth (corresponding to a crack depth, a_o to specimen width ratio, a_o/W of 0.1, 0.5 and 0.7), and in relation to the mechanisms of ductile crack initiation and growth. Finite element analyses have also been used throughout to enable the mixed mode fracture toughness of each laboratory specimen to be calculated and the mechanism of crack growth to be qualitatively modelled.

One method of improving the fracture performance of a structural component is to mechanically overstress it. One such technique, warm prestressing, particularly for ferritic steel components, involves loading a component at a temperature within the upper regime of the fracture transition curve. The subsequent performance of the component at lower in-service operating temperatures, for example, on the lower shelf of the fracture transition curve, has been found to improve the load bearing capacity and fracture toughness (Brothers and Yukawa, 1963 and Andrews 1970).

If an overload is applied in a controlled manner, causing localised yielding sufficient to blunt any existing crack like defect, residual stresses are created at the blunted crack tip. As a result, a higher in-service load at lower temperatures will be required to overcome the local residual stress to cause failure by cleavage fracture. The greatest benefits reported have been attributed to the controlled overload being applied in the same direction the component would be loaded during service.

There is however a limit to increased load bearing capacity and fracture toughness accrued through warm prestress which Brothers and Yukawa (1969) propose to be marginally lower than the stress required for crack initiation although a benefit is still obtained from the warm prestress if this optimum level is exceeded (Smith and Garwood, 1990a).

An additional aim of this research was to study the circumstances when precracked ferritic steel specimens are subjected to proof loading at room temperature and are then subsequently fractured at a lower temperature, close to the Mode I lower shelf behaviour of the steel. Experiments have been done to study low temperature mixed mode fracture of a pressure vessel steel without proof loading, and then mixed mode low temperature fracture after a Mode I or Mode II proof load at room temperature.

In this thesis, Chapter 1 provides a thorough review of the literature relevant to these studies. The mechanisms by which a material can fail are discussed together with current techniques, single and two-parameter approaches, used to assess mixed mode loading conditions, including an up to date review of the effects of constraint in terms of laboratory experiments. A review of the effects of warm prestress and the models available to assess these effects are also presented.

Chapter 2 provides the results of the mixed mode study in which the effects of warm prestressing have been addressed. Detail is also given to the experimental methods and techniques used throughout this study.

Chapter 3 details the experimental methods and results from the specimens used to assess the influence of shear and constraint in ductile fracture for mixed mode loading.

Chapter 4 describes the finite element techniques used to model the mixed mode behaviour of the material and chapter 5 discusses this research in relation to the experimental research presented in the open literature. Finally, chapters 6 and 7 give the main conclusions drawn from this research and provides recommendations for future studies to compliment this work and others.

CHAPTER 1 : LITERATURE REVIEW

In this chapter, the aspects of fracture mechanics methodology relevant to the present work are reviewed. This review is divided into five sections and forms the basis for discussing the forthcoming chapters.

In the first section, the failure mechanisms from brittle, through the transition temperature regime to fully ductile behaviour are discussed in the context of mixed mode I/II loading. The second section deals with the current methods used to describe linear elastic and elastic-plastic mixed mode I/II behaviour. Sections three and four describe two parameter methods currently used to quantify the effects of constraint. Also described are recent experimental investigations which address constraint in terms of material orientation, specimen type and size, and the effect of crack or flaw size. Finally, the effects of warm prestressing are reviewed. Warm prestressing is a process used to enhance the integrity of a structural component. Methods commonly used to assess the warm prestress effect are also reviewed.

The intention of this review is to address the aspects detailed above in relation to mixed mode I/II loading conditions. However, the majority of research conducted in these fields has been concerned mainly with Mode I type failure. In comparison, research into mixed mode loading is less well developed. Consequently, these reviews deal in the main with Mode I loading. However, where ever possible, mixed mode related issues are also discussed.

1.1 Failure Mechanisms in Ferritic Steels

There are primarily two distinct mechanisms by which failure will occur; brittle or ductile, depending on whether or not the micromechanism requires plastic flow for material separation or not. Brittle failure requires the separation of atomic planes by the attainment of a critical stress. Ductile failure requires plastic flow, sufficient to nucleate and grow voids until they coalesce, causing rupture. In this section these

failure mechanisms, along with the development of models that are capable of providing a qualitative description of the failure process, will be discussed.

1.1.1 The Micromechanisms of Brittle Fracture

Cleavage is a term commonly associated with metals that fail in a brittle manner, and is most likely to occur when plastic flow (dislocation motion) is restricted. The fracture path is transgranular and once nucleated, the crack propagates at such a velocity that failure is catastrophic.

The cleavage fracture of steels follows a critical tensile stress fracture criterion (Knott, 1966). For initiation to occur a critical stress must be achieved (greater than or equal to the cohesive strength of the material) that is sufficient to break the bonds between neighbouring atoms. However, yielding will occur before this stress can be achieved, unless there exists a local discontinuity ahead of the crack tip sufficient to raise the local stress level beyond the stress required for cleavage fracture. This is achieved in metals by inclusions and second phase particles which act as an effective barrier to dislocation movement.

In mild steels, cleavage initiates in grain boundary carbides (McMahon and Cohen, 1965, Smith, 1966, and Knott, 1977), however, in quenched and tempered alloy steels, initiation is due to cracking of spheroidal carbides (Liu and Gurland, 1968, and Curry and Knott, 1978). Susceptibility to cleavage can be enhanced by almost any factor that increases the yield strength, such as reduced temperature, triaxial stress state, high strain rate, strain ageing and heat treatment.

However, initiation is not the critical event that leads to cleavage fracture. Once a microcrack has initiated a propagating crack may arrest at a particle/matrix interface (figure 1.1a), a ferrite grain boundary (figure 1.1b), or, if a steep stress gradient exists (usually at low applied stress intensity levels) within a ferrite grain (figure 1.1c), unless there is sufficient driving force for the cleavage crack to propagate over one or two grain diameters (Rice and Tracey, 1973, and Ritchie et al., 1973).

Analytical Models Describing Cleavage Fracture

In 1920, Griffith developed a fracture theory for a brittle solid based on energy. Although limited to the fracture behaviour of glass, this was an important step in understanding the cleavage fracture behaviour of steels. Irwin (1948) and Orowan (1948) independently modified Griffith's (1920) theory to account for steels, materials that are capable of plastic flow. For cleavage fracture of mild steel, initiation occurs in grain boundary carbides as a 'through-thickness' microcrack, and for quenched and tempered steels, initiation occurs in spheroidal carbides as a 'penny-shaped' microcrack. The modified Griffith's (1920) equations, given by Orowan (1948), describing the cleavage fracture strength (σ_f) required for initiation in steel are given by

$$\sigma_f = \left[\frac{2E\left(\gamma_s + W_p\right)}{\pi\left(1-\nu^2\right)r}\right]^{1/2} \qquad \text{through-thickness microcrack} \qquad (1.1)$$

$$\sigma_f = \left[\frac{\pi E\left(\gamma_s + W_p\right)}{2\left(1-\nu^2\right)r}\right]^{1/2} \qquad \text{penny-shaped microcrack} \qquad (1.2)$$

where E is Young's modulus, ν the Poisson's constant, γ_s the surface energy of the matrix, W_p the plastic work necessary for crack propagation, and r the half thickness of the cracked carbide particle. Fracture is assumed to occur when the local stress ahead of the crack tip exceeds the cleavage fracture stress for a given critical carbide size.

Smith (1966) proposed a further modification to Griffith's theory. For failure to occur, the combination of cleavage fracture stress and the contribution from the pile-up of dislocations, had to be greater than, or equal to equation (1.1). In the absence of dislocation pile-ups the model would reduce to equation (1.2). However, dislocation pile-ups across the necessary one or two grain diameters (requirement for cleavage fracture to occur once initiation of a microcrack has been achieved) do not occur in quenched and tempered steels.

In 1973, Ritchie et al. proposed that due to the random nature of inclusions within the microstructure, cleavage fracture is a statistical event. They were the first to quantify that cleavage fracture initiation was a statistical event and concluded that the cleavage fracture stress must be achieved over a characteristic distance ahead of the crack tip.

The first true attempt to describe cleavage fracture as a statistical event was developed by Curry and Knott (1979). They proposed that the characteristic distance described by Ritchie et al. (1973) provided a description of the competition between small and large carbide particles initiating penny-shaped microcracks in spheroidal carbides. They based their model on the actual carbide size distribution (the probability of a carbide particle having a radius sufficient to nucleate cleavage fracture) and, combining it with Griffith's cleavage fracture criterion for a penny shaped crack and the stress distribution ahead of the crack tip determined numerically by Tracey (1973), calculated a probabilistic estimate for cleavage fracture toughness.

Although Curry and Knott's (1979) model qualitatively explained the temperature dependence of fracture toughness, it did not account for the experimentally observed size effects, which Landes and Shaffer (1980) demonstrated using a two parameter Weibull distribution.

More recently, 'weakest link' statistics have been used to qualitatively describe the phenomena of cleavage fracture toughness at the macroscopic level. The weakest link is concerned with one critical event that is sufficient to cause macroscopic failure. Pineau (1981), of the Beremin Research Group, was one of the first to present such an idea. He assumed pure weakest link behaviour for cleavage fracture, described the probability of finding a single initiator being critical with a two parameter Weibull distribution function, and used the plastic zone size as a measure of the cleavage fracture process zone. A number of workers, also associated with the Beremin Research Group have since modified this model.

The statistical nature of these models assumes that the material ahead of the crack tip contains a distribution of possible cleavage fracture initiators (a complex function of

the initiator size distribution, stress, strain, grain size, temperature and stress and strain rate). The shape and origin of the initiator is not detrimental to a component containing a sharp crack, but the only necessary assumption is that there is no global interaction between fracture initiating particles.

Wallin et al. (1984) developed a weakest link model (called the WST model) based on the actual cleavage fracture micromechanism, describing failure of a CrMoV steel with rod shaped chromium rich carbides. They derived a theoretical expression to determine the cumulative probability distribution of a single initiator being critical and assumed that the primary cleavage initiators comprised of brittle second phase particles. Although their model is capable of quantitatively explaining most of the experimental findings regarding cleavage fracture initiation, it can only provide a crude description of cleavage fracture initiation.

1.1.2 The Micromechanisms of Ductile Fracture

Dimple rupture, fibrous fracture and plastic fracture are terms commonly associated with metals that fail in a ductile manner. Unlike metals that fail by cleavage, ductile fracture usually involves the absorption of large amounts of energy. There are three principal stages that combine to cause ductile fracture

1. ***nucleation*** of internal cavities during plastic flow,
2. ***growth*** of the nucleated cavities with continued deformation, and
3. ***coalescence*** to cause fracture.

The fracture path is predominately intergranular. If the inclusions or second-phase particles are well bonded into the matrix, nucleation is often the critical stage in the fracture process since fracture occurs soon after. However, if nucleation readily occurs, the fracture properties are controlled by the growth and coalescence of the nucleated microvoids. A diagrammatic representation of the mechanisms of ductile fracture are shown in figure (1.2).

Mechanisms of Nucleation and Analytical Models in Ductile Fracture

Microvoid nucleation is concerned with the formation of a free surface and usually occurs at inclusions or second-phase particles by decohesion of the particle/matrix interface, particle cracking, or at blocked slip bands when second-phase particles are absent.

Nucleation is highly dependant on stress state and strength level (an increase in strength corresponds to a decrease in plastic strain for nucleation), which can vary considerably with particle size, shape, orientation and distribution, for different microstructures and microconstituents of steels (Cox and Low, 1974, French and Weinrich, 1974, Argon and Im, 1975 and Beremin, 1981).

Gurland (1972) and Beremin (1981) proposed that void nucleation is controlled by the attainment of a critical stress due to the creation of internal stresses as a result of mismatch in deformation between the inclusions and matrix. For a spheroidised steel, French and Weinrich (1974) demonstrated that nucleation is a function of strain as well as stress, particularly when large stresses are required for nucleation. Van Stone et al. (1985) proposed additional factors, such as inclusion size and local deformation mode should also be considered.

Large particles are more susceptible to cracking and small particles are more likely to nucleate voids by decohesion of the particle/matrix interface (McMahon and Cohen, 1965, Gurland, 1972, and Cox and Low, 1974). Beremin (1981) observed that orientation of Mn-S inclusions in a C-Mn steel (one of the most common void nucleation sites in low alloy steels) were detrimental to nucleation, since orientation dictates whether nucleation is due to cracking or decohesion. Rellick and McMahon (1974) demonstrated that a transition between cracking and decohesion can be achieved in heat treated steels by applying insufficient cooling time to promote non-equilibrium composition differences. Cox (1973) and Cox and Low (1974) observed decohesion of the particle/matrix interface and particle cracking in a quenched and tempered, and maraging steel, respectively. Although different nucleation mechanisms were observed, the influence of stress state on cavity formation in both steels was similar.

Argon, Im and Needleman (1975), Argon, Im and Safoglu (1975), Argon and Im (1975) and Goldenberg et al. (1978) suggested that there was no intrinsic particle size effect on void nucleation when a large volume fraction of inclusions was present. However, the influence of particle size of low volume fraction is caused by the interaction of stress fields (plastic zones) of closely spaced inclusions.

The majority of nucleation models presented consider Mode I loading only. Most models describe nucleation based on interfacial and nominal stress criteria, and are limited to specific steel conditions. Recent models present nucleation as a combination of stress, strain and energy criteria, and are highly dependent on the deformation modes of the particle and matrix, and have been extended to mixed mode behaviour. Some models describing nucleation are based on plastic continuum theory and others on dislocation-particle interactions. The former refers to particle diameters greater than 1μm and assumes critical stress to be independent of particle size, the latter are required for particle diameters less than 1μm.

Aoki et al. (1987) proposed that nucleation in mixed mode loading was controlled by the competition between the blunted (dominated by tensile stress) and sharpened (dominated by shear stress) sides of the deformed notch tip as a function of equivalent plastic strain, void volume fraction and mixed mode loading ratio. Knott (1980) suggested that the plastic strain in slip bands produces dislocation pile-ups at carbide particles thus stressing the particle and particle/matrix interface with increasing strain until, at a critical strain, either the interface or particle fractures.

Gurland and Plateau (1963) proposed one of the first continuum models for nucleation, and assumed that particle fracture was dependent on the elastic energy in the particle exceeding the surface energy of the newly formed void surfaces. Argon, Im and Safoglu (1975) demonstrated that the theory proposed by Gurland and Plateau (1963) was necessary, but an additional stress on the particle/matrix interface in excess of the interfacial strength should also be considered. They proposed that the critical stress required for decohesion was a critical combination of hydrostatic stress and effective stress, demonstrating a relationship between stress and strain (as the nucleation stress increases, the nucleation strain decreases).

Beremin (1981) proposed a similar continuum model, but based on a modification of elasticity theory that was extended by Berveiller and Zaoui (1979) for a plastically deforming matrix. The expression yielded a temperature dependence through a plastic equivalent Young's modulus (although he observed this dependence to be negligible), and a function, C which accounts for inclusion shape and loading direction. The model, given in equation (1.3) is independent of particle radius and, although a stress criterion, a critical nucleation strain can be determined through the relationship of both hydrostatic stress (σ_{hyd}) and effective stress (σ_{eff}) to the total plastic strain. Beremin (1981) proposed that the critical stress (σ_{crit}) required for void nucleation can be determined from this simplified model

$$\sigma_{crit} = \sigma_{hyd} + C\left(\sigma_{eff} - \sigma_{ys}\right) \tag{1.3}$$

For small particle radii (< 1μm) dislocation models are required to estimate the total interface stress on a particle. Brown and Stobbs (1976) developed a model describing the local flow stress based on the dislocation density around a particle. However, the presence of a particle imposes a local plastic constraint on the matrix, resulting in elevation of the local stress on the particle interface. Goods and Brown (1979) applied further modifications to account for the concentration of stress and derived an expression describing the critical condition for nucleation by decohesion of the particle/matrix interface. The model demonstrates that the local stress concentration increases with decreasing particle size, inferring that nucleation is more difficult with larger particles.

For mixed mode loading, Bhattacharjee and Knott (1994) proposed the localisation of strain at the sharp crack corner which leads to damage accumulation as the important feature for nucleation. Using a model developed by Smith and Barnby (1967) for nucleation by a series of coplanar dislocation pile-ups, Bhattacharjee and Knott (1994) proposed a model capable of predicting the shear strain for decohesion of a particle/matrix interface for a given particle diameter. They demonstrated two competing mechanisms during ductile failure under mixed mode loading, shear band formation and microvoid coalescence.

Void Growth and Coalescence in Ductile Fracture

Microvoid growth and coalescence is concerned with cavity enlargement due to localised plastic flow, and subsequent joining of the enlarged cavities when a local plastic instability occurs in the necked region between growing voids.

It can be assumed that under most conditions, the resultant stress free surfaces of the nucleated voids are sufficiently spaced so that there is no interaction between their local stress and strain fields (Gurland, 1972, and Van Stone et al., 1985). With continued plastic flow the growing voids exhibit a volumetric growth and shape change, causing eventual interaction between neighbouring voids. The concentration of strain between growing voids can provide sufficient plasticity to nucleate voids from smaller, closely spaced particles, effectively accelerating the fracture process.

Growth of cavities at nucleated microvoids depends on the flow properties of the matrix material surrounding the nucleated particle. Constraint is a structural feature which inhibits plastic flow and promotes stress triaxiality. As the level of constraint increases, the level of stress triaxiality also increases. The ratio of hydrostatic stress to effective stress provides a measure of stress triaxiality, and Cox and Low (1974) have demonstrated that hydrostatic stress has a significant influence on the rate of void growth. However, in mixed mode loading, as the degree of shear (Mode II) loading is increased, the influence of hydrostatic stress decreases and the effective stress becomes the dominant mechanism (Ghosal and Narasimhan, 1994, and Otsuka et al., 1987).

Cottrell (1959) proposed that coalescence of inclusion nucleated voids could be due to significant necking of the matrix between the voids. Rogers (1960) and Druyvesteyn et al. (1964) suggested that coalescence could occur by the formation of secondary voids in the intense shear bands between inclusion nucleated larger voids. Rosenfield and Hahn (1966) suggested that failure would occur when the ligament between nucleating voids failed when the growing voids achieved a critical size as a function of their spacing.

Beachem (1963, 1964) demonstrated at least three general appearances of void coalescence depending on the stress state existing between neighbouring voids using fractographic and metallographic techniques. The fracture surfaces shown by Beachem could be reconciled as having void coalescence occur by growth until impingement of the voids by normal rupture (Mode I loading), shear rupture (Mode II loading), or tearing (Mode III loading). Several processes have been identified as possible mechanisms of void coalescence based on experimental evidence on steels of different heat treatments and compositions. They consist of coalescence by void impingement, which can be accompanied by extensive plastic flow (over aged maraging steels, Roesch and Henry, 1969) or not (spheroidised carbon steels, King and Knott, 1981), and secondary void formation in bands of intense shear localised between large inclusions (Rogers, 1960).

For failure in mixed mode loading with a high shear component, Bhattacharjee and Knott (1994) observed that equivalent plastic strain and void volume fraction were higher on the sharpened side of the crack, but in the presence of a high tensile component they were higher on the blunted side. Results obtained by Aoki et al. (1987) collaborated these suggestions. However, results presented by Tohgo et al. (1988) revealed the opposite. Results obtained by Ghosal and Narasimhan (1994) demonstrated that the maximum void volume fraction always occurs near the blunted portion of the deformed notch irrespective of mode mixity, but confirm the statements of Aoki et al. (1987) and Bhattacharjee and Knott (1994) concerning the equivalent plastic strain being higher on the sharpened side of the notch in the presence of a high shear component during mixed mode loading.

There have been a number of models developed which attempt to describe void growth and coalescence. Some are based on continuum theory and others on dislocations. The majority of models tend to describe void growth since coalescence occurs rapidly and catastrophically, and is the most difficult stage to investigate.

Rice and Tracey (1969) used continuum theory to model the enlargement of a spherical void in a remote uniform stress and strain field in an infinite plastic solid.

They proposed a rate equation for void growth that can be determined by the following evolution equation

$$\frac{\dot{R}}{R} = 0.283\dot{\varepsilon}^{p}_{m} e^{\frac{3\sigma_{hyd}}{2\sigma_{eff}}} \qquad (1.4)$$

which depends exponentially on the triaxiality ratio; which is the ratio of the hydrostatic stress (σ_{hyd}) to the effective stress (σ_{eff}), where ε^{p}_{m} is the accumulated plastic strain and R is the void radius.

Gurson (1977) used equation (1.4) to describe the plastic yielding behaviour of a porous medium. However, although the Gurson relationship can qualitatively describe the initial stages of void growth, it cannot describe the final stage of coalescence since it assumes that the growth of each void is independent of the next. Tvergaard and Needleman (1984) introduced an empirical modification of the Gurson yield function, and proposed that coalescence occurs when the material looses its stress carrying capacity and when a critical void volume fraction is achieved. The model also exhibits a dilatational plastic behaviour which is consistent with a growing void.

Rousselier (1986) proposed a yield function to describe the growth of microvoids as a function of σ_{eff}, σ_{hyd}, the true stress-strain curve and the void volume fraction. The yield function is equivalent to the Von Mises yield criterion if the void volume fraction is set to zero. Coalescence is also implicitly included in the Rousselier model. As the damage increases due to an increase in load, the stresses decrease with increasing strains, simulating void coalescence. Seidenfuss (1992) introduced a critical void volume fraction into the Rousselier model to enable large amounts of crack growth to be modelled numerically. He found that numerical errors occurred since the drop in stress was not steep enough. His modification induced the necessary steep stress drop by reducing the materials stiffness to zero once the critical void volume fraction had been achieved.

Thomason (1990) developed a criterion for void coalescence based on the net section stress for uniaxial and multiaxial loading situations (shown in figure 1.3). For uniaxial loading, coalescence follows as a result of necking when a critical necking stress (σ_{nk}) has been achieved and takes account of void spacing (2d) and dimension (2b). The stress required for coalescence of a specimen loaded in uniaxial tension is given by

$$\sigma \geq \sigma_{nk}\left(\frac{d}{d+b}\right) \rightarrow \text{coalescence} \qquad (1.5)$$

For multiaxial loading where voids are orientated at some arbitrary angle with respect to each other, equation (1.6) gives the stress required for coalescence. In this more general case the driving force for coalescence is equal to the effective stress (σ_{eff}) and depends on the ligament size (d) achieving some critical fraction of the planar spacing (d_o).

$$\sigma_{eff} \geq \sigma_{nk}\left(\frac{d}{d_o}\right) \rightarrow \text{coalescence} \qquad (1.6)$$

1.1.3 Brittle to Ductile Fracture Transition

The fracture toughness characteristics of ferritic steels can change considerably with a change in temperature. At low temperature, steel is brittle and fails by cleavage as discussed previously. At high temperature, steel is ductile and fails due to microvoid nucleation, growth and coalescence. The transition from brittle to ductile failure occurs over a temperature range specific to the type of steel. Within this regime both failure mechanisms can occur. For each steel there exists a specific temperature within the brittle to ductile transition temperature range which corresponds to the onset of ductile tearing. Prior to achieving this temperature, failure is predominantly cleavage, but at temperatures above the initiation temperature for ductile tearing, there is an increasing influence of ductile fracture mechanism. Figure (1.4) illustrates

the change from cleavage to microvoid coalescence as the fracture temperature increases within the brittle to ductile transition temperature region.

Heerens and Read (1988) investigated the change in fracture mechanism of a quenched and tempered steel at several temperatures in the transition region. They observed a critical temperature which corresponded to the initiation of ductile tearing. For fracture below this temperature failure is due to cleavage since carbide particles of sufficient size to initiate cleavage are always available near the crack tip. However, above this temperature and the probability of finding a particle of sufficient size to initiate cleavage near the crack tip reduces progressively as the fracture temperature increases. In this region fracture initiation is effected by large scale yielding as well as the effect of ductile tearing prior to cleavage fracture initiation. For fracture to occur the crack has to grow until a critical particle, capable of initiating cleavage can be sampled.

Because the fracture toughness behaviour in the transition temperature region is governed by statistical sampling effects, data tends to be highly scattered. Wallin (1989, 1991) incorporated a ductile crack growth correction function into an existing weakest link statistical model for cleavage fracture (Wallin et al., 1984) and was able to provide a qualitative description of scatter and thickness effects on fracture toughness in the transition region.

1.1.4 Fracture Surface Features

Cleavage Fracture Surface Features

Once an appropriate driving force has been obtained a propagating crack will pass through each grain along a specific crystallographic plane (for body-centre-cubic materials the preferred cleavage planes are those with the lowest packing density {100}), continually changing direction, seeking the path that requires the least energy for cleavage crack propagation. The nominal orientation of a cleavage crack is

perpendicular to the maximum tensile stress, and direction changes are due to the random nature of the polycrystal grain structure.

The change of orientation from grain to grain contributes to a branching of the crack along different planes. A grain with the {100} plane orientated normal to the maximum tensile stress can be identified as a flat smooth facet. Misorientation of neighbouring grains can be identified by 'river patterns' that originate at grain boundaries. River patterns are due to the presence of screw dislocations threading through a cleavage plane, orientated at an angle (other than normal) to the maximum tensile stress.

When a propagating crack encounters a grain boundary, and the {100} plane of the neighbouring grain is orientated at a finite twist angle from the current {100} plane, the crack accounts for the mismatch by forming on several parallel planes within the grain. While propagating through the grain the multiple cracks converge to a single crack to minimise the energy of fracture, joining like river tributaries in the direction of crack growth. The directionality of river patterns can also provide information confirming the presence of fracture initiating inclusions and precipitates. These features are shown in figure (1.5).

The height of river patterns provides information regarding the orientation of the cleavage plane within a particular grain, relative to the maximum tensile stress. Therefore, a grain with little or no river patterns refers to a crack propagating easily on a single plane. The density of river patterns corresponds to the density of dislocations and to the degree of cold working present within the grain before cleavage occurs.

Ductile Fracture Surface Features

Microvoids grow under triaxial stress conditions ahead of the crack tip and expand until they coalesce to leave behind hemispherical cavities (known as dimples) on the fracture surface. The size and shape of the dimples can be related to the size of, and

spacing between, initiated particles to the condition of applied stress (Mode I, Mode II or Mode III), and to the fracture toughness of the specimen.

As mentioned previously, dimples have been classified into three groups (Beachem, 1963, 1964); equiaxed dimples (Mode I), shear dimples (Mode II) and tear dimples (Mode III). Equiaxed dimples do not always appear equiaxed in scanning electron fractographs due to specimen tilting. This is a technique that is often used to provide good contrast for other surface features. Therefore the dimples may appear slightly distorted. With shear dimples, identification of the site of initiation can be difficult because the particle may be hidden below the surface, rubbed or flattened out by the shear displacement during fracture. Elongated microvoids that become tear dimples usually form in a narrow band just ahead of a well developed crack front. Tear dimples are fairly rare since tensile tearing is not a predominant mechanism of fracture.

Tearing is a characteristic of both cleavage and ductile fracture, and is often found at a discontinuity in the path of a propagating crack by another fracture mechanism. Tearing occurs when small regions, or ligaments, fracture by plastic flow or necking, and is usually accompanied by the formation of tear ridges which are typically sharp and produce bright contrast when viewed with a scanning electron microscope.

1.2 Mixed Mode Elastic and Elastic-Plastic Fracture Criteria

One of the least understood problems of fracture mechanics has been concerned with the estimation of applied load at crack instability in combined mode loading situations, since a crack can spread in any direction depending on the relative orientation of the applied load and crack position. Accomplished fracture theories can be roughly classified into three main groups. The first group attempt to extend the classical theory of Griffith (1920) to mixed mode loading. The second group assumes that fracture is controlled by some component of the crack tip stress / strain field, and the third group assumes the strain energy density in the vicinity of the crack tip controls cracking behaviour. The applicability of these three groups to predict

both the direction for fracture and fracture toughness for combined mode I/II loading, and their subsequent modifications to extend the theories from elastic to elastic-plastic material behaviour are discussed below.

1.2.1 Maximum Energy Release Rate Criterion, G

Griffith (1920) stated that for a central crack in a large elastic plate, a crack extension of Δa corresponds to a decrease in stored elastic energy. He proposed a solution for the energy release rate, G as a function of applied stress. For pure Mode I and II loading Irwin (1958) demonstrated a relationship between G and Stress Intensity, K, and suggested that for combined mode loading

$$G = \frac{1}{E'}\left(K_I^2 + K_{II}^2\right) \tag{1.7}$$

where E′ is the modulus of elasticity corresponding to E for plane stress and $E/(1-\nu^2)$ for plane strain, where ν is Poisson's ratio, and K_I and K_{II} are stress intensity factors for Mode I and II, respectively.

In contrast to either Mode I or Mode II loading, the direction of crack propagation is not co-planar, that is, the crack grows at some angle θ from the plane of the original crack. For combined Mode I and II loading, Erdogan and Sih (1963) suggested that in order to apply the Griffith energy criterion correctly, G must be a function of θ, and crack propagation would be in the direction of maximum energy release rate, G_{max}, when G_{max} exceeded a critical value, G_{cr}.

Hussain et al. (1974) presented a numerical method to calculate G for a growing crack subject to combined tensile and shear loading. They proposed that if the Griffith - Irwin criterion is valid, then the crack would grow in a direction along which the elastic energy released per unit crack extension would be a maximum and the crack would start to grow when this energy achieved a critical value. The energy was calculated by path-independent integrals, using an elastic solution of a deflected

crack, having a main branch and a propagating branch. They proposed that the direction, as well as the energy release rate could be calculated from

$$G(\theta)=\frac{4}{E'}\left(\frac{1}{3+\cos^2\theta}\right)^2\left(\frac{1-\theta/\pi}{1+\theta/\pi}\right)^{\frac{\theta}{\pi}}\left[(1+3\cos^2\theta)K_I^2+4\sin 2\theta K_I K_{II}+(9-5\cos^2\theta)K_{II}^2\right] \quad (1.8)$$

Provided solutions for K_I and K_{II} are known for the cracked geometry of interest, the critical direction for fracture, θ_o corresponding to $G(\theta)$ achieving a maximum value, G_{max} can be found. Hussain et al. (1974) also present failure loci predicted by G_{max} in K_I, K_{II} space normalised with respect to the plane strain Mode I failure stress intensity factor, K_{Ic} which is a material property. The criterion predicts that K_{IIc}=0.63 K_{Ic}.

1.2.2 Maximum Tangential Stress Criterion, MTS

Using the singular term of the Williams (1957) series expansion, which defines the two-dimensional stress distribution in the vicinity of the crack tip, Erdogan and Sih (1963) proposed a criterion for fracture of a brittle solid in the presence of combined tensile (Mode I) and transverse shear (Mode II) loading. They called it the Maximum Tangential Stress (MTS) criterion. For fracture to occur, they proposed that a crack would extend in the direction along which the tangential stress ($\sigma_{\theta\theta}$) achieved a maximum and the shear stress a minimum. They based their theory on three main assumptions;

1. crack extension starts at its tip and propagates in a radial direction,
2. crack extension starts in the plane perpendicular to the direction of greatest tension, and
3. only the tangential components of the stresses can initiate crack growth.

In their analysis, Erdogan and Sih (1963) considered the problem of a central crack in a wide plate, loaded by a remote uniaxial tensile stress (see figure 1.6). The crack was orientated at an angle β with respect to the loading axis. For this situation the stress system can be related to the individual components of stress intensity for combined mode loading.

Erdogan and Sih (1963) proposed that the critical angle for fracture (θ_o) can be determined for any value of applied stress intensity, K_I and K_{II} by differentiating $\sigma_{\theta\theta}$ with respect to θ (polar angle about the crack tip), setting the derivative equal to zero, and setting $\theta=\theta_o$.

$$\frac{d\sigma_{\theta\theta}}{d\theta} = K_I(\sin\theta_o) + K_{II}(3\cos\theta_o - 1) = 0 \qquad (1.9)$$

For any combination of mixed mode I/II loading, θ_o can be shown to be a function of the equivalent crack angle, β given by equation (1.10), which varies from 90° for Mode I to 0° for Mode II. The locus of θ_o as a function of β is shown in figure (1.7). K_I and K_{II} can be eliminated by substituting into equation (1.9) their respective solutions. This result implies that the initial angle of crack growth is independent of the material properties, but dependent on θ and β.

$$\beta = \tan^{-1}\left(\frac{K_I}{K_{II}}\right) \qquad (1.10)$$

Having satisfied equation (1.9), θ_o can be used to predict the failure loci in K_I, K_{II} space from equation (1.11), which is non-dimensionalised with respect to the stress intensity factor, K_{Ic}. The resultant failure locus for mixed mode I/II loading is shown in figure (1.8).

$$\frac{K_I}{K_{Ic}}\cos^3\left(\frac{\theta_o}{2}\right) - \frac{3}{2}\frac{K_{II}}{K_{Ic}}\cos\left(\frac{\theta_o}{2}\right)\sin\theta_o = 1 \qquad (1.11)$$

Based on laboratory experiments using centre cracked panels manufactured from PMMA, Erdogan and Sih (1963) proposed that the MTS criterion gives a lower bound prediction of fracture toughness of a brittle solid subject to combined tensile and shear loading. The fracture angles predicted by equation (1.9), compared with the fracture angles for PMMA obtained from laboratory experiments (Erdogan and Sih, 1963), are conservative in the presence of significant shear loading ($\beta<40°$) and non-conservative in the presence of significant tensile loading ($\beta>40°$).

Cotterell (1966) discussed the inclusion of other terms from the Williams (1957) series expansion with reference to crack direction under tensile loading. In particular he found that the second, non-singular term (representative of a direct stress in the local direction of the crack) significantly improved the prediction of θ_o.

Williams and Ewing (1972) demonstrated that the inclusion of the second, non-singular term in the MTS criterion could also provide an improved correlation with fracture predictions for the angle of fracture and the critical stress intensity factor, for combined tensile and shear loading. They proposed that θ_o can be determined by differentiating $\sigma_{\theta\theta}$ with respect to θ. However, the singular term is dictated by a radial distance from the crack tip, r which does not appear in the second term. Therefore, the differential has to be solved for a given value of r. Williams and Ewing (1972) proposed a parameter α which is dependent on a relationship between the critical distance, r_{cr} (which they determined from experiments to be a constant and have a value of approximately 50μm), and crack length, a_o, and proposed an expression giving θ_o for any value of β. They reported significantly improved predictions of fracture toughness, especially for low values of β ($\beta<40°$) where the original MTS criterion (Erdogan and Sih, 1963) gave non-conservative predictions.

Unfortunately the solution presented by Williams and Ewing (1972) was incorrect since they neglected to include the effect of normal stress on the second term. Finnie and Saith (1973) corrected the mistake and proposed that θ_o for any given value of β can be predicted by solving

$$\tan^2\beta-\left[\frac{(1-3\cos\theta_o)}{\sin\theta_o}\right]\tan\beta-\left[\frac{16\alpha\sin\left(\frac{\theta_o}{2}\right)}{3\tan\theta_o}\right]\left(1-\tan^2\beta\right)=0 \qquad (1.12)$$

Based on equation (1.12), Williams and Ewing (1974) further proposed that the conditions for fracture can be given by substituting α (for $r=r_{cr}$) and θ_o into equation (1.13).

$$\frac{K_{Ic}}{K_{applied}}=\cos\frac{\theta_o}{2}\sin\beta\left(\sin\beta\cos^2\frac{\theta_o}{2}-\frac{3}{2}\cos\beta\sin\theta_o\right)+\alpha\cos^2\beta\sin^2\theta_o \qquad (1.13)$$

Shih (1974) proposed that the MTS criterion can also be used to predict the direction of crack propagation in the presence of small scale yielding. He extended the pure Mode I and II near tip solutions for stress and strain, developed by Hutchinson (1968a) and Rice and Rosengren (1968), to combined Mode I and II loading by defining near and far field mode mixity parameters, M^p and M^e, respectively. He proposed that the near field mode mixity parameter, M^p depends on θ, and that a unique relationship exists between the angular variation of stresses and strains for combined mode loading and a particular value of M^p. The critical angle for fracture, θ_o can be determined from the tangential stress distribution which varies as a function of strain hardening exponent, n. The failure locus for combined tensile and shear loading in small scale yielding is given by

$$\left(\frac{K_I}{K_{Ic}}\right)^2+\left(\frac{K_{II}}{K_{Ic}}\right)^2=\left(\frac{\tilde{\sigma}_{\theta\theta}\{\theta_o,M^p,n\}}{\tilde{\sigma}_{\theta\theta}\{\theta_o,M^p=1,n\}}\right)^{-(n+1)}\left(\frac{I_n\{M^p\}}{I_n\{M^p=1\}}\right) \qquad (1.14)$$

The dimensionless function $\tilde{\sigma}_{\theta\theta}\{\theta_o, M^p, n\}$ depends on its arguments; θ_o, M^p and n. The dimensionless function I_n is a function of M^p and is given by Shih (1974). The functions on the right hand side can be determined from graphs provided by Shih (1974) and Maccagno and Knott (1991). Equation (1.14) is identical to equation (1.11) when n=1.

1.2.3 Strain Energy Density Criterion, S

The strain energy density criterion, S, for mixed mode fracture was proposed by Sih (1973) based on the local density of the energy field in the crack tip region. Unlike conventional fracture theory, S requires no special assumptions regarding the direction in which the energy released by the separating crack faces is determined, but senses the direction of minimum resistance by achieving a stationary (minimum) value with respect to θ. The stationary value, S_{min} can be used as an intrinsic material parameter whose value at the point of crack instability, S_{cr} is independent of crack geometry and loading configuration, whether tensile or compressive. Although the criterion provides both a qualitative and quantitative measure of fracture due to tensile loading conditions, the theory can only indicate the trend of the failure stress variations with crack angle for fracture under compressive loading.

For an elastic material the strain energy (dW) stored in a volume element (dV) at some position near the crack tip, under a general three-dimensional stress system is given by

$$dW = \frac{1}{2E}\left[\left(\sigma_{xx}^2 + \sigma_{yy}^2 + \sigma_{zz}^2\right) - \frac{\nu}{E}\left(\sigma_{xx}\sigma_{yy} + \sigma_{yy}\sigma_{zz} + \sigma_{zz}\sigma_{xx}\right) + \frac{1}{2\mu}\left(\tau_{xy}^2 + \tau_{xz}^2 + \tau_{yz}^2\right)\right]dV \qquad (1.15)$$

where ν and μ are Poisson's ratio and shear modulus, respectively.

By substituting the singular terms of the stress components for combined mode loading, given by Sih and Liebowitz (1968), the amplitude of the strain energy density field (S) can be calculated

$$\frac{dW}{dV} = \frac{1}{r}S + \text{higher order terms} \qquad (1.16)$$

where S and the coefficients, a_{ij} are given by

$$S = \frac{1}{\pi}\left(a_{11}K_I^2 + 2a_{12}K_IK_{II} + a_{22}K_{II}^2\right) \tag{1.17}$$

$$a_{11} = \frac{1}{16\mu}\left[(\kappa - \cos\theta)(1+\cos\theta)\right] \tag{1.18}$$

$$a_{12} = \frac{1}{16\mu}\sin\theta\left[2\cos\theta - (\kappa - 1)\right] \tag{1.19}$$

$$a_{22} = \frac{1}{16\mu}\left[(\kappa+1)(1-\cos\theta) + (1+\cos\theta)(3\cos\theta - 1)\right] \tag{1.20}$$

where $\kappa=(3-4\nu)$ for plane strain, and $\kappa=(3-\nu)/(1+\nu)$ for plane stress.

The strain energy density concept is based on two main assumptions;

1. crack initiation will start in a radial direction along which the strain energy density is a minimum, and
2. the critical intensity, S_{cr} of the energy field governs the onset of crack propagation.

To achieve a stationary value, the derivative of S, from equation (1.17) must be equal to zero, thus satisfying hypothesis (1) and equation (1.21).

$$\frac{dS}{d\theta} = 0, \qquad \text{at } \theta = \theta_o \tag{1.21}$$

The direction of crack propagation, given by S_{min} corresponds to the direction of maximum potential energy, a position of unstable equilibrium (potential energy is equal to the negative of the strain energy). Therefore, S_{min} is a critical value (S_{cr}) at $\theta=\theta_o$ from which a critical value of stress, σ_{crit} can be determined, sufficient to initiate crack growth. However, S ceases to be valid as r becomes indefinitely small, hence Sih (1974) proposed a critical distance, r_{cr}, a core region surrounding the tip of a stress free crack. Sih (1974) proposed that the value of S_{cr} ($\theta=\theta_o$) at $r=r_{cr}$ is a

constant and a material property that varies from material to material, and can be used to determine the conditions for fracture. For cracks propagating in a self similar fashion S_{cr} can be related to K using the Irwin relationship (1960).

For combined tensile and shear loading, Sih (1973) studied the problem of a crack of length $2a_o$ inclined at an angle β with respect to the loading axis (figure 1.6). Sih proposed that θ_o can be found for any value of β by substituting the relevant coefficients, given in equations (1.18) through to (1.20), into equation (1.17), giving equation (1.22). Differentiating equation (1.22) with respect to θ to find the direction that S attains a minimum (corresponding to $\theta=\theta_o$) for a given β is given in equation (1.23). At $\theta=\theta_o$, $S_{min}=S_{cr}$. From S_{cr}, the critical values of K_I and K_{II} can be calculated and plotted in K_I, K_{II} space, similar to the MTS criterion discussed earlier.

$$S = \sigma^2 \pi a_o \left(a_{11} \sin^2\beta + 2a_{12} \sin\beta\cos\beta + a_{22} \cos^2\beta\right) \sin^2\beta \qquad (1.22)$$

$$(\kappa - 1)\sin(\theta_o - 2\beta) - 2\sin\left[2(\theta_o - \beta)\right] - \sin 2\theta_o = 0, \qquad \beta \neq 0 \qquad (1.23)$$

where σ is applied stress and a_o is the half crack length for a centre cracked M(T) specimen of length $2a_o$.

Following the demonstration by Williams and Ewing (1972) concerning the advantages of including higher order terms in the MTS criterion, Sih and Kipp (1974) demonstrated that the S criterion could also be modified to include higher order terms and provide a better correlation with experimental results. However, since S, defined by equation (1.17), is only present in the first term of equation (1.16) the direction of propagation can only be determined when the minimum value of dW/dV attains a critical value at $r=r_{cr}$.

Sih (1974), and Sih and MacDonald (1974) proposed that the S criterion could theoretically be adapted to apply to ductile material behaviour. They decomposed the strain energy density in the crack tip region into two component parts, one associated with a change in volume (dilatational, S_v, applicable mainly to elastic behaviour) and

the other associated with a change in shape (distortional, S_d, corresponding to plastic deformation) of a volume element, such that

$$S = S_v + S_d \tag{1.24}$$

This was done to demonstrate that in the direction of fracture, S_v was greater than S_d, which is consistent with the classical concept that fracture occurs along the plane where $S_v > S_d$ (Nadai, 1950).

Theocaris and Andrianopoulos (1982) proposed that the strain energy density should be evaluated around the elastic-plastic boundary as defined by the Von Mises yield criterion, and crack propagation would occur in the direction corresponding to the maximum dilatational strain energy density. They referred to this as the T criterion and proposed that the maximum value of T_v is a critical value and a material constant. Furthermore, they proposed that the T criterion is also suitable for both elastic and elastic-plastic material behaviour, since it accounts for distortional, as well as dilatational strain energy.

1.2.4 Summary of the Mixed Mode Fracture Criteria

All of the mixed mode I/II fracture criteria (G, MTS and S) described above are capable of predicting both the direction for fracture and the fracture toughness for combined tensile and shear loading. Although G is essentially confined to simple geometries and linear elastic material behaviour, both the MTS and S criteria can be used for more complex geometries, and extended to assess mixed mode I/II fracture behaviour under conditions of small scale yielding.

For linear elastic material behaviour these criteria complement each other for Mode I loading but deviate significantly for Mode II. For Mode II loading, the predicted direction for fracture ranges from -70.5° (MTS criterion) to -82.0° (S criterion for ν=0.3). As the S criterion is material dependent the direction for fracture is governed by ν. As ν increases the predicted direction for fracture also increases. However,

compared with the inevitable experimental scatter of test results there is very little difference between the three criteria.

The variation in fracture toughness predicted by these criteria is rather pronounced, ranging from $K_{IIc}=0.63K_{Ic}$ (G criterion) to $K_{IIc}=K_{Ic}$ (S criterion for $\nu=0.3$). The fracture toughness loci given by S is extremely sensitive to ν since as ν increases slightly, K_{IIc} decreases significantly (for $\nu=0.4$, $K_{IIc}=0.79K_{Ic}$). The most conservative estimate of fracture is given by the G criterion.

The G criterion is best suited to simple geometries where the stress intensity factors are known and the material behaviour is linear elastic. For the more complicated geometries the MTS and S criteria are more appropriate since the tangential stress and strain energy density can readily be obtained from finite element analyses. The MTS criterion has proven to be more popular with researchers and has suffered least from controversy compared with either the G or S criteria. Furthermore, the MTS criterion is not limited to linear elastic material behaviour (unlike the G criterion) and it is material independent (unlike the S criterion).

1.3 Two Parameter Characterisation of Elastic and Elastic-Plastic Fracture Mechanics

1.3.1 The Stress Field at the Tip of a Crack

The Elastic Crack Tip Stress Field

In 1957, Williams demonstrated that the elastic stresses at the tip of a crack, for both symmetric (Mode I) and antisymmetric (Mode II) crack problems can be expressed as an infinite series expansion. Assuming small scale yielding and isotropic linear elastic material behaviour, the stress field in any linear elastic cracked body can be expressed as

$$\sigma_{ij} = A_{ij}(\theta)r^{-1/2} + B_{ij}(\theta)r^{0} + C_{ij}(\theta)r^{1/2} + \ldots\ldots \qquad (1.25)$$

The development of linear elastic fracture mechanics has largely concentrated on the role of the leading term, where the $1/\sqrt{r}$ singularity dominates the stress field close to the crack tip. This has enabled the use of the stress intensity factor, K as a single fracture characterising parameter. Neglecting higher order terms, the singular term in equation (1.25) can be re-written as

$$\sigma_{ij} = \frac{K}{\sqrt{2\pi r}} f_{ij}(\theta) \qquad (1.26)$$

There exists a circular zone ahead of the crack tip, known as the region of K dominance (also referred to as a singularity dominated zone), within which K provides a unique measure of the intensity of the stress. The radius of the annulus where K dominates is determined by the radial distance at which the asymptotic singular solution (equation 1.26) deviates significantly (> 10%) from the full field solution (inclusive of higher order terms). A singularity dominated zone is a pre-requisite for a single parameter description of crack tip conditions.

Although equation (1.26) predicts infinite stress at the crack tip, plasticity causes the stress to redistribute, resulting in a truncated stress distribution in the near tip region. An elastic stress analysis becomes increasingly inaccurate as the size of the crack tip plastic zone increases.

The American Society for Testing and Materials (ASTM) propose strict specimen size requirements to ensure that plane strain conditions (limiting condition for K dominance) are achieved at the crack tip and equation (1.26) remains valid. These were based on experimental observations of the size dependence of K in steels and are represented by

$$a_o, B, (W - a_o) \geq 2.5\left(\frac{K_I}{\sigma_{ys}}\right)^2 \qquad (1.27)$$

where a_o, B and $(W-a_o)$ are crack length, specimen thickness and ligament length, respectively. K_I refers to the Mode I plane strain fracture toughness (a geometry independent material property) and σ_{ys} the yield stress. The thickness and in-plane dimensional requirements ensure that the plastic zone size is small and embedded within the singularity dominated zone. Equation (1.26) is valid as long as the requirements of equation (1.27) are achieved. Irwin (1956) proposed a simple correction for crack tip yielding by defining an effective crack length that is slightly longer than the actual crack size, thus extending the use of elastic analysis to conditions of small scale yielding.

If the plastic zone size becomes too large the singularity dominated zone is destroyed and an alternative description for crack tip stresses would be required to account for the increase in non-linear behaviour.

In a mixed mode problem (tension and in-plane shear, Mode I and II) the individual contributions of different modes of loading are additive, such that equation (1.26) can be re-written as

$$\sigma_{ij} = \frac{K_I}{\sqrt{2\pi r}} f_{ij}(\theta) + \frac{K_{II}}{\sqrt{2\pi r}} g_{ij}(\theta) \qquad (1.28)$$

where $f_{ij}(\theta)$ and $g_{ij}(\theta)$ are geometry functions that are dependent on mode of loading and polar angle θ.

The Elastic-Plastic Crack Tip Stress Field

For conditions of small scale yielding, Hutchinson (1968a, 1968b) and Rice and Rosengren (1968) independently studied the plane strain and plane stress asymptotic crack tip fields in strain hardening materials for symmetric (Mode I) and antisymmetric (Mode II) crack problems. They each assumed uniaxial stress-strain behaviour, characterised by the Ramberg-Osgood power law relationship and used J_2 deformation theory of plasticity to generalise the uniaxial relation to include multi-axial stress states.

Both Hutchinson, and Rice and Rosengren expressed the elastic-plastic stress field as a series expansion with a power law dependence on distance from the crack tip, r and an angular variation that is independent of r. The leading term of the expansion (known as the HRR field) has been widely used to characterise the distribution of stress in the near tip region. Similar to equation (1.25), the leading term is singular, where the stress is asymptotic to the crack tip and varies with $r^{-1/(n+1)}$. The HRR field is given below where the J-Integral (Rice, 1968) is used to define the amplitude of the singularity.

$$\sigma_{ij} = \sigma_{ys}\left(\frac{EJ}{\alpha\sigma_{ys}^2 I_n r}\right)^{\frac{1}{n+1}} \tilde{\sigma}_{ij}(n,\theta) \qquad (1.29)$$

where I_n is an integration constant that depends mildly on the strain hardening exponent, n and stress state (plane stress or plane strain), α is derived from the Ramberg-Osgood power law equation and $\tilde{\sigma}_{ij}$ is a universal function that varies with polar angle θ, n and stress state.

In a manner similar to the relationship between K and the elastic singularity, the J-Integral, defined by Rice (1968) is a measure of the amplitude of the crack tip fields. A unique relationship exists between the elastic (equation 1.26) and elastic-plastic (equation 1.29) near tip field equations. For the case of n=1, corresponding to linear elastic material behaviour, equation (1.29) is identical to equation (1.26).

The conditions where the elastic-plastic stress field in a cracked body corresponds to the HRR solution, as characterised by J (given in equation 1.29) is referred to as the J dominated region. Similar to the elastic singularity solution, as long as there exists a region of J dominance around the crack tip, the stresses can be characterised by the HRR singular solution. The noticeable difference between the elastic singularity, $1/\sqrt{r}$ and the HRR singularity, $r^{-1/(n+1)}$ is that the latter often persists long after the K dominated region has been destroyed by crack tip plasticity. Figure (1.9) illustrates

the effect of plasticity on the crack tip stress fields, identifying the regions of K and J dominance.

In order to maintain J dominance, similar size requirements as those proposed by ASTM for an elastic analysis, have been proposed by McMeeking and Parks (1979), Shih and German (1981), Shih (1985), Al-Ani and Hancock (1991) and Betegón and Hancock (1991). They demonstrated that in bending, J dominance is maintained as long as the ligament length ($W-a_o$) is greater than $25(J/\sigma_{ys})$, while in tension, the ligament length has to be greater than $200(J/\sigma_{ys})$. Similar size requirements have been proposed for shallow and deep crack specimen geometries, since shallow cracks exhibit a higher resistance to crack growth.

The basic assumption of the HRR field is that the crack tip remains sharp, however crack tip blunting is inevitable when the applied load is increased. McMeeking and Parks (1979) demonstrated that the HRR solution is still appropriate at distances from the crack tip where the effects of blunting can be neglected. They proposed a distance of approximately two or three crack opening displacements, or equivalently, distances of the order $2(J/\sigma_{ys})$. Within this distance it is necessary to adopt a large strain formulation to investigate the near tip blunting region (McMeeking, 1977).

Shih (1974) studied the plane strain plastic fields in hardening and non-hardening materials subject to combined tensile and shear loading. He demonstrated that the solutions had the same form as the pure mode solutions originally proposed by Hutchinson (1968a, 1968b), and Rice and Rosengren (1968). Shih (1974) proposed that the J-Integral could be extended to define the amplitude of the stresses in the near tip field for combined mode loading situations since the path independent qualities of J allows the near tip solution to be matched to any known remote field. Taking J as a measure of the intensity of the mixed mode field, Shih (1974) proposed the following relationship for stress

$$\sigma_{ij} = \sigma_{ys}\left(\frac{EJ}{\alpha\sigma_{ys}^2 I_n(M^p) r}\right)^{\frac{1}{n+1}} \tilde{\sigma}_{ij}(\theta, n, M^p) \qquad (1.30)$$

which is very similar to equation (1.29) except that $I_n(M^p)$ and $\tilde{\sigma}_{ij}(\theta, n, M^p)$ are also functions of M^p, a near field mixity parameter, defined by Shih (1974) as

$$M^p = \frac{2}{\pi}\tan^{-1}\left|\lim_{r\to 0}\frac{\sigma_{\theta\theta}(r,\theta=0)}{\sigma_{r\theta}(r,\theta=0)}\right| = \frac{2}{\pi}\tan^{-1}\left|\frac{\sigma_{\theta\theta}(\theta=0)}{\sigma_{r\theta}(\theta=0)}\right| \qquad (1.31)$$

For Mode I and Mode II loading, M^p=1.0 and 0.0, respectively. The functions on the right hand side of equation (1.30) can be determined from the tables provided by Shih (1983) and Symington et al. (1988) for seven mode mixities ranging from Mode I to Mode II. For each mode mixity the data is given for a range of hardening exponents from n=1 to 20, and angular intervals, $\Delta\theta$=5°.

1.3.2 J-T Characterisation

Based on the research of Larsson and Carlsson (1975), Betegón and Hancock (1991) demonstrated that a loss of J dominance can be quantified by considering the second term in the Williams (1957) asymptotic series expansion of the elastic field (equation 1.25).

The first term in equation (1.25) is dominated by K (see equation 1.26) which defines the amplitude of the elastic singularity. The second term is denoted T (Rice, 1974) and can be regarded as a uniform uni-axial stress, parallel to the crack flanks which is independent of radial distance ahead of the crack tip, r. For a crack in an isotropic elastic material subject to plane strain loading, the first two terms of the Williams solution (equation 1.25) can be re-written as

$$\begin{bmatrix}\sigma_{11} & \sigma_{12}\\ \sigma_{21} & \sigma_{22}\end{bmatrix} = \frac{K}{\sqrt{2\pi r}}\begin{bmatrix}f_{11}(\theta) & f_{12}(\theta)\\ f_{21}(\theta) & f_{22}(\theta)\end{bmatrix} + \begin{bmatrix}T & 0\\ 0 & 0\end{bmatrix} \qquad (1.32)$$

Leevers and Radon (1983) proposed that the magnitude of T can be defined through a biaxiality parameter, B, which is dependent on geometry and loading. Du et al. (1991) extended the use of the biaxiality parameter to combined mode loading by considering the relative contributions of the individual Mode I and Mode II components, K_I and K_{II}.

$$B = \frac{T\sqrt{\pi a}}{\sqrt{K_I^2 + K_{II}^2}} \tag{1.33}$$

They also inferred that since B is dependent on geometry and loading it can be used as a qualitative index of the relative crack tip constraint of any structural component. For Mode I loading Bilby et al. (1986), Betegón and Hancock (1991), Du and Hancock (1991) and O'Dowd and Shih (1991a; 1991b) used modified boundary layer (MBL) formulations, as shown in figure (1.10), to examine the effect of T. They imposed displacements corresponding to both K and T of the elastic field on a remote elastic boundary, with a radius sufficient to ensure that the size of the plastic zone was small compared to the crack length (in accord with procedures developed by Tracey, 1976 and Parks and Wang, 1988). The T term was calculated from equation (1.33) for a variety of B values.

MBL formulations conducted by Bilby et al. (1986) demonstrated the sensitivity of the plastic zone shape and the stresses deep inside the plastic zone to tensile (positive, +ve) and compressive (negative, -ve) T stress. They compared MBL formulations with the singular, self similar solution ($K_{T=0}$) and found that tensile T stress caused the maximum stress (σ_{max}) ahead of a blunting crack tip to increase slightly. With increasing deformation the stress eventually maintained a constant level corresponding to full plasticity, although below the HRR reference field. Moreover, they observed that compressive T stress caused σ_{max} to decrease significantly (proportional to an increase in deformation level) from both $K_{T=0}$ and HRR. Figure (1.11) illustrates the variation of tangential stress ($\sigma_{\theta\theta}$) obtained from an MBL formulation with distance ahead of the crack tip for different levels of T

stress (Betegón and Hancock, 1991) compared with the elastic ($K_{T=0}$) and elastic-plastic (HRR) small scale yielding solutions.

Betegón and Hancock (1991) proposed that geometries which lose J-dominance of the flow field feature compressive T stress, while those which maintain J-dominance feature tensile T stress. Furthermore, while a single parameter description can be used to characterise crack tip conditions for geometries exhibiting tensile T, those featuring compressive T can be adequately described by J combined with T (J-T).

Betegón and Hancock (1991) proposed that J-T characterisation can extend the formal limits of contained yielding into large scale yielding behaviour. They compared MBL formulations with a full field solution of a centre-cracked panel ($a_o/W=0.5$, compressive T, B=-1.06), which features a loss of J-dominance regardless of crack length, and examined the stresses at distances $2(J/\sigma_{ys})$ (McMeeking and Parks, 1979) and $5(J/\sigma_{ys})$ from the crack tip. Even at a significant deformation level, corresponding to full plasticity, the MBL formulation matched the full field solution. They observed similar results for shallow ($a_o/W=0.3$) and deeply ($a_o/W=0.9$) cracked single-edge bend bars, SE(B) corresponding to (T=0, B=0) and (tensile T, B=+1.1), respectively. Karstensen et al. (1997) proposed that J-T can be extended further if the T stress is calculated from the elastic component of the J-Integral.

Du and Hancock (1991) and Al-Ani and Hancock (1991) compared the effect of T stress on the size and shape of the plastic zone at the crack tip. They found that compressive T stress caused the plastic zone size to increase and the plastic lobes to rotate forwards (ahead of the crack tip). In contrast, tensile T stress caused a reduction of the plastic zone size and the plastic lobes to rotate backwards. In agreement with the discussions presented by Hancock and Cowling (1980) and Bilby et al. (1988), Al-Ani and Hancock (1991) also found that compressive T stress had a significant effect on the mechanism of void growth. They found that geometries that feature compressive T stress exhibit a lower level of triaxial stress within the plastic zone, resulting in lower void growth rates and enhanced ductilities.

Sumpter (1993) sought to characterise the effect of T experimentally. Using the applied stress from each experiment he was able to provide encouraging evidence demonstrating that different geometries, with the same T stress will have the same value of toughness at initiation (J_c).

Du et al. (1991) addressed the issue of J-dominance in mixed mode loading. They comparing MBL formulations with mixed mode, HRR singularity solutions given by Shih (1974). They observed that mode mixity caused asymmetry of the plastic zone distribution ahead of the crack tip. As they increased the Mode II component they observed the relative and absolute size of the plastic zone to increase. This also resulted in a rotation about the crack tip. However, although the plastic zone was distorted by T, the orientation of the minimum radial distance to the elastic-plastic boundary was unaffected.

Similar to the effects of T stress on Mode I loading, Du et al. (1991) observed that in mixed mode loading, compressive T stress decreased the tangential stress distribution and tensile T stress maintained stress levels close to the HRR field. In pure Mode II loading, zero T stress corresponded to a symmetric plastic zone about the crack plane. However, compressive T stress introduced asymmetry where plastic flow developed on one crack flank only. In contrast, tensile T stress caused the asymmetry to develop on the other crack flank, although the absolute size of the plastic zone was unaffected.

Hancock et al. (1997) compared the effect of constraint due to mixed mode loading with slip line fields (Prandtl, 1920 and Shih, 1974). Their initial studies demonstrated that for Mode I loading, tensile T stress enabled the development of a fully plastic slip line field. As they reduced the level of T stress a loss of J-dominance was observed with the development of elastic regions, symmetric about the crack flanks. An increase in the size of the elastic sectors was observed with a proportional decrease in T stress. In contrast, for the case of zero T stress, they found that the appearance of a Mode II component caused the elastic sector to appear on one crack flank only (contrasting observations were made by Shih, 1974). An increase in Mode II caused a proportional shift of the slip field. Hancock et al.

(1997) further proposed that for weak and moderately hardened materials, the stress profiles for all mode mixities can be described by a family of fields (parallel stress distributions and independent of distance ahead of the crack tip) and can further be correlated with the constraint of an unconstrained Mode I field.

A number of methods have been presented in the literature for calculating T and have been briefly reviewed above. Perhaps the most simplistic approach is that developed by Ayatollahi et al. (1998), who use crack flank nodal displacements obtained from an elastic finite element analysis to determine a value of T stress for any combination of mixed mode I/II loading. Their methods negate the need for additional calculations to determine values of stress intensity factor for a specific specimen geometry, or loading configuration and have been proven to give realistic values of T stress compared to those reported throughout the literature.

Moreover, Ayatollahi et al. (1998) applied their method to predict the values of T stress for a test specimen located within a loading fixture (Davenport and Smith, 1993) which is capable of imposing different combinations of Mode I and Mode II from pure tension to pure shear. Three models were analysed, a rigid connection between the specimen and loading fixture, contact elements between the specimen and loading fixture, and the specimen located within the loading fixture through four location pins. Although the actual transmission of load between the specimen and loading fixture in the experimental studies is best simulated by the contact element model, only the pin loaded model provided an antisymmetric stress field in Mode II loading. The effect of loading in Mode I was negligible between the three models.

1.3.3 J-Q Characterisation

Section 1.3.1 demonstrated that the stress distribution deep inside the plastic zone can be expressed by a series expansion. Conventional fracture mechanics methodology has concentrated on the use of the HRR term to describe the elastic-plastic near tip behaviour. However, as mentioned above, the HRR solution is restricted to high constraint geometries and can be over conservative, especially for

low constraint geometries such as centre cracked tensile specimens, M(T). To remove some of the conservatism inherent in the single-parameter approach and to account for the observed size effects in fracture, O'Dowd and Shih (1991) presented a two-parameter approach based on the J-Integral (Rice, 1968) and a dimensionless factor Q.

O'Dowd and Shih (1991) proposed that the higher order terms of the series expansion can be grouped together into a difference field and used to provide a quantitative measure of crack tip constraint, such that the stresses can be described by

$$\sigma_{ij} = \left(\sigma_{ij}\right)_A + \left(\sigma_{ij}\right)_{Diff} \tag{1.34}$$

where the subscript A corresponds to a reference stress field described by either the elastic-plastic HRR singular field, $(\sigma_{ij})_{HRR}$, given in equation (1.29), or the small scale yielding solution driven by K alone, $(\sigma_{ij})_{SSY}$, given in equation (1.26), where T=0. The use of the difference field as an appropriate measure of crack tip constraint has also been demonstrated by Faleskog and Nordland (1994).

For a non zero difference field the stress distribution shifts either up or down and the magnitude of the shift remains constant with increasing distance from the crack tip. Moreover, O'Dowd and Shih (1991) observed that the difference fields corresponding to σ_{yy} and σ_{xx} were approximately the same, but much larger than σ_{xy} over an angular region of $|\theta| \leq \pi/2$ ahead of the crack tip. Based on these results they proposed that the difference field corresponds approximately to a uniform hydrostatic shift of the stress field ahead of the crack tip. O'Dowd and Shih (1991) chose to express the amplitude of the second order field by a dimensionless factor, Q such that equation (1.34) can be re-written as

$$\sigma_{ij} = \left(\sigma_{ij}\right)_A + Q\sigma_{ys}\delta_{ij} \qquad \text{for } |\theta| \leq \pi/2 \tag{1.35}$$

where σ_{ys} is the yield stress and δ_{ij} the Kronecker delta.

O'Dowd and Shih (1991) defined Q as the difference between the full field and reference stress field, such that

$$Q = \frac{\sigma_{\theta\theta} - (\sigma_{\theta\theta})_{REF}}{\sigma_{ys}} \qquad \text{for } \theta = 0^{\circ},\ r = 2(J/\sigma_{ys}) \qquad (1.36)$$

Although either reference field, $(\sigma_{ij})_{SSY}$ or $(\sigma_{ij})_{HRR}$, can be used, O'Dowd and Shih (1994) recommend the use of the small scale yielding solution given by equation (1.26). The singular solution given by the HRR field is based on the J-Integral which assumes Ramberg-Osgood material behaviour. In general, not all materials display power law hardening, but the $(\sigma_{ij})_{SSY}$ solution does have the capability of characterising either state (O'Dowd, 1995).

O'Dowd and Shih (1991, 1994) recommend that the value of Q should be determined within a region directly ahead of the crack tip, $|\theta| \leq \pi/2$ at a normalised distance corresponding to $r=2(J/\sigma_{ys})$. They based this recommendation on small and finite strain analyses from which limiting normalised distances of $J/\sigma_{ys}<r<5(J/\sigma_{ys})$ were observed. Finite strains caused by crack tip blunting (McMeeking and Parks, 1979) are dominant up to J/σ_{ys} and higher order terms, other than Q can be significant at distances greater than $5(J/\sigma_{ys})$. Within these proposed limits the stress distributions for different Q are parallel and independent of r and polar angle, θ. The use of $r=2(J/\sigma_{ys})$ has generally been accepted throughout the literature as the corresponding normalised distance from which Q should be determined (O'Dowd and Shih, 1991; 1994, Wu and Mai, 1995, and Joyce and Link, 1997).

The lower limiting distance given above describes the inner boundary of a zone around the crack tip, referred to by O'Dowd and Shih (1994) as the J-Q annulus, that encompasses the microstructurally significant length scales for both brittle and ductile fracture.

To demonstrate the interpretation of Q as a triaxiality parameter, O'Dowd and Shih (1994) compared values of Q calculated from both the hoop and hydrostatic (mean) stress fields at $r=2(J/\sigma_{ys})$ and observed negligible differences.

Moreover, for Mode I loading, O'Dowd and Shih (1994) demonstrated that for different values of hardening coefficient, a unique relationship exists between T stress and Q for small and moderate scale yielding behaviour, given by

$$Q = a_1(n)\left(\frac{T}{\sigma_{ys}}\right) + a_2(n)\left(\frac{T}{\sigma_{ys}}\right)^2 + a_3(n)\left(\frac{T}{\sigma_{ys}}\right)^3 \qquad (1.37)$$

Tabulated values for the constants a_1, a_2 and a_3 for several values of n are given by O'Dowd and Shih (1994). However, in contrast to recommendations by Betegón and Hancock (1991), T stress can not have general applicability under conditions of large scale yielding since the elastic solution from which T stress is obtained is increasingly violated as plastic flow progresses beyond well contained yielding.

Ainsworth and O'Dowd (1995) proposed a simple, approximate relationship between T stress and Q independent of n, given by

$$Q = \frac{T}{\sigma_{ys}} \qquad \text{for } \frac{T}{\sigma_{ys}} < 0 \qquad (1.38)$$

$$Q = \frac{T}{2\sigma_{ys}} \qquad \text{for } \frac{T}{\sigma_{ys}} > 0 \qquad (1.39)$$

The curves corresponding to equation (1.37) for different n and equations (1.38) and (1.39) are shown in figure (1.12).

O'Dowd and Shih (1994) proposed that all near tip stress fields are members of a single family of crack tip fields. Moreover, each member field can be characterised by the degree of deformation and the corresponding level of crack tip stress triaxiality. They proposed that the amplitude of the stress field can be measured by

the J-Integral while Q scales the near tip stress distribution relative to a high triaxiality reference stress state (either $\sigma_{ij,HRR}$ or $\sigma_{ij,SSY}$).

Since Q quantifies both the hoop, $\sigma_{\theta\theta}$ and hydrostatic stress, σ_{hyd} components it can be used to interpret both brittle and ductile behaviour. Cleavage fracture is controlled by the attainment of a critical $\sigma_{\theta\theta}$ over a critical distance, X_o (Ritchie et al., 1973 and Dodds et al., 1991; 1993) and void growth, which is associated with ductile tearing, is controlled by σ_{hyd} (Needleman et al., 1992).

O'Dowd and Shih (1994) investigated the critical toughness associated with initiation for different geometries of different constraint. They investigated shallow and deeply cracked three-point single edge bend, 3P SE(B), single edge tension, SE(T) and centre crack tension, M(T) specimens and constructed a J-Q failure locus (shown in figure 1.13). They proposed that the J-Q locus provides a qualitative assessment of a structural component in service. By imposing the driving force curve for the structural component onto figure (1.13), both the failure mechanism and the critical initiation toughness can be predicted. The use of a J-Q failure locus is illustrated in figure (1.14).

Wu and Mai (1995) introduced a theoretical model for ductile fracture based on void nucleation and growth in the J-Q fields ahead of the crack tip and found good agreement with experimental studies. O'Dowd et al. (1995) introduced a theoretical model of cleavage fracture based on the RKR criterion (Ritchie et al., 1973). Using $(\sigma_{ij})_{HRR}$ as the reference stress and assuming that X_o was within the J-Q annulus they also found good agreement with experimental studies.

A number of investigators have used experiments to verify the use of the J-Q failure locus to quantify cleavage failure. Sumpter and Forbes (1992) investigated shallow and deep cracked SE(B) and moderately deep M(T) mild steel specimens. Kirk et al. (1993) investigated SE(B) specimens of varying thickness and crack depth, manufactured from A515 steel. All data was within the upper and lower limits of the J-Q failure locus shown in figure (1.13).

O'Dowd et al. (1995) investigated the effects of crack growth using MBL formulations governed by a K_c resistance curve. They observed that under tensile T stresses the crack grew under high stress triaxiality which remained high throughout continued growth. Under compressive T stresses, crack growth initiated under low stress triaxiality. However, as crack growth continued the level of stress triaxiality increased, approaching levels similar to those under positive T stress. The results of these studies indicated that a high triaxiality stress field, described by the HRR solution dominates the near tip field for a steadily growing crack. They also observed an increase in the magnitude of the near tip stress field relative to those for a stationary crack, as well as a reduction in the size of the J-Q annulus. Such an increase in the near tip stresses can cause premature cleavage failure following some stable crack growth by tearing (Wallin, 1991). Therefore, it is not desirable to use current two-parameter methodologies for a propagating crack.

Although the J-Q theory is completely general, the approach can apply to both plane stress and plane strain conditions. O'Dowd and Shih (1991) have also proposed that the theory could also be used to quantify mixed mode fields, however the theory has yet to be proven for such conditions.

1.3.4 Summary of the Two Parameter Methods for Characterising Crack Tip Constraint

In general, the most convenient method of quantifying the crack tip constraint in the presence of mixed mode I/II loading is via J-T characterisation. However, the underlying problem with this approach is that it is confined to small-to-moderate scale yielding although limit studies by Betegón and Hancock (1991) suggest that this approach can be extended further. Essentially, T is an elastic term which is known for most standard specimen types. For the more complicated types, T can be readily determined from a simple elastic finite element analysis (Ayatollahi, Pavier and Smith, 1998).

The J-Q approach is more complex and values of Q are not as openly available as for T. Nevertheless, the J-Q approach can be used to quantify the crack tip constraint under both contained yielding and fully plastic conditions although in the presence of mixed mode I/II loading this has to be investigated further. Q is dependent on both specimen geometry and type of loading and can only be determined from an elastic plastic analysis.

O'Dowd and Shih (1994) have shown that a relationship exists between T and Q but only for contained yielding and at present, to Mode I loading since the elastic solution from which T is obtained is increasingly violated as plastic flow progresses beyond well contained yielding.

1.4 Experimental Investigations of Constraint Effects

The best method of assessing the integrity of a cracked structural component is to test the component itself. However, the inherent costs associated with testing a full size component often precludes such an approach. As a consequence it is often more convenient to perform experiments in the laboratory on smaller, less expensive specimens and then to translate the laboratory results to the performance of the real component.

The majority of models and analytical techniques are for Mode I loading situations. However, structural components are usually subject to complex loading situations, resulting in combinations of Mode I, Mode II and Mode III loading. At present the methods of inferring the integrity of the real component from mixed mode loading laboratory tests is uncertain. There are additional problems associated with the behaviour of laboratory test specimens. For example, when the specimen dimensions or geometry are varied, but the length of crack remains the same, the value of fracture toughness is known to vary considerably, particularly for Mode I (Garwood, 1982, Gibson et al., 1987 and Joyce and Link, 1995).

The general approach to considering the influence of specimen dimensions and geometry is to attribute the effects to varying levels of constraint. There has been considerable effort in addressing such problems of constraint, although principally for Mode I loading conditions only. A single parameter characterisation of fracture, using parameters such as, Stress Intensity (Irwin, 1957), J-Integral (Rice, 1968) or Crack Opening Displacement (Wells, 1961), has limited success when there are different levels of constraint. Instead two parameter methodologies such as J-T (Betegón and Hancock, 1991) and J-Q (O'Dowd and Shih, 1991; 1992) have been developed and have been thoroughly reviewed in section 1.3.

Although a number of approaches to the problems of constraint have been proposed, no one approach has been shown to be universally applicable and therefore theoretical and experimental work in this area is continuing.

1.4.1 The Effects of Specimen Orientation

Orientation is an important variable in fracture toughness measurements, since materials are seldom homogenous and isotropic in nature. The sensitivity to orientation can be particularly pronounced since a microstructure with a preferred orientation may contain planes of weakness, where crack propagation is relatively easy.

For fracture toughness specimens extracted from a rolled plate or forging, ASTM (E616-89) assign the letters L, T and S to denote the longitudinal, transverse and short transverse rolling directions, relative to the rolling direction or forging axis, respectively. Two letters are used to specify the orientation of a fracture toughness specimen. The first indicates the principal straining axis and the second denotes the crack propagation direction, thus there are six possible orientations. Figure (1.15) demonstrates the convention globally used to represent the six orientations for specimens extracted from rolled plates and forgings.

Willoughby et al. (1978) investigated the effect of specimen orientation on initiation toughness, J_{Ic} and the slope of the tearing resistance curve, dJ/da for mild steel, side grooved (SG) single edge bend, SE(B) specimens loaded in three point bend (3PB). They developed crack growth resistance curves for all six possible orientations of the test specimen. However, they presented their results in terms of the principal straining directions only and provided no indication of crack propagation direction. Their illustrations demonstrate that J_{Ic} is similar in the L and T orientations but significantly lower in S. For crack growth, $\Delta a<1.5$mm, dJ/da is similar in the T and S orientations but significantly higher in L. However, for $\Delta a>1.5$mm, dJ/da appears to be orientation independent.

Lautridou and Pineau (1981) tested A508 C-Mn steel using full thickness, plain sided (PS) compact tension, C(T) specimens in Mode I loading. They investigated two orientations, L-T and T-L, and observed that J_{Ic} for the L-T direction was greater than for the T-L direction. During the initial stages of crack growth, $\Delta a<0.8$mm, dJ/da for the L-T direction was significantly greater than for the T-L direction, however for $\Delta a>0.8$mm, the L-T direction was equivalent to the T-L direction. They also investigated an alternative heat of A508, where the heat treatment resulted in a significant reduction of the void volume fraction of Mn-S inclusions present and furthermore, reduced their overall size. For comparison, PS C(T) specimens were used, extracted from the L-T orientation. Although J_{Ic} was similar for both steels the heat treated specimens exhibited a reduction in dJ/da, albeit slight.

Also in Mode I loading, Garwood (1982) investigated orientation effects using PS, L-T and T-L 3PB SE(B) and cracked middle tension, M(T) specimens extracted from API 5LX65 C-Mn pipe steel. Independent of geometry, he observed that J_{Ic} for the L-T direction was greater than for the T-L direction and for $\Delta a<5$mm, dJ/da for the L-T direction was greater than for the T-L direction. However, similar to observations made by Lautridou and Pineau (1981), for further crack growth the M(T) L-T specimen demonstrated a significant reduction in dJ/da, resulting in dJ/da for the T-L direction being greater than for the L-T direction. Garwood (1982) correlated these effects with the formation of shear lips. He observed that shear lip formation was suppressed in SE(B) specimens for the T-L direction and, although

present in both M(T) in the L-T and T-L directions, the shear lips observed in M(T) L-T direction were significantly greater than for the M(T) T-L direction.

Shi and Zhou (1995) investigated the effects of orientation in Mode II using two steels, HT80 and HT100. They used SE(B) specimens in the T-L and L-T directions with a crack depth corresponding to an a_o/W ratio of 0.5, where W=2B=24mm. The SE(B) specimens were tested in four point bend (4PB). They determined a value of J_{IIc} from the intersection of the resistance curve with the Mode II blunting line. They proposed that although the onset of crack growth may occur in Mode II, once the crack started to grow it rapidly transformed into a mixed mode crack. Furthermore, since σ_{ys} is approximately equal to $2\tau_{ys}$, where σ_{ys} and τ_{ys} are tensile and shear yield stress, respectively, a Mode II blunting line can be estimated from the Mode I blunting relationship, thus giving

$$J_{II} = 4\tau_{ys}\Delta a \qquad (1.40)$$

Although their results demonstrate that J_{IIc} is orientation independent, J_{IIc} is dependent on material, since J_{IIc} for HT80 was greater than for HT100. For HT80, dJ/da is also orientation independent, however for HT100, dJ/da for the T-L direction was significantly greater than for the L-T direction.

1.4.2 The Effects of Side Grooves

Grooves are often machined into the sides of fracture toughness specimens with the primary purpose of suppressing the formation of shear lips and crack tunnelling. Side grooves effectively remove the free surfaces where plane stress conditions prevail and introduce a higher level of lateral constraint at the specimen edges. If done properly, shear lip formation can be suppressed and a straight crack front can be achieved. The depth of side grooves required to achieve these features has been found to be material dependent. If they are too deep, they produce lateral singularities which causes the crack to grow more rapidly at the outer edges. In general, ASTM E813-89$^{\epsilon 1}$ recommend that a 20 to 25% reduction in thickness

achieved through side grooving is applicable to a wide range of engineering materials.

Gudas et al. (1979) tested HY130, a high strength low alloy (HSLA) steel, using standard plain sided (PS) and side grooved (SG) C(T)25 specimens, extracted from the T-L orientation. The specimens were side grooved to a total depth corresponding to 12.5% and 25% of the specimen thickness. Their results demonstrated that side grooving to a depth of 12.5% or greater produced a lower bound dJ/da. Side grooving also reduced J_{Ic}, albeit by only a small amount, although an increase in side grooving did not correspond to a further decrease in J_{Ic}. Their tests covered a range of crack depths, where a_o/W=0.55, 0.65 and 0.8, which had little influence on their observations.

Similar observations have been reported by a number of investigators verifying the effects of side grooving on Mode I fracture toughness for a variety of different steels. Andrews and Shih (1979) tested A533B at 93°C using PS, 25%SG and 50%SG C(T)100 specimens. Gibson (1986) tested BS4360 43A C-Mn steel using PS and 25%SG C(T)25 specimens. Gordon and Challenger (1989) tested HSLA HY100 using PS, 20%SG, 40%SG and 60%SG 3P SE(B) specimens. Sommer and Aurich (1991) also used PS and 25%SG C(T)25 specimens to test StE 460 C-Mn steel.

Garwood (1982) tested API 5LX65 C-Mn pipe steel using PS and 50%SG 3PB SE(B) and M(T) specimens extracted from the T-L orientation. He observed that the effect of side grooving on J_{Ic} was negligible in either geometry. However, he also observed that side grooving caused a significant decrease in dJ/da when compared with plain sided specimens of identical global dimensions.

1.4.3 The Effects of Specimen Size

In the literature, size effects are expressed in a number of different ways; constant width variation in thickness, constant thickness variation in width, and proportional

increases in both thickness and width. In contrast to Mode II, Mode I size effects have been studied extensively.

The Effects of Specimen Thickness, Constant Width

Andrews and Shih (1979) tested A533B at 93°C using C(T)100 specimens in the L-T orientation. They investigated specimens of varied thickness, B=25, 63 and 101mm. They observed that dJ/da decreased with increasing thickness, however they observed the value of J_{Ic} to increase as B was reduced from 101mm to 63mm and then decrease for the 25mm thick specimen.

Gibson (1986) and Gibson et al. (1987) tested BS4360-43A, a normalised C-Mn steel also using C(T) specimens 100mm thick in the L-T orientation. They investigated specimen thickness in the range, $13mm \leq B \leq 50mm$ and observed tearing behaviour similar to that reported by Andrews and Shih (1979). However, the effect on J_{Ic} of specimen thickness was negligible. Turner (1986) reported similar results from tests on EN32 SE(B) specimens for thickness, B=10mm and 24mm.

In contrast, Joyce and Link (1995) observed the effect of specimen thickness ($12.5mm \leq B \leq 50mm$) to have a negligible effect on both J_{Ic} and dJ/da, from tests on HSLA HY100 using 20%SG SE(B) specimens.

The Effects of Specimen Width, Constant Thickness

Gibson (1986), who tested BS4360-43A using C(T) specimens 100mm thick observed dJ/da to increase slightly with increasing specimen width. They examined specimen widths in the range $26mm \leq W \leq 100mm$. The observed effects on J_{Ic} were negligible.

Turner (1986) observed similar behaviour from tests on EN32 using SE(B) specimens of width, W=10mm and 24mm. However, Jones and Gordon (1989), who tested HSLA HY100 using SE(B) specimens observed dJ/da to decrease with increasing specimen width ($30mm \leq W \leq 150mm$).

Gordon and Challenger (1989) examined HSLA HY100 using 3P SE(B) specimens. For constant thickness, B=30mm they observed that dJ/da decreased with increasing specimen width (15mm ≤ W ≤ 120mm). However, for W less than 60mm a reduction in dJ/da was only observed when $\Delta a > 6mm$. For $\Delta a < 6mm$, the resistance curve for W equal to 60mm produced a lower bound reference curve. They also observed J_{Ic} to be independent of specimen width.

Effects due to Proportional Increases in Specimen Thickness and Width

Turner (1986) investigated the effect of specimen size in A533B C-Mn steel using C(T) specimens of constant crack depth, a_o. He tested specimens of thickness, B in the range, 10mm ≤ B ≤ 100mm and width, W which corresponded to a proportional increase with B, such that $B=(W-a_o)$. His results demonstrated that both J_{Ic} and dJ/da are independent of a proportional increase in specimen size for the range of dimensions examined. Gibson et al. (1987) who investigated BS4360-43A using C(T) specimens in the L-T orientation also found J_{Ic} and dJ/da to be independent of specimen size. They examined specimens of various thickness, B=13, 25, 37.5 and 50mm and varied width corresponding to W=2B.

Gordon and Challenger (1989) examined HSLA HY100 using 3PB SE(B) specimens. They examined a range of specimen thickness, B=15, 30, 45, 60 and 75mm with a proportional increase in specimen width, where W=2B. They observed that J_{Ic} was independent of specimen size, however, in contrast to the observations of Turner (1986), they found dJ/da to decrease as specimen size increased.

Sommer and Aurich (1991) tested 20MnMoNi55 steel at 80°C using C(T) specimens. He examined three different size specimens where W=2B=25, 50 and 96mm and produced similar results to those presented by Gordon and Challenger (1989), although the decrease in dJ/da with increasing size was albeit slight.

1.4.4 The Effect of Crack Depth (a_o) and Crack Depth to Width (a_o/W) Ratio

Gudas et al. (1979) tested HSLA HY100 using PS, 12.5%SG and 25%SG C(T)25 specimens with crack depths corresponding to a_o/W=0.55, 0.65 and 0.8. They observed that J_{Ic} for both PS and SG specimens were independent of crack depth. However, although dJ/da was independent of a_o/W for both sets of side grooved specimens they observed that dJ/da increased with increasing crack depth for PS specimens.

Sommer and Aurich (1991) tested StE 460 steel using M(T) specimens. They examined three different crack depths corresponding to a_o/W=0.1, 0.5 and 0.8 respectively. Although they observed that J_{Ic} was independent of crack depth, they found that dJ/da for a_o/W=0.1 was equivalent to dJ/da for a_o/W=0.8. However, both were higher than dJ/da for a_o/W=0.5.

Joyce and Link (1993) tested HSLA HY100 at 25°C and A533B at 100°C. The specimens they examined were SE(B) and SE(T) of different size and crack depths. For the HY100 steel, dJ/da decreased with increasing a_o/W from 0.14 to 0.6. However, although they observed J_{Ic} to decrease with increasing crack depth for the smaller specimens (B=W=50mm and 2B=W=50mm), for the larger specimen (4B=W=50mm) J_{Ic} increased with increasing crack depth. For the SE(T) geometry tested, J_{Ic} was independent of a_o/W but dJ/da decreased with increasing a_o/W. All A533B specimens were side grooved 20% and both the SE(B) and SE(T) geometries exhibited a decrease in dJ/da with increasing a_o/W and although J_{Ic} was independent of a_o/W for the SE(B) geometry an increase was observed with increasing a_o/W for the SE(T) geometry. Joyce and Link (1997) also examined HSLA HY80 using 20%SG 3PB SE(B) specimens for a range of crack depths ($0.13<a_o/W<0.83$). They observed that J_{Ic} was independent of a_o/W however with increasing crack depth ($0.13<a_o/W<0.7$) dJ/da decreased. As they increased the crack depth further ($a_o/W>0.7$) they observed dJ/da to increase.

MacLennan and Hancock (1994) tested HSLA HY80 using SE(B) for a_o/W=0.1, 0.2, 0.3 and 0.5. Their results demonstrated that deeply cracked geometries ($a_o/W\geq0.3$)

exhibit a geometry independent toughness, providing a lower bound toughness associated with highly constrained flow fields. In contrast, with decreasing crack depth, dJ/da increased. Their results were in excellent agreement with results presented by Hancock et al. (1993) who tested A710 pressure vessel steel, also using SE(B) specimens.

Panontin and Sheppard (1995) examined the effect of crack depth on crack initiation for A516 Gr70 C-Mn steel using SE(T) (a_o/W=0.15, 0.3 and 0.7) and 3PB SE(B) (a_o/W=0.3 and 0.7) specimens. For the SE(T) specimens they observed that J_{Ic} was a_o/W independent, however for the SE(B) specimens they found J_{Ic} to decrease with increasing a_o/W, albeit slightly.

1.4.5 The Effect of Specimen Geometry

Garwood (1982) tested API 5LX65 C-Mn steel using PS and 50%SG 3PB SE(B) and M(T)-PS and 50%SG specimen geometries in Mode I loading, and found a considerable effect of change of geometry on J_{Ic} and dJ/da. Comparing the PS SE(B) and M(T) results, the SE(B) geometry produced a slightly lower J_{Ic} but a significantly lower dJ/da. Side grooving to a depth of 50% was employed to suppress shear lip formation and ensure that each specimen geometry was subject to plane strain behaviour. After side grooving, although J_{Ic} for the SE(B) specimens were still slightly lower, the difference in dJ/da was negligible. Garwood proposed that, even if shear lip formation is suppressed, there is a geometric effect between the bend and tension geometries which can probably be attributed to the differences in plastic zone formation.

Gibson et al. (1987) tested BS4360-43A C-Mn steel using tension; M(T) and double-edge DE(T), and bend; C(T), 3PB and 4PB SE(B) specimen geometries in the L-T orientation, in Mode I loading. All specimens were 25mm thick, and the width of the tension and bend specimens were 25mm and 50mm, respectively. Their results show that there was no effect of geometry, either bend or tension, on J_{Ic} regardless of specimen size, and dJ/da for the bend geometries were all similar. The tension

specimens demonstrated an increase in dJ/da compared to the bend specimens, but due to two different methods used to determine J, the comparisons of dJ/da between the M(T) and DE(T) geometries are confusing. The results presented by Gibson et al. (1987) are comparable with those presented by Garwood (1982) for PS 3PB SE(B), where the values of J_{Ic} are all similar, however there is a significant difference in dJ/da which could be attributed to size effects.

Sommer and Aurich (1991) tested StE 460 steel using M(T), DE(T) and C(T) specimens in Mode I. They observed that J_{Ic} for the C(T) specimens was less than J_{Ic} for the M(T) specimens which was similar to J_{Ic} for the DE(T) specimens. They also observed that dJ/da for the M(T) specimens was greater than for the DE(T) specimens which was similar to dJ/da for the C(T) specimens. However, the relationship of these specimens with material orientation, and the consistency of each geometry to be orientated in the same direction is unclear.

Joyce and Link (1993, 1995) tested HY100 using 20%SG SE(T), DE(T) and SE(B) specimens, and A533B using 20%SG SE(T), DE(T), C(T) and SE(B) specimens, all in Mode I. For the tests on HY100, J_{Ic} for the SE(T) specimens was greater than for the SE(B) specimens which was greater than for the DE(T) specimens. Also, dJ/da for the SE(T) specimens was greater than for the DE(T) specimens which was greater than for the SE(B) specimens. However, for A533B there was no discernible difference in J_{Ic} for all geometries tested, but dJ/da for the DE(T) specimens was greater than for the SE(T) specimens which was greater than for the SE(B) specimens which was greater than for the C(T) specimens.

Green and Miles (1983) tested two C-Mn steels in Mode I using PS C(T)25 specimens, and in Mode II using side grooved compact double shear (CDS) and double punch shear (DPS) specimens. They found that J_{Ic} for each geometry, regardless of mode of loading, was similar and only a slight variation in dJ/da, however, dJ/da for SG DPS (Mode II) was greater than for the SG C(T)25 (Mode I) specimens which was greater than for the SG CDS (Mode II). Their results suggest that between the three geometries tested the effect of loading mode, either Mode I or

Mode II is negligible, however there are differences in J_{Ic} and dJ/da, albeit only slight.

1.4.6 Summary of the Experimental Investigations of Constraint Effects

It is evident from the literature that constraint effects have been studied predominantly in Mode I loading. There have been limited studies in Mode II loading, but none have sought to investigate the effects of combined mode loading. In general, mixed mode fracture studies reported in the open literature have been confined to assessing the influence of mode mixity for a particular combination of B, W and a_o/W. To date, these studies have not progressed to consider how variations of B, W, a_o/W or even material orientation can affect the fracture behaviour of these materials in the presence of combined mode loading.

A review of the literature shows that R-curves are dependent on material orientation. For Mode I loading, T-L and S-L orientated specimens generally produce lower bound R-curves compared to any other orientation (Davenport, 1993). However, Shi and Zhou (1995) and Davenport (1993) have shown that this may not be the case for Mode II loading.

In general, both J_{Ic} and J_{IIc} do not vary significantly as B, W and a_o/W vary (Gibson, 1986, Turner, 1986, Gibson et al., 1987 and Joyce and Link, 1993; 1995). However, dJ/da varies considerably, especially when W and a_o/W are varied (Gibson, 1986 and Turner, 1986). The greatest effects on dJ/da are reported for HSLA steels such as HY80 and HY100 (Gudas et al., 1979, Jones and Gordon, 1989, Gordon and Challenger, 1989, Sommer and Aurich, 1991 and MacLennan and Hancock, 1994).

The results of this present study (refer to chapter 3) are unique since they address how variations of B, W and a_o/W ratio affect the fracture behaviour of A508, a C-Mn steel in the presence of combined tension (Mode I) and shear (Mode II) loading. Mode I studies of A508 C-Mn steel by Davenport (1993) have already established that a lower bound R-curve is produced by S-L orientated specimens. Moreover,

Davenport (1993) has also shown that specimen orientation has a negligible effect on the R-curve in Mode II loading.

1.5 Warm Prestressing in Structural Steels

In this section the process of Warm Prestressing (WPS), an overstressing operation used to assess, and enhance the integrity of a component is reviewed. The review focuses on the reported, and proven benefits gained using WPS on the behaviour of a range of C-Mn steels, which are commonly used in the manufacture of structural components such as pressure vessels and piping. A number of reviews have been published which cover the work of the past few decades. More detailed overviews are given by Nichols (1968a; 1968b), Pickles and Cowan (1983) and Smith and Garwood (1990a).

Although this review will appear biased toward a select band of researchers, there is a wealth of information currently available, comprising experimental, analytical and numerical investigations. It is also recognised that this review neglects such detail as material orientation and specimen size (Smith and Garwood, 1990a; 1990b) effects, although it is appreciated that these factors do significantly affect the degree of benefit achieved from WPS.

1.5.1 The Effects of Warm Prestress and Experimental Verification

On completion of manufacture, and at periodic intervals during service, pressure vessels are required to undergo a hydrostatic pressure test according to British Standards and ASME codes of practice, to demonstrate their structural integrity. The pressure test requires the vessel to be overstressed to a level which exceeds 125%, but is not greater than 150%, of its maximum in-service design stress. However, specific cases may be tested at a lower pressure if it assumed that significant yielding of any part of the vessel would occur beyond the lower level of 125%. The limits ensure that gross yielding of the vessel does not occur which would invariably cause

irreversible damage. The hydrostatic pressure test is usually performed by hydraulic pressurisation at water temperatures within the region of 7°C to 20°C, the only precaution being that the temperature is not low enough to cause the narrower sections of the vessel to freeze.

Although the principal aim of the pressure test is to assess the integrity of the structure and ensure that it will safely perform that for which it was designed, it has been found that the operating life of the vessel can be greatly enhanced. In particular, pressure testing a vessel containing flaws or defects that have obtained a critical size (a size that would have originally prompted the vessel to be removed from service) can significantly reduce the critical stress concentrations produced by these flaws, thus resulting in prolonged in-service life. This has been found to be beneficial to welded structures where the application of a controlled tensile overload can effectively reduce the peak residual stresses (Burdekin, 1969 and Leggatt and Davey, 1987). The application of a uniform elastic tensile strain causes the initial residual stress field to rise sufficiently thus causing localised yielding where significant tensile strain already exists.

There has been considerable effort to characterise the mechanisms which contribute to an increase in vessel life and there appears to be a strong dependence on which method of prestressing is used. For instance, the vessel could either be prestressed at its operating temperature, or at a different temperature. The level of applied prestress has also been thoroughly investigated. In particular the optimum prestress level to achieve the maximum benefit from the vessel. Brothers and Yukawa (1963) identified this optimum level as corresponding to the initiation of ductile tearing.

One prestressing technique, warm prestress (WPS) has already been the subject of significant detailed research over the past few decades, and has been found to be of particular value to ferritic steel components (other than pressure vessels) which fail by cleavage at reduced temperature (Brothers and Yukawa, 1963, Succop et al., 1970, Chell et al., 1978, Curry, 1981, Beremin, 1981, Smith and Garwood, 1990a; 1990b; 1992, Reed and Knott, 1992; 1996a; 1996b, and MacDonald et al., 1997). WPS involves loading a component to a predetermined prestress level at a higher

temperature than the component is required to operate during service life, a temperature sufficient to reduce the risk of failure. The basic theory behind WPS is that by performing the prestress operation at a higher temperature, usually within the upper regime of the fracture transition curve, the material will flow plastically. If the prestress is applied in a controlled manner, plastic flow can invariably reduce the potentially damaging critical stress concentrations of any existing defects. When the component is cooled, usually to a temperature within the lower regime of the fracture transition curve, corresponding to the in-service operating conditions, there is sufficient increase in the low temperature yield strength to enable a higher load to be achieved before failure occurs. Thus, the distinction between a standard proof test and a WPS is that a proof test is basically a method of demonstrating the structural integrity of a component, whereas in addition, a WPS is intended to enhance the in-service reliability of a vessel.

Yukawa (1969) proposed that the influence of a proof test and WPS cycle can be used to assess the integrity of a vessel containing small, medium and long surface cracks, as a function of critical pressure to cause failure (either brittle or ductile) and temperature (shown in figure 1.16). Assuming T1 and T3 are lower and upper shelf temperatures, respectively, and P1 and P2 are operating and prestress load levels, respectively, applying P2 at either T1, T2 or T3 would simulate a typical proof test. If P2 is applied at T1, where $P2>P_c^1$, and the vessel does not fail, figure (1.16) infers that no large flaws exist within the vessel. If however the vessel operates at either T2 or T3, the information obtained from P2 at T1 would infer that there is a considerable margin of safety between P_c^1 and the operating condition, P1 at T2 or T3. For WPS, the vessel is preloaded to a predetermined pressure P2 at $T \geq T3$, and unloaded if required and cooled to a lower temperature to simulate the in-service operating temperature of the vessel. For WPS however, the existence of flaws is postulated, therefore by subjecting the vessel to P2 at T3 there is assumed to be a benefit on the operation of the vessel at P1 T1. This would suggest that for pressures and temperatures up to P2 and T3 the vessel could contain a large flaw without sacrificing structural integrity.

The type of WPS loading cycle can have a significant bearing on the in-service fracture properties of a component (Brothers and Yukawa, 1963). A variety of loading histories have been used in experimental work to investigate WPS effects; load-cool-unload-fracture (LCUF), load-unload-cool-fracture (LUCF) and load-cool-fracture (LCF). All three WPS cycles are shown schematically in figure (1.17), in relation to an idealised brittle-to-ductile fracture transition curve.

A considerable amount of research, conducted by many researchers on a variety of different ferritic steels, have all demonstrated that each of the three WPS cycles, detailed above, provide a benefit in terms of enhancing the low temperature fracture properties of a material. Some of the data has been collated by Yukawa (1969), and is shown in figure (1.18). It can be seen that for a specific prestress level, a greater benefit in terms of fracture toughness can be achieved by applying an LCF WPS. The least benefit (or the most conservative loading cycle) is achieved by applying an LUCF WPS, where LCF and LUCF provide upper and lower bounds, respectively. However, although the LCF WPS cycle produces the greatest benefit in terms of fracture toughness, the increment of applied load to cause failure is not as great as the LUCF WPS, although the absolute value of applied load is invariably higher (idealised in figure 1.18).

For any WPS cycle, the greatest reported benefits have been attributed to the controlled prestress being applied in the same direction as the component would be loaded during service. As a result the load required to cause brittle fracture would need to be sufficient to exceed the zone of local compressive residual stress created during unloading of the prestress cycle (Brothers and Yukawa, 1963, Harrison and Fearnehough, 1972 Loss et al., 1977, Chell et al., 1979, Curry, 1979 and Smith and Garwood, 1990a). Hall et al., (1962) demonstrated that strain hardening can also contribute to the benefits achieved through WPS. However the attainment of an increase in benefit is strongly dependent on an increase in yield strength, thus enabling the critical stress for cleavage fracture to be obtained. An increase in yield strength is usually associated with a decrease in temperature, hence the greatest benefits have been achieved at very low temperatures.

There has been significantly less investigations associated with the application of a prestress achieved by shear loading. Steigerwald (1961) examined the effects of notch blunting and concluded that while plastic flow can geometrically reduce the acuity of the notch by increasing the notch root radius, the contribution to improved notch strength in his tests was not believed to be the dominant mechanism. Steigerwald found that WPS increased the notch strength even when a shear crack was generated during the prestress. However, compressive residual stress is generally accepted as one of the principal mechanisms which contribute a beneficial increase in material behaviour at low temperature following WPS. In the presence of a prestress achieved by shear loading, the crack tip is flanked by both 'beneficial' compressive residual stress and 'damaging' tensile residual stress. On loading a structure to failure, following a prestress achieved by shear loading, the non-equilibrium residual stress states would influence the growing crack to propagate in a direction that requires the least energy for fracture, the direction of tensile residual stress, hence ignoring the compressive residual stress zone (total stress is the sum of the applied and residual stress contributions).

Strain ageing embrittlement is of relative importance to pressure vessels and piping that have been in service for a long time, and may tend to offset any intended benefit from the application of a WPS (Succop et al., 1970 and Harrison and Fearnehough, 1972). Ageing is caused by the diffusion of carbon and nitrogen to dislocations, which results in them being pinned. Consequently a loss of ductility may occur if yielded material is exposed to elevated temperature for a prolonged period. This, together with an increase in apparent strength, may also promote a change in failure mechanism from ductile to cleavage fracture.

Succop et al., (1970) observed that the degree of benefit achieved from LUCF WPS can be reduced by strain ageing. In contrast however, Harrison and Fearnehough (1972) observed little effect on the response of either the LUCF or the LCF WPS cycles.

Haigh (1984) observed that ductile crack initiation toughness was reduced, but load bearing capacity was increased by strain ageing. The reduction of ductile crack

initiation toughness was also observed by Satoh et al., (1983) and the apparent increase in load bearing capacity was observed by Ripling and Lindberg (1965). However, MacDonald et al., (1997) proposed that the effect of strain ageing on the WPS benefit is of no consequence for A508 and A533B C-Mn steels over a wide range of prestress and fracture temperatures. They further proposed that ductile tearing, on the other hand, may cause significant damage to the crack tip plastic zone thereby decreasing the WPS benefit.

1.5.2 Predicting the Warm Prestress Effect

Standard fracture mechanics criteria, such as the MTS criterion proposed by Erdogan and Sih (1963), do not have the ability to qualitatively predict the fracture toughness of a component subject to a prior loading history. As a result a number of researchers (Harrison and Fearnehough, 1972, Harrop, 1979, Chell et al., 1979, Curry, 1981, Smith, 1987 and Smith and Garwood, 1990a) have derived analytical solutions which attempt to describe the WPS effect and provide a tool capable of predicting whether the application of a WPS will enhance the performance of a structural component subject to specific in-service conditions. However, experimental evidence describing the WPS effect found in the open literature appear to favour the models proposed by Chell et al., (1979), Curry (1981) and Smith and Garwood (1990a). The major limitation to all models reported in the open literature is that they are all specific to the case of Mode I WPS followed by Mode I fracture.

The model proposed by Chell et al., (1979) is based on a definition of the J-integral and a dislocation model similar to that proposed by Dugdale (1960). They define a parameter J_e, evaluated only from elastic strains and distortions, unlike the normal J-integral, proposed by Rice (1967), which accounts for the elastic and plastic contributions of total strains and distortions. Also, in contrast to the J-integral, Chell et al., (1979) suggest that the parameter J_e has a real physical meaning; it is the force acting on all singularities and inhomogeneities enclosed by a contour of integration (that is, the force acting on both the crack tip and the deformation associated with it). However, the critical event for fracture is still associated with a critical value of

J-integral, J_{crit} and hence directly related to a critical value of stress intensity factor, K_{crit}, such that failure occurs when

$$J_e = J_{crit} = \frac{(1-\nu^2)}{E} K_{crit}^2 \qquad (1.41)$$

After unloading of the WPS, a zone of residual stress is created around the crack tip and a plastic zone is formed. As the component is cooled the yield strength of the material increases, consequently impeding plastic flow and hence reducing dislocation movement. At the lower temperature, plastic flow will only resume when additional load is applied, sufficient to raise the local stress level beyond the low temperature yield stress. Chell et al., (1979) describe the unloading plastic zone as a residual zone, consisting of immobile 'in-active' dislocations. Only when the load, applied at the low temperature, is sufficient to induce plastic flow, will the dislocations once again become mobile, 'active'. The theory assumes that failure at low temperature will be by cleavage, occurring when a critical force on all dislocations that are active at the lower temperature is achieved in the crack tip region, hence equation (1.41). On this basis Chell et al., (1979) evaluated J_e around a contour which coincides with the boundary which separates the low temperature 'active' plastic zone from the surrounding 'in-active' residual zone. J_e is given by

$$J_e = \overline{\sigma}_3 \left[\phi(c) - \phi(a_3) \right] \qquad (1.42)$$

where $\overline{\sigma}_3$ is the flow stress at the lower temperature for fracture, $\phi(c)$ is effectively the crack tip opening displacement, and $\phi(a_3)$ is the displacement discontinuity across the plastic zone at $x=a_3$ ($x=0$, refers to the crack tip). The basic assumption is that the stress in the plastic zone is uniform and equals the flow stress. The evaluation of $\phi(c)$ and $\phi(a_3)$ is relatively involved and requires the summation of the various contributions of the stress distributions which arise from the different loading and un-loading stages between WPS and fracture.

There are however limitations of the model. The first is that the model only applies to a stationary crack and any sub-critical crack growth would have a significant influence on the associated stress distributions. Second, the model is relatively in-sensitive to the values of yield stress associated with the WPS and fracture events, respectively. However, it is a necessity that the yield stress increases as the fracture temperature decreases. Despite this, Chell and Haigh (1986) propose a lower bound equation, eliminating the yield stress from the model so that the only dependence is on K_I and K_{Ic}, the applied stress intensity factor following proof loading and fracture, respectively, which they verified through experiments.

$$\frac{K_{If}}{K_{Ic}} = 0.2\frac{K_I}{K_{Ic}} + 0.87 \qquad (1.43)$$

Curry (1981) developed a model based on the cleavage fracture criterion developed by Ritchie et al., (1973), who proposed that cleavage will occur when the stress level, σ_{yy}, ahead of the crack tip exceed the cleavage fracture stress, σ_f, over a characteristic distance, X_0. Curry proposed that a value of σ_f can be derived from experiments on notched bars, and a value of X_o can also be determined by superposition of appropriate near tip σ_{yy} distributions, derived from finite element analysis by Tracey (1976) and Ostergren (1969).

For LUCF, Curry proposed (in agreement with Chell et al., 1979) three possible loading cases, determined by the relative size of the initial loading (S1), unloading (S2), and final loading (S3) plastic zone size. Once the appropriate loading case had been identified the corresponding stress distributions given by Tracey (1976) and Ostergren (1969) can be combined to generate crack tip stress distributions for any specific WPS loading history and the final stress intensity factor at failure, K_{If} following WPS can be calculated.

For case 1, S1>S2>S3. The plastic zone forms under the final loading with an effective yield stress of (σ_{ys2} + σ_{ys1}) where σ_{ys1} and σ_{ys2} refer to the yield stress values at WPS and fracture temperatures respectively. As a result the final plastic zone will be smaller than the unloading zone if the following inequality is true

$$\frac{K_{If}}{\sigma_{ys2}+\sigma_{ys1}} < \frac{K_I}{2\sigma_{ys1}} \tag{1.44}$$

and the stress distribution at fracture will be

$$\sigma_{yy}\left\{K_{If}\right\} = \sigma_{yy}\left\{K_I,\sigma_{ys1}\right\} - \sigma_{yy}\left\{K_I,2\sigma_{ys1}\right\} + \sigma_{yy}\left\{K_{If},\left(\sigma_{ys2}+\sigma_{ys1}\right)\right\} \tag{1.45}$$

For case 2, S1>S3>S2. During the final loading the effects of unloading are removed and the final plasticity develops under a load equivalent to (K_{If} - K_I) and with an effective yield stress of (σ_{ys2} - σ_{ys1}). As a result, S1>S3>S2 must be true if the inequality given by equation (1.46) is true and the corresponding final stress distribution, which involves contributions from the two loading steps only, will be given by equation (1.47).

$$\frac{K_{If}-K_I}{\sigma_{ys2}-\sigma_{ys1}} < \frac{K_I}{\sigma_{ys1}} \tag{1.46}$$

$$\sigma_{yy}\left\{K_{If}\right\} = \sigma_{yy}\left\{K_I,\sigma_{ys1}\right\} + \sigma_{yy}\left\{\left(K_{If}-K_I\right),\left(\sigma_{ys2}-\sigma_{ys1}\right)\right\} \tag{1.47}$$

Finally, for case 3, S3>S1>S2. When the plastic zone becomes larger than that due to the initial loading, all the effects of prior plasticity are removed, hence there will be no WPS effect. If this is true the following inequality, given by equation (1.48) must be true.

$$\frac{K_{If}-K_I}{\sigma_{ys2}-\sigma_{ys1}} > \frac{K_I}{\sigma_{ys1}} \tag{1.48}$$

Curry (1981) validated his model by experiments on mild steel SE(B) specimens in 3PB, preloaded at room temperature and fractured at -150°C, which he assumed to be low enough to ensure that cleavage failure was slip dominated (a requirement of the RKR cleavage fracture model proposed by Ritchie et al., 1973). This model can also be used to predict the effect of WPS on pressure vessel steels containing a bainitic

microstructure, such as A533B, since the results presented by Parks (1976) suggest that the RKR criterion is also applicable to this family of steels.

In contrast, Smith and Garwood (1992) reported that commonly used elastic-plastic fracture mechanics parameters: J-Integral (J) and Crack Opening Displacement (δ) did not qualitatively describe the WPS effect based on earlier studies on A533B in the presence of WPS (Smith and Garwood, 1990a). This was despite cleavage fracture being the dominant failure mechanism. They also reported that the earlier models proposed by Chell et al., (1979) and Curry (1981) were not capable of adequately describing the WPS for this type of bainitic steel and their analyses were further limited by specimen orientation (see figure 1.15).

In an attempt to model these phenomena, Smith and Garwood (1990a) proposed a modification to an existing model developed by Smith (1983). The model, given by equation (1.49), assesses the global behaviour of a component across the ligament area ahead of a crack and is based on reference stress, a technique commonly used in creep analysis. Smith observed that a point exists, which he termed a reference stress point, in a singular crack tip field where the stress is approximately independent of the materials strain hardening exponent. Smith termed the stress at this point, the reference stress, σ_R which in general is some fraction of the yield stress of the material, and is approximated by the ratio of applied load, P_{app} to collapse load, P_{col}.

$$\frac{\sigma_{Rf}}{\sigma_{Rc}} = \left(\frac{\sigma_{ys2}}{\sigma_{ys2}+\sigma_{ys1}}\right)\left(1-\frac{\sigma_{ys1}}{\sigma_{ys2}}\frac{\sigma_{R1}}{\sigma_{Rc}}\right) \qquad (1.49)$$

where σ_{Rf}, σ_{Rc} and σ_{R1} refer to the predicted failure reference stress following WPS, the predicted failure reference stress and the applied reference stress, respectively, and σ_{ys1} and σ_{ys2} are the representative values of yield stress at temperatures corresponding to the WPS and fracture events, respectively. By definition $\sigma_{Rc}<\sigma_{ys2}$ and $\sigma_{R1}<\sigma_{ys1}$, thereby setting strict limits on the degree of benefit and applied proof load levels obtainable, thus enabling a structure to be proof loaded without the possibility of gross yielding occurring. Equation (1.49) can also be expressed in

terms of stress intensity factor by replacing σ_{Rf}/σ_{Rc} with K_f/K_{Rc} and σ_{RI}/σ_{Rc} with K_I/K_{Rc}. where K_f, K_{Rc} and K_I refer to the predicted stress intensity factor following WPS, the predicted failure stress intensity factor and the applied stress intensity factor, respectively.

Analytical models based on continuum and micro-structural investigations have all been used successfully to predict the response of a component subject to WPS. However, obtaining a reasonable prediction to verify experimental observations becomes increasingly difficult due to scatter of fracture toughness data as the fracture temperature is increased. However, the models discussed are capable of predicting trends.

1.5.3 Summary of the Effects of Warm Prestressing in Structural Steels

The preceding review of warm prestressing has shown that there is a significant amount of experimental data, generated from a variety of fracture mechanics specimens such as C(T) and SE(B) specimens, that is available to assess the effect of WPS on the tensile properties of ferritic steels.

However, it is evident from the literature that WPS investigations are biased to situations where the prestress is applied in the same sense as the operating load, that is, in Mode I. In addition, all of the models that are used to assess the degree of benefit achieved from a prior overload on the cleavage fracture toughness of ferritic steels are also for Mode I loading.

To date there has been no work reported that has attempted to investigate the effect of WPS when a component is subject to combinations of tension (Mode I) and shear (Mode II) loading. Unfortunately this is an extremely important oversight since structural components are rarely subject to just Mode I loading but complex loading situations, resulting in combinations of Mode I, II and III loading. These issues have been addressed in chapter 2 by studying the low temperature mixed mode I/II fracture

behaviour of a pressure vessel steel in the absence of a prior overload and after a Mode I or Mode II proof load at room temperature.

CHAPTER 2 : THE EFFECT OF WARM PRE-STRESS ON MIXED MODE BRITTLE AND DUCTILE FRACTURE

The aim of these experiments was to study the circumstances when pre-cracked ferritic steel specimens are subject to proof loading at room temperature and then fractured under combined tension and shear at a lower temperature, close to the Mode I lower shelf behaviour of the steel (Smith and Garwood, 1992). Experiments were carried out on BS1501-224 Gr490B, a Carbon Manganese (C-Mn) steel commonly used in the manufacture of pressure vessels. Tests were carried out to study the mixed mode low temperature (-120°C) fracture behaviour of a pressure vessel steel without proof loading, and then mixed mode low temperature fracture after Mode I or Mode II proof loading at room temperature (approximately 20°C), corresponding to LUCF (load-unload-cool-fracture) conditions. The experiments comprised of the following sets of tests;

1. Non proof (NP) loaded specimens subjected to mixed mode loading and fractured at -120°C,
2. Mode I proof load (MIP) at 20°C followed by mixed mode loading to fracture at -120°C, and
3. Mode II proof load (MIIP) at 20°C followed by mixed mode loading to fracture at -120°C.

In this chapter, section (2.1) describes in detail the material used in this study. Sections (2.2) and (2.3) describe the loading fixture which was used to apply mixed mode loading conditions at the crack tip of each specimen and details the method of testing and the test apparatus used throughout this study. Section (2.4) describes the analysis method, and sections (2.5) through to (2.7) present the experimental results and microscopic studies. Finally, section (2.8) compares the experimental results presented in sections (2.5) through to (2.7).

2.1 Material Used

BS1501-224 Gr490B C-Mn steel was used for the experimental studies. The choice of this material was bound by existing experimental activities (Fowler, 1998) to characterise the influence of warm pre-stressing and proof loading on the cleavage fracture toughness of ferritic steels.

The material was supplied by TWI (formerly known as The Welding Institute), Cambridge, UK as 50mm thick end pieces of previously tested large scale wide plate specimens. From these initial studies, Smith (1986) was able to fully characterise the uniaxial behaviour of this steel at room temperature and on the lower shelf. Limited studies on as-received properties were performed by Fowler (1998) who reported results consistent with those presented by Smith (1986). The chemical composition of the plate material (Smith and Garwood, 1992) is given in table (2.1) and the as-received, average basic material properties (Swankie and Smith, 1998) are given in table (2.2).

Fowler (1998) found this material to exhibit fully brittle fracture behaviour at -110°C based on Mode I experimental studies using C(T) specimens. Preliminary studies for Mode I and Mode II fracture at -120°C with prior loading history have been reported by Xavier (1995). His results for Mode I and Mode II ductile fracture at 20°C of single edge notch, SEN specimens, identical to the specimen geometry and dimensions used in this study, are presented in figures (2.1a) and (2.1b), respectively. The figures illustrate the load and displacement response of the material and specimen for Mode I (see figure 2.1a) and Mode II (see figure 2.1b).

2.2 Description of Mixed Mode Loading Fixture and Specimen Design

2.2.1 Mixed Mode Loading Fixture

To facilitate mixed mode I/II loading a special purpose loading fixture, designed by Davenport (1993), was used (see figure 2.2). The loading fixture enables mixed mode I/II loading to be achieved in a standard uniaxial testing machine. The fixture comprises four pieces which bolt together as two halves around a specimen which is located using four hardened pins. When the fixture is loaded through α=0.0°, pure tensile (Mode I) loading of the specimen is achieved. If loaded through α=90.0°, pure shear (Mode II) loading is achieved. Mixed mode (combined tension and shear) conditions are obtained by loading through α=18.0°, 36.0°, 54.0° and 72.0°, corresponding to loading angle increments of $\Delta\alpha$=18°. For each test configuration, loading is applied directly through the crack tip of each specimen.

2.2.2 Mixed Mode Specimen Design

SEN specimens were used in the experiments (see figure 2.3), and extracted from the plate in the T-L orientation. The specimens were 100mm long with a square cross section of 20mm, machined to an accuracy of ±0.01mm by surface grinding. Four location holes, diameter 10mm, were drilled and reamed to enable a close fit assembly between the halves of the test fixture, specimen and location pins. A 3.175mm, 60° inclusive, chevron slitting saw was used to produce a starter notch 7mm deep from which each specimen was fatigue pre-cracked to an approximate overall crack depth corresponding to a ratio of crack depth to width, a_o/W of 0.5. Specimens for Mode I loading were 130mm long. This was to ensure that the two halves of the loading fixture did not come into contact with each other as the loading arrangement rotated about the specimen crack tip with increasing applied load.

2.3 Description of Test Apparatus and Method of Testing

2.3.1 Description of Test Apparatus

A 250kN load capacity, Instron servo-hydraulic test machine with an analogue control system was used. Clevis grips were used to couple the test machine to the mixed mode loading fixture. An extensometer (see figure 2.4), used to measure local load point displacement, providing a measure of the rotation and displacement of the specimen and loading fixture, was positioned securely on the faces of the loading fixture. To enable fracture testing at the lower shelf temperature of -120°C an environmental chamber, cooled with liquid nitrogen, was used with a control thermocouple attached to each specimen, which enabled the temperature to be controlled within ±1°C. A computer data-logging system was used to record DC voltage signals from the test machine load cell, which provided a measure of applied load. The linear variable differential transducer (LVDT), located within the extensometer (see figure 2.4), provided a measure of local load point displacement.

2.3.2 Specimen Fatigue Pre-Cracking

Each test specimen was fatigue pre-cracked at 10Hz and at a ratio of minimum to maximum load of 0.1 in the servo-hydraulic test machine at room temperature (approximately 20°C), in accordance with the guidelines stipulated within ASTM E399-90$^{\epsilon 1}$. Fatigue pre-cracking was employed to produce, as near as possible, a natural crack with an a_o/W of approximately 0.5. To maintain an acceptable plastic zone size the load range was decreased approximately every millimetre of crack growth, ensuring that the maximum load did not exceed 80% of the estimated fracture toughness of the material at the fracture test temperature. Since fracture was at -120°C, to ensure that the effect of pre-cracking was negligible on final fracture conditions, the maximum applied stress intensity for pre-cracking was determined from

$$K_{max} < 0.6\left(\frac{\sigma_{ys1}}{\sigma_{ys2}}\right)K_Q \qquad (2.1)$$

where σ_{ys1} and σ_{ys2} are yield strength at pre-crack (20°C) and fracture test (-120°C) temperatures, respectively and K_Q was determined from figure (2.1a), using the 95% secant interception method. The corresponding maximum load (P_{max}) for each stage of pre-cracking was calculated from equation (2.1) using the relationship

$$P_{max} = \frac{B\sqrt{W}K_{max}}{f_I(a_o/W)} \qquad (2.2)$$

where B and W are specimen thickness and width, respectively and $f_I(a_o/W)$ is the Mode I geometry function determined from an analytical solution developed by Tada et al. (1973, 1985), given by

$$f_I\left(\frac{a_o}{W}\right) = \frac{\sqrt{2\tan\left(\frac{\pi a_o}{2W}\right)}}{\cos\left(\frac{\pi a_o}{2W}\right)}\left[0.752 + 2.02\left(\frac{a_o}{W}\right) + 0.37\left(1-\sin\left(\frac{\pi a_o}{2W}\right)\right)^3\right] \qquad (2.3)$$

2.3.3 Proof Loading

Proof loading took place under displacement control at a rate of approximately 0.5mm/min at room temperature (approximately 20°C), where the material exhibits ductile behaviour and can therefore withstand loads in excess of yield strength. Proof loading involved loading a pre-cracked specimen in either Mode I or Mode II to a percentage of an experimentally determined collapse load (P_{col}), shown in figures (2.1a) and (2.1b), respectively. The applied load for those specimens subject to a Mode I proof load was 80% of the Mode I experimental collapse load, P_{app}=70kN, and for a Mode II proof load, the load was 95% of the Mode II experimental collapse load, P_{app}=62.5kN.

2.3.4 Fracture Test Method

For fracture, the SEN specimen and mixed mode loading fixture were cooled down to the fracture test temperature of -120°C in an environmental chamber at zero load, under load control of the servo-hydraulic test machine. Once the desired temperature was obtained the test temperature was held constant for approximately ten minutes to enable a uniform temperature distribution throughout the specimen thickness. The specimens were then fractured under displacement control at a rate of approximately 0.5mm/min. For each test, DC voltage output signals from the test machine load cell and displacement LVDT were used to develop representative load versus load point displacement curves for loading at low temperature for NP, MIP and MIIP tests.

When each specimen had fractured they were immediately removed from the environmental chamber and loading fixture. The fracture surfaces were wetted with acetone to ensure oxidation and corrosion were kept to a minimum, and heated to room temperature using a heat gun.

A digital XY stage comprising magnifying optics was used to measure the initial crack lengths (a_o) of each fractured specimen to an accuracy of ±1μm. The ASTM (E399-90$^{\epsilon 1}$) recommendation for crack length measurements was used to derive an averaged value of a_o and each measurement was repeated to ensure accuracy.

The fracture path of each failed specimen was then photographed using a Polaroid camera and fracture angles were measured directly from the photographs. The fractured surfaces were examined using a Joel 6400 scanning electron microscope (SEM) to determine the mechanism of fracture.

2.4 Analysis of Mixed Mode Fracture Toughness

For each test the maximum load (P_{max}) achieved by each specimen (definition of P_{max} given in figure 2.5) was used to determine linear-elastic stress intensity factors for Mode I (K_I) and Mode II (K_{II}) loading from equations (2.4) and (2.5)

$$K_I = \frac{P_{max}}{B\sqrt{W}} f_I\left(\alpha, \frac{a_o}{W}\right) \tag{2.4}$$

$$K_{II} = \frac{P_{max}}{B\sqrt{W}} f_{II}\left(\alpha, \frac{a_o}{W}\right) \tag{2.5}$$

where $f_I(\alpha, a_o/W)$ and $f_{II}(\alpha, a_o/W)$ are elastic geometry functions dependent on loading angle (α, given in figure 2.2) and initial crack depth to width (a_o/W) ratio.

The crack depths of each specimen, achieved by fatigue pre-cracking, ranged between $10.00mm \leq a_o \leq 11.40mm$. Mode I and II reference curves for an initial crack length, a_o=10.00mm, for $0° \leq \alpha \leq 90°$ at mixed mode loading hole increments of $\Delta\alpha$=18° were determined from a plane strain, two-dimensional, elastic finite element analysis of the loading fixture and specimen (Davenport and Smith, 1993). To allow for variation in crack length following fatigue pre-cracking, an analytical solution (Tada et al., 1973; 1985), for $f_I(\alpha, a_o/W)$ is given by equation (2.3). The function $f_{II}(\alpha, a_o/W)$ is given by,

$$f_{II}\left(\frac{a_o}{W}\right) = \frac{1.30 - 0.65\left(\frac{a_o}{W}\right) + 0.37\left(\frac{a_o}{W}\right)^2 + 0.28\left(\frac{a_o}{W}\right)^3}{\sqrt{1-\left(\frac{a_o}{W}\right)}} \tag{2.6}$$

Equations (2.3) and (2.6), were used to develop calibration curves for a series of different crack lengths, at increments, Δa=0.20mm to a total crack depth, a_o=11.40mm. The results are given in tables (2.3) and (2.4), and are shown in figures (2.6a) and (2.6b) for $f_I(\alpha, a_o/W)$ and $f_{II}(\alpha, a_o/W)$, respectively. From these calibration curves, representative values of Mode I and Mode II elastic geometry function were interpolated for each specimen, for each corresponding value of average initial crack length, a_o.

Mixed Mode failure stress intensity factors (K_T) can be calculated from the relationship

$$K_T = \sqrt{K_I^2 + K_{II}^2} \tag{2.7}$$

where K_I and K_{II} are given by equations (2.4) and (2.5), respectively.

2.5 Non Proof Load, Mixed Mode Fracture Studies

Eleven specimens were tested in mixed mode loading to characterise the as-received, non proof loaded (NP) mixed mode fracture behaviour of BS1501 C-Mn pressure vessel steel at -120°C. The experimental results for the NP mixed mode fracture studies are given in table (2.5) and shown in figure (2.5) and figures (2.7) through to (2.11).

2.5.1 Mixed Mode Fracture Toughness

Failure in Mode I loaded specimens occurred catastrophically, with no evidence of non linearity of the load versus displacement curves (see figure 2.5). For mixed mode loading of the NP specimens there was evidence in the load versus load point displacement curves of increasing plasticity with increasing shear (Mode II) load, illustrated in figure (2.5). Although there was significant plasticity near Mode II, the maximum load, P_{max}, sustained by each specimen either at or prior to fracture was used to determine linear-elastic stress intensity factors from equations (2.4) and (2.5).

In Mode I loading the pressure vessel steel exhibited an average fracture toughness, K_{If} of 77.8MPa$\sqrt{m}$ based on 4 NP tests, given in table (2.5). Here the onset of catastrophic failure is given the notation K_{If} (for Mode I) to avoid ambiguity with plane strain definitions of linear-elastic fracture toughness.

For a valid plane strain value of linear-elastic fracture toughness in Mode I loading, denoted K_{Ic}, it is recommended that initially a significantly large specimen should be employed to obtain an overestimated value of K_{Ic} (ASTM E399-90$^{\epsilon 1}$). From this result, specimen dimensions can then be reduced to an appropriate thickness (B) and

corresponding crack depth (a_o) for subsequent tests. However, these size reductions should not invalidate the size requirements given in equation (2.8), such that

$$a_o, B \geq 2.5\left(\frac{K_{Ic}}{\sigma_{ys2}}\right)^2 \qquad (2.8)$$

Substituting K_{Ic} with K_{If} yields approximate values for a_o and B in excess of 47mm, which are significantly larger than the dimensions of the specimens used in these experiments ($10.00mm \leq a_o \leq 11.40mm$ and B=20.0mm). However, each specimen loaded in Mode I failed by transgranular cleavage in a catastrophic manner. Any through thickness necking due to the Poisson's effect was found to be negligible and the formation of shear lips was completely suppressed. Hence it was concluded that for BS1501 pressure vessel steel, the dimensional requirements of equation (2.8) were conservative and the SEN specimen, detailed in figure (2.3), was used for each subsequent test.

For combinations of tensile and shear loading the change in proportion of K_{II} with respect to K_{If} is shown in figure (2.7). The apparent average Mode II fracture toughness, K_{II} for NP specimens was approximately 48.1MPa$\sqrt{m}$. This is based on 3 NP tests, resulting in K_{II} being approximately 62% of the NP Mode I (K_{If}) fracture toughness. However, for fracture in Mode II it is evident from figure (2.5) that ductile tearing preceded fracture and that an equivalent Mode II fracture toughness, estimated from an elastic-plastic analysis, would be more appropriate in these conditions.

2.5.2 Mixed Mode Fracture Angles and Fracture Surface Examinations

The fracture angles for the pressure vessel steel for NP conditions are given in table (2.5) and shown in figures (2.8) as a function of loading angle, α and (2.9) as a function of equivalent crack angle, β, given by

$$\beta = \tan^{-1}\left(\frac{K_I}{K_{II}}\right) \tag{2.9}$$

Scanning electron microscope (SEM) examinations of the fracture surface features revealed a transition from cleavage fracture to ductile tearing with increasing Mode II (see figures 2.10a and 2.10b). Cleavage fracture occurred for Mode I loading (β=90.0°) and loading through α=36.0° (β=75.2°), shown in figure (2.10a), and there was no evidence of ductile tearing preceding fracture. From SEM examinations of the fracture surface features of specimens loaded through Mode I and α=36.0°, there was a significant number of fracture initiating carbide particles positioned randomly about the crack front. However, a quantitative analysis of carbides present was not conducted.

Loading through α=54.0° (β=64.4°) produced ductile tearing of approximately 150μm directly ahead of the fatigue pre-crack (see figure 2.11). Within this region, large voids were created at carbide locations across the specimen thickness. For distances greater than 150μm, the fracture surface was a mixture of dimple and cleavage fracture.

For loading through α=72.0° (β=44.0°), ductile tearing extended to 1.5mm (see figure 2.11). Again, large voids were apparent where carbide particles were located. At larger distances from the crack tip the fracture surface was, again, a mixture of dimple and cleavage fracture although a greater proportion of dimple features were present in comparison with features seen for α=54.0°.

For pure shear, α=90.0° (β=0.0°), the fracture mechanism was entirely ductile tearing. Typical of a Mode II fractured specimen, portions of each fracture surface examined were destroyed due to contact between the upper and lower shearing crack surfaces during loading. Mode II fracture surface features are shown in figure (2.10b). The crack propagation direction is easily identifiable from visual examination of the plastically deformed grain structure. Compared with Mode I cleavage fracture surface features, the appearance of fracture initiating carbides is

less obvious. However, there was evidence of carbides in the form of smooth elongated voids, suggesting that the interaction between the upper and lower shearing crack surfaces had expelled the carbides from the matrix.

2.6 Mode I Proof Load, Mixed Mode Fracture Studies

Eight specimens that had received an initial Mode I proof load (MIP) were tested in mixed mode loading to characterise the LUCF WPS mixed mode fracture behaviour of BS1501 C-Mn pressure vessel steel at -120°C. The experimental results for the MIP mixed mode fracture studies are given in table (2.6) and figures (2.12) through to (2.18).

2.6.1 Mixed Mode Fracture Toughness

As demonstrated in figure (2.12), failure in Mode I of the MIP specimen occurred catastrophically, with no evidence of non-linearity of the load versus load point displacement curve. For mixed mode loading of the MIP specimens there was evidence in the load versus load point displacement curves of increasing plasticity with increasing Mode II when $\Delta\alpha>54°$. Once again, even though significant plasticity was observed near Mode II, P_{max} achieved by each specimen either at or prior to fracture (refer to figure 2.5 for definition of P_{max}) was used to determine linear-elastic stress intensity factors from equations (2.4) and (2.5).

In Mode I loading the pressure vessel steel exhibited a fracture toughness, K_{If} of 103.2MPa$\sqrt{m}$ based on 1 MIP test, given in table (2.6). Once again the notation K_{If} has been used to avoid ambiguity with plane strain definitions of linear-elastic fracture toughness.

For combinations of tensile and shear loading the change in proportion of K_{II} with respect to K_{If} is shown in figure (2.13). The apparent MIP average K_{II} was approximately 49.0MPa$\sqrt{m}$, based on 4 MIP tests, resulting in K_{II} being

approximately 47% of MIP K_{If}. For fracture in Mode II, following MIP, ductile tearing preceded fracture and an elastic-plastic analysis should have been employed to determine an appropriate value of fracture toughness.

2.6.2 Mixed Mode Fracture Angles and Fracture Surface Examinations

The fracture angles for the pressure vessel steel subject to an initial Mode I proof load are given in table (2.6). Each fractured specimen (shown in figure 2.14) was photographed using a Polaroid camera and the fracture angle, relative to the plane of the fatigue pre-crack (corresponding to $\theta=0°$), was measured directly from enlarged copies of the photographs. Measured fracture angles are shown in figure (2.15) as a function of the equivalent crack angle β, given by equation (2.9).

Similar to the NP mixed mode fracture surface features observed using an SEM, a transition from cleavage fracture to ductile tearing with increasing Mode II loading was also found in MIP specimens. Typical fracture surface features for Mode I ($\beta=90.0°$, $\alpha=0.0°$) loading are shown in figure (2.16). Shown in this figure are typical features of an ambient temperature Mode I proof load where large voids form within a zone directly ahead of the fatigue precrack prior to low temperature fracture. For Mode II fracture, microvoids were again present along the fatigue precrack front. However, the fracture surface features resembled those shown in figure (2.10b).

It was evident from the fracture surface examinations that the Mode I proof load had caused significant damage at the crack tip prior to fracture. The accumulation of damage caused by the high level Mode I (80% P_{col}) proof load was assessed using a specimen that was sectioned along its length, and one half mounted and polished. Examination of the specimen cross section revealed that proof loading in Mode I had caused the initial fatigue pre-crack to extend by approximately 80μm (see figure 2.17). Microcracking parallel to the applied tensile load was observed at the crack tip along ferrite and pearlite grain boundaries. Small micro-voids along the grain boundary were also observed up to a radial distance ahead of the crack tip of approximately 50μm. SEM examination of the characteristic features of the crack

growth region revealed eqi-axed dimples of random size. Throughout the specimen thickness there were also numerous, large, nucleated voids, approximately 25μm in diameter, in the centre of which were located small spherical carbide particles.

Cleavage fracture occurred for Mode I loading and α=36.0° (β=75.2°) although ductile dimple features, a product of the Mode I proof load, were apparent between the fatigue pre-crack and the final fracture front over a region of approximately 80μm (see figure 2.18).

For α=54.0° (β=63.8°) there was no further ductile crack growth in addition to that produced by the initial Mode I proof load, but a transition from cleavage to a ductile dimple failure mechanism was observed. Detailed examinations revealed that there was a greater emphasis on cleavage facets rather than ductile dimples.

For α=72.0° (β=42.4°), ductile tearing extended to 250μm, an increase of 130μm from the initial ductile crack growth induced by the Mode I proof load (see figure 2.18). The characteristic features of the ductile tearing region were clearly identifiable from the MIP crack growth region and fracture front, since the dimple features of the ductile tearing region were planished and elongated in the crack propagation direction, and there was a significant reduction in the number of carbide particles present. Although the fracture surface was, again, a mixture of cleavage and ductile dimple features, there was a greater emphasis on ductile dimples in comparison with fracture for α=54.0°.

For failure in pure shear, loading through α=90.0° (β=0.0°), the fracture mechanism was entirely ductile tearing.

2.7 Mode II Proof Load, Mixed Mode Fracture Studies

Seven specimens that had received an initial Mode II proof load (MIIP) were tested in mixed mode loading to characterise the LUCF WPS mixed mode fracture behaviour of BS1501 C-Mn pressure vessel steel at -120°C. The experimental

results for the MIIP mixed mode fracture studies are given in table (2.7) and figures (2.19) through to (2.25).

2.7.1 Mixed Mode Fracture Toughness

Load versus load point displacement curves for MIIP specimens fractured in Mode I, Mode II and combined tensile and shear loading are shown in figure (2.19). It is evident that failure in Mode I and for mixed mode loading, where $\alpha \leq 72.0°$, occurred catastrophically, since the load versus load point displacement curves were all linear to failure. Non-linearity of the load versus load point displacement curve was only observed for Mode II loading, where significant ductile tearing preceded fracture. As with NP and MIP studies, linear-elastic stress intensity factors were determined from equations (2.4) and (2.5), where P_{max} was taken as the maximum load achieved in each test (refer to figure 2.5 for definition of P_{max}).

In Mode I loading the pressure vessel steel exhibited an average K_{If} of 25MPa$\sqrt{m}$ based on 3 MIIP tests, given in table (2.7). The same notations, K_{If} and K_{II} as used in the NP and MIP analyses have been used to describe the mixed mode fracture behaviour of MIIP specimens.

For combinations of tensile and shear loading the change in proportion of K_{II} with respect to K_{If} is shown in figure (2.20). The apparent Mode II fracture toughness, K_{II} based on 1 test was 47.2MPa$\sqrt{m}$, resulting in an increase in Mode II fracture toughness of approximately 89% with respect to MIIP K_{If}. However, the MIIP K_{II} value given in table (2.7) is based on equation (2.4) and is therefore conservative, since significant plastic deformation preceded failure and the analysis used was based on linear-elastic material behaviour.

2.7.2 Mixed Mode Fracture Angles and Fracture Surface Examinations

The fracture angles for the pressure vessel steel subject to an initial Mode II proof load are given in table (2.7). Again, Polaroid photographs were taken of each fractured specimen (see figure 2.21) and fracture angles were measured from enlarged copies of the photographs. The fracture angles are shown in figure (2.22) as a function of equivalent crack angle β, given in equation (2.9).

Although a Mode II proof load was applied to each specimen, a transition from cleavage fracture to ductile tearing with increasing Mode II loading was, again, observed. Typical fracture surface features for Mode I loading (β=90.0°, α=0.0°) are shown in figure (2.23). Shown in this figure are typical features of shear decohesion produced by the ambient temperature proof load, directly ahead of the fatigue precrack. Interestingly, the cleavage facets observed on the Mode I fracture surface directly ahead of the Mode II proof load are smaller than those seen in the Non and Mode I proof load Mode I fracture experiments. However, failure was via a cleavage mechanism at low temperature. For Mode II fracture, the fracture surface features resembled the surface features created by the Mode II proof load (see figure 2.10b for an example of typical Mode II fracture surface features).

Again, although a Mode II proof load cycle was used throughout these series of tests, a significant degree of crack tip damage was caused by the high level Mode II (95% P_{col}) proof load. Using an identical procedure adopted in the MIP studies, examination of the specimen cross section revealed that proof loading in Mode II had caused the initial fatigue pre-crack to extend by approximately 370μm (see figure 2.24) and at an angle of approximately 15°, from the plane of the initial fatigue pre-crack.

Plastic flow induced by the applied load had caused global deformation of the grain structure ahead of the crack tip. Consistent with the observations of Maccagno and Knott (1992), the applied load caused one side of the crack tip to blunt and the other to remain sharp. Blunting of the crack tip may have been formed by dislocation

pile-ups. Knott (1980) suggests that accumulated plastic strain in slip bands causes dislocation pile-ups at carbide particles thus stressing the particle and particle-matrix interface until, at a critical strain, either the interface or particle fractures. The energy released from the pile-up once a critical strain has been achieved may have been sufficient to cause the formation and linking of other cavities within the slip band (requiring the least energy for crack propagation), causing the shear crack to propagate. The microcracking and plastic deformation of the grain structure at the blunt region of the deformed crack tip (see figure 2.24) is possibly a product of these pile ups where the energy released was insufficient to promote continued growth. Grain boundary micro-voids were only observed below the shear crack (as indicated in figure 2.24), extending to a radial distance of up to 150μm. Plastic deformation above the shear crack was minimal and the appearance of micro-voids was negligible.

SEM examination of the characteristic features of the initial shear crack growth region revealed dimples of random size, elongated and planished in the direction of crack propagation. An interesting observation was the lack of carbide particle presence within the crack growth region, suggesting that the interaction between the upper and lower shearing crack surfaces had expelled the carbides from the matrix.

Cleavage fracture occurred for Mode I loading (β=90.0°, α=0.0°). The average fracture angle was θ=15.8°, which is similar to the angle of the ductile tearing resulting from the Mode II proof load.

For mixed mode loading at α=36.0° (β=75.2°), 54.0° (β=64.4°) and 72.0° (β=42.4°) following MIIP, the fracture mechanism was also cleavage and there was no additional ductile tearing greater than that incurred from Mode II proof loading (see figure 2.25).

For Mode II (pure shear) conditions, loading at α=90.0° (β=0.0°), the fracture mechanism was entirely ductile tearing.

2.8 Comparison of Non, Mode I and Mode II Proof Load Studies

2.8.1 Load Bearing Capacity

Typical mixed mode load versus load point displacement curves from the experiments are compared in figure (2.26) for NP, MIP and MIIP loaded mixed mode fracture. The load bearing capacity (LBC) of the NP loaded specimens increased with increasing Mode II. For near Mode II loading, plasticity preceded fracture. For specimens subject to an initial MIP load the variation in LBC throughout the range of mixed mode loading was negligible. However, there was significant scatter in the LBC of specimens subject to an initial MIIP load throughout the range of mixed mode loading.

For specimens loaded in Mode I (α=0.0°), an MIP load caused an increase in LBC of approximately 39% and an MIIP load resulted in a significant decrease in load bearing capacity of approximately 70% compared with NP load conditions.

For specimens loaded in Mode II (α=90.0°) the effect of either a MIP or MIIP load was negligible in terms of LBC. Although unstable tearing was observed in the NP, MIP and MIIP loaded specimens beyond maximum load, stable tearing prior to maximum load was only observed in the NP and MIP loaded specimens.

For α=36.0° and 54.0°, respectively, an initial MIP load caused an increase in LBC of 13% and 15%, respectively. For α=72.0° the effect of an MIP load was negligible in terms of LBC.

In contrast, for fracture through α=36.0°, 54.0° and 72.0° the failure loads for those specimens subject to an initial MIIP load were consistently lower than the NP mixed mode specimens by approximately 50%.

2.8.2 Mixed Mode Fracture Toughness

For combinations of tensile and shear load the change in proportion of K_{II} normalised with respect to K_{If} (the average fracture toughness based on 4 NP tests) is shown in figure (2.27) as a function of K_I/K_{If} for the NP, MIP and MIIP loaded specimens to enable an assessment of benefit in terms of fracture toughness.

For fracture in Mode I (α=0.0°) an increase in fracture toughness of approximately 32% resulted from an initial MIP load. With increasing shear load the benefit achieved from an MIP load in terms of fracture toughness was found to decrease to the extent that for Mode II fracture the difference was negligible.

In contrast, for fracture in Mode I (α=0.0°), an initial MIIP load resulted in a significant reduction in fracture toughness of approximate 70%. The reduction seen in Mode I was not as great with increasing shear load. For pure shear loading, similar to MIP conditions, the change in fracture toughness following an MIIP load was negligible.

2.8.3 Mixed Mode Fracture Angles

The fracture angles following mixed mode fracture of NP, MIP and MIIP loaded specimens are compared in figure (2.28). The variation in fracture angle for MIP and MIIP loaded specimens are similar throughout the range of mixed mode loading. NP load mixed mode fracture angles are also similar up to α=54.0°, however the 2 NP tests performed at α=72.0° varied considerably. The fracture angles for NP, MIP and MIIP loaded specimens that were tested in Mode II are also similar.

2.8.4 Ductile Tearing

Figure (2.29) shows both the initiation and extent of ductile tearing, δ_a associated with NP, MIP and MIIP specimens subject to mixed mode fracture. Examination of

each specimen subject to an initial proof load in either Mode I or Mode II revealed initial tearing prior to fracture. For the MIP specimens, proof loading caused the initial fatigue pre-crack length (a_o) to extended approximately 80μm. For the MIIP specimens, proof loading caused a_o to extend a further 370μm while kinking at an angle of approximately 15° to the plane of the initial crack. The kink angle appeared to be attributed to the development of plasticity at the crack tip.

For the NP specimens, ductile tearing initiated at α=54.0° (β=64.4°), extending the initial fatigue pre-crack by approximately 150μm prior to fracture. With increasing shear (Mode II) there was a greater degree of ductile tearing prior to fracture.

Similar observations were found in fractured specimens subject to an initial Mode I or Mode II proof load. However, for the MIP specimens, additional tearing initiated from α=72.0° (β=42.4°) and for the MIIP specimens, from α=54.0° (β=64.4°), albeit slight. With increasing shear load, for either MIP or MIIP specimens, the amount of ductile tearing prior to fracture increased significantly.

CHAPTER 3 : THE EFFECT OF SHEAR AND CONSTRAINT ON MIXED MODE DUCTILE FRACTURE

The aim of these experiments was to study the effects of shear loading and varying constraint conditions on mixed mode I and II loading of ferritic steel components. The effect of increasing shear was studied using a special purpose, unique loading fixture that enabled Mode I, Mode II and combinations of Mode I and II loading to be applied through the tip of a crack in a typical single edge notch (SEN) specimen. Constraint was quantified in terms of increasing thickness (B), width (W) and crack depth (a_o). The experiments were carried out on A508 Class 3, a C-Mn steel forging, commonly used in the manufacture of pressure vessels. All investigations were done at room temperature (20°C ±2°C) where a previous study (Davenport 1993), has shown that the material behaves in an elastic-plastic manner.

Throughout the available literature (refer to section 1), for steels it is reported that Mode II toughness is either equivalent, or higher than Mode I. In contrast, investigations by Davenport (1993) have demonstrated for A508 that Mode II toughness is significantly lower than Mode I. Moreover, Davenport (1993) has shown that increasing Mode II, from pure Mode I loading, corresponds to a continuous decrease in both crack initiation toughness (J_{init}) and tearing resistance (described by the slope of the resistance curve, dJ/da), where Mode II provides lower bound values.

The main body of experiments performed in this study extended Davenport's (1993) experiments to quantify the effect of constraint in mixed mode I/II loading. First, the effects of side grooving on both J_{init} and dJ/da have been addressed and compared with Davenport's (1993) results. Second, fracture mechanics test specimens and metallographic techniques have been used to quantify the effect of constraint in the presence of mixed mode I/II loading conditions, and identify the relevant failure mechanisms. Finally, the apparent decrease in J_{init} and dJ/da, seen with increasing Mode II, was examined using small sized specimens that had been subject to a range of different prior heat treatments.

Sections (3.1) through to (3.6) describe in detail the material used in this study, the different types of specimen used, the different fixtures used to apply the load and the analyses used to quantify fracture toughness. Sections (3.7) through to (3.12) present the experimental results and microscopic studies. Finally, limit load solutions are presented in section (3.13) and the results from additional studies designed to investigate the effect of microstructure on Mode II loading are presented in section (3.14).

3.1 Material Used

A508 Class 3 C-Mn steel forging was used for the experimental studies. It is a steel that is widely used in the manufacture of pressure vessels used in the nuclear industry, which is tough in nature and exhibits elastic-plastic behaviour under room temperature conditions. The material was supplied by Framatome (France) via British Energy Plc. and was part of a nozzle cut-out undergoing characterisation as a candidate PWR reactor vessel material.

The chemical composition of A508 class 3 C-Mn steel was obtained by spark discharge emission spectroscopy by British Energy Plc. and the results of their analysis are given in table (3.1). Mechanical properties (Davenport, 1993) for each of the three primary rolling directions, L, T and S (see figure 1.15) are given in table (3.2). Davenport (1993) observed only a 2% scatter between both the yield and ultimate strengths for each orientation thus concluding that A508 class 3 is isotropic in nature. Moreover, negligible orientation effects were seen in the ductility of the material.

Two billets of A508 were supplied by British Energy Plc. for the experiments. Both billets were cut from the same nozzle and were approximately 225mm thick. To determine the orientation of the material a small corner section was removed from each billet. The three primary surfaces of each corner section were sequentially polished and etched to reveal the microstructure. Orientation was determined from microscopic examination of the size, shape and orientation of the inherent Mn-S

inclusions, since grain directionality was negligible. Typical features used to assess the orientation are shown in figure (3.1). The significance of these studies was to ensure that all tests were performed on specimens of the same orientation.

Figure (3.2) shows the equi-axed pearlitic grain structure found throughout both billets of A508 steel forging. The lack of directionality of the grain structure suggests that a final heat treatment, post rolling may have been performed while the material was being manufactured. The average grain size of approximately 16.0μm was calculated using the Mean Linear Intercept Method (to an accuracy of 5%). The lamellae thickness of ferrite within the pearlite grains was approximately 1.5μm, while the cementite lamellae were slightly thinner, approximately 0.75μm.

3.2 Description of Mixed Mode Loading Fixture and Specimen Designs

Three series of tests on A508 Class 3 C-Mn steel forging were carried out.

The first set of tests was aimed at extending initial studies on plain sided (PS) and side grooved (SG) single edge notch (SEN) specimens by Davenport (1993). Using PS SEN specimens (see figure 2.3) Davenport developed crack growth resistance curves (R-curves) for pure tensile loading (Mode I), pure shear loading (Mode II) and combinations of tension and shear. In Mode I, Davenport (1993) also tested SG SEN specimens (see figure 3.3) and compared his results with the PS SEN results to study the effect of SG on crack initiation toughness and tearing resistance. The loading fixture (see figure 2.2) designed by Davenport (1993) was used to apply Mode I, Mode II and combinations of tension and shear.

The second set of tests was aimed at investigating the issues of constraint in mixed mode loading (combinations of tension and shear loading) using PS SEN specimens. To investigate constraint effects, variations of specimen thickness (B=10mm, 20mm and 40mm), width (W=20mm, 40mm and 80mm) and crack length (a_o/W=0.1, 0.5 and 0.7) were used. A plan of the proposed tests is shown in figure (3.4). A number

of the larger specimens (highlighted in figure 3.4) could not be tested since the theoretical load that would be required to initiate a crack would have exceeded the rated load capacity of the test machine. To enable Mode I, Mode II and mixed mode loading of each different sized PS SEN specimen, a unique loading fixture (see figure 3.5), geometrically similar to that used by Davenport (1993), was designed and manufactured. To quantify the effect of constraint, R-curves were generated for each specimen size, crack depth and mode of loading. In addition a Scanning Electron Microscope (SEM) was used to study the mechanism of crack growth.

The final set of experiments were performed on heat treated, small scale Mode II specimens. The reason for investigating Mode II only was to gain an understanding as to why the initiation toughness and tearing resistance were so low in Mode II compared to Mode I. As discussed in the preceding subsections of section (1.4), a number of investigators have observed that the converse is true. The objectives of this study was to examine whether the pearlitic microstructure had a detrimental effect on the shearing characteristics of the material. A shear punch test fixture, shown in figure (3.6) was used to apply the necessary shearing loads.

Many specimens were needed to satisfy the requirements of each test program. Consequently, to minimise both time and expense of specimen manufacture, each specimen was notched using electro-discharge machining (EDM) and not fatigue pre-cracked as suggested in various testing standards (BSI BS7448:Part 1:1991 and ASTM E813-89$^{\epsilon 1}$, 1989).

The notch root radius, ρ of all PS and SG SEN specimens used throughout this experimental program were measured prior to fracture and found to be less than 0.10mm. A number of investigators have examined the effects of ρ on fracture toughness of C-Mn steels, each concluding that as long as ρ was sufficiently small then fracture properties would be unaffected. Yoda (1987) proposed that as long as $\rho<0.10$mm for Mode I loading and $\rho<0.3$mm for Mode II loading then a notch can be used in place of fatigue pre-cracking. Miles and Gladwin (1991) observed similar effects in Mode II, but proposed that ρ should be no greater than 0.20mm.

3.2.1 Mixed Mode Loading Fixture

To facilitate Mode I, Mode II and mixed mode loading a special purpose loading fixture was designed (see figure 3.5) which was larger than the earlier loading fixture of Davenport (1993), shown in figure (2.2). The fixture was designed to enable the complete range of specimen thickness, width and crack depth (see figure 3.4) to be tested in a standard uniaxial testing machine. The loading fixture, manufactured from EN24T steel, comprises four sections which bolt together as two halves around an SEN specimen which is located within the fixture using two EN24T hardened pins.

To enable each size of SEN specimen (see figure 3.4) to be tested, an assembly of different sized spacer blocks and side plates were used. These were located within a recess which was machined into the inner face of each of the four sections of the loading fixture. The side plates were manufactured from gauge plate and used to alter the depth of each recess according to the thickness of each specimen being tested. The spacer blocks were manufactured from EN24T steel and hardened to reduce wear. They were used to alter the width of the recess and to position each specimen such that any combination of mixed mode loading was applied directly through the crack tip of each specimen. The spacer blocks were positioned into the two halves of the loading fixture using dovetail slots and hardened pins. The hardened pins were used to ensure accurate location of each spacer block and side plate within the loading fixture. The general arrangement of the spacer blocks, within the mixed mode loading fixture, is shown in figure (3.7)

When the fixture (see figure 3.5) is loaded through holes 1 (loading angle α=0°), pure tensile (Mode I) loading is achieved. If the load is applied through holes 5 (loading angle α=90°), pure shear (Mode II) loading is achieved. Mixed mode I/II conditions are achieved by loading through holes 2, 3 and 4, which correspond to loading angle increments of $\Delta\alpha$=22.5°.

3.2.2 Side Grooved SEN Mixed Mode Specimens

The side grooved SEN specimens, used to complement the initial studies by Davenport (1993), are shown in figure (3.3). The specimens, extracted from each A508 steel billet in the S-L orientation were 100mm long with a square cross section of 20mm, machined to an accuracy of ±0.01mm by surface grinding. Four location holes, diameter 10mm were drilled and reamed to enable a close fit assembly within the test fixture. A two stage wire feed EDM process was used to produce a 10mm deep notch in the L direction, in each specimen, corresponding to an a_o/W of 0.5. The EDM process introduced an initial notch, 8mm deep, 0.5mm wide and a finishing notch approximately 0.15mm (ρ=75μm) wide, to an overall depth of 10mm. A 90° inclusive, chevron slitting saw was used to side groove each specimen to an overall depth of 2mm, thus reducing the specimen net thickness (B_N) in the plain of the EDM notch to 16mm (20%).

The specimens tested in Mode I were 130mm long. This was to ensure that the two halves of the loading fixture did not come into contact with each other as the loading arrangement rotated about the specimen crack tip as the applied load was increased.

3.2.3 Plain Sided SEN Mixed Mode Specimens

Plain sided SEN specimens were used to study the influence of shear and constraint on ductile mixed mode I/II fracture. All specimens were extracted from the two A508 steel billets in the S-L orientation. Due to the high load levels required to ensure crack growth in some of the larger specimens, the end sections of those specimens were redesigned to ensure that there was no plastic deformation of the specimen loading holes when maximum load was achieved throughout the notched region of each specimen. Dependent on crack depth, the ends of some of the specimens were increased across their width and others, their thickness. Throughout the text these specimens have been referred to as 'dog-bone' specimens.

Although each specimen was EDM notched to an overall depth corresponding to a_o/W=0.1, 0.5 or 0.7, some of the larger width specimens were initially notched using a 60° inclusive, chevron slitting saw and finish machined using EDM. The primary purpose of using the slitting saw was to reduce machining times and overall cost of specimen manufacture. The notch root radius of each specimen was less than 0.1mm and the width and depth of each initial notch, machined with the slitting saw, was produced according to ASTM guidelines (E813-89$^{\epsilon 1}$, 1989). Parallel sided and dog-bone SEN specimens, similar to those used in the experiments, are shown schematically in figures (2.3) and (3.8).

Surface grinding was used to finish machine each specimen and ensure a dimensional accuracy of ±0.01mm. Two location holes were drilled and reamed (either 15mm or 20mm in diameter, depending on specimen size) to enable a close fit assembly within the test fixture. The specimen was located within each half of the loading fixture using hardened steel pins, manufactured from EN24T steel, ensuring that the crack tip was directly in line with the loading axis. The distance between the two loading holes of the specimens used for mixed mode and Mode II loading was 130mm. For Mode I loading this distance was extended to 160mm. This was to ensure that the two halves of the loading fixture did not come into contact with each other as the loading arrangement rotated about the specimen crack tip as the applied load was increased.

3.2.4 Small Scale Plain Sided SEN Mode II Specimens

Small scale SEN specimens, shown in figure (3.9), were used to investigate whether the pearlitic microstructure had a detrimental effect on the shearing characteristics of A508 class 3 steel. The specimens, extracted from the S-L orientation, were 10mm long with a square cross section of 5mm. Surface grinding was used to finish machine each specimen and ensure a dimensional accuracy of ±0.01mm was achieved. Finally, a notch, 2.5mm deep (corresponding to a_o/W=0.5), was machined in the L direction of each specimen using EDM.

3.3 Description of Test Apparatus and Method of Testing

A computer data-logging system was used to monitor and record DC voltage signals obtained from load cells, and displacement transducers used in each test. Although each series of tests were performed on different test machines, in each case, applied load and global axial displacement were measured and recorded. During the SG and PS, mixed mode experimental programs, DC voltage signals were recorded from additional extensometers (see figure 3.10a), used to measure local axial load line (Δ_{lll}), local crack normal (Mode I, Δ_{lcn}) and local crack parallel (Mode II, Δ_{lcp}) specimen displacements (see figure 3.10b). The local specimen displacement convention is illustrated in figure (3.11). Additional extensometry was not used to test the small scale SEN Mode II specimens.

An analogue XY chart recorder was used also to monitor the applied load and axial load line displacement during each test. The load versus displacement curve, plotted using the chart recorder, was used to monitor the current state of deformation during each test. Based on this visual representation, each test was manually stopped and unloaded once the desired level of deformation had been achieved.

3.3.1 Apparatus used to Test the Side Grooved SEN Specimens

An Instron, servo-hydraulic, uniaxial test machine with a load capacity of 250kN was used throughout these tests. Clevis grips were used to couple the mixed mode loading fixture (see figure 2.2) to the upper and lower loading rods of the test machine. Three displacement extensometers, shown in figure (3.10a), were used to measure specimen deformation. Each extensometer was located onto the faces of the loading fixture using two specially designed mounting blocks (see figure 3.10b), which enabled each extensometer to be located in line with the crack tip of each specimen. The mounting blocks were designed such that the gauge length of each extensometer, simultaneously measuring the local specimen displacements (Δ_{lll}, Δ_{lcn} and Δ_{lcp}), measured across the same gauge length (105mm) in each test. An active

electronic filter was used to refine the LVDT signals from each extensometer prior to recording.

3.3.2 Apparatus used to Test the Plain Sided SEN Specimens

A Mayes, servo-hydraulic, uniaxial test machine with a load capacity of 500kN was used throughout these tests. Clevis grips were used to couple the mixed mode loading fixture (see figure 3.5) to the test machine. The clevis grips were manufactured from EN24T steel and designed to withstand approximately twice the loading capacity of the test machine. Again, three extensometers (the same as those used in the side grooved experiments, see figure 3.10a) were used to measure local specimen displacements. Each extensometer was located onto the faces of the loading fixture using two specially designed mounting blocks (see figure 3.10b) which ensured that each measuring device was axially aligned with the specimen crack tip and measured across the same gauge length (160mm).

3.3.3 Apparatus used to Test the Small Scale Plain Sided SEN Mode II Specimens

An Autograph, servo-electric uniaxial test machine with a load capacity of 10kN was used throughout these tests. The shear punch test fixture, shown in figure (3.6), was positioned centrally within the load frame. The base of the test machine provided a stable support for the test fixture and the location recess in the upper loading rod ensured axial loading throughout each test.

3.3.4 Test Machine Stiffness Tests

Stiffness tests were performed on each specimen geometry to enable the elastic system energy associated with flexure of the loading assembly to be calculated. To measure the elastic-plastic toughness (J-Integral) of each specimen, corresponding only to a growing crack, stiffness calibration functions were incorporated into the

analysis, detailed in section (3.4), to enable the extraneous system energy to be removed. The stiffness functions were calculated from load versus local specimen displacement records of solid, un-cracked A508 calibration specimens of each specimen size used in both of the mixed mode experimental test programs. Each calibration specimen was located within the appropriate mixed mode loading fixture (see figures 2.2 and 3.5) and positioned within the clevis grips of the uniaxial test machine. Extensometry was attached to the loading fixture to measure local specimen displacements, corresponding to local load line (Δ_{lll}), local crack normal (local Mode I, Δ_{lcn}) and local crack parallel (local Mode II, Δ_{lcp}) displacements (see figure 3.11).

Each specimen was loaded elastically and then unloaded. This was repeated four times, and the applied load and local displacements were recorded. Non-linearity in the load versus displacement curves was seen at the onset of loading since pin loading was used to locate the specimen within the loading fixture which, in turn, was located via pins within the clevis grips, thus forming the load train. The initial non-linearity in the load versus displacement response decreased as the load was increased since the slack in the load train was taken up by the increasing load. This portion of the load versus displacement curves was not representative of direct loading on the specimen and was therefore omitted from the stiffness calculations. The unloading curves were also omitted since the analysis technique used to derive representative values of mixed mode fracture toughness (section 3.4) required only the loading portion of the load versus displacement curves. Stiffness calibration functions, k (corresponding to the applied load, P divided by the displacement, Δ) were calculated from the average of the remaining linear loading portions of the four load versus displacement curves.

The stiffness functions for the side grooved specimens are given in table (3.3) and shown in figure (3.12). The plain sided specimen stiffness calibration functions are given in tables (3.4) through to (3.11).

3.3.5 Mixed Mode Fracture Toughness Test Method

Although the side grooved and plain sided SEN mixed mode specimens were tested in different machines, using different loading fixtures, the analyses procedures were the same in each test program.

In general, either three or four specimens were used to characterise the crack growth resistance of a particular specimen size and crack length for each combination of tension and shear loading. This method of testing is commonly referred to as a multiple-specimen technique and the test procedure is described in detail by ASTM (E813-89$^{\epsilon 1}$). ASTM recommend that a minimum of five specimens should be tested to generate an R-curve for a specific size of specimen, depth of crack and mode of loading. However, to test a minimum of five specimens for each combination of specimen thickness, width, crack depth and mode of loading (detailed in figure 3.4) would have required more material than was available for testing. It was found that for Mode II and near Mode II loading, where crack tunnelling was limited, three specimens provided sufficient information to develop a representative R-curve. However, for those specimens subject to a high Mode I component, crack tunnelling was evident and some discrepancies in crack growth measurements were seen. To improve the accuracy of the R-curves developed for near Mode I loading, in some cases, four or more specimens were tested.

All specimens were tested under displacement control, at a rate of approximately 0.6mm/min, and at room temperature (20°C ±2°C). The first specimen of each set was loaded beyond maximum load to obtain the complete load versus displacement record and significant crack growth. After unloading the specimen to zero load, the specimen was removed from the loading fixture and the crack growth marked by heat tinting. This was done by placing the specimen in a furnace, heating to approximately 300°C and waiting until the specimen surface had changed colour slightly. Although ASTM recommend an approximate soak time of 10 minutes this was found to be inadequate, especially for the larger size specimens. Visual inspection was found to be the best method of assessing an appropriate time for heat tinting.

After heat tinting, the specimen was marked with an identification code in four locations by etching the specimen surface on either side of the crack growth region, and on both sides of the specimen. The specimen was then sectioned along its length. One half was polished and etched using a 2% nital solution (2% nitric acid, 98% methylated spirit) to reveal the microstructure and damage accumulation at the crack tip for microscopic analysis. The other half was cooled in liquid nitrogen and broken open to reveal the crack growth region. To protect the fracture surface features, the specimen surfaces were wetted with acetone to ensure oxidation and corrosion were kept to a minimum, then heated to room temperature using a heat gun.

A digital XY stage, comprising magnifying optics, was used to measure the stretch zone width (SZW) and crack growth (Δa) attributed to each tested specimen, to an accuracy of $\pm 1\mu m$. For the thin specimen tests (B=10mm), SZW and Δa measurements were recorded at 0.5mm intervals along the crack front. For the thicker specimens (B=20mm and 40mm), measurements were recorded at 1.0mm intervals. The SZW was measured since it provides a direct measure of crack tip blunting up to the critical point of crack initiation.

A scanning electron microscope (SEM) and a standard binocular type microscope were used to analyse the mechanism of crack growth and deformation characteristics of each specimen.

Following the initial test, each subsequent specimen in each set of tests was then loaded to selected different displacement levels (but less than the initial test). Toughness values, calculated from each test, together with the corresponding SZW and Δa measurements for each specimen, were then used to develop a series of R-curves.

3.3.6 Small Scale Mode II Fracture Toughness Test Method

Three sets of tests were completed to enable a preliminary investigation into the effects of the pearlitic microstructure on the crack growth resistance of A508 in Mode II loading. All tests were done at room temperature (20°C ±2°C). Each set of tests comprised six small scale SEN specimens, shown in figure (3.9). The first set of tests were performed on parent material and the remaining two sets were heat treated to change the microstructural characteristics of the material. The heat treatments performed were

set 2 : austenitised by heating to 950°C, 15 minute soak time, oil quench

set 3 : austenitised by heating to 950°C, 15 minute soak time, furnace cool

The different microstructures achieved by the variation in heat treatment are shown in figure (3.13). During heating and cooling, set 3 was wrapped in a ceramic wool to retain heat and enable a slow cooling rate to be achieved (approximately 2.5°C/min). The temperature was measured throughout the heat treatment process using a K-type thermocouple, spot welded onto the specimen surface.

One specimen from each of the two sets of heat treated specimens was used to enable microstructural features and material composition to be compared with the parent material. Microstructural examinations were performed using a binocular type microscope and material composition was obtained by optical emission spectroscopy.

Representative values of each element were found by first examining the parent material. Although the values did not reflect the true weight percentage of each element, they were used as a comparator to determine whether the composition of each of the two different heat treated specimens were similar to the parent material.

Each specimen was located within the shear punch test fixture and positioned within the frame of the test machine. The cross head, which housed the load cell, was then lowered until it came into contact with the test fixture and displayed a contact force of zero load (read on the test machine console). The cross-head was then lowered at

a rate of 0.6mm/min until the desired shear displacement was achieved. The load was then removed. Throughout each test a computer data-logging system and an analogue XY chart recorder were used to record shear load and shear displacement data. Representative values of Mode II fracture toughness were then calculated from the recorded data and R-curves were generated using averaged stretch zone width and crack growth measurements from each test.

The first specimen of each of the three sets was loaded until the remaining specimen ligament had failed by plastic collapse. With reference to the global shear displacement recorded from the initial test, each of the four remaining specimens were then loaded to different global displacements, each less than the previous. The specimens were then heat tinted, broken open in liquid nitrogen, and the crack growth was measured at 0.5mm intervals along the crack front using a digital XY measuring stage, as described above.

3.4 Analysis of Mixed Mode Fracture Toughness

The elastic-plastic fracture toughness, J of each specimen was calculated from the area beneath the loading portion of the applied load versus displacement curve, using a method developed by Sumpter and Turner (1976). A more elaborate method for correcting J for a growing crack has also been developed. In the limit of a stationary crack the two formulae predict identical values of initiation toughness. However, the more elaborate method which updates the ligament length per increment of crack extension is more often used in the single specimen test technique. Throughout this study multiple specimens have been used to develop R-curves, hence the simpler approach proposed by Sumpter and Turner (1976) has been used. The area beneath each loading curve was calculated using the trapezoidal rule and J was calculated from the sum of the elastic and plastic components where,

$$J = J_e + J_p \tag{3.1}$$

The subscripts 'e' and 'p' refer to the elastic and plastic components of the J-Integral, respectively.

Two methods of analysis were used. The first method used applied load (P) and load line (Δ_{ll}) displacement data to determine a value of J for each specimen. A second method was used to determine the individual effects of crack opening (local Mode I, Δ_{lcn}) and crack sliding (Mode II, Δ_{lcp}) displacement attributed to combined mode loading. To enable the individual contributions to be calculated, P was resolved into crack normal (Mode I, $P\cos\alpha$) and crack parallel (Mode II, $P\sin\alpha$) components with respect to the mixed mode loading angle, α and analysed with respect to the corresponding Mode I (Δ_{lcn}) and Mode II (Δ_{lcp}) displacements.

Since the J-Integral is proportional to the energy associated with fracture or crack growth, the separated components of equation (3.1) can be calculated from their equivalent energies (U), thus equation (3.1) can be re-written as

$$J = \frac{\eta_e U_e}{B(W-a_o)} + \frac{\eta_p U_p}{B(W-a_o)} \qquad (3.2)$$

where the geometry dependent functions, η_e and η_p, which are sensitive to mode of loading and crack length, were determined from finite element analyses (described in section 4.2.2). The quantities B, W and a_o refer to specimen thickness, width and initial crack length, respectively. For the SG specimens, B was replaced with B_N, the specimen net section thickness between the side grooves.

Each of the load versus displacement curves that were generated from an experiment comprised not only of elastic and plastic energy associated with growing a crack but extraneous system energy, U_k corresponding to flexure of the loading fixture and test machine. Using stiffness calibration functions (detailed in section 3.3.4), calculated for each size of specimen and mode of loading, it was possible to remove the extraneous system energy and hence determine the energy associated only with crack growth using,

$$J = \frac{\eta_e\left(U_e\right)}{B\left(W-a_o\right)} + \frac{\eta_p\left(U_T - U_e - U_k\right)}{B\left(W-a_o\right)} \qquad (3.3)$$

U_p from equation (3.2) has been replaced by the total and elastic energy components, since U_p cannot be directly derived from the area beneath the load versus displacement curve. U_T corresponds to the total area beneath the loading portion of the load versus displacement curve and U_e can be calculated from the elastic stress intensity.

The elastic energy associated with a growing crack, U_e was calculated from,

$$J_e = \frac{K^2}{E'} \qquad (3.4)$$

where the stress intensity factors for Mode I (K_I) and Mode II (K_{II}) loading of PS specimens are given by equations (2.5) and (2.6), respectively and E′ is the elastic modulus, which for plane stress, E′=E, and for plane strain, $E' = E/\left(1-\nu^2\right)$, where ν is Poisson's ratio.

For combinations of tension and shear loading, K is given by equation (2.7). However, for side grooved specimens the denominator shown in equations (2.5) and (2.6) becomes $\sqrt{BWB_N}$.

Substituting the appropriate solutions for K into equation (3.4) and solving for U_e in equations (3.2) and (3.3) gives,

$$U_e = \frac{K^2 B\left(W-a_o\right)}{\eta_e E'} \qquad (3.5)$$

Finally, from the stiffness calibration functions (k) calculated for each size of specimen and mode of loading, the system energy was calculated from,

$$U_k = \frac{P_{max}^2}{2k} \tag{3.6}$$

where P_{max} is the maximum load achieved during each test and k is dependent on whether the analysis is based on Δ_{III}, Δ_{Icn} or Δ_{Icp} displacements.

Substituting equations (3.5) and (3.6) into equation (3.3) gives equations (3.7) and (3.8) for SG and PS analysis of J, respectively, based on applied load and local load line displacement (Δ_{III}).

$$J_{T(SG)} = \frac{P_{max}^2(1-\nu^2)\left\{f\left(\frac{a_o}{W}\right)_I^2 + f\left(\frac{a_o}{W}\right)_{II}^2\right\}}{BWB_N E}\left\{1-\frac{\eta_p}{\eta_e}\right\} + \frac{\eta_p}{B_N(W-a_o)}\left\{U_T - \frac{P_{max}^2}{2k_{III}}\right\} \tag{3.7}$$

$$J_{T(PS)} = \frac{P_{max}^2(1-\nu^2)\left\{f\left(\frac{a_o}{W}\right)_I^2 + f\left(\frac{a_o}{W}\right)_{II}^2\right\}}{B^2WE}\left\{1-\frac{\eta_p}{\eta_e}\right\} + \frac{\eta_p}{B(W-a_o)}\left\{U_T - \frac{P_{max}^2}{2k_{III}}\right\} \tag{3.8}$$

where the values of η_e and η_p are dependent on the mode of loading.

For mixed mode loading the individual components of J_T, denoted J_{Icn} and J_{Icp}, corresponding to Mode I and Mode II alone are given by

$$J_{Icn} = \frac{(P_{max}\cos\alpha)^2(1-\nu^2)\left\{f\left(\frac{a_o}{W}\right)_I^2\right\}}{BWB_N E}\left\{1-\frac{\eta_{pI}}{\eta_{eI}}\right\} + \frac{\eta_{pI}}{B_N(W-a_o)}\left\{U_{Icn} - \frac{(P_{max}\cos\alpha)^2}{2k_{Icn}}\right\} \tag{3.9}$$

$$J_{lcp} = \frac{\left(P_{max}\sin\alpha\right)^2\left(1-\nu^2\right)\left\{f\left(\frac{a_o}{W}\right)^2_{II}\right\}}{BWB_NE}\left\{1-\frac{\eta_{pII}}{\eta_{eII}}\right\} + \frac{\eta_{pII}}{B_N\left(W-a_o\right)}\left\{U_{lcp}-\frac{\left(P_{max}\sin\alpha\right)^2}{2k_{lcp}}\right\} \quad (3.10)$$

for side grooved specimens, and

$$J_{lcn} = \frac{\left(P_{max}\cos\alpha\right)^2\left(1-\nu^2\right)\left\{f\left(\frac{a_o}{W}\right)^2_{I}\right\}}{B^2WE}\left\{1-\frac{\eta_{pI}}{\eta_{eI}}\right\} + \frac{\eta_{pI}}{B\left(W-a_o\right)}\left\{U_{lcn}-\frac{\left(P_{max}\cos\alpha\right)^2}{2k_{lcn}}\right\} \quad (3.11)$$

$$J_{lcp} = \frac{\left(P_{max}\sin\alpha\right)^2\left(1-\nu^2\right)\left\{f\left(\frac{a_o}{W}\right)^2_{II}\right\}}{B^2WE}\left\{1-\frac{\eta_{pII}}{\eta_{eII}}\right\} + \frac{\eta_{pII}}{B\left(W-a_o\right)}\left\{U_{lcp}-\frac{\left(P_{max}\sin\alpha\right)^2}{2k_{lcp}}\right\} \quad (3.12)$$

for plain sided specimens. The subscripts I, and II refer to Mode I and Mode II, respectively. Here η_e and η_p are dependent on either Mode I or Mode II (indicated by the subscripts I and II) while the elastic geometry functions, which are given by $f(a_o/W)_{I\text{ or }II}$, are dependent on the mixed mode loading angle α.

For the case of pure Mode I loading, parallel displacement of the crack faces was negligible, hence equations (3.10) and (3.12) can be neglected and equations (3.9) and (3.11) correspond to equation (3.7) and (3.8). Similarly, for pure Mode II loading, crack normal displacement of the crack faces was negligible, hence equations (3.9) and (3.11) can be neglected and equations (3.10) and (3.12) correspond to equations (3.7) and (3.8).

3.5 Analysis of Small Scale Mode II Fracture Toughness

Analyses of the small scale Mode II specimens was done by integrating the area beneath the load versus shear displacement curve to determine the Mode II fracture energy, U_{II} which is given by

$$U_{II} = \int_0^{\Delta} P_s d\Delta_s \qquad (3.13)$$

where P_s and Δ_s are the shear load and shear displacement, respectively. To convert these energy values into fracture toughness using Sumpter and Turner's (1976) method would have required extensive numerical analyses to determine both the elastic and plastic geometry functions (equation 3.2). Since, the purpose of these experiments was to study the role of microstructure it was decided that a qualitative assessment of this effect, if any, could be made directly from a comparison of energy.

3.6 Crack Growth Resistance Curves

Crack growth resistance curves (R-curves), described in terms of the J-Integral (J) and the amount of apparent crack growth (Δa), were used to quantify constraint as a function of crack initiation toughness (J_{init}) and tearing resistance (described by the slope of the tearing resistance curve, dJ/da). The guidelines proposed by ASTM (E813-89$^{\epsilon 1}$, 1989) where followed when possible and the power law expression, given in equation (3.14), was used to fit the applicable fracture toughness data.

$$J = C_1(\Delta a)^{C_2} \qquad (3.14)$$

C_1 and C_2 are curve fitting parameters which were derived from an initial first order fit of all applicable data for a specific specimen size, crack depth and mode of loading.

ASTM propose strict validity limits which govern the range of allowable crack growth over which the power law expression is applicable. The proposed limits however are specific to Mode I loading and as this study seeks to quantify the effects of mixed mode loading, the limits have not been applied.

3.7 Results From Mixed Mode I/II Side Grooved Studies

3.7.1 Mixed Mode Fracture Toughness

Test results for the 20% side grooved (SG) and plain sided (PS) SEN specimens are given in table (3.12) and shown in figure (3.14). The data for each set of specimens shown in figure (3.14) is fit using a linear equation. Experiments were performed in Mode I (α=0.0°), Mode II (α=90.0°) and mixed mode loading (α=54.0°), using the experimental loading fixture designed by Davenport (1993), shown in figure (2.2). The PS results given by Davenport (1993) are shown in figure (3.14) as hollow symbols and his results for 20% SG specimens loaded in Mode I are also shown.

In Mode I loading Davenport (1993) demonstrated that 20% SG resulted in decreases in both the slope of the tearing resistance curve, dJ/da and initiation toughness, J_{init} (the value of J_T at Δa=0.2mm) of approximately 45% and 12%, respectively.

In Mode II loading 20% SG resulted in a decrease in J_{init} of approximately 25%, however the effect on dJ/da was found to be negligible. Similar observations were found for α=54.0°. Although the reduction in J_{init} was not as great, approximately 20%, once again, the effect on dJ/da was found to be negligible.

The results also demonstrated that the difference between dJ/da for Mode II loading and mixed mode loading for α=54.0° was negligible. However, both the PS and 20% SG specimens loaded in Mode I demonstrated a significant increase in dJ/da.

3.7.2 Microscopic Analyses

The crack growth profiles of each of the 20% SG specimens, photographed using a Polaroid camera, are shown in figure (3.15).

Examinations of specimens loaded in Mode I indicated significant crack tip blunting (see figure 3.16) prior to crack initiation. At the tip of the blunting crack, multiple microscopic cracks were found to have initiated. Global crack growth was in the plane of the initial crack (θ_o=0°), orientated normal to the applied tensile loading. However, microscopic examination identified that the preferred direction of crack growth was towards regions where there was a higher density of pearlite present. Examination from the crack tip, within a radial distance of approximately 50μm revealed grain boundary separation and microcracking in highly populated pearlite regions and microvoid nucleation along grain boundaries, though normal to the plane of the initial crack (parallel to the applied load), as shown in figure (3.17).

Examination of specimens loaded in Mode II revealed anti-symmetric blunting of the crack tip (see figure 3.18) prior to crack initiation. At the tip of the sharpened region of the blunted tip a shear crack initiated and grew in the plane of the initial crack. Plastic deformation at the tip of the initiated shear crack had caused the grains to deform and re-orientate themselves. For the Mode II specimens subject to increased crack growth, although similar anti-symmetric blunting features were seen at the initial crack tip, a second blunting region was seen ahead of the initial crack. In addition, shear crack propagation was also seen from this second blunting region although propagating at an angle of approximately +28° to the plane of the initial crack as shown in figure (3.18). Plastic deformation was widespread throughout the ligament ahead of the propagating crack, causing the ferrite and pearlite grains to re-shape and re-orientate. The intensity of deformation was found to be greatest around the second blunting region where significant, randomly orientated microcracking was observed (see figure 3.19). Substantial microvoid formation was also seen within the grain boundaries of the plastically deformed grains at a distance of approximately 250μm from the crack tip. The density of microvoids was found to

reduce at increasing distance from the flanks of the propagating crack. An interesting observation was of the limited plastic deformation and limited number of nucleated microvoids above the growing crack as shown in figure (3.18).

Anti-symmetric blunting of the initial crack tip was also seen in specimens for α=54.0°. However, unlike that seen in Mode II specimens, it was evident that there was a significant contribution from crack opening displacement (Mode I) in addition to crack sliding displacement (Mode II). Once again crack initiation and propagation occurred in the plane of the initial crack, from the tip of the sharpened corner of the blunted crack tip. Examinations of specimens with significantly more crack growth demonstrated that the preferred direction for crack growth was in the plane of the initial crack. As with loading in Mode II, microvoids nucleated along grain boundaries, parallel to the advancing crack. With increasing load, the localised shearing between the grain boundaries increases until the ligament between neighbouring microvoids is unable to withstand further load and coalescence occurs thus forming a shear crack.

3.8 Mixed Mode Fracture Toughness, a_0/W=0.5

A total of 109 plain sided (PS) SEN specimens of varying thickness, B (10mm, 20mm and 40mm) and width, W (20mm, 40mm and 80mm) were tested in mixed mode loading, ranging from pure tension (Mode I) to pure shear (Mode II). From each set of tests (corresponding to a particular size of specimen) crack growth resistance curves (R-curves) were generated. In addition, a selection of the tested specimens from each combination of B, W and mode of loading were sectioned, metallographically prepared and examined using a Scanning Electron Microscope (SEM). The results of the metallographic analyses are described in section (3.12).

A total of 32 specimens were tested in Mode I (α=0.0°). The number of specimens used to examine each combination of W and B are given in table (3.13), and the corresponding fracture toughness results for each specimen are given in table (3.14). The results comprise calculated values of J-Integral, crack growth (Δa) and stretch

zone width (SZW). The SZW was used as a measure of blunting up to, and including crack initiation. R-curves (detailed in section 3.6) were generated for each data set and are shown in figure (3.20) as J versus Δa, where Δa refers to the average crack growth measurements of the two fracture surfaces of each specimen. Equation (3.14) was used to fit a curve through each data set. The constants, C_1 and C_2 which define the shape of each R-curve are given in Table (3.15).

For W=20mm specimens, tested in Mode I, the effect of thickness (10mm≤B≤40mm) on crack initiation toughness, J_{init}, measured at Δa=0.2mm (J_{init} is based on extrapolating the fitted curves (using equation 3.14) back to Δa corresponding to the average SZW), and tearing resistance (measured by the slope of the R-curve, dJ/da) was negligible. However, J_{init} and dJ/da decreased significantly as W increased for a given B. In general, regardless of W, the SZW at crack initiation was constant, approximately 0.2mm. As can be seen in figure (3.20), some of the data points for the B=10mm specimens lie outside the general trends. Examination of the fracture surfaces while measuring the amount of crack growth revealed that the main cause for this was the presence of inclusions in the path of the propagating crack.

For Mode II loading (α=90.0°), 35 specimens were used to investigate the effect of specimen size. Table (3.13) shows the number of specimens that were used to generate an R-curve for each combination of W and B. Figure (3.21) summarises the Mode II results given in table (3.16) and shows that all data, regardless of specimen size, can be described by a single curve. The results suggest that Mode II loading is size independent and moreover, a 'master curve' can be used to describe the crack initiation and tearing behaviour of this material when subject to pure shear loading conditions. The average SZW measurements were found to be approximately 0.1mm. The constants, C_1 and C_2 which define the shape of each R-curve and the master curve for Mode II are given in Table (3.15).

To investigate the effect of mixed mode loading, 10mm thick specimens were used. This is because the range of thickness' tested in both Mode I and Mode II demonstrated that thickness effects were negligible, in terms of J_{init} and dJ/da. For each combination of tensile and shear loading (α=22.5°, 45.0° and 67.5°), specimens

with W=20mm, 40mm and 80mm were tested. An additional 4 tests were done for α=45.0° on B=40mm specimens (W=20mm), to establish whether the negligible effect of thickness seen in the pure mode studies could be confirmed.

The R-curves for mixed mode loading are shown in figures (3.22), (3.23) and (3.24) for α=22.5°, 45.0° and 67.5°, respectively. In each figure, results are shown for B=10mm and W=20mm, 40mm and 80mm, respectively. The fracture toughness data for each specimen is given in tables (3.17), (3.18) and (3.19), for α=22.5°, 45.0° and 67.5°, respectively, together with the total number of completed tests for each size of specimen. The constants, C_1 and C_2 which define the shape of each R-curve are given in Table (3.15).

For α=22.5°, the R-curves for B=10mm and W=20mm, 40mm and 80mm (see figure 3.22) are similar. For each W tested, the variation in J_{init} (the value of J at the intersection between the R-curve and average SZW measurement) is negligible and there is only a slight difference in dJ/da. Essentially, the data can be described by a single R-curve. A similar trend is seen in the R-curves for α=45.0° (see figure 3.23) and α=67.5° (see figure 3.24).

Essentially, the R-curves shown in figures (3.20) through to (3.24) are independent of B and with the exception of Mode I (figure 3.20), they are also independent of W. The R-curves for increasing Mode II (figures 3.22 for α=22.5°, 3.23 for α=45.0°, 3.24 for α=67.5° and 3.21 for Mode II) show that when a component of shear loading (Mode II) is present, the R-curves are relatively independent of specimen size but decrease with increasing Mode II. Similarly, the average SZW measurements decrease with increasing Mode II from approximately 0.2mm for Mode I loading (α=0.0°) to approximately 0.1mm for Mode II loading (α=90.0°).

R-curves for a given B and W are shown in figures (3.25) through to (3.27) for different combinations of tension and shear. For B=10mm, W=20mm, figure (3.25) shows that the R-curves steadily decrease with increasing Mode II. However, at Δa=0.2mm, J_{init} for Mode I loading is similar to J_{init} for α=45.0°. The R-curves for

B=10mm, W=40mm, shown in figure (3.26) also decrease with increasing Mode II and at Δa=0.2mm, J_{init} for Mode I loading is similar to J_{init} for Mode II. For B=10mm, W=80mm (see figure 3.27) the R-curve for Mode I loading lies between the R-curves for α=45.0° and 67.5°. At Δa=0.2mm, J_{init} for Mode I loading is similar to J_{init} for α=67.5°. The R-curve for α=22.5° is the highest and with increasing Mode II the R-curves steadily decrease.

By measuring the crack normal (Δ_{Icn}) and crack parallel (Δ_{Icp}) displacements during each mixed mode test, the individual Mode I (J_{Icn}) and Mode II (J_{Icp}) components of J were evaluated. However, unlike J it was not possible to determine how much of Δa was attributed to either opening (Mode I) or sliding (Mode II) of the crack faces during mixed mode loading.

The Mode I, J_{Icn} and Mode II, J_{Icp} R-curves are shown in figures (3.28a) and (3.28b) for W=20mm, figures (3.29a) and (3.29b) for W=40mm and figures (3.30a) and (3.30b) for W=80mm, respectively.

The Mode I, J_{Icn} R-curves for the 20mm wide specimens shown in figure (3.28a), are similar to the R-curves generated using the full mixed mode J-integral analysis shown in figure (3.25). That is, an increase in Mode II corresponds to a decrease in both J_{init} (at Δa=0.2mm) and dJ/da for the Mode I component, J_{Icn}, such that the R-curve for pure Mode I loading is higher than the R-curve for α=22.5° which is higher than the R-curve for α=45.0° which is higher than the R-curve for α=67.5°. For the Mode II component (see figure 3.28b), the Mode II, J_{Icp} R-curve for α=22.5° lies between the Mode II, J_{Icp} R-curves for α=45.0° (the highest R-curve for J_{Icp}) and 67.5°. The lowest Mode II, J_{Icp} R-curve corresponds to Mode II loading. For α=22.5°, the Mode I, J_{Icn} R-curve is greater than the Mode II, J_{Icp} R-curve hence the likely mechanism of failure is microvoid coalescence. In contrast, for α=45.0° the R-curve for the Mode I component, J_{Icn} is less than the R-curve for the Mode II component, J_{Icp} hence the likely mechanism of failure is shear localisation. Therefore, it is possible that a transition from microvoid coalescence to shear localisation for W=20mm occurs between α=22.5° and 45.0°.

For the 40mm wide specimen tests, the Mode I, J_{Icn} and Mode II, J_{Icp} R-curves are shown in figures (3.29a) and (3.29b), respectively. In figure (3.29a), for the Mode I component, J_{Icn}, dJ/da decreases with increasing Mode II. However, at Δa=0.2mm, J_{init} for Mode I was less than J_{init} for α=45.0° but greater than J_{init} for α=67.5°. For the Mode I component, J_{Icn}, J_{init} achieved a maximum at α=22.5°. In figure (3.29b) the Mode II, J_{Icp} R-curve for α=22.5° was lower than the Mode II, J_{Icp} R-curve for α=67.5° but higher than the J_{Icp} R-curve for pure Mode II loading. The highest R-curve for the Mode II component, J_{Icp} was for α=45.0°. For α=22.5°, the Mode I, J_{Icn} R-curve is greater than the Mode II, J_{Icp} R-curve hence the likely mechanism of failure is microvoid coalescence. In contrast, for α=45.0° the Mode I, J_{Icn} R-curve is less than the Mode II, J_{Icp} R-curve hence the likely mechanism of failure is shear localisation. Therefore it is possible that a transition from microvoid coalescence to shear localisation for W=40mm occurs between α=22.5° and 45.0°.

For the 80mm wide specimen tests, the Mode I, J_{Icn} and Mode II, J_{Icp} R-curves are shown in figures (3.30a) and (3.30b), respectively. In figure (3.30a), for the Mode I component, J_{Icn}, dJ/da decreases with increasing Mode II although dJ/da for Mode I loading is similar to dJ/da for α=22.5°. However, at Δa=0.2mm, J_{init} for Mode I was equivalent to J_{init} for α=45.0°. For the Mode I component, J_{Icn}, J_{init} achieved a maximum at α=22.5°. In figure (3.30b) the Mode II, J_{Icp}, R-curve for α=22.5° was lower than the Mode II, J_{Icp} R-curve for α=67.5° but higher than the J_{Icp} R-curve for pure Mode II loading. The highest R-curve for the Mode II component, J_{Icp} was for α=45.0°. For α=22.5°, the Mode I, J_{Icn} R-curve is much higher than the Mode II, J_{Icp} R-curve hence the likely mechanism of failure is microvoid coalescence. In contrast, for α=45.0° the Mode I, J_{Icn} R-curve is only slightly less than the Mode II, J_{Icp} R-curve hence the likely mechanism of failure is shear localisation. Therefore it is possible that a transition from microvoid coalescence to shear localisation for W=80mm occurs at approximately α=45.0°.

The differences between the Mode I, J_{Icn} and Mode II, J_{Icp} R-curves seen throughout the mixed mode tests may be due to a change in failure mechanism from microvoid

coalescence to shear localisation. This can only be confirmed by microscopic analyses, the details of which are described in section (3.12).

3.9 Mixed Mode Fracture Toughness, $a_o/W=0.7$

A total of 27 PS SEN specimens of thickness, B=10mm and 20mm, and width, W=20mm and 80mm, were tested in Mode I, Mode II and mixed mode loading through $\alpha=45.0°$. Testing was limited to these specific combinations of B and W due to limited material availability. In Mode I, 10 specimens were tested. Thickness effects, B=10mm and 20mm, were examined using specimens that were 20mm wide. The objective of testing the 10mm and 20mm thick specimens was to clarify that, as for $a_o/W=0.5$ (section 3.8.1), J_{init} and dJ/da were thickness independent. In Mode II, 11 specimens were tested to confirm whether a unique 'master curve' could also be used to quantify specimen size effects for $a_o/W=0.7$. For mixed mode studies, loading was applied through $\alpha=45.0°$. A total of 6 specimens were tested using 10mm thick specimens to examine the effect of increasing specimen width (W=20mm and 80mm). A selection of the tested specimens from each combination of B, W and mode of loading were sectioned, metallographically prepared and examined using an SEM. The results of the metallographic analyses are described in section (3.12).

The number of specimens used to examine specific combinations of W, B and mode of loading are shown in table (3.20) and the corresponding fracture toughness data for each specimen are given in tables (3.21) to (3.23). Equation (3.14) was used to fit a curve through each data set and the constants, C_1 and C_2 which define the shape of each R-curve are given in table (3.24).

The results for Mode I loading are shown in figure (3.31) and the fracture toughness data are given in table (3.21). The SZW measurements, which give a direct measure of the amount of crack tip blunting corresponding to crack initiation, are all similar and give an average value of 0.17mm. The effect of varying thickness (B=10mm and 20mm) and specimen width (W=20mm and 80mm) on J_{init}, measured at $\Delta a=0.17$mm

for Mode I loading is negligible. There is a slight effect on dJ/da with increasing thickness since dJ/da for B=20mm is slightly less than dJ/da for B=10mm. However, there is a significant decrease in dJ/da for W=80mm compared with W=20mm.

The results for Mode II loading are shown in figure (3.32) and the fracture toughness data are given in table (3.23). The SZW measurements give an average value of approximately 0.10mm. For Mode II loading the R-curves are independent of specimen size and can therefore, as for Mode II loading for $a_o/W=0.5$, be described by a master curve. The tearing moduli for each size of specimen are given in table (3.24) and as can be seen, the values are fairly similar.

To investigate the effects of mixed mode loading for $a_o/W=0.7$, only 10mm thick specimens were used. This was because the most significant effect on the shape and magnitude of the R-curves for pure mode loading was due to specimen width, hence W=20mm and 80mm were examined. The data for $\alpha=45.0°$ are given in table (3.22) and the results are shown in figure (3.33). The SZW measurements were similar between the two sets of specimens and gave an average value of approximately 0.17mm. Unlike loading in Mode I and Mode II, for $\alpha=45.0°$ at $\Delta a=0.17$mm there is a significant difference in J_{init} which is greater for W=80mm than for W=20mm. Although the fracture toughness data for W=80mm exhibits a large degree of scatter when crack growth is small, dJ/da for W=80mm is similar to dJ/da for W=20mm.

The R-curves for Mode I, Mode II and $\alpha=45.0°$ are shown in figure (3.34) with respect to J_T for W=20mm. Although the R-curves decrease with increasing Mode II, at $\Delta a=0.2$mm J_{init} for Mode I loading is similar to J_{init} for $\alpha=45.0°$. However, for Mode II loading there is a significant decrease in J_{init}. Similarly, in figure (3.35) for W=80mm, dJ/da decreases with increasing Mode II. However, at $\Delta a=0.2$mm J_{init} for Mode I loading is significantly lower than J_{init} for $\alpha=45.0°$. Again, at $\Delta a=0.2$mm J_{init} for Mode II loading is considerably lower.

As for the $a_o/W=0.5$ mixed mode experiments, the individual Mode I component, J_{Icn} and Mode II component, J_{Icp} of J were calculated for the R-curves shown in figure (3.33). The Mode I, J_{Icn} and Mode II, J_{Icp} R-curves are shown in figures (3.36a) and

(3.36b), respectively, for W=20mm and 80mm. As can be seen, for α=45.0° both J_{init} at Δa=0.2mm and dJ/da for the Mode II, J_{Icp} R-curves (see figure 3.36b) are higher than the Mode I, J_{Icn} R-curves (see figure 3.36a), thus inferring that regardless of specimen width, failure for α=45.0° may be due to shear localisation since the Mode II, J_{Icp} R-curves are higher than the Mode I, J_{Icn} R-curves. Although dJ/da for the Mode II, J_{Icp} R-curve for W=20mm is higher than for W=80mm, at Δa=0.2mm J_{init} is significantly lower for W=20mm than for W=80mm. Consequently, the Mode II, J_{Icp} R-curve for W=20mm is lower than for W=80mm. However, the data for W=80mm was limited and there were no results obtained between 0.5mm<Δa<2.5mm, therefore comparison of results by dJ/da may be misleading.

Figures (3.37a), (3.37b), (3.38a) and (3.38b) compare the R-curves shown in figures (3.31), (3.32), (3.34a) and (3.34b) for W=20mm and 80mm, respectively, demonstrating the effect of increasing shear load in terms of Mode I, J_{Icn} and Mode II, J_{Icp}. The Mode I, J_{Icn} R-curves shown in figures (3.37a) and (3.38a) demonstrate that both J_{init} at Δa=0.2mm and dJ/da for α=45.0° are significantly lower than for pure Mode I loading. However, the Mode II, J_{Icp} R-curves shown in figures (3.37b) and (3.38b) demonstrate that for α=45.0° both J_{init} at Δa=0.2mm and dJ/da are significantly higher than for Mode II.

3.10 Mixed Mode Fracture Toughness, a_o/W=0.1

A total of 13 specimens were tested in mixed mode I/II loading for B=10mm and 40mm, and W=20mm.

For Mode I loading, 2 specimens were tested for B=10mm and W=20mm and 2 specimens were tested for B=40mm and W=20mm. The specimens tested in Mode I were unsuccessful since gross yielding occurred throughout the entire specimen. Figure (3.39) shows Luders banding throughout the length of a specimen loaded in Mode I. Crack growth did not occur in any of these specimens. Similar features were seen in the 2 specimens subject to mixed mode loading through α=45.0°.

For Mode II loading only specimens of W=20mm were examined, 4 specimens were tested for B=10mm and 3 specimens were tested for B=40mm (see table 3.25). Unlike the Mode I specimens, crack growth occurred in each specimen and R-curves were generated from data given in table (3.26). Equation (3.14) was used to fit a curve through each data set and the constants, C_1 and C_2 which define the shape of each R-curve are given in table (3.27).

The average SZW measurements for each data set were 0.04mm for B=10mm and 0.11mm for B=40mm. Although only one data point for B=40mm lies between the data points for B=10mm, all the crack growth data can essentially be described by a master curve (see figure 3.40) thus demonstrating that both J_{init} and dJ/da are independent of specimen size for $a_o/W=0.1$.

3.11 Influence of Crack Depth on Mixed Mode Fracture

A selection of the R-curves detailed in sections (3.8), (3.9) and (3.10) for $a_o/W=0.5$, 0.7 and 0.1, respectively, are compared in figures (3.41), (3.42) and (3.43) for similar specimen sizes.

In figure (3.41) the Mode I R-curves in terms of J_T for $a_o/W=0.5$ and 0.7 are compared. As can be seen, for the four R-curves which correspond to W=20mm, the differences in J_{init} at $\Delta a=0.2$mm and dJ/da are negligible. However, for W=80mm the R-curve for $a_o/W=0.5$ is lower than the R-curve for $a_o/W=0.7$. Although dJ/da for the two R-curves is similar, J_{init} at $\Delta a=0.2$mm for $a_o/W=0.7$ is much greater than for $a_o/W=0.5$. Moreover, J_{init} for $a_o/W=0.7$ is similar to J_{init} for the four R-curves for W=20mm. Although Mode I R-curves could not be generated for $a_o/W=0.1$ due to gross yielding throughout each specimen (see figure 3.39) and no apparent crack growth, the high loads achieved in each test demonstrated that J_{init} for $a_o/W=0.1$ would be higher than for $a_o/W=0.5$ and 0.7.

In figure (3.42) the Mode II R-curves in terms of J_T for $a_o/W=0.1$, 0.5 and 0.7 are compared. Each data set, regardless of specimen size, is represented by a master

curve which is dependent on a_o/W ratio only. As can be seen the R-curves for a_o/W=0.5 and 0.7 are very similar. However, for a_o/W=0.1, J_{init} at Δa=0.1mm and dJ/da are higher than for a_o/W=0.5 and 0.7.

In figure (3.43) the mixed mode R-curves in terms of J_T for α=45.0° are shown for a_o/W=0.5 and 0.7. As for Mode I loading, R-curves for a_o/W=0.1 could not be generated due to gross yielding of each test specimen although the load achieved in each specimen for a_o/W=0.1 suggests that J_{init} would be higher than J_{init} for a_o/W=0.5 and 0.7. Although the data used to generate the R-curves is limited and scattered (which has a significant affect on the shape of the R-curve) a trend in the available data can be seen. The scatter in the experimental data for a_o/W=0.5 and 0.7 suggests that a master curve can be used to describe mixed mode I/II loading through α=45.0°.

The separated Mode I component, J_{Icn} and Mode II component, J_{Icp} from the R-curves for α=45.0° compared in figure (3.43) are compared in figures (3.44a) and (3.44b), respectively. For W=20mm (a_o/W=0.5 and 0.7) the R-curves suggest that failure may be due to shear localisation since both J_{init} and dJ/da for Mode II, J_{Icp} are greater than for Mode I, J_{Icn}. Similarly for W=80mm, the R-curves for a_o/W=0.7 also suggest that failure may be controlled by shear. However, for a_o/W=0.5 both J_{init} and dJ/da for Mode I, J_{Icn} are similar to Mode II, J_{Icp} which suggests that failure may be controlled equally by tensile and shear loading. In figure (3.44a) the Mode I, J_{Icn} R-curves for a_o/W=0.5 are higher than the Mode I, J_{Icn} R-curves for a_o/W=0.7. However, in figure (3.44b), although the difference between the Mode II, J_{Icp} R-curves for W=20mm is negligible, for W=80mm the Mode II, J_{Icp} R-curve for a_o/W=0.5 is lower than the Mode II, J_{Icp} R-curve for a_o/W=0.7.

3.12 Microscopic Analyses

Of the specimens tested and subsequently reported in sections (3.8) for a_o/W=0.5 and (3.9) for a_o/W=0.7, a selection of them, representative of each combination of specimen thickness and width, and mode of loading, were examined using a standard binocular type microscope. Each specimen was sectioned along its length and

prepared using metallographic techniques to enable the crack growth, at specimen mid-thickness, to be examined. The procedure used for preparing each specimen is detailed in section (3.3.5).

Regardless of mode of loading and crack depth ($0.5<a_o/W<0.7$), blunting of the initial notch, followed by crack growth, was seen. Typical features are schematically illustrated in figure (3.45).

Essentially, for Mode I loading, notch tip blunting was symmetrical about the plane of the initial notch. The introduction of a Mode II component during loading, however small, caused asymmetric blunting of the notch tip where one side became blunt while the other remained sharp. The extent of asymmetry was proportional to the amount of Mode II present, as indicated in figure (3.45), and on the constraint imposed by the different size of specimen tested.

Crack initiation occurred from the nose of the blunted notch in the specimens loaded in Mode I. For Mode II loading, crack initiation occurred from the sharpened side of the deformed notch. However, for combined tension and shear loading, initiation occurred from the blunt side of the deformed notch.

The crack growth mechanism was also different in Mode I than in Mode II. In Mode I, the crack propagated in a zig-zag pattern, in the plane of the initial notch and additional blunting of the propagating crack tip was seen. In Mode II, a shear crack propagated near the original plane of the initial notch, in a self-similar manner and the tip of the propagating crack was always sharp. Essentially, for mixed mode loading, Mode II type crack growth was seen in each specimen. However, the acuity of the propagating crack tip was seen to decrease as the mode of loading decreased from Mode II to Mode I.

3.12.1 Pure Mode I Loading

For the specimens loaded in Mode I, regardless of specimen size, a variety of 'crack forming' processes were evident. In particular, deformation of the equi-axed grain structure was in close proximity of the newly formed crack flanks, within a 60μm boundary (normal to the crack flanks) and approximately 30μm ahead of the crack tip. The majority of nucleated microvoids were found within pearlite grains as cracked cementite platelets. However, there was evidence of microvoids having nucleated along the primary ferrite-pearlite and pearlite-pearlite grain boundaries (see figure 3.46). All grain boundary microvoids had nucleated along the grain boundaries orientated normal to the plane of the initial notch (parallel to the direction of applied load).

In each specimen, crack initiation occurred at the tip of the blunted notch. The preferred direction for the crack to propagate was towards pearlite colonies where a higher density of nucleated microvoids were present. In some specimens both Mn-S and carbide inclusions were found to assist the nucleation process and influence the crack propagation direction. In each specimen, although the local direction of crack propagation was typically zig-zag in shape, the global direction was in the plane of the initial notch, normal to the applied load.

3.12.2 Pure Mode II Loading

All specimens loaded in Mode II exhibited similar crack growth characteristics (see figure 3.47). As discussed above, asymmetric blunting of the notch tip caused one side to blunt and the other to sharpen. Ahead of the blunting notch tip, slip motion invariably caused distortion and elongation of the pearlite and ferrite grains, which increased with increasing load. The interaction between slip, which causes local discontinuities (dislocations) in the lattice structure, and blunting caused a pile-up of dislocations at the blunted notch tip. A crack initiated from the sharpened side of the blunted notch tip when the density of dislocation pile-ups had achieved a critical value. The subsequent release of stored energy at crack initiation caused the crack to

propagate. The distortion and dilation of the grain structure caused microvoids to nucleate (see figure 3.48), although mainly due to cracking of the cementite platelets within the pearlite grains. It was not clear though whether the nucleated microvoids grew as loading increased although failure of the inter-lamellae ferrite between the cementite platelets was seen in a large number of the pearlite grains. The initiated crack propagated at an approximate angle of θ=+22° from the plane of the initial notch, along the slip line field and through the thinner sections of the elongated grains (see figure 3.47). With increasing crack growth, the initiation angle decreased such that the overall crack propagation direction was parallel to the plane of the initial notch.

Distortion and dilation of the grain structure along the lower crack flank and ahead of the crack tip was wide spread and nucleated microvoids were abundant. Typical features seen around the blunting region and crack tip are shown in figures (3.49a) and (3.49b). Equi-axed grains were seen close to the upper crack flank where microvoid nucleation was both negligible and localised.

3.12.3 Mixed Mode Loading Through α=22.5°

For mixed mode loading through α=22.5°, two different size specimens were examined. One specimen was representative of high constraint (B=20mm, W=80mm), and the other of lower constraint (B=10mm, W=20mm). The main observation from comparing the two specimens (see figures 3.50a and 3.50b) was a difference in failure mechanism. Although both specimens exhibited asymmetric blunting of the initial notch tip, the degree of asymmetry (rotation and opening of the blunting notch tip) was more acute in the lower constraint geometry. The rotation angle from the plane of the initial notch for B=10mm, W=20mm was approximately 55° and for B=20mm, W=80mm the rotation angle was approximately 75°. Ahead of the deformed tip, dilation and distortion of the primary ferrite and pearlite grain structure was visible, although to a lesser extent at the tip of the sharpened side. The sharpened tip of both specimens was capped by a thin layer of pearlite grains and

there was no evidence of microcracking (see figure 3.51). Within this region, the appearance of nucleated microvoids was negligible.

Crack initiation occurred in both specimens from the blunt side of the deformed notch where the density of microvoids was highest. In the lower constraint geometry (B=10mm, W=20mm), crack propagation was via a shear type mechanism at an angle of approximately θ=+25° from the plane of the initial notch. Failure in the higher constraint geometry (B=20mm, W=80mm) was via a tensile type mechanism.

In the higher constraint geometry, local crack propagation was in a zig-zag pattern (see figure 3.50b) towards the densely populated pearlite regions, characteristic of a Mode I type failure mechanism. The appearance of microvoids was negligible throughout and the global direction of crack propagation was planar to the original notch. In the lower constraint geometry, crack propagation was via a shear type mechanism (see figure 3.50a), which was assisted by the presence of nucleated microvoids and plastic flow of the surrounding grain structure. The shear crack was seen to propagate along primary ferrite-primary ferrite and primary ferrite-pearlite grain boundaries, assisted by grain boundary microvoids. Propagation through pearlite grains due to cementite platelets cracking under the influence of plastic strain was also evident as shown in figure (3.52). Nucleated microvoids were seen along both flanks of the shear crack, although confined to within 15μm of either crack flank. The overall direction of crack growth was planar to the original notch. The crack propagated through the thinnest region of the dilated primary ferrite and pearlite grains. However, in some cases the density of nucleated microvoids within pearlite grains caused the crack to propagate through the grains length (see figure 3.52).

3.12.4 Mixed Mode Loading Through α=45.0°

For mixed mode loading through α=45.0° a range of different size specimens, typical of variations in geometric constraint, were examined where B=10mm and W=20mm, 40mm and 80mm, respectively for a_o/W=0.5. Each specimen exhibited asymmetric

blunting of the original notch tip due to simultaneous opening of the crack faces and clockwise rotation of the upper crack flank about the deforming notch tip. The rotation angle from the plane of the initial notch for B=10mm, W=20mm was approximately 43°. This is illustrated in figure (3.45). This combined motion caused one side of the notch tip to remain sharp while the other became blunt. Compared to the observed blunting characteristics of specimens loaded through α=22.5° and 67.5°, specimens loaded through α=45.0° exhibited a greater degree of notch tip rotation than α=22.5° (between 55° and 75° from the plane of the initial notch) but less than α=67.5° (approximately 30° from the plane of the initial notch). The converse was seen with the amount of crack face opening.

Microvoid nucleation around the sharpened side of the blunted notch of each specimen regardless of W was negligible. Moreover, as seen in specimens loaded through α=22.5° (for B=10mm, W=20mm) and 67.5° (for B=10mm, W=20mm), the nose of the sharpened side of the deformed notch tip in each specimen was capped by a thin layer of pearlite grains (as an example see figure 3.51 for α=22.5°). Plastic deformation, due to asymmetric loading, was wide spread and dilation and distortion of the surrounding grains was significant ahead of the deformed notch tip.

Regardless of the variation in constraint imposed by the different size of specimen studied, in each case a crack initiated from the blunt side of the deformed notch tip (see figure 3.53) where the density of nucleated microvoids was highest. The crack initiated at an angle of approximately θ=+23° from the plane of the original notch. Crack propagation was via a shear type mechanism, which was assisted by the presence of nucleated microvoids and plastic flow of the surrounding grain structure. A shear crack propagated along primary ferrite-primary ferrite and primary ferrite-pearlite grain boundaries, assisted by grain boundary microvoids, in the direction of the plastically deforming grains. Propagation through pearlite grains due to cementite platelets cracking under the influence of plastic strain was also evident. Nucleated microvoids were seen along both flanks of the shear crack, within 15 to 20μm of either crack flank.

3.12.5 Mixed Mode Loading Through α=67.5°

For mixed mode loading through α=67.5°, a range of different size specimens were examined which were representative of high (B=20mm, W=80mm), medium (B=10mm, W=40mm) and low (B=10mm and W=20mm) constraint conditions. The crack profiles for B=10mm, W=20mm is shown in figure (3.54). Each specimen exhibited asymmetric blunting of the notch tip due to simultaneous opening of the crack faces and clockwise rotation of the upper crack flank about the deforming notch tip. This combined motion caused one side of the notch tip to remain sharp while the other became blunt. Compared to the observed blunting characteristics of specimens loaded through α=22.5° and 45.0°, specimens loaded through α=67.5° exhibited a greater degree of notch tip rotation. The rotation angle for B=10mm, W=20mm was approximately θ=+30° from the plane of the original notch. The converse was seen with the amount of crack face opening.

As shown in figure (3.55) microvoid nucleation on the sharpened side of the deformed notch tip was negligible although there was evidence of microcracking. Moreover, as seen in specimens loaded through α=22.5° and 45.0°, the tip of the sharpened side of each specimen was capped by a thin layer of pearlite grains (see figure, 3.55). Plastic deformation, due to asymmetric loading, was wide spread and dilation and distortion of the surrounding grains was significant ahead of the crack tip, although to a much lesser extent at the sharpened tip.

Regardless of the variation in constraint imposed by the different size of specimen studied, in each case a crack initiated from the blunt side of the deformed notch tip where there was a high population of nucleated microvoids. The initiation angle was influenced by the development of the slip line field. However, the angle was less (approximately θ=+13° to the plane of the original notch for B=10mm, W=20mm) than seen during Mode II loading. The variation of initiation angle for the different size of specimen examined was negligible. As seen in Mode II, the initiation angle decreased with increasing crack growth such that the final direction of crack growth was planar with the original notch.

Crack propagation was via a shear type failure mechanism, traversing through the thinner sections of the dilated primary ferrite and pearlite grains. Nucleated microvoids were seen along the upper and lower crack flanks. Although not as wide spread as seen in Mode II, microvoids were found within a 10μm distance from the upper crack flank and approximately 30μm from the lower crack flank. Nucleated microvoids were abundant at the shear crack tip and the crack propagation path was seen to depend on the location of the microvoids, especially those within pearlite patches. It was ahead of the propagating crack and beneath the lower crack flank that dilation and distortion of the surrounding grains was wide spread. The grain structure remained relatively equi-axed above the upper crack flank, beyond the region of nucleated microvoids.

3.13 Mixed Mode I/II Limit Load Solutions

When failure conditions are governed by plastic collapse Miller (1988) proposes the use of limit load analyses to calculate the maximum load (the limit load) that a given structure made of a perfectly plastic material can sustain. Complete solutions are hard to calculate, but upper and lower bound limit load theorems can be determined by considering the strain and stress fields, respectively. However, usually a safe (conservative) estimate of the load carrying capacity of a structure is required and a lower bound is more appropriate.

A plastic analysis may be used to determine the limit load for a given combination of loads on a given structure. Experimentally, the limit load can be determined directly from a load versus displacement (or load versus strain) curve. The angle that the linear part of the load versus displacement curve makes with the load (Y) axis is called γ. A second straight line (the collapse limit line) is drawn through the origin so that it makes an angle ϕ (equation 3.15) with the load axis, such that

$$\phi = \tan^{-1}(2\tan\gamma) \tag{3.15}$$

The collapse load is the load at the intersection of the load versus displacement (or load versus strain) curve and the collapse limit line.

For each combination of B, W and mode of loading from which R-curves were generated, the limit loads for $a_o/W=0.5$, given in table (3.28), were calculated from experimental load versus load line displacement curves from specimens that had been loaded to maximum load, using the procedure described above. Figure (3.56a) shows the effect of specimen width (constant thickness, B=10mm) and figure (3.56b) shows the effect of specimen thickness (constant width, W=20mm) for mixed mode I/II loading as loci of shear load (Q) versus tensile load (N). The analytical expression for combined tension and shear loading, proposed by Miller (1988) for a deep crack SEN specimen, given by equation (3.16) is also shown for comparison for each different size of specimen tested.

$$\left(\frac{N}{N'}\right)^2 + 1.03\left(\frac{Q}{Q'}\right) = 1 \qquad (3.16)$$

where N′ and Q′ depend on the flow strength (σ_{flow}) of the material and the size of specimen.

$$N' = \sigma_{flow}\left(W - a_o\right)B \qquad (3.17)$$

$$Q' = \frac{\sigma_{flow}\left(W - a_o\right)B}{2} \qquad (3.18)$$

where

$$\sigma_{flow} = \frac{\sigma_{ys} + \sigma_{UTS}}{2} \qquad (3.19)$$

The data for W=20mm and 40mm, shown in figure (3.56a), compare well with Miller's (1988) solution. The data for W=80mm also exhibit similar behaviour

except for Mode I loading which is much lower than predicted. Using the material properties given in table (3.2), the flow strength (σ_{flow}) of A508 is typically 497MPa. Based on the ligament area ahead of the crack tip, given by $B(W-a_o)$, for W=80mm a limit load of approximately 199kN would be expected. For W=20mm and 40mm the estimated limit loads based on σ_{flow} are 49.7kN and 99.4kN, respectively, which are very close to the experimental Mode I limit loads given in figure (3.56a). Although limited for B=20mm and 40mm, the data presented in figure (3.56b) appear to follow the locus given by Miller's (1988) analytical expression. However, for B=40mm, Miller's (1988) is very conservative.

Figures (3.57a) and (3.57b) show the mixed mode I/II experimental limit loads (given in table 3.29) for $a_o/W=0.7$, which are also compared with Miller's (1988) analytical expression (equation 3.16). Miller's limit load predictions for B=10mm and W=20mm, shown in figures (3.57a) and (3.57b) are conservative, however they are consistent throughout the range of mixed mode loading. For B=10mm and W=80mm (see figure 3.57a), the data for Mode I loading is significantly lower than the value predicted by Miller (1988). However, for Mode II and mixed mode loading through $\alpha=45.0°$, although conservative, equation (3.16) does show the data trend. Similarly, in figure (3.57b) for B=20mm, equation (3.16), although very conservative, does show the data trend.

3.14 Small Scale Plain Sided Mode II Specimen Results

In sections (3.8), (3.9) and (3.10) it was demonstrated that the effect of specimen size had a negligible effect on the size and shape of the R-curve for specimens subject to Mode II loading. Moreover, it has been demonstrated that master curves, unique only to a_o/W, can be used to describe the tearing behaviour of any size of specimen subject to Mode II loading. This section addresses the issue of a master curve by investigating whether the controlling mechanism of Mode II failure is governed by the microstructure.

Three sets of 5 specimens were used in these investigations. The first set of tests were done on parent material. The second and third sets of tests were done on specimens subject to two completely different heat treatments which are described in detail in section (3.3.6). The microstructures of set 1 (parent material), set 2 and set 3 are shown in figures (3.2) and (3.13).

The results of each test are given in table (3.30) and the corresponding shear load (P_s) versus shear displacement (Δ_s) curves are shown in figure (3.58). Both sets 1 and 3 exhibited similar maximum loads prior to load drop off which was seen to be more rapid in set 1. The specimens in set 2 achieved substantially higher loads and less ductility (Δ_s beyond yield) than sets 1 and 3.

Using the analysis procedure detailed in section (3.5) resistance curves were generated for each set of specimens as a function of fracture energy, U_{II} (calculated using equation 3.13) and crack growth, Δa. The data for each material condition are shown in figure (3.59). It is clear that regardless of microstructure and the differences seen in the P_s versus Δ_s curves (see figure 3.58), all of the data can be described by a master curve.

It is clear from figure (3.59) that the data beyond Δa=0.7mm does not compare well with the master curve. That is because the shear crack in each of these specimens has propagated through a significant proportion of the initial uncracked ligament length ($W-a_o$) of 2.5mm. For Δa=0.7mm, the shear crack has propagated through 28% of the initial ligament length. Essentially, for such a high percentage of crack growth unstable tearing would be prominent.

CHAPTER 4 : FINITE ELEMENT ANALYSES

Finite Element (FE) analyses using ABAQUS (1997) were employed to determine elastic and plastic functions that are necessary to enable the J-Integral to be calculated directly from load and displacement data. These results were recorded from laboratory test specimens (Chapter 3.0). Further studies in this research have demonstrated the applicability of the analyses to provide a qualitative prediction of the direction of crack propagation for loading in Mode I, Mode II and mixed mode loading through α=45.0°. The calculated elastic and plastic functions were found to compare well with the limited data available in the open literature. Moreover, the capability of the model to predict the direction of crack propagation for a range of mode mixities also compared well with the direction of crack propagation observed in the experiments.

Section (4.1) provides a complete description of the FE model. Section (4.2) describes the methods used to determine the elastic and plastic functions that enabled J to be calculated from a load versus displacement record of a laboratory test specimen. Section (4.3) demonstrates how the FE model can be used to provide a qualitative description of the direction of ductile crack propagation and section (4.4) compares the results from the model with those reported in the open literature.

4.1 The Finite Element Model

A full scale 2-dimensional plane strain FE model of a single edge notch (SEN) specimen (figure 2.3) located within the mixed mode loading fixture (figure 3.4) was developed using ABAQUS (1997). The FE mesh is shown in figure (4.1). The fixture and specimen were designed as a single unit with a rigid connection between the internal edges of the loading fixture and the outer surface of the specimen. Mode I loading was applied by loading through nodes 1. Mode II loading was applied by loading through nodes 5. Mixed mode loading was applied by loading through either nodes 2, 3 or 4. For combinations of tension and shear, until Mode II loading, the x-y

co-ordinates of the nodal points which were used to define the overall mesh size, shape and orientation, were translated through increments of $\Delta\alpha$=22.5°, corresponding to the required mode mixity. That is, regardless of mode mixity, the load was always applied in the +Y direction (see figure 4.1), directly through the crack tip. For each analysis, the lower loading node was constrained to inhibit displacement in the X and Y directions but, at the same time enable friction free rotation about the anchored node. The upper loading node was constrained in the X direction only thus enabling friction free rotation about the node and movement in the Y direction. The loading was always applied through the node in the upper loading fixture.

As described in sections (2.3.1), (3.3.1) and (3.3.2), clevis grips were used to couple the mixed mode loading fixture to the upper and lower loading rods of the test machine. Essentially, clevis grips constrain movement in the X, Y and Z directions but allow free rotation in the X-Y plane due to pin loading. The clevis grip that was used to couple the mixed mode loading fixture to the hydraulic ram, the moving part of the test machine, moved with the hydraulic ram in the vertical, Y, direction while the specimen was being loaded. For these reasons the boundary conditions described in the preceding paragraph were imposed on the upper and lower loading nodes of the FE model.

Eight-noded plane strain quadrilateral elements (type CPE8R) were used to construct the mesh. The crack tip was modelled as a key-hole notch with a radius of 0.05mm (see figure 4.1). This was to ensure that the profile of the crack tip resembled as near as possible the profile of the crack tip in the specimens since each notch was produced by electrical discharge machining (EDM) and not fatigue precracked.

The crack tip region was modelled using 24 rows of 32 circumferential elements, biased so that the size of each element increased with increasing distance from the crack tip. Regardless of crack depth (a_o/W=0.1, 0.5 and 0.7) 24 rows of elements were always used to define the core region. However, the size and position of the core region in relation to the specimen boundary surfaces did vary. Figure (4.2)

shows the size, position and relevant dimensions of each core region, corresponding to the different crack depths investigated.

The nodal positions of the loading fixture were fixed regardless of size of specimen and crack length. However, the nodal co-ordinates used to define the specimen boundary and the internal edges of the loading fixture were adjusted to suit the range of specimen widths examined in the experiments (W=20mm, 40mm and 80mm) and to ensure that the load was always applied directly through the crack tip.

A Young's modulus (E), of 400GPa (approximately two times the value of the A508 Class 3 C-Mn steel forging used in the experiments) was used to describe the stiffness of the loading fixture. This was considered sufficient to ensure that plastic deformation occurred in the specimen only and the results from the FE analyses were representative of the crack tip region only. Stress and plastic strain data for A508 (Davenport, 1993) was converted to true stress and log plastic strain, and used in the ABAQUS input file to define the plastic behaviour of the specimen material. The stress versus plastic strain data corresponding to the short transverse rolling direction was used since this direction corresponded to the principal straining direction of each specimen used in the laboratory experiments.

The FE model was designed to enable a series of elastic and plastic functions, used for fracture mechanics calculations, to be calculated for each size of SEN specimen shown in figure (3.3). From these functions the fracture toughness of each specimen can be calculated directly from a laboratory test record of load and displacement. However, additional studies have demonstrated that the model can also be used to predict the direction of crack propagation regardless of mode of loading. The technique has been validated from experiments for specimens loaded in Mode I, Mode II and mixed mode (α=45.0°).

The results from the analyses to determine the elastic and plastic functions, and a description of the technique used to predict the direction of crack propagation are detailed in the proceeding sections.

4.2 Elastic and Plastic Functions for Mixed Mode Loading

Both linear-elastic and elastic-plastic studies, using the FE models described in section (4.1) were performed to enable the elastic geometry functions, $f_I(\alpha, a_o/W)$, $f_{II}(\alpha, a_o/W)$ and the elastic and plastic factors, η_e and η_p for mixed mode loading to be calculated. Each function is sensitive to mode of loading, crack length and to a lesser extent specimen size. The subscripts I and II refer to the Mode I and Mode II components of mixed mode loading, respectively and the subscripts e and p refer to the elastic and plastic components of load, respectively. The symbol α refers to the mixed mode loading angle (for Mode I and Mode II loading α=0.0° and 90.0°, respectively) and a_o/W refers to the crack depth in relation to the specimen width. For the case of pure Mode I loading, $f_{II}(\alpha, a_o/W)$ is zero. Likewise, for Mode II loading, $f_I(\alpha, a_o/W)$ is zero. For mixed mode loading however, $f_I(\alpha, a_o/W)$ and $f_{II}(\alpha, a_o/W)$ are dependent on the relative magnitude of mode mixity. Moreover, regardless of mode of loading, η_e and η_p are non-zero. However, for the elastic case only, η_p is zero.

4.2.1 Mixed Mode Elastic Geometry Functions

The use of geometry functions to derive values of linear-elastic fracture toughness (stress intensity factor, K) is well established. Although a number of analytical solutions have been developed for an extensive range of specimen geometry and crack configurations, they mainly refer to pure mode loading situations (Tada et al., 1973, 1985). There have been limited studies that attempt to extend the solutions to mixed mode loading (Hellen and Blackburn, 1975 and Davenport, 1993). Davenport (1993) used BERSAFE, an FE code developed for 'in-house' use by British Energy plc., to model mixed mode loading of an SEN specimen in a unique mixed mode loading fixture which has been used in this present experimental study (chapter 2). He calculated values of $f_I(\alpha, a_o/W)$ and $f_{II}(\alpha, a_o/W)$ using displacement separations of an effective stress intensity factor, K_{eff} that was calculated from the energy release rate, G (Hellen, 1975).

A simpler technique was employed using ABAQUS to determine $f_I(\alpha, a_o/W)$ and $f_{II}(\alpha, a_o/W)$ for different mode mixities. For each mode mixity, stress intensity factors, K_I and K_{II} were calculated from the displacements of a pair of nodes along the crack faces. Using the asymptotic stress field, the stress intensity factor ratio of K_{II}/K_I can be expressed using the formulae given in the ABAQUS users manual (1997) which is

$$\frac{K_{II}}{K_I} = \lim_{(x_1 \to 0)} \left[\frac{u_1(x_1,+) - u_1(x_1,-)}{u_2(x_1,+) - u_2(x_1,-)} \right] = R_\Delta \qquad (4.1)$$

where u_1 and u_2 refer to nodal displacement in the x and y directions, respectively, and + and - is the sign convention used to define the upper and lower crack faces, respectively. The ratio K_{II}/K_I was obtained from the numerical results by taking the displacements at a pair of nodes behind the crack tip (at a distance not greater than 10% of the crack length). Once J and R_Δ were known, the separate stress intensity factors were estimated assuming plane strain conditions and $K_{III}=0$, using the equation (ABAQUS, 1997) given below

$$K_I \cong \sqrt{\frac{EJ}{(1+R_\Delta^2)(1-\nu^2)}} \qquad (4.2)$$

$$K_{II} \cong R_\Delta K_I \qquad (4.3)$$

where ν refers to Poisson's ratio.

Having calculated K_I and K_{II}, $f_I(\alpha, a_o/W)$ and $f_{II}(\alpha, a_o/W)$ were calculated from equations (2.4) and (2.5), respectively. The results for $f_I(\alpha, a_o/W)$ and $f_{II}(\alpha, a_o/W)$, calculated from the plane strain FE analyses are given in tables (4.1) through to (4.3) and shown in figures (4.3) through to (4.5) for each combination of a_o/W and W.

4.2.2 Mixed Mode η Factors

The use of η factors to convert load and displacement data into representative values of fracture toughness based on the J-Integral is well established (Sumpter and Turner, 1976, Wu et al., 1990, Sharobeam and Landes, 1991 and Davenport, 1993). However, for mixed mode loading, η factors are less well known. Using FE, Davenport (1993) determined values of η_e and η_p for an SEN specimen (B=W=20mm, a_o/W=0.5) subject to combinations of tensile and shear loading under plane strain conditions. He achieved similar values to those presented in the literature for loading in Mode I and Mode II.

Using an approach similar to the method proposed by Davenport (1993), the FE code ABAQUS was used in the present study to determine η_e and η_p. Regardless of specimen geometry and mode of loading the procedure used to determine η factors was consistent throughout this study.

The method to determine η_e and η_p is relatively straight forward. The analysis for calculating η_p however requires more computational time than for η_e. The value of η_e is constant regardless of applied load and was calculated from the initial load increment, using equation (3.2), where the magnitude of U_p (plastic dissipation) is zero compared to U_e (recoverable strain energy). As U_p is zero, equation (3.2) could be rearranged to find η_e such that

$$\eta_e = \frac{JB(W-a_o)}{U_e} \tag{4.4}$$

Having calculated η_e, equation (3.2) could be rearranged to calculate η_p for increasing plastic deformation. The solution for η_p could be expressed as

$$\eta_p = \frac{JB(W-a_o)-\eta_e U_e}{U_p} \tag{4.5}$$

As the load increases, U_p increases and the terms from the elastic part become relatively small in comparison. Values of η_p were calculated from equation (4.5) as the load was incremented in the FE model. The loci of η_e and η_p for increasing plasticity (defined by the ratio of U_p/U_e) are shown in figure (4.6). The initial value of η_p was large but decreased with increasing plasticity until a steady state value was achieved. It is the steady state value of η_p, and the corresponding constant η_e that was used to calculate J from the area beneath a load versus displacement curve. In contrast, the locus of η_p presented by Davenport (1993) shows η_p increasing with increasing plasticity until a steady state value is achieved. By definition (see equation 4.5), as U_p approaches zero η_p would approach infinity, hence the reason for η_p to approach zero in Davenport's (1993) analyses is somewhat confusing. Nevertheless, the values of η_p calculated by Davenport (1993) for large values of U_p/U_e compared well with the present results.

For the 10mm thick specimens, η_e and η_p for each combination of W (20mm, 40mm and 80mm), a_o/W (0.1, 0.5 and 0.7) and mode of loading are given in tables (4.4) through to (4.6). The results are also shown graphically in figures (4.7) through to (4.10). Plane strain analyses were performed throughout, hence the η factors for B=10mm also refer to B=20mm and 40mm.

For the short crack geometries ($a_o/W=0.1$) steady state values of η_p could not be achieved since J, calculated by ABAQUS for each increment of load, became progressively path dependent with increasing plasticity. For J to be valid, path independence must be maintained regardless of applied load and the plastic zone must be able to develop uninhibited. However, at a relatively small load the plastic zone in the short crack specimens spreads to the boundary of the specimen, hence the J integral was no longer valid since J dominance was lost.

During the experiments, size effects in short crack ($a_o/W=0.1$) specimens were studied only in Mode I and Mode II loading since there was insufficient material to do further studies. Consequently, η_e and η_p were determined for Mode I and Mode II loading only. For each loading case, η_p was calculated for decreasing a_o/W

(a_o/W=0.4, 0.3 and 0.2) until a solution for η_p could not be found. The results for W=80mm are shown in figure (4.7). The values of η_p for decreasing a_o/W were then fitted with a polynomial curve and the resultant equation was used to extrapolate a value of η_p for a_o/W=0.1. This technique was used to calculate η_p in Mode I and Mode II loading for W=20mm, 40mm and 80mm, respectively.

As shown in figures (4.8), (4.9) and (4.10) the η factors are relatively insensitive to changes in W and a_o/W. To illustrate this further, loci of η_e and η_p for W=40mm are plotted as a function of α for a_o/W=0.1, 0.5 and 0.7 in figure (4.11). However, for a_o/W=0.1, η_e are higher throughout the range of mixed mode loading compared with a_o/W=0.5 and 0.7 which are similar. Also, the locus for W=20mm and a_o/W=0.1 does not compare with the curves for mixed mode loading (α=22.5°, 45.0° and 67.5°) for W=40 and 80mm which are similar. The differences however are not observed in Mode I or Mode II loading.

4.3 Simulation of Mixed Mode Crack Propagation

The aim of these investigations was to demonstrate the capability of the FE model to give a qualitative description of the direction of crack propagation. As discussed in chapter 3, ductile fracture occurs by growth and coalescence of microvoids that have nucleated from inclusions and second phase particles. The bulk of past research has been concerned with the case of Mode I loading. However, more recently, investigations have attempted to model the ductile fracture processes of steels subject to mixed mode I/II loading.

For Mode I loading a number of investigators have concluded that microvoid initiation obeys a critical stress criterion. However, for some steels, such as A508, the critical stage for ductile fracture is void growth (Beremin, 1981 and Lautridou and Pineau, 1981). For A508, the state of stress at the tip of a crack at initiation is of sufficient magnitude that the corresponding strains are relatively small. McClintock (1968), Rice and Tracey (1969) and Gurson (1977) have demonstrated that, in addition to an exponential dependence on stress state, void growth is controlled by

plastic equivalent strain. The potential of these models has been improved upon since their introduction and they now take into account, for example, variations in size, shape and distribution of microvoid initiating particles, and interactions between neighbouring voids.

Employing Gurson's (1977) constitutive equation, Aoki et al. (1987) demonstrated that, in the presence of mixed mode I/II loading, one side of the notch tip sharpened while the other side blunted. Plotting the void volume fraction and equivalent plastic strain near the notch tip for various mixed mode I/II ratios, Aoki et al. (1987) proposed that a competition exists between the blunted and sharpened sides of the deformed notch tip, moreover that there exists a change in failure mechanism (a competition between tensile and shear dominated failure). They proposed that for a high Mode I loading component, crack initiation occurred from the blunted side where the plastic equivalent strain and void volume fraction were higher. In contrast, for a high Mode II loading component, the equivalent plastic strain and void volume fraction were higher on the sharpened side, corresponding to the direction of maximum shear. Bhattacharjee and Knott (1994) observed that although Aoki et al. (1987) correctly predicted the shape of the deforming notch tip, their analysis did not accurately predict the damage accumulation and crack initiation direction. Bhattacharjee and Knott (1994) concluded that the observed change in failure mechanism was dependent on a number of factors such as strength, work hardening characteristics, inclusion size and distribution and the nature of the carbide precipitates and that a true mixed mode fracture criterion should account for each of these factors combined.

However, the existing ductile fracture criteria for mixed mode loading fail to predict the path of crack propagation in the ductile regime. The intention of the investigations in this study was to examine the feasibility of a simple FE analysis to qualitatively predict the path of crack propagation for the material examined in the laboratory experiments: A508 class 3 C-Mn pressure vessel steel.

For this study, only one SEN specimen size was considered (B=20mm, W=20mm and $a_o/W=0.5$), subject to three different loading conditions: Mode I ($\alpha=0.0°$), Mode II ($\alpha=90.0°$) and mixed mode loading through $\alpha=45.0°$.

Each analyses comprised of incrementally loading the specimen to a collapse load which was determined from the laboratory experiments. Seven loading increments were used. For each load increment, plastic equivalent strain (ε_{eq}) contours were analysed with respect to r (radial distance from the crack tip) and θ (polar angle measured from the plane of the crack where $\theta=\theta_o=0.0°$) to find the maximum distance and corresponding direction from the crack tip that ε_{eq} achieved a value corresponding to yield.

For mode I loading, the strain contours, compared with the crack propagation path observed in a typical laboratory experiment (in specimens of identical dimensions), are shown in figure (4.12). Although the FE method does not demonstrate the zig-zag nature of a propagating crack as seen in the experiments, it does show that the global direction of crack propagation can be qualitatively described by the competition between the ε_{eq} loci which are symmetrical about the crack tip with increasing load. The apparent competition between the two loci may give rise to the zig-zag path of the propagating crack.

The same method was used to predict the direction of crack propagation for Mode II loading and mixed mode loading through $\alpha=45.0°$. The FE predictions compare well with the crack propagation path observed in typical laboratory experiments as shown in figure (4.13) for Mode II, and figure (4.14) for mixed mode loading through $\alpha=45.0°$. Moreover, as seen in the experiments, the FE model predicts that the crack initially propagates at an angle to the plane of the initial notch and as the crack continues to propagate the angle decreases until propagation is in the plane of the initial notch.

4.4 Comparison with Other Studies

In a separate study, using ABAQUS, Ayatollahi (1998) also developed a full size, 2-dimensional FE model of the mixed mode loading fixture and SEN specimen used in the laboratory experiments. He designed the crack tip region using 27 rows of 36 circumferential eight-noded plane strain elements. However, unlike the model described in section (4.1), Ayatollahi (1998) modelled the crack tip as an infinitely sharp crack such that the first circumferential row of nodes were collapsed onto a single co-ordinate point. The mixed mode loading fixture was assumed linear elastic and given a Young's modulus value of three times that of A508 (see table 2.9). This was to account for rigidity of the loading fixture, thus ensuring that all plastic deformation was confined to the specimen. The deformation characteristics of the specimen, described in section (4.1), were also used by Ayatollahi (1998).

He developed three models to simulate various methods of connecting the loading fixture to the SEN specimen. However, only the model which incorporated contact elements between the internal edges of the loading fixture and SEN specimen was used to compare the results calculated from the model described in section (4.1). An SEN specimen (B=10mm, W=20mm, a_o/W=0.5mm) was analysed in Mode I, Mode II and mixed mode loading through α=45.0°.

In figure (4.15) the load versus displacement curves from the FE models and laboratory experiments are compared. Since neither FE model reflects the stiffness associated with the elastic loading of the test machine used in the experiments, the experimental loci shown have been corrected for extraneous elastic displacements. This has been done using the stiffness calibration functions given in tables (3.4) through to (3.11). It is evident that regardless of mode mixity, the FE curves compare well with the experiments.

There was also good agreement between the elastic geometry functions, $f_I(\alpha, a_o/W)$ and $f_{II}(\alpha, a_o/W)$, calculated for each mode of loading (see figure 4.16). The numerical results presented by Davenport (1993), and the pure Mode I and Mode II

analytical solutions proposed by Tada et al. (1973, 1985), given in equations (2.3) and (2.6), are also in good agreement for $a_o/W=0.5$. The results shown in figure (4.16) also suggest that the elastic geometry function is independent of specimen size but dependent on mode of loading. The analytical solutions proposed by Tada et al. (1973, 1985) also confirm this since they consider crack length in relation to specimen width (a_o/W) only.

Mixed mode I/II solutions for elastic and plastic η factors are not common and only Davenport (1993) has presented results for a mixed mode I/II loading fixture and SEN specimen geometry similar to the fixture and loading combination used in this study. Davenport's (1993) results are shown in figure (4.17), compared with the η factors calculated from limited mode mixity plane strain studies using Ayatollahi's (1998) contact model and the results presented in table (4.5) for a similar size specimen.

Irrespective of the variation of load and displacement between the contact model and the results presented in table (4.5), the η factors are in good agreement with those reported by Davenport (1993). Moreover, elastic mixed mode η factors, like the elastic geometry functions (figures 4.3, 4.4 and 4.5), are independent of specimen size but dependent on mode mixity.

Wu et al. (1990) proposed a series of analytical solutions for η_p although only for pure Mode I loading. These are

$$\eta_p = \frac{\left(1-a_o/W\right)\left[1.702-\dfrac{2.144\left(2a_o/W-1\right)}{\left[\left(2a_o/W-1\right)^2+0.5876\right]^{0.5}}\right]}{0.3507-1.702a_o/W+1.072\left[\left(2a_o/W-1\right)^2+0.5876\right]^{0.5}} \qquad (4.8)$$

for $a_o/W \geq 0.545$, and for $a_o/W < 0.545$

$$\eta_p = 1 + \left[\frac{2.205}{\zeta} - \frac{0.441}{0.9 + 0.4\zeta + 0.6\sqrt{0.9 + 0.4\zeta}}\right]\frac{a_o/W}{\left(1 - a_o/W\right)^2} \qquad (4.9)$$

where

$$\zeta = 1 + 1.1025\left(\frac{a_o/W}{1 - a_o/W}\right)^2 \qquad (4.10)$$

Wu et al. (1990) based the solutions on slip line field analyses for a variety of commonly used fracture mechanics specimens, comprising deep and shallow notches. Their results for an SEN specimen, calculated from equations (4.8) through to (4.10), are shown in figure (4.18) together with the results presented in tables (4.4), (4.5) and (4.6) for Mode I loading. Wu et al. (1990) also proposed that η_p was independent of specimen size but dependent on a_o/W. Both the numerical and analytical results, shown in figure (4.18), compare well for a_o/W=0.5 and 0.7, although the numerical results indicate a dependence on W, albeit slight. However, the results do not agree for a_o/W=0.1.

A possible reason for the disagreement may be due to the boundary conditions in the FE model between the specimen boundary and loading fixture (refer to section 4.1). Essentially, the rigid connection between the specimen and loading fixture constrains the development of the plastic zone around the crack tip since necking of the specimen is inhibited due to the idealised stiffness of the loading fixture. For the deeply cracked specimens (a_o/W=0.5 and 0.7) the crack tip may have been sufficiently far from the specimen boundary that any effect imposed by the boundary conditions was small. Consequently, any possible error in η_p would be less than for the shallow crack specimens. As the depth of crack decreases, the crack tip approaches the specimen boundary and any subsequent error in η_p would therefore increase. As a result the η_p factors calculated in this present study for a_o/W=0.1 may be artificially high.

Despite the rigidity of the FE model described in section (4.1), from the comparisons of results presented above it is evident that the rigid model can be successfully used to calculate the elastic and plastic functions that are necessary to determine the fracture toughness of a laboratory specimen directly from the load and displacement record. Moreover, the rigid model can also be used to give a qualitative description of the direction of crack propagation by examination of the contours of equivalent plastic strain.

CHAPTER 5 : DISCUSSION

The experimental results and metallurgical studies presented in Chapters 2 and 3 are discussed in terms of previous work in the field of mixed mode I/II fracture. The aim of this chapter is to present a general discussion of the trends and major findings, and to make comparisons with investigations presented in the literature. Some of the results discussed here are unique to this research and have not been previously presented by other researchers. However, a rationalisation concerning their effect on mixed mode fracture will be made taking account of current theory.

Section 5.1 deals with the research investigating the effect of warm prestress on mixed mode brittle and ductile fracture while section 5.2 deals with the research investigating the effect of shear and constraint on ductile mixed mode fracture.

5.1 The Effect of Warm Pre-Stress on Mixed Mode Brittle and Ductile Fracture

5.1.1 Fracture Toughness

For brittle fracture, without the presence of near crack tip plasticity, the maximum tangential stress (MTS) criterion (Erdogan and Sih, 1963), detailed in section (1.2.2), postulates that the ratios of K_{II}/K_{Ic} and K_I/K_{Ic} vary according to

$$\frac{K_I}{K_{Ic}}\cos^3\left(\frac{\theta_o}{2}\right)-\frac{3}{2}\frac{K_{II}}{K_{Ic}}\cos\left(\frac{\theta_o}{2}\right)\sin\theta_o=1 \qquad (5.1)$$

where θ_o is the fracture angle that satisfies

$$K_I\sin\theta_o+K_{II}\left(3\cos\theta_o-1\right)=0 \qquad (5.2)$$

The fracture locus for the MTS criterion is shown in figure (5.1) together with the experimental results shown in figures (2.7, 2.13 and 2.20) which have been normalised with respect to K_{If}. K_{If}, the average Mode I non-proof loaded (NP) fracture toughness (see table 2.5) has been used instead of K_{Ic} to avoid ambiguity with plane strain definitions of fracture toughness. For $K_I/K_{If}>0.4$, the mixed mode experimental results, for the NP condition, lie near to the predicted MTS fracture locus. It appears that irrespective of increasing plasticity with increased mixed mode loading, fracture for $K_I/K_{If}>0.4$ can be adequately described by the MTS criterion. However for $K_I/K_{If}<0.4$ this criterion would overestimate the failure load. This is because with increasing plasticity, failure was close to plastic collapse.

The MTS criterion, however, does not take account of the influence of prior loading and hence cannot provide a qualitative assessment. Nevertheless, there are models in the literature (Curry, 1983, Chell and Haigh, 1986 and Smith, 1987) which are capable of predicting the benefits produced by the application of LUCF, LCUF or LCF WPS cycles. These models are only capable of assessing the benefits of a Mode I proof load on Mode I fracture toughness. A simplified and lower bound form of the model proposed by Chell and Haigh (1986) is given by

$$\frac{K_{LUCF}}{K_{Ic}} = 0.2\frac{K_I}{K_{Ic}} + 0.87 \qquad (5.3)$$

where K_{LUCF} is the applied stress intensity factor for low temperature after an LUCF WPS proof load, K_I is the applied proof load stress intensity factor and K_{Ic} is the fracture toughness at the low temperature.

Using equation (5.3), the Mode I fracture toughness, K_{LUCF} based on an initial Mode I proof load (MIP) can be determined. At room temperature, MIP gave K_I to be 131MPa$\sqrt{m}$ and by equating K_{If} at fracture (-120°C) to K_{Ic} in equation (5.3) gives K_{LUCF}=94MPa$\sqrt{m}$. This is an increase of 20% on the low temperature load bearing capacity. The experimental value of K_{LUCF} was 103MPa$\sqrt{m}$, corresponding to an actual increase of 32%. However, the magnitude of this increase may be misleading since the NP experimental data exhibits significant scatter.

The increase in toughness arises because near crack tip compressive residual stresses are generated following an MIP (Curry, 1983, Chell and Haigh, 1986 and Smith and Garwood, 1990a). If it is postulated that the inherent material toughness remains unchanged, there is an apparent increase in lower shelf fracture toughness because compressive residual stresses have to be overcome prior to fracture. With the introduction of plasticity prior to final fracture, compressive residual stresses are relaxed and their beneficial effect can be diminished. This was observed by Smith and Garwood (1990b; 1992) where the benefit of the WPS decreased as the fracture temperature increased.

Chell et al. (1979) proposed that the relative size of plastic zone created during the initial loading and unloading, and final fracture events could also provide a measure of benefit, again specific to Mode I WPS followed by Mode I fracture. They propose three cases which can be used to assess whether, in Mode I loading an LUCF WPS can enhance the low temperature fracture characteristics of a structural component. Each case has been described in detail in Chapter 1, section 1.5.2.

Applying each case to assess the influence of a Mode I, room temperature proof load, on Mode I fracture behaviour at -120°C, using approximate values of K_{If} and K_I of 103MPa$\sqrt{m}$ and 87.6MPa$\sqrt{m}$ respectively, and σ_{ys1} and σ_{ys2} of 358MPa and 565MPa, respectively, the models given in equation (1.44), (1.46) and (1.48) predict that a Mode I benefit is gained from a Mode I WPS. This is based on satisfying case 2, given by equation (1.46), where the size of the plastic zone at fracture is greater than the unloading plastic zone but smaller than the initial loading plastic zone.

This can be justified further by estimating the size of plastic zone created during initial loading and unloading, and at fracture. Given that the plane strain plastic zone size, r_p is proportional to $(K/\sigma_{ys})^2/3\pi$, on initial loading, r_p=6.35mm, and at fracture, r_p=3.53mm. The unloading plastic zone is approximately one quarter of the size of the initial loading plastic zone, giving r_p=1.59mm.

For increasing shear loading the experiments show that there was not as great an increase in low temperature toughness after MIP as there was for Mode I. This was a

direct consequence of the increase in plasticity relaxing the compressive residual stresses. In pure shear after MIP, compressive residual stresses had been completely removed, and there was no increase in toughness.

Following proof loading in pure shear (MIIP) the near crack tip residual stresses are more complex than for MIP conditions. MIIP conditions produce compressive and tensile residual stresses lying either side of the plane of the crack. Tensile residual stresses enhance the fracture conditions, and the experiments demonstrated that lower tensile loads, compared to NP conditions, were required to produce low temperature fracture. Consequently the load bearing capacity following MIIP was lower than for NP conditions, as shown in figure (2.26). Increasing the shear component introduced plasticity at the lower temperature, and diminished the influence of the tensile residual stresses. Finally, for pure shear, there was no influence of MIIP loading on Mode II fracture, similar to conditions after MIP loading.

For failure in Mode II, fracture toughness appeared to be unaffected by the application of a proof load, whether Mode I or Mode II, and plastic collapse occurred prior to the onset of brittle fracture in each case. As a result, the actual toughness in Mode II, K_{II} would have to be derived by applying a simply geometric function times the Mode II collapse load.

Compared with the Mode I fracture toughness data the scatter was significantly reduced in Mode II. Ideally, additional tests are needed to determine the extent of experimental scatter throughout the range of mixed mode loading. However, the data that has been obtained is sufficient to illustrate how the mixed mode failure loci for MIP and MIIP loaded specimens compare with NP load conditions for low temperature mixed mode I/II fracture.

5.1.2 Fracture Faces and Angles

The predicted variation of θ_o according to the MTS criterion, equation (5.2), is shown in figure (5.2). For loading at α=0.0° (Mode I, β=90.0°), α=36.0° (β=75.2°) and

α=54.0° (β=64.4°) the measured angles for cleavage fracture for NP, MIP and MIIP conditions are in general agreement with those predicted by the MTS criterion. However for greater amounts of shear loading (β<64.4°, α>54°), for NP conditions, the fracture angles deviated significantly from values predicted by the MTS criterion. This is not surprising since it was observed that the fracture mechanism was not cleavage but a shear mechanism. The change in failure mechanism indicated by fracture angle measurements is also in close agreement with evidence of significant plasticity shown in the non-linearity of the load versus load point displacement curves (figure 2.26), and the deviation of K_I/K_{If}, failure stress intensity ratio from the fracture locus given by the MTS criterion (figure 5.1).

For shear fracture, near crack tip slip line fields (Shih, 1974, Budden, 1988 and Budden and Jones, 1989) suggest that the angle of maximum shear stress (and strain) for plane strain conditions ranges from 70° for Mode I to 0° for Mode II. The predicted directions (θ) of the plastic zones obtained by Budden and Jones (1989) are shown in figure (5.2) as a function of the equivalent crack angle β (equation 2.9).

For loading at α=54.0° for NP conditions, final fracture was predominately a cleavage mechanism, and the measured fracture angle agrees with the MTS criterion (figure 5.2). This is regardless of ductile tearing (figure 2.29) prior to failure. For lower values of β it is evident that the fracture angles lie between the predictions from the MTS criterion and the predictions from the maximum extent of the plastic zone. Fracture surface examination of the two NP loaded specimens for α=72.0° revealed similar features which suggests that at this combination of tension and shear loading, a change in failure mechanism is occurring.

Following MIP and MIIP loading the measured fracture angles suggest that the MTS criterion is more appropriate for a greater range of equivalent crack angles, β than for the NP case. Prior Mode I loading generated compressive residual stresses and thereby constrained the onset of further plasticity. For example, for mixed mode loading at α=72.0° (β=44.0°), although there was only a minor change in the load

bearing capacity compared to NP conditions, the measured fracture angle coincided more closely with the MTS criterion.

Prior Mode II loading generated compressive and tensile residual stresses. Brittle fracture conditions were more favourable for a combination of applied mechanical stresses and tensile residual stresses. Consequently, the critical fracture stress was achieved before the onset of further plasticity, and the fracture angle again agrees more closely with the MTS criterion for mixed mode loading at α=72.0° than for NP conditions.

Ideally, further tests are needed at α=72.0° to confirm the apparent transition in failure mechanism which was observed from the limited data.

5.2 The Effect of Shear and Constraint on Mixed Mode Ductile Fracture

The purpose of these experiments was to characterise the mixed mode ductile fracture characteristics of A508 Class 3 C-Mn forging steel which is commonly used in the manufacture of pressure vessels, particularly in the nuclear industry. Previous studies (Davenport, 1993) have demonstrated that the chemical composition of the material is within specification (A508/A508M-95) and room temperature mechanical tests have shown that the material is isotropic. However, Davenport (1993) found slight orientation effects in Mode I fracture mechanics studies using cracked C(T) specimens. This was not the case for Mode II loading. The sensitivity of specimen orientation in Mode I, and the insensitivity in Mode II, could be due to the volume fraction of Mn-S inclusions present within the material. Lautridou and Pineau (1991) addressed the issue of void volume fraction of inclusions for A508 Class 3 steel and concluded that fracture in Mode I is strongly dependent on their orientation and distribution.

As mentioned in Chapter 3, section 3.1, two billets of A508 steel were supplied by British Energy plc. for characterisation. Each had an equi-axed pearlitic grain

structure (see figure 3.2) and an average grain size of approximately 16μm. The equi-axed nature of the grains suggests that a final heat treatment, post rolling may have been performed while the material was being manufactured. Material orientation has two important implications;

1. the isotropic equiaxed grain structure would have a negligible effect on fracture toughness and tearing resistance, since their behaviour would be similar in all orientations, and
2. for fracture in Mode I, the size, shape and distribution of second phase particles and inclusions is dominant. The results suggest that higher plastic strains are required for hole growth to occur around inclusions orientated in specific directions.

Because of the very low void volume fraction of inclusions in A508 steel (Lautridou and Pineau, 1991), fracture in mode I is only achieved when the energy required for fracture exceeds the energy requirements of a volume of material containing the orientated inclusions in the un-cracked ligament region of a cracked specimen (Figure 5.3a). In mode II, the energy required for fracture is principally concerned with the separation of a plane of material directly ahead of the crack tip in shear (Figure 5.3b). Since there was no microscopic evidence of shearing through inclusions, it is proposed that the preferred path for fracture involves shearing along inclusion grain boundaries. For mode I, the size, shape, orientation and volume fraction of inclusions causes a variation in global strength over the volume of material in the un-cracked ligament region, subject to tensile loading. In mode II, these effects appear to be negligible for a crack propagating in shear. The relationship between the specimen crack orientation, S-L, used in these tests, and inclusion orientation is shown in Figure (5.4) for clarity.

Contrary to the behaviour of other steels reported in the open literature (refer to Chapter 1, section 1.4), Davenport (1993) has shown that A508 has a significantly lower initiation toughness (J_{init}) and tearing resistance (dJ/da) in Mode II loading than in Mode I loading. This was one of the principal reasons for pursuing this current

research and to extend investigations to determine the effect of constraint on mixed mode ductile fracture.

Since the specimens in this current study were from the same forging that was used by Davenport (1993) it is not surprising that the level of anisotropy, displayed via a series of mechanical tests, was negligible. Moreover, to determine the orientation of each billet was a difficult task and could only be assessed from the size, shape and orientation of the Mn-S inclusions present, which were minimal.

A lack of anisotropy is important since one of the features of mixed mode loading is that crack growth is not always planar to the original crack or crack like defect. For this reason, with the exception of the study detailed in Chapter 3, section 3.7, none of the specimens were side grooved. Moreover, since the level of anisotropy is negligible, the differences observed in the size and shape of the different R-curves for different combinations of B, W and a_o/W in mixed mode loading, reported in Chapter 3, are therefore relatively independent of the structure of the material.

For a crack depth ratio, a_o/W of 0.5 Davenport (1993) has shown using SEN specimens that the Mode I R-curve is significantly higher than the Mode II R-curve and that the effect of increasing Mode II is to reduce the value of J_{init} and dJ/da until the limiting condition of pure Mode II is reached. The mixed mode R-curves for B=10mm, W=20mm were compared with Davenport's (1993) R-curves for B=20mm, W=20mm (see figure 5.5), since previous studies have shown that the R-curves are independent of specimen thickness. The results compared reasonably well, with the exception for Mode I loading. Throughout the tests the method of loading and instrumentation used to monitor the local displacements (Δ_{III}, Δ_{Icn} and Δ_{Icp}) were identical. In addition the same analyses techniques were used. The only differences were in the size of the loading fixtures (see figures 2.2 and 3.5) used to apply conditions of mixed mode loading, and η_e and η_p which were determined by finite element analyses and enabled the J-Integral to be determined from a laboratory record of applied load and displacement.

The distance between the opposing loading holes (example: Mode I, α=0.0°) in Davenport's (1993) loading fixture is 160mm and in the loading fixture used in this present study, 330mm. In comparison, Davenport's (1993) loading fixture introduces a higher bending moment about the crack tip since the loading holes are closer together. Consequently, the crack tip constraint is different in the two specimens since the level of triaxial stress is different. As a result Davenport's (1993) R-curves are lower than the R-curves developed in this study where the ligament ahead of the crack tip is subject to predominantly tensile loading.

The introduction of a Mode II component diminishes the effect of bending. As can be seen in figure (5.5) the mixed mode results from the two loading fixtures compare well. For Mode II loading, the R-curves should be identical regardless of loading fixture since the crack faces are simply being slid over one another. However, although the difference in dJ/da is negligible, Davenport's (1993) R-curve is higher since the toughness required for initiation is higher. The magnitude of J is dependent on η factors (see equation 3.2) which scale the elastic and plastic regions under the load versus displacement curve, thus defining the magnitude of J_e and J_p. Davenport's (1993) elastic and plastic η factors are 60% and 21% higher, respectively than the current values (viz. 0.12 and 0.87 compared with 0.075 and 0.72) which would account for the differences in the R-curves. Davenport (1993) determined his η factors using the finite element software package, BERSAFE. Davenport collapsed the nodes defining the crack tip onto a single point to represent an infinitely sharp crack tip. In the present study the package ABAQUS was used and the crack tip was modelled as a key-hole notch of radius, r=50μm (see figure 4.1), which is thought to be more representative of the specimen being tested since the cracks were produced by EDM (as were Davenport's, 1993).

Although the effect of friction in Mode II and near Mode II loading has not been quantified in this present study it is recognised as having an effect on the magnitude and shape of the R-curve. The specimens used in this study, and during Davenport's (1993) experiments were notched using EDM to reduce the variation in initial crack depth (hence variation in a_o/W) which could have been significant if fatigue precracking had been employed. Essentially this technique ensures that any frictional

effects are associated with initiation and the surface roughness of the newly formed crack surfaces of the propagating shear crack sliding against each other. A number of experimentalists have pre-fatigued their specimens to achieve a desired a_o/W, apparently unaware that for nominally the same a_o/W, the variation in length of the fatigue precrack, as well as roughness of the newly formed crack surfaces, has a significant effect on the amount of friction present and on the magnitude of the R-curve. This could possibly be due to the high degree of scatter reported in some Mode II investigations. To date, there has not been any quantitative investigations into the effect of friction although a number of researchers have recognised this as a potential problem in Mode II and mixed mode loading with a high component of shear.

A direct comparison of the mixed mode data presented in this thesis with the limited data presented in the open literature is difficult due to the different levels of constraint imposed by the different methods used to apply mixed mode conditions. A number of experimentalists have applied mixed mode conditions via three- and four-point-bend loading fixtures which for Mode I loading are generally recognised as giving lower bound R-curves since the specimens maintain a higher level of constraint under fully plastic conditions compared to tensile loaded specimens. Additional problems arise due to the different methods used to analyse mixed mode loading, such as crack tip opening and sliding displacement which has been used by Maccagno and Knott (1992) and Bhattacharjee and Knott (1994).

5.2.1 Mode I Fracture

Initial studies have investigated the effect of specimen size when the crack tip is subject to conditions of pure Mode I loading for a crack depth ratio, a_o/W of 0.5. The experiments demonstrate that an increase in specimen thickness (B=10, 20 and 40mm) has a negligible effect on J_{init} and dJ/da in Mode I (see figure 3.20). This is in agreement with Joyce and Link (1995) who tested HSLA HY100 using SEN specimens up to 50mm thick. In contrast a number of investigators, also examining C-Mn steels (Andrews and Shih, 1979 tested A533B, Gibson, 1986 tested

BS4360-43A, Turner, 1986 tested EN32 and Gibson et al., 1987 tested BS4360-43A), have found that an increase in specimen thickness causes dJ/da to decrease but the reported effects on J_{init} are varied.

Also shown in figure (3.20) is the effect of specimen width. As can be seen, a variation in specimen width has a significant effect on both J_{init} and dJ/da since J_{init} for W=20mm is greater than for W=40mm which is similar to W=80mm and dJ/da for W=20mm is greater than for W=40mm which is greater than for W=80mm. Jones and Gordon (1989) and Gordon and Challenger (1989) examined HSLA HY100 using SEN specimens and although they reported that J_{init} was independent of W they demonstrated that dJ/da decreases as W increases. The range of W tested by Jones and Gordon (1989) and Gordon and Challenger (1989) was $30mm \leq W \leq 150mm$ and $15mm \leq W \leq 120mm$, respectively. In contrast, Gibson (1986) who tested BS4360-43A using C(T) specimens and Turner (1986) who tested EN3B using SEN specimens found dJ/da to increase, albeit slightly, as W increased.

Similar effects of specimen size on J_{init} and dJ/da in Mode I loading were observed in the deeper cracked specimens, corresponding to an a_o/W of 0.7. However, although the R-curves for B=10mm, W20mm and B=20mm, W=20mm were similar to the R-curves for $a_o/W=0.5$, the R-curve for B=10mm, W=80mm for $a_o/W=0.7>0.5$ (see figure 3.41). Moreover, J_{init} was similar for each R-curve except for B=10mm, W=80mm, where $a_o/W=0.5$ was significantly lower. Recently Joyce and Link (1997) have presented R-curves for SEN specimens of HSLA HY80 over a range of a_o/W ratios from 0.13 to 0.83. They reported that the wide range of constraint present over this range of a_o/W resulted in R-curves with nearly constant J_{init} but with widely varying dJ/da. They plotted dJ/da versus a_o/W and showed that dJ/da decreased as a_o/W increased, that is until 0.7 when dJ/da began to increase. The results presented in figure (3.41) for W=20mm agree with their observations, however the results for W=80mm suggest that an increase in specimen size (an increase in constraint) causes the lower limit value of a_o/W to decrease (that is, a shift in the limiting value of a_o/W is observed).

In Mode I loading, failure occurs by microvoid nucleation, growth and coalescence. As reported by many researchers, blunting of the crack tip was observed prior to crack initiation at the centre of the notch followed by crack propagation. Microvoids nucleated along grain boundaries, parallel to the loading direction and within the pearlite grains due to cracking of the cementite platelets. With increasing load the voids grew and eventually coalesced when the net section ligament area between neighbouring voids could no longer sustain a further increase in load. On a global scale the crack propagated (via microvoid coalescence) in the plane of the initial notch (θ=0°), although locally this was achieved in a zig-zag pattern at ±45° to the plane of the initial notch (Gudas, 1985 and Beachem and Yoda, 1973). The tip of the propagating crack of all specimens examined was blunt and nucleated microvoids were clearly visible ahead of the crack front.

Tunnelling was observed in all Mode I loaded specimens. In the thinner specimens this effect was more pronounced (B=10mm) since the triaxial stress at the crack tip is low in comparison to thicker specimens, such as B=40mm. However, the increase in triaxial stress associated with an increase in B is not reflected in the size and shape of the R-curves presented in Chapter 3.

5.2.2 Mode II Fracture

The Mode II experiments (figures 3.21, 3.32 and 3.40 for a_o/W=0.5, 0.7 and 0.1, respectively) demonstrate that specimen size has a negligible effect on J_{init} and dJ/da, and microscopic examination has shown that failure is due to shear localisation. There is a lack of experimental evidence in the open literature to corroborate these findings. However, Ayatollahi (1998) has recently presented results from numerical analyses for an SEN specimen with an a_o/W of 0.5. His results confirm that the mechanism of shear localisation is almost independent of the geometry and loading conditions in Mode II loading where the hydrostatic stress in the vicinity of the crack tip is significantly reduced compared to Mode I loading. However, the decrease in stress triaxiality is overcome by an increase in plastic strain with respect to void nucleation. As an aside, Davenport (1993) investigated the effects of orientation in

Mode I and Mode II loading. Although there was significant scatter in Mode I between the six combinations of specimen orientation with respect to L, S and T (see figure 1.15) for both J_{init} and dJ/da this was not seen in the Mode II studies. Essentially for Mode II loading of A508 C-Mn steel the effect of orientation was negligible. Moreover, the effect of specimen size and microstructure was found to have a negligible effect on Mode II loading also (see Chapter 3, sections 3.8 to 3.10 and 3.14).

Green and Miles (1983) tested two C-Mn steels in Mode II using side grooved compact double shear (CDS) and double punch shear (DPS) specimens at ambient temperature. They found that J_{init} for each specimen geometry was similar and only a slight variation in dJ/da was observed. The results presented by Green and Miles (1983) compare well with the Mode II side grooved results presented in Chapter 3, suggesting that the effect of geometry in Mode II loading is negligible (see figure 5.6).

Unlike Mode I, at the onset of shear loading asymmetric blunting of the notch tip causes one side to blunt and the other to sharpen. Similar features have been observed by Aoki et al. (1987) who demonstrated that the strain and void volume fraction were higher at the sharpened corner with increasing load due to the distribution of equivalent plastic strain. In the present experiments a higher density of microvoids nucleated at the sharpened corner where the localisation of plastic strain was high. This led to a loss in stress carrying capability and subsequent failure of the ligament between neighbouring voids by a localised shear mechanism. In contrast to the failure mechanism in Mode I (microvoid nucleation, growth and coalescence), microvoids initiated in Mode II but there was no evidence of growth. This is attributed to the lack of hydrostatic stress which is necessary for growth to occur. These features have been demonstrated in detailed finite element analyses by Aoki et al. (1987) and Ghosal and Narasimhan (1996) who studied the stress and strain distributions in the vicinity of a crack tip subject to mixed mode loading. They also examined the effect of void density and the interaction between neighbouring voids around the crack tip.

5.2.3 Mixed Mode Fracture

R-curves for mixed mode loading have mainly been developed for an a_o/W of 0.5. Thickness effects were only investigated for α=45.0° and like Mode I and Mode II they were found to have a negligible effect on the size and shape of the R-curve. The effect of specimen width was examined for α=22.5°, 45.0° and 67.5° and can be seen in figures (3.22), (3.23) and (3.24), respectively.

The R-curves for α=22.5° are independent of specimen size when the amount of crack growth, Δa<1mm. For Δa>1mm the R-curves are size dependent. The results demonstrate that J_{init} is independent of specimen size, unlike dJ/da for extended crack growth. Moreover, similar observations were made for α=45.0° and 67.5°.

Mixed mode loading causes asymmetric blunting of the crack tip where the angle of the blunted tip, caused by the forward rotation of the upper crack flank in relation to the lower, corresponds approximately to the mixed mode loading angle, α. For α=45.0° and 67.5°, shear cracks initiated at the blunt side of the deformed notch. In contrast, competing failure mechanisms were observed for loading through α=22.5° which was probably due to the variation in specimen width causing a change in constraint. Essentially the wider specimens (W=80mm) failed in a manner similar to that observed in Mode I while the smaller width specimens (W=20mm) failed by shear localisation.

For mixed mode loading, Ghosal and Narisimhan (1996) used finite elements to study the contours of equivalent plastic strain in the vicinity of the notch. In agreement with Aoki et al. (1987) and Budden (1988) they showed the deformation of the crack tip as a function of mode mixity, detailing the sharpening and blunting characteristics of the notch during deformation which are evident in the present experiments. Moreover, they demonstrated that the maximum plastic strain occurs near the blunted part of the notch tip which, also in agreement with the present experiments, they predict to be the location for microvoid nucleation and localised shear localisation.

The mixed mode R-curves for B=10mm, W=20, 40 and 80mm are shown in figures (3.25), (3.26) and (3.27), respectively for $a_o/W=0.5$. Similarly, the mixed mode R-curves for B=10mm, W=20 and 80mm are shown in figures (3.35) and (3.36), respectively for $a_o/W=0.7$.

Figures (3.25) and (3.35) for W=20mm show a proportional decrease in both J_{init} and dJ/da with increasing Mode II until the limiting condition of pure Mode II is reached. With the exception of the Mode I R-curves, the R-curves for W=40 and 80mm also follow this trend. However, the Mode I R-curves are no longer upper bound curves. The increase in constraint associated with an increase in specimen width is reflected only in the Mode I R-curves and not when a component of Mode II is present. This is possibly due to the competition between ductile tearing and shear localisation diminishing the effect of bending. The Mode I R-curves suggest that in addition to tensile loading at the crack tip, a proportion of this load is attributed to bending. Bend loading is not reflected in the curve for W=20mm but becomes increasingly effective as W increases.

In the experiments, if the tensile force was applied along the centreline of the uncracked ligament ahead of the crack, the effect of bending would be zero and the applied load would be predominantly tensile. However, the load was always applied directly through the crack tip in the experiments. Consequently, the effect of bending increased as the uncracked ligament ahead of the initial notch increased since the centre of eccentric loading, 'e' moved progressively further from the crack tip. For W=20mm the bending moment is small since 'e' is close to the crack tip thus the effect of bending is small. However, for W=80mm the bending moment is much larger since 'e' is further from the crack tip, hence the effect of bending becomes more instrumental.

The analytical solutions (Miller, 1988) for combined tension (N) and shear (Q) loading, compared with the experimental data were presented in figures (3.56a) and (3.57a) for $a_o/W=0.5$ and 0.7, respectively. The loci for W=20mm compare well with the experimental data since the effect of bending is negligible. Similarly, good agreement was also seen for W=80mm, that is, except for pure tension. Miller

(1988) also gives solutions for combined tension, shear and bend (M) loading. These curves are plotted with the experimental data in figures (5.7a) and (5.7b) for a_o/W=0.5 and 0.7, respectively. As shown, although conservative, the analytical solutions predict well the limit loads for mixed mode loading, effectively demonstrating the significance of bending.

In an attempt to obtain a simple relationship between the tensile and shear loading characteristics for ductile tearing of A508 steel, Davenport (1993) proposed a simple scaling factor interpolation relationship between the Mode I and Mode II load line R-curves, demonstrating that only tests in pure modes of loading need to be performed to enable the R-curves to be predicted for any combination of tension and shear loading. Davenport's (1993) interpolation plot is given by

$$J = \beta J_I + (1-\beta) J_{II} \qquad (5.6)$$

$\beta=\cos^2\alpha$, where α is the mixed mode loading angle (units: degrees) shown in figures (2.2) and (3.5) for the different loading fixtures used throughout this research. Davenport (1993) used β since the component of load (P) responsible for Mode I crack growth is found by multiplying P with the factor $\cos(\alpha)$. As J is proportional to the square of the load, $\beta=\cos^2\alpha$. Davenport (1993) found this relationship to predict his mixed mode R-curves for A508 reasonably well (see figure 5.8) with the greatest error in J of 16% (equivalent to an 8% error in toughness) occurring for loading though α=36.0° (see figure 2.2).

Davenport's (1993) interpolation model has been applied to the present data for B=10mm, W=20, 40 and 80mm (see figures 5.9, 5.10 and 5.11, respectively) with a crack depth ratio corresponding to a_o/W=0.5. As can be seen, this method does not apply to the present mixed mode data.

Davenport's (1993) experimental results (figure 5.8) demonstrate that the change in dJ/da between Mode I and Mode II loading is small but J_{init} is large since initiation for Mode I loading requires more energy than for Mode II loading. The reason for

dJ/da being similar is due to bend loading being significant during Mode I loading. Consequently, the scaling factor approach works well. In this present study the experiments for B=10mm and W=20mm (figure 5.9) show that dJ/da for Mode I is much greater than for α=22.5°, 45.0°, 67.5° and Mode II which are all similar and failed via shear localisation. Unlike Davenport's (1993) Mode I R-curve, Mode I loading in the present study was predominantly tensile since 'e' was small, hence dJ/da was large.

As the specimen width increases 'e' increases, hence dJ/da decreases (see figure 3.20). However, the introduction of Mode II diminishes the effect of bending by allowing the crack faces to slide as well as open, even when a significant amount of Mode I loading is present. For near Mode I loading crack opening displacement is much greater than crack sliding displacement hence J_{init} is large. For near Mode II loading crack opening displacement is much less than crack sliding displacement hence J_{init} is much lower. The experiments suggest that once initiation has occurred, as long as failure is via shear localisation, dJ/da is similar regardless of mode mixity (see figures 3.26 and 3.27 for B=10mm and W=40 and 80mm, respectively). Ductile tearing is always the failure mechanism for Mode I loading despite the increasing contribution from bend loading with increasing constraint.

5.3.3 Separation of Mode I and Mode II Contributions to Mixed Mode Loading

During the experiments, displacements perpendicular and parallel to the original notch were recorded. From these measurements and a record of the applied load, individual values of J corresponding to simultaneous opening (Mode I, J_{Icn}) and sliding (Mode II, J_{Icp}) of the crack faces during mixed mode loading were determined. The R-curves for an a_o/W of 0.5 are shown in figures (3.28a) through to (3.30b) for B=10mm, W=20, 40 and 80mm. For an a_o/W of 0.7 the R-curves are shown in figures (3.37a) through to (3.38b) for B=10mm, W=20 and 80mm.

Interestingly, these curves agree well with the microscopic observations (Chapter 3, section 3.12), since they demonstrate the competition between the two failure mechanisms; ductile tearing and shear localisation.

For $a_o/W=0.5$ and B=10mm, W=20 (figures 3.28a and 3.28b) and 40mm (figures 3.29a and 3.29b), the Mode I, J_{Icn} R-curves were much greater than the Mode II, J_{Icp} R-curves for Mode I loading and $\alpha=22.5°$, inferring that failure was dominated by tensile loading for $\alpha<22.5°$. For loading through $\alpha=45.0°$, $\alpha=67.5°$ and Mode II the Mode II, J_{Icp} R-curves were much greater than the Mode I, J_{Icn} R-curves thus inferring that failure was dominated by shear loading and a transition from ductile tearing to shear localisation occurred between $\alpha=22.5°$ and 45.0°. However, for B=10mm, W=80mm, the Mode I, J_{Icn} and Mode II, J_{Icp} R-curves for $\alpha=45.0°$ were similar suggesting that an increase in specimen width (corresponding to an increase in constraint) suppresses shear localisation.

This can be further clarified by plotting curves of dJ/da versus α and J_{init} versus α for Mode I, J_{Icn} and Mode II, J_{Icp} to see the competition between crack opening and crack sliding for increasing W. For $a_o/W=0.5$, B=10mm, W=20mm, 40mm and 80mm the curves are shown in figures (5.12) to (5.14) for dJ/da and figures (5.15) to (5.17) for J_{init}. As can be seen, for increasing W the variation in dJ/da and J_{init} are negligible for Mode II, J_{Icp}. However, when tensile loading is significant, the loci of dJ/da and J_{init} for Mode I, J_{Icn} differ significantly. Moreover, the change in failure mechanism with mixed mode loading, as seen under the microscope, coincides approximately with the crossover over of the Mode I, J_{Icn} and Mode II, J_{Icp} loci. For W=20, 40 and 80mm the loci based on tearing resistance predict a change in failure mechanism at $\alpha=30.0°$, 32.5° and 42.5°, respectively. Similarly, the loci based on J_{init} predict $\alpha=34.0°$, 41.0° and 45.0° for W=20, 40 and 80mm respectively. This method is not restricted to $a_o/W=0.5$ but works just as well for $a_o/W=0.7$.

CHAPTER 6 : CONCLUSIONS

6.1 The Effect of Warm Pre-Stress on Mixed Mode Brittle and Ductile Fracture

1. The mixed mode fracture toughness, expressed in terms of stress intensity factor, of a ferritic pressure vessel steel tested at -120°C, using non proof loaded specimens, were found to agree with the elastic MTS criterion for $K_I/K_{If}>0.4$. For $K_I/K_{If}<0.4$ the failure load would be overestimated using the MTS criterion.

2. An increase of approximately 30% in Mode I load bearing capacity and fracture toughness at low temperature was produced by an initial room temperature Mode I proof load. This increase is also in broad agreement with predictions. With increasing shear loading the increase in low temperature toughness was not as great.

3. The enhancement in fracture toughness and load bearing capacity following Mode I proof loading is essentially limited to conditions promoting cleavage fracture.

4. A reduction of approximately 60% in Mode I load bearing capacity and fracture toughness at low temperature was produced by an initial room temperature Mode II proof load.

5. The Mode II load bearing capacity and fracture toughness at low temperature was unaffected by the application of an initial room temperature Mode I or Mode II proof load. This is due to plastic collapse occurring prior to the onset of brittle fracture, and removing the influence of prior history.

6. With increasing shear loading there was a transition in the fracture angle that closely corresponded with a change of failure mechanism. The transition from cleavage to ductile fracture was suppressed when Mode I and Mode II proof loading was introduced, with cleavage fracture being more prominent.

6.2 The Effect of Shear and Constraint on Mixed Mode Ductile Fracture

1. A new loading fixture is presented that enables combinations of Mode I and Mode II loading to be applied directly through the crack tip of SEN specimens of different width, thickness and crack depth ratio.

2. A full matrix of tests have been carried out to determine the ductile crack initiation and tearing resistance of a C-Mn steel at ambient temperature.

3. Finite element analyses have been used to determine elastic and plastic geometry dependent functions for SEN specimens of different width, thickness and crack depth ratio subject to mixed mode loading. These results have been used to calculate the elastic-plastic fracture toughness of laboratory test specimens.

4. Stiffness calibration functions have been determined for each combination of specimen width and thickness and for each mode of loading. These results have been used in the analysis of fracture toughness to extract the extraneous energy associated with flexure of the test machine and loading fixture.

5. The ductile fracture results have shown that there is an increase in constraint with increasing specimen width in Mode I loading such that the slope of the R-curve decreases. It has been demonstrated that this is due to an increase in bend load at the crack tip with increasing W. The effect of increasing specimen thickness is negligible.

6. Mode II fracture toughness is independent of specimen size and can be described by a Master Curve. The master curve is dependent of a_o/W ratio. Experiments have shown that an increase in a_o/W causes a decrease in tearing resistance in Mode II loading.

7. The application of shear loading diminishes the effect of bend loading due to the competition between tension and shear. Furthermore, unlike Mode I, an increase in specimen width and/or thickness does not influence the size and shape of the R-curve.

8. The mixed mode ductile fracture characteristics of a C-Mn steel revealed that there is competition between void growth and shear localisation mechanisms which is affected by specimen width. This can be explained by loci of either dJ/da or J_{init} as a function of the mixed mode loading angle α, for local Mode I, J_{Icn} and Mode II, J_{Icp} components of load.

9. In Mode I loading, ductile fracture is via microvoid nucleation, growth and coalescence. In Mode II, nucleated microvoids do not grow but coalesce by local failure between neighbouring voids. A principal site for void nucleation is at grain boundaries. For Mode II, microvoids also nucleate within pearlite grains due to cracking of the cementite platelets. If shear loading is dominant the tearing behaviour is independent of specimen size. If tensile loading is dominant the tearing behaviour is dependent on specimens width but independent on change in thickness.

10. By plotting the direction of maximum plastic equivalent strain for increasing applied load a qualitative prediction of the direction of crack propagation has been done using finite element analyses. The results compare well with the crack paths observed in the laboratory experiments.

CHAPTER 7 : RECOMMENDATIONS FOR FUTURE WORK

To enhance the experimental results and numerical studies presented in the preceding chapters, some recommendations for future work are given below.

7.1 The Effect of Warm Prestress on Mixed Mode Brittle and Ductile Fracture

1. Near Mode II fracture toughness experiments failed in a ductile manner at -120°C. At this temperature, fracture near Mode I loading was via a brittle mechanism. This suggests that there is a shift in the brittle-to-ductile transition temperature with mixed mode loading. The lower shelf temperature for Mode II loading should be determined and the experiments repeated to generate a true, linear elastic K_{II} vs. K_I fracture toughness locus. This would enable a true understanding of the effect of a prior overload at ambient temperature on mixed mode brittle fracture, particularly for near Mode II loading.

2. Although a benefit in terms of load bearing capacity and fracture toughness at low temperature is achieved by an LUCF WPS cycle, it has been shown that this is a rather conservative method (Yukawa, 1969). The greatest benefits are reported to be achieved by an LCF WPS cycle. It would be interesting to see how these results would compare with the present data and what would result for loading near Mode II.

3. Ayatollahi (1998) used FE to demonstrate a change in failure mechanism for non proof load mixed mode fracture using a plastic collapse analysis and the strain energy density criterion to describe the ductile and brittle behaviour respectively. His predictions were in good agreement with the data presented in this thesis. It would be beneficial if these studies were extended in an attempt to quantify the WPS effect. Models exist (chapter 1, section 1.5) for Mode I loading that are capable of predicting the low temperature benefits

achieved by a proof load applied in the ductile regime. It may be possible to adapt one of these models to describe the benefit for mixed mode fracture.

7.2 The Effect of Shear and Constraint on Ductile Mixed Mode Fracture

1. Mixed mode ductile fracture studies were unsuccessful for low constraint investigations ($a_o/W=0.1$), since strain hardening at the crack tip promoted gross yielding throughout each specimen and prevented crack initiation. Consequently, specimens with slightly deeper cracks ($a_o/W=0.2$ to 0.3) should be studied to enable the R-curves to be compared for a complete range of low, medium and high constraint conditions.

2. A method for separating the relative contributions of Mode I, J_{Icn} and Mode II, J_{Icp} loading for mixed mode loading situations has been presented. This method has been shown to give a good approximation of a change in failure mechanism from dimple rupture (Mode I dominated failure) to shear localisation (Mode II dominated failure). In addition it has been shown that when shear is the dominant failure mechanism (either J_{init} or dJ/da for Mode II, J_{Icp} is greater than for Mode I, J_{Icn}), for increasing shear load dJ/da can be considered constant but the R-curves are scaled by J_{init}. When failure is dominated by tension, both dJ/da and J_{init} are a function of mode mixity. It would be interesting to see if these features could be studied using FE where the local Mode I and II components are quantified in terms of failure criteria such as the models proposed by Gurson (1977) and Bhattacharjee and Knott (1994) for dimple rupture and shear localisation respectively.

3. Bend loading was found to have a significant effect on the size and shape of the R-curve for pure Mode I loading, especially for increasing W. For non Mode I loading the effect of bend load was diminished due to competition between Mode I and Mode II loading. For each test the load was applied directly through the specimen crack tip. Effectively, for Mode I loading, this produced

eccentric loading through the uncracked ligament ahead of the crack tip. the degree of eccentricity increased as W increased. Consequently the level of constraint also increased thus producing lower R-curves. It would be interesting to compare the current Mode I R-curves with those generated by applying the load directly through the centre of eccentricity, a pure tensile loading condition, to see the margins of conservatism in the present results.

4. The shear characteristics of A508 C-Mn steel should be studied further. It has been shown that the Mode II R-curves are independent of specimen size but dependent on crack depth ratio, a_o/W. Preliminary studies have also suggested that shear loading is independent of microstructure. Microscopic analysis has demonstrated that a significant proportion of nucleated microvoids occur due to cracking of the cementite platelets within the pearlite grains, and the subsequent plastic deformation of the surrounding grain structure ensures coalescence via localised shear. Controlled heat treatment should be done to achieve specific microstructures (i.e., thicker cementite platelets and variation in grain size) and chemical analysis employed to ensure that the material is still within specification. Each sample should then be subject to Mode II ductile crack growth studies and the damage accumulation at the crack tip quantified.

REFERENCES

ASTM E399-90$^{\epsilon 1}$, 1990, Standard test method for plane strain fracture toughness of metallic materials, *Annual Book of ASTM Standards*, Vol. 03.01

ASTM E616-89, 1989, Standard terminology relating to fracture testing, *Annual Book of ASTM Standards*, Vol. 03.01

ASTM E813-89$^{\epsilon 1}$, 1989, Standard test method for J_{Ic}, a measure of fracture toughness, *Annual Book of ASTM Standards*, Vol. 03.01

ABAQUS, 1997, *User's manual*, Hibbit, Karlsson and Sorrensen Inc., Providence, Rhode Island, Version 5.7

Ainsworth R.A. and O'Dowd N.P., 1995, Constraint in the failure assessment diagram approach for fracture assessment, *Journal of Pressure Vessel Technology - Transactions of the ASME*, Vol. 117, No. 3, pp. 260-267

Al-Ani A.M. and Hancock J.W., 1991, J-dominance of short cracks in tension and bending, *Journal of the Mechanics and Physics of Solids*, Vol. 39, pp. 23-43

Andrews W.R. and Shih C.F., 1979, Thickness and side-groove effects on J- and δ-resistance curves for A533-B steel at 93°C, *Elastic-Plastic fracture, ASTM STP 668*, (Edited by Landes, Begley and Clarke), ASTM, Philadelphia, pp. 426-450

Aoki S., Kishimoto K., Yoshida T. and Sakata M., 1987, A finite element study of the near crack tip deformation of a ductile material under mixed mode loading, *Journal of the Mechanics and Physics of Solids*, Vol. 35, pp. 431-455

Argon A.S., Im J. and Safoglu R., 1975, Cavity formation from inclusions in ductile fracture, *Metallurgical Transactions*, Vol. 6A, pp. 825-837

Ayatollahi M.R., 1998, Geometry and constraint effects in mixed mode fracture, *PhD Thesis*, November, Department of Mechanical Engineering, University of Bristol, BS8 1TR, UK

Ayatollahi M.R., Pavier M.J. and Smith D.J., 1998, Determination of T-stress from finite element analysis for mode I and mixed mode I/II loading, *International Journal of Fracture*, accepted for publication

BSI BS7448, 1991, Methods for determination of K_{Ic}, critical CTOD and critical J values of metallic materials, *British Standards Institution, London*

Beachem C.D., 1963, An electron fractographic study of the influence of plastic strain conditions upon ductile rupture processes in metals, *Transactions of the ASM*, Vol. 56, pp. 318-326

Beremin F.M., 1981, Numerical modelling of the warm prestress effect using a damage function for cleavage fracture, *Proceedings of the 5th International Conference on Fracture, ICF5*, Pergammon Press, Oxford, Vol. 2, pp. 825-832

Betegón C. and Hancock J.W., 1991, Two-parameter characterisation of elastic-plastic crack-tip fields, *Journal of Applied Mechanics*, Vol. 58, pp. 104-110

Bhattacharjee D. and Knott J.F., 1994, Ductile fracture in HY100 steel under mixed mode I/mode II loading, *Acta Metallurgica et Materialia*, Vol. 42, pp. 1747-1754

Bilby B.A., Cardew G.E., Goldthorpe M.R. and Howard I.C., 1986, A finite element investigation of the effects of specimen geometry on the fields of stress and strain at the tips of stationary cracks, *Size Effects in Fracture*, IMechE, London, pp. 37-46

Brothers A.J. and Yukawa S., 1963, The effect of warm prestressing on notch fracture strength, *Journal of Basic Engineering*, Transactions ASME, Ser. D, Vol. 85(I), pp. 97-104

Brown L.M. and Stobbs W.M., 1976, The work-hardening of copper-silicate v. equilibrium plastic relaxation by secondary dislocations, *Philosophical Magazine*, Vol. 34, pp. 351-372

Chell G.G., Haigh J.R. and Vitek V., 1979, A theory of warm prestressing: Experimental validation and the implications for elastic-plastic failure criteria, *CEGB Report*, report no. CERL RD/L/N63/79

Chell G.G. and Haigh J.R., 1986, The effect of warm prestressing on proof tested pressure vessels, *International Journal of Pressure Vessels and Piping*, Vol. 23, pp. 121-132

Cotterell B., 1966, Notes on the paths and stability of cracks, *International Journal of Fracture Mechanics*, Vol. 2, No. 3, pp. 526-533

Cottrell A.H., 1959, Theory of brittle fracture in steel and similar metals, *Transactions of the AIME*, Vol. 212, No. 2, pp. 192-203

Cox T.B., 1973, *PhD Thesis*, Carnegie-Mellon University, Pittsburgh, Pa.

Cox T.B. and Low J.R., 1974, An investigation of the plastic fracture of AISI 4340 and 18 nickel-200 grade maraging steels, *Metallurgical Transactions*, Vol. 5, No. 6, pp. 1457-1470

Curry D.A., 1979, A micromechanistic approach to the warm prestressing of ferritic steels, *CERL Laboratory Note*, note RD/L/N103/79, September

Curry D.A., 1981, A micromechanistic approach to the warm prestressing of ferritic steels, *International Journal of Fracture*, Vol. 17, No. 3, pp. 335-343

Curry D.A. and Knott J.F., 1978, Effects of microstructure on cleavage fracture stress in steel, *Metal Science*, November, pp. 511-514

Curry D.A. and Knott J.F., 1979, Effect of microstructure on cleavage fracture toughness of quenched and tempered steels, *Metals Science*, Vol. 13, pp. 341-345

Davenport J.C.W., 1993, Mixed mode elastic-plastic fracture, *PhD Thesis*, August, Department of Mechanical Engineering, University of Bristol, BS8 1TR, UK

Davenport J.C.W. and Smith D.J., 1993, A study of superimposed fracture modes I, II and III on PMMA, *Fatigue and Fracture of Engineering Materials and Structures*, Vol. 16, No. 10, pp. 1125-1133

Dodds R.H., Anderson T.L. and Kirk M.T., 1991, A framework to correlate a/W ratio effects on elastic-plastic fracture toughness (J_c), *International Journal of Fracture*, Vol. 48, pp. 1-22

Dodds R.H., Shih C.F. and Anderson T.L., 1993, Continuum and micromechanics treatment of constraint in fracture, *International Journal of Fracture*, Vol. 64, pp. 101-133

Druyresteyn M.H., Klosterman F.T., Roos J., Van Dijk P.M., Los P. and Radelaar S., 1964, Deformation bands in hard rolled copper foil, *Journal of the Mechanics and Physics of Materials*, Vol. 12, pp. 219-230

Du Z.Z. and Hancock J.W., 1991, The effect of non-singular stresses on crack-tip constraint, *Journal of the Mechanics and Physics of Solids*, Vol. 39, pp. 555-567

Du Z.Z., Betegón C. and Hancock J.W., 1991, J-dominance in mixed mode loading, *International Journal of Fracture*, Vol. 52, pp. 191-206

Dugdale D.S., 1960, Yielding in steel sheets containing slits, *Journal of the Mechanics and Physics of Solids*, Vol. 8, pp. 100-104

Erdogan F. and Sih G.C., 1963, On the crack extension in plates under plane and transverse shear, *Journal of Basic Engineering*, Transactions ASME, December, pp. 519-527

Evans A.G., 1983, Statistical aspects of cleavage fracture in steel, *Metallurgical Transactions*, Vol. 14A, pp. 1349-1255

Finnie I. and Saith A., 1973, A note on the angled crack problem and the directional stability of cracks, *International Journal of Fracture*, Vol. 9, pp. 484-486

Fowler H, 1998, The influence of warm prestressing and proof loading on the cleavage fracture toughness of ferritic steels, *PhD Thesis*, January, Department of Mechanical Engineering, University of Bristol, BS8 1TR, UK

French I.E. and Weinrich D.F., 1974, Unusual variation of the tensile fracture strain of brasses at high pressures, *Scripta Metallurgica*, Vol. 8, pp. 7-9

Garwood S.J., 1979, Effect of specimen geometry on crack growth resistance, *Fracture Mechanics, ASTM STP 677*, (Edited by Smith), ASTM, Philadelphia, pp. 511-532

Garwood S.J., 1982, Geometry and orientation effects on ductile crack growth resistance, *International Journal of Pressure Vessels and Piping*, Vol. 10, pp. 297-319

Gibson G.P., 1986, Prediction of specimen size and geometry effects on ductile crack growth resistance, *Size Effects in Fracture: IMechE*, Farnborough, UK, 10th November, pp. 33-36

Gibson G.P., Druce S.G. and Turner C.E., 1987, Effect of specimen size and geometry on ductile crack growth resistance in a C-Mn steel, *International Journal of Fracture*, Vol. 32, pp. 219-240

Goods S.H. and Brown L.M., 1979, The nucleation of cavities by plastic deformation, *Acta Metallurgica*, Vol. 27, pp. 1-15

Gordon J.R. and Challenger N.V., 1989, *TWI Report*

Goshal A.K. and Narasimhan R., 1994, A finite element analysis of mixed-mode fracture initiation by ductile failure mechanisms, *Journal of the Mechanics and Physics of Solids*, Vol. 42, pp. 953-978

Green G. and Miles L., 1983, Use of J-integral estimation techniques to determine critical fracture toughness in ductile steels, *Elastic-Plastic Fracture: Second Symposium, Volume I - Inelastic Crack Analysis, ASTM STP 803*, (Edited by Shih and Gudas), ASTM, Philadelphia, pp. 458-479

Griffith A.A., 1920, The phenomenon of rupture and flow in solids, *Philosophical Transactions of the Royal Society*, Vol. 221, pp. 163-198

Gudas J.P., Joyce J.A. and Davis D.A., 1979, Investigation of specimen geometry modifications to determine the conservative J_I-R curve tearing modulus using the HY-130 steel system, *Fracture Mechanics, ASTM STP 677*, (Edited by Smith), ASTM, Philadelphia, pp. 474-485

Gurland J. and Plateau J., 1963, The mechanism of ductile rupture of metals containing inclusions, *Transactions of the ASM*, Vol. 56, pp. 443-454

Haigh J.R., 1984, Effects of combined warm prestressing, strain ageing and ductile crack growth on the toughness and load bearing capacity of a C-Mn steel, *CEGB Report*, report no. NWR/SSD/84/0012/N

Hall W.J., Nordell W.J. and Munse W.H., 1962, Studies of welding procedures, *Welding Journal*, No. 11, Vol. 41, pp. 505s-517s

Hancock J.W. and Cowling M.J., 1980, Role of state of stress in crack-tip failure processes, *Metal Science*, August-September, pp. 293-304

Hancock J.W, Nekkal A. and Karstensen A.D., 1997, Constraint effects in mixed mode loading, *Advances in Fracture*, Proceedings of the Ninth International Conference on Fracture, Sydney, Australia, Vol. 4, pp. 2015-2022

Hancock J.W., Reuter W.A. and Parks D.M., 1993, Toughness and constraint parameterized by T, *Constraint Effects in Fracture, ASTM STP 1171*, (Edited by Hackett, Schwalbe and Dodds), ASTM, Philadelphia, pp. 121-140

Harrison T.C. and Fearnehough G.D., 1972, The influence of warm prestressing on the brittle fracture of structures containing sharp defects, *Journal of Basic Engineering*, June, pp. 373-376

Harrop L.P., 1979, Warm prestressing during severe thermal shock loading of a pressure vessel, *International Journal of Pressure Vessels and Piping*, Vol. 7, No. 6, pp. 463-482

Heerens J. and Read D.T., 1988, Fracture behaviour of a pressure vessel steel in the ductile-to-brittle transition region, *NISTIR 88-3099*, National Institute for Standards and Technology, Boulder, CO, December

Hellen T.K., 1975, On the method of virtual crack extensions, *International Journal of Numerical Methods in Engineering*, Vol. 9, pp. 187-207

Hellen T.K. and Blackburn W.S., 1975, The calculation of stress intensity factors for combined tensile and shear loading, *International Journal of Fracture*, Vol. 11, pp. 605-617

Hussain M.A., Pu S.L. and Underwood J., 1974, Strain energy release rate for a crack under combined mode I and II, *Fracture Analysis, ASTM STP 560*, pp. 2-28

Hutchinson J.W., 1968a, Singular behaviour at the end of a tensile crack in a hardening material, *Journal of the Mechanics and Physics of Solids*, Vol. 16, pp. 13-31

Hutchinson J.W., 1968b, Plastic stress and strain fields at a crack tip, *Journal of the Mechanics and Physics of Solids*, Vol. 16, pp. 337-347

Irwin G.R., 1948, Fracture dynamics, *Fracturing of Metals*, American Society for Metals, Cleveland, pp. 147-166

Irwin G.R., 1956, Onset of fast crack propagation in high strength steel and aluminium alloys, *Sagamore Research Conference Proceedings*, Vol. 12, pp. 289-305

Irwin G.R., 1957, Analysis of stresses and strains near the end of a crack traversing a plate, *Journal of Applied Mechanics*, Vol. 24, pp. 361-364

Irwin G.R., 1958, Fracture, *Encyclopaedia of Physics*, 6th Edition, S. Flugge, Springer-Verlag, Berlin, pp. 551-590

Irwin G.R., 1960, Fracture mechanics, *Structural Mechanics,* Pergamon Press, London, England, pp. 560-574

Joyce J.A. and Link R.E., 1995, Effects of constraint on upper shelf fracture toughness, *Fracture Mechanics: Twenty-Sixth Volume, ASTM STP 1256*, (Edited by Reuter, Underwood and Newman Jr.), ASTM, Philadelphia, pp. 142-177

Joyce J.A. and Link R.E., 1997, Application of two parameter elastic-plastic fracture mechanics to analysis of structures, *Engineering Fracture Mechanics*, Vol. 57, pp. 431-446

Karstensen A.D., Nekkal A. and Hancock J.W., 1997, The constraint of elastic-plastic crack tip fields, *Advances in Fracture*, Proceedings of the Ninth International Conference on Fracture, Sydney, Australia, Vol. 4, pp. 2007-2014

Kirk M.T., Koppenhoefer K.C. and Shih C.F., 1993, Effect of constraint on specimen dimensions needed to obtain structurally relevant toughness measures, *Constraint Effects in Fracture, ASTM STP 1171*, (Edited by Hackett, Schwalbe and Dodds), ASTM, Philadelphia, pp. 79-103

Kirk M.T., Dodds R.H. Jr. And Anderson T.L., 1994, An approximate technique for predicting size effects on cleavage fracture toughness (J_C) using the elastic T stress, *Fracture Mechanics: Twenty-Fourth Volume, ASTM STP 1207*, (Edited by Landes, McCabe and Boulet), ASTM, Philadelphia, pp. 62-86

Knott J.F., 1977, Micromechanisms of fracture and the fracture toughness of engineering alloys, *International Conference on Fracture (ICF4) - Fracture 1977*, Waterloo, Canada, June 1977, pp. 61-91

Knott J.F., 1980, Micromechanisms of fibrous crack extension in engineering alloys, *Metal Science*, Vol. 14, pp. 327-336

Landes J.D. and Shaffer D.H., 1980, Statistical characterisation of fracture in the transition region, *Fracture Mechanics: Twelfth Conference, ASTM STP 700*, ASTM, Philadelphia, pp. 368-382

Larsson S.G. and Carlsson A.J., 1973, Influence of non-singular stress terms and specimen geometry on small scale yielding at crack tips in elastic-plastic materials, *Journal of the Mechanics and Physics of Solids*, Vol. 21, pp. 263-278

Lautridou J.C. and Pineau A., 1981, Crack initiation and stable crack growth resistance in A508 steels in relation to inclusion distribution, *Engineering Fracture Mechanics*, Vol. 15, pp. 55-71

Leevers P.S. and Radon J.C., 1983, Inherent stress biaxiality in various fracture specimen geometries, *International Journal of Fracture*, Vol. 19, pp. 311-325

Leggatt R.H. and Davey T.V., 1987, Measurements of the reduction due to proof loads of residual-stresses in simulated pressure-vessel welds, *ASTM Specialists' Symposium on Mechanical Relaxation of Residual Stresses*, pp. 30-41

Liu C.T. and Gurland J., 1968, The fracture behaviour of spheroidised carbon steels, *Transactions of the ASM*, Vol. 61, pp. 156-167

Loss F.J., Gray R.A. and Hawthorne J.R., 1977, Significance of warm prestress to crack initiation during thermal shock, *NRL/NUREG Report*, report no. 8165, September

Maccagno T.M. and Knott J.F., 1991, The low temperature brittle fracture behaviour of steel in mixed modes I and II, *Engineering Fracture Mechanics*, Vol. 38, No. 2/3, pp. 111-128

Maccagno T.M. and Knott J.F., 1992, The mixed mode I/II fracture behaviour of lightly tempered HY130 steel at room temperature, *Engineering Fracture Mechanics*, Vol. 41, pp. 805-820

Macdonald B.D., Embley G.T., Irizarry-Quinones H., McAfee W.J., McCabe D.E., Smith P.D. and Wuthrich J.W., 1997, Analysis of warm prestress data, *Fatigue and Fracture Mechanics: 27th Volume, ASTM STP 1296*, (Edited by Piascik, Newman and Dowling), ASTM, Philadelphia, pp. 243-263

MacLennan I. And Hancock J.W., 1994, Constraint based failure assessment diagrams, *Constraint and the Definition of Upper Shelf Behaviour*, HSE/TWI Handbook, TWI, Abington, Cambridge, UK, 12th April.

McMahon C.J. Jr and Cohen M., 1965, Initiation of cleavage in polycrystalline iron, *Acta Metallurgica*, Vol. 13, pp. 591-604

McMeeking R.M., 1977, Finite deformation analysis of crack-tip opening in elastic-plastic materials and implications for fracture, *Journal of the Mechanics and Physics of Solids*, Vol. 25, pp. 375-381

McMeeking R.M. and Parks D.M., 1979, On criteria for J-dominance of crack tip fields in large-scale yielding, *Elastic Plastic Fracture ASTM STP 668*, (Edited by Landes, Begley and Clarke), ASTM, Philadelphia, pp. 175-194

Miles L. and Gladwin D.N., 1991, Evaluation of mode II fracture toughness using single punch specimens, *Nuclear Electric Memorandum, TD/SIP/MEM/1216/91*

Nadai A., 1950, Theory of flow and fracture of solids, Vol. 1, 2nd Edition, McGraw-Hill Book Co., New York, Toronto, London

Needleman A., Tvergaard V. and Hutchinson J.W., 1992, Void growth in plastic solids, *Topics in Fracture and Fatigue*, (Edited by Argon), Springer-Verlag, pp. 145-178

Nichols R.W., 1968(a), The use of overstressing techniques to reduce the risk of subsequent brittle fracture - Part 1, *British Welding Journal*, January, pp. 21-42

Nichols R.W., 1968(b), The use of overstressing techniques to reduce the risk of subsequent brittle fracture - Part 2, *British Welding Journal*, February, pp. 75-84

O'Dowd N.P., 1995, Applications of two parameter approaches in elastic-plastic fracture mechanics, *Engineering Fracture Mechanics*, Vol. 52, pp. 445-465

O'Dowd N.P. and Shih C.F., 1991a, Family of crack-tip fields characterised by a triaxiality parameter: part I - structure of fields, *Journal of the Mechanics and Physics of Solids*, Vol. 39, pp. 939-963

O'Dowd N.P. and Shih C.F., 1991b, Family of crack-tip fields characterised by a triaxiality parameter: part II - fracture applications, *Journal of the Mechanics and Physics of Solids*, Vol. 40, pp. 989-1015

O'Dowd N.P. and Shih C.F., 1994, Two-parameter fracture mechanics: theory and applications, *Fracture Mechanics: Twenty-Fourth Volume, ASTM STP 1207*, (Edited by Landes, McCabe and Boulet), ASTM, Philadelphia, pp. 21-47

O'Dowd N.P., Shih C.F. and Dodds Jr. R.H., 1995, The role of geometry and crack growth on constraint and implications for ductile/brittle fracture, *Constraint Effects in Fracture Theory and Applications: Second Volume, ASTM STP 1244*, (Edited by Kirk and Baker), ASTM, Philadelphia, pp. 134-159

Orowan, E., 1948, Fracture and Strength of Solids, *Reports on Progress in Physics*, Vol. 12, pp. 185

Ostergren W.J., 1969, *Masters' Thesis*, Brown University, USA

Otsuka A., Tohgo K. and Okamoto Y., 1987, Relationship between ductile crack initiation and void volume fraction, *Nuclear Engineering and Design*, Vol. 105, pp. 121-129

Panontin T.L. and Sheppard S.D., 1995, The relationship between constraint and ductile fracture initiation as defined by micromechanical analyses, *Fracture Mechanics: Twenty-Sixth Volume, ASTM STP 1256*, (Edited by Reuter, Underwood and Newman Jr.), ASTM, Philadelphia, pp. 54-85

Parks D.M. and Wang Y.Y., 1988, Elastic-plastic analysis of part-through surface cracks, *Analytical, Numerical and Experimental Aspects of 3-D Fracture Processes*, (Edited by Rosakis et al.), ASME, AMD-91, New York, pp. 19-32

Pickles B.W. and Cowan A., 1983, A review of warm prestressing studies, *International Journal of Pressure Vessels and Piping*, Vol. 14, pp. 95-131

Pineau A., 1981, Review of fracture micromechanisms and a local approach to predicting crack resistance in low strength steels, *Advances in Fracture Research, 5th International Conference on Fracture*, Vol. 2, pp. 553-577

Reed P.A.S. and Knott J.F., 1992, An investigation of the warm prestressing (WPS) effect in A533B weld metal, *Fatigue and Fracture of Engineering Materials and Structures*, Vol. 15, No. 12, pp. 1251-1270

Reed P.A.S. and Knott J.F., 1996a, Investigation of the role of residual stresses in the warm prestress (WPS) effect. Part I - Experimental, *Fatigue and Fracture of Engineering Materials and Structures*, Vol. 19, No. 4, pp. 485-500

Reed P.A.S. and Knott J.F., 1996b, Investigation of the role of residual stresses in the warm prestress (WPS) effect. Part II - Analysis, *Fatigue and Fracture of Engineering Materials and Structures*, Vol. 19, No. 4, pp. 501-513

Rellick J.R. and McMahon C.J., 1974, Intergranular embrittlement of iron-carbon alloys by impurities, *Metallurgical Transactions*, Vol. 5, pp. 2339-2450

Rice J.R., 1967, Mechanics of crack tip deformation and extension by fatigue, *Fatigue Crack Propagation, ASTM STP 415*, ASTM, Philadelphia, pp. 247-311

Rice J.R., 1968, A path independent integral and the approximate analysis of strain concentration by notches and cracks, *Journal of Applied Mechanics*, Vol. 35, pp. 379-386

Rice J.R., 1972, The line spring model for surface flaws, *The Surface Crack: Physical Problems and Computational Solutions*, (Edited by Swedlow J.L.), ASME, New York, 171-186

Rice J.R., 1974, Limitations to the small scale yielding approximation for crack tip plasticity, *Journal of the Mechanics and Physics of Solids*, Vol. 22, pp. 17-26

Rice J.R. and Rosengren G.F., 1968, Plane strain deformation near a crack tip in a power law hardening material, *Journal of the Mechanics and Physics of Solids*, Vol. 16, pp. 1-12

Rice J.R. and Tracey D.M., 1969, On the ductile enlargement of voids in triaxial stress fields, *Journal of the Mechanics and Physics of Solids*, Vol. 17, pp. 201-217

Rice J.R. and Tracey D.M., 1973, Computational fracture mechanics, *Numerical and Computer Methods in Structural Mechanics*, Academic Press, New York, pp. 585-623

Ripling E.J. and Lindberg R.S., 1965, Toughness of warm worked martensitic steels, *Journal of Basic Engineering - Transactions of the ASME*, Series D, Vol. 87, June, pp. 307-312

Ritchie R.O., Knott J.F. and Rice J.R., 1973, On the relationship between critical tensile stress and fracture toughness in mild steel, *Journal of the Mechanics and Physics of Solids*, Vol. 21, pp. 395-410

Rogers H.C., 1960, Tensile fracture of ductile metals, *Transactions of the Metal Society, AIME*, Vol. 218, pp. 498-506

Roos E., Eisele U. and Silcher H., 1993, Effect of stress state on the ductile fracture behaviour of large-scale specimens, *Constraint Effects in Fracture, ASTM STP 1171*, (Edited by Hackett, Schwalbe and Dodds), ASTM, Philadelphia, pp. 41-63

Rosenfield A.R. and Hahn G.T., 1966, Numerical descriptions of ambient low-temperature, and high strain rate flow and fracture behaviour of plain carbon steel, *Transactions of the ASM*, Vol. 59, No. 4, pp. 962-980

Rousselier G., 1986, Les modèles de rupture ductile et leurs possibilités actuelles dans le cadre de l'approche, *EDF, Service Réacteurs Nucléaires et Echangeurs, Les Renardières, BP 1, F-77250, MORET-SUR-LOING, FRANCE*

Satoh K., Toyoda, M. and Mutoh Y., 1983, Effect of prestrain at elevated temperature on the fracture behaviour of high strength steels, *Journal of Engineering Materials and Technology*, Vol. 105, pp. 16-20

Seidenfuss M., 1992, Untersuchungen zur beschreibung des versagensverhaltens mit hilfe von schadigungsmodellen am beispiel des werkstoffes 20 MnMoNi 5 5, *PhD Thesis, MPA Stuttgart, GERMANY*

Sharobeam M.H. and Landes J.D., 1991, The local separation criterion and methodology in ductile fracture mechanics, *International Journal of Fracture*, Vol. 47, pp. 81-104

Shi Y.W. and Zhou N.N., 1995, Comparison of microshear toughness and mode II fracture toughness for structural steels, *Engineering Fracture Mechanics*, Vol. 51, pp. 669-676

Shih C.F., 1974, Small-scale yielding analysis of mixed mode plane-strain crack problems, *Fracture Analysis ASTM STP 560*, ASTM, Philadelphia, pp. 187-210

Shih C.F., 1983, Tables of Hutchinson-Rice-Rosengren singular field quantities, *Brown University Technical Report*, MRL E-147, June

Shih C.F., 1985, J-dominance under plane strain fully plastic conditions: the edge crack panel subject to combined tension and bending, *International Journal of Fracture*, Vol. 29, pp. 73-84

Shih C.F. and German M.D., 1981, Requirements for a one parameter characterisation of crack tip fields by the HRR singularity, *International Journal of Fracture*, Vol. 17, pp. 27-43

Sih G.C., 1973, A special theory of crack propagation, *Methods of Analysis and Solutions to Crack Problems*, (Edited by Sih), Noordhoff International, pp. 21-45

Sih G.C., 1974, Strain-energy-density factor applied to mixed mode crack problems, *International Journal of Fracture*, Vol. 10, No. 3, pp. 305-321

Sih G.C. and Kipp M.E., 1974, Discussion on "fracture under complex stress - the angled crack problem" by Williams J.G. and Ewing P.D., *International Journal of Fracture*, Vol. 10, No. 2, pp. 261-265

Sih G.C. and Liebowitz H., 1968, *Mathematical Fundamentals of Fracture*, Academic Press, New York, p. 67

Sih G.C. and MacDonald B., 1974, Fracture mechanics applied to energy problems - strain energy density fracture criterion, *Engineering Fracture Mechanics*, Vol. 6, pp. 361-386

Smith, D.J., 1983, Creep crack growth in low alloy steels under steady and cyclic loading, *PhD Thesis*, University of London

Smith D.J., 1986, The influence of proof testing on component reliability: progress report 1 - parent material characterisation, *TWI Report Number 5561/1/86*, The Welding Institute, Cambridge, CB1 6AL, UK

Smith, D.J., 1987, The significance of prior overload with regard to the risk of subsequent fracture in A533B steel, *The Welding Institute Report*, report no. 339/1987

Smith, D.J. and Garwood, S.J., 1990a, The significance of prior overload on fracture resistance: a critical review, *International Journal of Pressure Vessels and Piping*, Vol. 41, pp. 255-296

Smith, D.J. and Garwood, S.J., 1990b, Experimental study of the effects of prior overload on fracture toughness of A533B steel, *International Journal of Pressure Vessels and Piping*, Vol. 41, pp. 297-331

Smith, D.J. and Garwood, S.J., 1992, The application of fracture mechanics to assess the significance of proof loading, *Fracture Mechanics: Twenty-Second Symposium (Volume I), ASTM STP 1131*, (Edited by Ernst, Saxena and McDowell), ASTM, Philadelphia, pp. 833-849

Smith E., 1966, The nucleation and growth of cleavage microcracks in mild steel, *Proceedings of the Conference on the Physical Basis of Fracture*, pp. 36-46

Sommer E and Aurich D., 1991, On the effect of constraint on ductile fracture, *Defect Assessment in Components - Fundamentals and Applications, ESIS/EGF9*, (Edited by Blauel and Schwalbe), Mechanical Engineering Publications, London, pp. 141-174

Steigerwald E.A., 1961, Influence of warm prestressing on the notch properties of several high strength alloys, *Transactions of the ASM*, Vol. 54, pp. 445-455

Succop L.N., Pense A.W. and Stout R.D., 1970, The effects of warm overstressing on pressure vessel steel properties, *Welding Research Supplement*, August, pp. 354s-364s

Sumpter J.D.G., 1993, An experimental investigation of the T-stress approach, *Constraint Effects in Fracture ASTM STP 1171*, (Edited by Hackett, Schwalbe and Dodds Jr.), ASTM, Philadelphia, pp. 492-502

Sumpter J.D.G. and Forbes A.T., 1992, Constraint based analysis of shallow cracks in mild steel, *Proceedings of TWI/EWI/IS International Conference on Shallow Crack Fracture Mechanics, Toughness Tests and Applications*, (Edited by Dawes), Cambridge, UK, 23-24 September, Ch. 28, pp. 52-60

Sumpter J.D.G. and Turner C.E., 1976, Method of laboratory determination of Jc, *Cracks and Fracture, ASTM STP 601*, ASTM, Philadelphia, pp. 3-18

Swankie T.D., 1995, The role of shear and constraint in mixed mode brittle and ductile fracture, *Internal Research Report*, April, Department of Mechanical Engineering, University of Bristol, BS8 1TR, UK

Swankie T.D. and Smith D.J., 1998, Low temperature mixed mode fracture of a pressure vessel steel subject to prior loading, *Engineering Fracture Mechanics*, Vol. 61, pp. 387-405

Symington M., Shih C.F. and Ortiz M., 1988, Tables of plane strain mixed-mode plastic crack tip fields, *Brown University Technical Report*, MRG/DMR-8714665/1, October

Tada H., Paris P.C. and Irwin G.R., 1973, The stress analysis of cracks handbook - 1st edition, *Del Research corporation*

Tada H., Paris P.C. and Irwin G.R., 1985, The stress analysis of cracks handbook - 2nd edition, *Del Research corporation*

Theocaris P.S. and Andrianopoulos N.P., 1982, The T-criterion applied to ductile fracture, *International Journal of Fracture*, Vol. 20, R125-R130

Thomason P.F., 1990, *Ductile Fracture of Metals*, Pergamon Press, Oxford, UK

Tohgo K., Otsuka A. and Gao H-W, 1988, Behaviour of ductile crack initiation from a notch under mixed mode loading, *Journal of the Society of Materials Science*, Japan, Vol. 37, No. 419, pp. 885-890

Tracey D.M., 1973, *PhD Thesis*, Brown University

Tracey D.M., 1976, Finite element solutions for crack-tip behaviour in small scale yielding, *Journal of Engineering Materials and Technology*, ASME, Vol. 98, pp. 146-151

Turner C.E., 1986, Size effects in ductile fracture: a plasticity view, *Size Effects in Fracture: IMechE*, Farnborough, UK, 10th November, pp. 25-32

Tvergaard V. and Needleman A., 1984, Analysis of the cup-cone fracture in a round tensile bar, *Acta Metallurgica*, Vol. 32, pp. 157-169

Van Stone R.H., Cox T.B., Low Jr. J.R. and Psioda J.A., 1985, Microstructural aspects of fracture by dimple rupture, *International Metals Review*, Vol. 30, pp. 157-179

Wallin K., 1989, The effect of ductile tearing on cleavage fracture probability in fracture toughness testing, *Engineering Fracture Mechanics*, Vol. 32, No. 4, pp. 523-531

Wallin K., 1991, Statistical modelling of fracture in the ductile to brittle transition region, *Defect Assessment in Components - Fundamentals and Applications*, ESIS/EGF9 (Edited by Blauel and Schwalbe), Mechanical Engineering Publications, London, pp. 415-445

Wallin K., Saario T. and Törrönen K., 1984, Statistical model for carbide induced brittle fracture in steel, *Metal Science*, Vol. 18, pp. 13-16

Wells A.A., 1961, Unstable crack propagation in metals: cleavage and fast fracture, *Proceedings of the Crack Propagation Symposium*, Vol. 1, Paper 84, Cranfield, UK

Williams M.L., 1957, On the stress distribution at the base of a stationary crack, *Journal of Applied Mechanics*, Vol. 24, pp. 109-114

Williams J.G. and Ewing P.D., 1972, Fracture under complex stress - the angled crack problem, *International Journal of Fracture Mechanics*, Vol. 8, No. 4, pp. 441-446

Willoughby A.A., Pratt P.L. and Turner C.E., 1978, The effect of specimen orientation on the R-curve, *International Journal of Fracture*, Vol. 14, pp. R249-R251

Wu S.-X., Mai Y.-W. and Cotterell B., 1990, Plastic η-factor (η_p) of fracture specimens with deep and shallow cracks, *International Journal of Fracture*, Vol. 45, pp. 1-18

Wu S.-X. and Mai Y.-W., 1995, Two parameter (J-Q) fracture characterisation of ductile tearing, *Fracture Mechanics: Twenty-Sixth Volume, ASTM STP 1256*, (Edited by Reuter, Underwood and Newman Jr.), ASTM, Philadelphia, pp. 43-54

Xavier A., 1995, Interaction of proof loading and mixed mode fracture, *Undergraduate Report Number 95/54*, June, Department of Mechanical Engineering, University of Bristol, BS8 1TR, UK

Yoda M., 1987, The effect of the notch root radius on the J-integral fracture toughness under mode I, II and III loadings, *Engineering Fracture Mechanics*, Vol. 26, pp. 425-431

Yukawa S., 1969, Evaluation of periodic proof testing and warm prestressing procedures for nuclear reactor vessels, *General Electric Report*, report no. HSSTP-TR-1

Element	C	S	P	Si	Mn	Ni	Cr	Mo	V
Wt %	0.180	0.011	0.016	0.330	1.130	0.020	0.020	<0.005	0.01

Element	Cu	Sb	Ti	Al	B	Sn	Co	As	
Wt %	0.020	0.033	<0.002	0.029	0.0003	<0.005	0.010	<0.005	

Table 2.1. BS1501-224 Gr490B Chemical Analysis

(after Smith and Garwood, 1992)

Temperature degrees C	E GPa	σ_{ys} MPa	σ_{UTS} MPa
20	203.0	358.0	546.0
-120	207.3	565.0	708.0

E = Elastic modulus, σ_{ys} = Yield strength, and σ_{UTS} = Tensile strength

Table 2.2. BS1501-224 Gr490B Averaged Tensile Properties (T-L orientation)

(after Swankie and Smith, 1998)

α	Crack Length (increments, Δa = 0.20mm) mm								
	10.00	10.20	10.40	10.60	10.80	11.00	11.20	11.40	11.60
M I	**3.5436**	3.6972	3.8593	4.0305	4.2114	4.4029	4.6059	4.8212	5.0500
18°	**3.4503**	3.5999	3.7577	3.9244	4.1005	4.2870	4.4846	4.6943	4.9170
36°	**3.0540**	3.1864	3.3261	3.4736	3.6295	3.7946	3.9695	4.1550	4.3522
54°	**2.3546**	2.4567	2.5643	2.6781	2.7983	2.9256	3.0604	3.2035	3.3555
72°	**1.3521**	1.4107	1.4726	1.5379	1.6069	1.6800	1.7574	1.8396	1.9269
M II	**0.0466**	0.0486	0.0507	0.0530	0.0554	0.0579	0.0605	0.0634	0.0664

α = Mixed mode loading angle and Ref. = reference crack length

Table 2.3. **Mode I** : Variation of $f_I(\alpha, a_o/W)$ with Increasing Crack Depth

(after Davenport and Smith, 1993, and Tada et al., 1973; 1985)

α	Crack Length (increments, Δa = 0.20mm) mm								
	10.00	10.20	10.40	10.60	10.80	11.00	11.20	11.40	11.60
M I	**0.0000**	0.0000	0.0000	0.0000	0.0000	0.0000	0.0000	0.0000	0.0000
18°	**0.4176**	0.4216	0.4258	0.4302	0.4348	0.4396	0.4447	0.4499	0.4555
36°	**0.8889**	0.8974	0.9063	0.9157	0.9255	0.9357	0.9464	0.9577	0.9695
54°	**1.3080**	1.3205	1.3337	1.3474	1.3618	1.3769	1.3927	1.4093	1.4266
72°	**1.5691**	1.5841	1.5998	1.6163	1.6336	1.6517	1.6707	1.6905	1.7114
M II	**1.5662**	1.5813	1.5970	1.6134	1.6307	1.6487	1.6677	1.6875	1.7083

α = Mixed mode loading angle and Ref. = reference crack length

Table 2.4. **Mode II** : Variation of $f_{II}(\alpha, a_o/W)$ with Increasing Crack Depth

(after Davenport and Smith, 1993, and Tada et al., 1973; 1985)

α degrees	a_o/W	P_{max} kN	K_I MPa√m	K_{II} MPa√m	β degrees	θ_o degrees
Mode I, α = 0°	0.510	46.79	61.16	0.00	90.00	0.00
Mode I, α = 0°	0.570	47.10	80.28	0.00	90.00	1.00
Mode I, α = 0°	0.500	62.50	78.30	0.00	90.00	0.00
Mode I, α = 0°	0.524	65.72	91.34	0.00	90.00	1.00
α = 36°	0.531	72.15	88.65	23.37	75.23	-29.50
α = 54°	0.537	78.38	76.46	37.61	63.81	-37.00
α = 72°	0.538	84.51	47.36	48.67	44.22	0.00
α = 72°	0.538	81.95	46.01	47.19	44.23	-42.00
Mode II, α = 90°	0.550	80.50	0.00	46.92	0.00	9.50
Mode II, α = 90°	0.540	85.00	0.00	49.01	0.00	10.00
Mode II, α = 90°	0.530	84.70	0.00	48.31	0.00	-8.50

α = Mixed mode loading angle, P_{max} = Maximum load, β = equivalent crack angle and θ_o = Mixed mode fracture angle

Table 2.5. Mixed Mode Experimental Test Data for Non Proof Load Specimens

(BS1501-224 C-Mn Steel, at -120°C)

α degrees	a_o/W	P_{max} kN	K_I MPa√m	K_{II} MPa√m	β degrees	θ_o degrees
Mode I, α = 0°	0.520	77.40	103.23	0.00	90.00	2.00
α = 36°	0.537	81.56	103.47	26.61	75.58	-32.50
α = 54°	0.535	90.30	87.52	43.26	63.70	-42.00
α = 72°	0.529	83.46	45.22	47.66	43.50	-53.00
Mode II, α = 90°	0.529	87.02	0.00	49.61	0.00	-7.50
Mode II, α = 90°	0.541	77.93	0.00	44.95	0.00	32.00
Mode II, α = 90°	0.550	91.30	0.00	53.22	0.00	-7.00
Mode II, α = 90°	0.520	85.30	0.00	48.16	0.00	-10.5

α = Mixed mode loading angle, P_{max} = Maximum load, β = equivalent crack angle and θ_o = Mixed mode fracture angle

Table 2.6. Mixed Mode Experimental Test Data for Mode I Proof Load Specimens

Mode I Proof Load, P_{app} = 70.0kN

(BS1501-224 C-Mn Steel, at -120°C)

α degrees	a_o/W	P_{max} kN	K_I MPa√m	K_{II} MPa√m	β degrees	θ_o degrees
Mode I, α = 0°	0.550	15.44	24.03	0.00	90.00	15.60
Mode I, α = 0°	0.540	18.05	26.88	0.00	90.00	16.00
Mode I, α = 0°	0.548	15.84	24.10	0.00	90.00	42.40
α = 36°	0.528	37.77	45.90	12.20	75.12	-40.00
α = 54°	0.536	32.95	32.03	15.79	63.76	-40.75
α = 72°	0.518	43.54	22.47	24.58	42.43	-48.00
Mode II, α = 90°	0.537	82.13	0.00	47.18	0.00	-7.00

α = Mixed mode loading angle, P_{max} = Maximum load, β = equivalent crack angle and θ_o = Mixed mode fracture angle

Table 2.7. Mixed Mode Experimental Test Data for Mode II Proof Load Specimens

Mode II Proof Load, P_{app} = 62.5kN

(BS1501-224 C-Mn Steel, at -120°C)

Element	C	S	P	Si	Mn	Ni	Cr	Mo
Wt %	0.160	0.007	0.004	0.220	1.340	0.670	0.170	0.510

Element	V	Cu	Sb	Ti	Al	Sn	As	Nb
Wt %	<0.010	0.060	0.004	<0.010	0.010	0.004	0.019	<0.010

Analysis obtained by Spark Discharge Emission Spectroscopy

Table 3.1. A508 Class 3 C-Mn Steel Chemical Analysis

(after Davenport, 1993)

Specimen orientation	E GPa	σ_{ys} MPa	σ_{UTS} MPa	n	Elongation at failure
L	201.0	430.0	561.0	7.7	26.0 %
T	225.0	440.0	578.0	8.0	30.0 %
S	213.8	423.0	571.0	7.8	27.5 %

E=Elastic modulus, σ_{ys}=Yield strength, σ_{UTS}=Tensile strength, and n=Strain hardening exponent

Table 3.2. A508 Class 3 C-Mn Steel Averaged Uniaxial Test Data, at 20°C

(after Davenport, 1993)

Loading mode	k_{III} kN/mm	k_{Icn} kN/mm	k_{Icp} kN/mm
Mode I (α=0.0°)	138.0	354.0	∞
α=18.0°	138.0	335.0	400.0
α=36.0°	143.0	445.0	170.0
α=54.0°	130.0	1000.0	200.0
α=72.0°	125.0	1333.3	160.0
Mode II (α=18.0°)	107.0	∞	138.0

α=Mixed mode loading angle, k_{III}, k_{Icn} and k_{Icp}=local load line, local crack normal and local crack parallel stiffness

Table 3.3. A508 Stiffness Calibration Functions for SG SEN Specimens

(B=20mm, W=20mm)

Loading mode	k_{III} kN/mm	k_{Icn} kN/mm	k_{Icp} kN/mm
Mode I (α=0.0°)	152.0	152.0	∞
α=22.5°	158.7	195.3	223.7
α=45.0°	153.6	290.5	175.6
α=67.5°	144.5	879.8	145.3
Mode II (α=90.0°)	145.0	∞	145.0

α=Mixed mode loading angle, k_{III}, k_{Icn} and k_{Icp}=local load line, local crack normal and local crack parallel stiffness

Table 3.4. A508 Stiffness Calibration Functions (B=10mm, W=20mm)

Loading mode	k_{III} kN/mm	k_{Icn} kN/mm	k_{Icp} kN/mm
Mode I (α=0.0°)	262.9	262.9	∞
α=22.5°	253.6	372.0	264.6
α=45.0°	206.3	389.7	235.7
α=67.5°	193.9	818.7	197.3
Mode II (α=90.0°)	194.3	∞	194.3

Table 3.5. A508 Stiffness Calibration Functions (B=10mm, W=40mm)

Loading mode	k_{III} kN/mm	k_{Icn} kN/mm	k_{Icp} kN/mm
Mode I (α=0.0°)	578.0	578.0	∞
α=22.5°	465.2	622.3	578.3
α=45.0°	370.3	706.6	400.8
α=67.5°	393.3	1385.2	400.8
Mode II (α=90.0°)	429.9	∞	429.9

Table 3.6. A508 Stiffness Calibration Functions (B=10mm, W=80mm)

Loading mode	k_{III} kN/mm	k_{Icn} kN/mm	k_{Icp} kN/mm
Mode I (α=0.0°)	116.3	116.3	∞
α=22.5°	245.9	340.0	280.5
α=45.0°	275.6	639.8	276.6
α=67.5°	266.8	1256.0	256.2
Mode II (α=90.0°)	253.1	∞	253.1

α=Mixed mode loading angle, k_{III}, k_{Icn} and k_{Icp}=local load line, local crack normal and local crack parallel stiffness

Table 3.7. A508 Stiffness Calibration Functions (B=20mm, W=20mm)

Loading mode	k_{III} kN/mm	k_{Icn} kN/mm	k_{Icp} kN/mm
Mode I (α=0.0°)	259.5	259.5	∞
α=22.5°	241.6	296.0	411.3
α=45.0°	222.8	356.7	282.8
α=67.5°	230.7	518.1	256.9
Mode II (α=90.0°)	257.0	∞	257.0

Table 3.8. A508 Stiffness Calibration Functions (B=20mm, W=40mm)

Loading mode	k_{III} kN/mm	k_{Icn} kN/mm	k_{Icp} kN/mm
Mode I (α=0.0°)	306.5	306.5	∞
α=22.5°	274.7	340.7	424.1
α=45.0°	245.9	384.5	316.2
α=67.5°	255.3	562.7	285.7
Mode II (α=90.0°)	294.3	∞	294.3

Table 3.9. A508 Stiffness Calibration Functions (B=20mm, W=80mm)

Loading mode	k_{III} kN/mm	k_{Icn} kN/mm	k_{Icp} kN/mm
Mode I (α=0.0°)	337.9	337.9	∞
α=22.5°	300.4	389.3	430.9
α=45.0°	277.0	462.7	339.6
α=67.5°	288.3	682.8	322.5
Mode II (α=90.0°)	318.8	∞	318.8

α=Mixed mode loading angle, k_{III}, k_{Icn} and k_{Icp}=local load line, local crack normal and local crack parallel stiffness

Table 3.10. A508 Stiffness Calibration Functions (B=40mm, W=20mm)

Loading mode	k_{III} kN/mm	k_{Icn} kN/mm	k_{Icp} kN/mm
Mode I (α=0.0°)	379.9	379.9	∞
α=22.5°	348.0	446.3	542.7
α=45.0°	318.1	511.3	397.1
α=67.5°	322.7	803.2	362.1
Mode II (α=90.0°)	359.0	∞	359.0

Table 3.11. A508 Stiffness Calibration Functions (B=40mm, W=40mm)

	Specimen ID	Proof Load	a_o/W	Failure Load kN	K_I MPa√m	K_{II} MPa√m	K_{TOT} MPa√m
Mode I Fracture (α=0.0°)							
*	M04-1	N	0.51	46.79	61.16	0.00	61.16
*	M04 5	N	0.57	47.10	80.28	0.00	80.28
*	M04-6	N	0.50	62.50	78.30	0.00	78.30
	PM1-3	N	0.52	65.72	91.34	0.00	91.34
	PM1-1P	MI	0.52	77.40	103.23	0.00	103.23
*	M04 G	MII	0.55	15.44	24.03	0.00	24.03
*	M04 J	MII	0.54	18.05	26.88	0.00	26.88
	MM12-2P	MII	0.55	15.84	24.10	0.00	24.10
Mixed Mode Loading (α=36.0°)							
	NPH3FA	N	0.53	72.15	88.65	23.37	91.68
	M1PHSFA	MI	0.54	81.56	103.47	26.61	106.84
	M2PH3FA	MII	0.53	37.77	45.90	12.20	47.50

α=mixed mode loading angle, K_I, K_{II} and K_{TOT}=Mode I, Mode II and total Stress Intensity Factor

Table 3.12. BS1501 Experimental Test Data (* refers to data given by Xavier, 1993) (contd.)

	Specimen ID	Proof Load	a_o/W	Failure Load kN	K_I MPa√m	K_{II} MPa√m	K_{TOT} MPa√m
Mixed Mode Loading (α=54.0°)							
	MM12-3	N	0.54	78.38	76.46	37.61	85.23
	MM12-5P	MI	0.54	90.30	87.52	43.26	97.62
	MM12-4P	MII	0.54	32.95	32.03	15.79	35.72
Mixed Mode Loading (α=72.0°)							
	MM12-6P	N	0.54	84.51	47.36	48.67	67.91
	MM12-9	N	0.54	81.95	46.01	47.19	65.91
	MM12-8P	MI	0.53	83.46	45.22	47.66	65.70
	MM12-7P	MII	0.52	43.54	22.47	24.58	33.30
Mode II Fracture (α=90.0°)							
*	M04 2	N	0.55	80.50	0.00	46.92	46.92
*	M04 3	N	0.54	85.00	0.00	49.01	49.01
*	M04 4	N	0.53	84.70	0.00	48.31	48.31

α=mixed mode loading angle, K_I, K_{II} and K_{TOT}=Mode I, Mode II and total Stress Intensity Factor

Table 3.12. BS1501 Experimental Test Data (* refers to data given by Xavier, 1993) (contd.)

	Specimen ID	Proof Load	a_o/W	Failure Load kN	K_I MPa√m	K_{II} MPa√m	K_{TOT} MPa√m
	M1PM2FB	MI	0.53	87.02	0.00	49.61	49.61
	MM12-1P	MI	0.54	77.93	0.00	44.95	44.95
*	M04 I	MI	0.55	91.30	0.00	53.22	53.22
*	M04 H	MI	0.52	85.30	0.00	48.16	48.16
*	M2PM2FA	MII	0.54	82.13	0.00	47.18	47.18

α=mixed mode loading angle, K_I, K_{II} and K_{TOT}=Mode I, Mode II and total Stress Intensity Factor

Table 3.12. BS1501 Experimental Test Data (* refers to data given by Xavier, 1993)

Mode I (Tension)

α=0.0°

	B=10	B=20	B=40
W=20	3	7	4
W=40	4	5	1
W=80	5	3	X

Mixed mode (combination of tension and shear)

α=22.5°

	B=10	B=20	B=40
W=20	5		
W=40	3		
W=80	3		X

Mixed mode (combination of tension and shear)

α=45.0°

	B=10	B=20	B=40
W=20	8		4
W=40	4		
W=80	3		X

Mixed mode (combination of tension and shear)

α=67.5°

	B=10	B=20	B=40
W=20	5		
W=40	4		
W=80	3		X

Mode II (Shear)

α=90.0°

	B=10	B=20	B=40
W=20	8	4	4
W=40	4	4	3
W=80	4	4	X

4	Number of completed specimens
X	Configuration exceeds load capacity of test machine

Table 3.13. A508: Matrix of Test Specimen Configurations, a_o/W=0.5

(dimensions in millimetres, W=width, B=thickness)

Specimen	B mm	W mm	a_o mm	J_T MPa mm	J_{Icn} MPa mm	J_{Icp} MPa mm	SZW mm	Δa mm
A21-E	10.02	20.00	9.80	2103.0	-	2103.0	0.210	0.774
A21-F	10.02	20.00	9.77	3422.4	-	3422.4	0.191	1.261
A21-G	10.02	20.00	9.84	1953.0	-	1953.0	0.173	0.680
A22-E	10.02	40.00	19.92	2460.0	-	2460.0	0.175	1.970
A22-F	10.02	40.00	19.92	1519.1	-	1519.1	0.182	2.000
A22-G	10.02	40.00	19.80	2021.5	-	2021.5	0.195	1.603
A22-H	10.03	40.00	19.78	1525.8	-	1525.8	0.278	1.344
A23-A	10.00	80.00	39.93	1579.7	-	1579.7	0.309	2.893
A23-B	10.01	80.00	39.96	2018.4	-	2018.4	0.296	3.566
A23-C	10.00	80.00	40.00	1339.5	-	1339.5	0.235	3.740
A23-D	10.00	80.01	39.76	921.9	-	921.9	0.244	1.175
A23-L	10.01	80.02	39.69	1209.7	-	1209.7	0.227	2.044
B21-C	20.00	20.00	10.00	343.9	-	343.9	0.168	0.168
B21-D	20.00	20.00	10.00	1600.5	-	1600.5	0.164	0.404

B=thickness, W=width, a_o=initial crack length, SZW=stretch zone width and Δa=crack growth (including SZW)

Table 3.14. A508: Mode I Fracture Toughness Data, $a_o/W=0.5$ (contd.)

Specimen	B mm	W mm	a_o mm	J_T MPa mm	J_{Icn} MPa mm	J_{Icp} MPa mm	SZW mm	Δa mm
B21-E	20.00	20.00	10.00	2323.4	-	2323.4	0.170	0.579
B21-H	19.94	20.05	9.76	2241.4	-	2241.4	0.166	0.826
B21-I	19.99	20.04	9.89	3063.2	-	3063.2	0.186	1.130
B21-J	19.99	20.05	9.77	1815.2	-	1815.2	0.176	0.598
B21-K	20.00	20.00	9.98	1318.4	-	1318.4	0.193	0.396
B22-E	20.02	40.01	19.82	2908.9	-	2908.9	0.223	2.197
B22-F	20.02	40.01	19.91	587.8	-	587.8	0.231	0.505
B22-G	20.00	40.01	19.94	2375.5	-	2375.5	0.284	1.679
B22-H	20.01	40.01	19.92	1444.3		1444.3	0.263	1.375
B22-I	20.00	40.00	20.01	1067.5	-	1067.5	0.229	0.841
C21-A	40.01	20.00	9.98	3064.9	-	3064.9	0.194	1.388
C21-B	40.00	20.00	10.01	1727.2	-	1727.2	0.227	0.731
C21-C	40.01	20.01	9.97	2358.3	-	2358.3	0.213	0.995
C21-D	40.01	20.01	9.99	3641.3	-	3641.3	-	-

B=thickness, W=width, a_o=initial crack length, SZW=stretch zone width and Δa=crack growth (including SZW)

Table 3.14. A508: Mode I Fracture Toughness Data, $a_o/W=0.5$

Loading angle	B mm	W mm	Local Load Line			Local Crack Normal (Mode I)			Local Crack Parallel (Mode II)		
			C_1	C_2	dJ/da	C_1	C_2	dJ/da	C_1	C_2	dJ/da
Mode I	10.0	20.0	2741.3	0.9327	2587	2741.3	0.9327	2587	-	-	-
α=0.0°	10.0	40.0	1081.0	1.2404	1472	1081.0	1.2404	1472	-	-	-
	10.0	80.0	792.8	0.6846	452	792.8	0.6846	452	-	-	-
	20.0	20.0	2772.7	0.6777	2553	2772.7	0.6777	2553	-	-	-
	20.0	40.0	1223.3	1.0784	1392	1223.3	1.0784	1392	-	-	-
	40.0	20.0	2313.1	0.8932	2018	2313.1	0.8932	2018	-	-	-
α=22.5°	10.0	20.0	1581.6	0.4011	643	1107.5	0.3916	434	527.4	0.3757	206
	10.0	40.0	1735.7	0.4441	596	1338.8	0.4131	420	443.7	0.5275	191
	10.0	80.0	1607.1	0.4288	353	1302.8	0.4314	298	371.4	0.4763	95
α=45.0°	10.0	20.0	1329.4	0.4151	723	444.8	0.3616	228	859.8	0.3783	437
	10.0	40.0	1141.3	0.4151	383	493.6	0.3788	143	751.8	0.4123	244
	10.0	80.0	1269.0	0.4780	394	648.9	0.4496	184	686.6	0.4592	205
	40.0	20.0	1229.1	0.4327	377	405.8	0.3197	91	936.5	0.4119	280

B=thickness, W=width, C_1 and C_2=R-curve parameters and dJ/da=slope of the R-curve (units: MPa)

Table 3.15. A508: R-Curve Parameters for Different Size Specimens, a_o/W=0. 5 (contd.)

Loading angle	B mm	W mm	Local Load Line			Local Crack Normal (Mode I)			Local Crack Parallel (Mode II)		
			C_1	C_2	dJ/da	C_1	C_2	dJ/da	C_1	C_2	dJ/da
α=67.5°	10.0	20.0	460.1	0.4864	241	47.8	0.3494	18	439.4	0.4753	226
	10.0	40.0	593.3	0.4092	229	80.9	0.2660	20	549.8	0.3884	204
	10.0	80.0	568.0	0.4327	156	94.1	0.3407	19	518.9	0.4217	135
Mode II α=90.0°	10.0	20.0	248.2	0.5303	174	-	-	-	248.2	0.5303	174
	10.0	40.0	263.7	0.6363	166	-	-	-	263.7	0.6363	166
	10.0	80.0	249.7	0.6838	127	-	-	-	249.7	0.6838	127
	20.0	20.0	288.8	0.6658	221	-	-	-	288.8	0.6658	221
	20.0	40.0	268.5	0.6035	172	-	-	-	268.5	0.6035	172
	40.0	20.0	266.8	0.6294	196	-	-	-	266.8	0.6294	196
	40.0	40.0	260.3	0.7920	195	-	-	-	260.3	0.7920	195
	Mode II master curve		269.1	0.6278	151	-	-	-	269.1	0.6278	151

B=thickness, W=width, C_1 and C_2=R-curve parameters and dJ/da=slope of the R-curve (units: MPa)

Table 3.15. A508: R-Curve Parameters for Different Size Specimens, a_o/W=0.5

Specimen	B mm	W mm	a_o mm	J_T MPa mm	J_{Icn} MPa mm	J_{Icp} MPa mm	SZW mm	Δa mm
A21-A	10.00	20.01	9.98	6.7	-	6.7	0.000	0.000
A21-B	10.00	20.01	9.99	90.7	-	90.7	0.067	0.154
A21-C	10.00	20.01	9.97	190.3	-	190.3	0.039	0.515
A21-D	9.99	20.01	9.96	255.1	-	255.1	0.037	0.842
A21-N	10.00	20.01	9.95	145.4	-	145.4	0.118	0.399
A21-O	9.99	19.99	9.90	210.6	-	210.6	0.109	0.959
A22-A	10.00	40.00	19.98	233.4	-	233.4	0.046	0.812
A22-B	9.99	40.01	19.98	361.4	-	361.4	0.100	1.653
A22-D	10.00	40.01	19.95	161.5	-	161.5	0.094	0.467
A23-E	10.00	80.00	40.00	217.3	-	217.3	0.128	0.849
A23-F	10.00	80.01	40.00	309.8	-	309.8	0.129	1.300
A23-G	10.00	79.99	39.97	667.9	-	667.9	0.102	4.276
B21-A	20.0	20.0	9.97	83.7	-	83.7	0.061	0.151
B21-B	20.0	20.0	9.95	99.9	-	99.9	0.074	0.221

B=thickness, W=width, a_o=initial crack length, SZW=stretch zone width and Δa=crack growth (including SZW)

Table 3.16. A508: Mode II Fracture Toughness Data, a_o/W=0. 5 (contd.)

Specimen	B mm	W mm	a_o mm	J_T MPa mm	J_{Icn} MPa mm	J_{Icp} MPa mm	SZW mm	Δa mm
B21-F	20.0	20.0	9.98	241.3	-	241.3	0.048	0.664
B21-G	20.0	20.0	10.01	306.8	-	306.8	0.046	1.192
B22-A	20.00	40.00	20.02	271.9	-	271.9	0.038	0.998
B22-B	20.00	40.00	19.91	202.2	-	202.2	0.036	0.536
B22-C	19.93	40.00	19.88	330.1	-	330.1	0.040	1.377
B22-D	20.00	40.00	20.05	181.8	-	181.8	0.037	0.638
C21-E	39.99	19.96	9.98	274.6	-	274.6	0.141	1.034
C21-F	39.99	19.99	10.00	148.7	-	148.7	0.115	0.392
C21-G	39.98	20.00	9.97	213.7	-	213.7	0.121	0.717
C22-E	39.99	40.01	20.16	397.2	-	397.2	0.148	1.828
C22-F	40.00	40.00	20.07	585.9	-	585.9	0.147	2.656
C22-G	40.00	40.00	20.01	224.3	-	224.3	0.144	0.811

B=thickness, W=width, a_o=initial crack length, SZW=stretch zone width and Δa=crack growth (including SZW)

Table 3.16. A508: Mode II Fracture Toughness Data, $a_o/W=0.5$

Specimen	B mm	W mm	a_o mm	J_T MPa mm	J_{Icn} MPa mm	J_{Icp} MPa mm	SZW mm	Δa mm
A21-V	10.00	20.02	9.95	1943.0	1333.6	654.3	0.390	1.823
A21-W	10.00	19.98	9.95	1126.3	779.1	390.4	0.127	0.315
A21-X	10.00	20.00	9.95	687.1	485.7	243.0	0.126	0.277
A21-Y	10.01	20.00	9.9	1744.7	1249.7	562.7	0.154	1.266
A21-Z	10.01	20.00	9.91	1282.2	928.5	425.2	0.158	0.337
A22-P	10.00	40.01	19.74	3131.5	2316.6	898.3	0.128	3.427
A22-Q	9.99	40.01	19.81	1486.2	1158.7	369.5	0.127	0.684
A22-R	9.99	40.01	19.76	2389.8	1803.9	644.9	0.149	2.333
A23-M	10.03	79.97	39.72	3409.5	2820.6	857.1	0.795	6.134
A23-N	10.00	80.00	39.70	1370.8	1127.6	311.6	0.127	0.732
A23-O	10.02	79.99	39.73	2344.0	1845.8	563.5	0.288	2.141

B=thickness, W=width, a_o=initial crack length, SZW=stretch zone width and Δa=crack growth (including SZW)

Table 3.17. A508: Mixed Mode, α=22.5° Fracture Toughness Data, a_o/W=0.5

Specimen	B mm	W mm	a_o mm	J_T MPa mm	J_{Icn} MPa mm	J_{Icp} MPa mm	SZW mm	Δa mm
A21-H	10.00	20.00	10.00	564.4	213.4	395.7	0.124	0.198
A21-I	10.00	20.00	10.00	787.9	281.6	555.6	0.121	0.228
A21-J	10.00	20.00	10.00	1040.8	364.4	616.3	0.173	0.341
A21-K	10.00	20.00	10.00	1280.0	441.1	808.6	0.093	1.012
A21-L	10.01	20.00	9.99	885.6	299.6	606.0	0.201	0.156
A21-M	10.00	20.00	9.91	1144.0	387.6	805.5	0.183	0.593
A22-I	10.00	40.00	20.02	1777.4	723.4	1160.4	0.362	2.989
A22-J	10.00	40.00	19.95	683.4	320.3	455.5	0.137	0.424
A22-K	10.01	40.01	20.02	950.1	408.2	640.0	0.179	0.471
A22-L	10.00	40.00	20.01	1365.2	587.0	878.2	0.322	1.405
A23-I	10.00	80.02	39.98	2259.6	1110.3	1202.1	0.231	3.601
A23-J	9.99	80.02	39.94	1010.3	519.0	556.5	0.106	0.697
A23-K	9.99	80.01	39.97	1588.7	813.3	839.5	0.145	1.323

B=thickness, W=width, a_o=initial crack length, SZW=stretch zone width and Δa=crack growth (including SZW)

Table 3.18. A508: Mixed Mode, α=45.0° Fracture Toughness Data, a_o/W=0.5 (contd.)

Specimen	B mm	W mm	a_o mm	J_T MPa mm	J_{Icn} MPa mm	J_{Icp} MPa mm	SZW mm	Δa mm
C21-I	39.99	19.99	10.05	1415.2	441.4	1075.0	0.166	1.966
C21-J	40.00	20.00	9.99	1093.0	379.8	830.7	0.142	0.540
C21-K	39.99	20.01	9.97	533.3	213.1	425.5	0.235	0.235
C21-L	40.01	20.01	10.00	1217.3	414.2	927.0	0.280	0.602

B=thickness, W=width, a_o=initial crack length, SZW=stretch zone width and Δa=crack growth (including SZW)

Table 3.18. A508: Mixed Mode, α=45.0° Fracture Toughness Data, a_o/W=0.5

Specimen	B mm	W mm	a_o mm	J_T MPa mm	J_{Icn} MPa mm	J_{Icp} MPa mm	SZW mm	Δa mm
A21-S	9.99	20.01	9.95	617.1	56.0	591.3	0.179	1.845
A21-T	9.99	20.00	9.98	240.0	30.1	231.9	0.158	0.247
A21-U	10.00	20.01	9.95	433.5	43.8	418.2	0.160	0.886
A21-AA	10.00	20.00	9.95	535.7	59.4	498.5	0.163	1.272
A21-AB	10.00	19.99	9.87	324.7	36.7	314.8	0.173	0.552
A22-L	10.00	40.00	19.95	1016.8	114.7	921.6	0.204	3.296
A22-M	10.00	40.00	19.90	282.9	49.7	275.9	0.143	0.149
A22-N	10.00	40.02	19.97	794.5	97.1	734.2	0.212	2.115
A22-O	10.00	40.01	19.95	482.5	71.8	438.3	0.182	0.724
A23-Q	10.00	80.02	39.72	1165.7	164.9	1035.6	0.282	5.032
A23-R	10.01	80.01	39.67	473.4	81.3	432.0	0.289	0.639
A23-S	10.01	80.02	39.69	796.0	123.8	732.2	0.283	2.345

B=thickness, W=width, a_o=initial crack length, SZW=stretch zone width and Δa=crack growth (including SZW)

Table 3.19. A508: Mixed Mode, α=67.5° Fracture Toughness Data, a_o/W=0.5

Mode I (Tension)

α=0.0°

	B=10	B=20	B=40
W=20	4	3	
W=40			
W=80	3		X

Mixed mode (combination of tension and shear)

α=22.5°

	B=10	B=20	B=40
W=20			
W=40			
W=80			X

Mixed mode (combination of tension and shear)

α=45.0°

	B=10	B=20	B=40
W=20	3		
W=40			
W=80	3		

Mixed mode (combination of tension and shear)

α=67.5°

	B=10	B=20	B=40
W=20			
W=40			
W=80			

Mode II (Shear)

α=90.0°

	B=10	B=20	B=40
W=20	4	4	
W=40			
W=80	3		

4	Number of completed specimens
X	Configuration exceeds load capacity of test machine

Table 3.20. A508: Matrix of Test Specimen Configurations, a_o/W=0.7

(dimensions in millimetres, W=width, B=thickness)

Specimen	B mm	W mm	a_o mm	J_T MPa mm	J_{Icn} MPa mm	J_{Icp} MPa mm	SZW mm	Δa mm
A31-E	10.01	20.00	13.96	2021.2	-	2021.2	0.143	0.623
A31-F	10.00	20.01	13.99	2452.3	-	2452.3	0.109	0.712
A31-G	10.00	20.01	13.94	1521.3	-	1521.3	0.110	0.408
A31-H	10.01	20.01	14.01	2135.9	-	2135.9	0.144	0.680
A33-A	10.01	80.01	55.94	3174.9	-	3174.9	0.158	4.411
A33-B	10.01	80.01	55.90	1449.8	-	1449.8	0.175	0.940
A33-C	10.01	80.01	55.93	2356.1	-	2356.1	0.196	3.008
B31-E	20.01	20.02	13.93	1830.6	-	1830.6	0.142	0.672
B31-F	20.01	20.02	14.04	1410.9	-	1410.9	0.137	0.427
B31-G	20.01	20.01	13.99	2150.5	-	2150.5	0.167	0.807

B=thickness, W=width, a_o=initial crack length, SZW=stretch zone width and Δa=crack growth (including SZW)

Table 3.21. A508: Mode I Fracture Toughness Data, $a_o/W=0.7$

Specimen	B mm	W mm	a_o mm	J_T MPa mm	J_{Icn} MPa mm	J_{Icp} MPa mm	SZW mm	Δa mm
A31-I	10.02	19.87	14.05	1282.5	385.8	929.2	0.147	1.277
A31-J	10.02	20.01	14.05	915.3	316.1	638.1	0.158	0.518
A31-K	10.02	19.89	14.04	517.0	184.5	369.0	0.000	0.173
A33-I	10.01	80.02	55.95	1871.8	736.9	1202.8	0.162	2.552
A33-J	10.01	80.02	55.95	1331.3	555.6	847.8	0.213	0.482
A33-K	10.00	80.02	55.95	1044.1	433.2	676.1	0.138	0.436

B=thickness, W=width, a_o=initial crack length, SZW=stretch zone width and Δa=crack growth (including SZW)

Table 3.22. A508: Mixed Mode, α=45.0° Fracture Toughness Data, a_o/W=0.7

Specimen	B mm	W mm	a_o mm	J_T MPa mm	J_{Icn} MPa mm	J_{Icp} MPa mm	SZW mm	Δa mm
A31-A	9.99	20.01	14.00	29.4	-	19.4	0.000	0.000
A31-B	10.00	19.99	14.00	78.3	-	78.3	0.042	0.165
A31-C	9.99	20.00	13.97	109.6	-	109.6	0.037	0.290
A31-D	9.99	19.99	13.96	144.7	-	144.7	0.040	0.554
A33-E	10.01	80.01	55.96	585.7	-	585.7	0.139	3.527
A33-F	10.01	80.01	55.99	242.4	-	242.4	0.127	0.806
A33-G	10.01	80.01	55.95	421.6	-	421.6	0.137	1.980
B31-A	20.00	20.00	13.98	179.2	-	179.2	0.044	0.508
B31-B	20.00	20.00	13.95	126.2	-	126.2	0.043	0.327
B31-C	20.00	20.00	13.99	154.8	-	154.8	0.044	0.525
B31-D	20.00	20.00	13.99	225.5	-	225.5	0.059	0.838

B=thickness, W=width, a_o=initial crack length, SZW=stretch zone width and Δa=crack growth (including SZW)

Table 3.23. A508: Mode II Fracture Toughness Data, $a_o/W=0.7$

Loading angle	B mm	W mm	Local Load Line			Local Crack Normal (Mode I)			Local Crack Parallel (Mode II)		
			C_1	C_2	dJ/da	C_1	C_2	dJ/da	C_1	C_2	dJ/da
Mode I	10.0	20.0	2993.6	0.7669	2725	2993.6	0.7669	2725	-	-	-
α=0.0°	10.0	80.0	1470.6	0.4861	493	1470.6	0.4861	493	-	-	-
	20.0	20.0	2426.0	0.6454	1918	2426.0	0.6454	1918	-	-	-
α=45.0°	10.0	20.0	1177.8	0.4569	659	369.7	0.3735	168	842.2	0.4634	487
	10.0	80.0	1456.2	0.2747	329	590.9	0.2427	117	935.3	0.2747	212
Mode II	10.0	20.0	186.9	0.4833	153	-	-	-	186.9	0.4833	153
α=90.0°	10.0	80.0	277.0	0.5992	125	-	-	-	277.0	0.5992	125
	20.0	20.0	251.3	0.6252	195	-	-	-	251.3	0.6252	195
	Mode II master curve		254.4	0.6803	152	-	-	-	254.4	0.6803	152

B=thickness, W=width, C_1 and C_2=R-curve parameters and dJ/da=slope of the R-curve (units: MPa)

Table 3.24. A508: R-Curve Parameters for Different Size Specimens, a_o/W=0.7

Mode I (Tension)

α=0.0°

	B=10	B=20	B=40
W=20	2		2
W=40			X
W=80		X	X

Mixed mode (combination of tension and shear)

α=22.5°

	B=10	B=20	B=40
W=20			
W=40			X
W=80		X	X

Mixed mode (combination of tension and shear)

α=45.0°

	B=10	B=20	B=40
W=20	2		
W=40			X
W=80		X	X

Mixed mode (combination of tension and shear)

α=67.5°

	B=10	B=20	B=40
W=20			
W=40			X
W=80		X	X

Mode II (Shear)

α=90.0°

	B=10	B=20	B=40
W=20	4		3
W=40			
W=80			X

4	Number of completed specimens
X	Configuration exceeds load capacity of test machine

Table 3.25. A508: Matrix of Test Specimen Configurations, a_o/W=0.1

(dimensions in millimetres, W=width, B=thickness)

Specimen	B mm	W mm	a_o mm	J_T MPa mm	J_{Icn} MPa mm	J_{Icp} MPa mm	SZW mm	Δa mm
A11-A	10.00	20.01	1.970	74.3	-	74.3	0.000	0.000
A11-B	10.00	20.01	1.986	150.3	-	150.3	0.039	0.103
A11-D	10.00	20.00	1.980	238.4	-	238.4	0.039	0.438
A11-C	10.00	20.00	1.990	318.1	-	318.1	0.049	0.619
C11-C	40.00	20.00	2.000	283.1	-	283.1	0.103	0.415
C11-A	40.00	20.00	2.000	515.6	-	515.6	0.101	1.197
C11-B	40.00	20.00	2.000	666.7	-	666.7	0.114	2.583

B=thickness, W=width, a_o=initial crack length, SZW=stretch zone width and Δa=crack growth (including SZW)

Table 3.26. A508: Mode II Fracture Toughness Data, $a_o/W=0.1$

Loading angle	B mm	W mm	C_1	C_2	dJ/da
Mode II α=90.0°	10.0	20.0	357.9	0.3889	317
	40.0	20.0	442.2	0.4744	169
	Mode II master curve		420.8	0.4836	204

B=thickness, W=width, C_1 and C_2=R-curve parameters and dJ/da=slope of the R-curve (units: MPa)

Table 3.27. A508: R-Curve Parameters for Different Size Specimens, a_o/W=0.1

Loading mode	Width, W	Thickness, B		
		10.0mm	20.0mm	40.0mm
Mode I α=0.0°	20.0mm	52.0 kN	102.1 kN	224.0 kN
	40.0mm	96.4 kN	173.6 kN	-
	80.0mm	123.7 kN	-	-
α=22.5°	20.0mm	49.3 kN	-	-
	40.0mm	70.5 kN	-	-
	80.0mm	162.2 kN	-	-
α=45.0°	20.0mm	29.4 kN	-	173.8 kN
	40.0mm	64.5 kN	-	-
	80.0mm	102.0 kN	-	-
α=67.5°	20.0mm	28.5 kN	-	-
	40.0mm	59.6 kN	-	-
	80.0mm	121.2 kN	-	-
Mode II α=90.0°	20.0mm	31.5 kN	50.9 kN	145.7 kN
	40.0mm	59.1 kN	141.2 kN	-
	80.0mm	112.8 kN	-	-

α=Mixed mode loading angle

Table 3.28. A508: Experimental Mixed Mode I/II Maximum Loads, a_o/W=0.5

Loading mode	Width, W	Thickness, B		
		10.0mm	20.0mm	40.0mm
Mode I	20.0mm	36.3 kN	73.5 kN	-
α=0.0°	80.0mm	71.5 kN	-	-
α=45.0°	20.0mm	23.4 kN	-	-
	80.0mm	86.4 kN	-	-
Mode II	20.0mm	20.2 kN	45.0 kN	-
α=90.0°	80.0mm	78.8 kN	-	-

α=Mixed mode loading angle

Table 3.29. A508: Experimental Mixed Mode I/II Maximum Loads, a_o/W=0.7

Specimen ID	Average fracture face measurements			P_{max}	Fracture Energy
	Face A	Face B	(A+B)/2		
	mm	mm	mm	N	N mm
Parent Material					
1	1.173	0.467	0.820	5849.2	4942.4
2	0.477	0.152	0.314	5570.7	2598.6
3	0.000	0.137	0.068	5459.2	1347.5
4	0.000	0.213	0.107	6139.8	2076.7
5	0.468	1.038	0.753	5531.8	2797.2
Set 2					
1	1.702	0.800	1.251	10081.4	4971.7
2	0.000	0.092	0.046	9581.0	1675.9
3	0.000	0.125	0.063	10208.4	2765.2
4	0.863	0.405	0.634	9900.2	4214.5
5	0.477	0.155	0.316	9852.0	3352.5
Set 3					
1	0.887	0.902	0.894	6468.0	6783.7
2	0.503	0.188	0.346	6222.8	3069.7
3	0.090	0.298	0.194	5849.2	2274.3
4	0.000	0.188	0.094	6016.4	1988.4
5	0.083	0.163	0.123	6182.4	2458.0

P_{max}=maximum load

Table 3.30. A508: Results of the Small Scale SEN Mode II Specimens

Specimen heat	B mm	W mm	C_1	C_2	dU/da N
Parent	5.0	5.0	4670	0.345	3295
Set 2	5.0	5.0			
Set 3	5.0	5.0			

B=thickness, W=width, C_1 and C_2=R-curve parameters and dU/da=slope of the R-curve

Table 3.31. A508: R-Curve Parameters for Small Scale SEN Mode II Specimens

Mode	α	W=20.0mm		W=40.0mm		W=80.0mm	
	(°)	$f_I(a_o/W)$	$f_{II}(a_o/W)$	$f_I(a_o/W)$	$f_{II}(a_o/W)$	$f_I(a_o/W)$	$f_{II}(a_o/W)$
Mode I	00.0	2.576	-	2.523	-	2.487	-
	22.5	1.746	0.300	2.338	0.339	2.357	0.204
	45.0	1.354	0.394	1.847	0.462	1.950	0.363
	67.5	0.885	0.524	1.236	0.646	1.027	0.628
Mode II	90.0	-	0.827	-	0.868	-	0.946

α=Mixed mode loading angle, W=Specimen width

Table 4.1. Mixed Mode Linear Elastic Geometry Functions, a/W=0.1

(plane strain analyses)

Mode	α	W=20.0mm		W=40.0mm		W=80.0mm	
	(°)	$f_I(a_o/W)$	$f_{II}(a_o/W)$	$f_I(a_o/W)$	$f_{II}(a_o/W)$	$f_I(a_o/W)$	$f_{II}(a_o/W)$
Mode I	00.0	3.358	-	3.298	-	3.269	-
	22.5	2.894	0.564	3.013	0.604	3.018	0.572
	45.0	2.214	0.762	2.295	0.829	2.341	0.831
	67.5	1.422	0.900	1.472	0.950	1.500	1.000
Mode II	90.0	-	0.968	-	0.983	-	1.071

Table 4.2. Mixed Mode Linear Elastic Geometry Functions, a/W=0.5

(plane strain analyses)

Mode	α	W=20.0mm		W=40.0mm		W=80.0mm	
	(°)	$f_I(a_o/W)$	$f_{II}(a_o/W)$	$f_I(a_o/W)$	$f_{II}(a_o/W)$	$f_I(a_o/W)$	$f_{II}(a_o/W)$
Mode I	00.0	4.352	-	4.279	-	4.221	-
	22.5	3.726	0.719	3.713	0.745	3.875	0.699
	45.0	2.846	0.989	2.826	1.020	2.923	1.117
	67.5	1.820	1.150	1.804	1.170	1.819	1.200
Mode II	90.0	-	1.180	-	1.185	-	1.242

Table 4.3. Mixed Mode Linear Elastic Geometry Functions, a/W=0.7

(plane strain analyses)

Mode	α (°)	W=20.0mm		W=40.0mm		W=80.0mm	
		η_e	η_p	η_e	η_p	η_e	η_p
Mode I	00.0	1.970	2.650	1.676	2.500	1.743	2.300
	22.5	0.947	-	1.578	-	1.681	-
	45.0	0.652	-	1.125	-	1.251	-
	67.5	0.280	-	0.522	-	0.429	-
Mode II	90.0	0.104	0.780	0.116	0.650	0.137	0.640

α=Mixed mode loading angle, W=Specimen width

Table 4.4. Mixed Mode Elastic and Elastic-Plastic η Factors, a/W=0.1

(plane strain analyses)

Mode	α (°)	W=20.0mm		W=40.0mm		W=80.0mm	
		η_e	η_p	η_e	η_p	η_e	η_p
Mode I	00.0	1.318	2.710	1.384	2.530	1.450	2.365
	22.5	1.160	2.500	1.294	2.425	1.337	2.300
	45.0	0.814	2.100	0.913	2.080	0.973	1.950
	67.5	0.355	1.300	0.395	1.310	0.451	1.110
Mode II	90.0	0.075	0.720	0.079	0.680	0.093	0.686

Table 4.5. Mixed Mode Elastic and Elastic-Plastic η Factors, a/W=0.5

(plane strain analyses)

Mode	α (°)	W=20.0mm		W=40.0mm		W=80.0mm	
		η_e	η_p	η_e	η_p	η_e	η_p
Mode I	00.0	1.239	2.740	1.287	2.620	1.347	2.460
	22.5	1.105	2.560	1.174	2.500	1.230	2.350
	45.0	0.773	2.153	0.820	2.120	0.868	2.040
	67.5	0.332	1.342	0.350	1.325	0.380	1.235
Mode II	90.0	0.065	0.680	0.066	0.690	0.072	0.660

Table 4.6. Mixed Mode Elastic and Elastic-Plastic η Factors, a/W=0.7

(plane strain analyses)

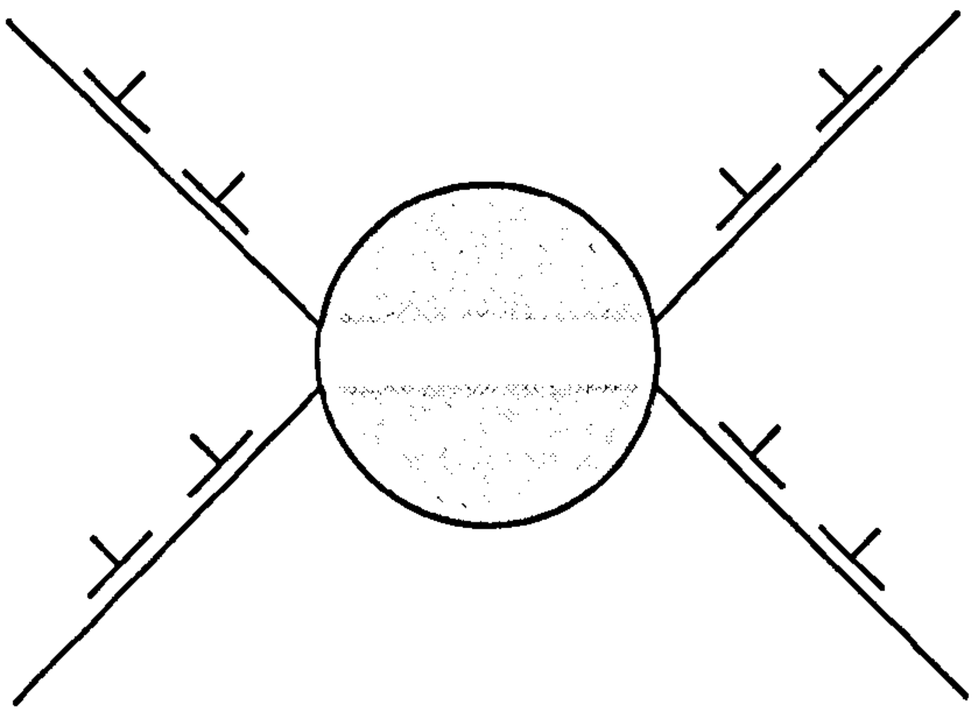

(a) Arrest at a particle/matrix interface

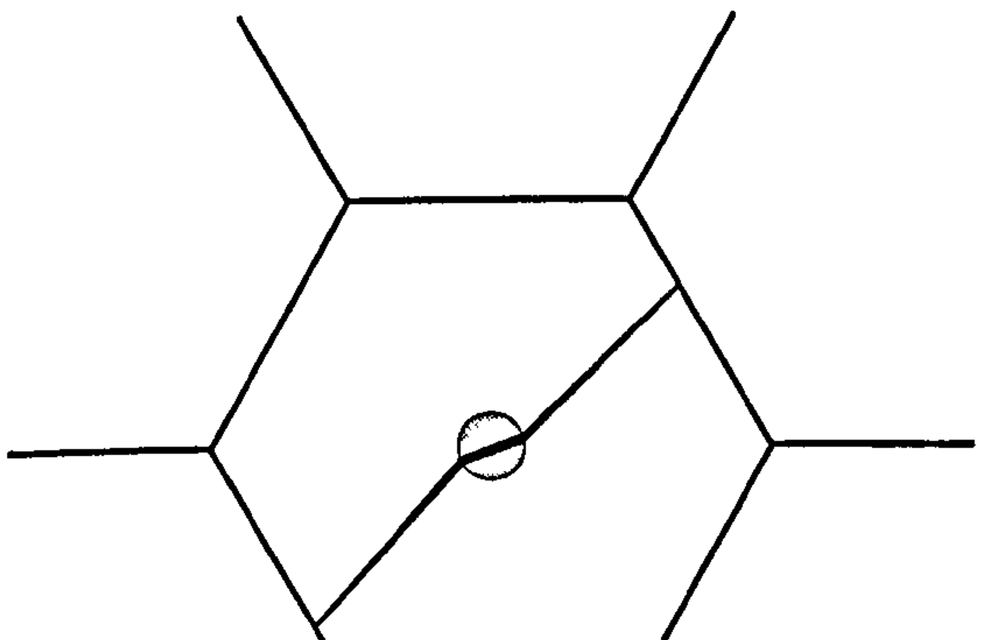

(b) Arrest at a grain boundary

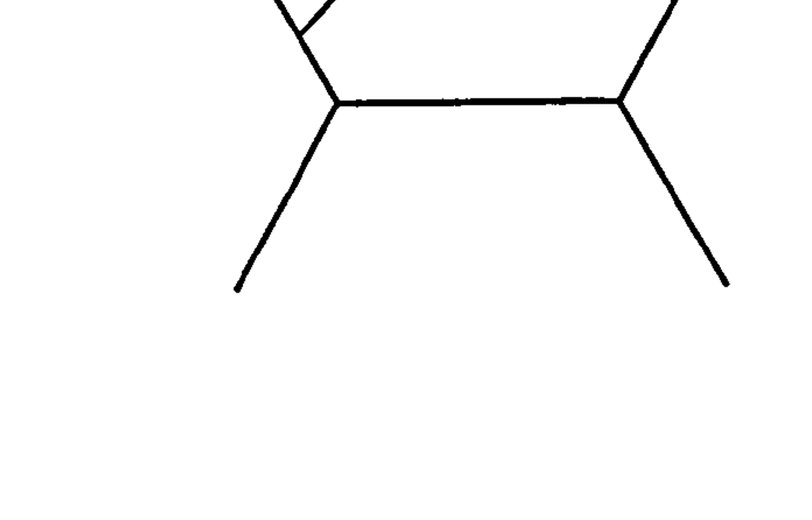

(c) Arrest due to a steep stress gradient

Figure 1.1. Examples of Unsuccessful Cleavage Events

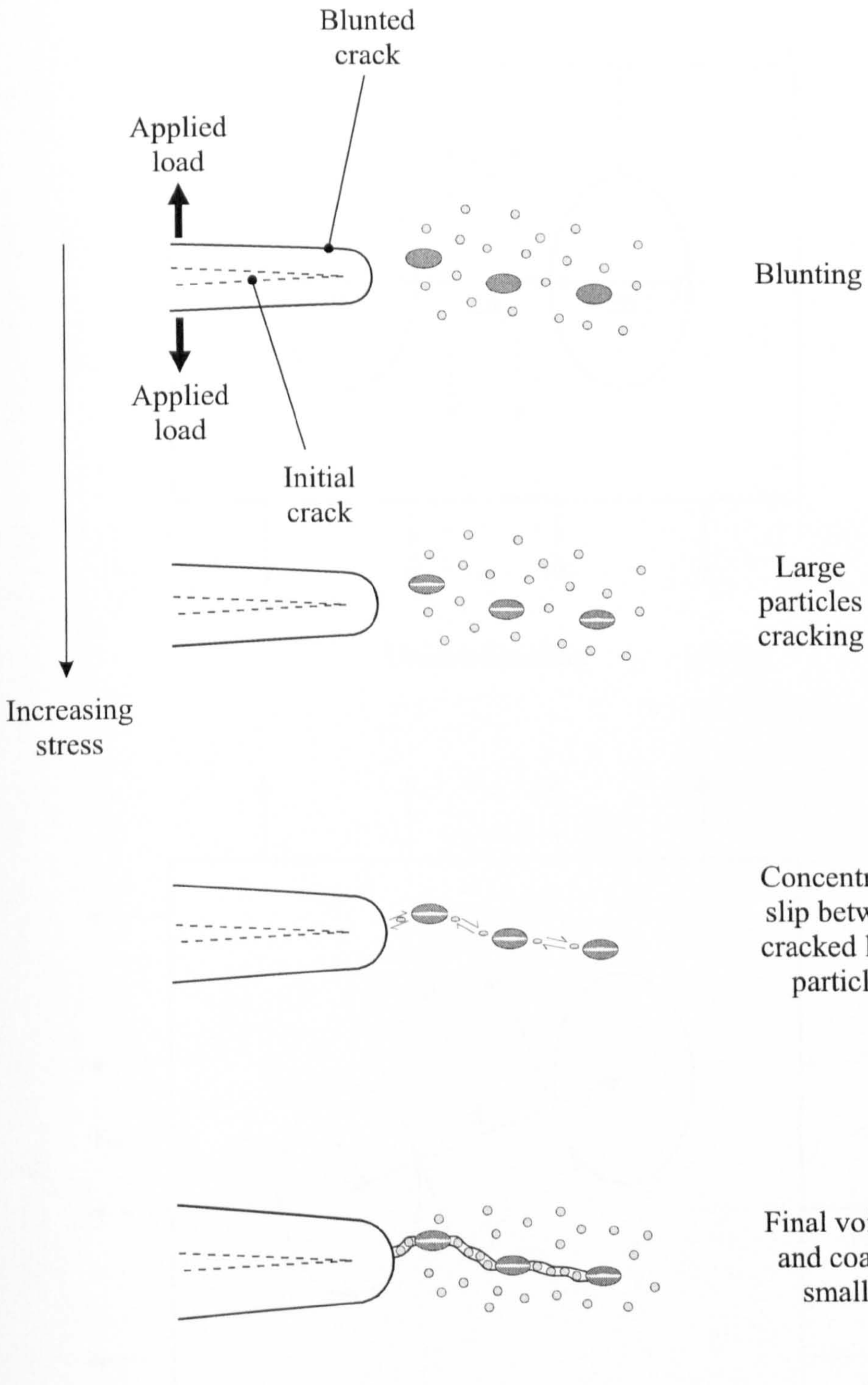

Figure 1.2. Mechanisms of Ductile Crack Growth

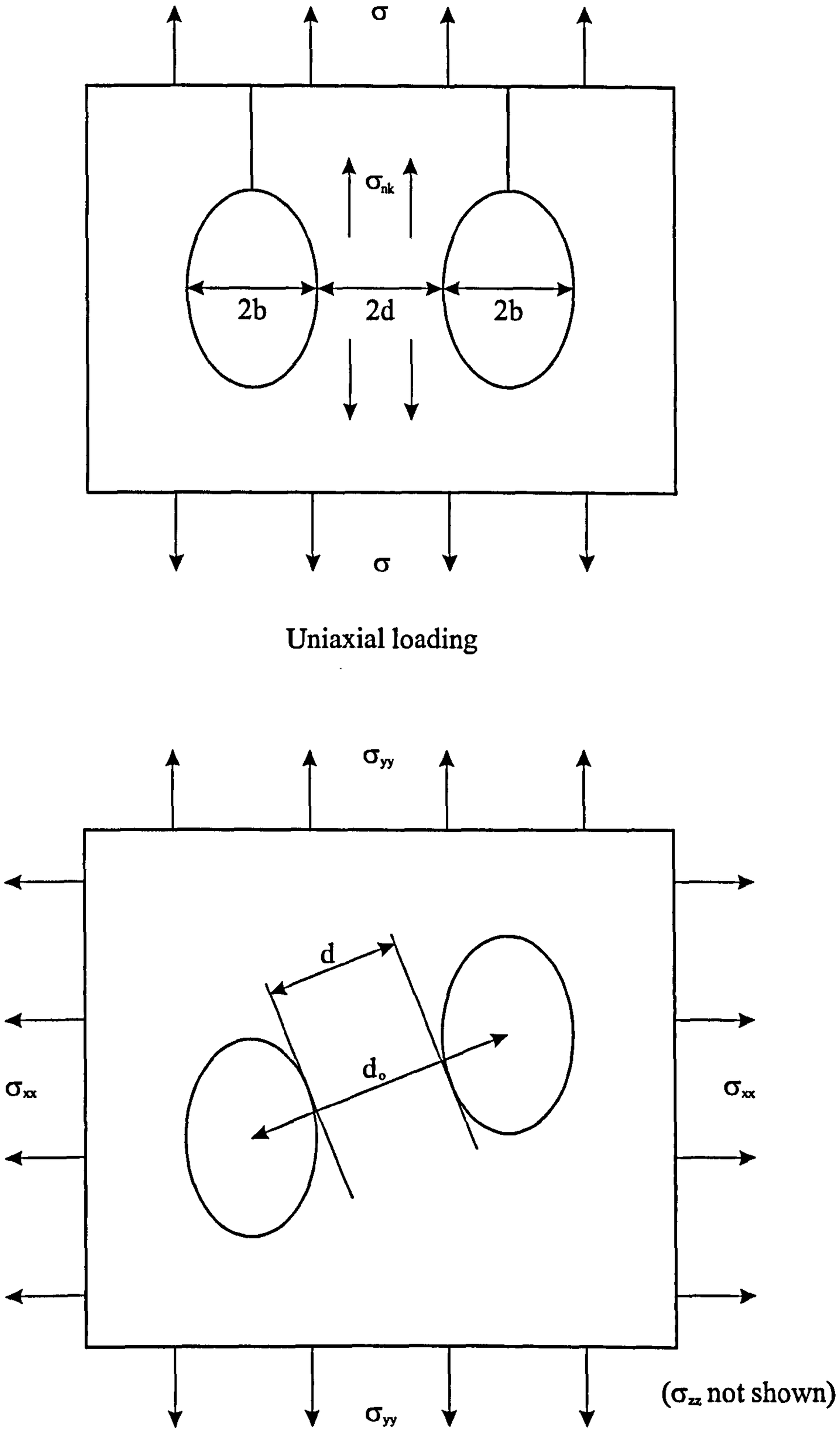

Figure 1.3. Coalescence Criteria Used by Thomason (1990)

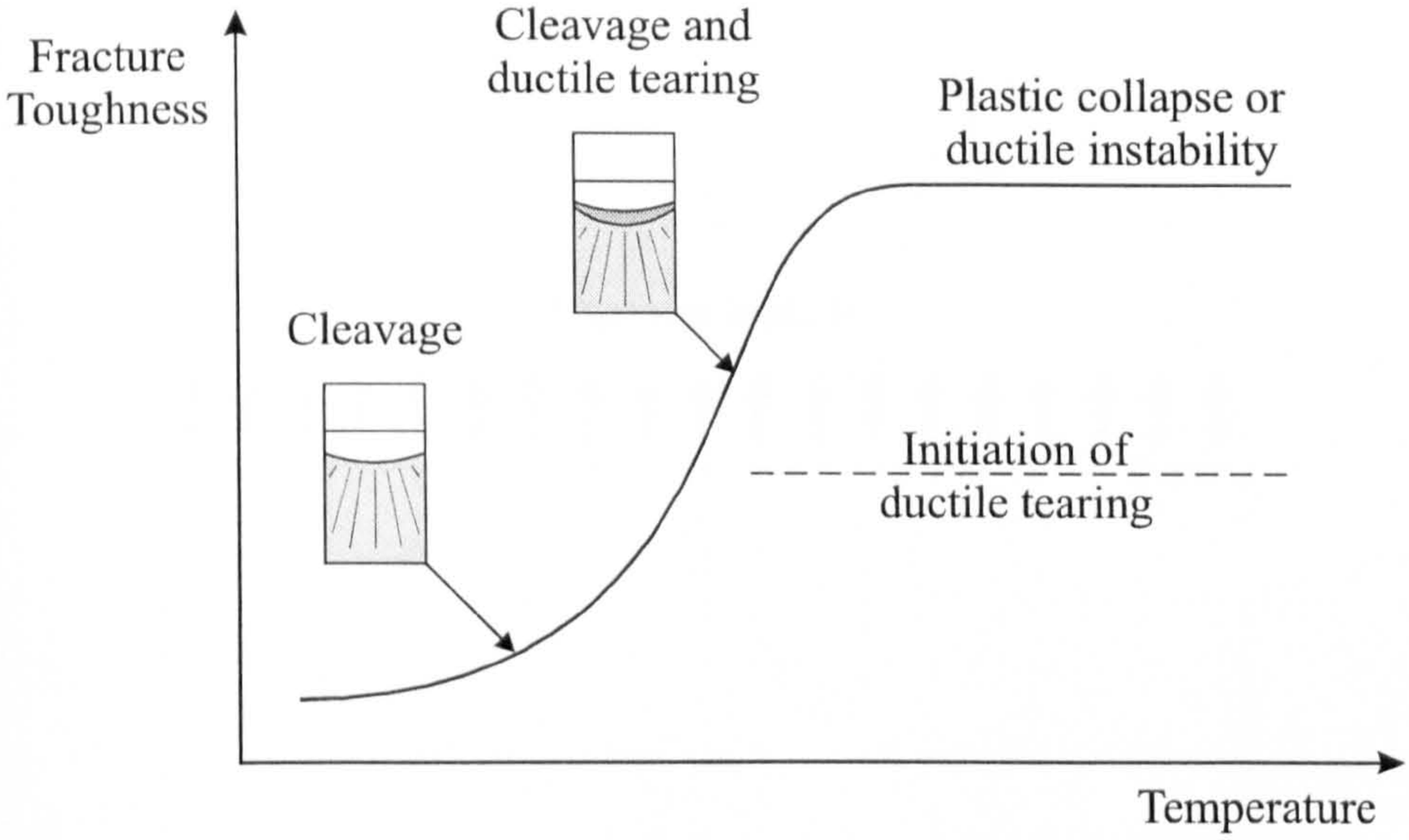

Figure 1.4. The Transition from Brittle to Ductile Fracture
as a Function of Temperature

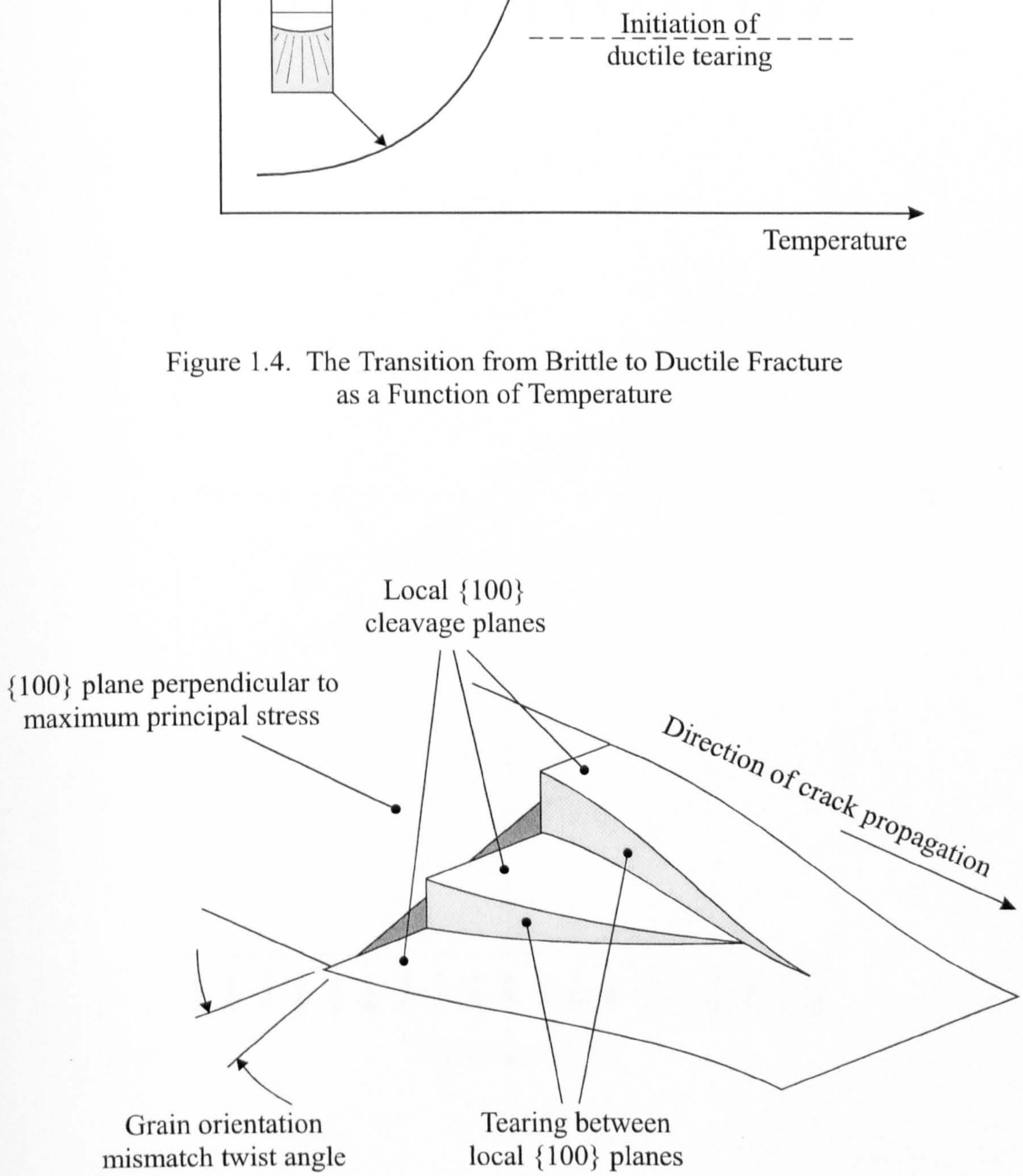

Figure 1.5. Characteristics of Cleavage Crack Growth
Propagating Through Neighbouring Grains

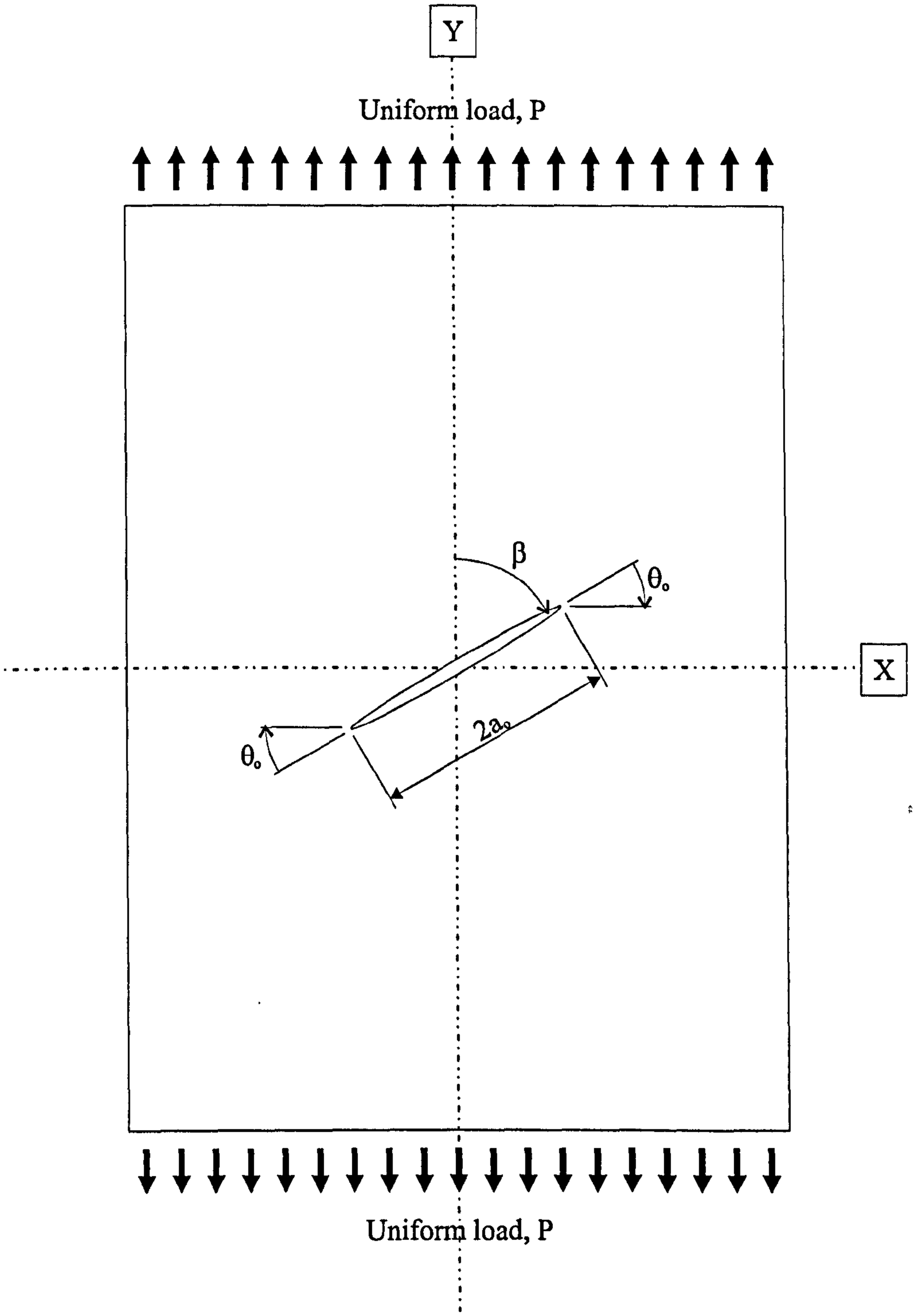

Figure 1.6. An Angled Through Crack in a Large Panel Subject to Uniaxial Tension

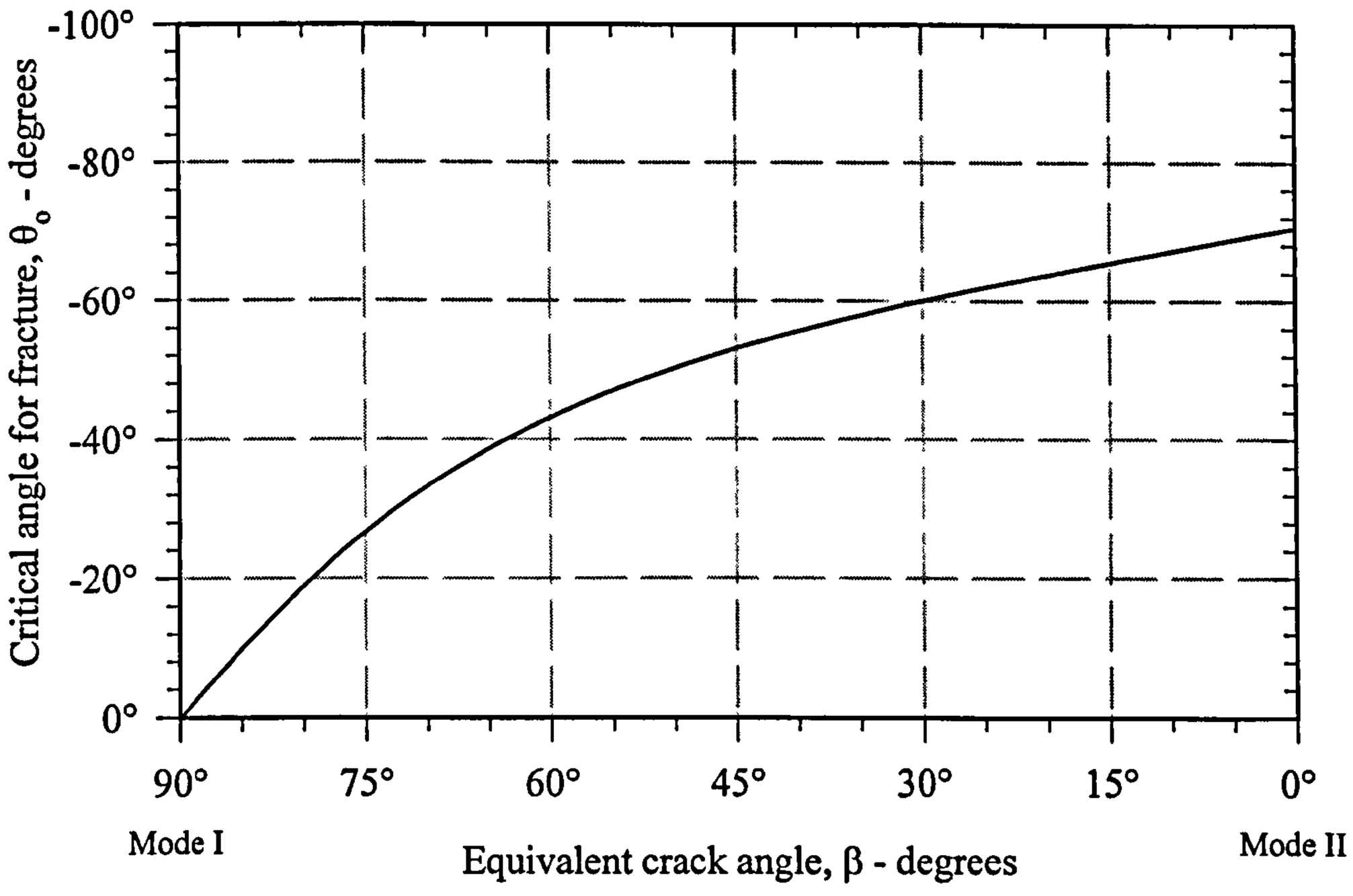

Figure 1.7. Variation of Fracture Angle for Combined Tensile and Shear Loading
(The MTS criterion, proposed by Erdogan and Sih, 1963)

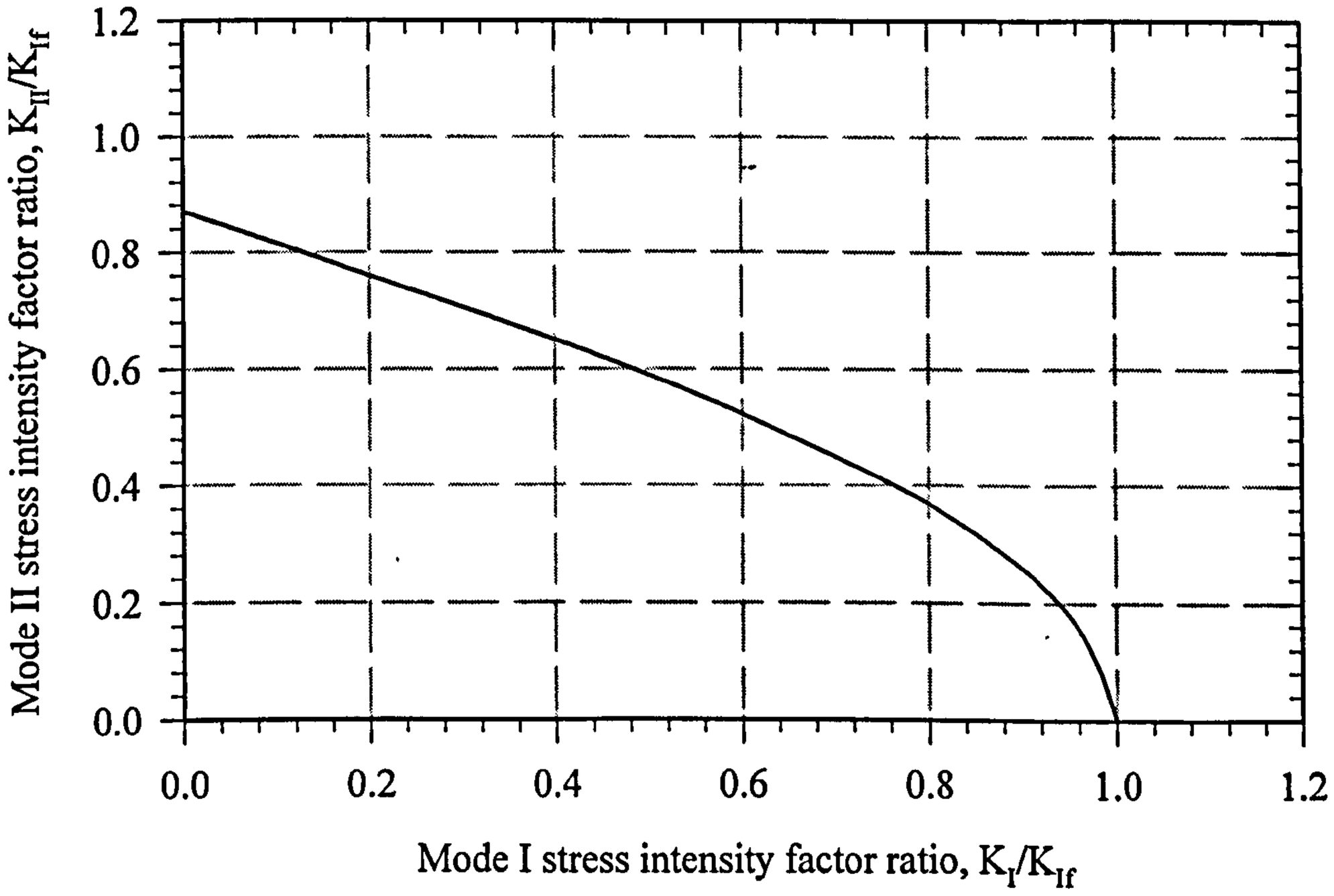

Figure 1.8. Variation of Fracture Toughness for Combined Tensile and Shear Loading
(The MTS criterion, proposed by Erdogan and Sih, 1963)

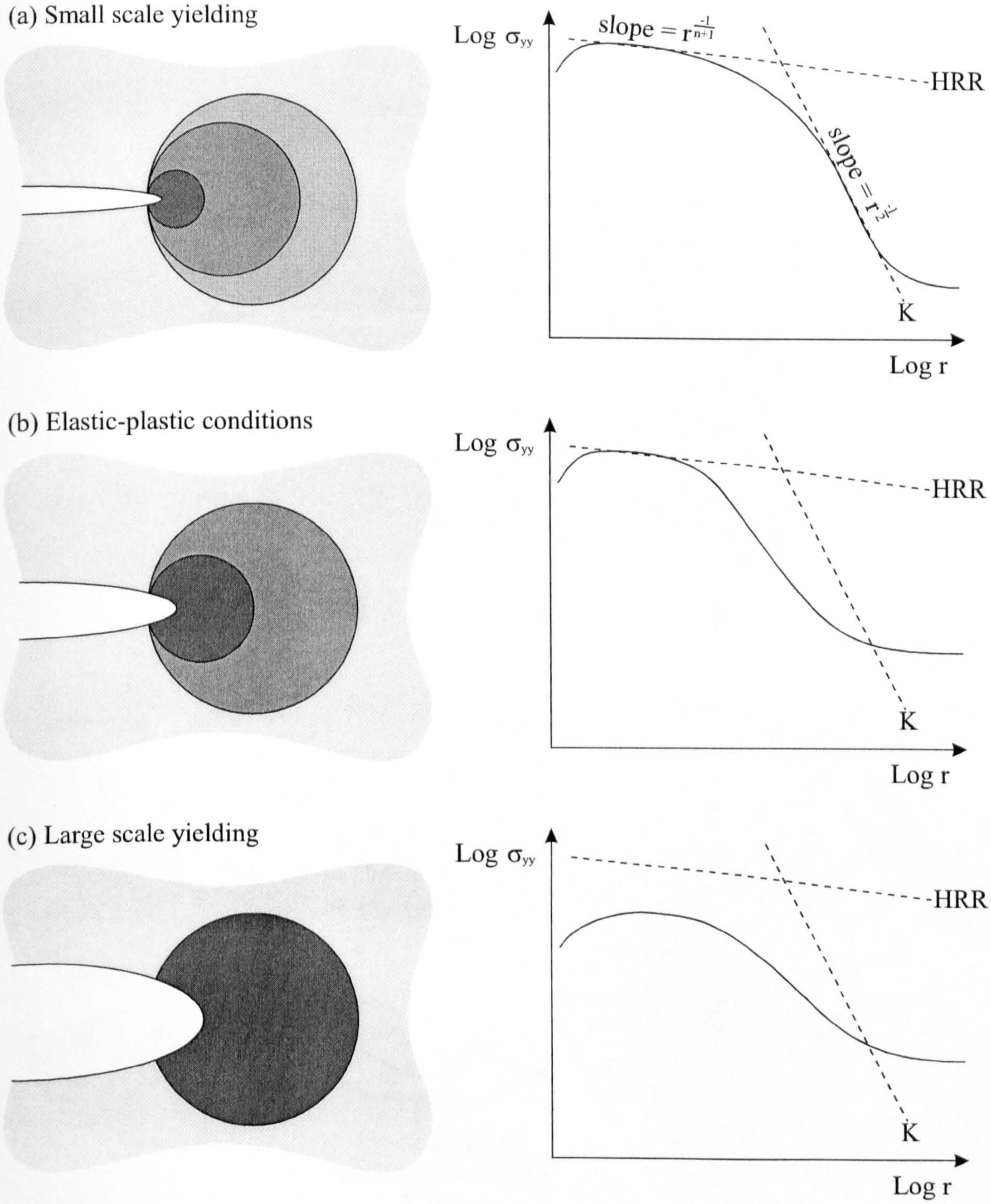

Figure 1.9. Effect of Plasticity on the Crack Tip Stress Fields

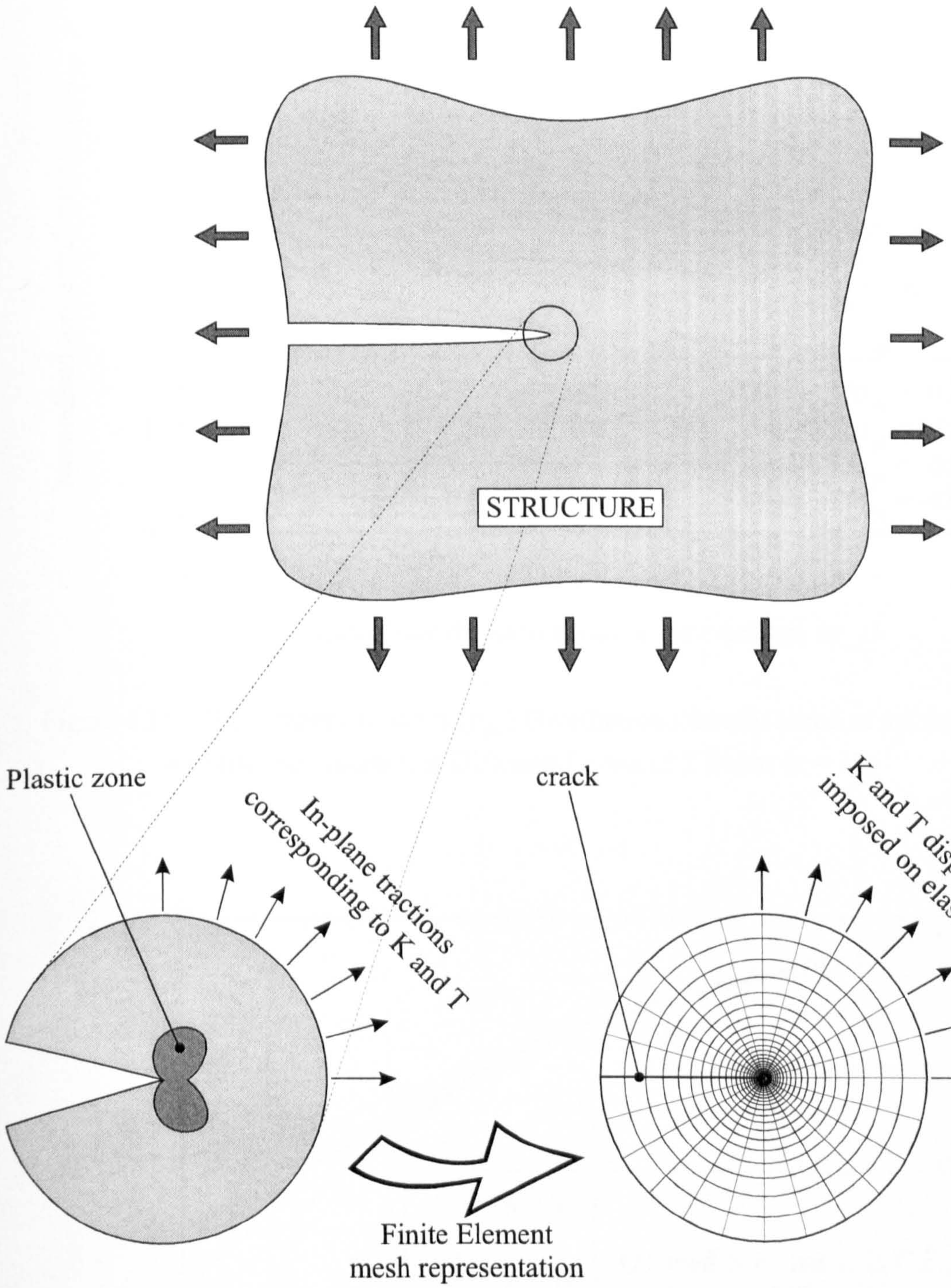

Region surrounding crack tip with imposed loading conditions

Typical boundary layer model comprising imposed u_x and u_y nodal displacements corresponding to K and T

Figure 1.10. Modified Boundary Layer Analysis

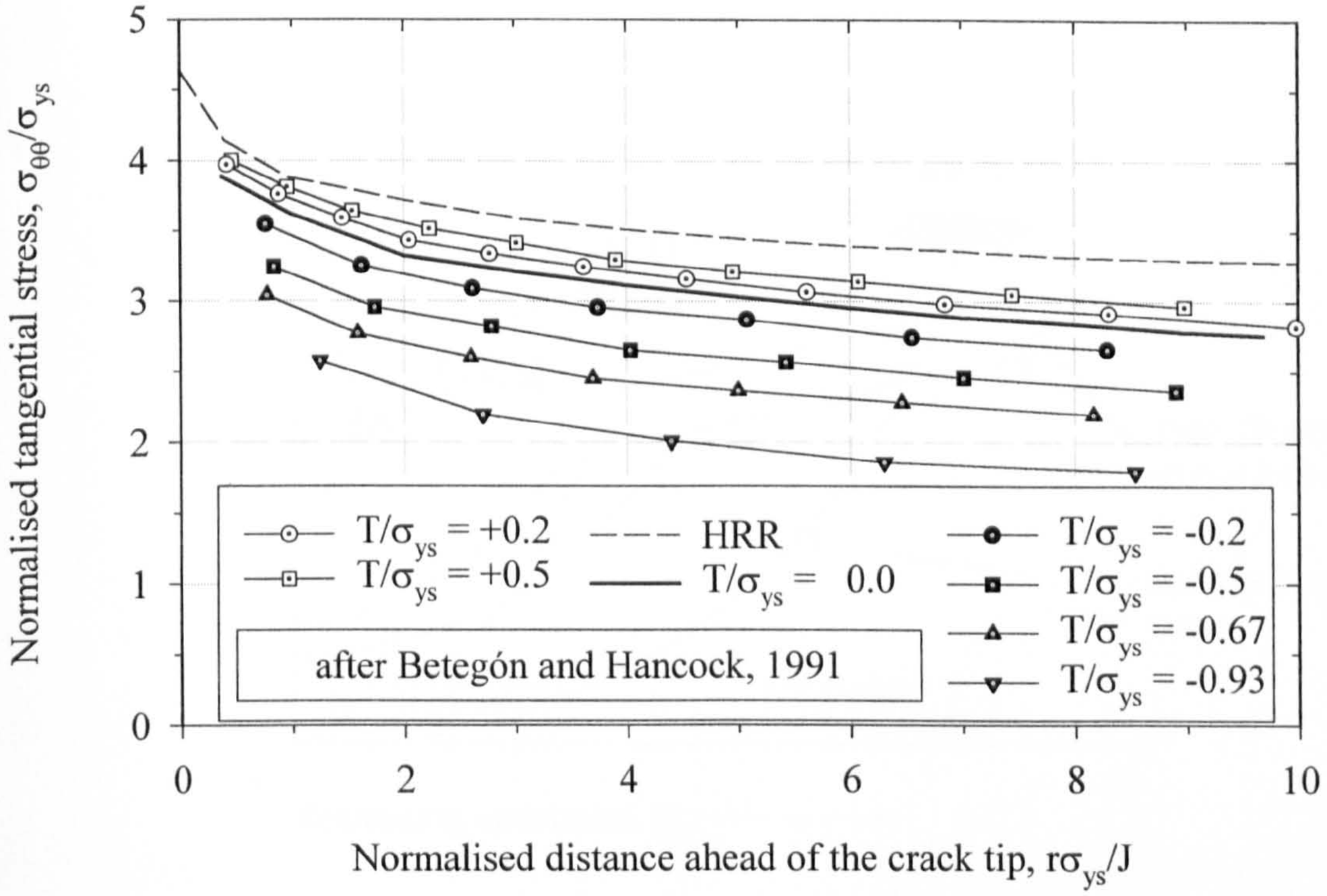

Figure 1.11. The Tangential Stress ($\sigma_{\theta\theta}$) Distribution Directly ahead of a Crack in an MBL Formulation at Different Levels of T Stress (n = 13)

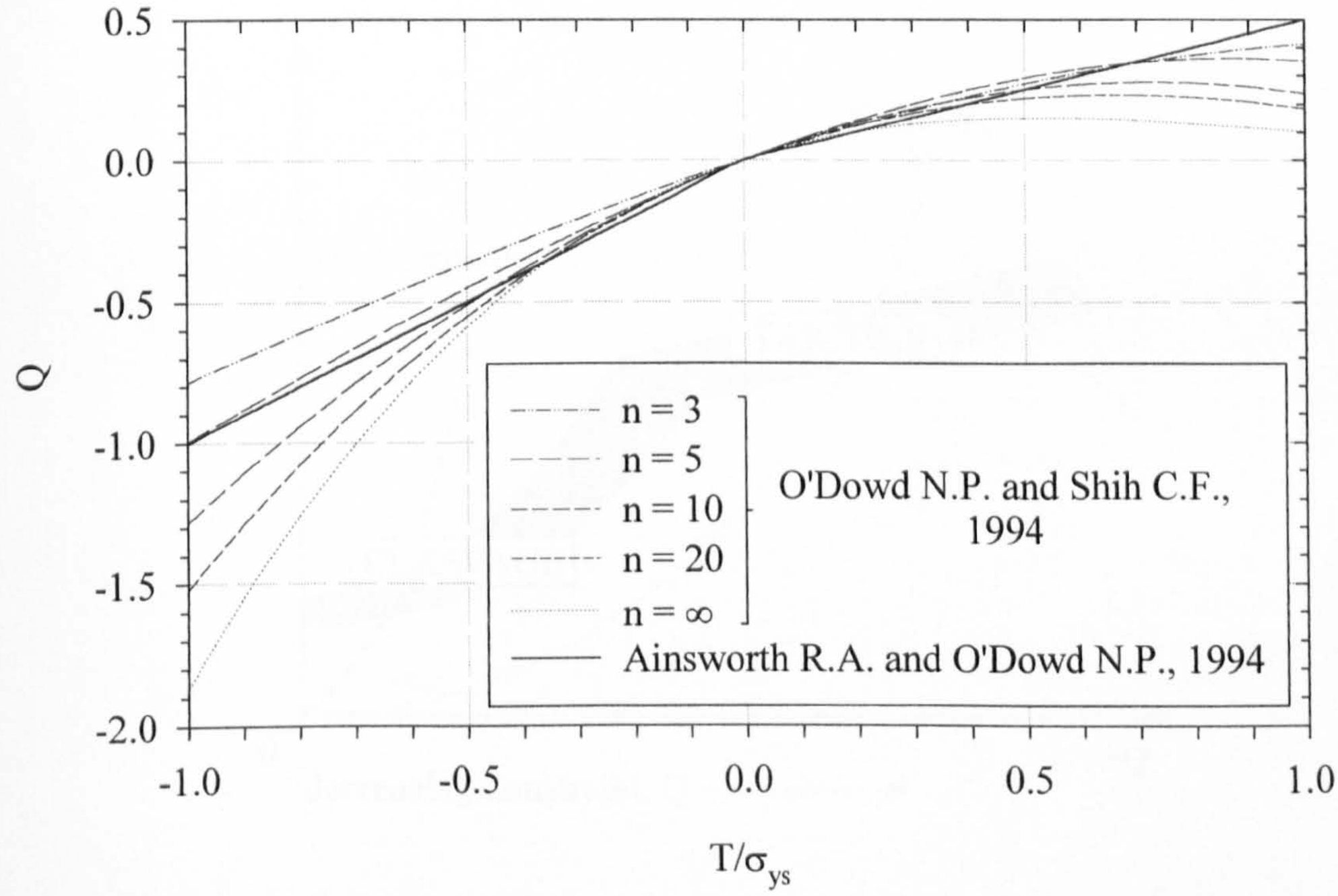

Figure 1.12. Variation of Q with T/σ_{ys} Under Contained Yielding for a Range of Hardening Exponent, n

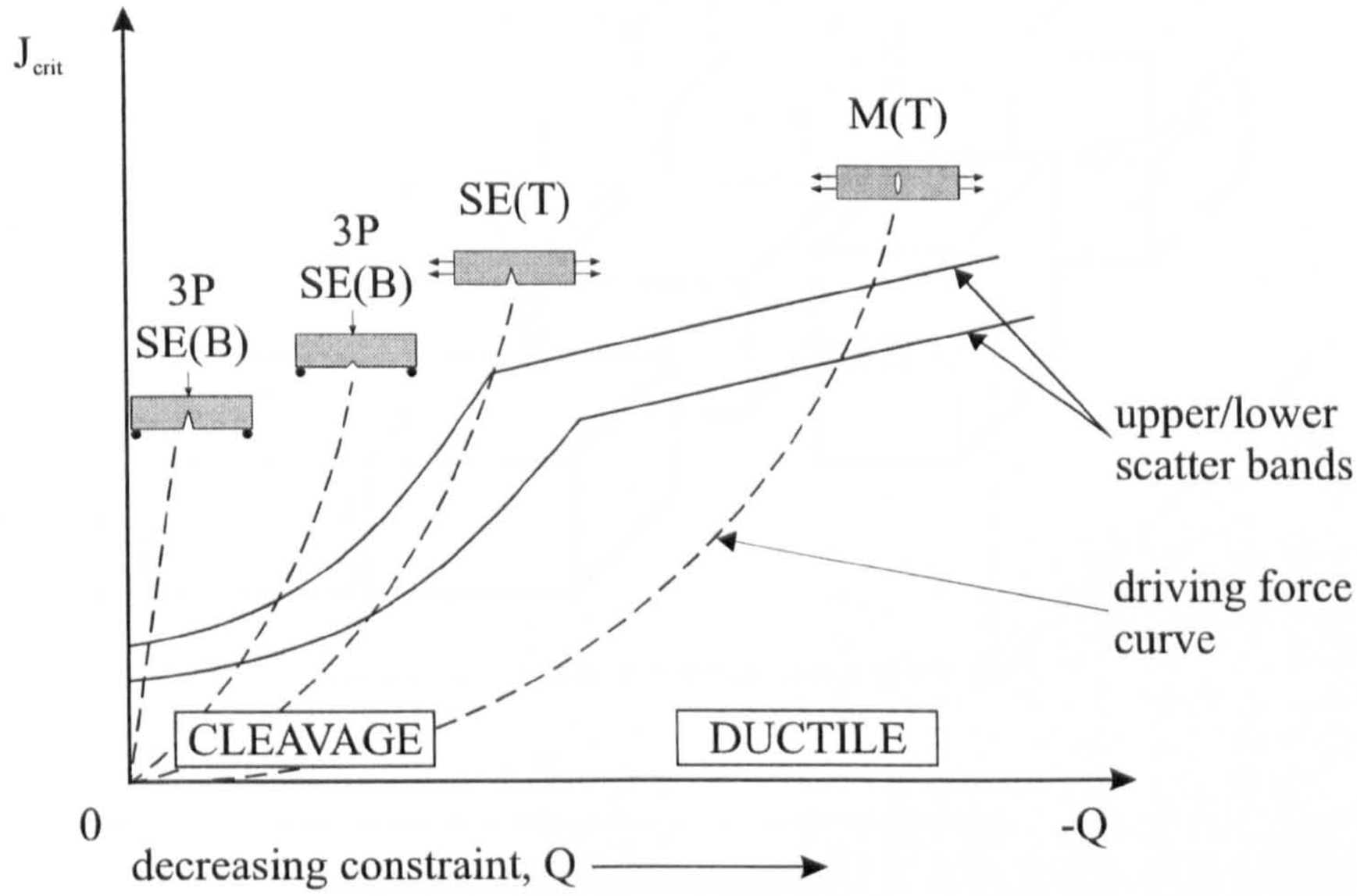

Figure 1.13. Illustration of J-Q Methodology from Laboratory Testing

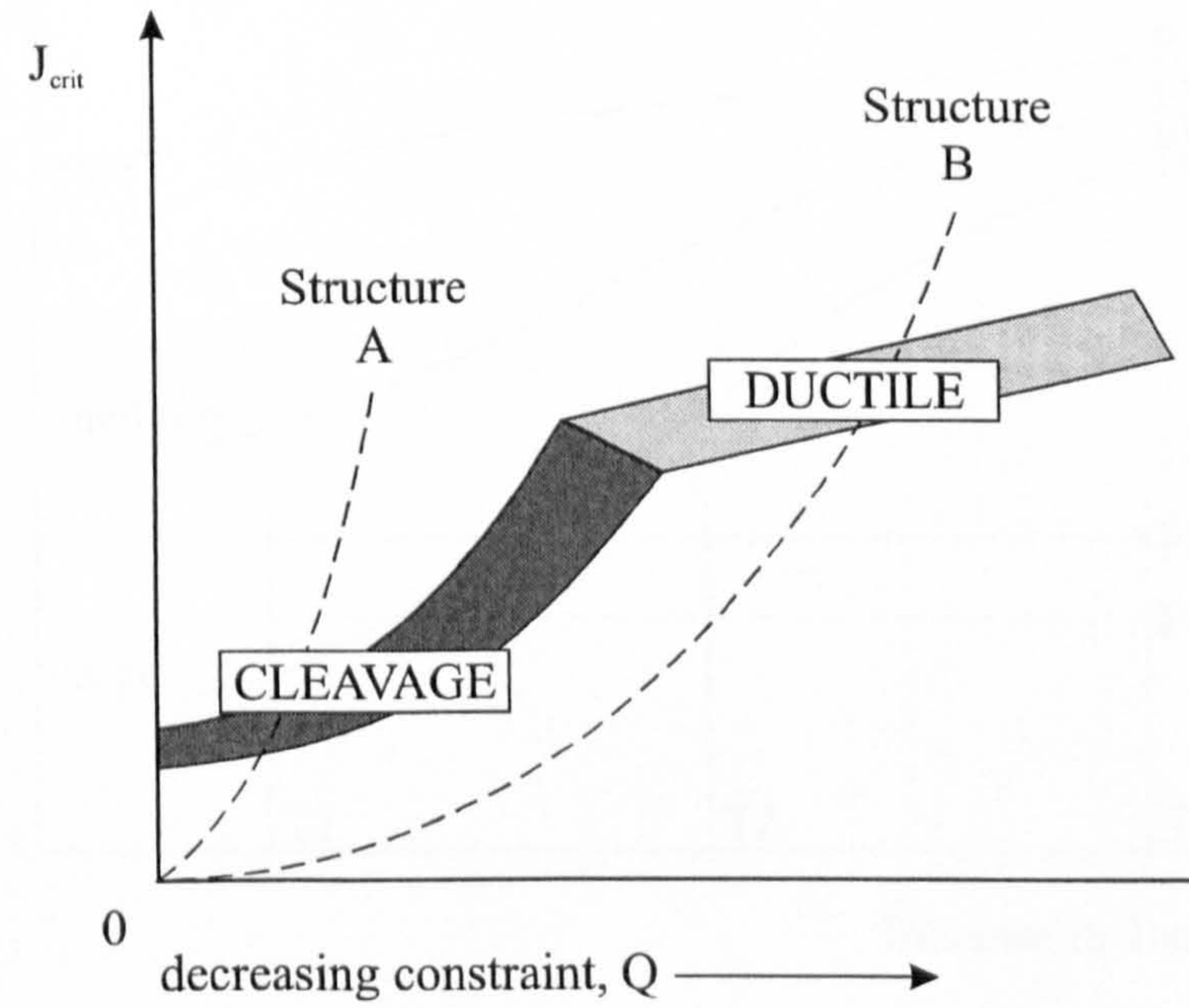

Figure 1.14. Illustration of J-Q Methodology for Structural Integrity Assessment

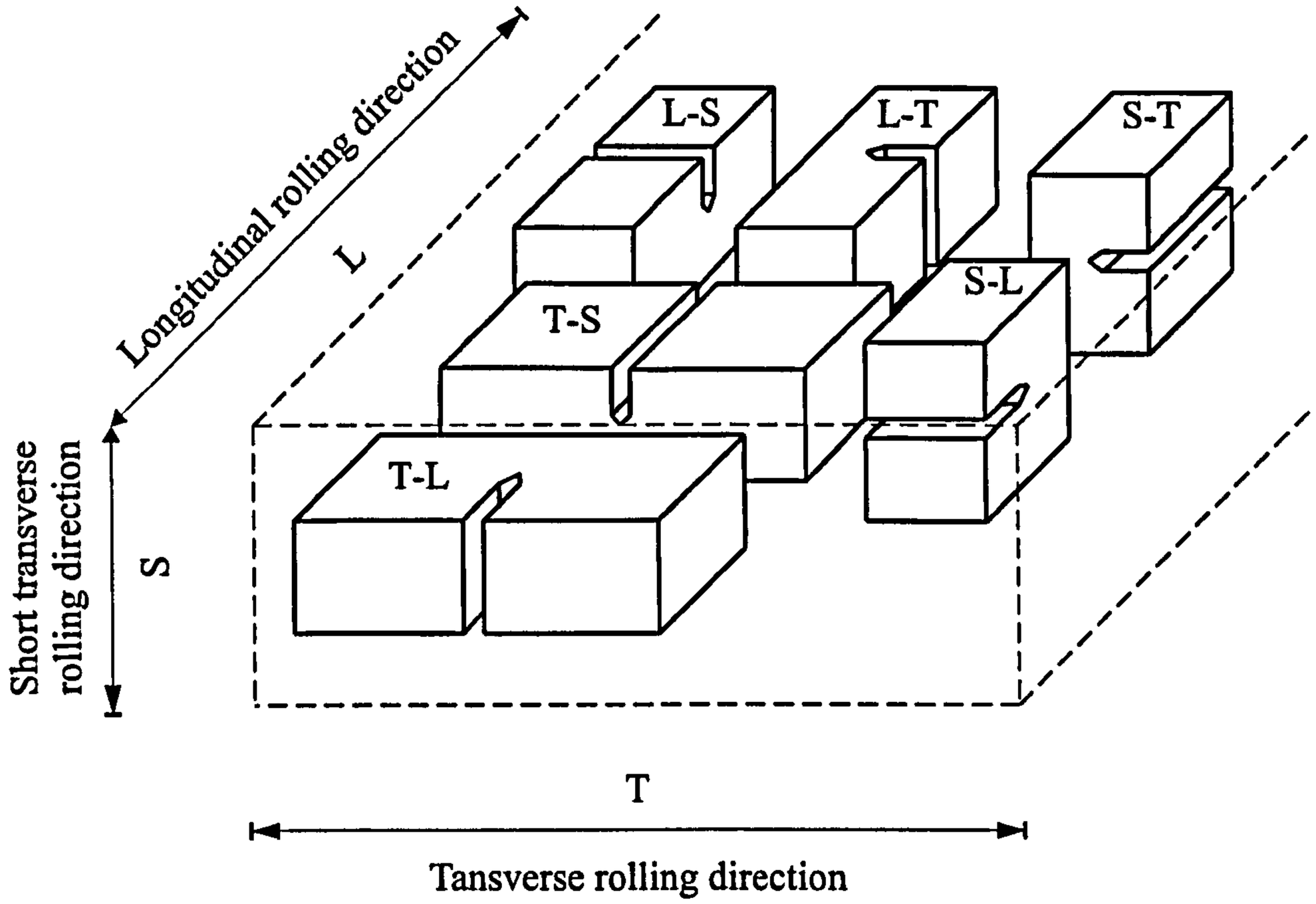

Figure 1.15. Terminology for Orientation of Fracture Specimens

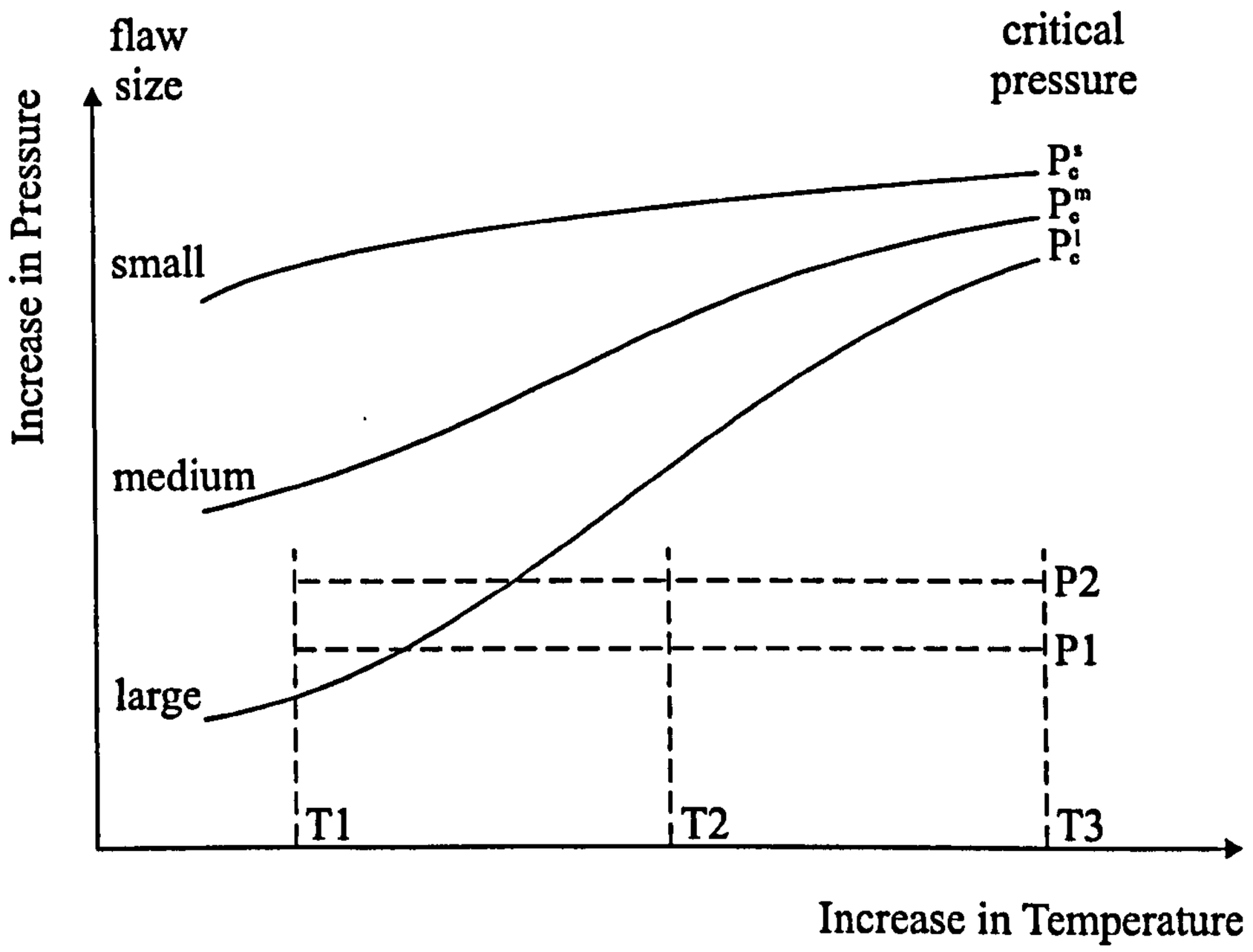

Figure 1.16. Schematic Representation of Proof Testing and Warm Prestressing
(after Yukawa, 1969)

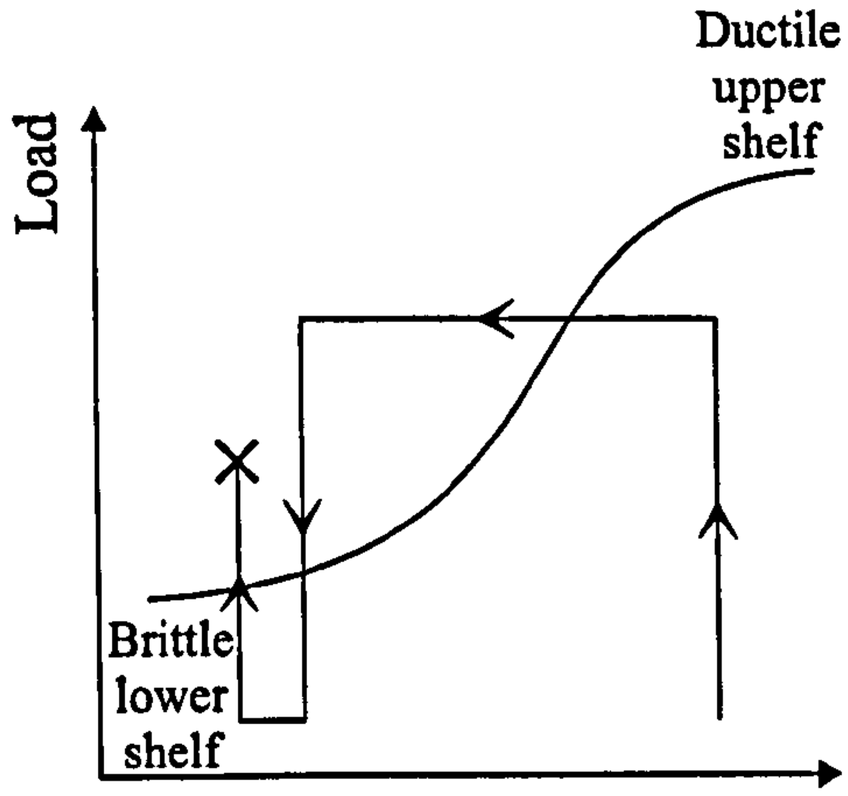

LCUF
load-cool-unload-fracture

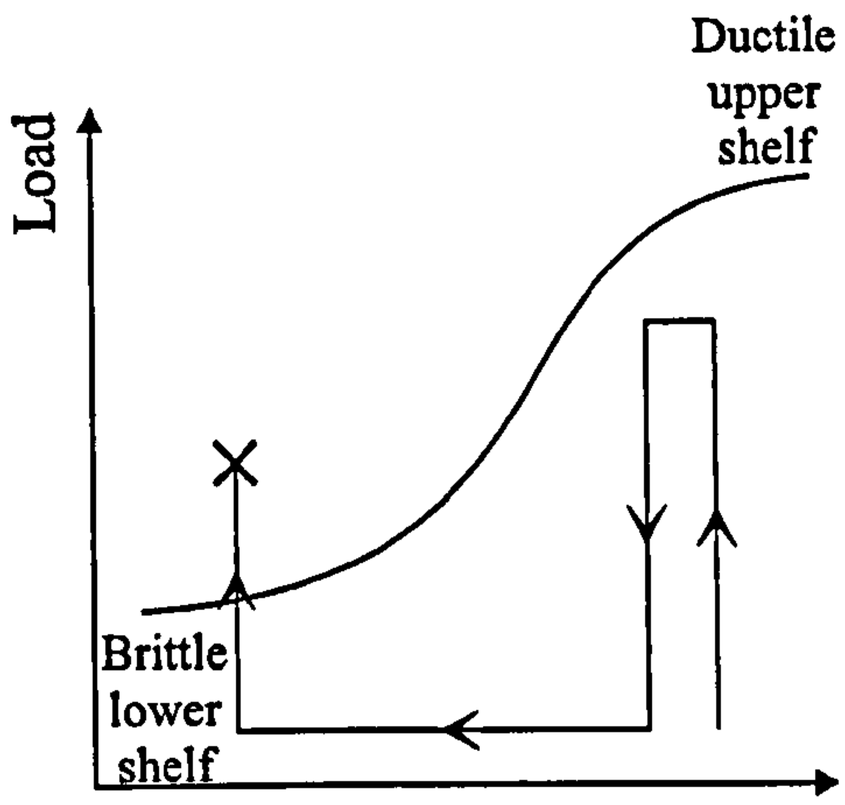

LUCF
load-unload-cool-fracture

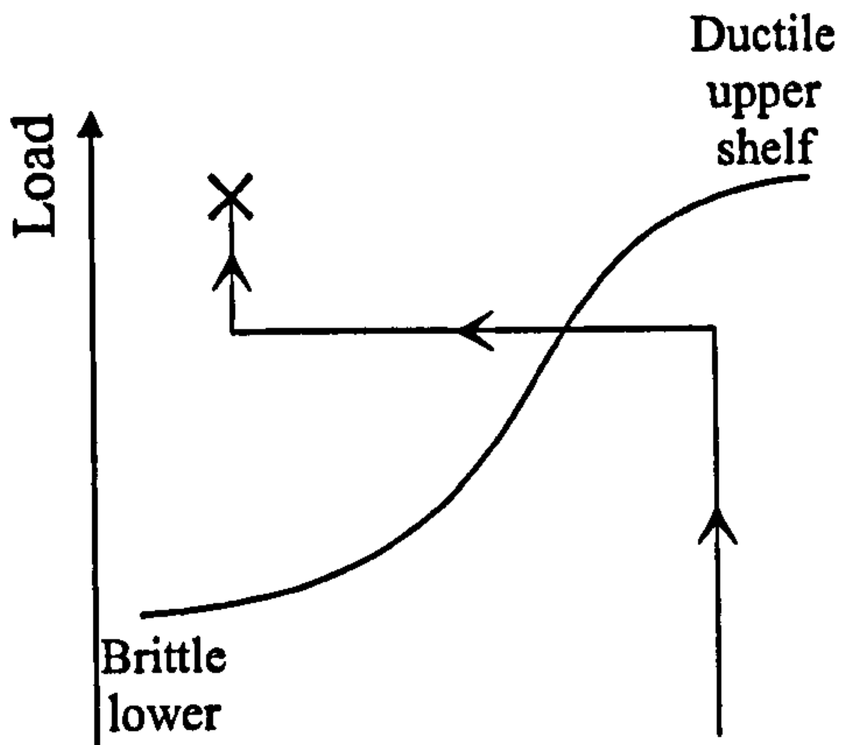

LCF
load-cool-fracture

Figure 1.17. Schematic Illustrations of Warm Prestress Cycles

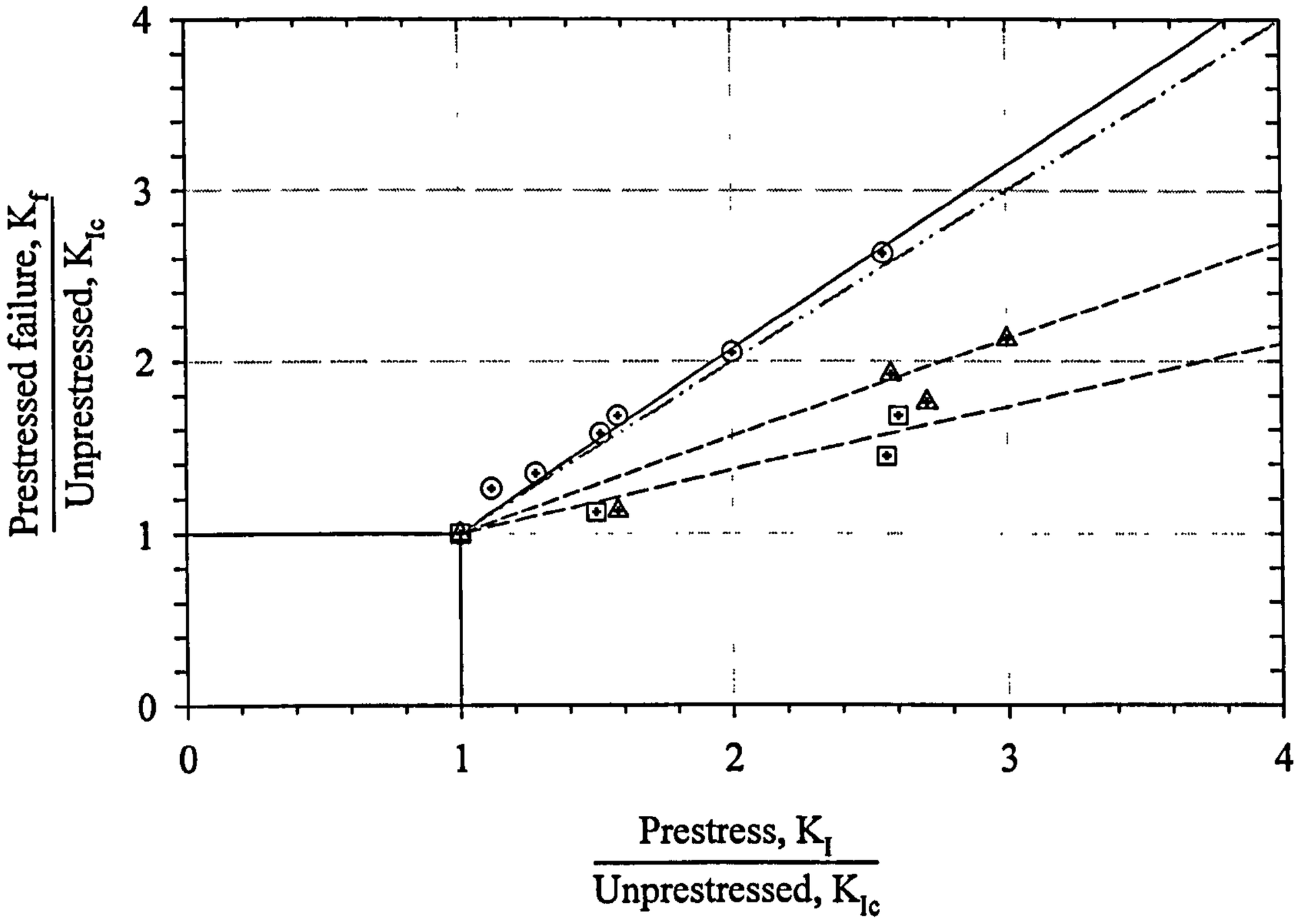

Figure 1.18. The Effects of Different Loading Paths on Warm Prestressing of A508 Steel

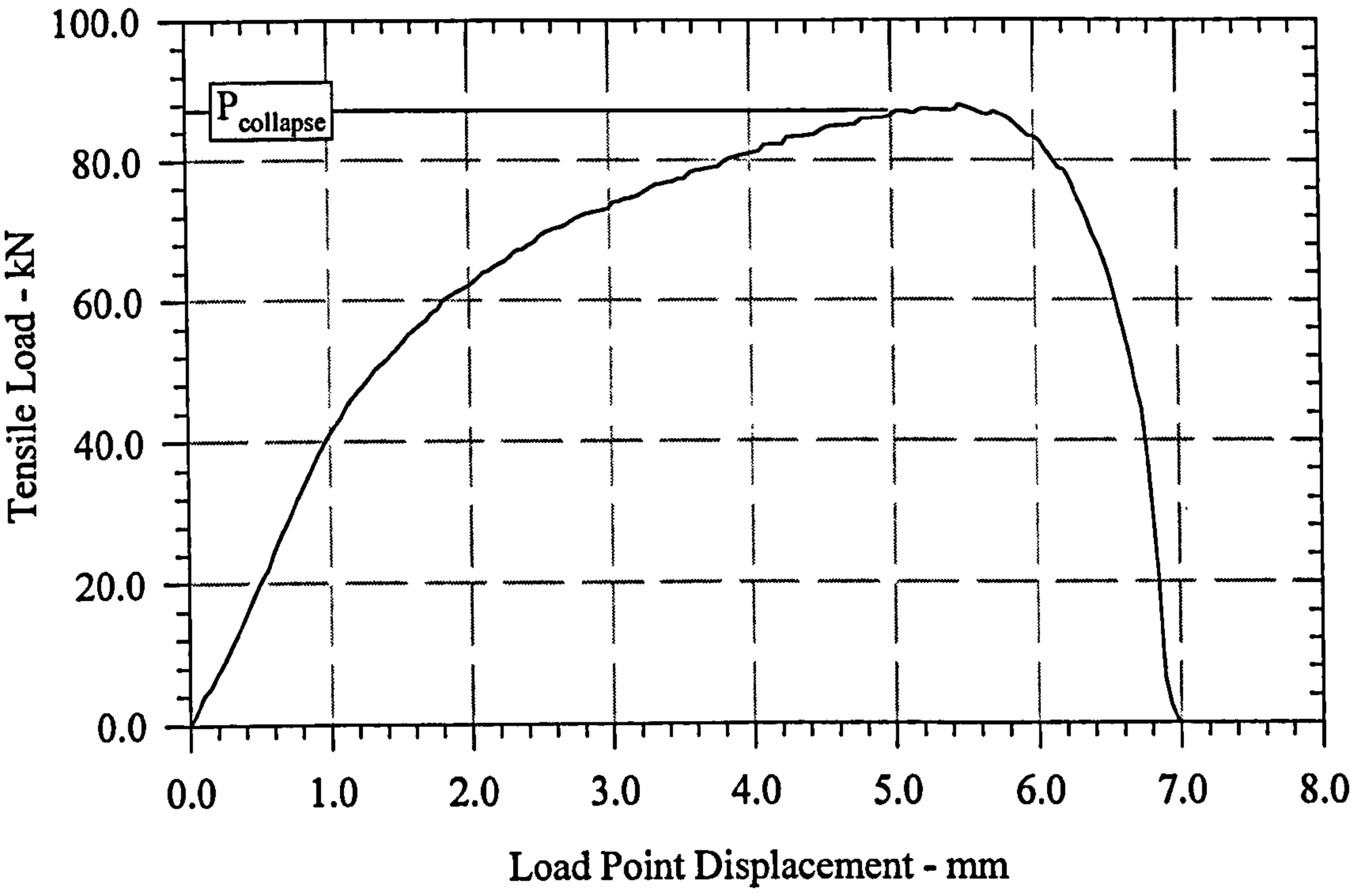

Figure 2.1a. **Mode I** : BS1501-224 C-Mn Steel, Ductile Fracture at 20°C
(after Xavier, 1995).

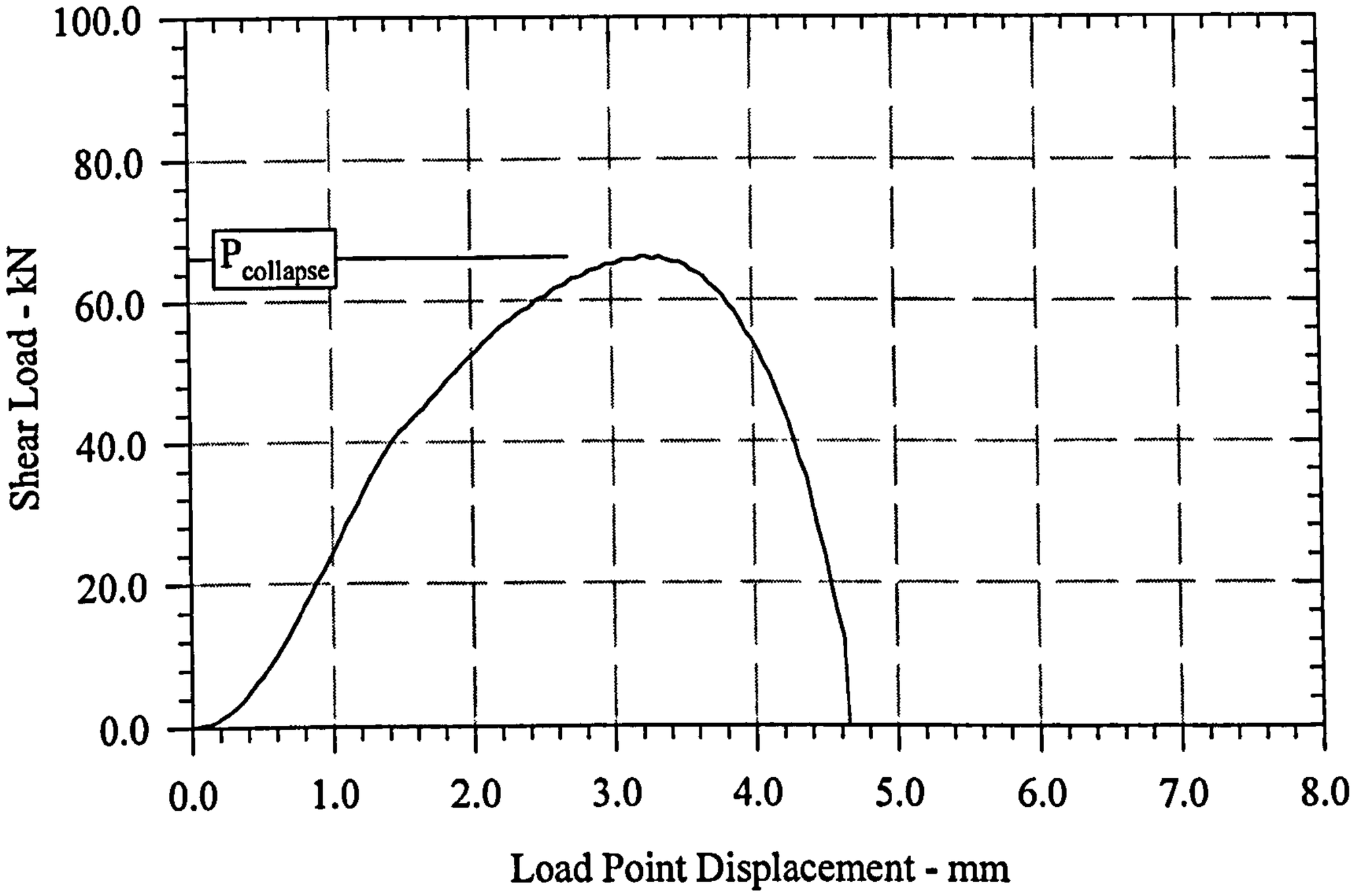

Figure 2.1b. **Mode II** : BS1501-224 C-Mn Steel, Ductile Fracture at 20°C
(after Xavier, 1995)

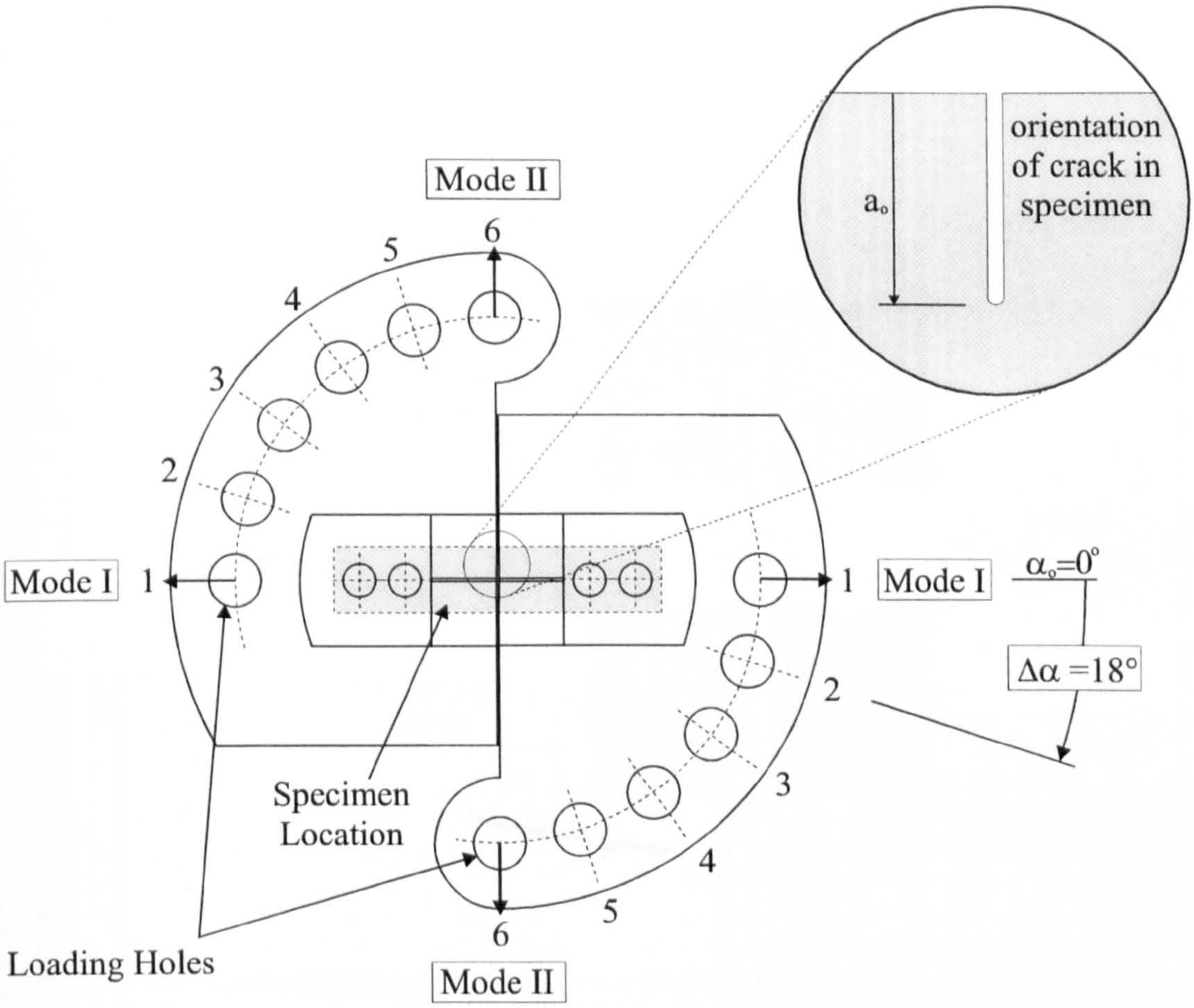

Figure 2.2. Mixed Mode I/II Loading Fixture
(after Davenport, 1993)

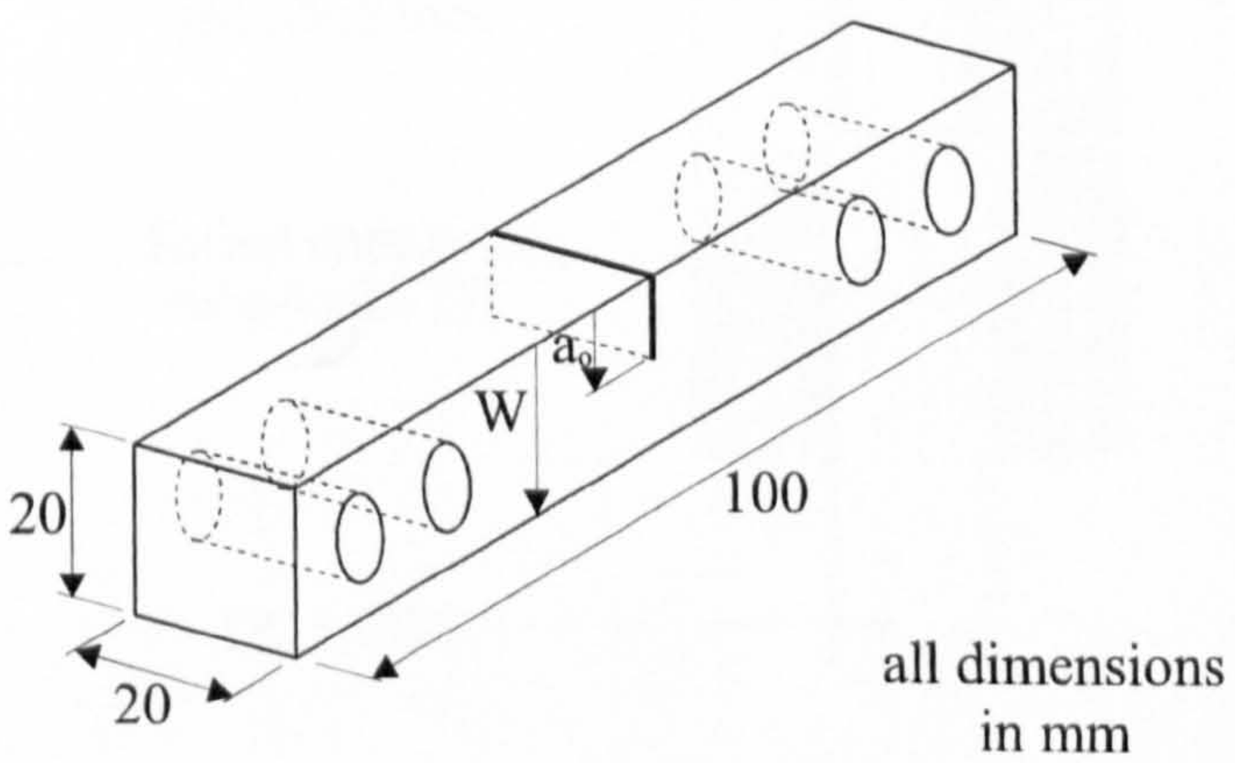

Figure 2.3. Single Edge Notch, SEN Specimen Geometry

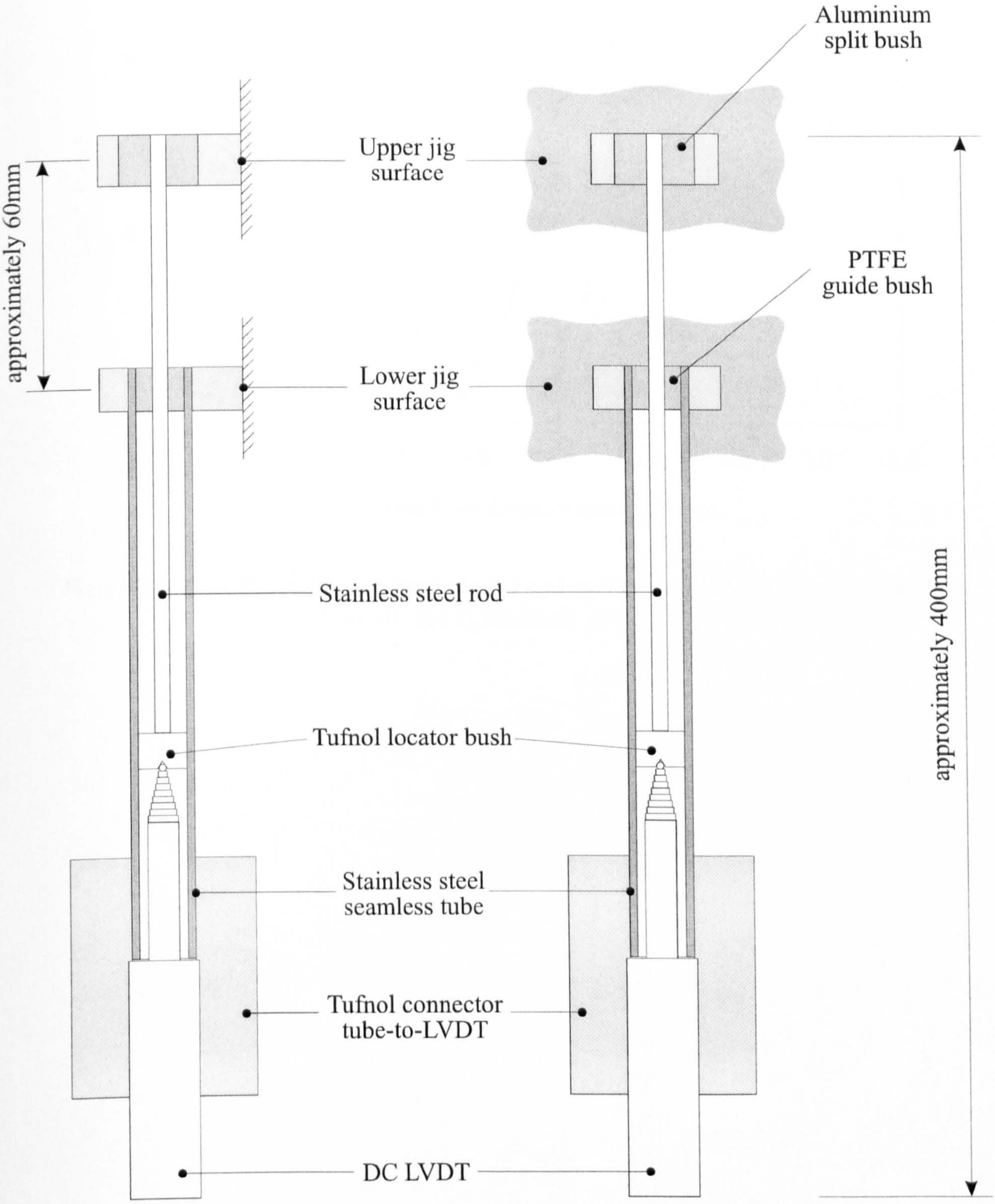

Figure 2.4. Extensometry Assembly for BS1501-224 Experiments

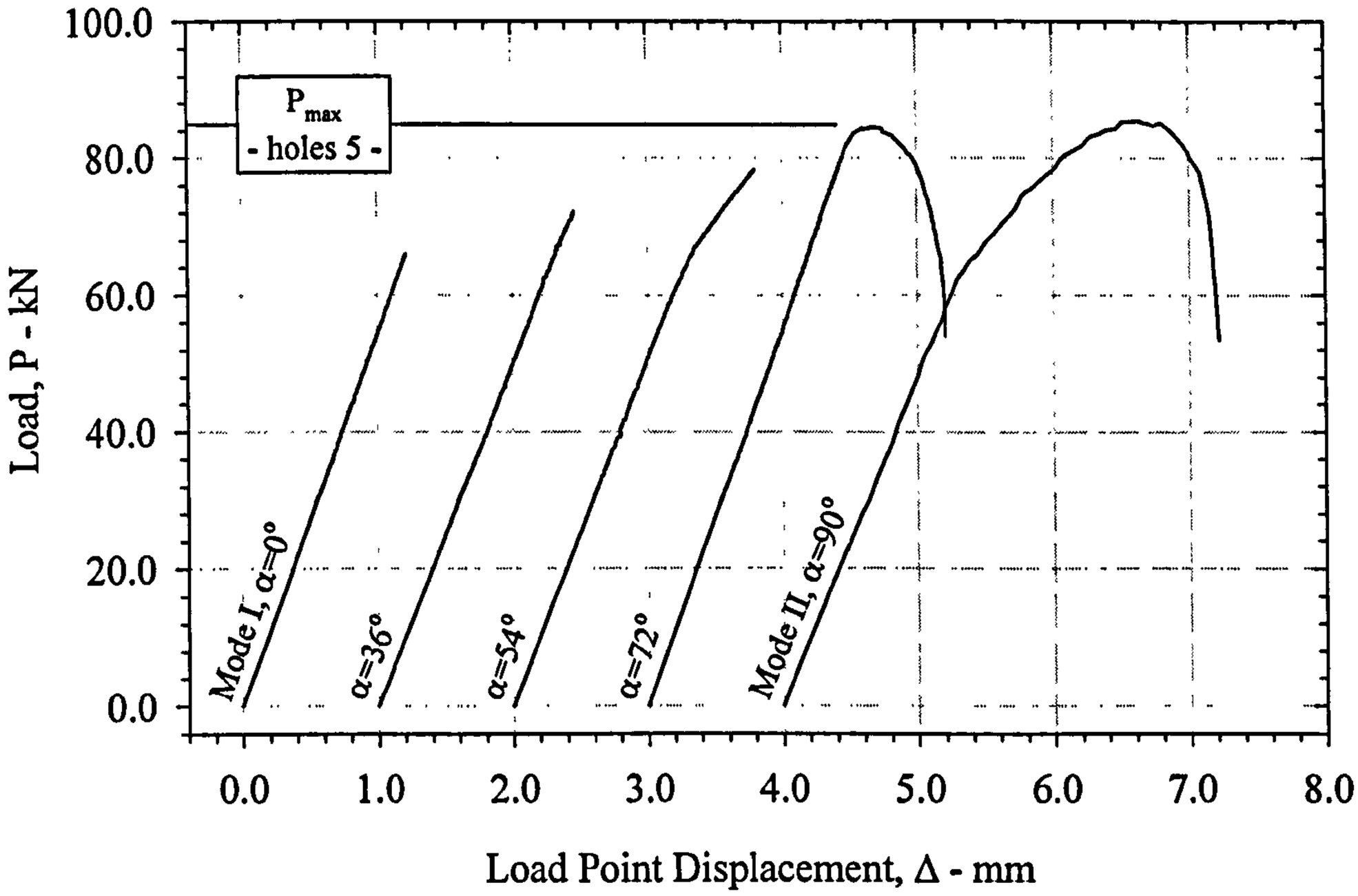

Figure 2.5. **Non Proof Load,** Mixed Mode Load vs. Load Point Displacement Curves
(BS1501-224 C-Mn Steel, at -120°C)

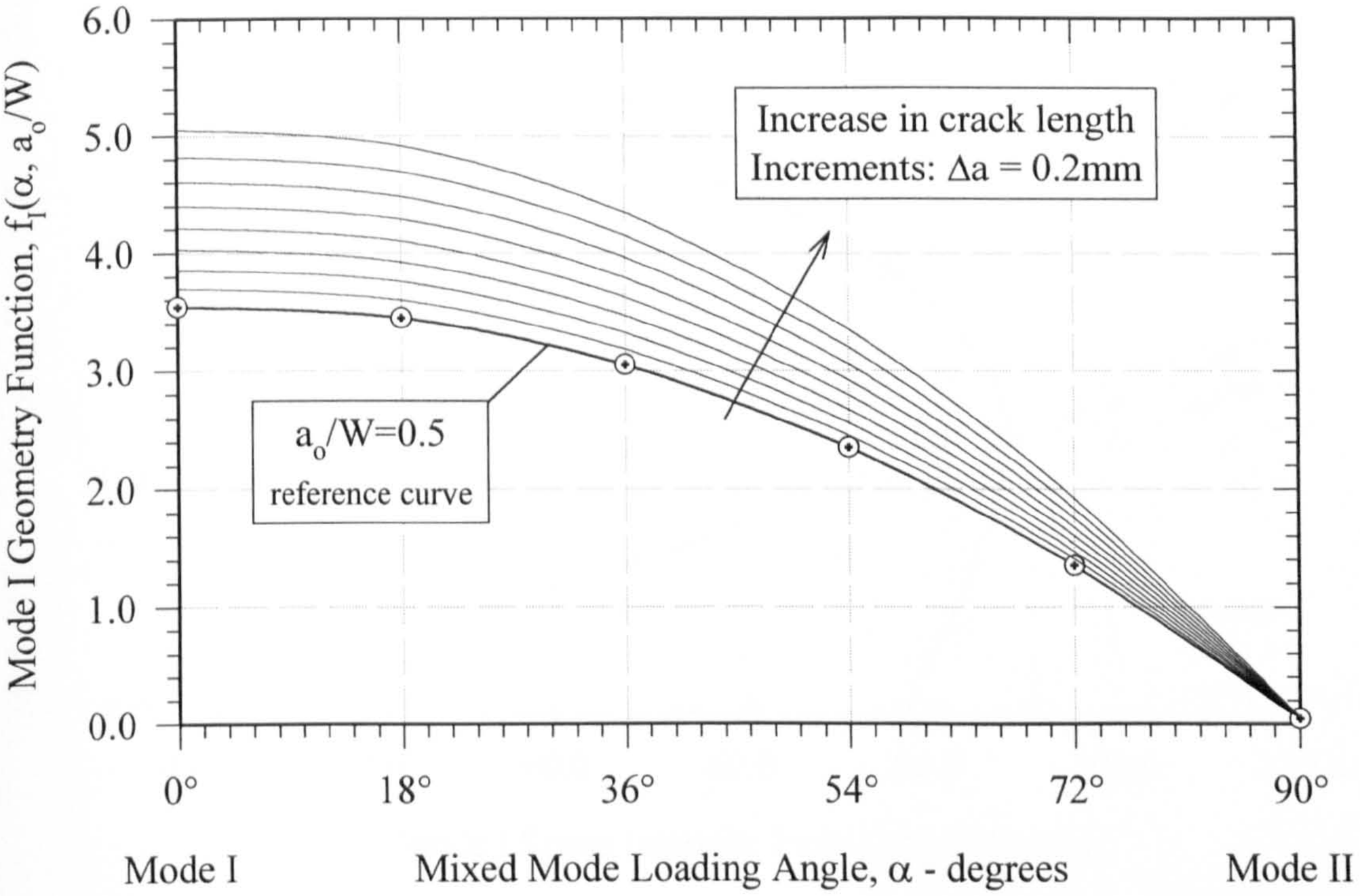

Figure 2.6a. **Mode I** : Elastic Geometry Function for Mixed Mode Loading
(after Davenport and Smith, 1993, and Tada et al., 1973, 1985)

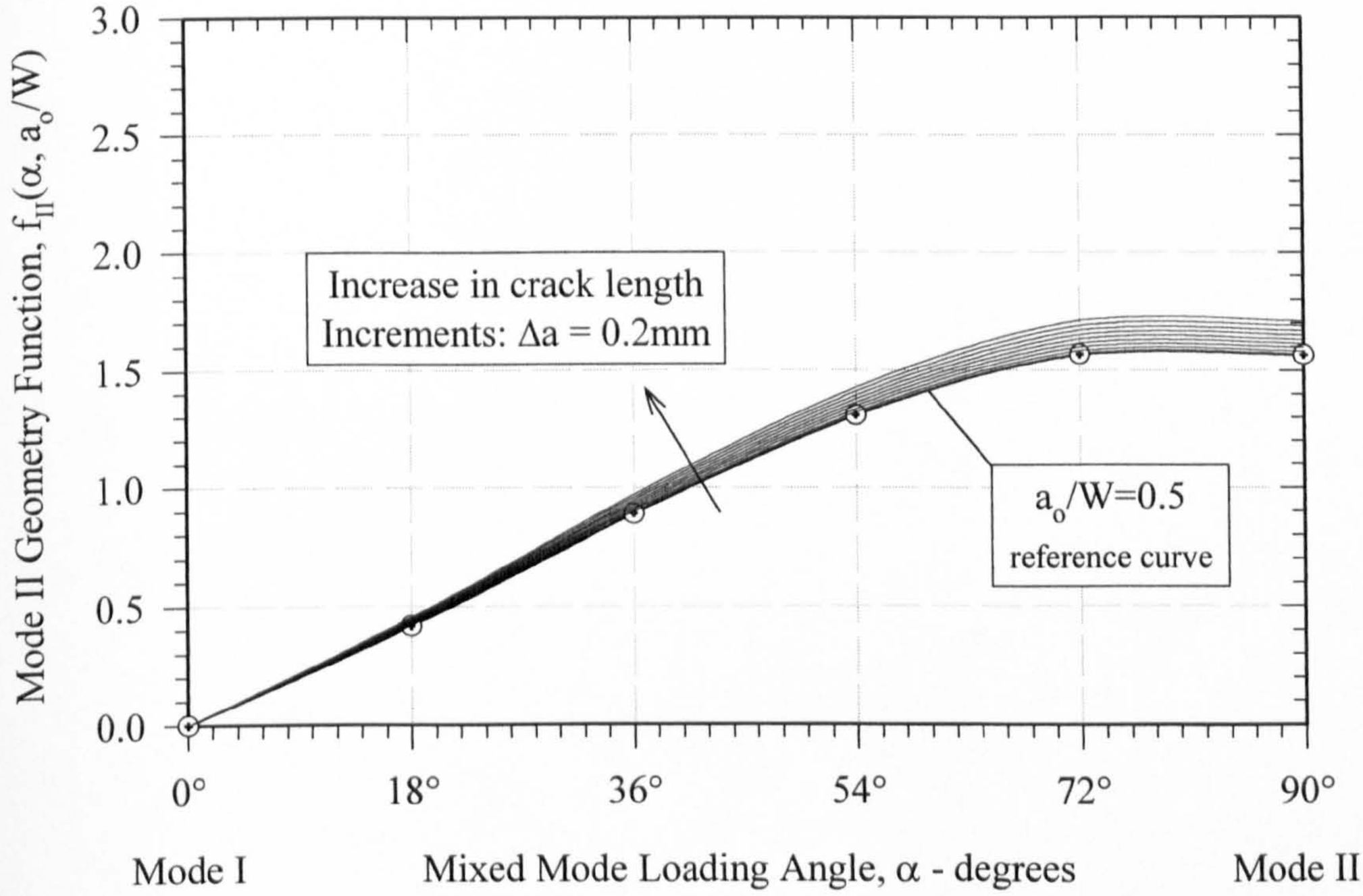

Figure 2.6b. **Mode II** : Elastic Geometry Function for Mixed Mode Loading
(after Davenport and Smith, 1993, and Tada et al., 1973, 1985)

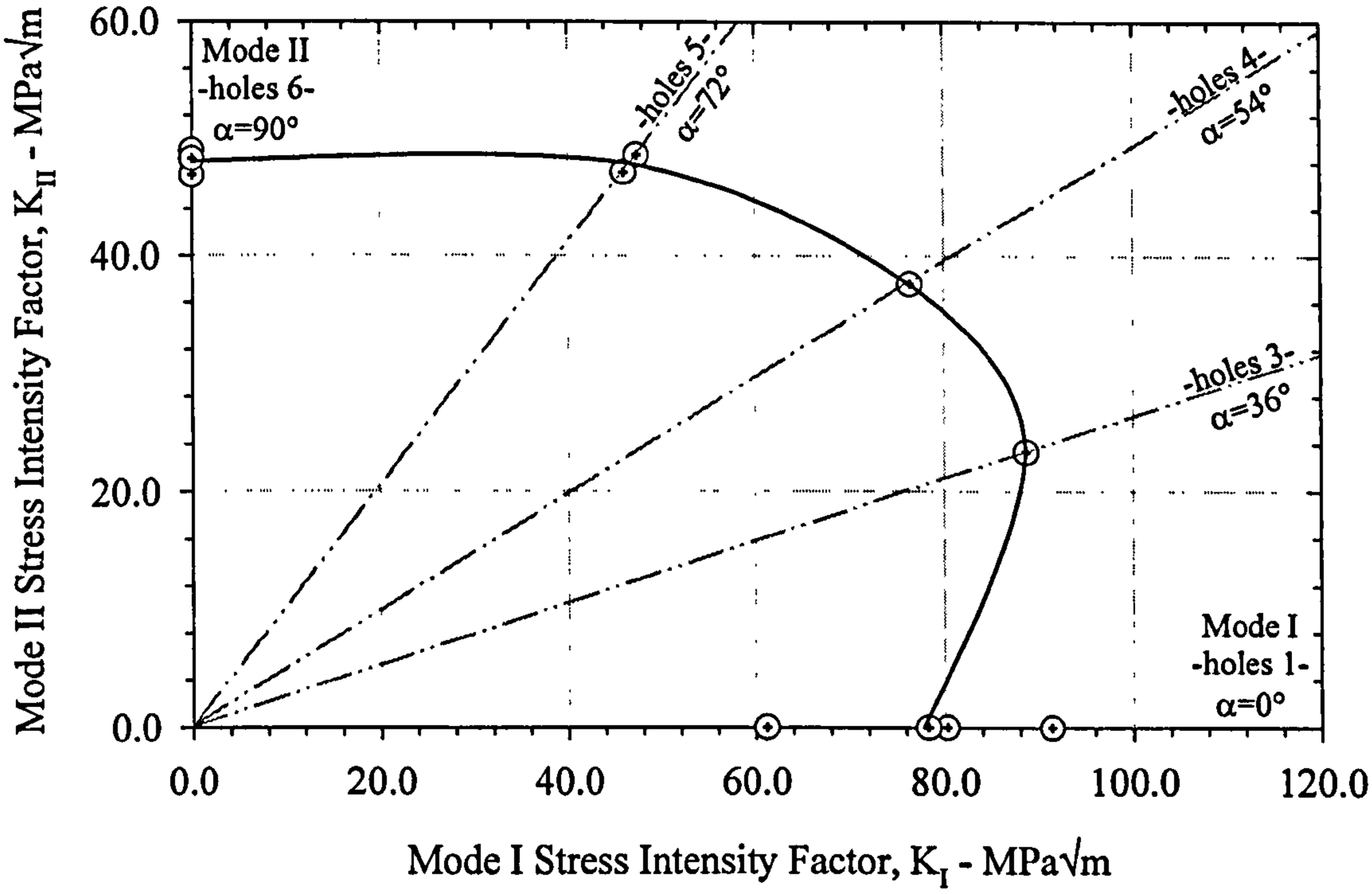

Figure 2.7. **Non Proof Load**, Mixed Mode Fracture Toughness
(BS1501-224 C-Mn Steel, at -120°C)

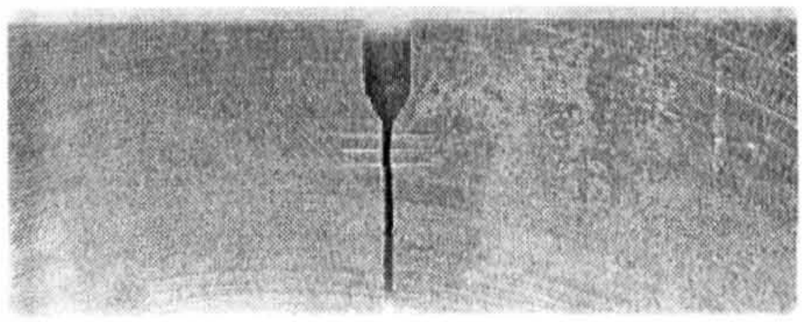

(a) Mode I Fracture (loading holes 1)
loading angle, α= 0°
fracture angle, θ= 0.0°

(b) Mixed Mode, Hole 3 Fracture
loading angle, α= 36°
fracture angle, θ= -29.5°

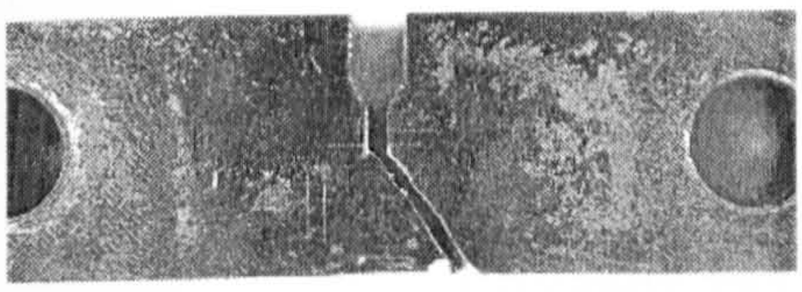

(c) Mixed Mode, Hole 4 Fracture
loading angle, α= 54°
fracture angle, θ= -37.0°

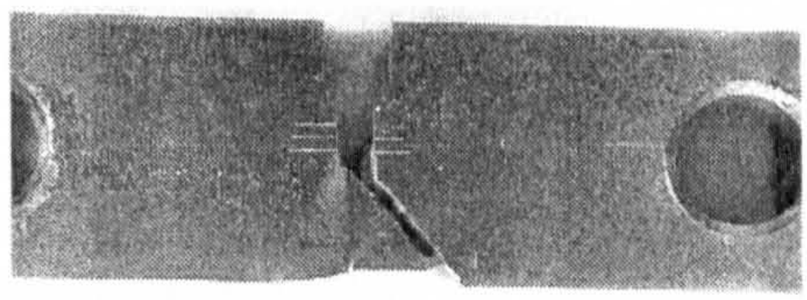

(d) Mixed Mode, Hole 5 Fracture
loading angle, α= 72°
fracture angle, θ= -42.0°

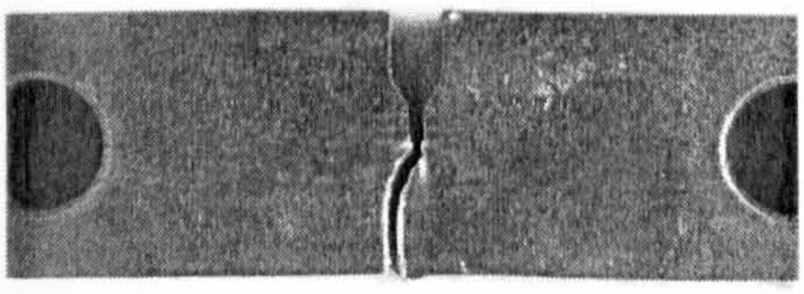

(e) Mode II Fracture (loading holes 6)
loading angle, α= 90°
fracture angle, θ= 9.5°

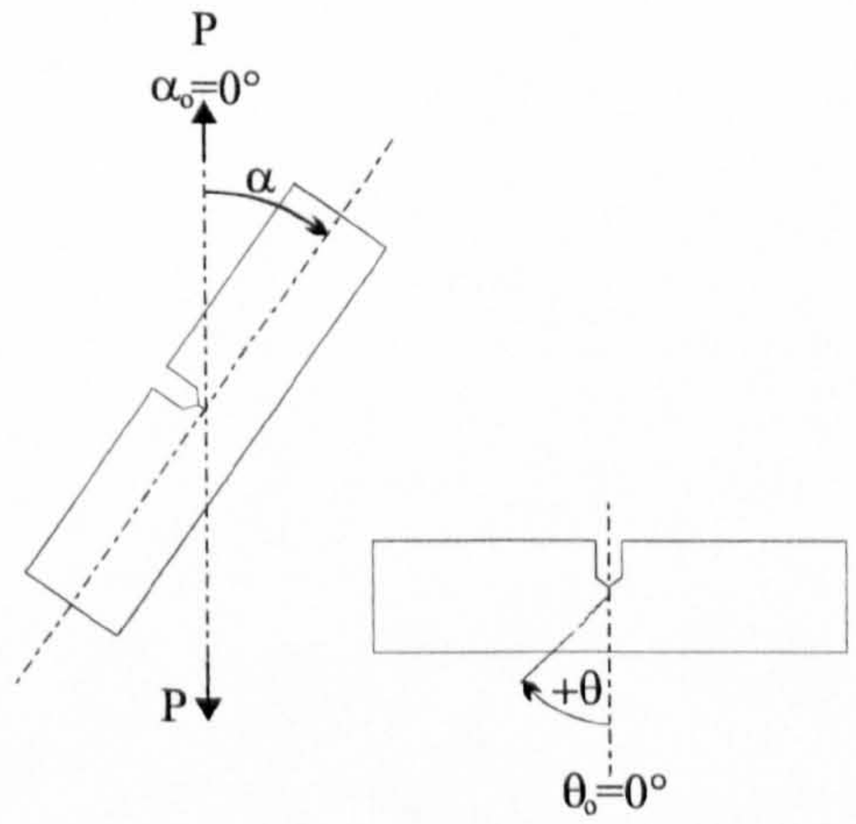

Figure 2.8. **Non Proof Load**, Mixed Mode Fracture Angles
(BS1501-224 C-Mn Steel, at -120°C)

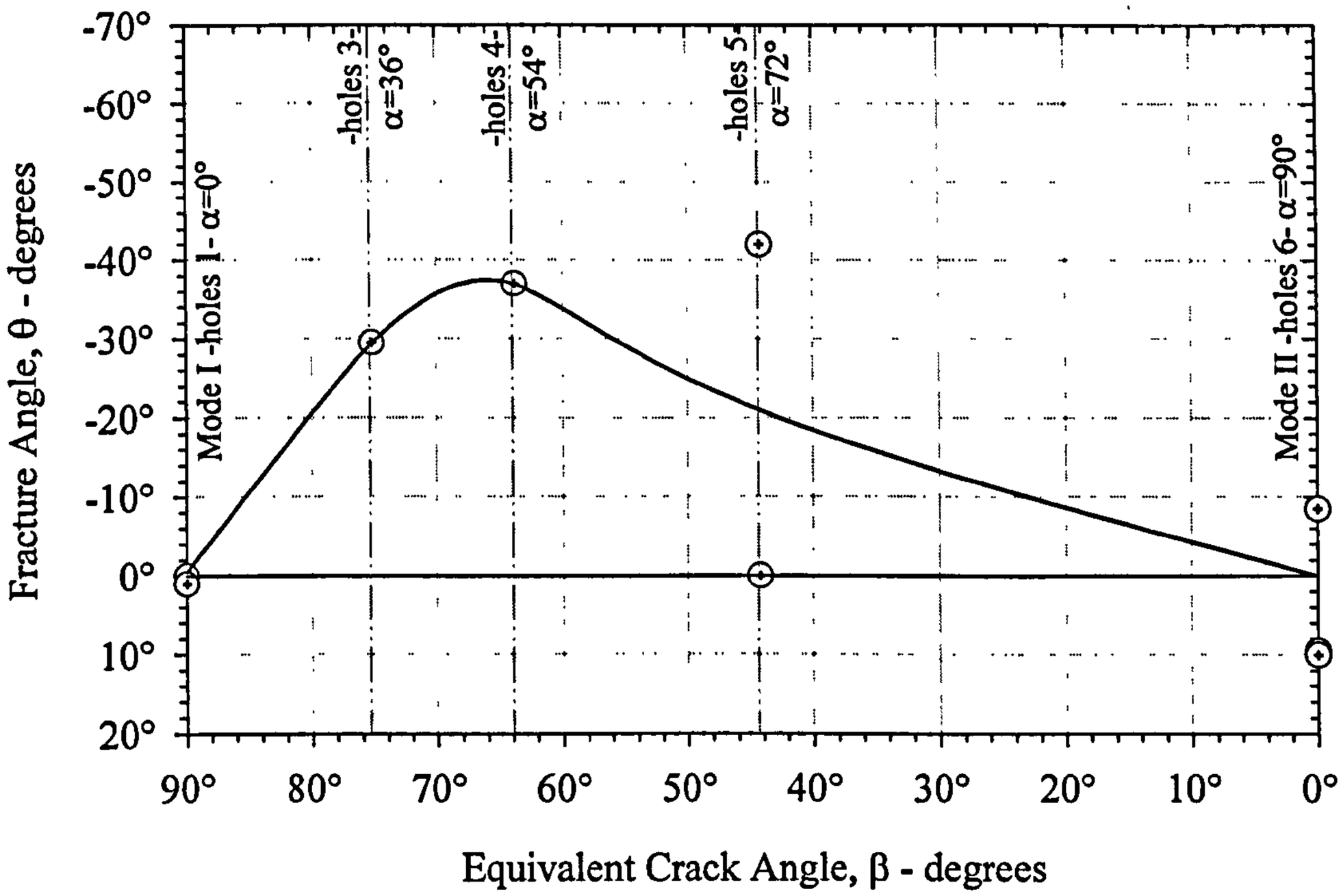

Figure 2.9. **Non Proof Load,** Mixed Mode Fracture Angles
(BS1501-224 Gr490B C-Mn Steel, at -120°C)

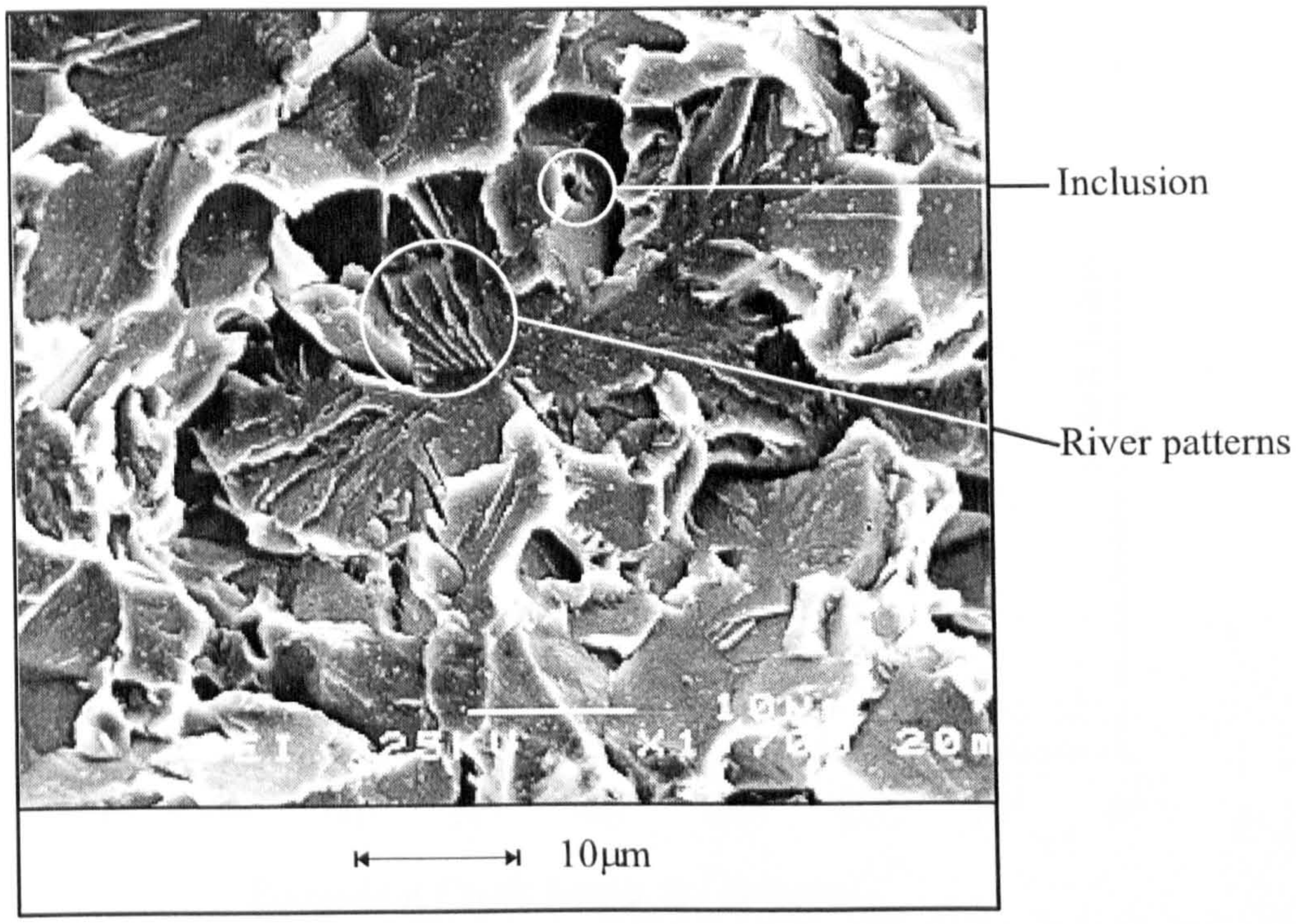

Figure 2.10a. BS1501-224 Fracture Surface Features : Non Proof Load, Mode I Fracture (magnification x1200)

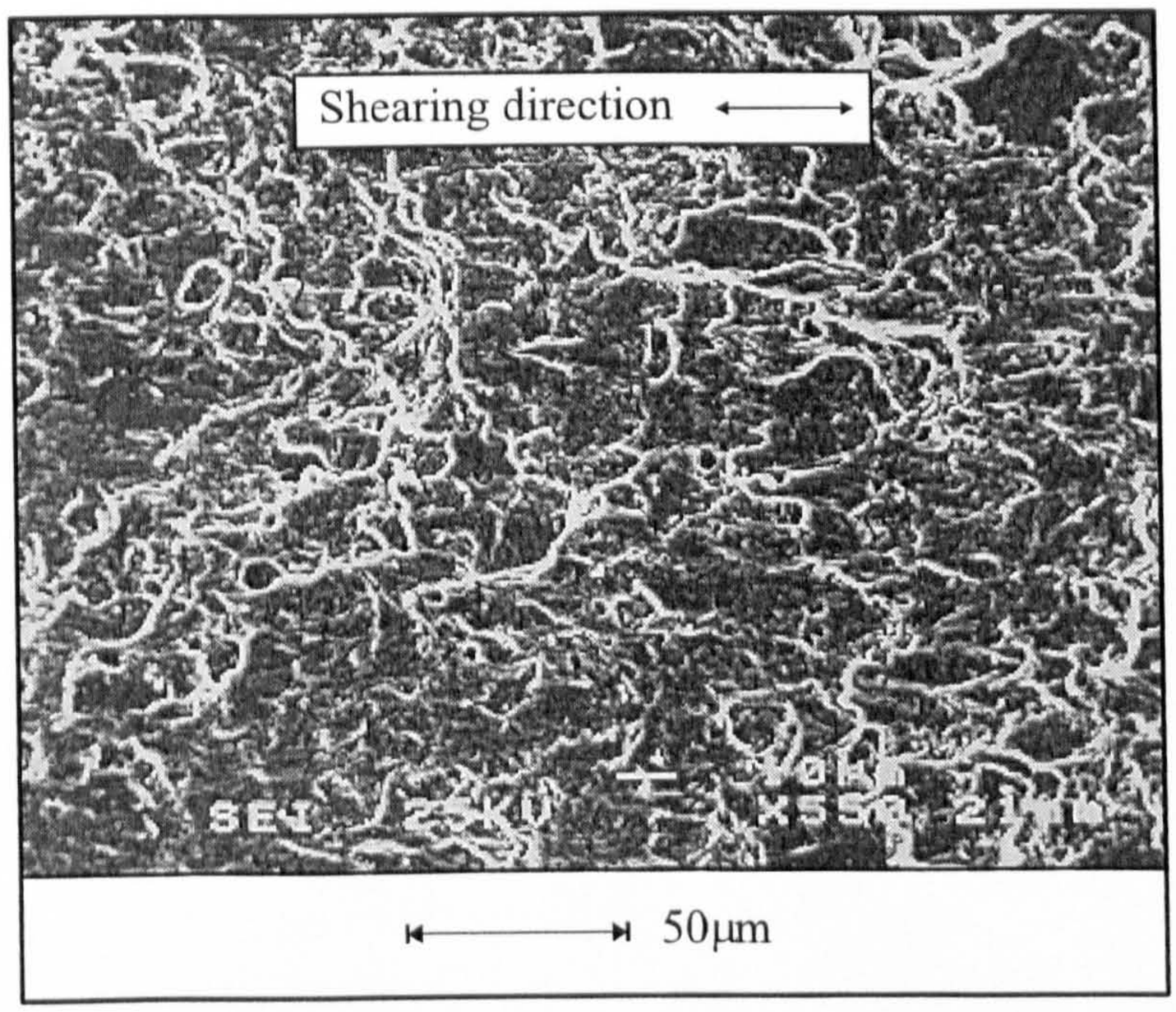

Figure 2.10b. BS1501-224 Fracture Surface Features : Non Proof Load, Mode II Fracture (magnification x550)

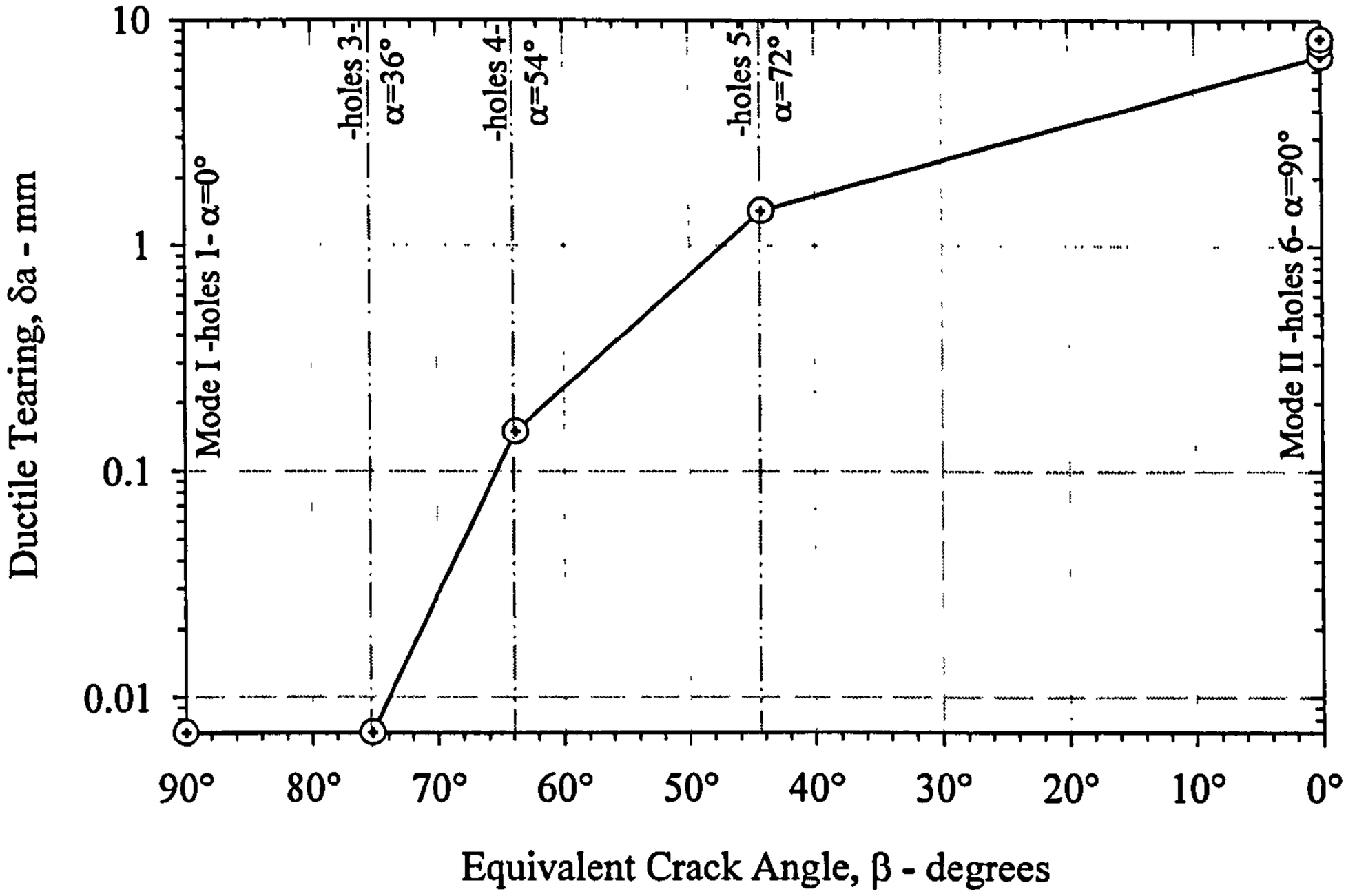

Figure 2.11. **Non Proof Load,** Ductile Tearing During Mixed Mode Fracture
(BS1501-224 C-Mn Steel, at -120°C)

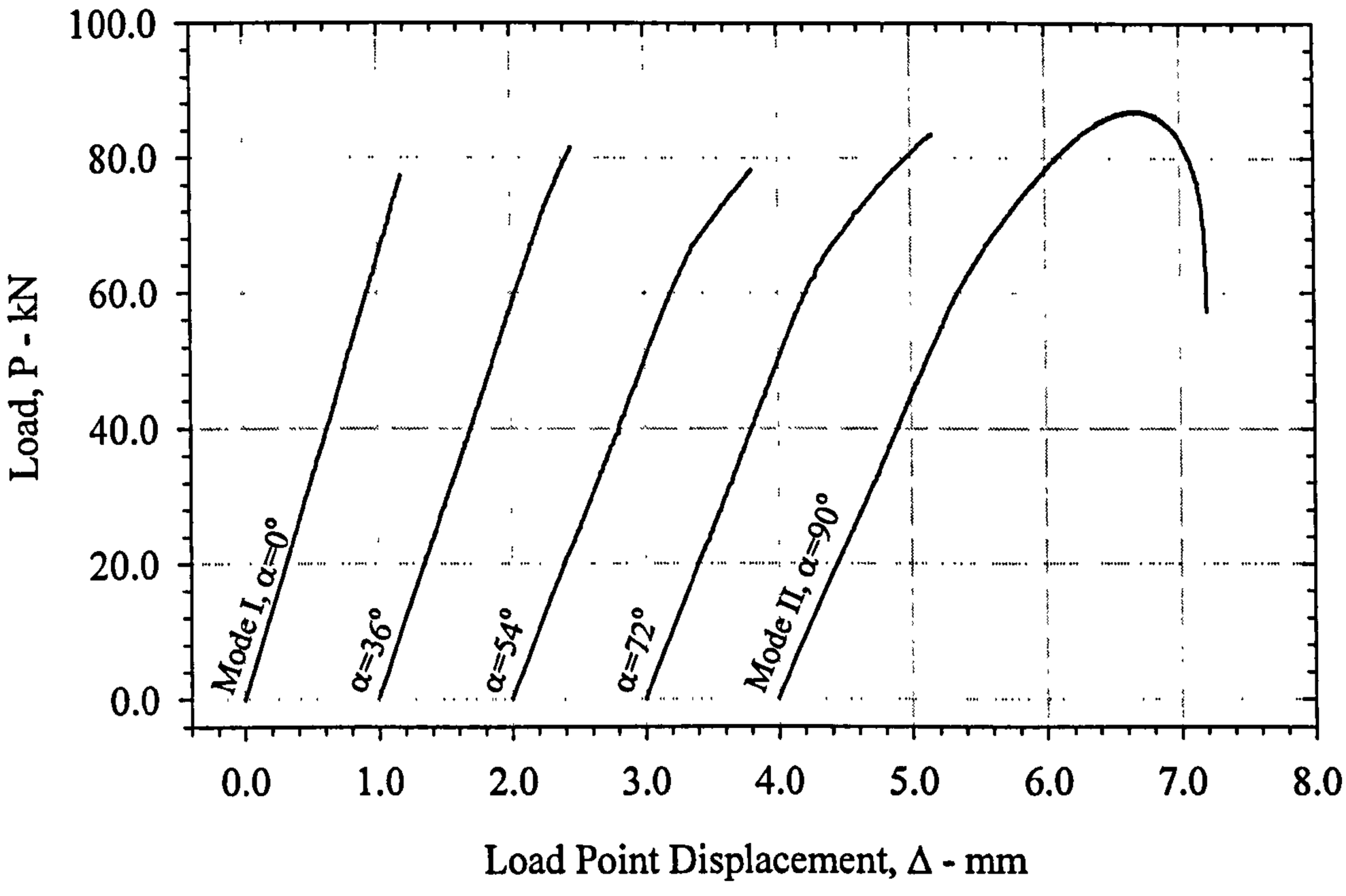

Figure 2.12. **Mode I Proof Load,** Mixed Mode Load vs. Load Point Displacement Curves
(BS1501-224 C-Mn Steel, at -120°C)

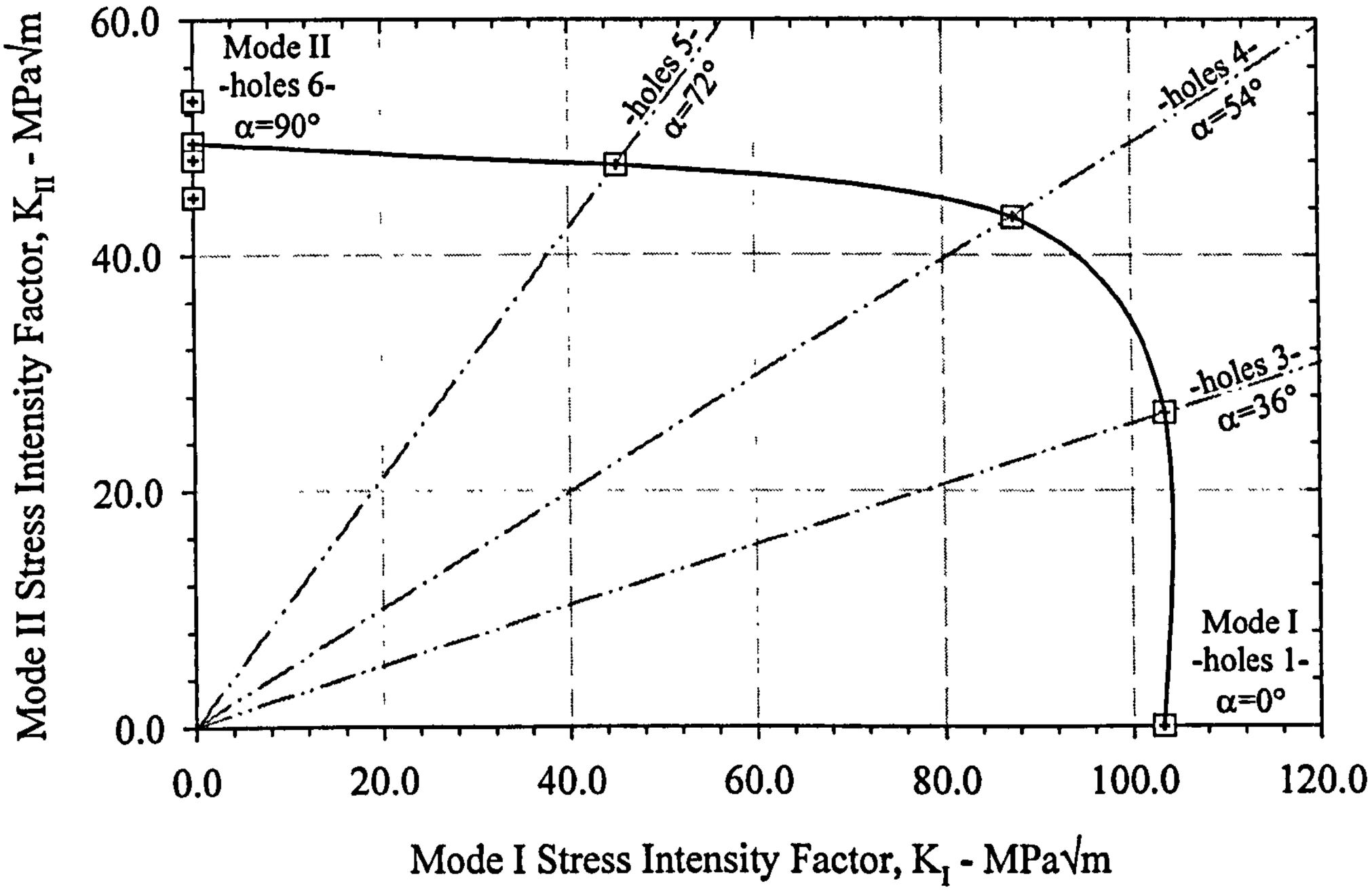

Figure 2.13. **Mode I Proof Load,** Mixed Mode Fracture Toughness
(BS1501-224 C-Mn Steel, at -120°C)

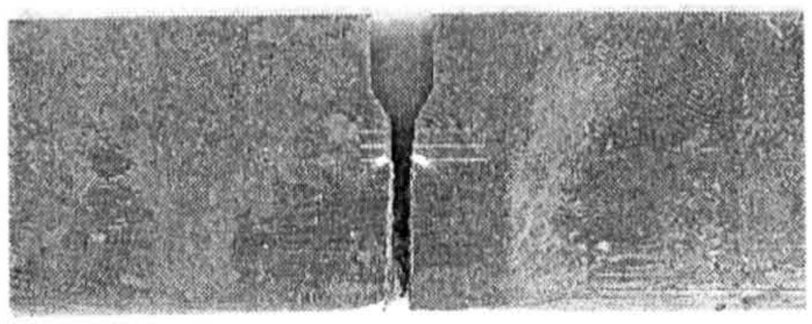

(a) Mode I Fracture (loading holes 1)
loading angle, $\alpha = 0°$
fracture angle, $\theta = 2.0°$

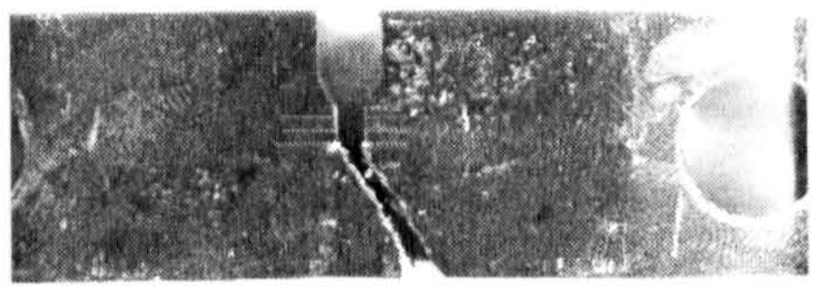

(b) Mixed Mode, Hole 3 Fracture
loading angle, $\alpha = 36°$
fracture angle, $\theta = -32.5°$

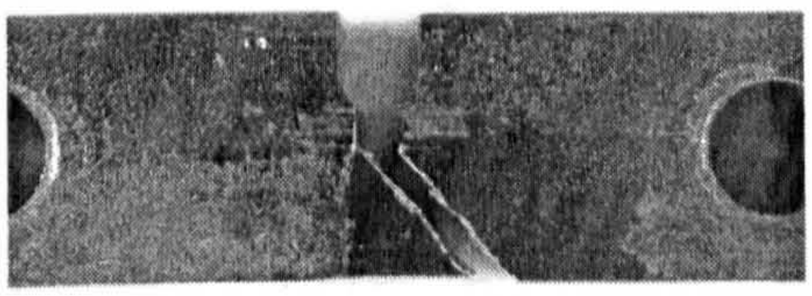

(c) Mixed Mode, Hole 4 Fracture
loading angle, $\alpha = 54°$
fracture angle, $\theta = -42.0°$

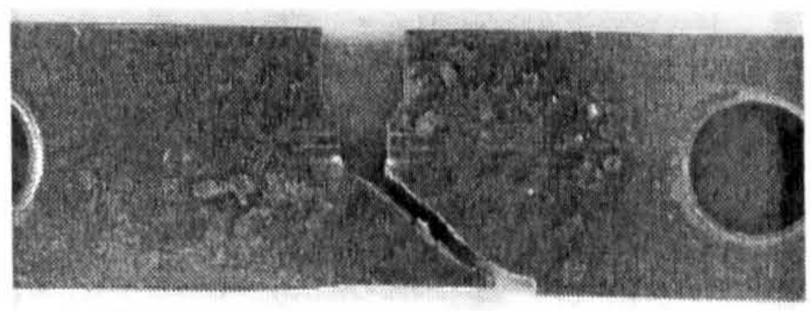

(d) Mixed Mode, Hole 5 Fracture
loading angle, $\alpha = 72°$
fracture angle, $\theta = -53.0°$

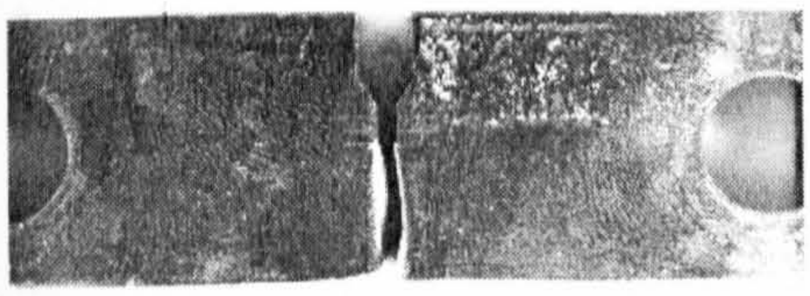

(e) Mode II Fracture (loading holes 6)
loading angle, $\alpha = 90°$
fracture angle, $\theta = -7.5°$

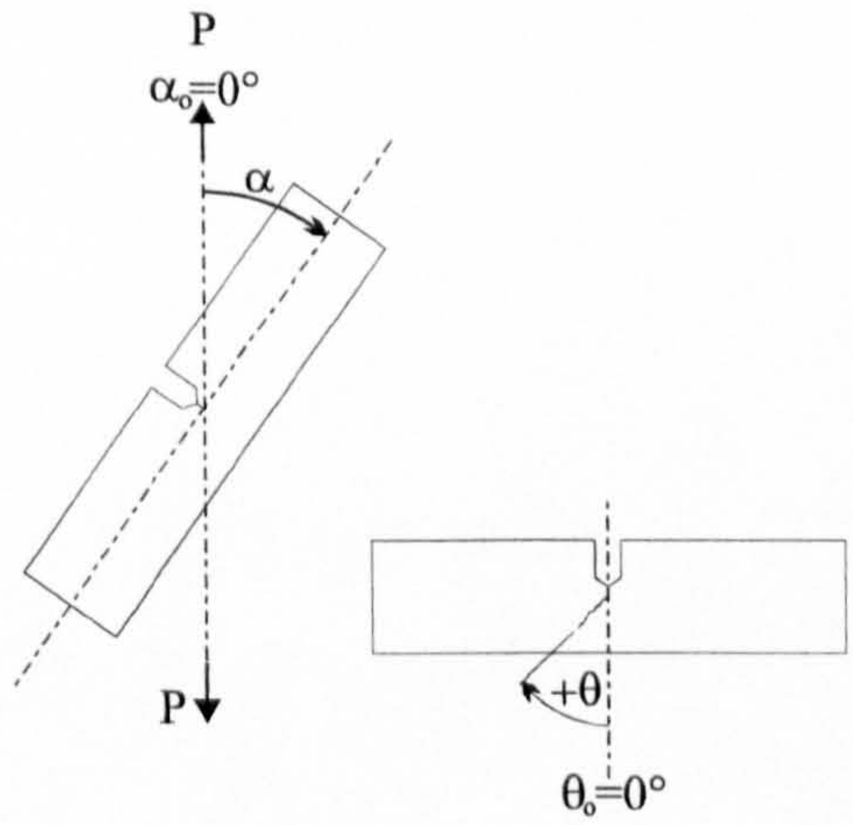

Figure 2.14. **Mode I Proof Load**, Mixed Mode Fracture Angles
(BS1501-224 C-Mn Steel, at -120°C)

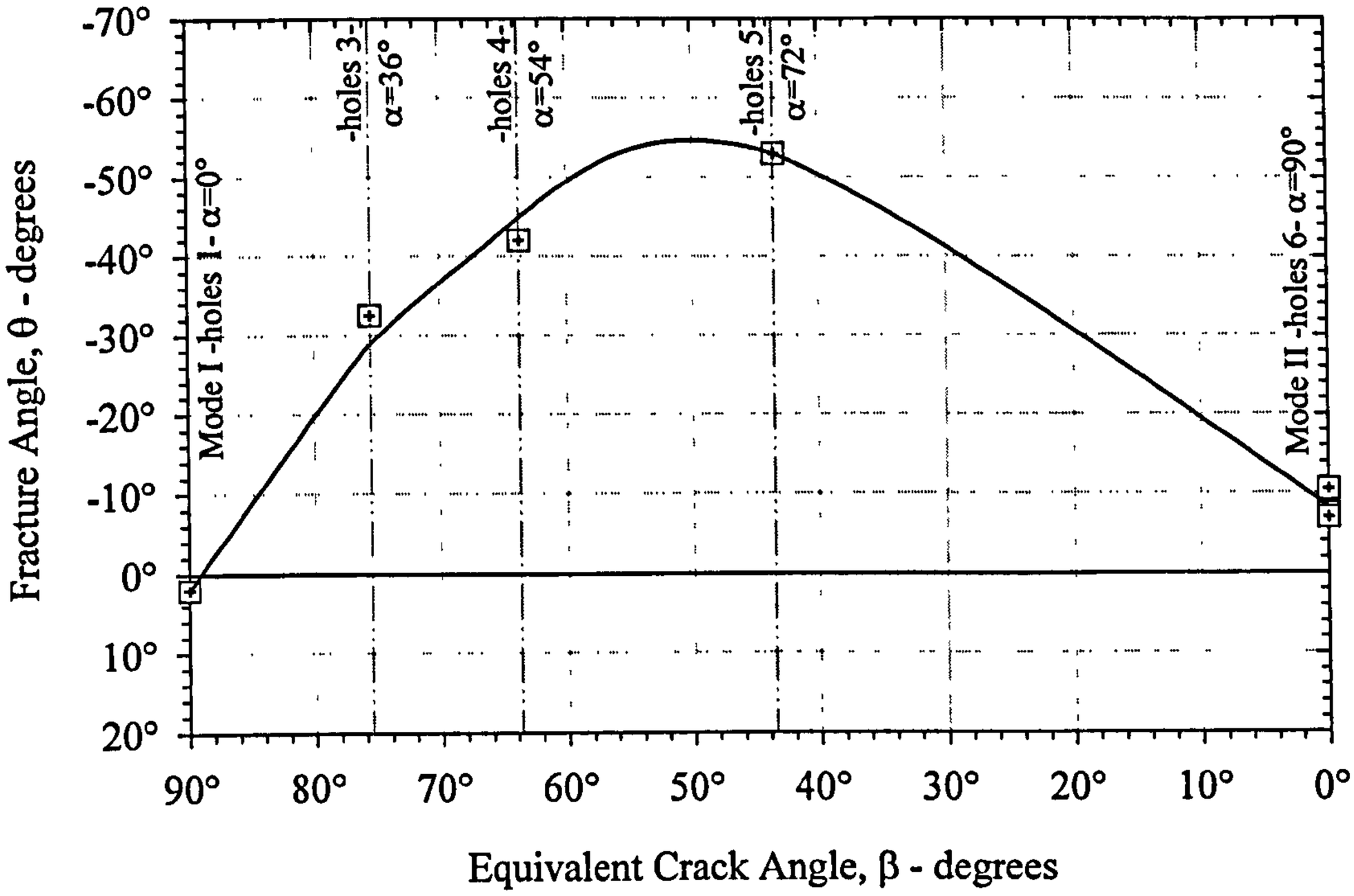

Figure 2.15. **Mode I Proof Load,** Mixed Mode Fracture Angles
(BS1501-224 C-Mn Steel, at -120°C)

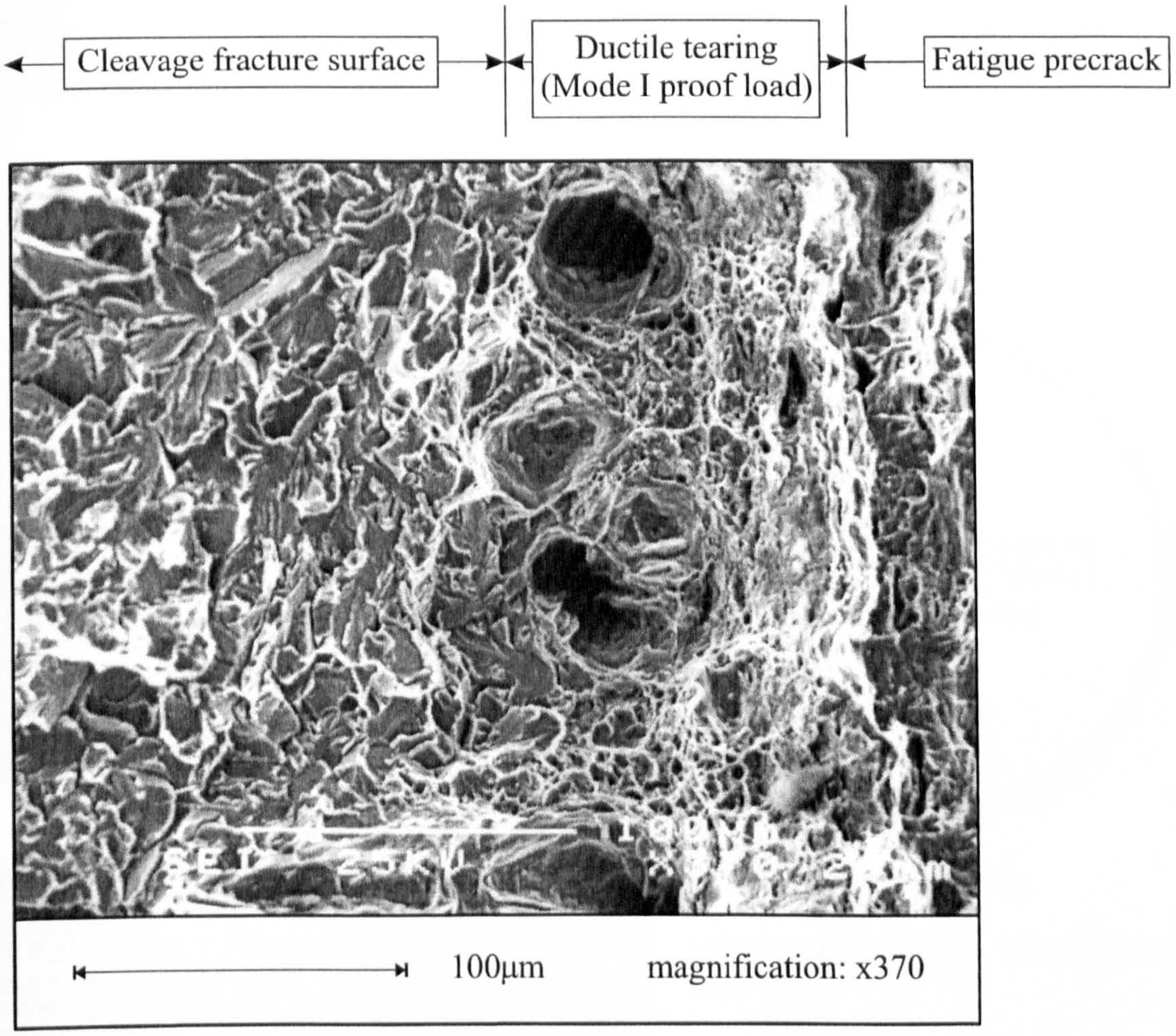

Figure 2.16. BS1501-224 Fracture Surface Features : Mode I Proof Load, Mode I Fracture

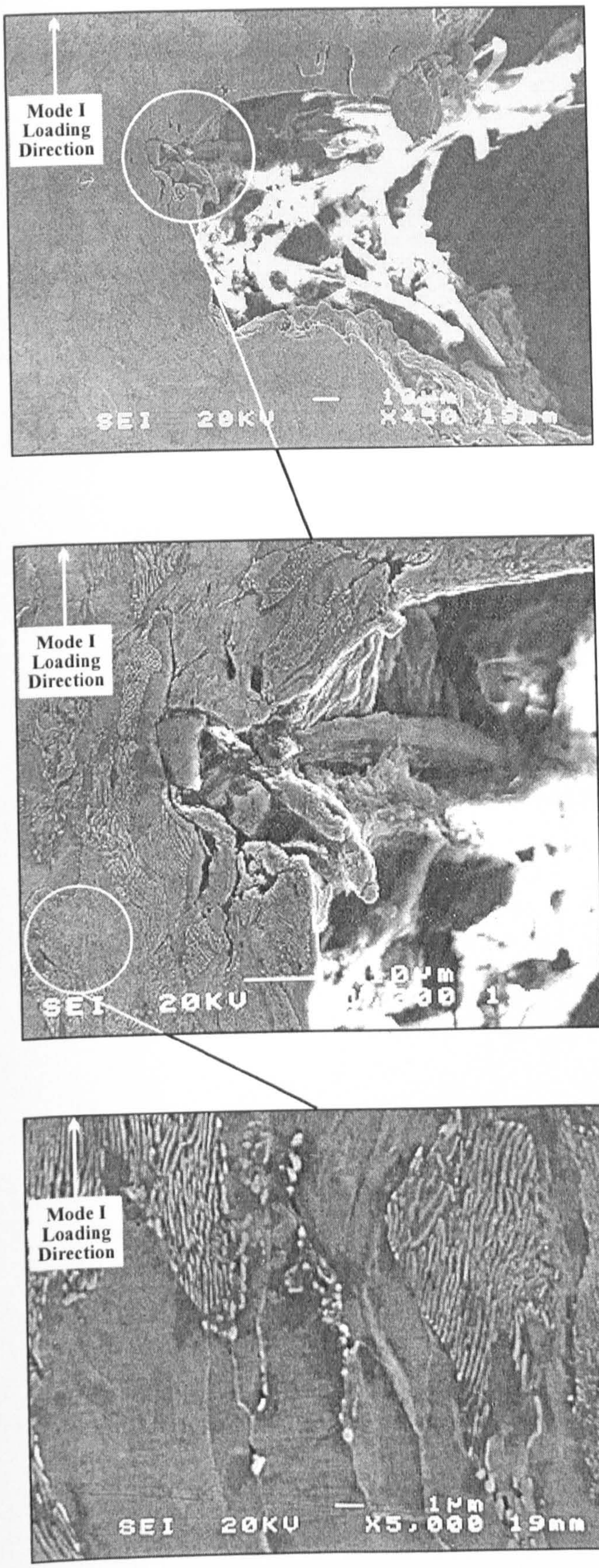

(a) X450 magnification

Crack growth caused by Mode I proof load

(b) X1200 magnification

Local damage at crack tip

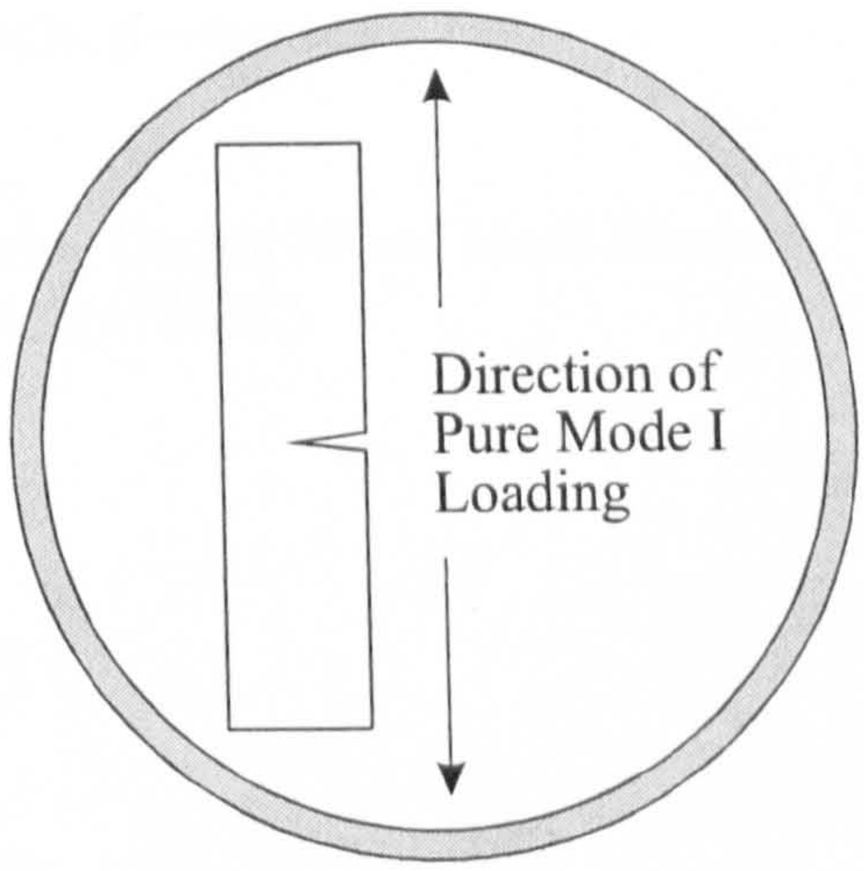

(c) X5000 magnification

Micro-void formation along grain boundaries

Figure 2.17. SEM Examination of Damage Accumulated at the Crack Tip due to a Mode I Proof Load (BS1501-224, at 20°C)

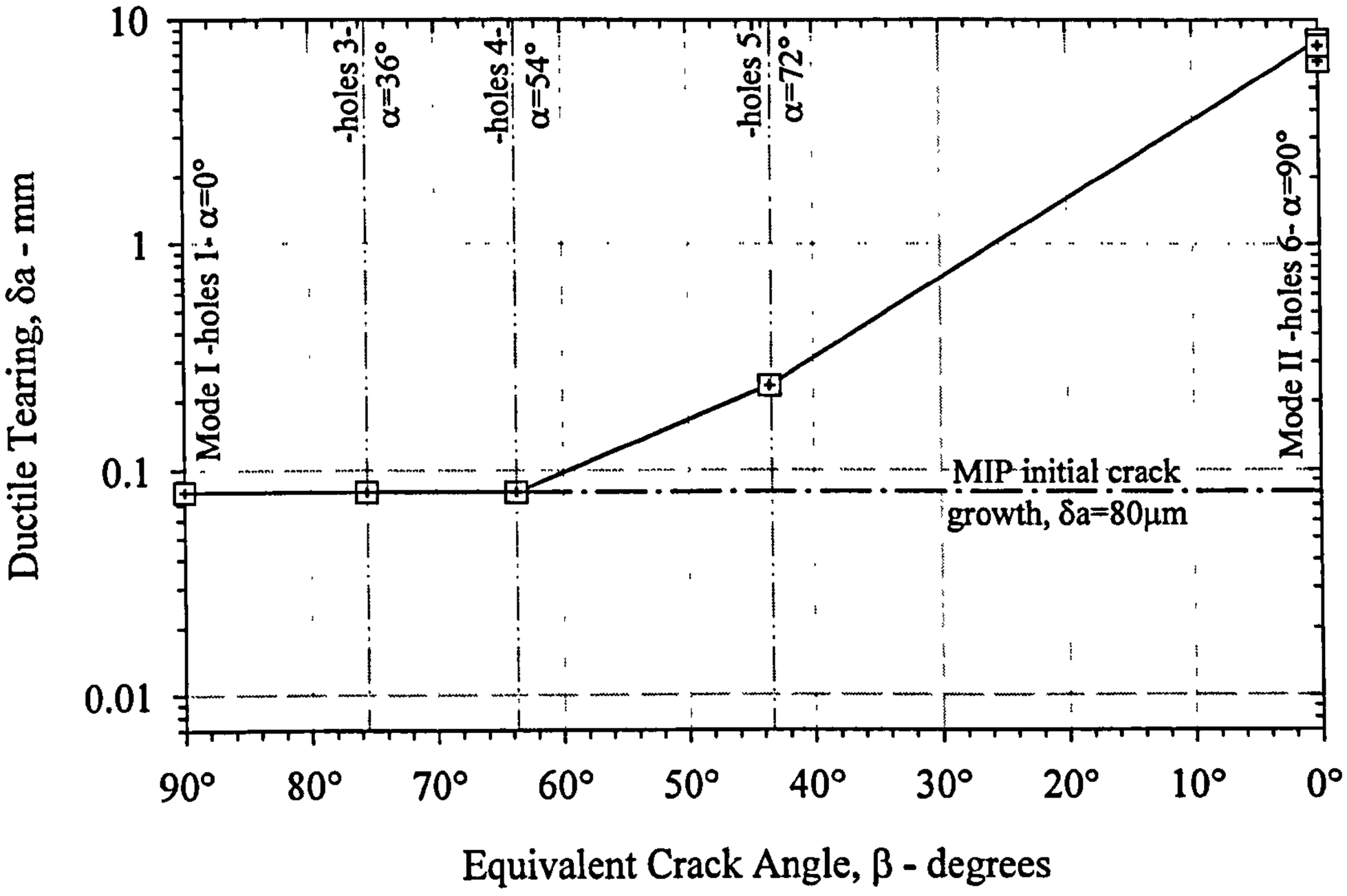

Figure 2.18. **Mode I Proof Load,** Ductile Tearing During Mixed Mode Fracture
(BS1501-224 C-Mn Steel, at -120°C)

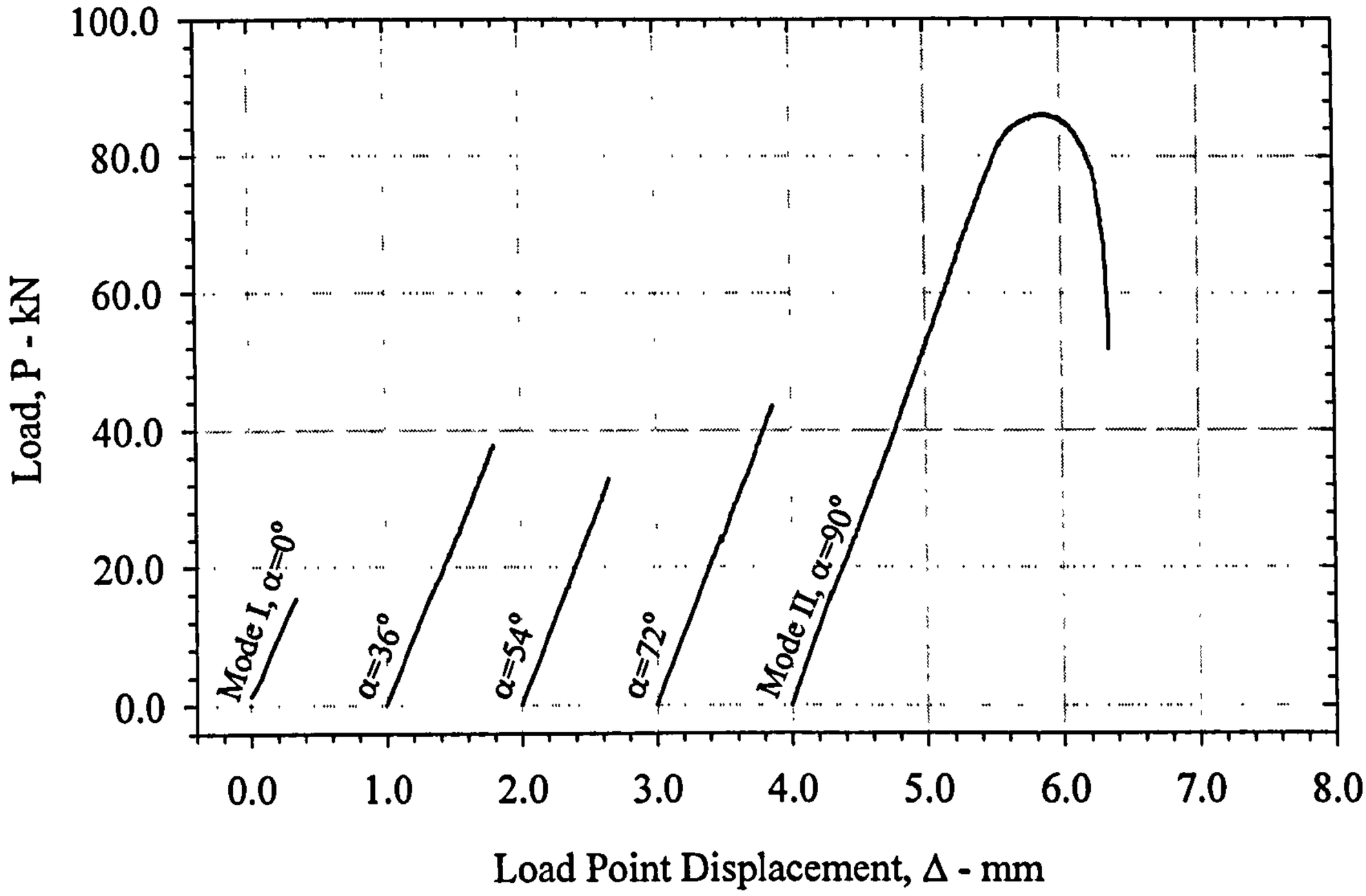

Figure 2.19. **Mode II Proof Load,** Mixed Mode Load vs. Load Point Displacement Curves
(BS1501-224 C-Mn Steel, at -120°C)

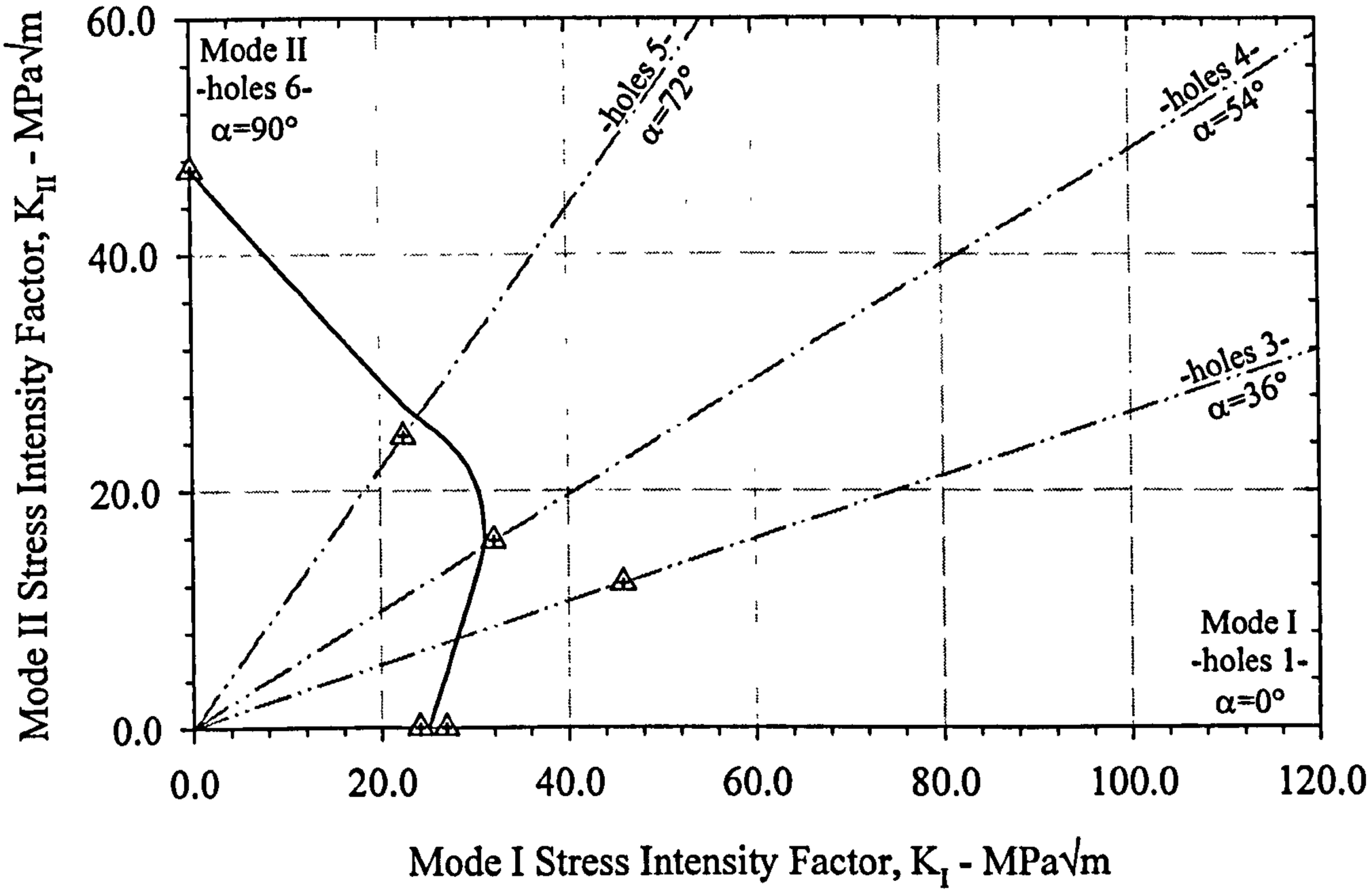

Figure 2.20. **Mode II Proof Load,** Mixed Mode Fracture Toughness
(BS1501-224 C-Mn Steel, at -120°C)

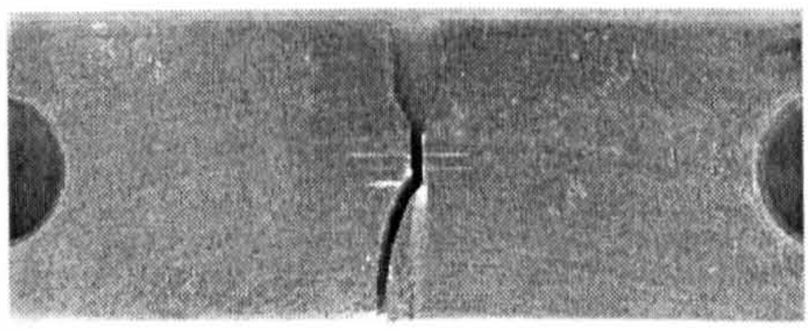

(a) Mode I Fracture (loading holes 1)
loading angle, $\alpha = 0°$
fracture angle, $\theta = 15.6°$

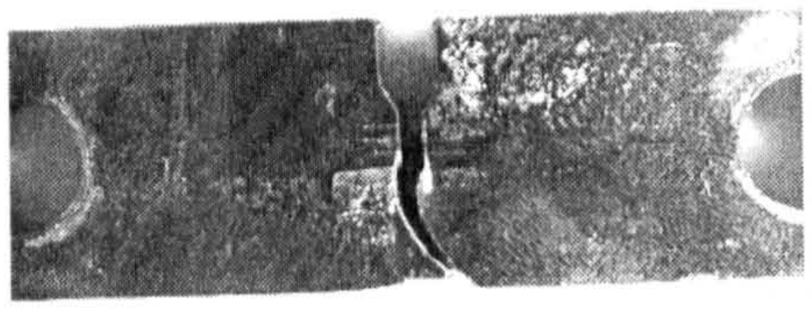

(b) Mixed Mode, Hole 3 Fracture
loading angle, $\alpha = 36°$
fracture angle, $\theta = -40.0°$

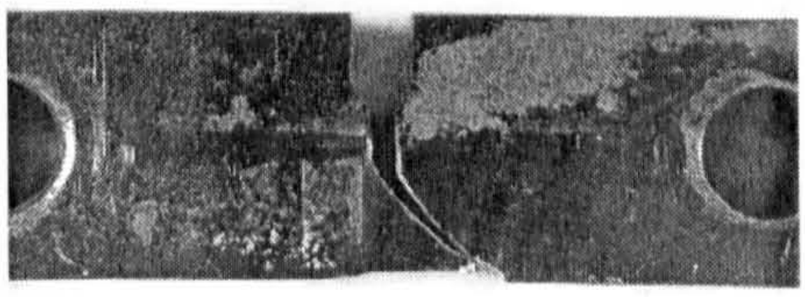

(c) Mixed Mode, Hole 4 Fracture
loading angle, $\alpha = 54°$
fracture angle, $\theta = -40.8°$

(d) Mixed Mode, Hole 5 Fracture
loading angle, $\alpha = 72°$
fracture angle, $\theta = -48.0°$

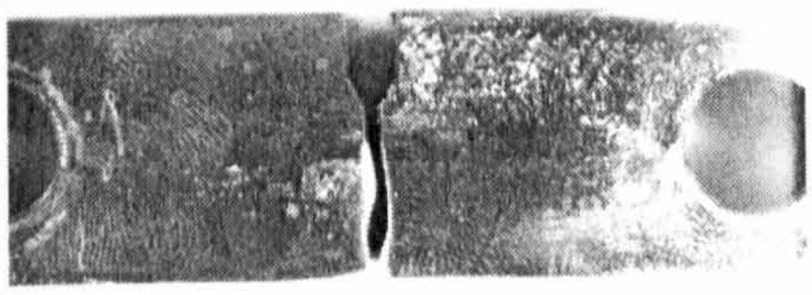

(e) Mode II Fracture (loading holes 6)
loading angle, $\alpha = 90°$
fracture angle, $\theta = -7.0°$

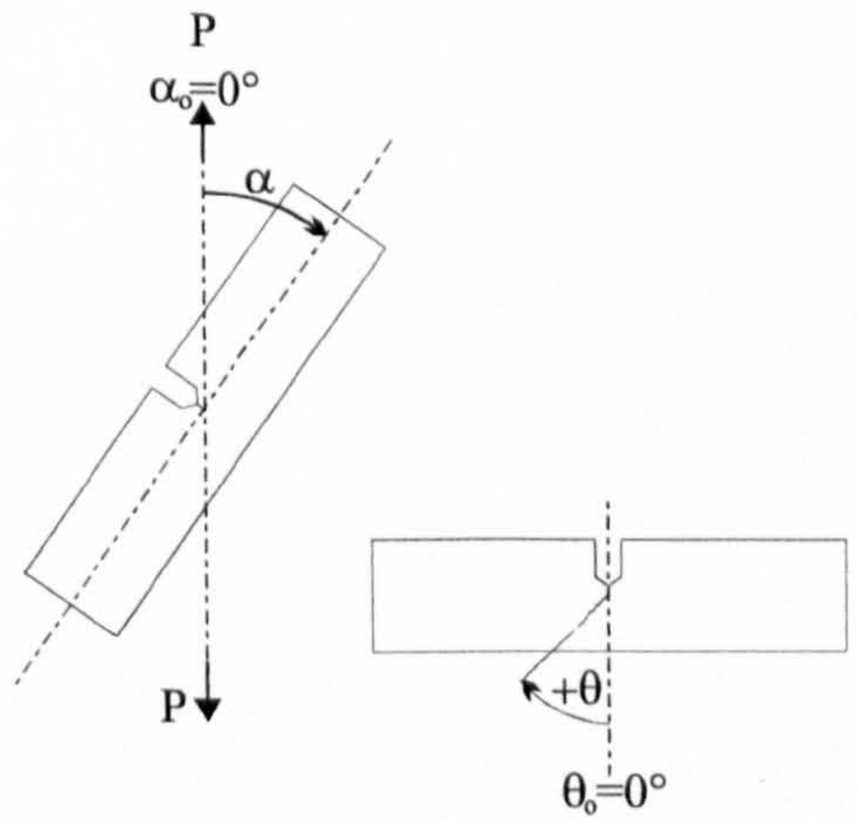

Figure 2.21. **Mode II Proof Load**, Mixed Mode Fracture Angles
(BS1501-224 C-Mn Steel, at -120°C)

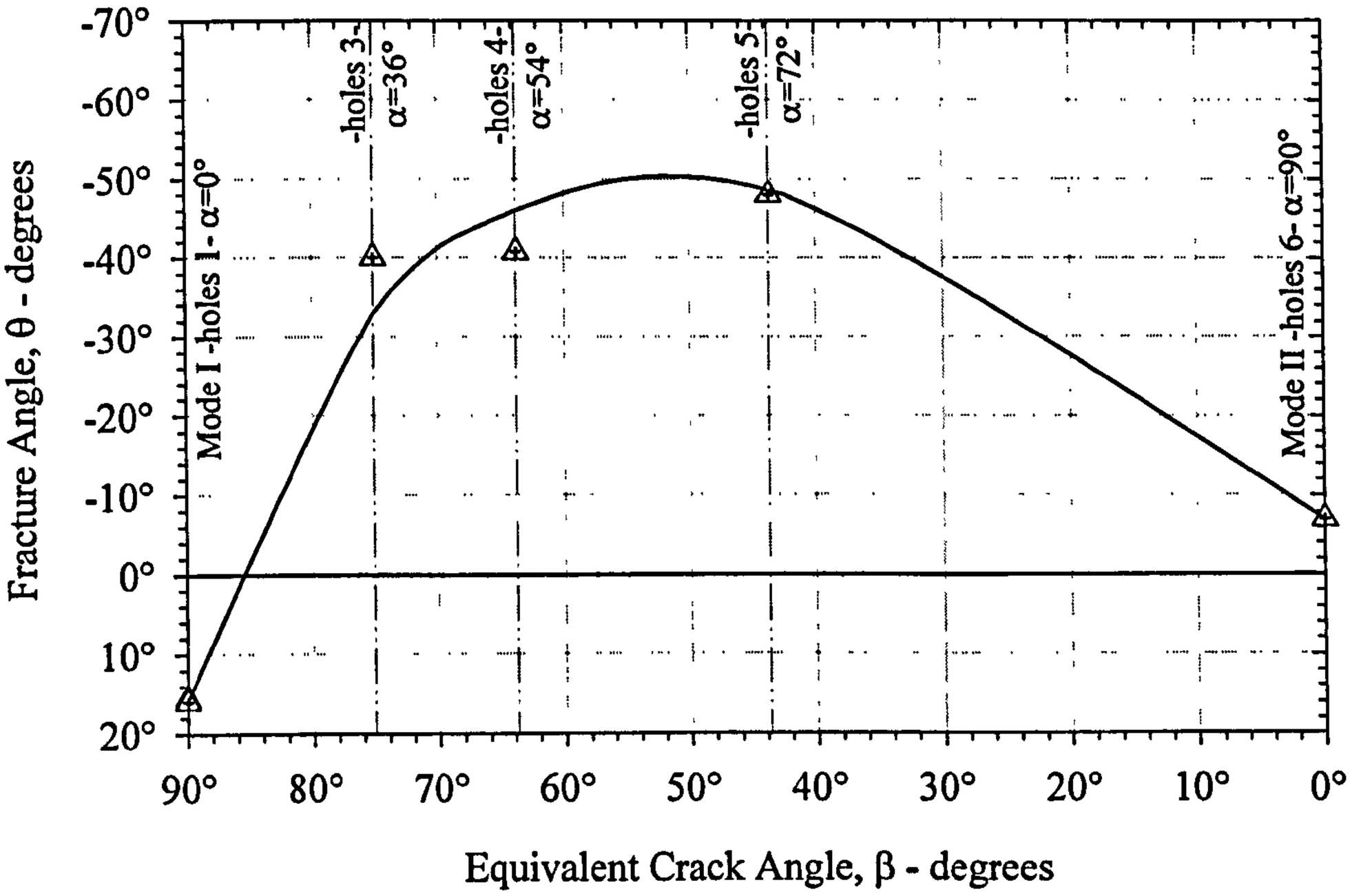

Figure 2.22. **Mode II Proof Load,** Mixed Mode Fracture Angles
(BS1501-224 C-Mn Steel, at -120°C)

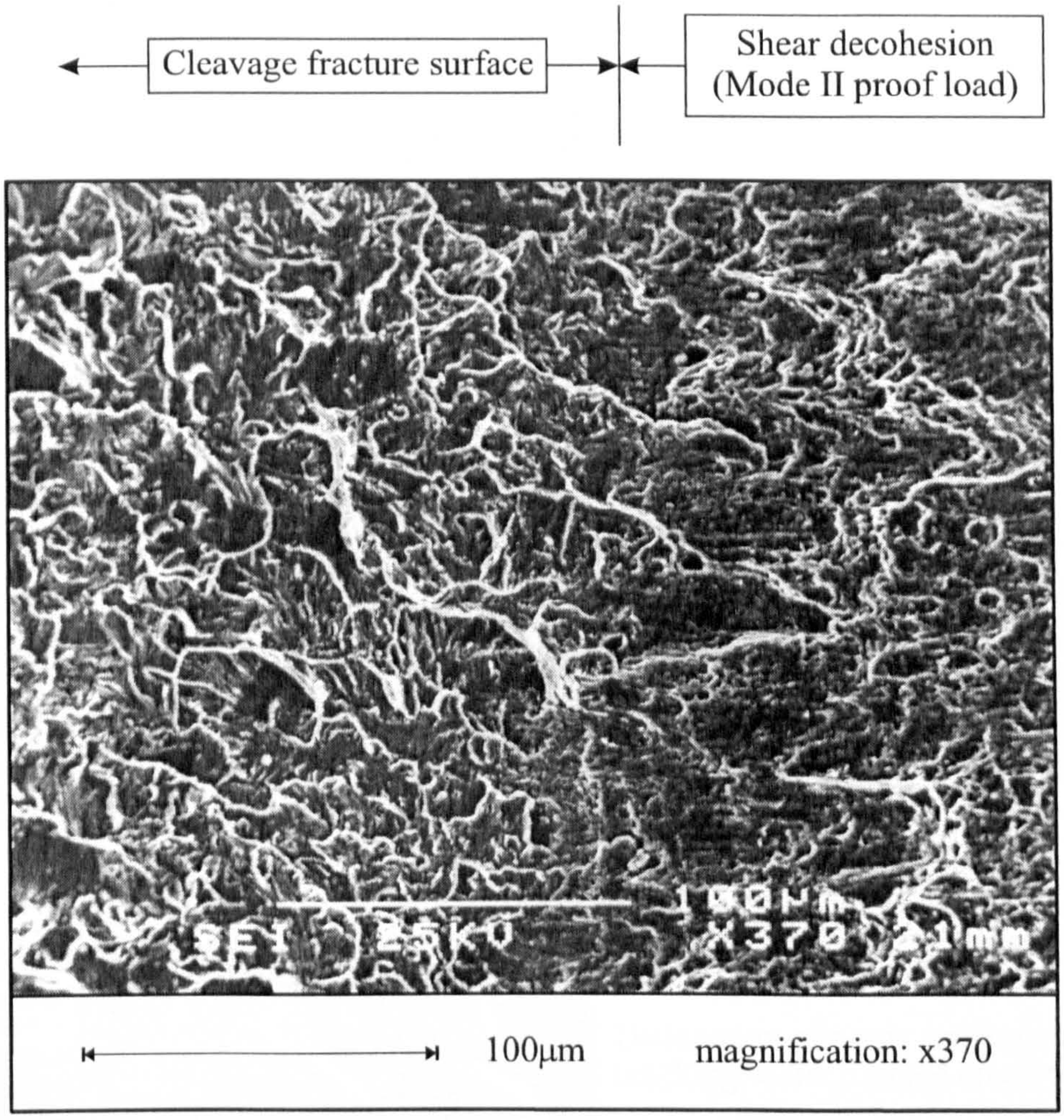

Figure 2.23. BS1501-224 Fracture Surface Features : Mode II Proof Load, Mode I Fracture

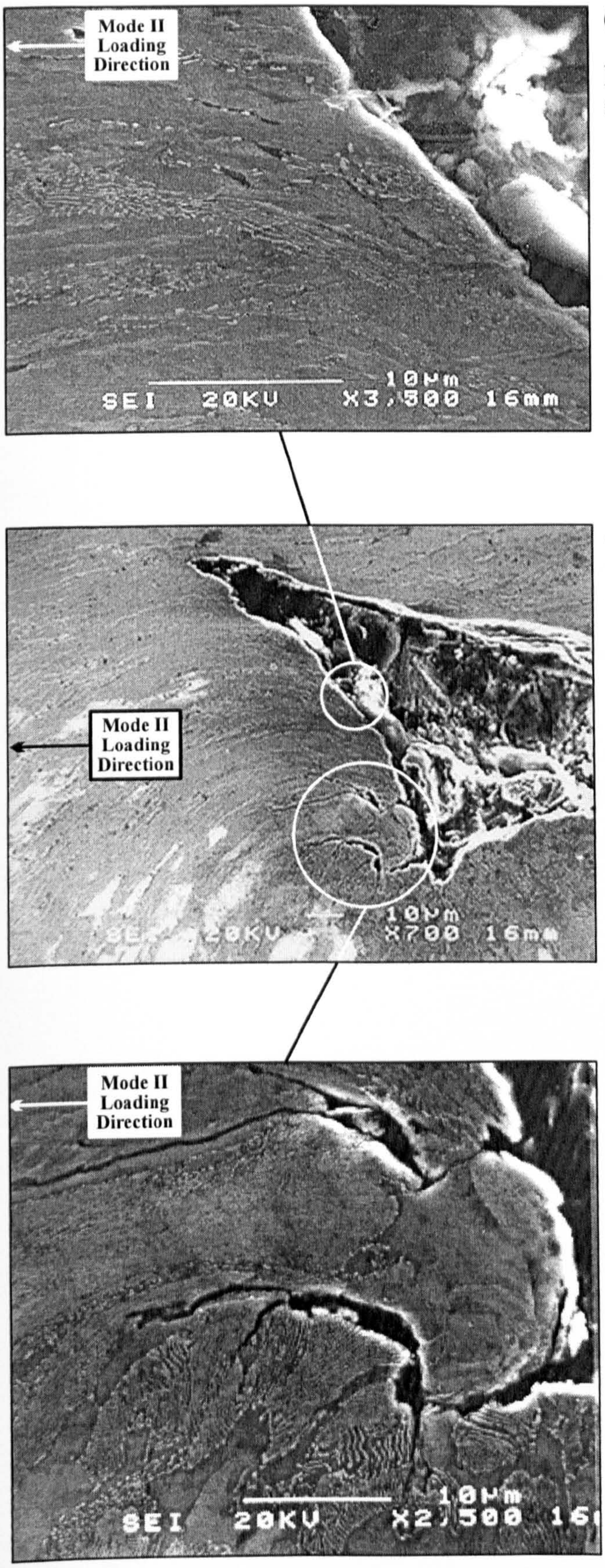

(a) X3500 magnification

Micro-void formation below the shear crack

(b) X700 magnification

Crack tip formation and plastic flow ahead of the crack

(c) X2500 magnification

Dislocation pile-ups causing micro cracking at the blunted crack tip

Figure 2.24. SEM Examination of Damage Accumulated at the Crack Tip due to a Mode II Proof Load (BS1501-224, at 20°C)

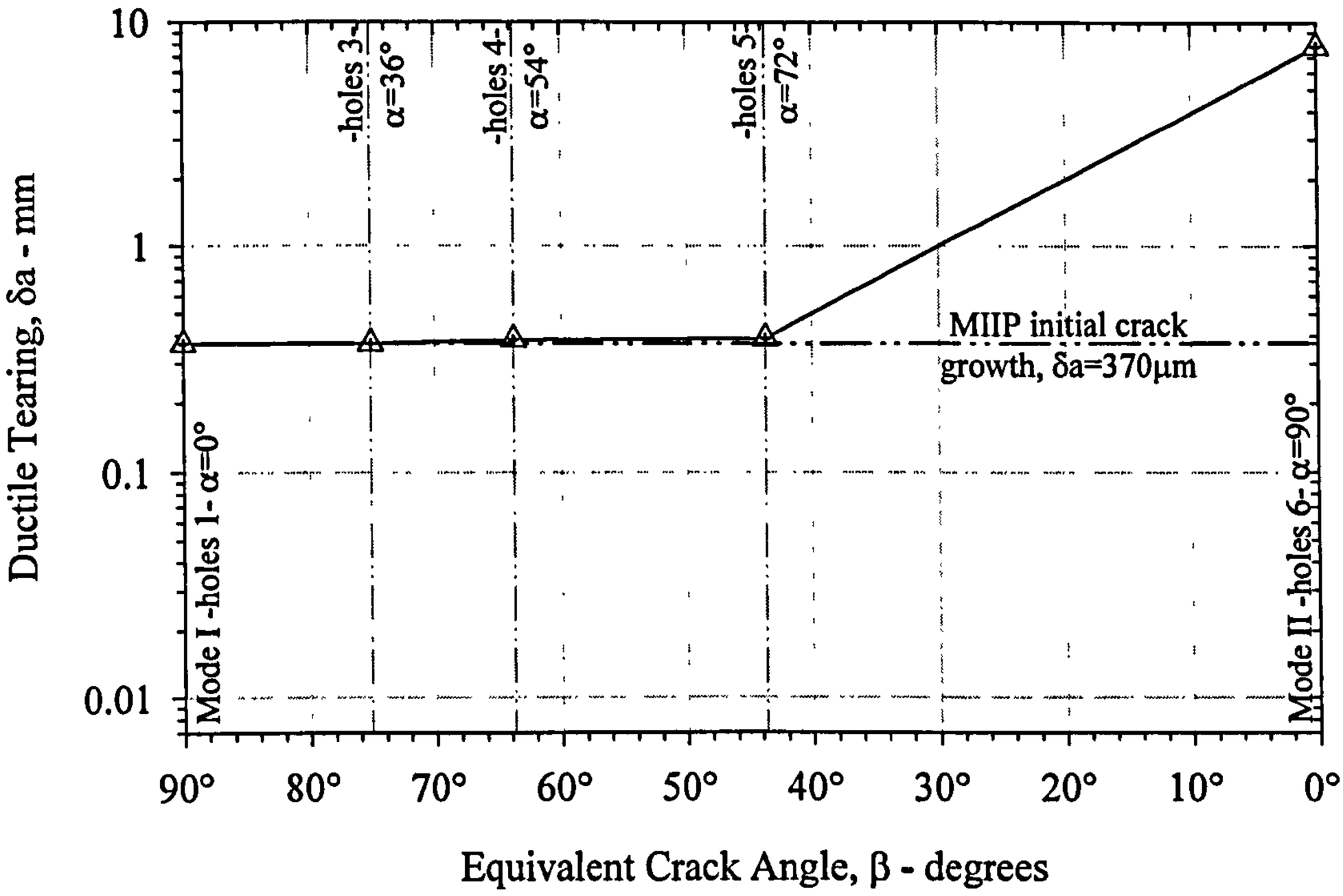

Figure 2.25. **Mode II Proof Load**, Ductile Tearing During Mixed Mode Fracture
(BS1501-224 C-Mn Steel, at -120°C)

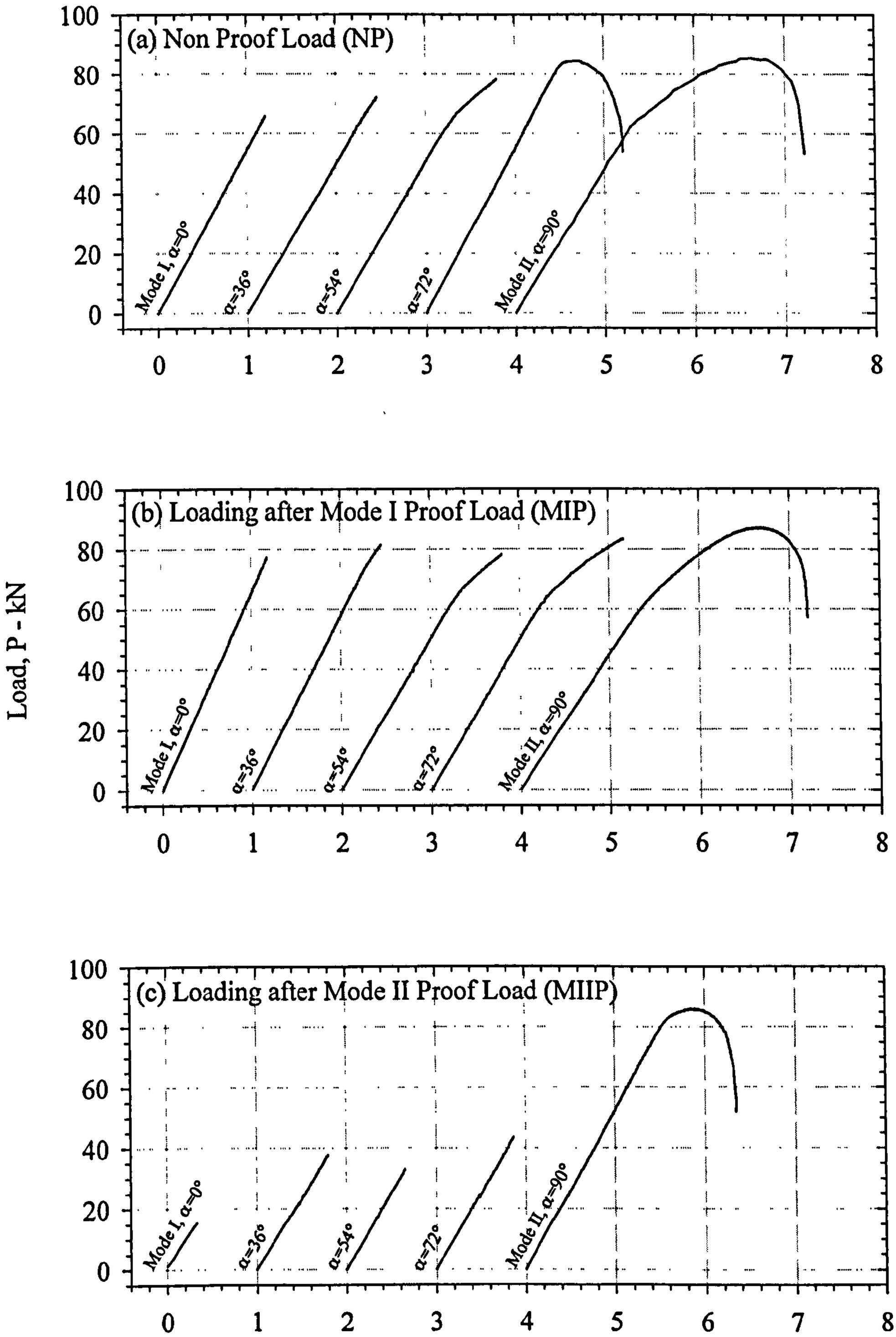

Figure 2.26. Comparison of Load vs. Load Point Displacement for (a) NP, (b) MIP and (c) MIIP Conditions (BS1501-224 C-Mn Steel, at -120°C)

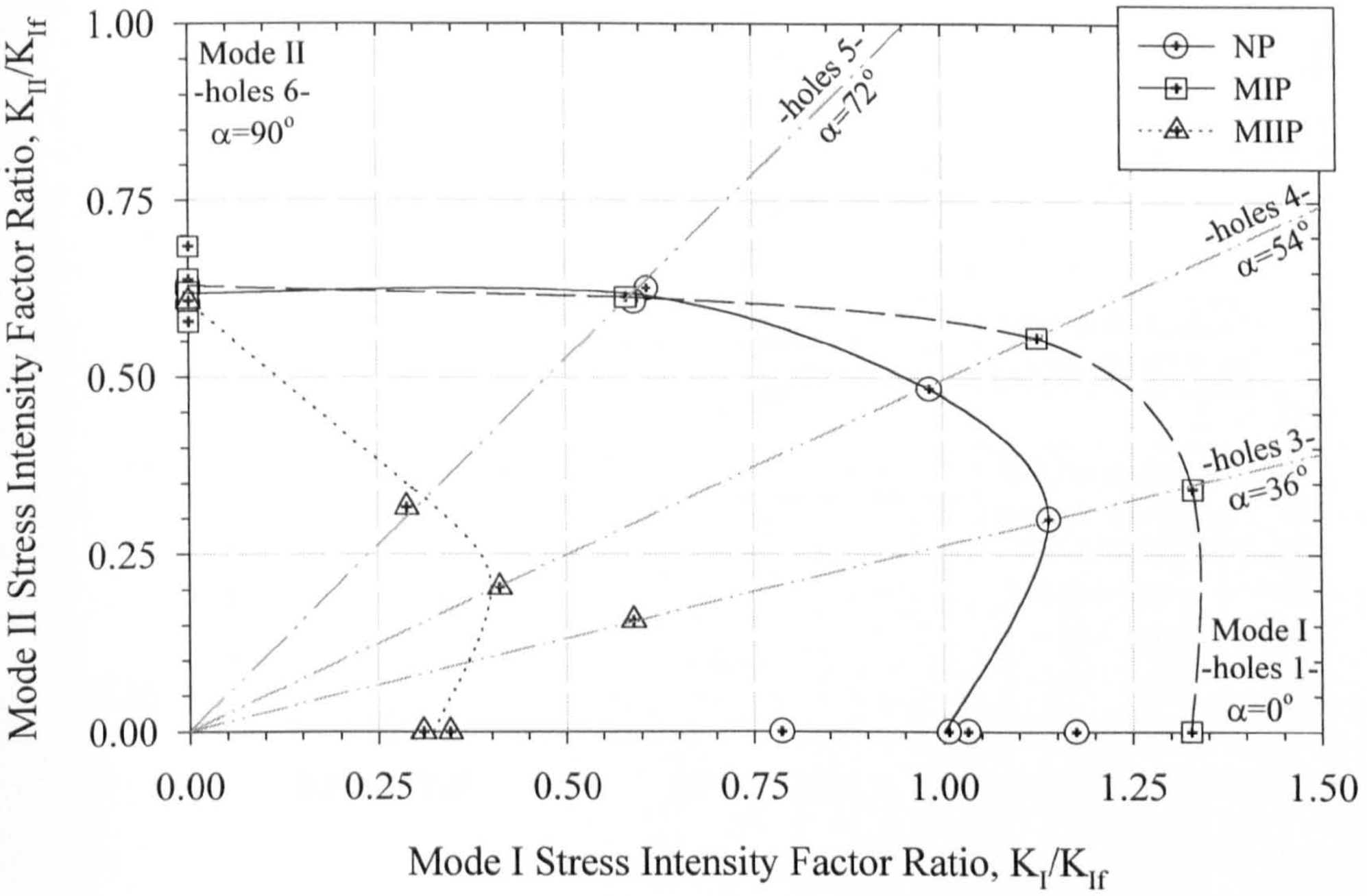

Figure 2.27. Non, Mode I and Mode II Proof Load, Mixed Mode Fracture Toughness
(BS1501-224 C-Mn Steel, at -120°C)

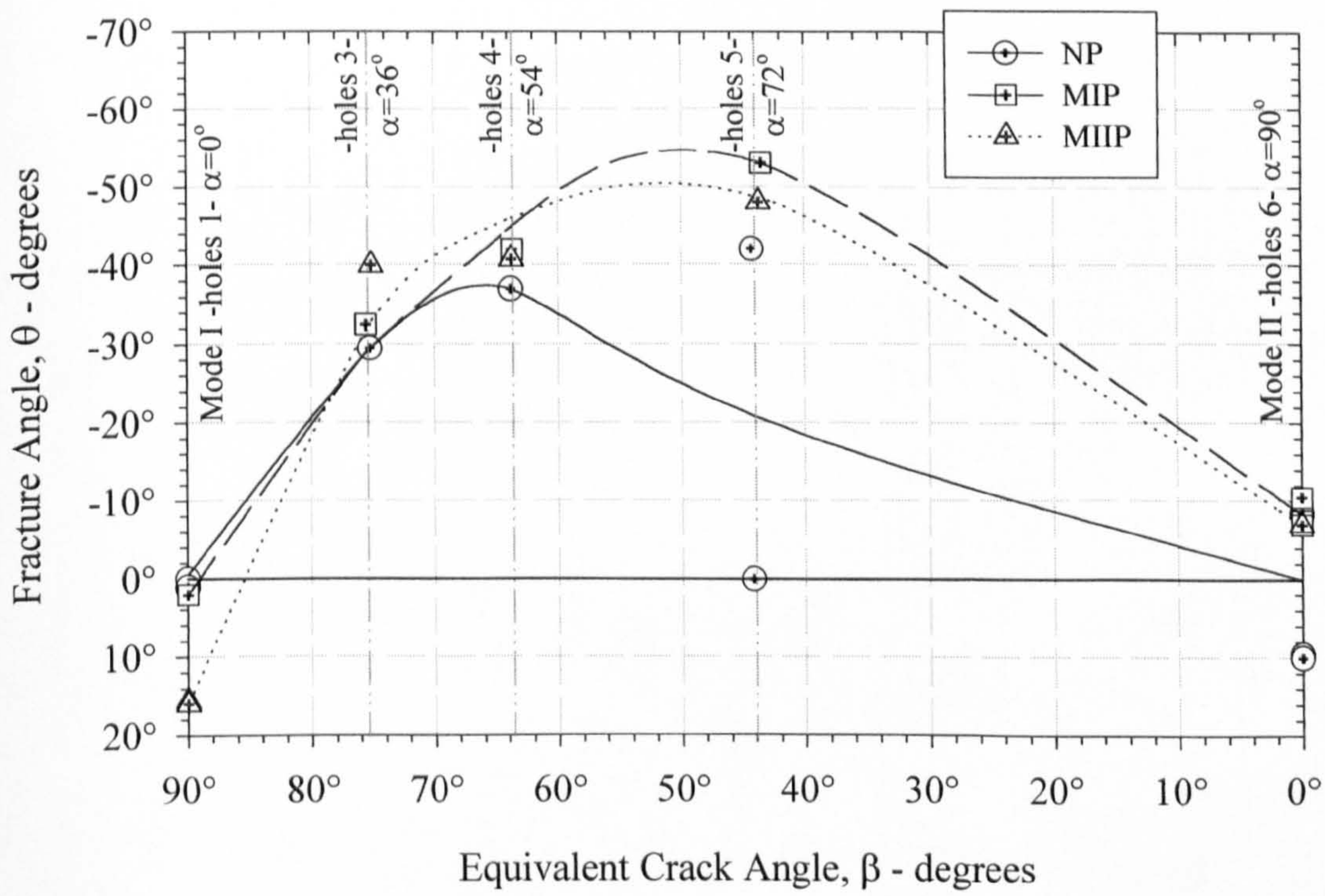

Figure 2.28. Non, Mode I and Mode II Proof Load, Mixed Mode Fracture Angles
(BS1501-224 C-Mn Steel, at -120°C)

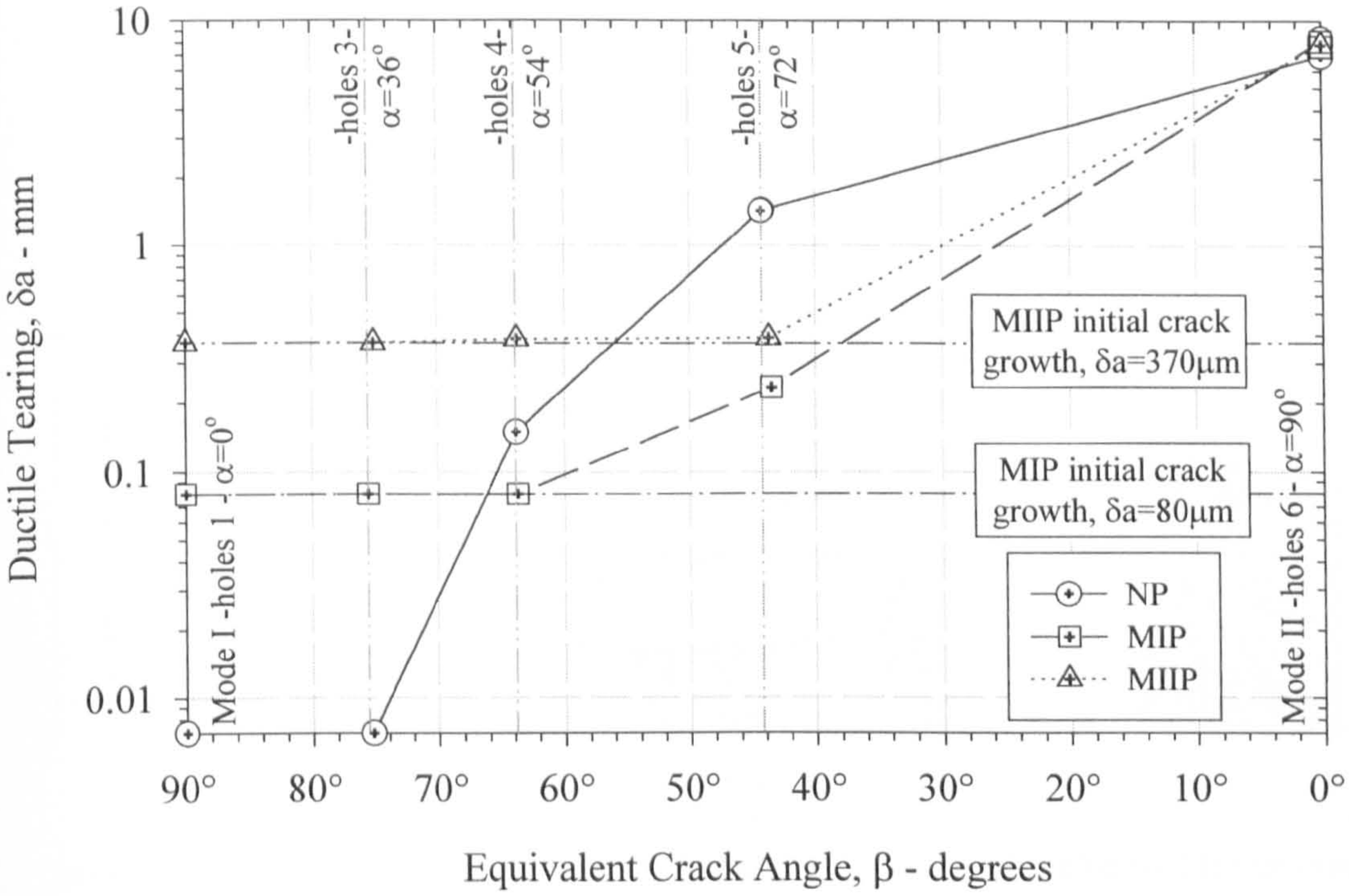

Figure 2.29. Non, Mode I and Mode II Proof Load Ductile Tearing During Mixed Mode Fracture (BS1501-224 C-Mn Steel, at -120°C)

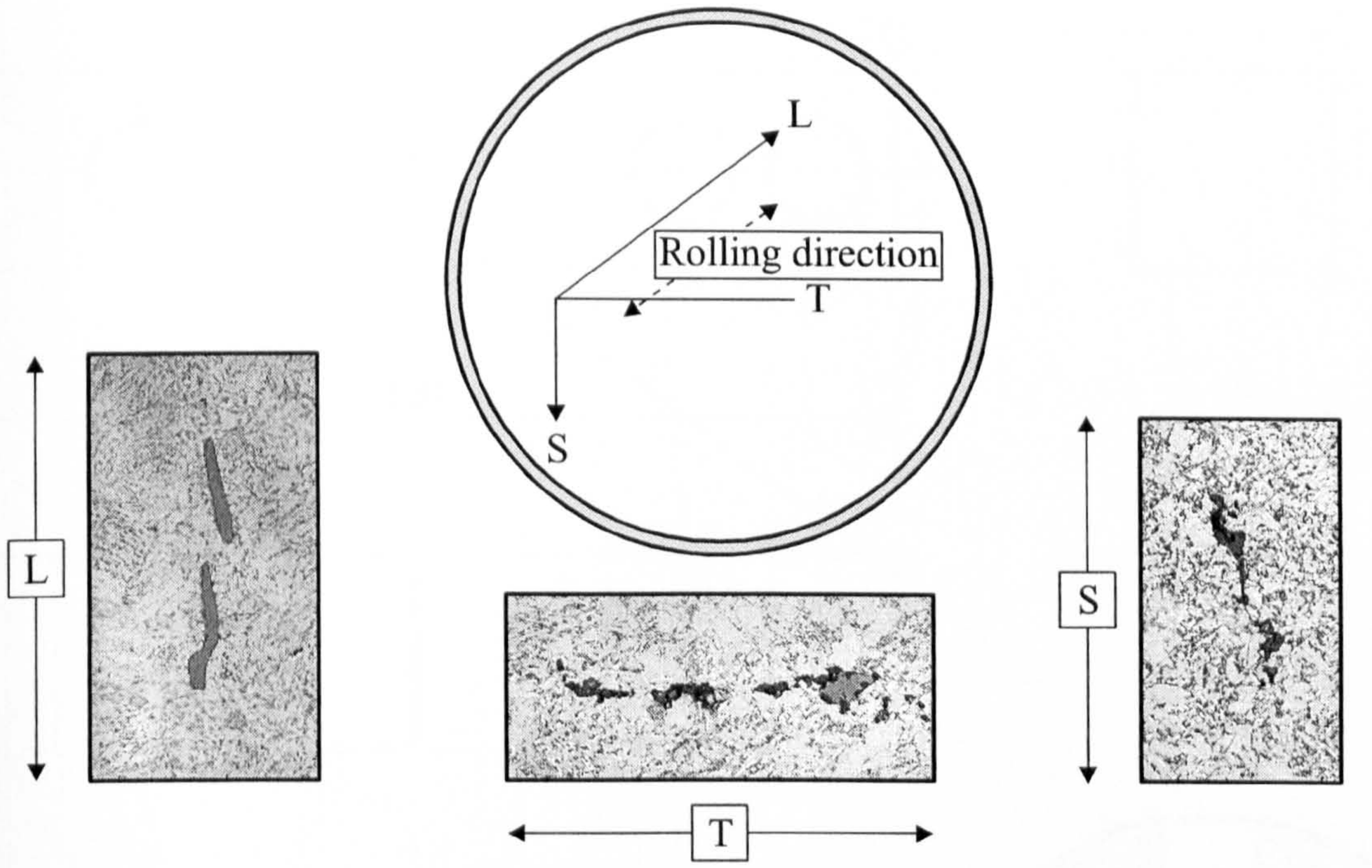

(a) Longitudinal inclusions

(b) Transverse inclusions

(c) Short transverse inclusions

Figure 3.1. Mn-S Inclusions in Relation to Orientation

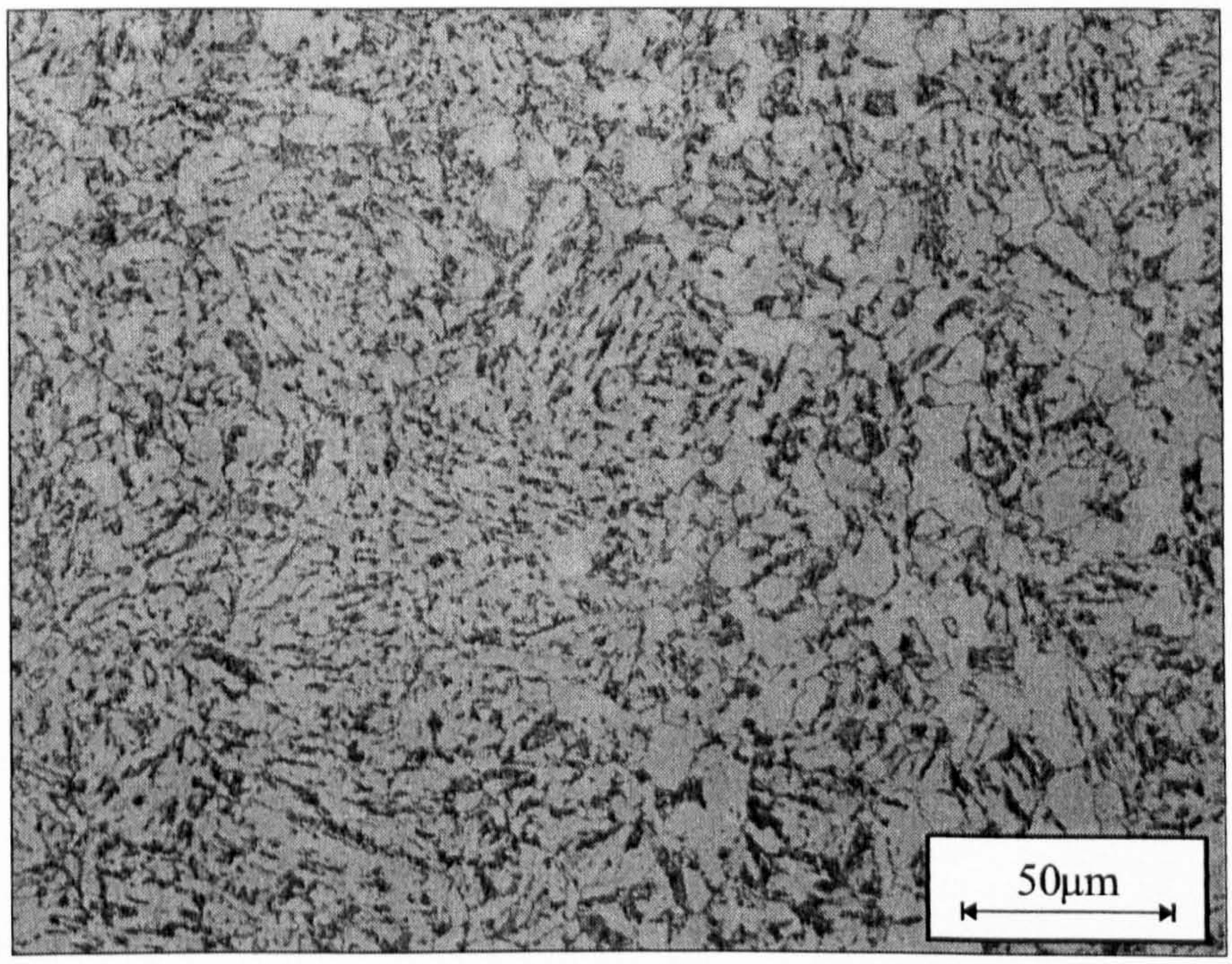

Figure 3.2. Pearlitic Grain Structure of A508 Class 3 C-Mn Steel

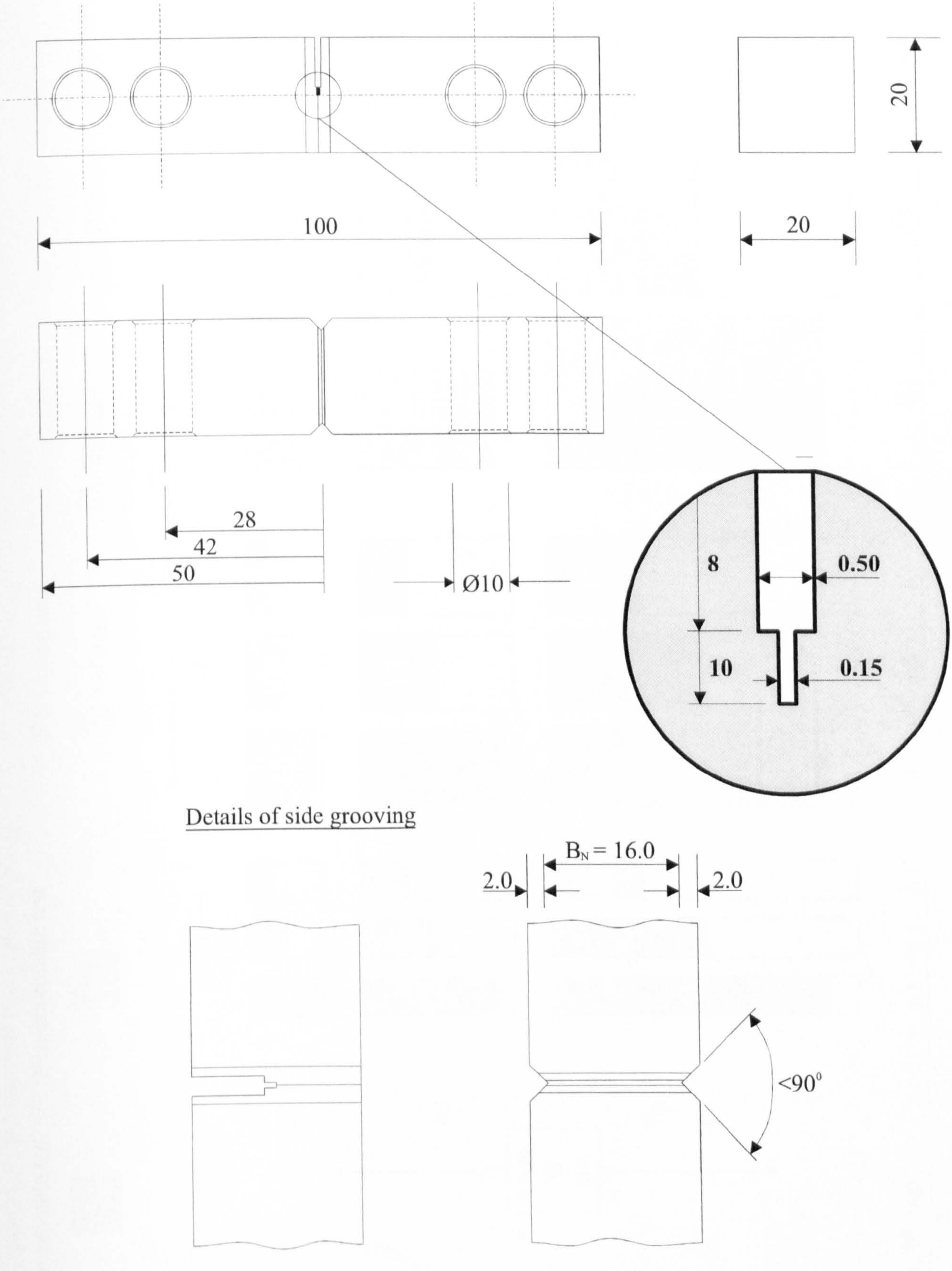

Figure 3.3. 20% Side Grooved Single Edge Notch, SEN Specimen
(dimensions in millimetres)

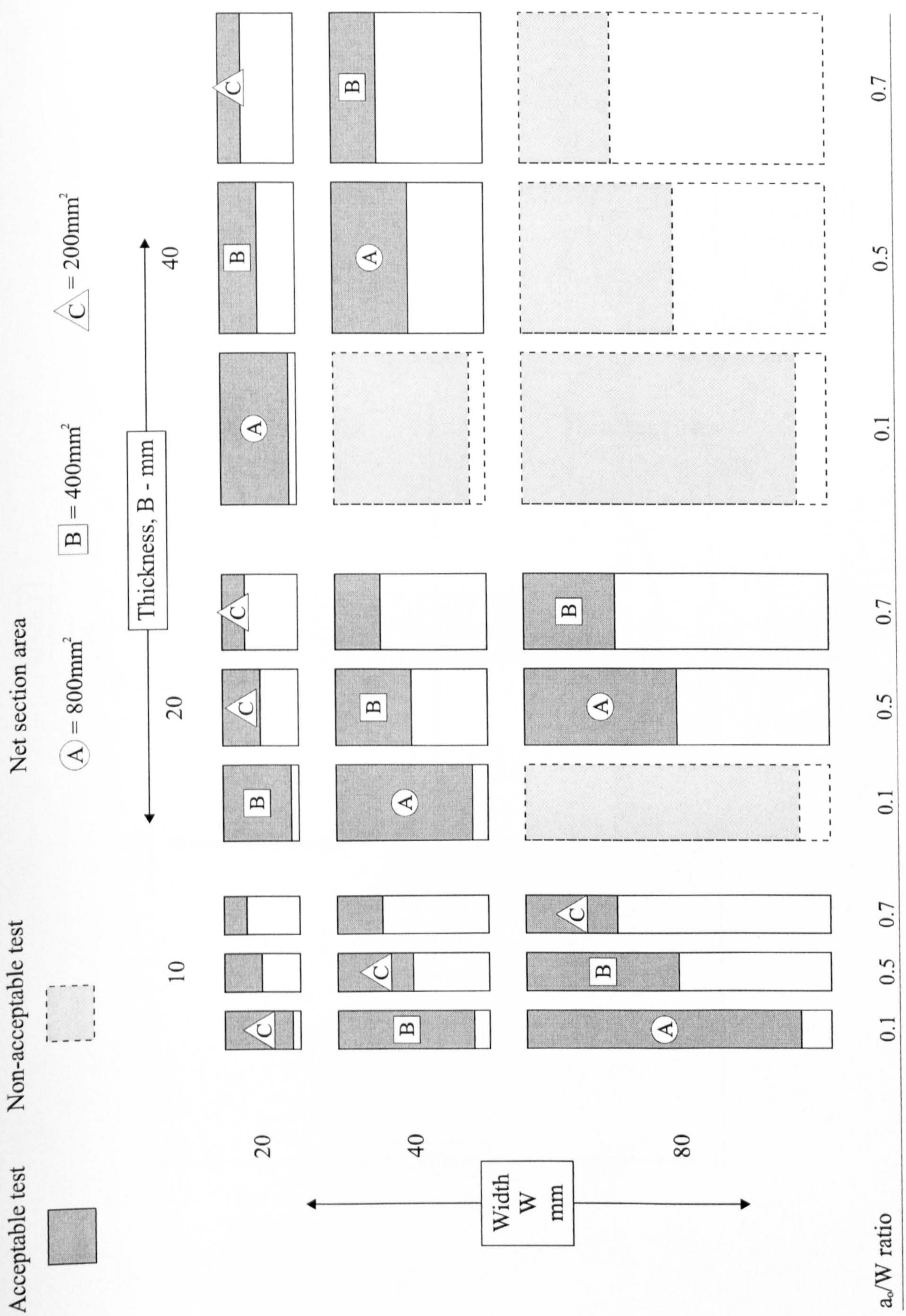

Figure 3.4. A508 Mixed Mode Test Matrix

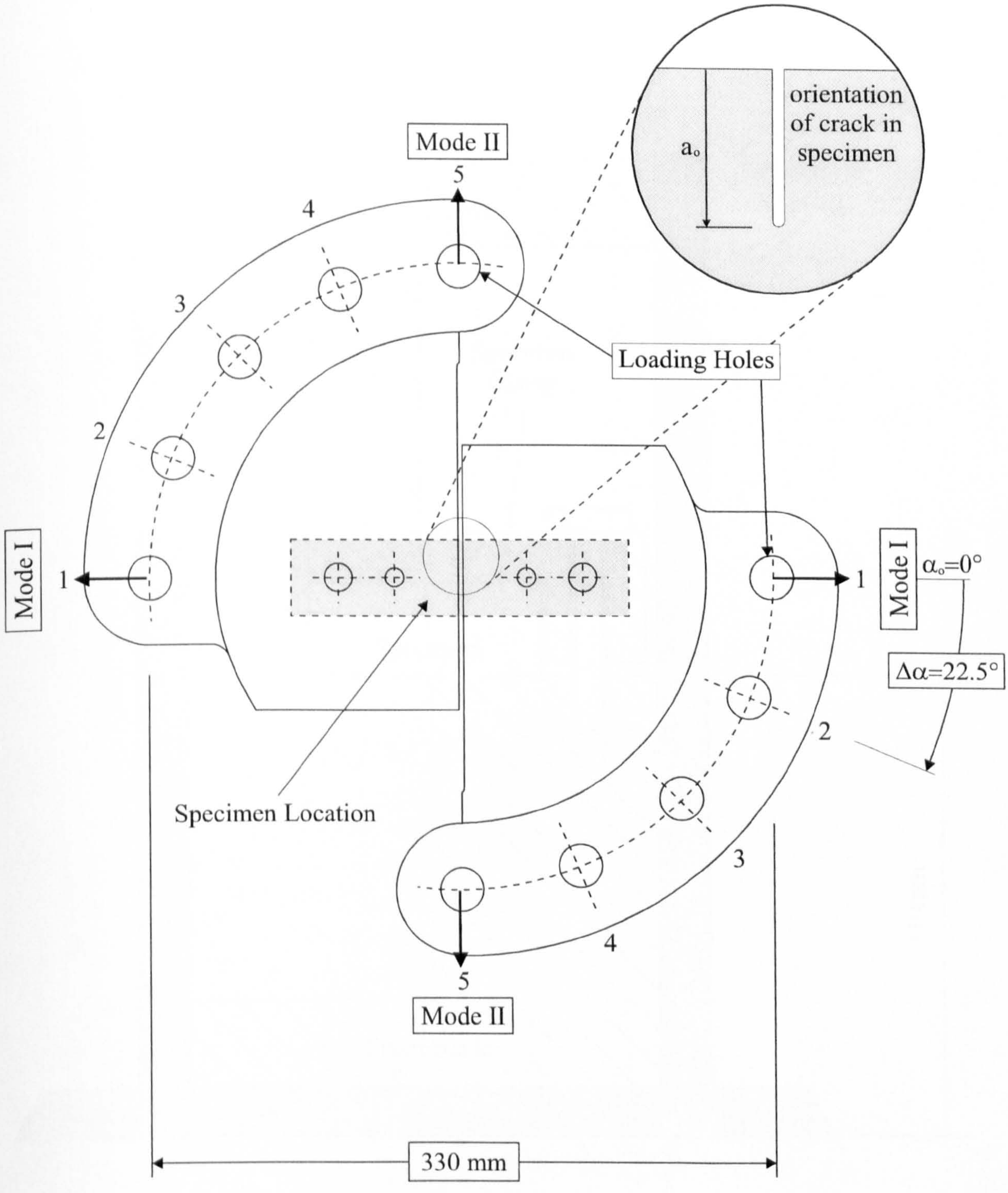

Figure 3.5. Mixed Mode I/II Loading Fixture for Constraint Experiments

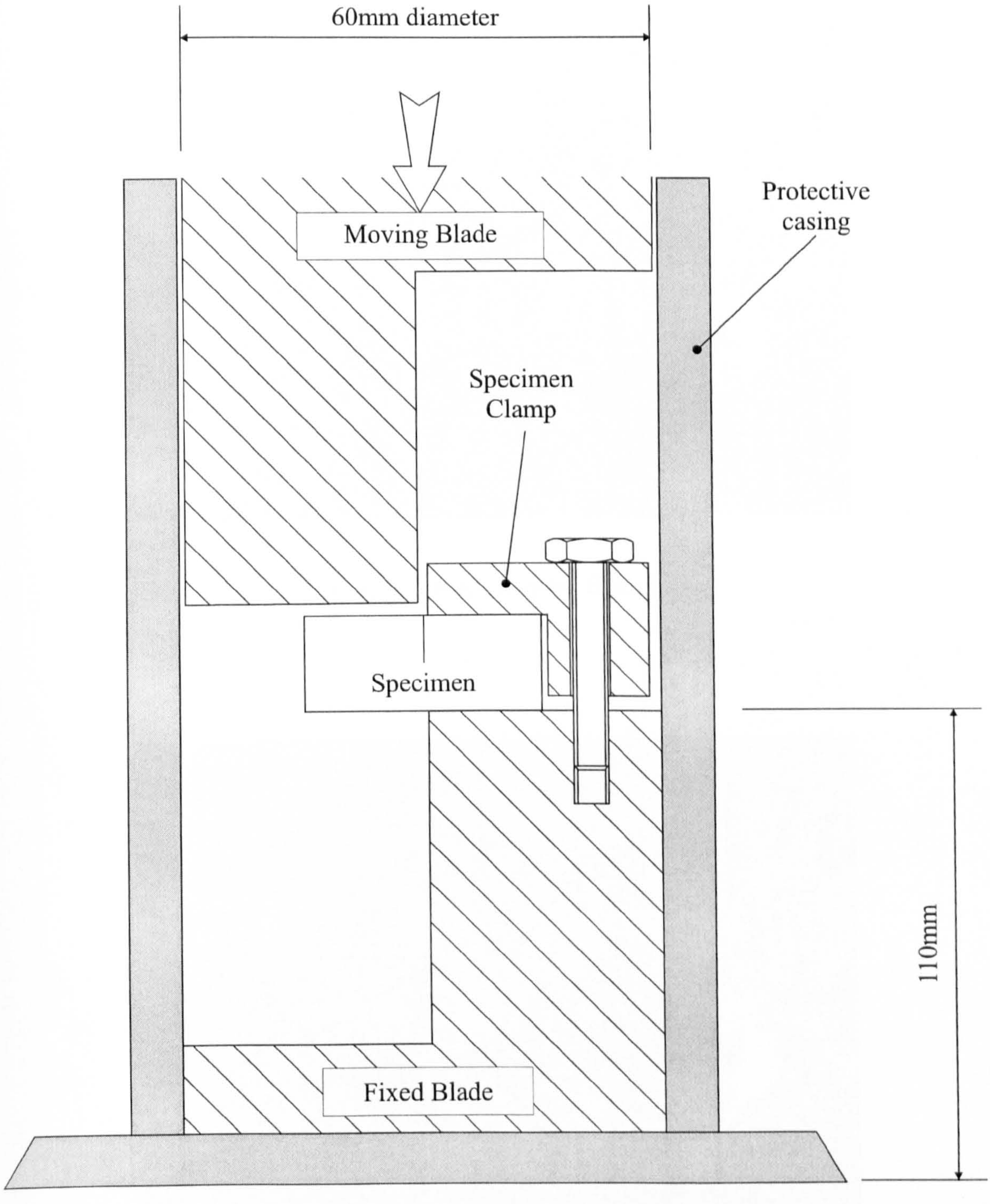

Figure 3.6. Shear Punch Loading Fixture
(not to scale)

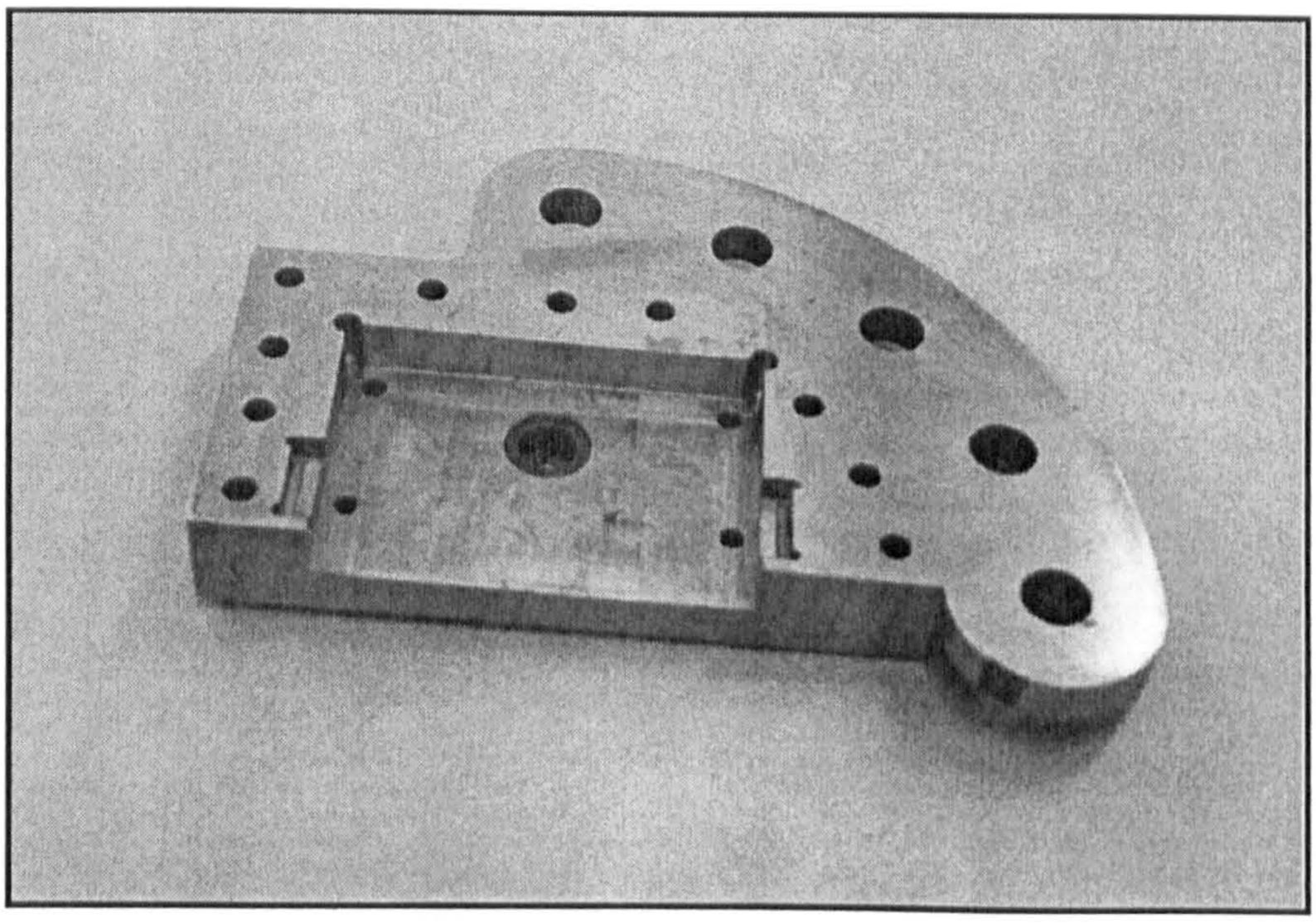

a) Mixed mode loading fixture

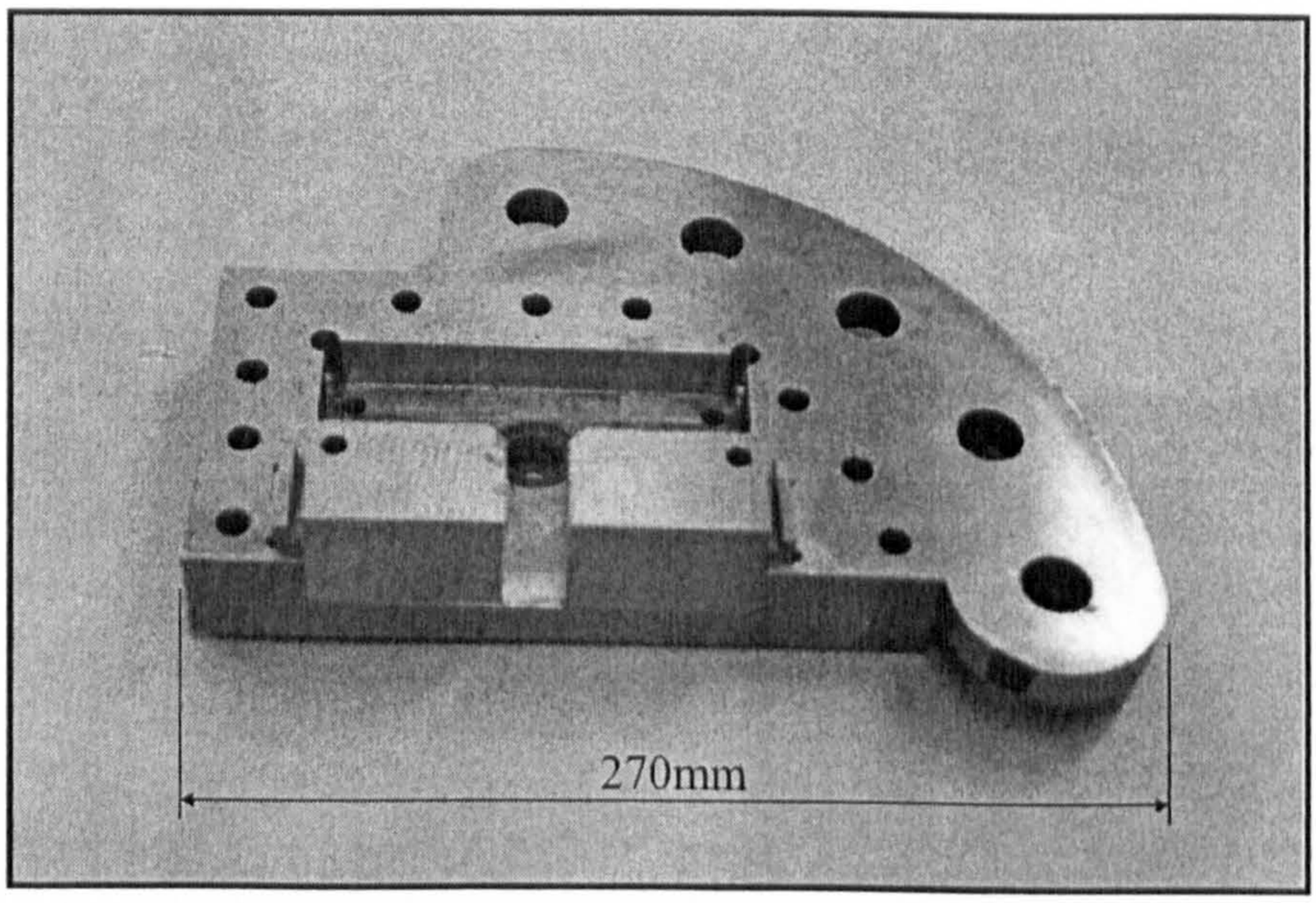

b) Spacer blocks located in mixed mode loading fixture

Figure 3.7. Positioning of Spacer Blocks in Mixed Mode Loading Fixture

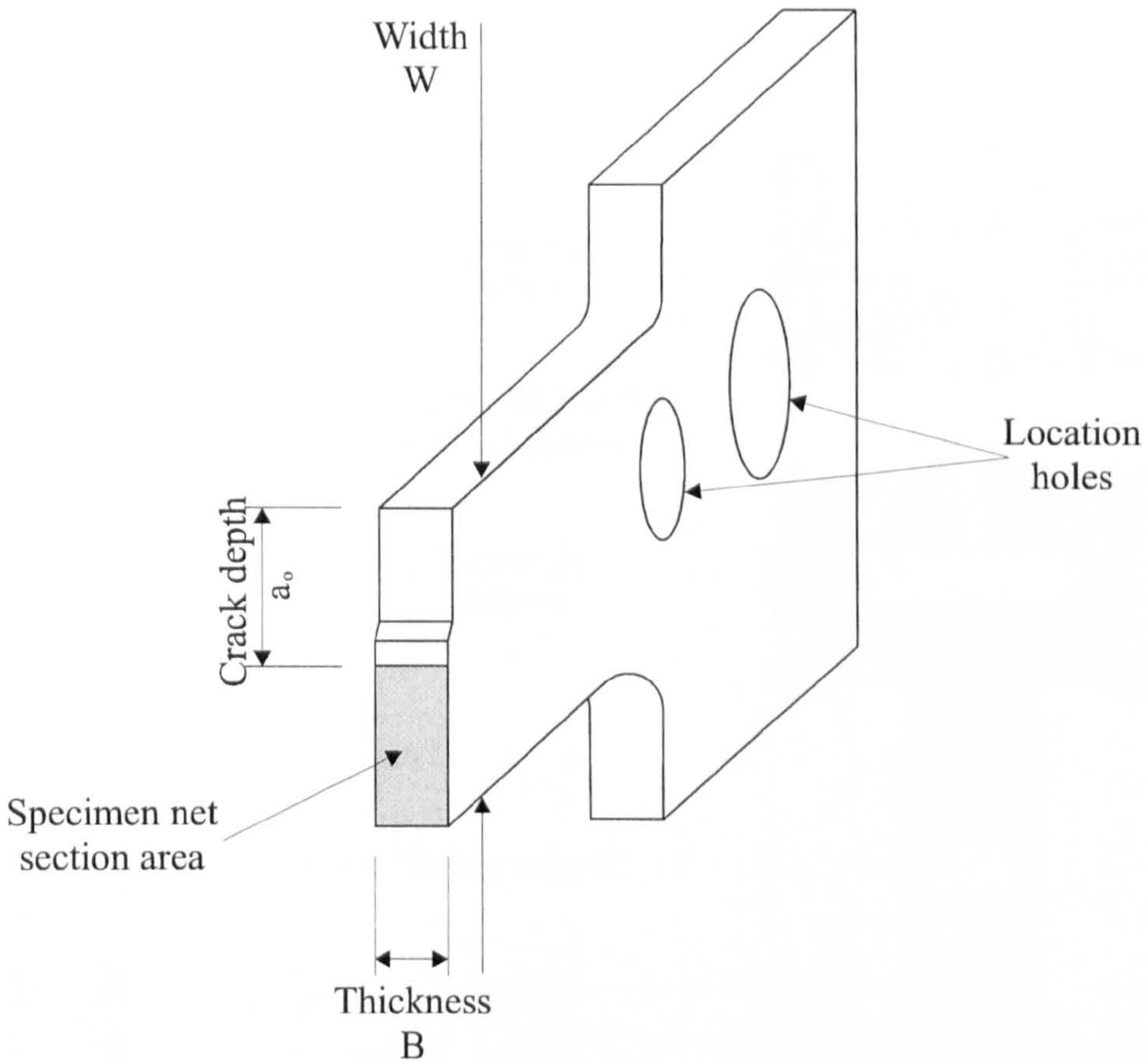

Figure 3.8. Dog-Bone SEN Specimen, Sectioned about the Plane of the Crack

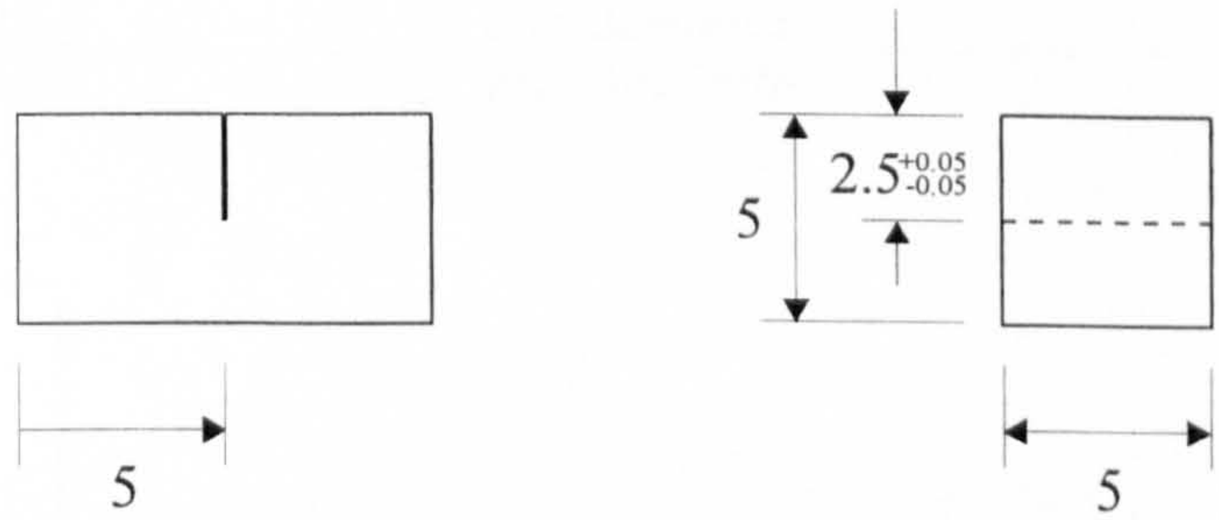

Figure 3.9. Small-Scale Single Punch Shear Specimen

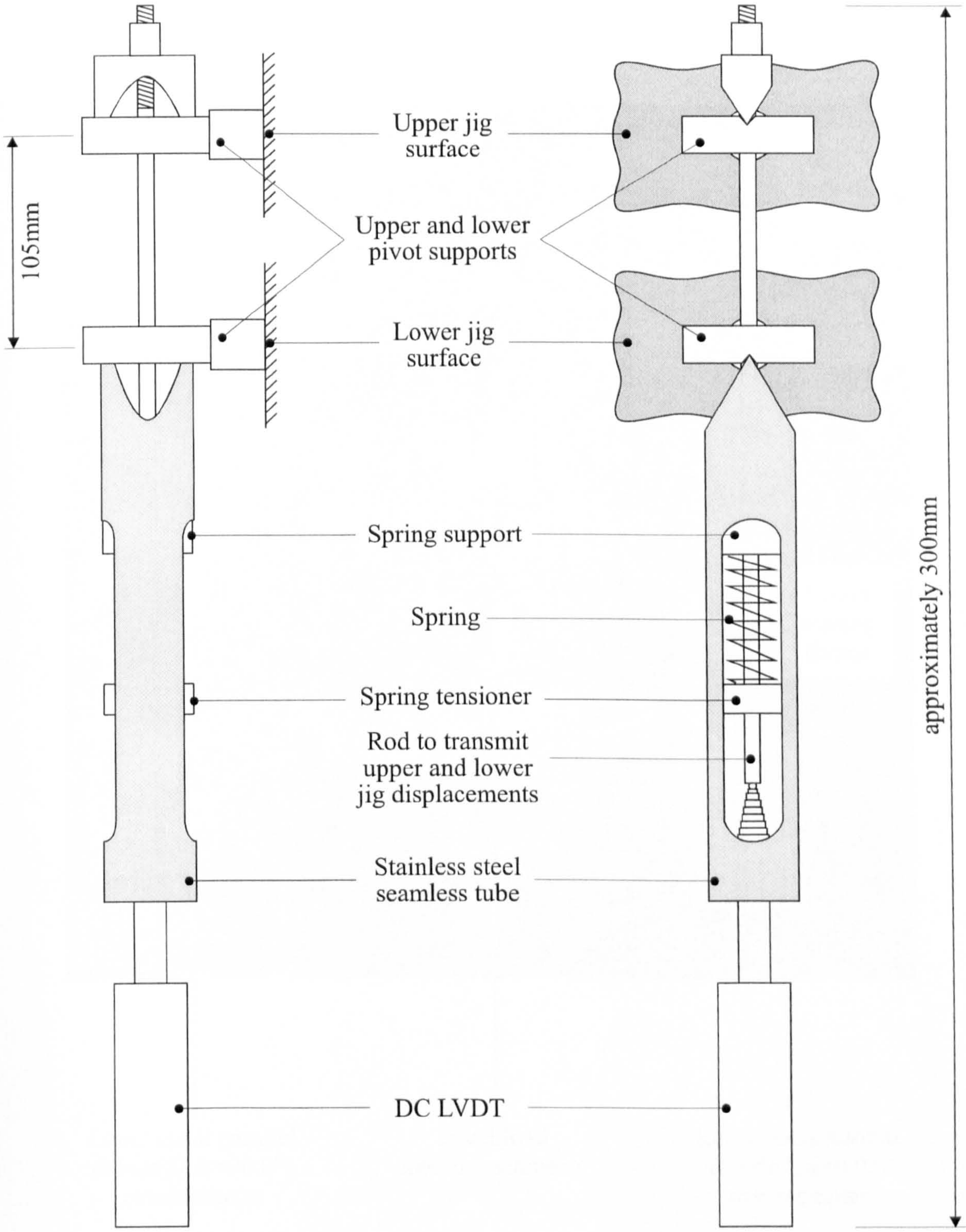

Figure 3.10a. Extensometry Assembly for A508 Experiments
(not to scale)

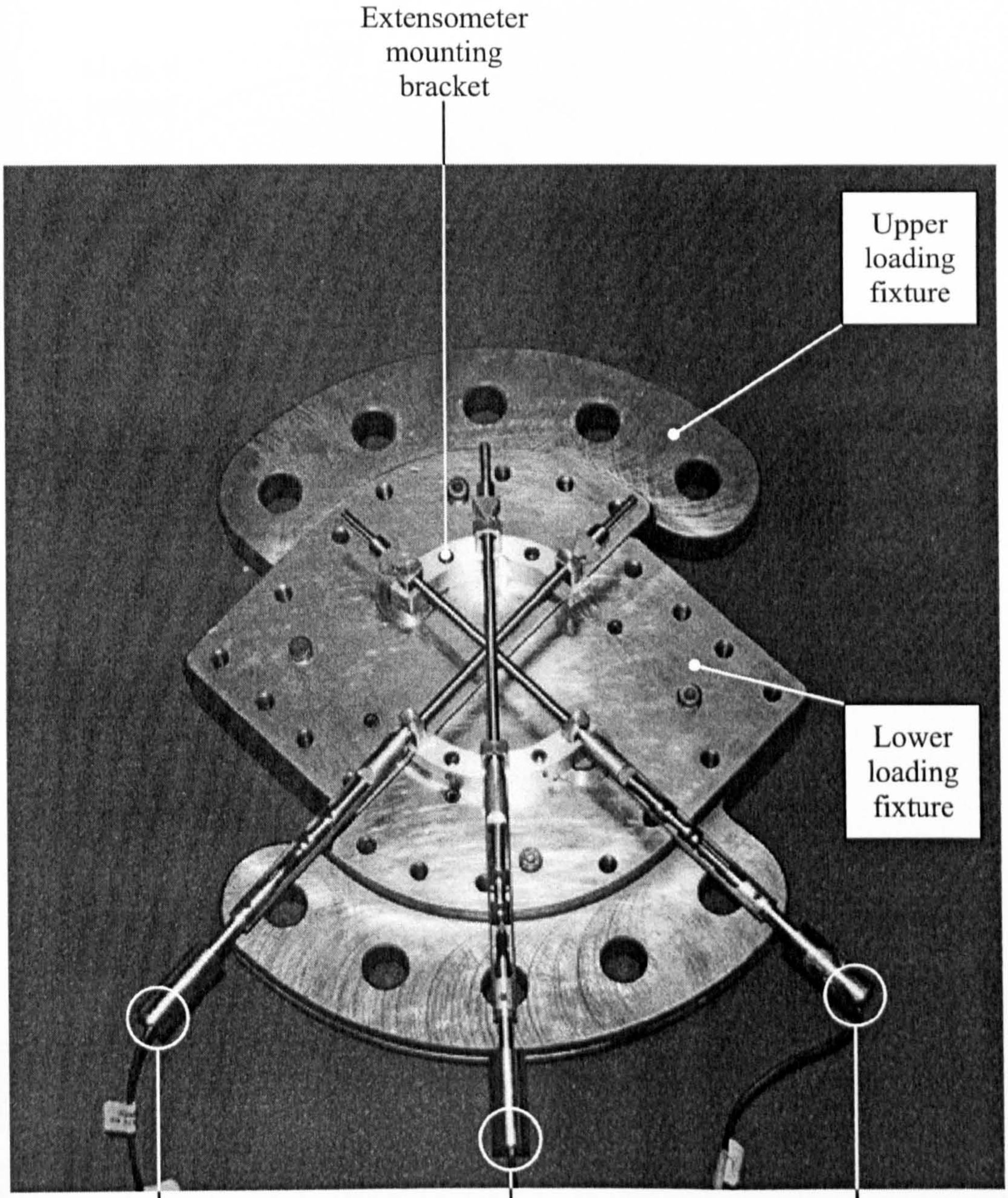

Figure 3.10b. Schematic Illustration Showing Extensometer Location on Loading Fixture (configuration for α=45.0° shown)

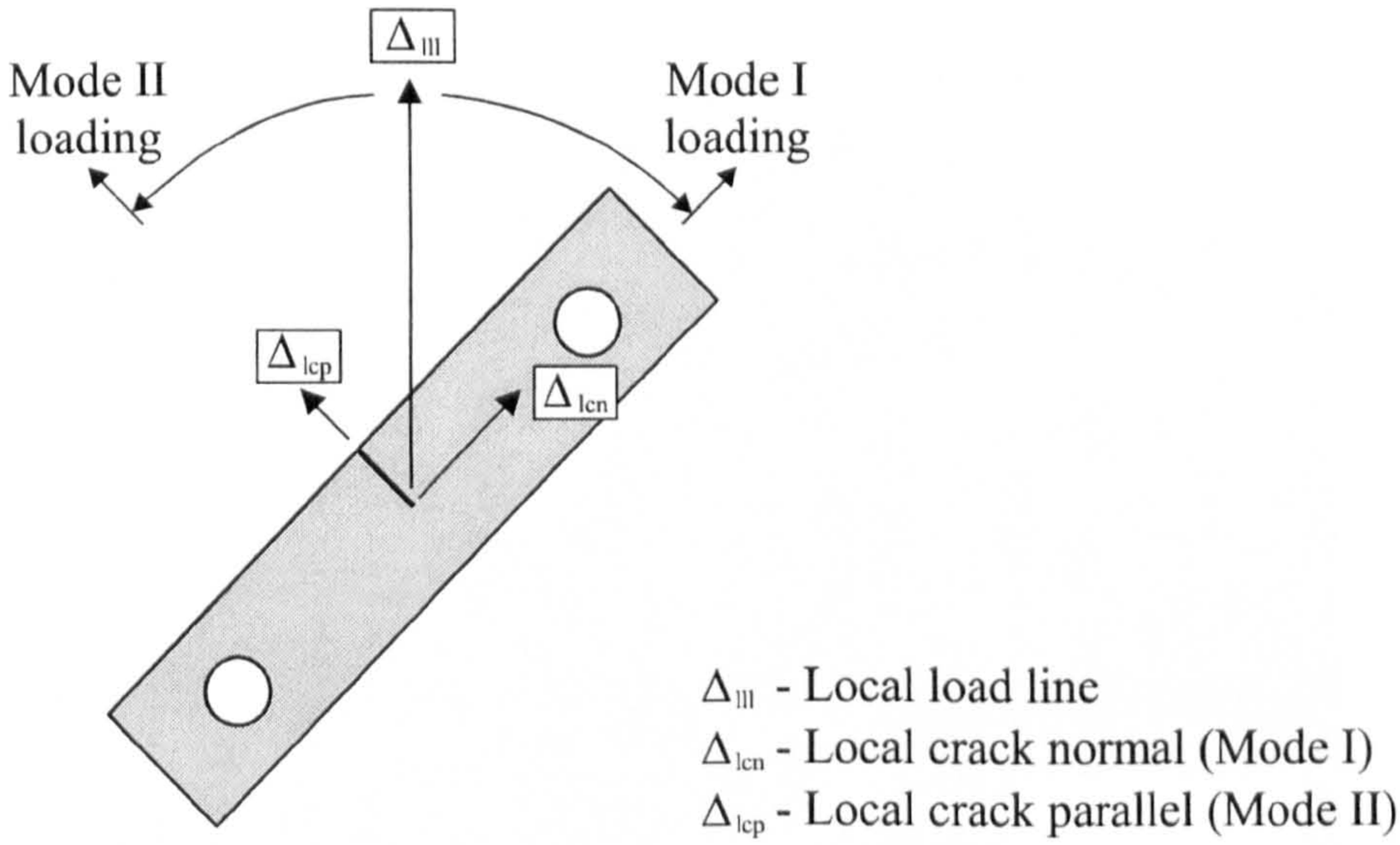

Figure 3.11. Measured Specimen Displacements

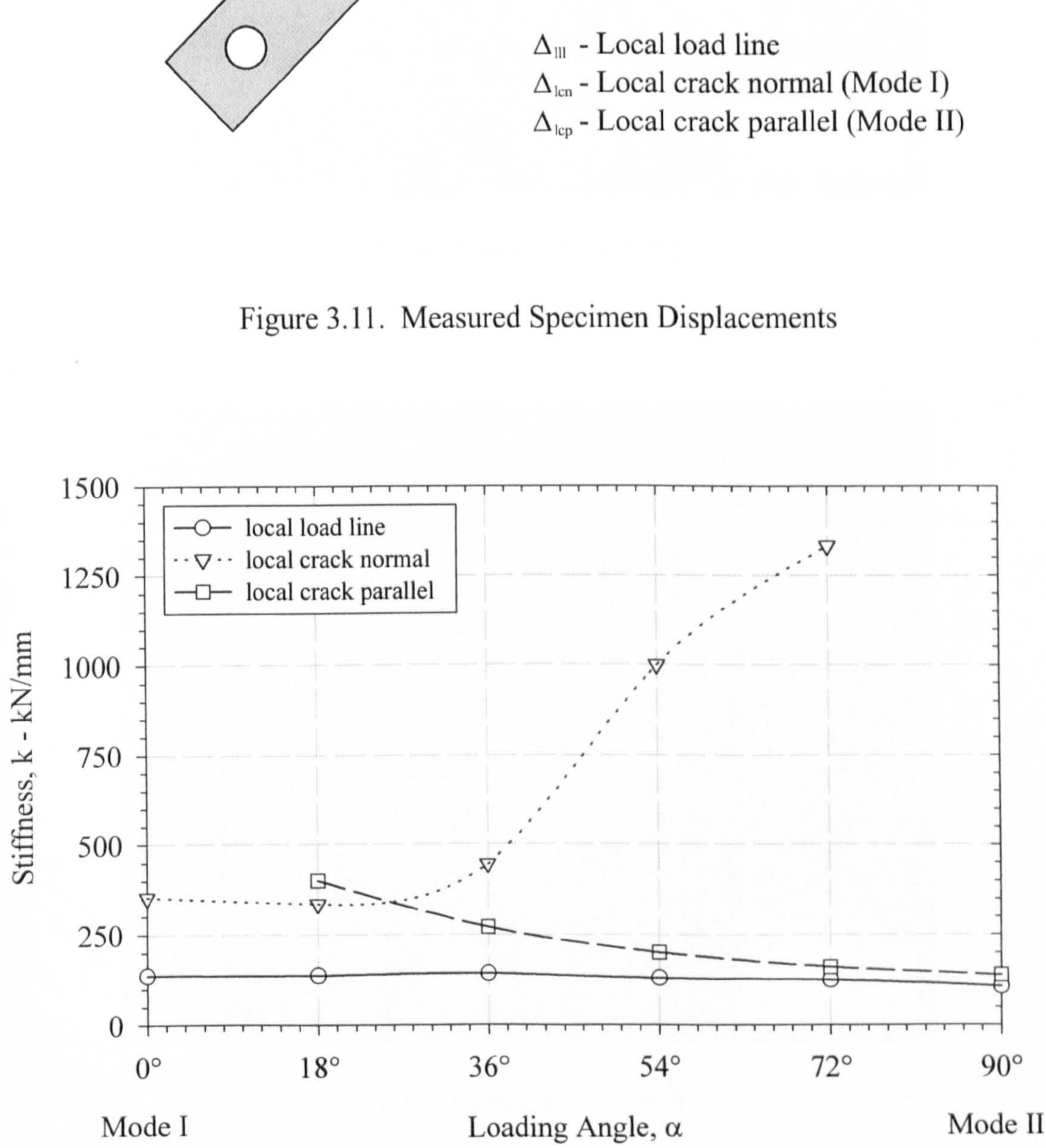

Figure 3.12. Stiffness Calibration Curves for 20% Side Grooved SEN Specimens

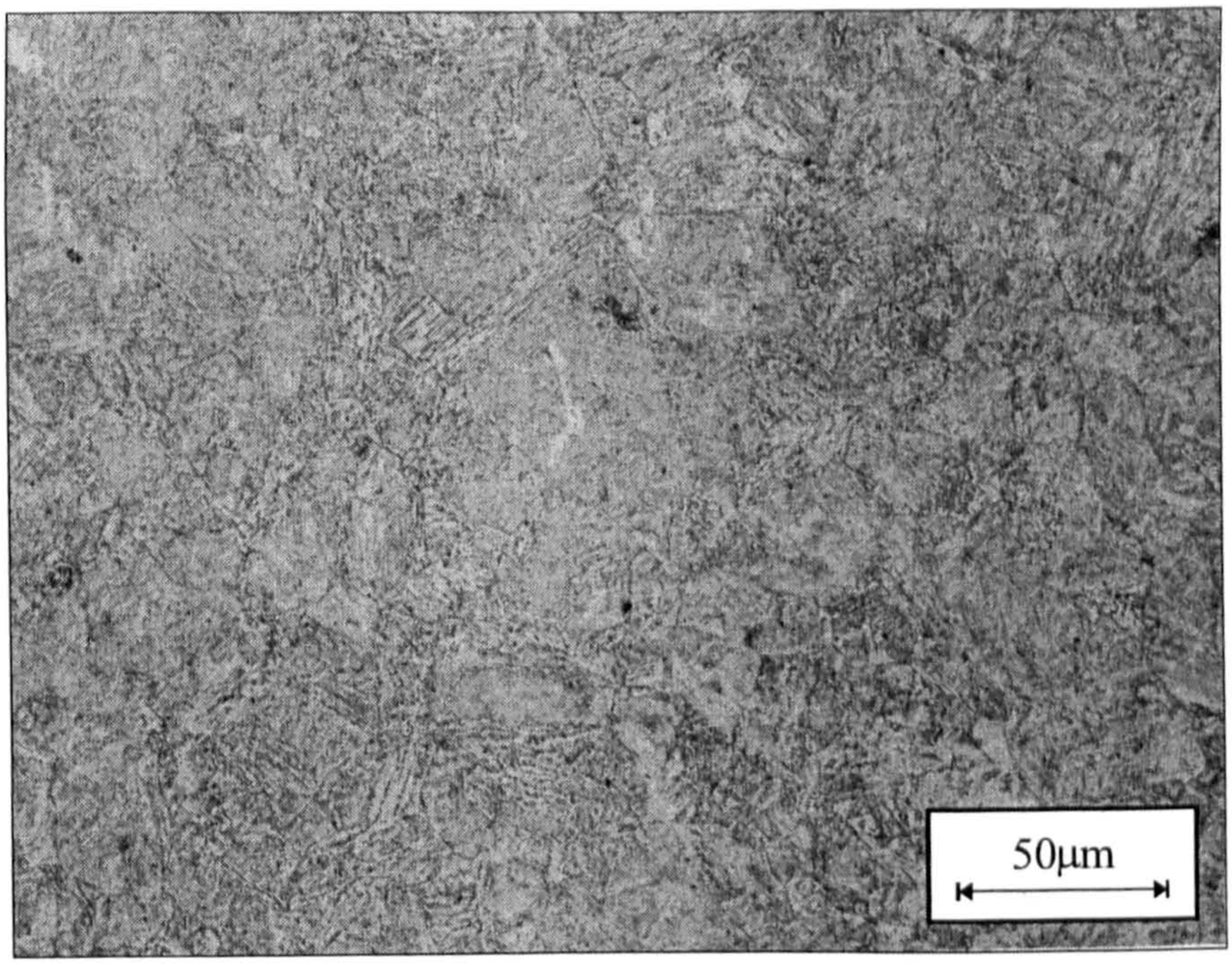

a) Microstructure of Set 2

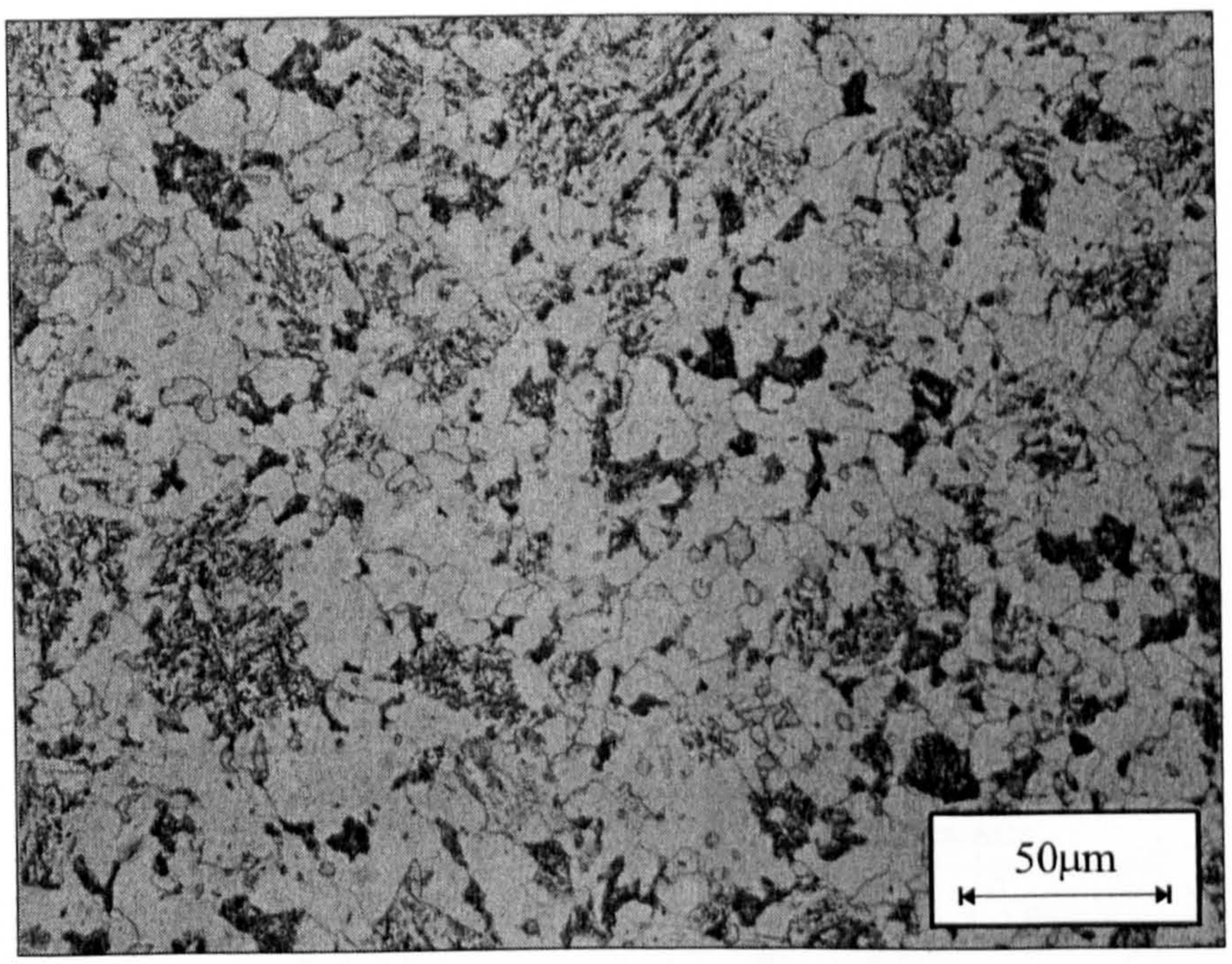

b) Microstructure of Set 3

Figure 3.13. Microstructure of Heat Treated Steel Samples used in the Small Scale Mode II Test Program

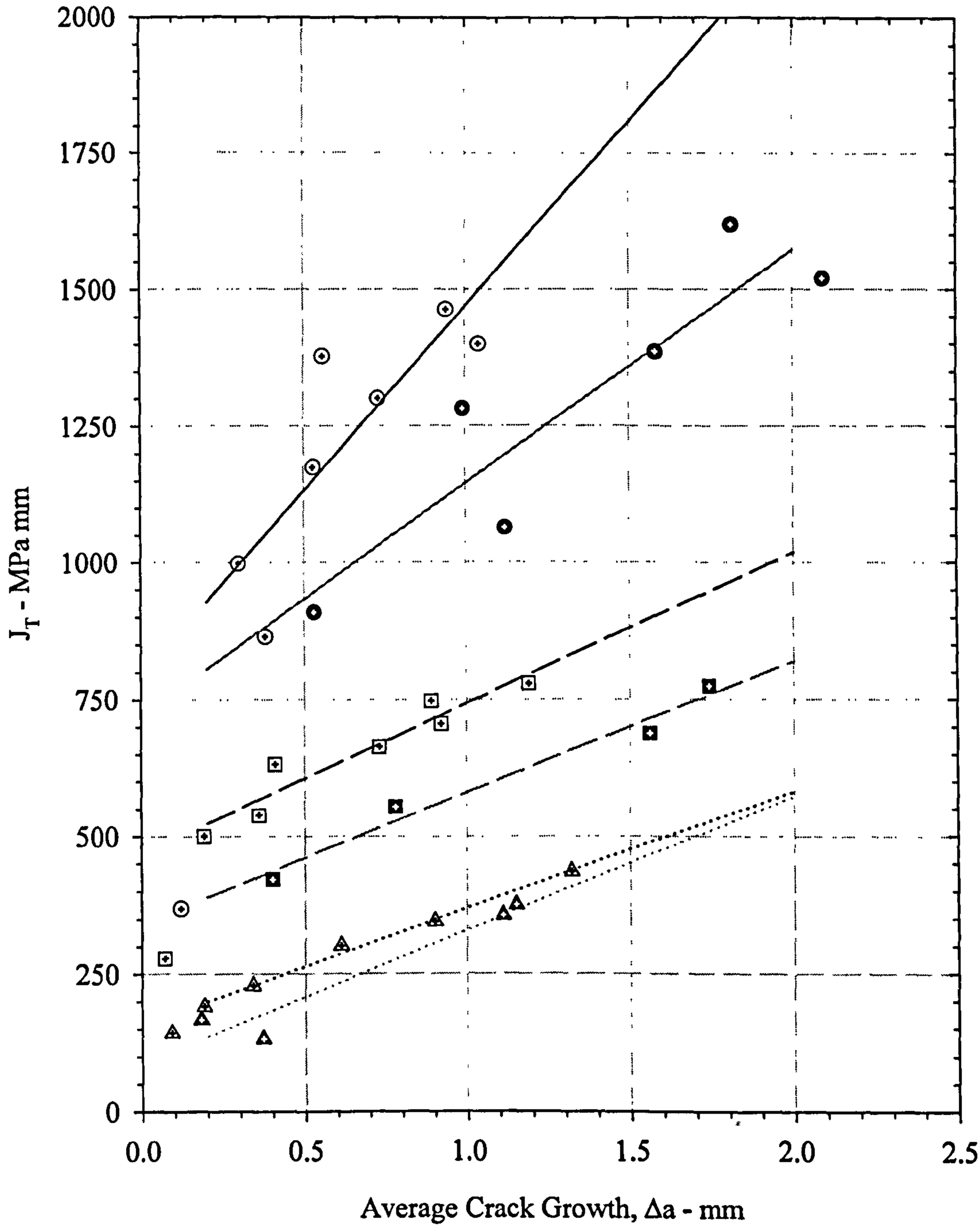

PS specimens	SG specimens
Mode I, α = 0°	*Mode I, α = 0°*
α = 54°	α = 54°
Mode II, α = 90°	Mode II, α = 90°

Figure 3.14. R-Curves: PS and 20%SG Mixed Mode I/II SEN Specimens
(Legends in italics refer to results given by Davenport, 1993)

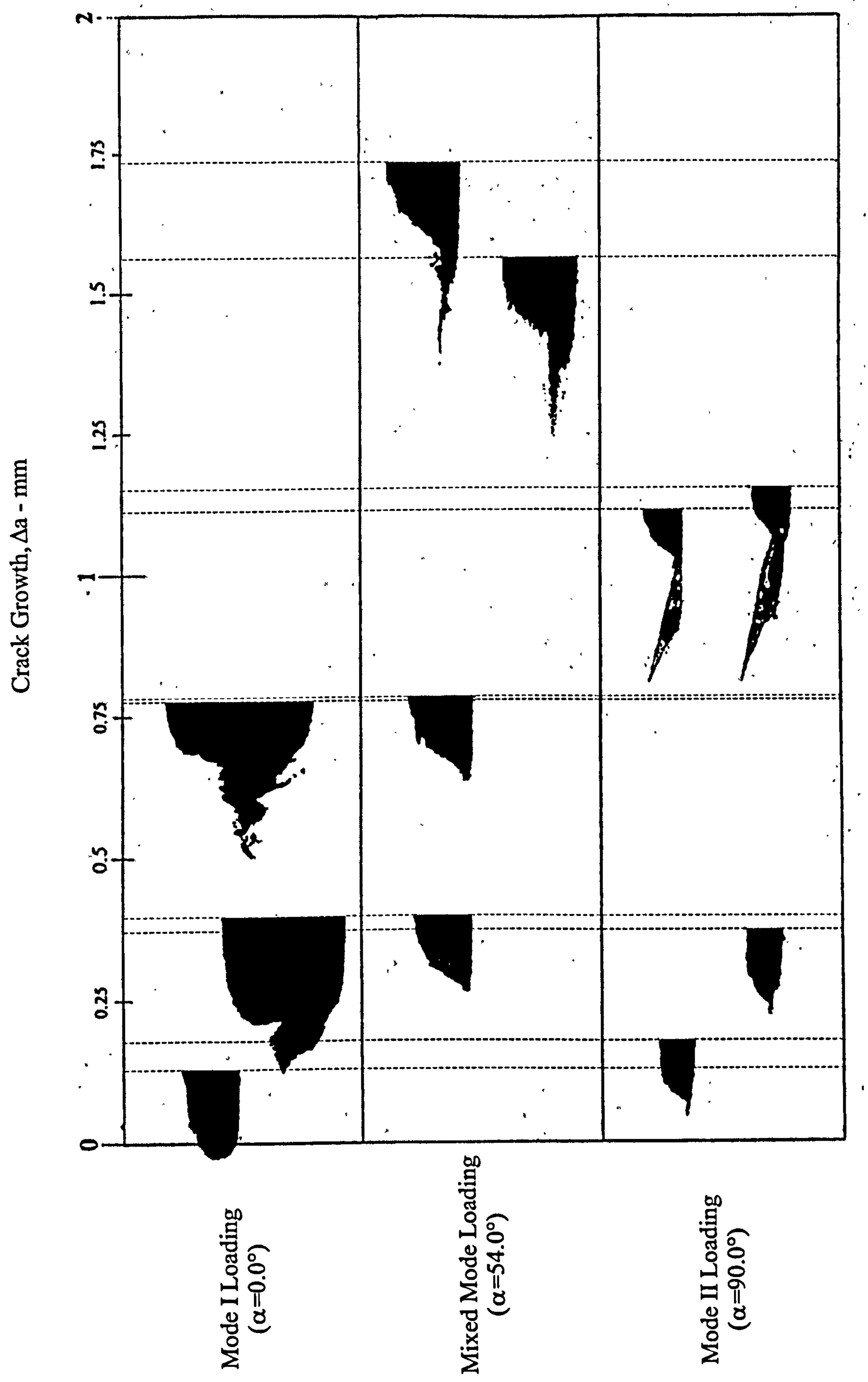

Figure 3.15. 20% Side Grooved SEN Specimens - Crack Profiles

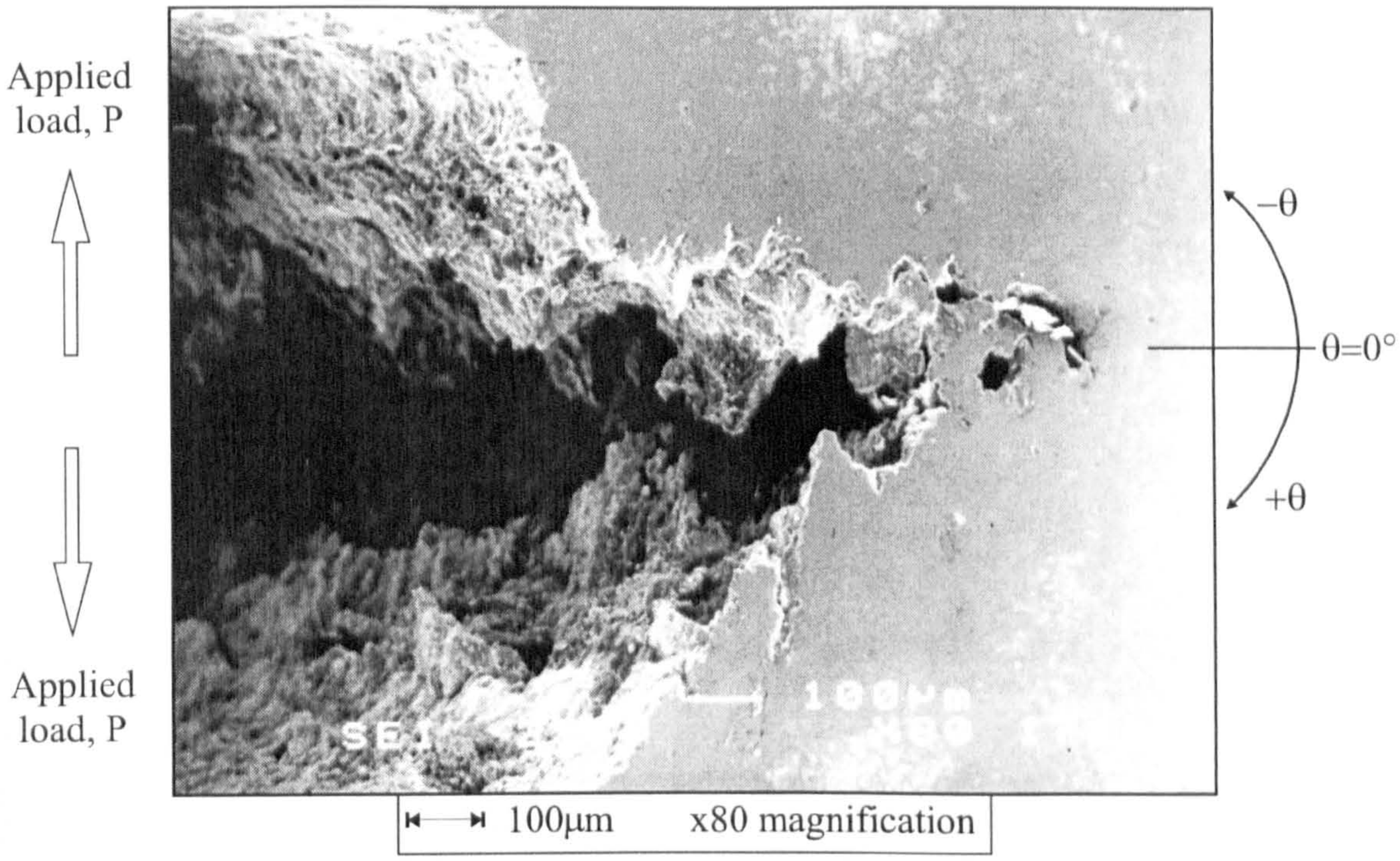

Figure 3.16. 20% SG SEN Specimen Loaded in Mode I

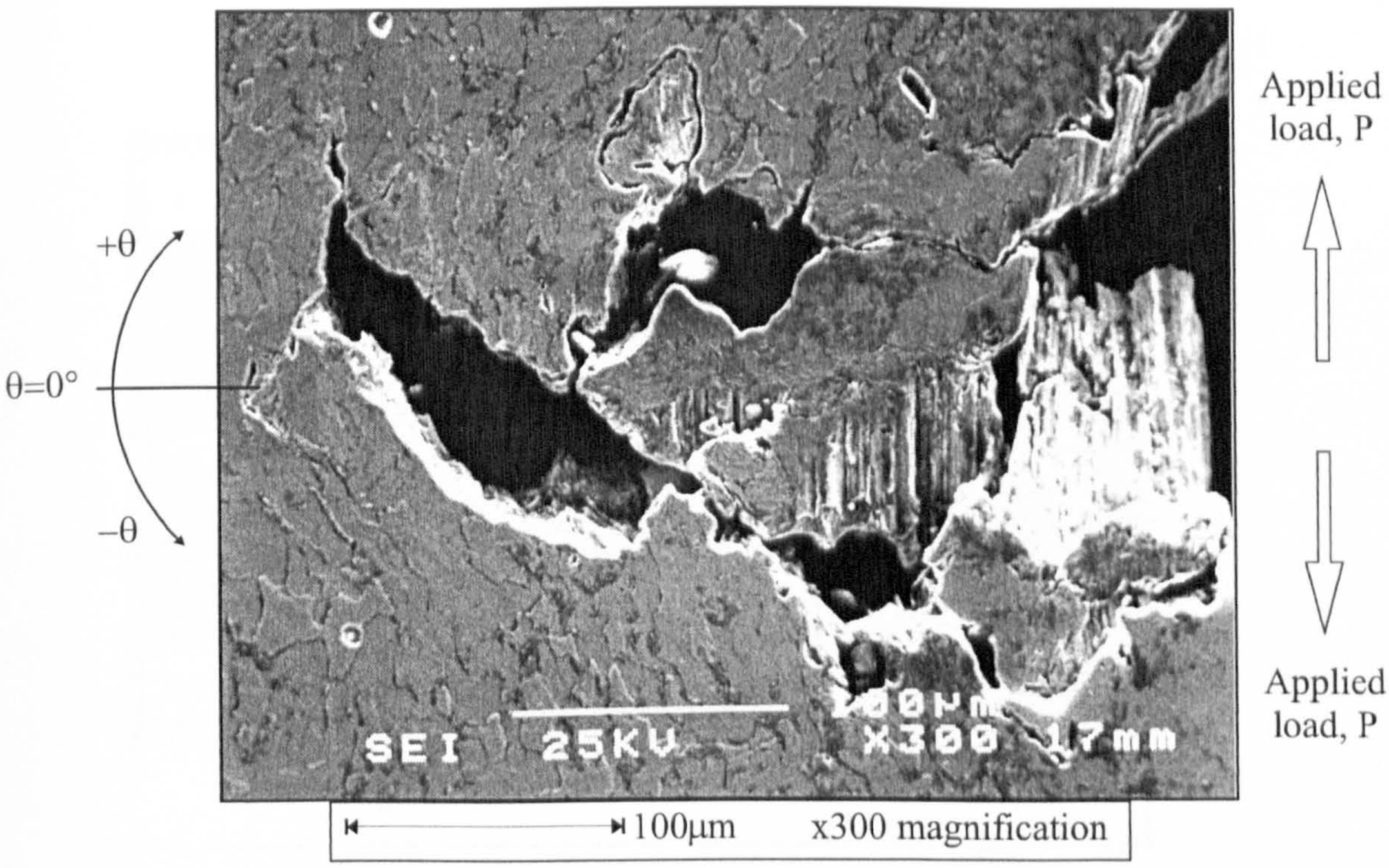

Figure 3.17. Grain Boundary Separation and Microcracking
in an SEN Specimen Loaded in Mode I

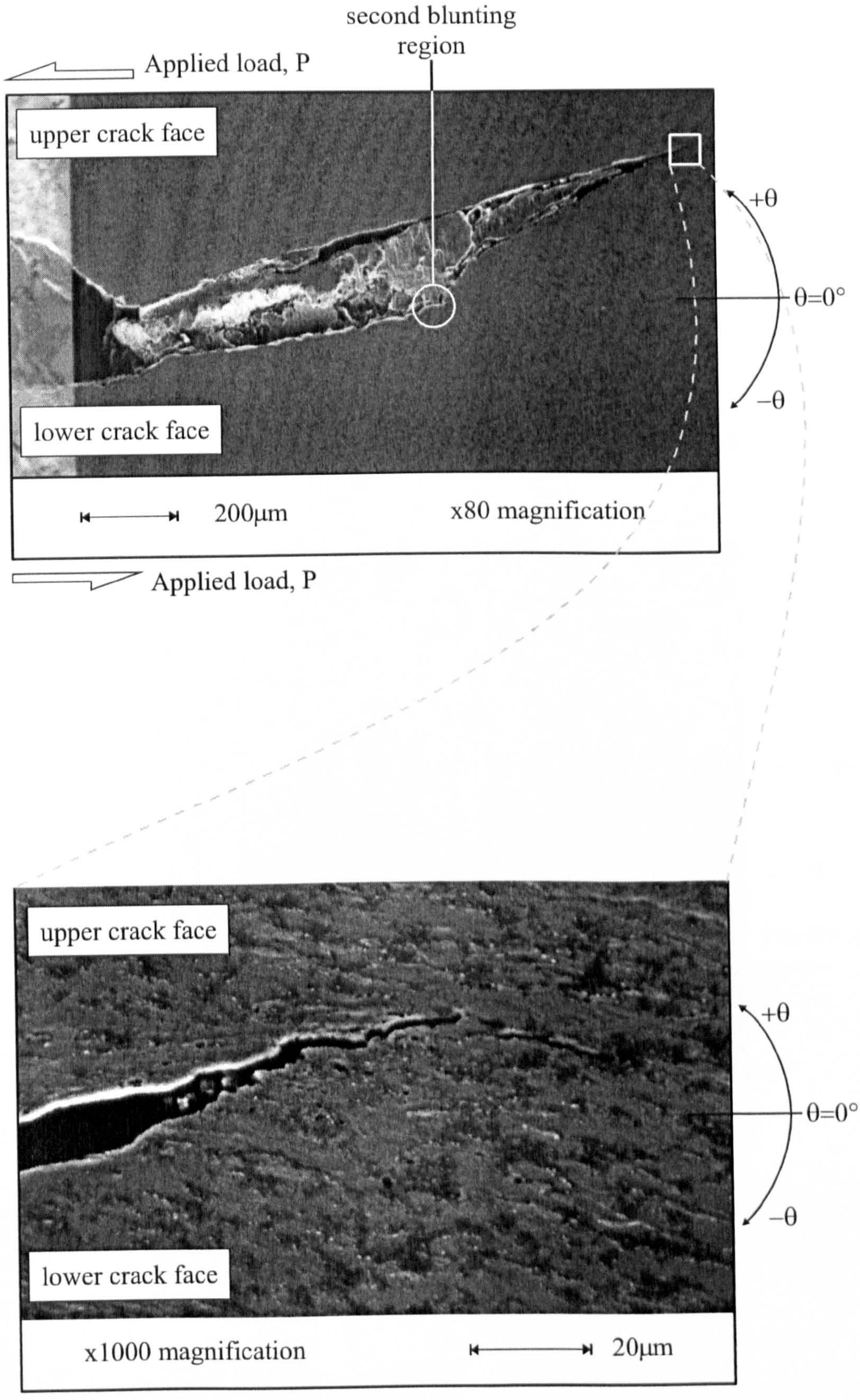

Figure 3.18. 20% SG SEN Specimen Loaded in Mode II

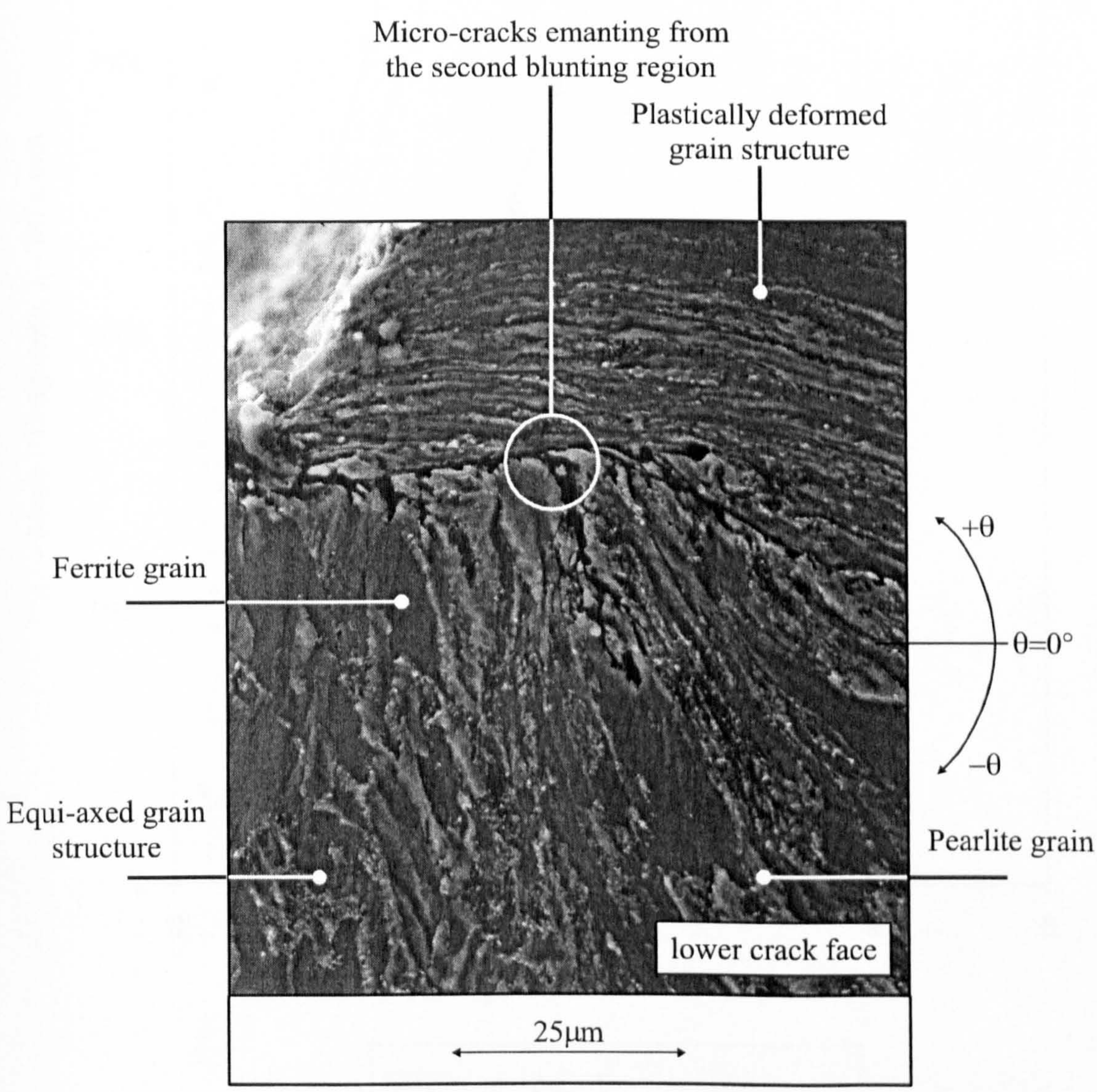

Figure 3.19. Mode II Loading : Detail of the Second Blunting Region

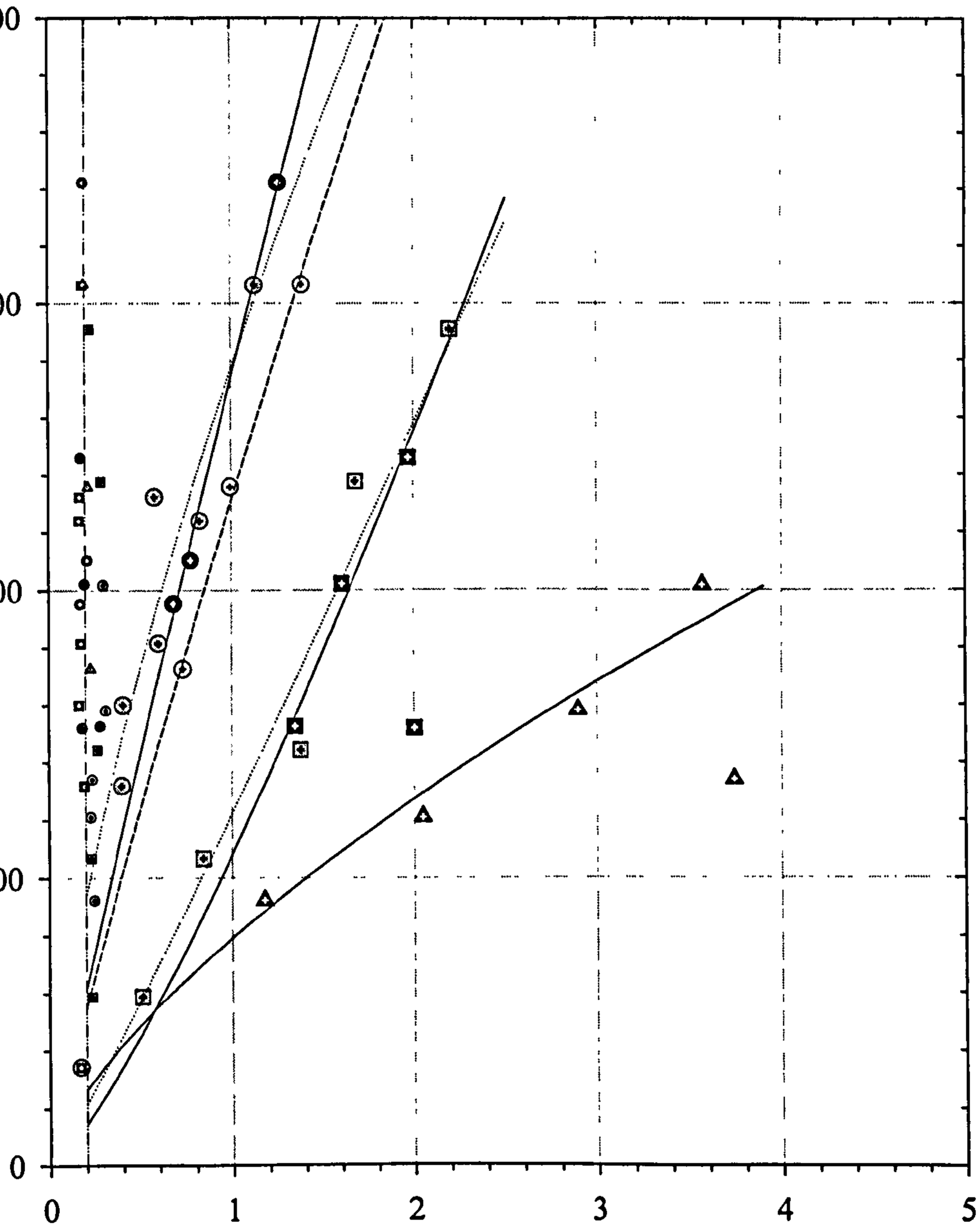

Figure 3.20. Mode I R-Curves : Size Effects, $a_o/W=0.5$

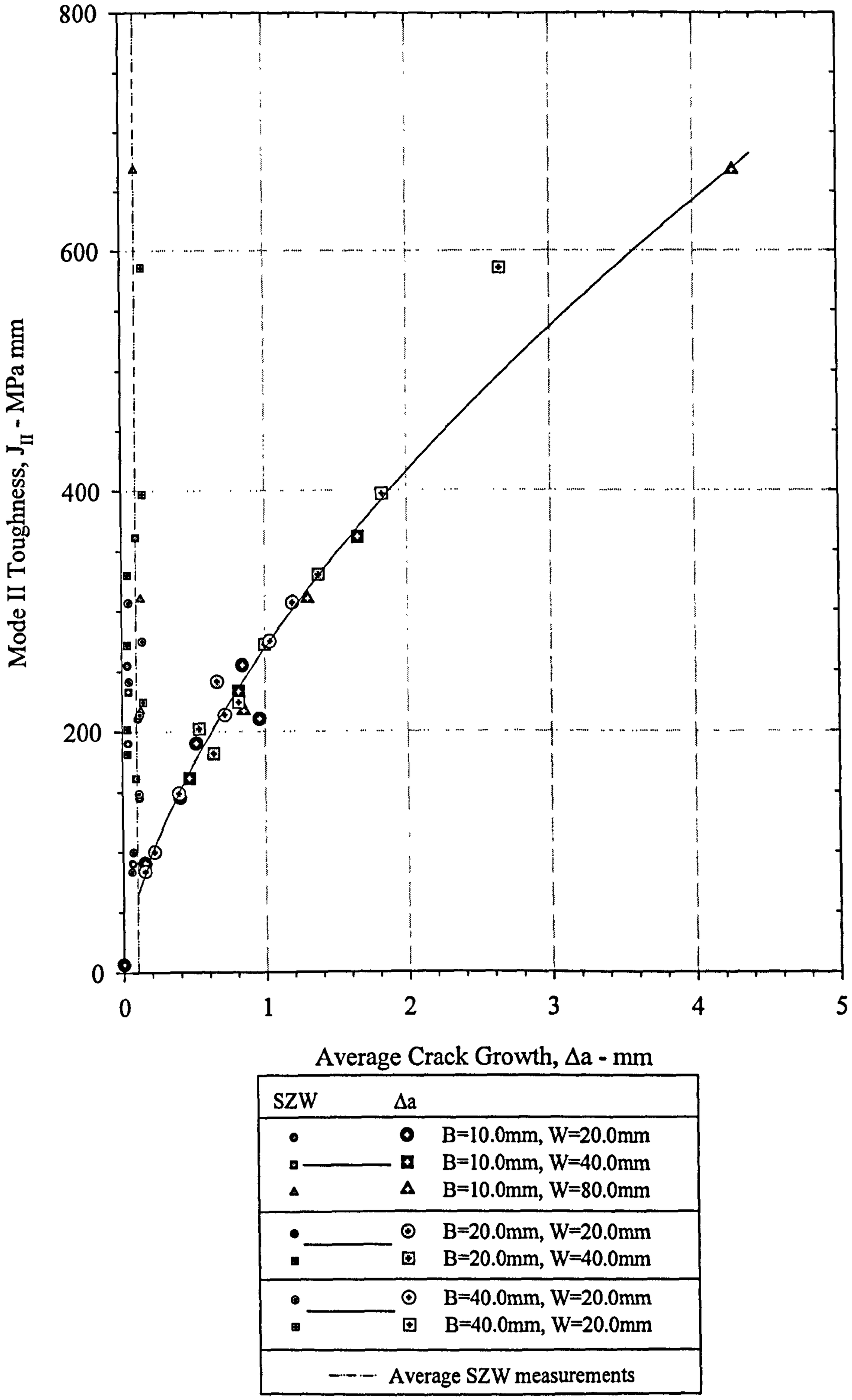

Figure 3.21. Mode II R-Curves : Size Effects, $a_o/W=0.5$

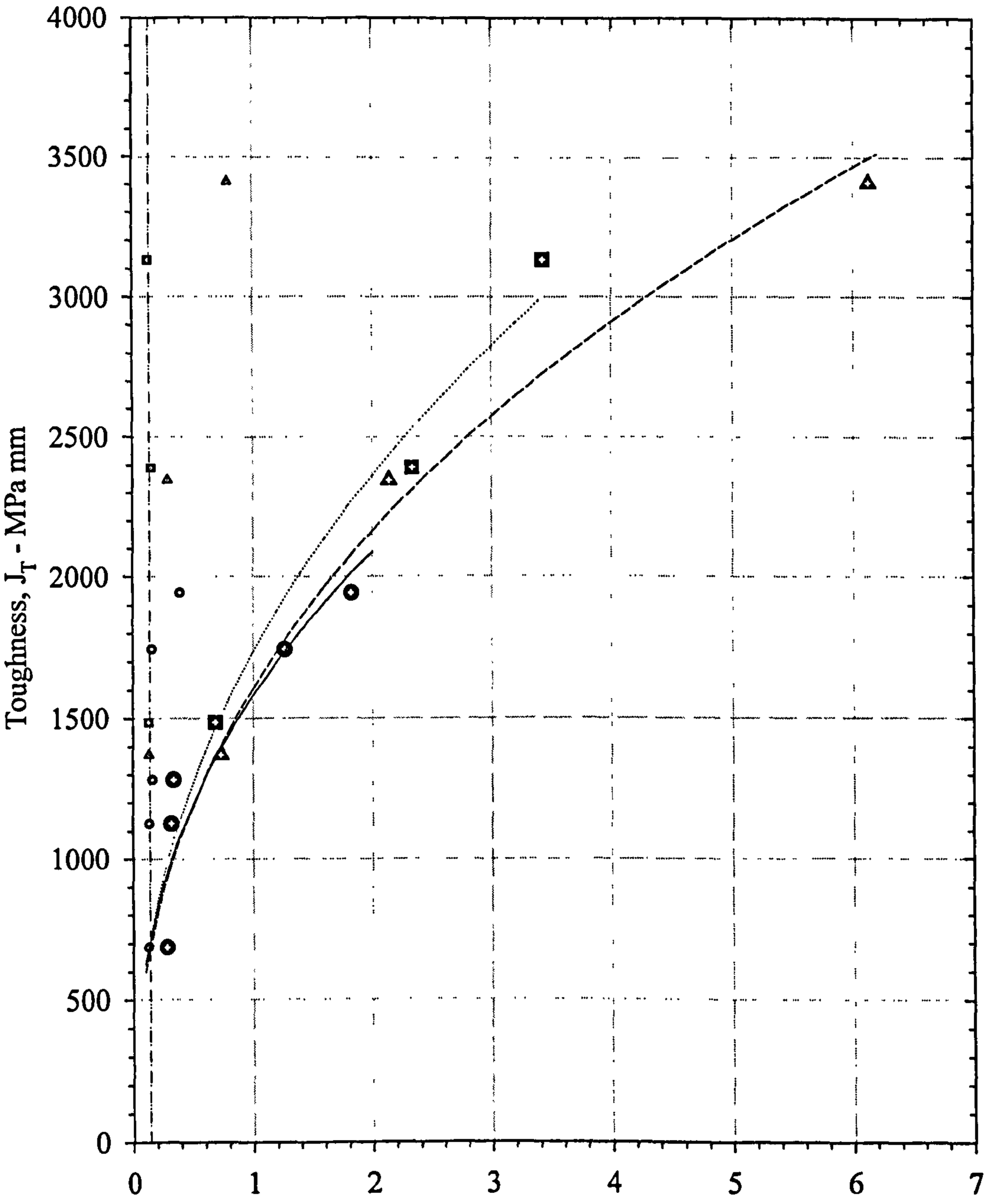

SZW		Δa	
○	———	●	B=10.0mm, W=20.0mm
□	.....	■	B=10.0mm, W=40.0mm
△	- - - - -	▲	B=10.0mm, W=80.0mm
—·—·— Average SZW measurements			

Figure 3.22. Mixed Mode I/II (α = 22.5°) R-Curves : Size Effects, a_o/W=0.5

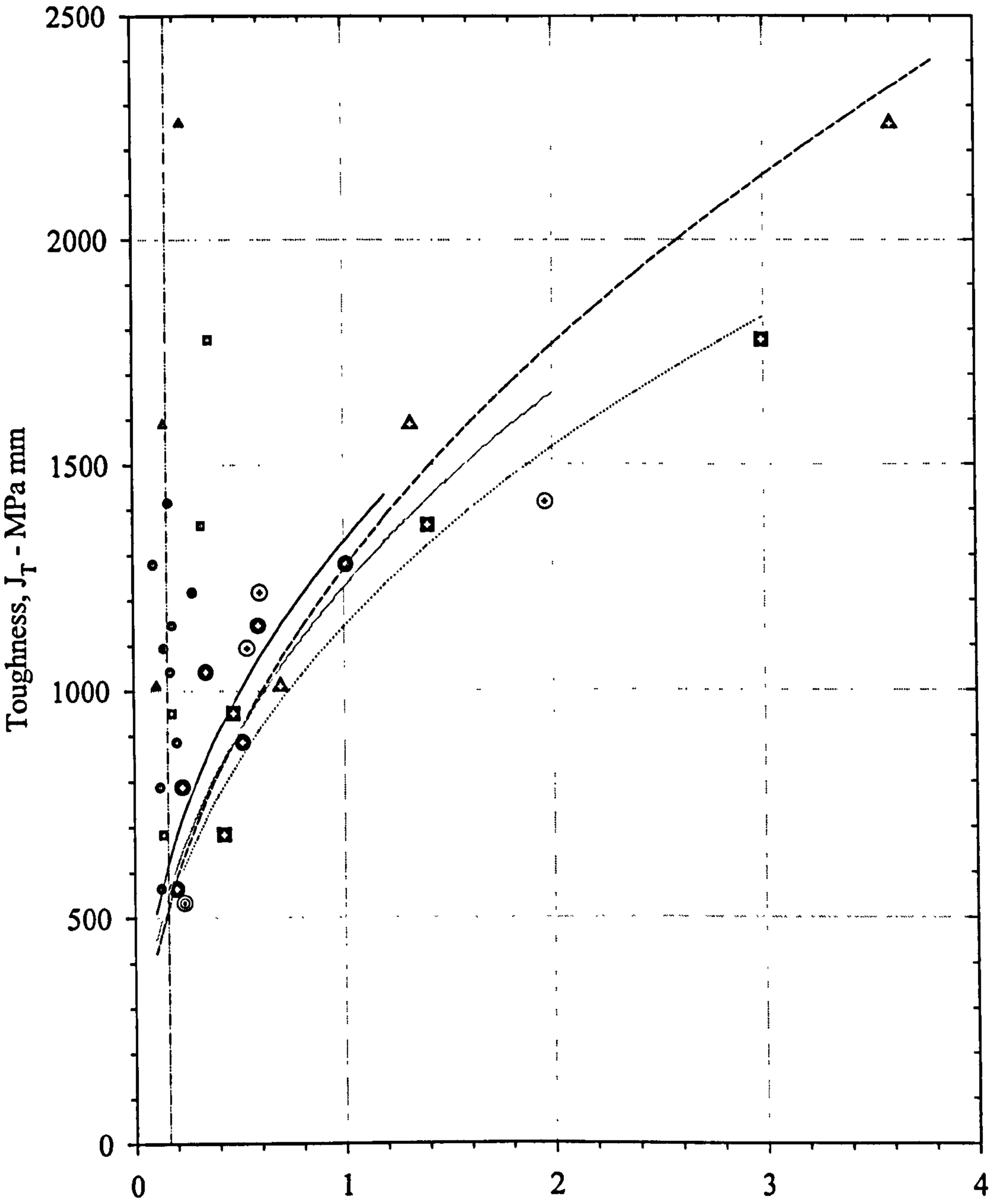

Figure 3.23. Mixed Mode I/II (α=45°) R-Curves : Size Effects, a_o/W=0.5

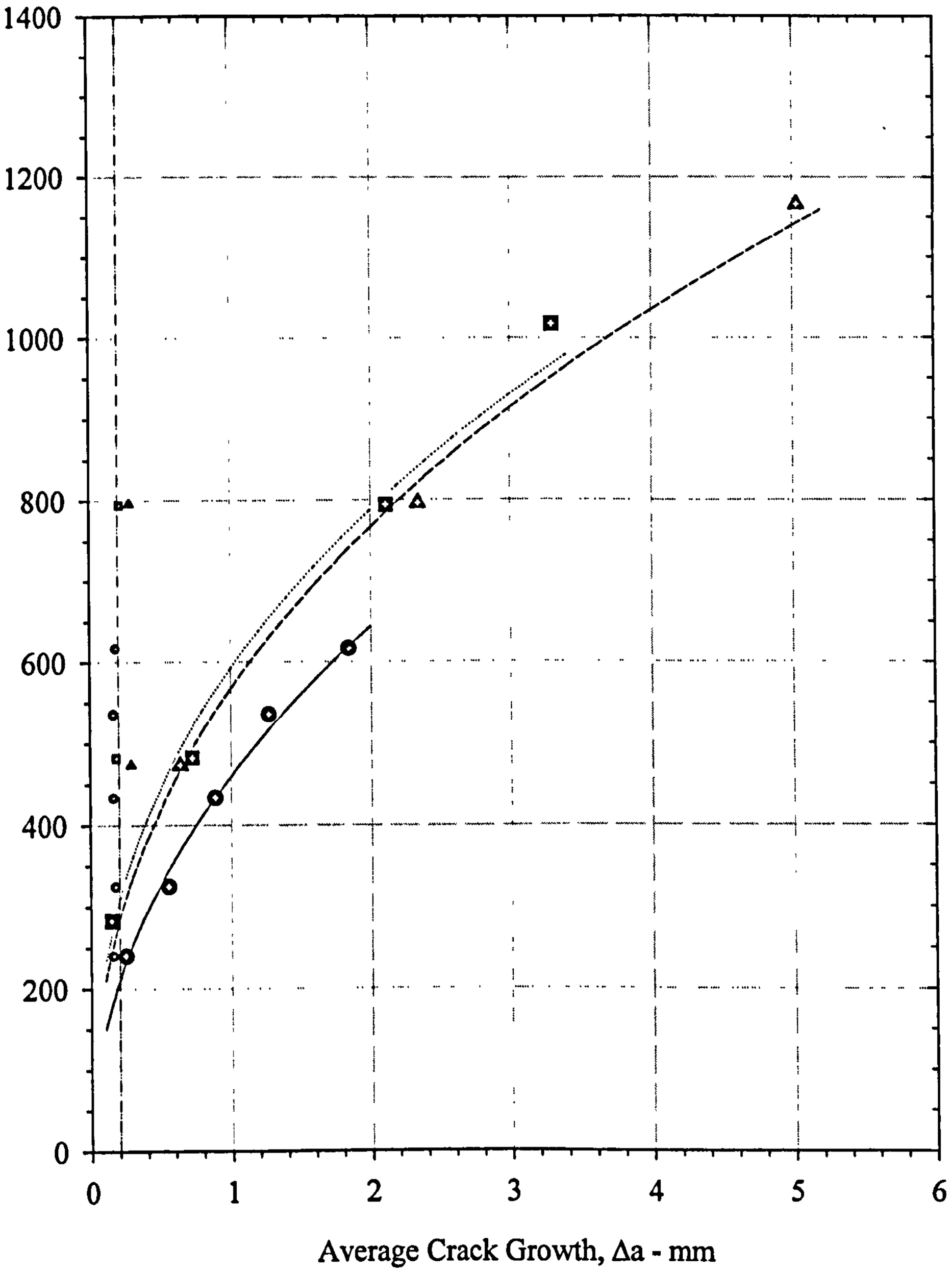

Figure 3.24. Mixed Mode I/II ($\alpha = 67.5°$) R-Curves : Size Effects, $a_o/W=0.5$

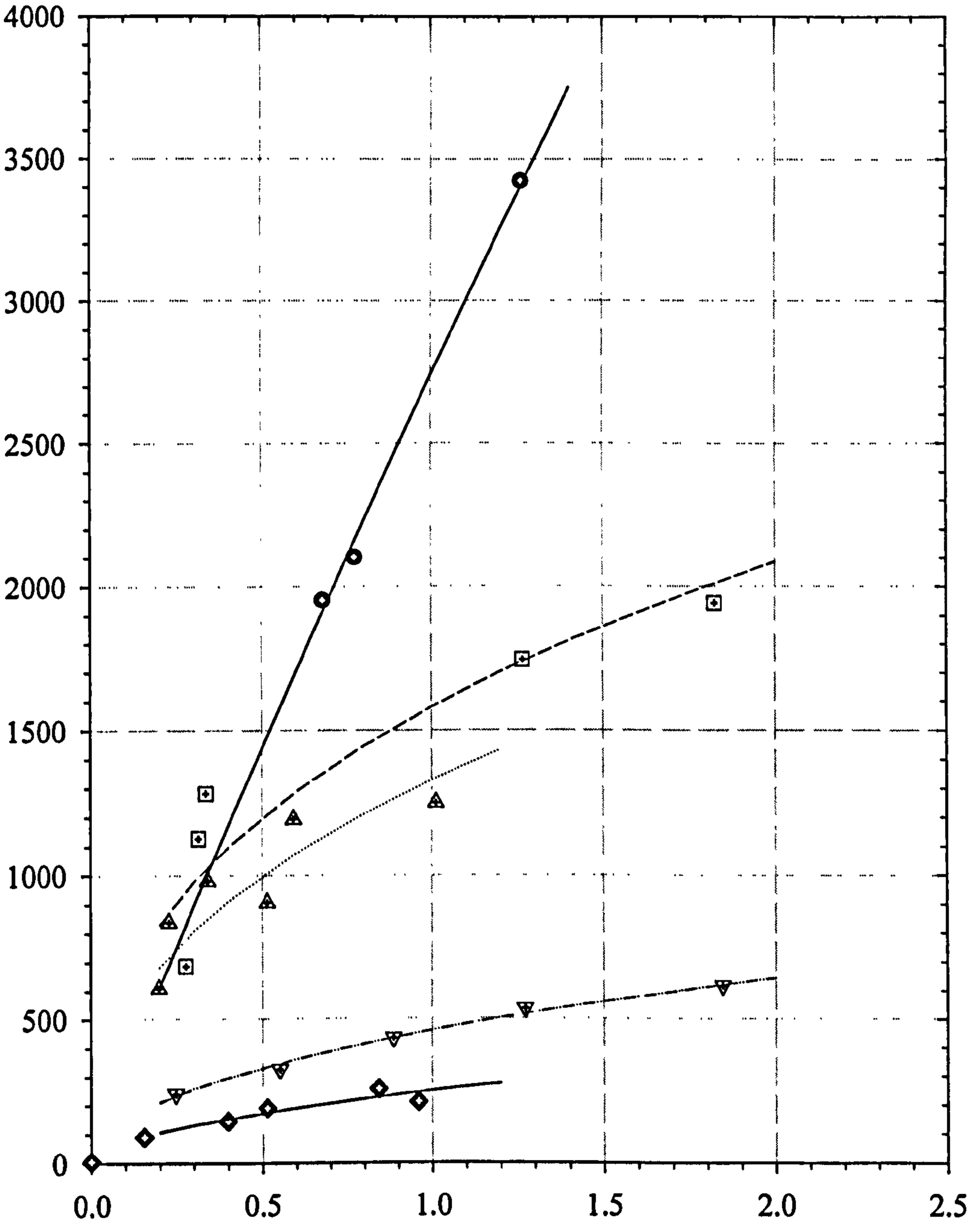

Figure 3.25. Mixed Mode I/II R-Curves : B=10.0mm, W=20.0mm, a_o/W=0.5

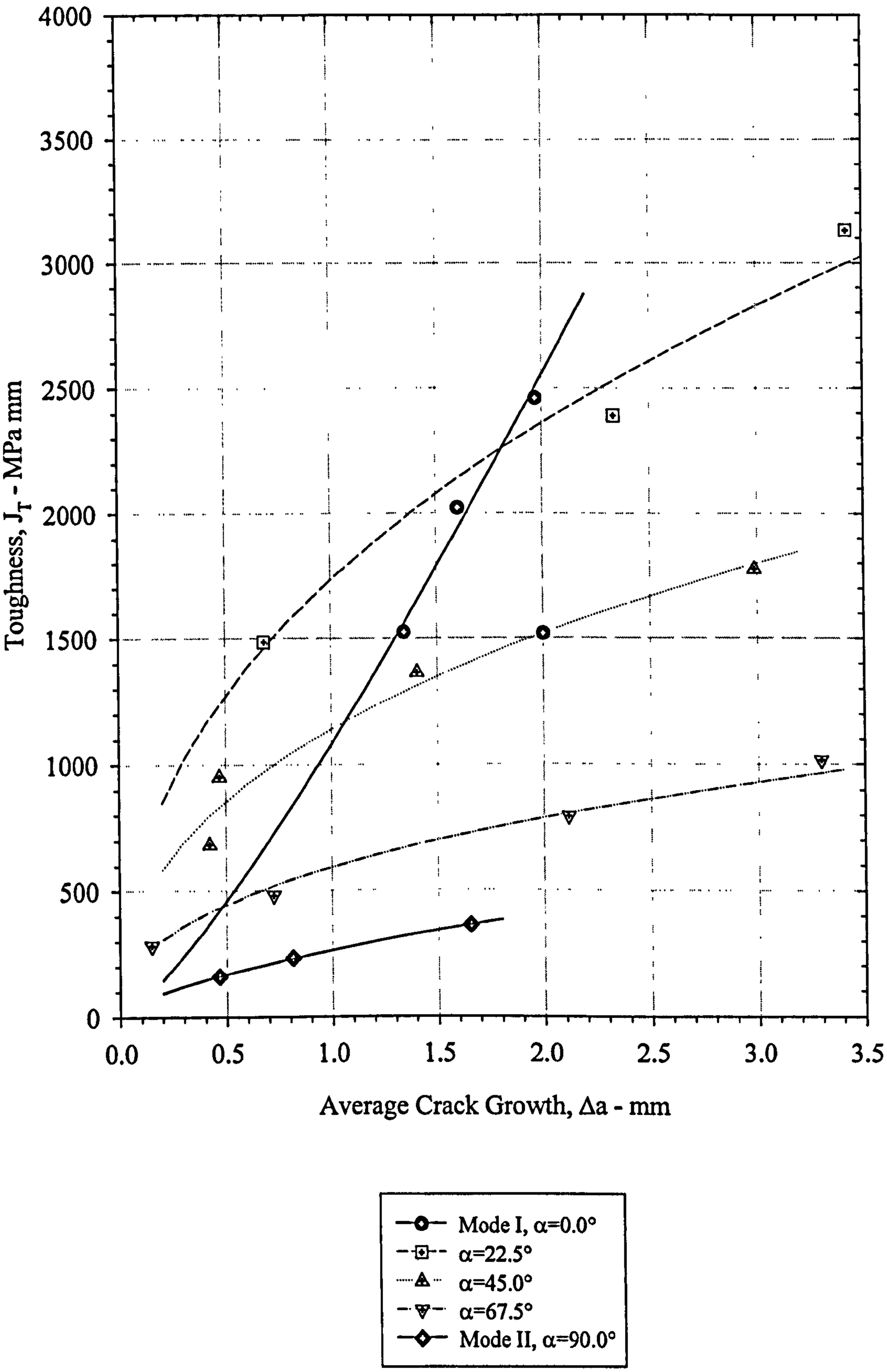

Figure 3.26. Mixed Mode I/II R-Curves : B=10.0mm, W=40.0mm, a_0/W=0.5

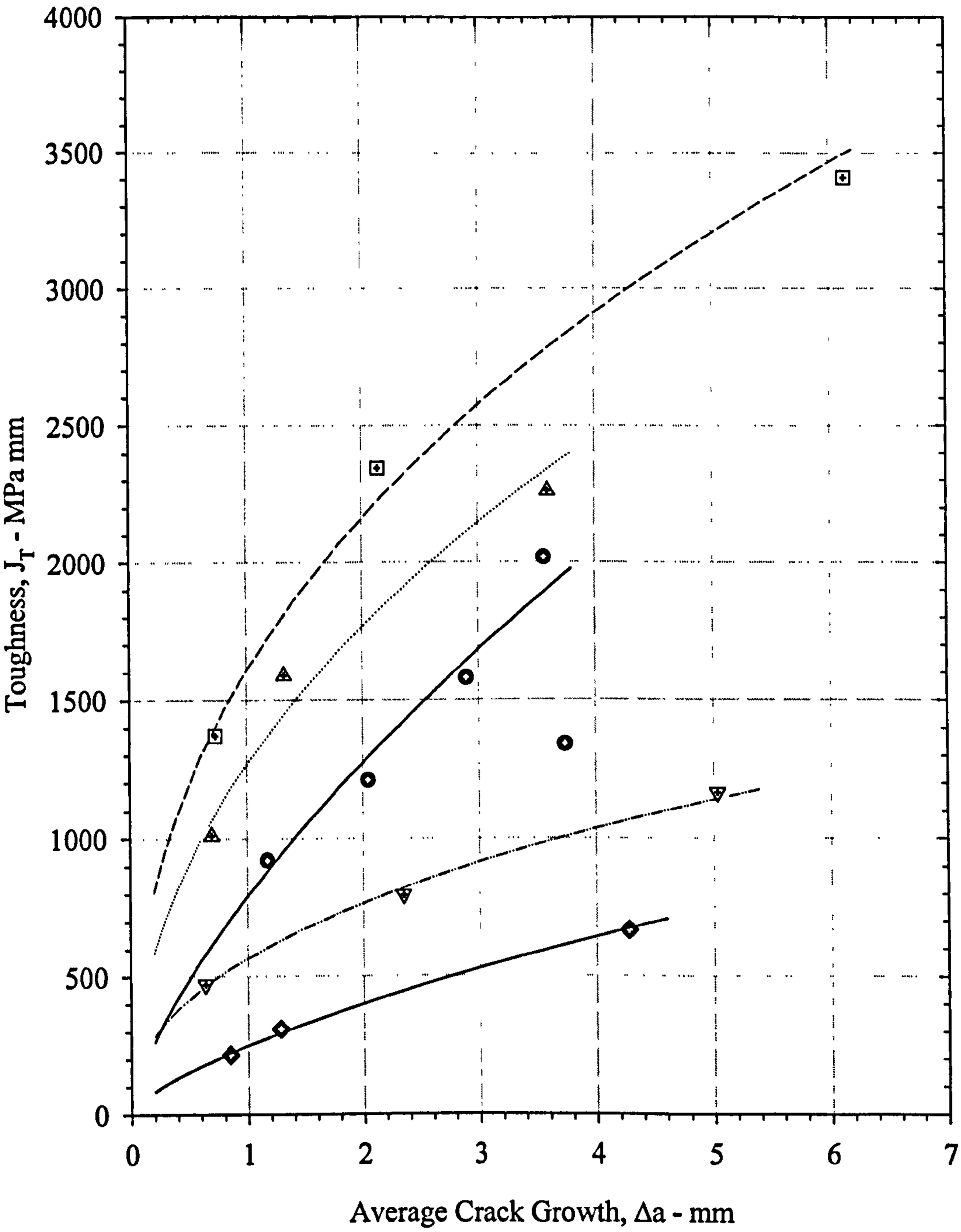

Figure 3.27. Mixed Mode I/II R-Curves : B=10.0mm, W=80.0mm, a_0/W=0.5

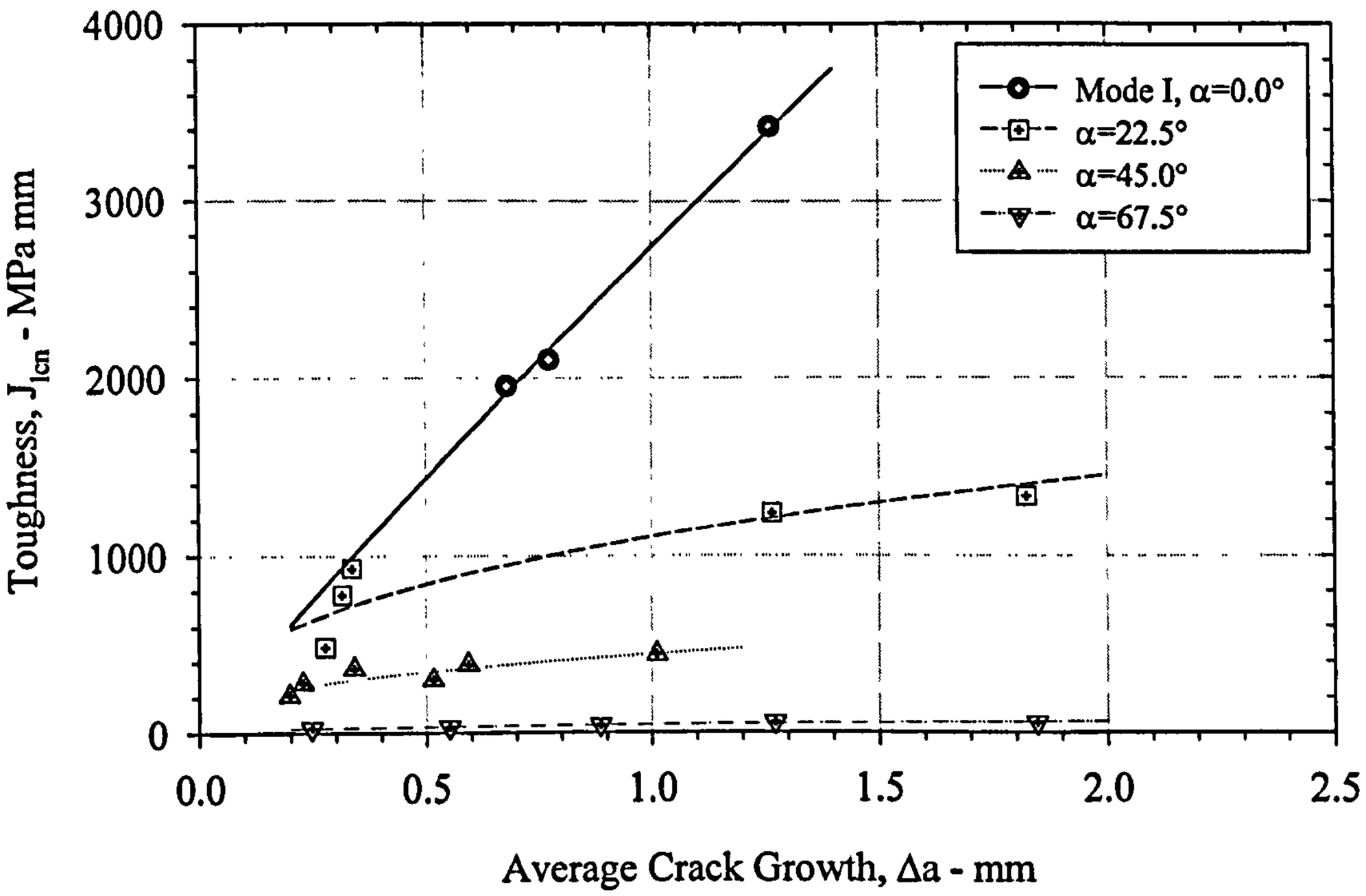

Figure 3.28a. Local Mode I, Mixed Mode I/II R-Curves
B=10.0mm, W=20.0mm, a_o/W=0.5

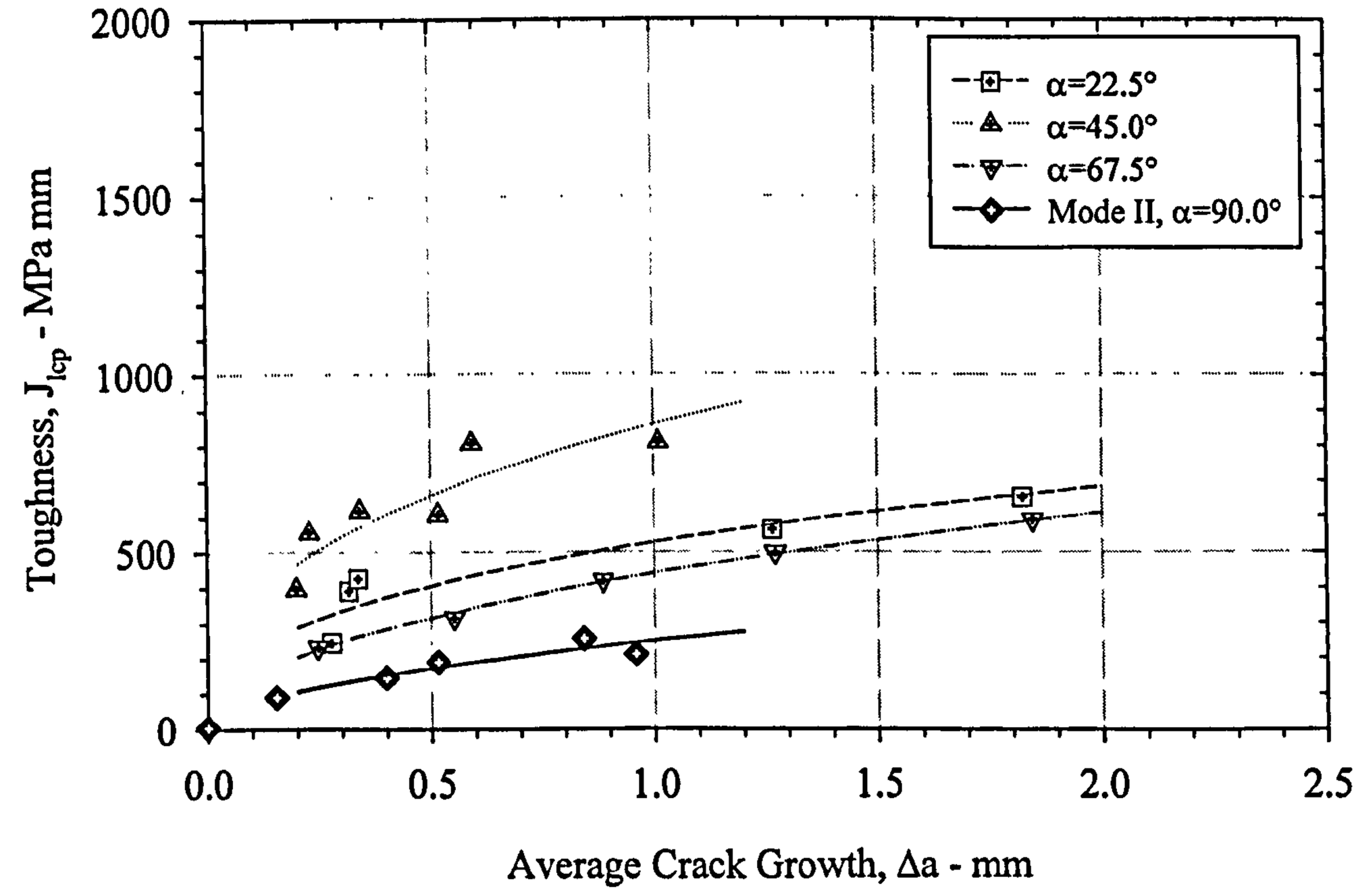

Figure 3.28b. Local Mode II, Mixed Mode I/II R-Curves
B=10.0mm, W=20.0mm, a_o/W=0.5

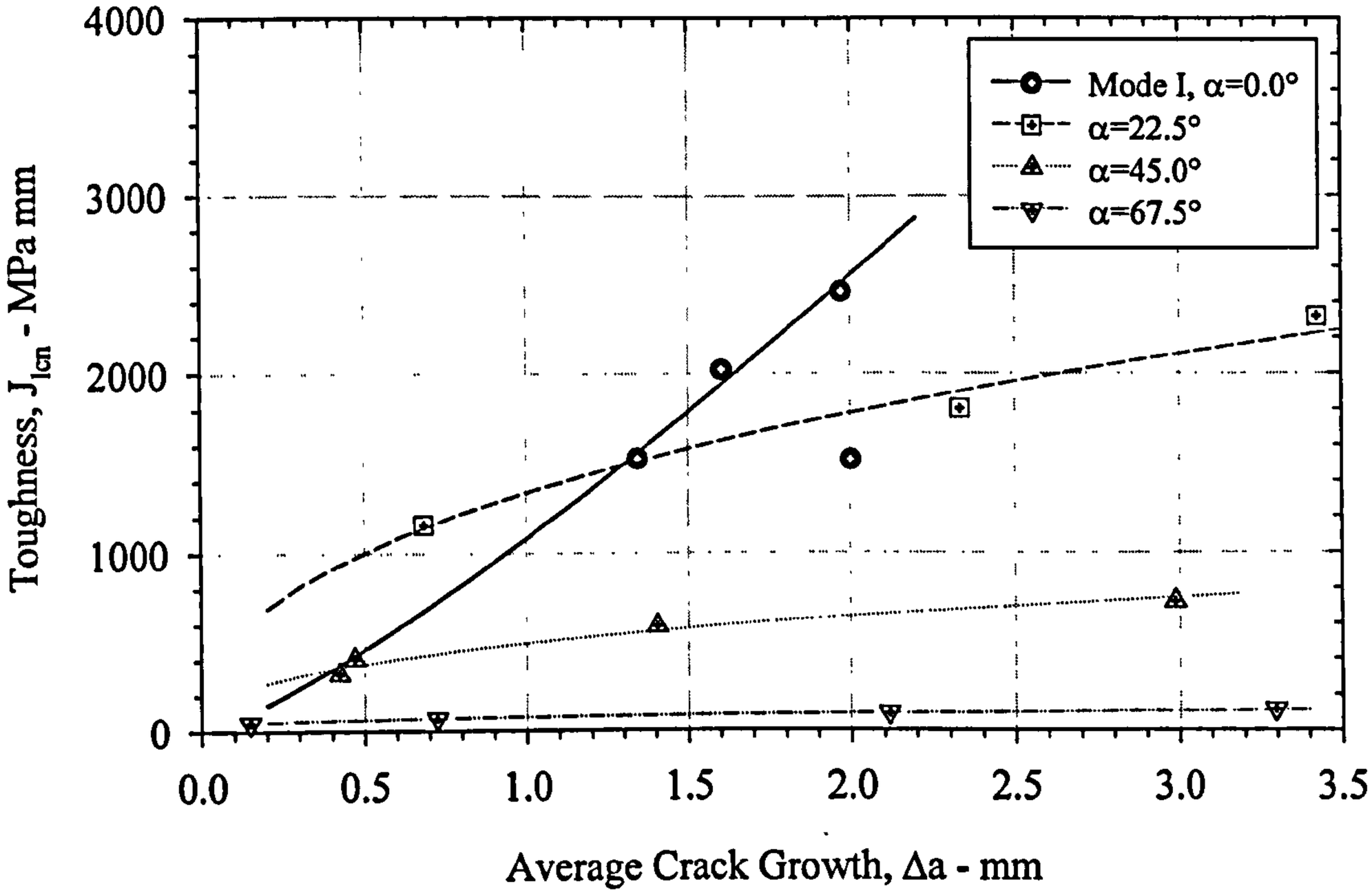

Figure 3.29a. Local Mode I, Mixed Mode I/II R-Curves
B=10.0mm, W=40.0mm, a_o/W=0.5

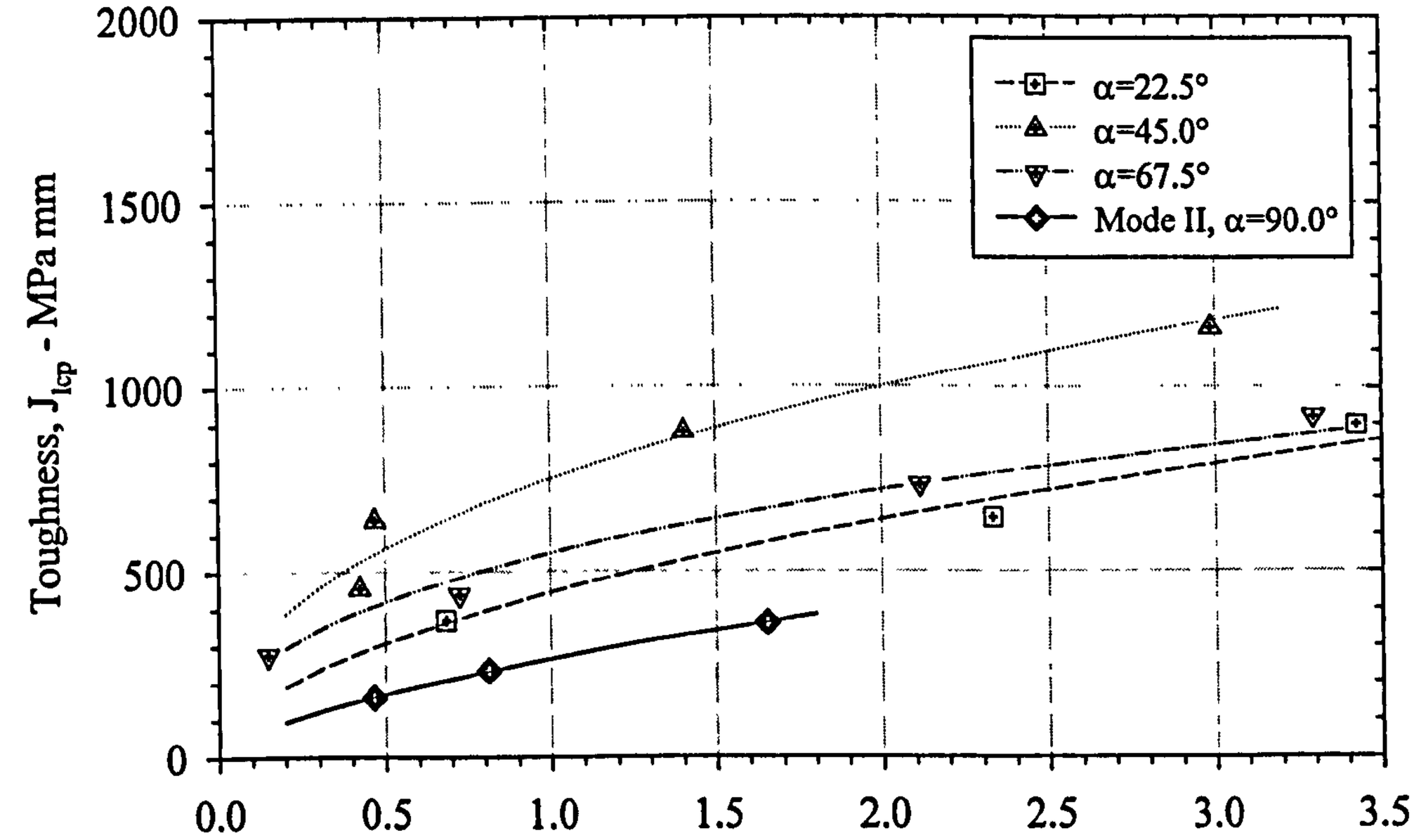

Figure 3.29b. Local Mode II, Mixed Mode I/II R-Curves
B=10.0mm, W=40.0mm, a_o/W=0.5

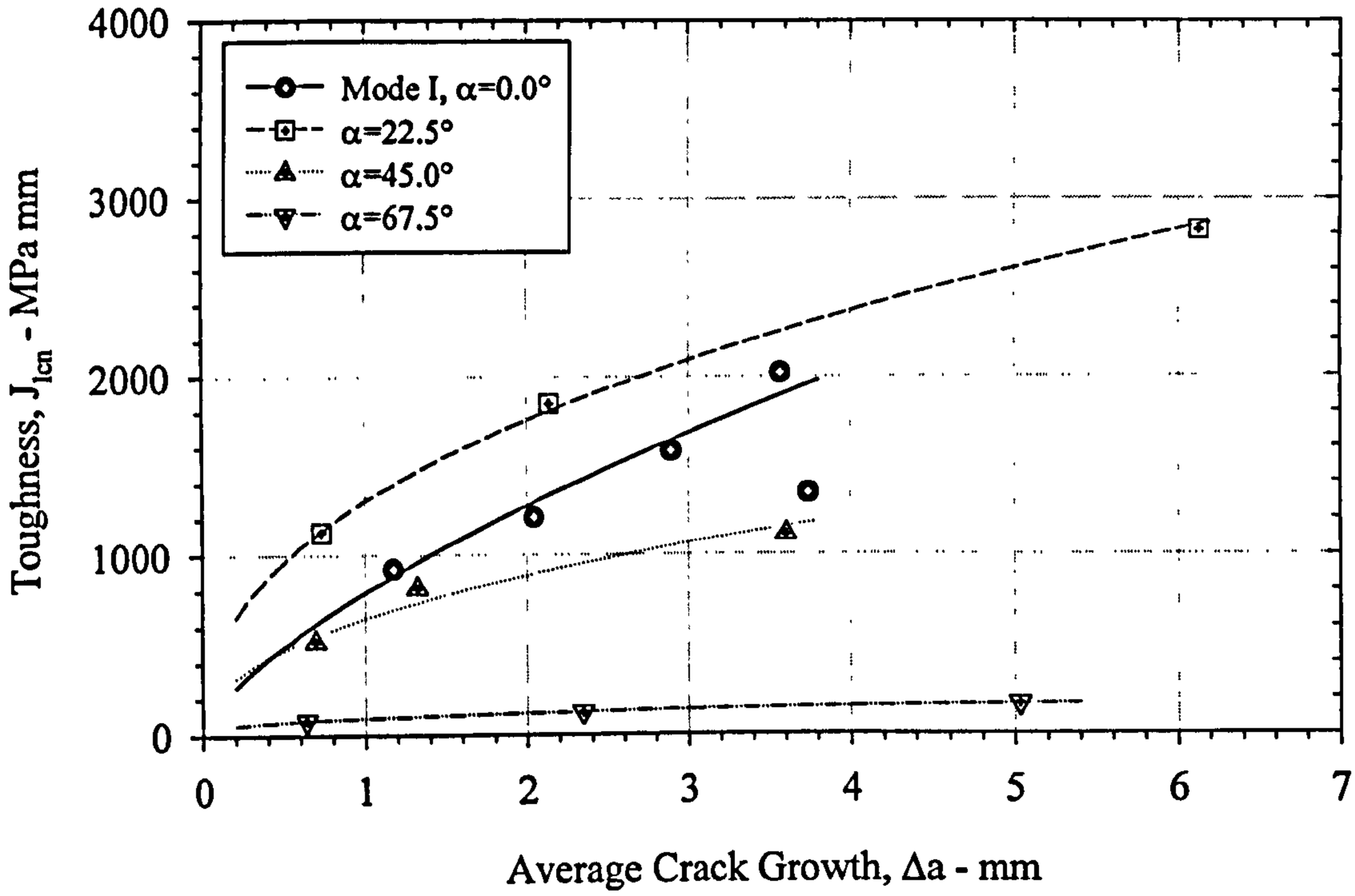

Figure 3.30a. Local Mode I, Mixed Mode I/II R-Curves
B=10.0mm, W=80.0mm, a_o/W=0.5

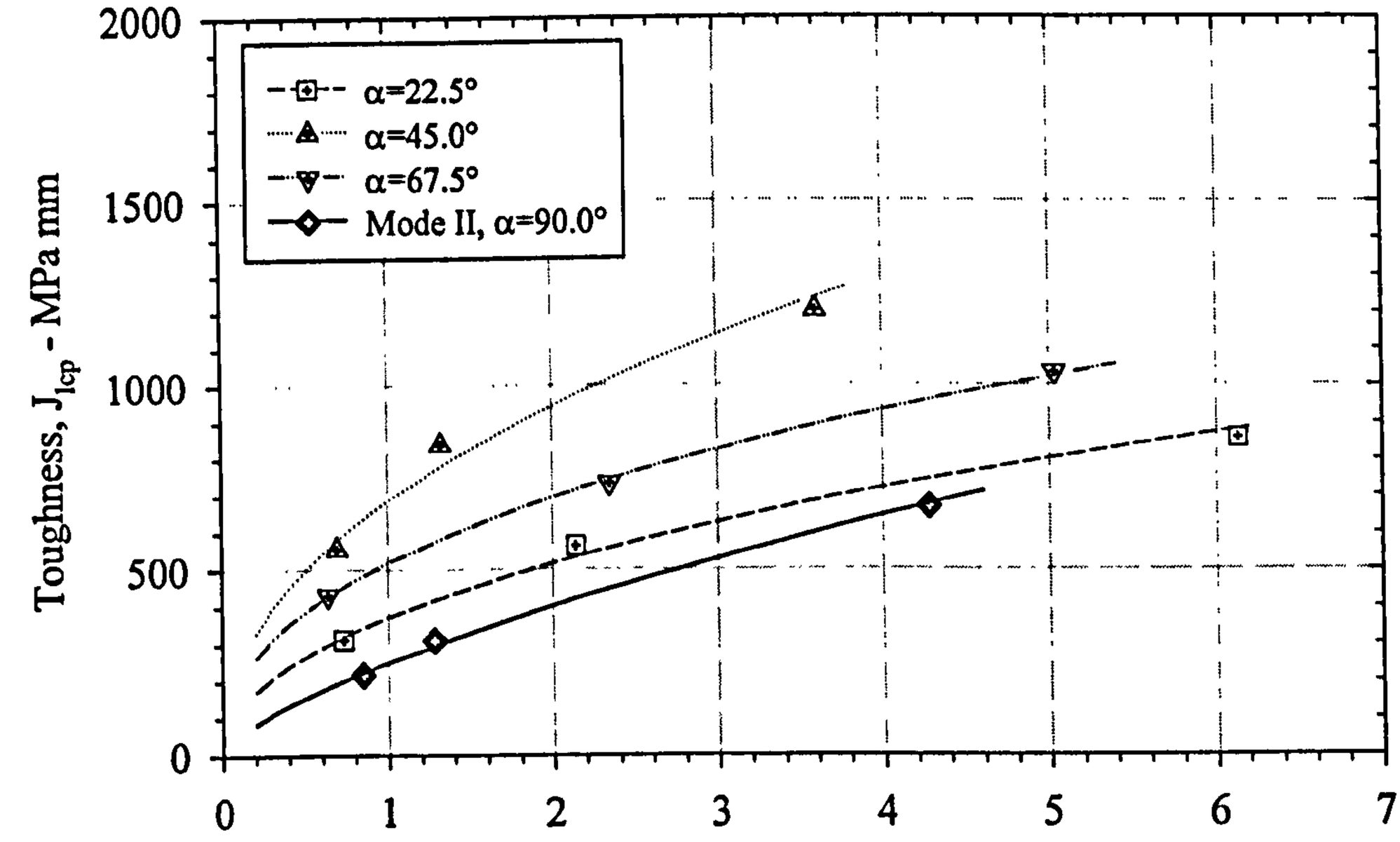

Figure 3.30b. Local Mode II, Mixed Mode I/II R-Curves
B=10.0mm, W=80.0mm, a_o/W=0.5

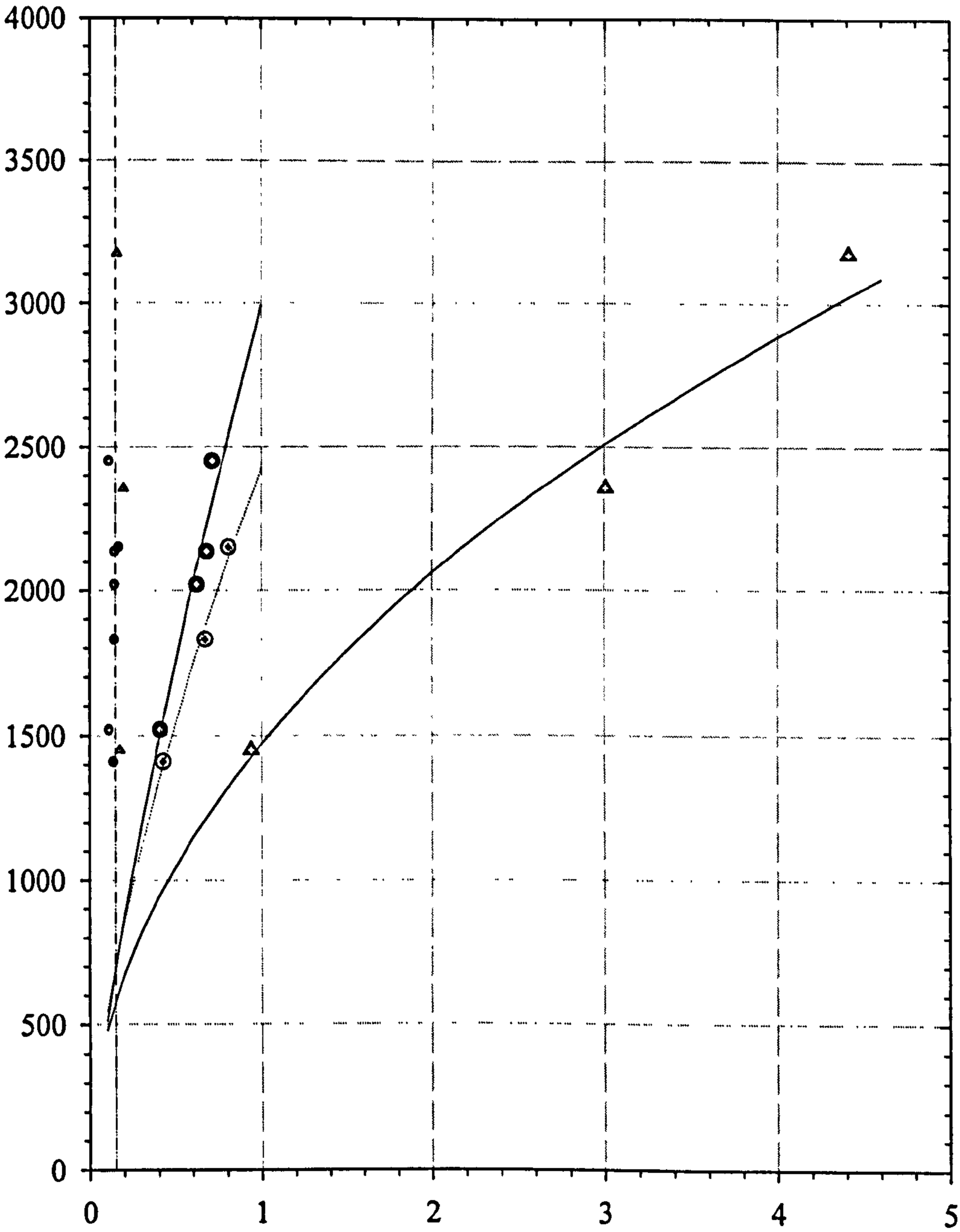

Figure 3.31. Mode I R-Curves : Size Effects, $a_o/W=0.7$

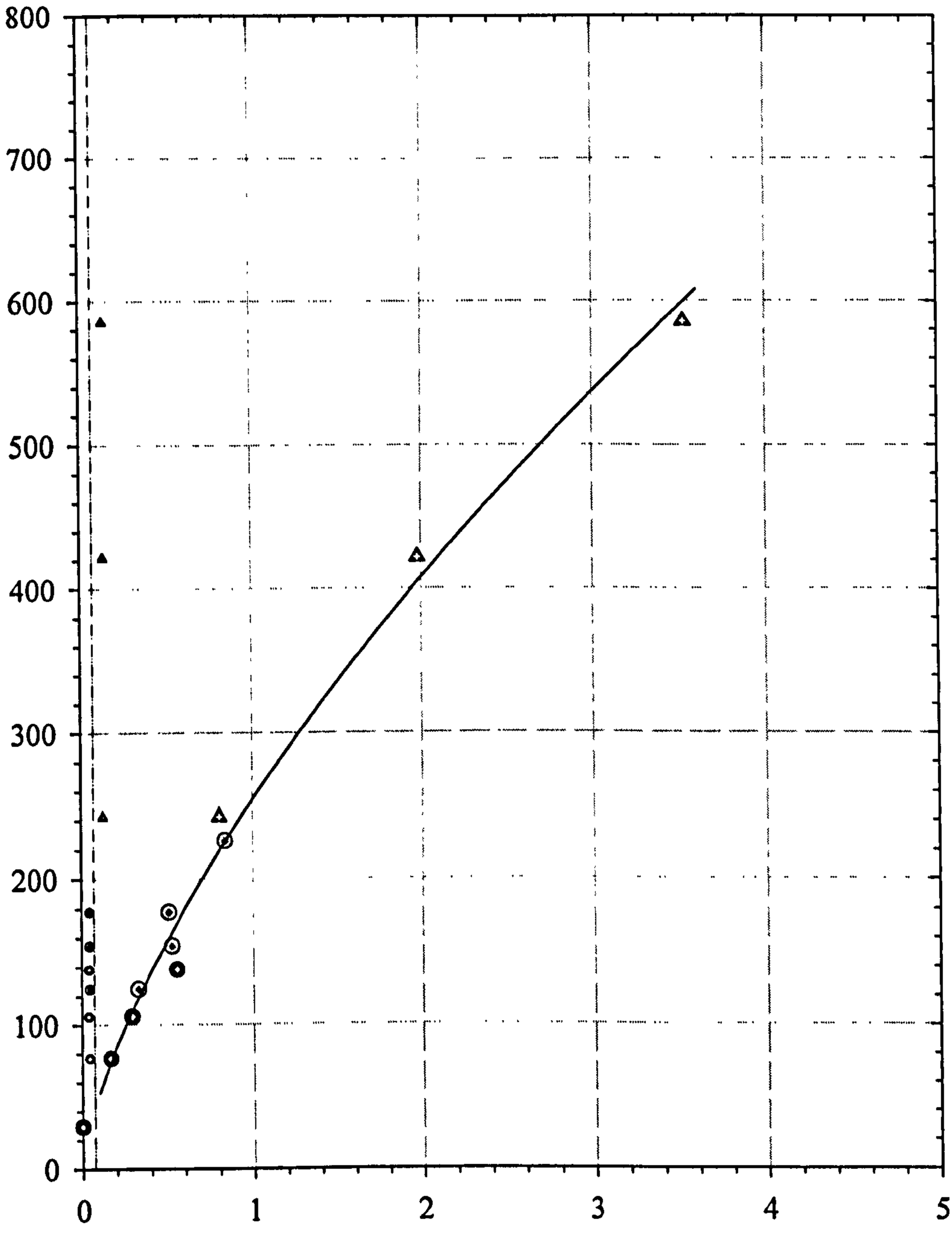

Figure 3.32. Mode II R-Curves : Size Effects, $a_o/W=0.7$

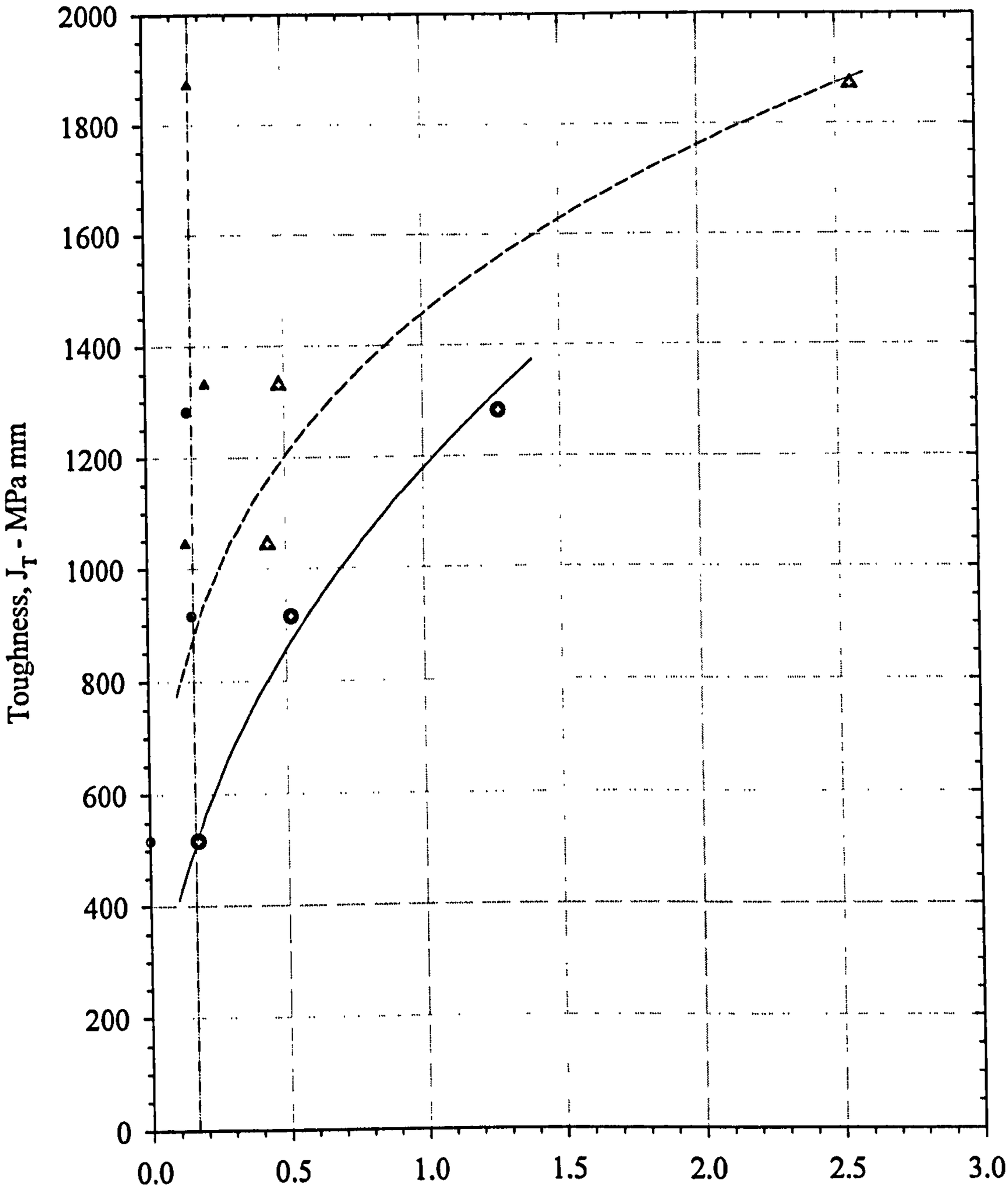

Figure 3.33. Mixed Mode I/II ($\alpha = 45.0°$) R-Curves : Size Effects, $a_o/W=0.7$

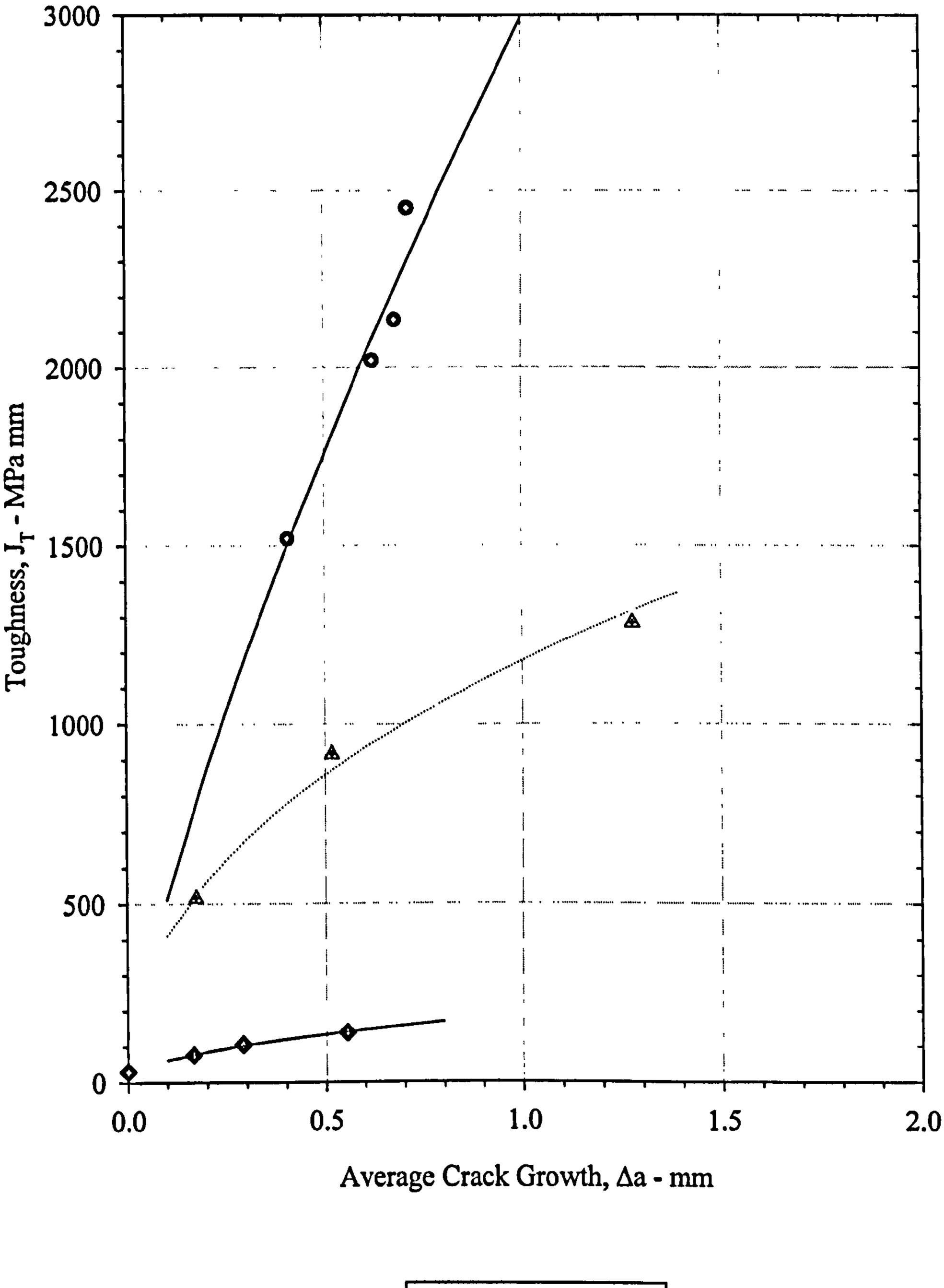

Figure 3.34. Mixed Mode I/II R-Curves : B=10.0mm, W=20.0mm, a_o/W=0.7

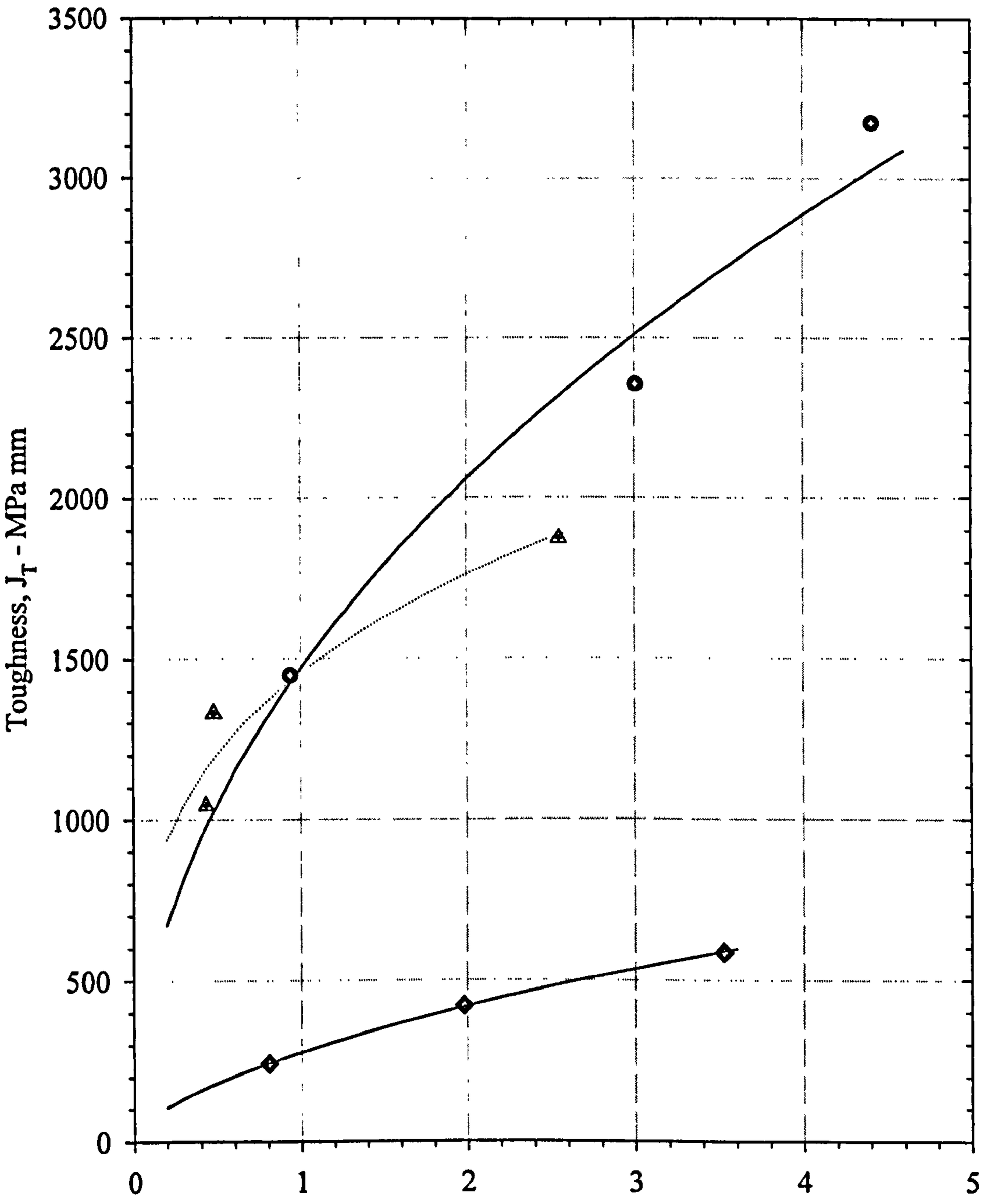

Figure 3.35. Mixed Mode I/II R-Curves : B=10.0mm, W=80.0mm, a_o/W=0.7

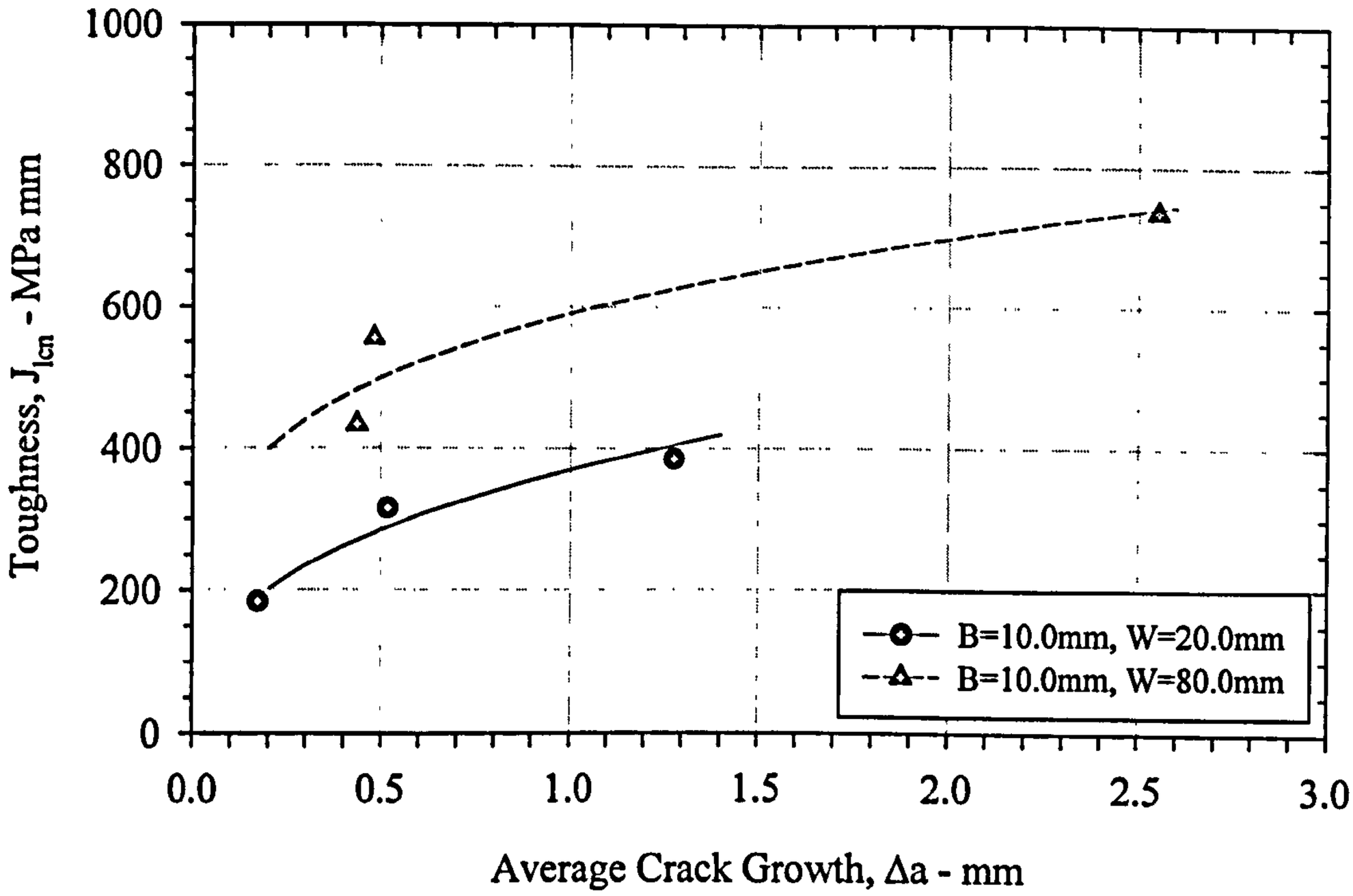

Figure 3.36a. Local Mode I, Mixed Mode I/II R-Curves, $a_o/W=0.7$
($\alpha = 45.0°$)

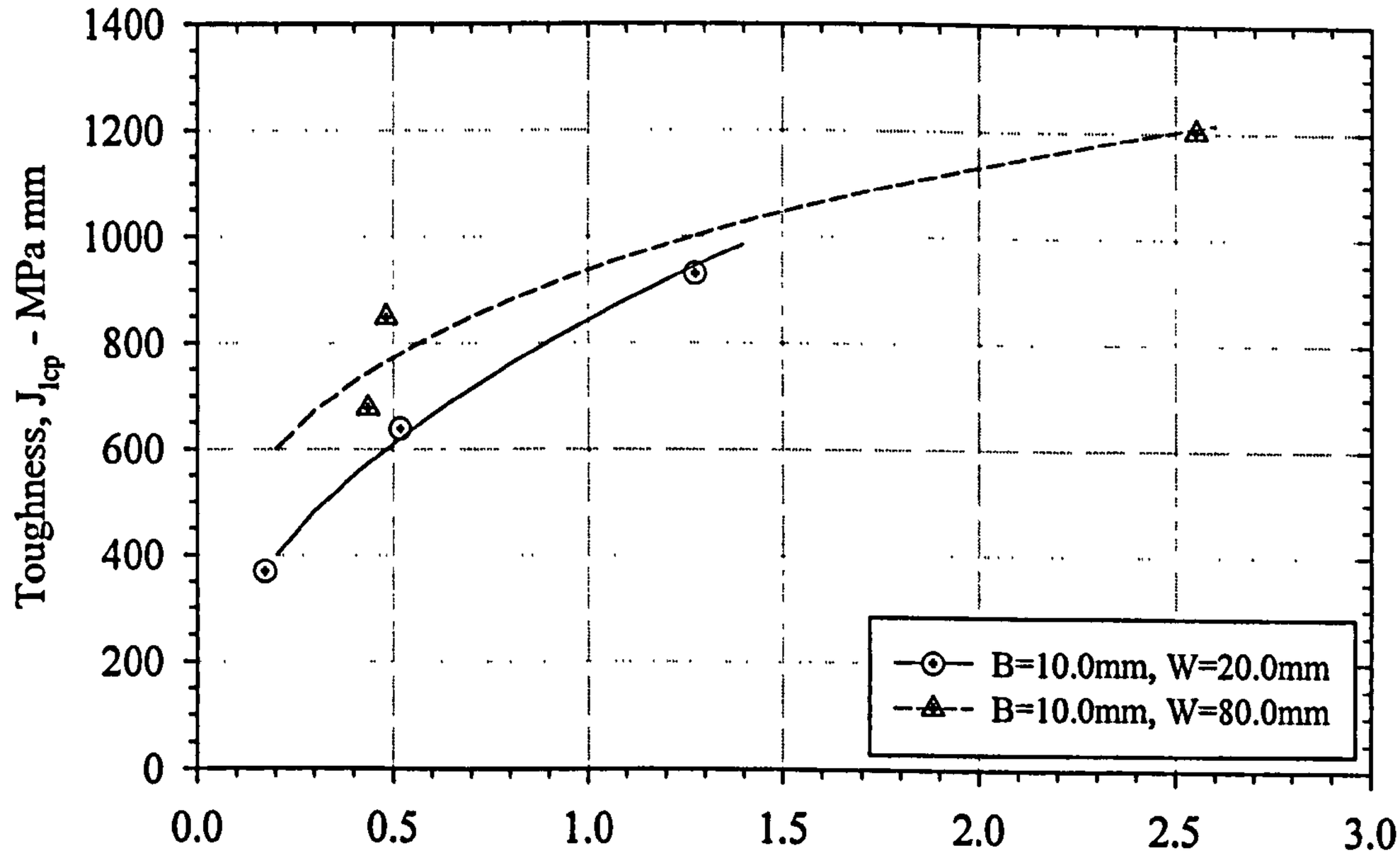

Figure 3.36b. Local Mode II, Mixed Mode I/II R-Curves, $a_o/W=0.7$
($\alpha = 45.0°$)

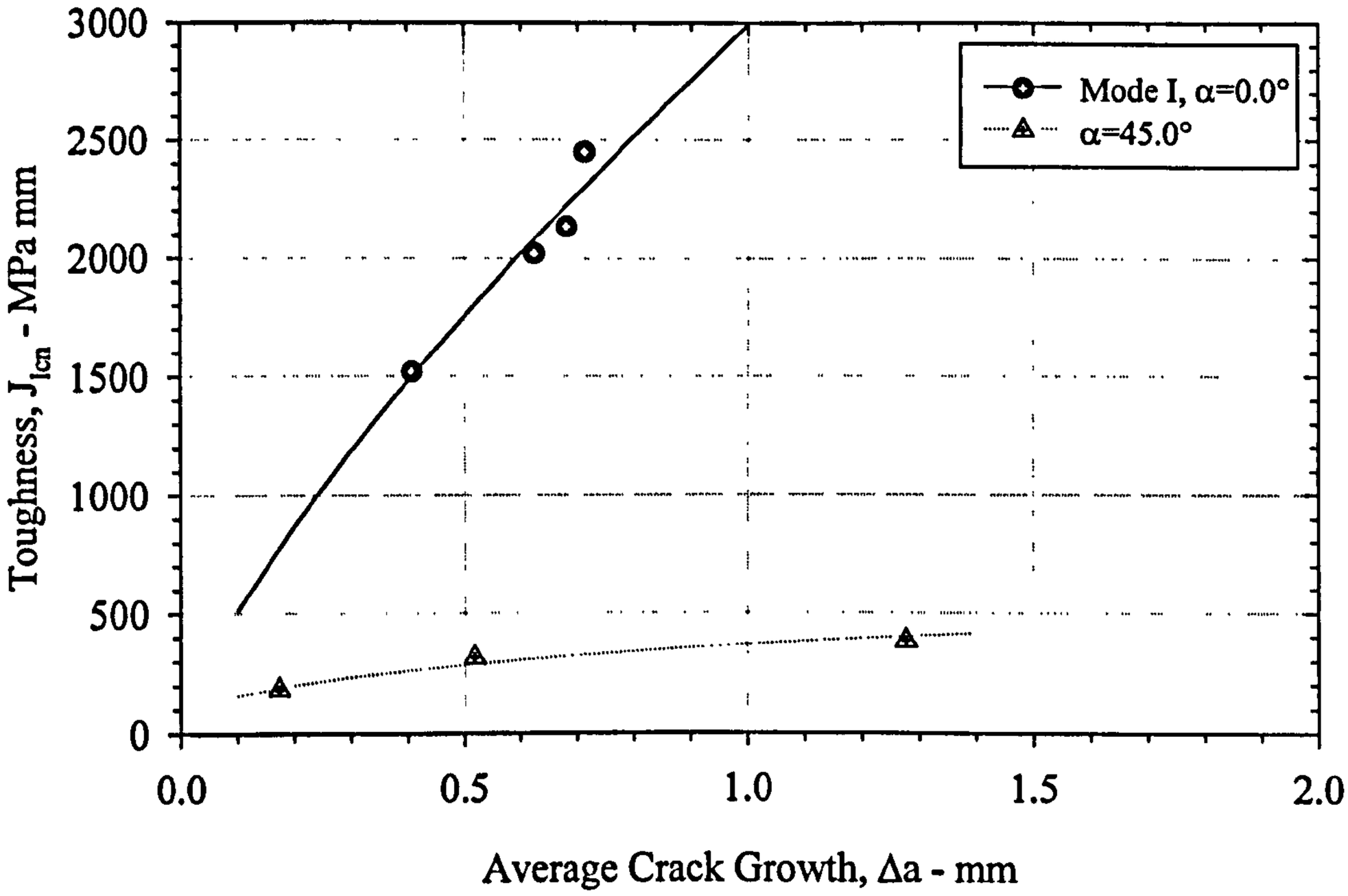

Figure 3.37a. Local Mode I, Mixed Mode I/II R-Curves
B=10.0mm, W=20.0mm, a_o/W=0.7

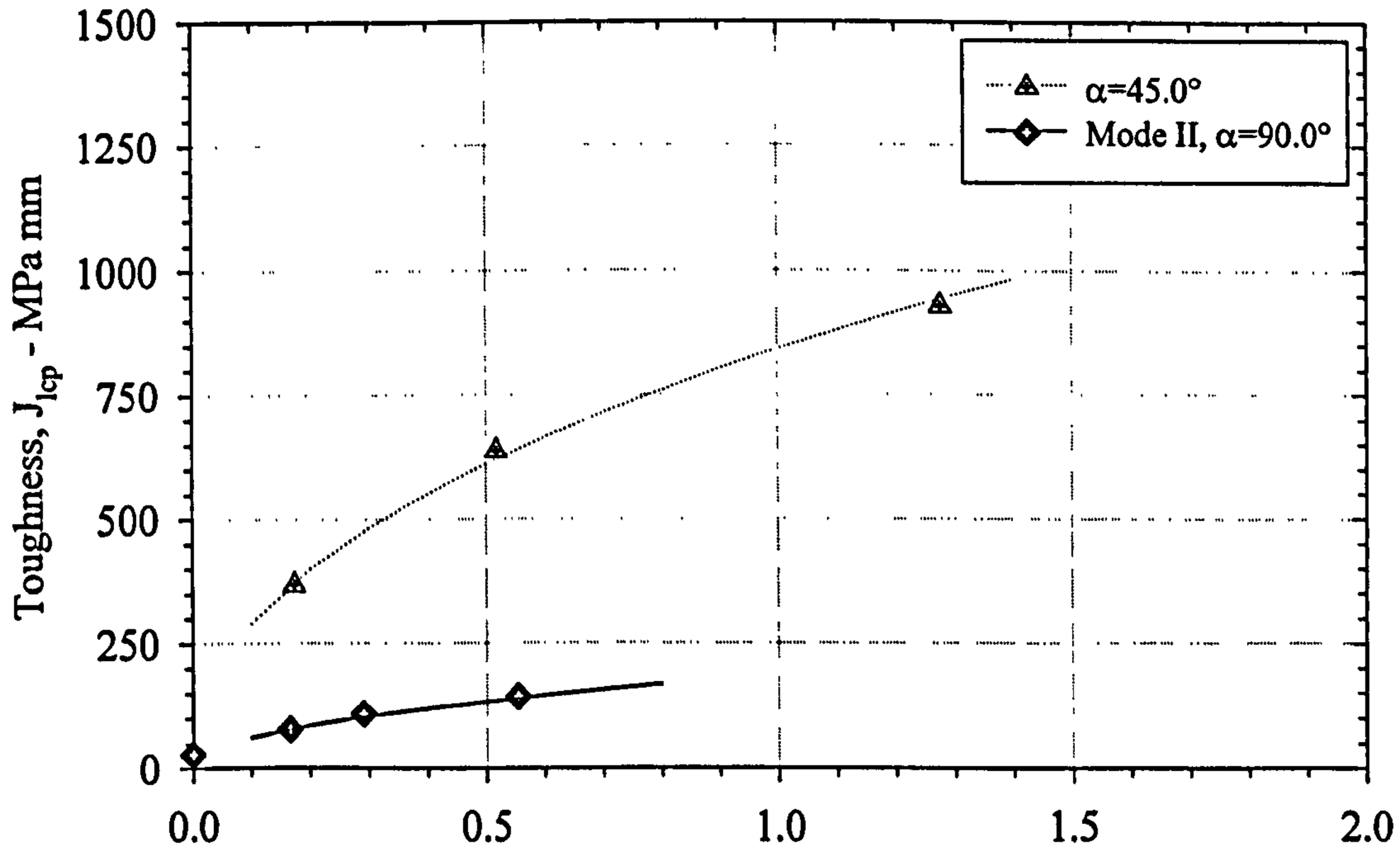

Figure 3.37b. Local Mode II, Mixed Mode I/II R-Curves
B=10.0mm, W=20.0mm, a_o/W=0.7

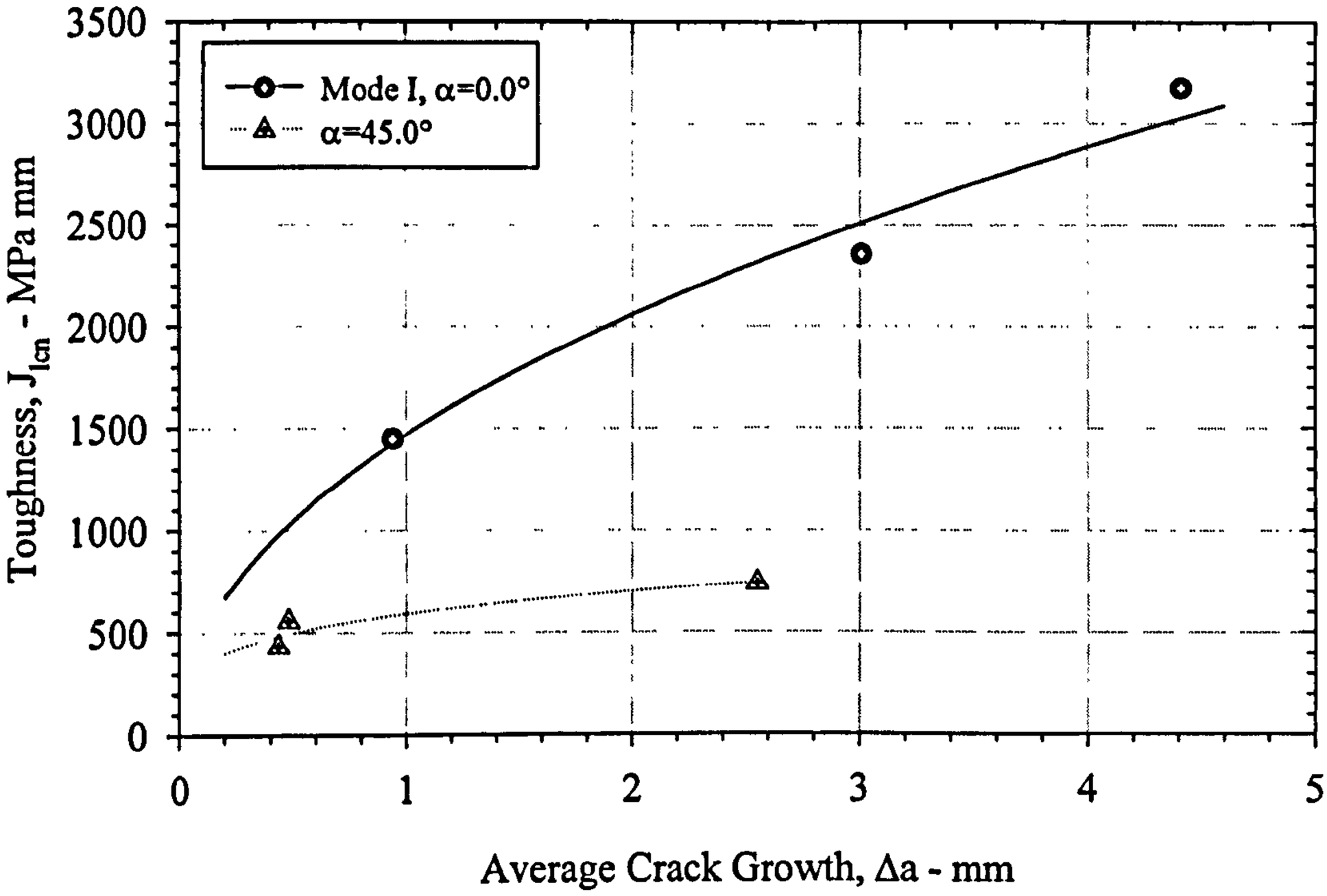

Figure 3.38a. Local Mode I, Mixed Mode I/II R-Curves
B=10.0mm, W=80.0mm, a_o/W=0.7

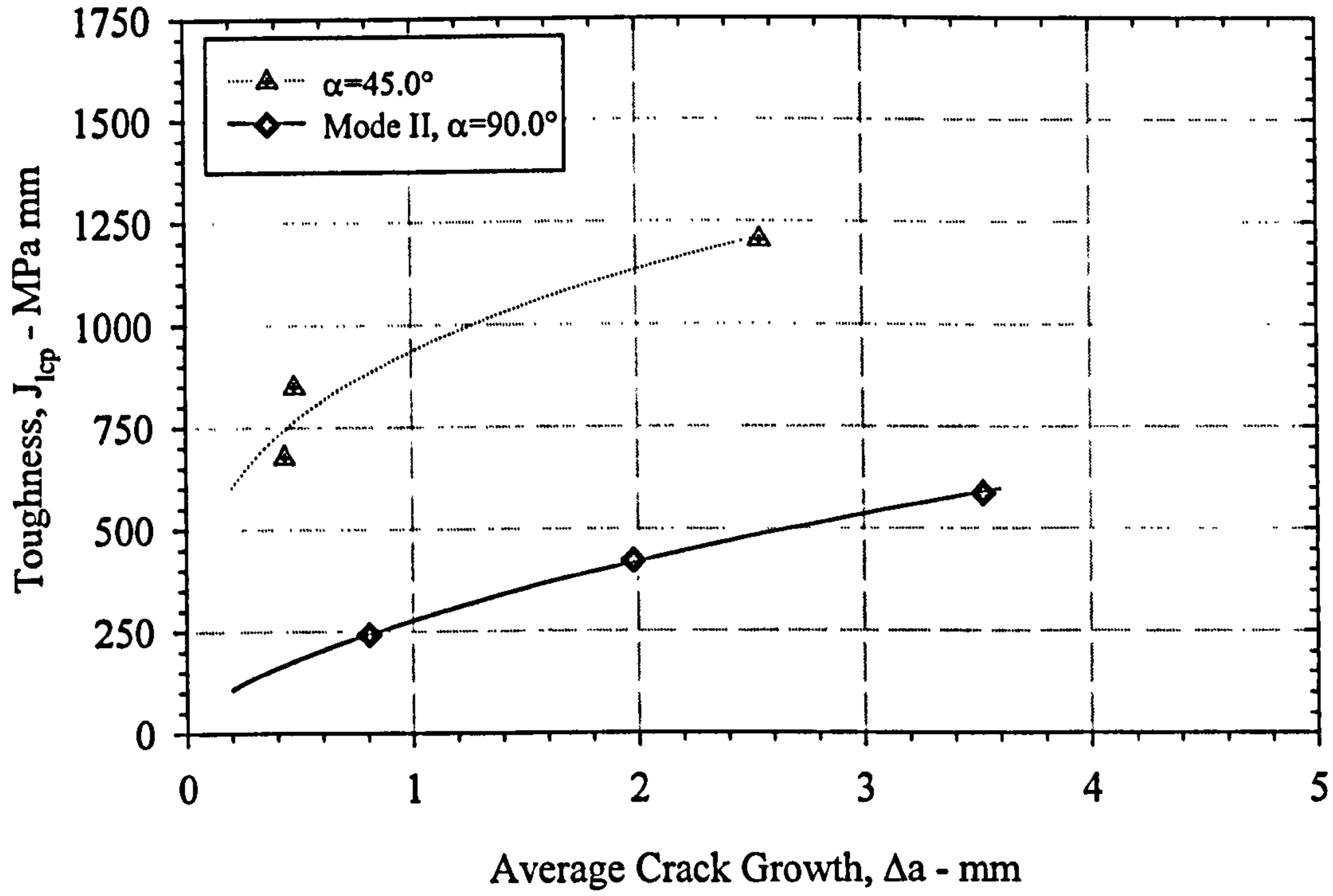

Figure 3.38b. Local Mode II, Mixed Mode I/II R-Curves
B=10.0mm, W=80.0mm, a_o/W=0.7

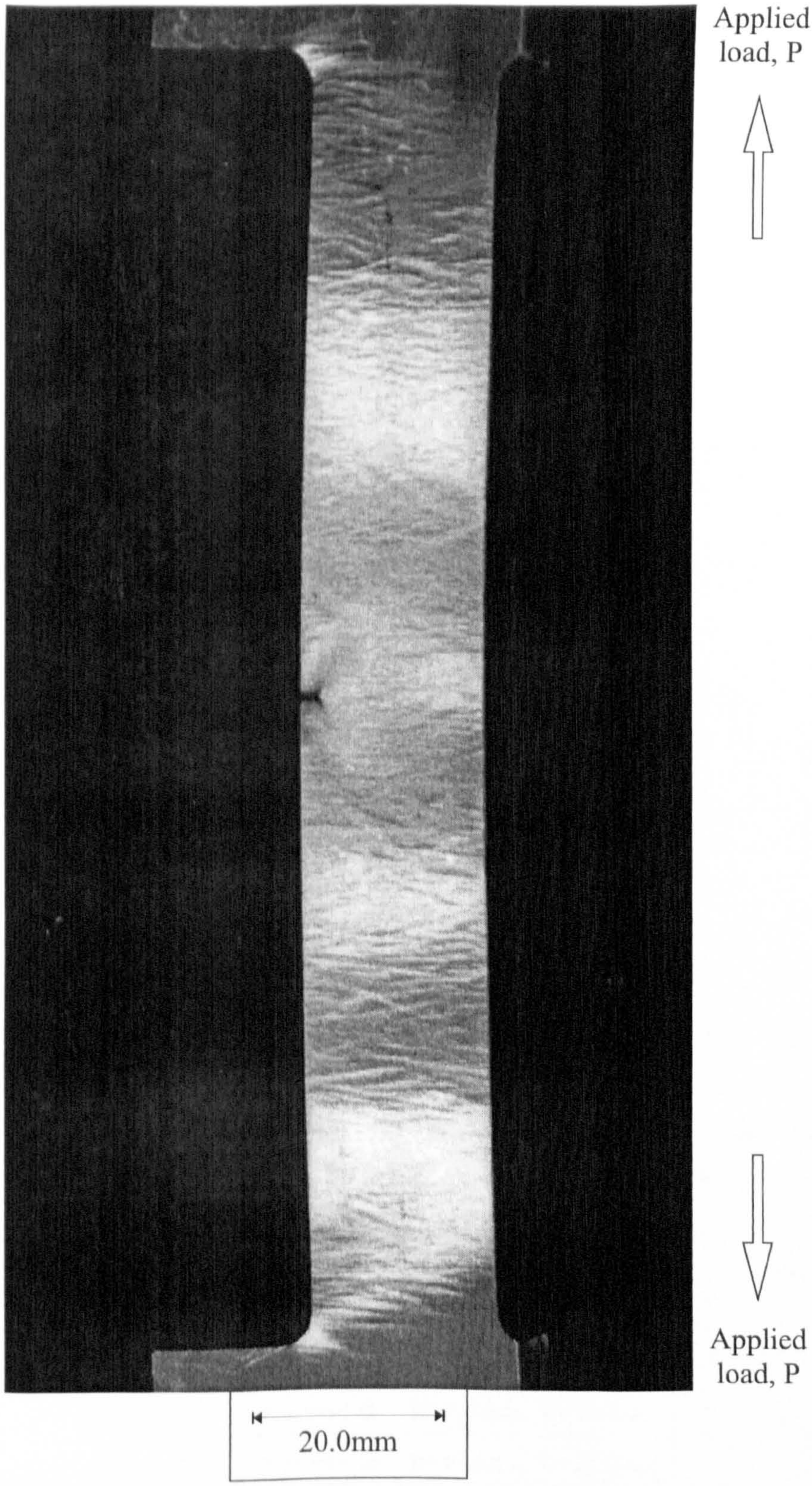

Figure 3.39. Luders Bands throughout an $a_o/W = 0.1$, Mode I Loaded SEN Specimen.

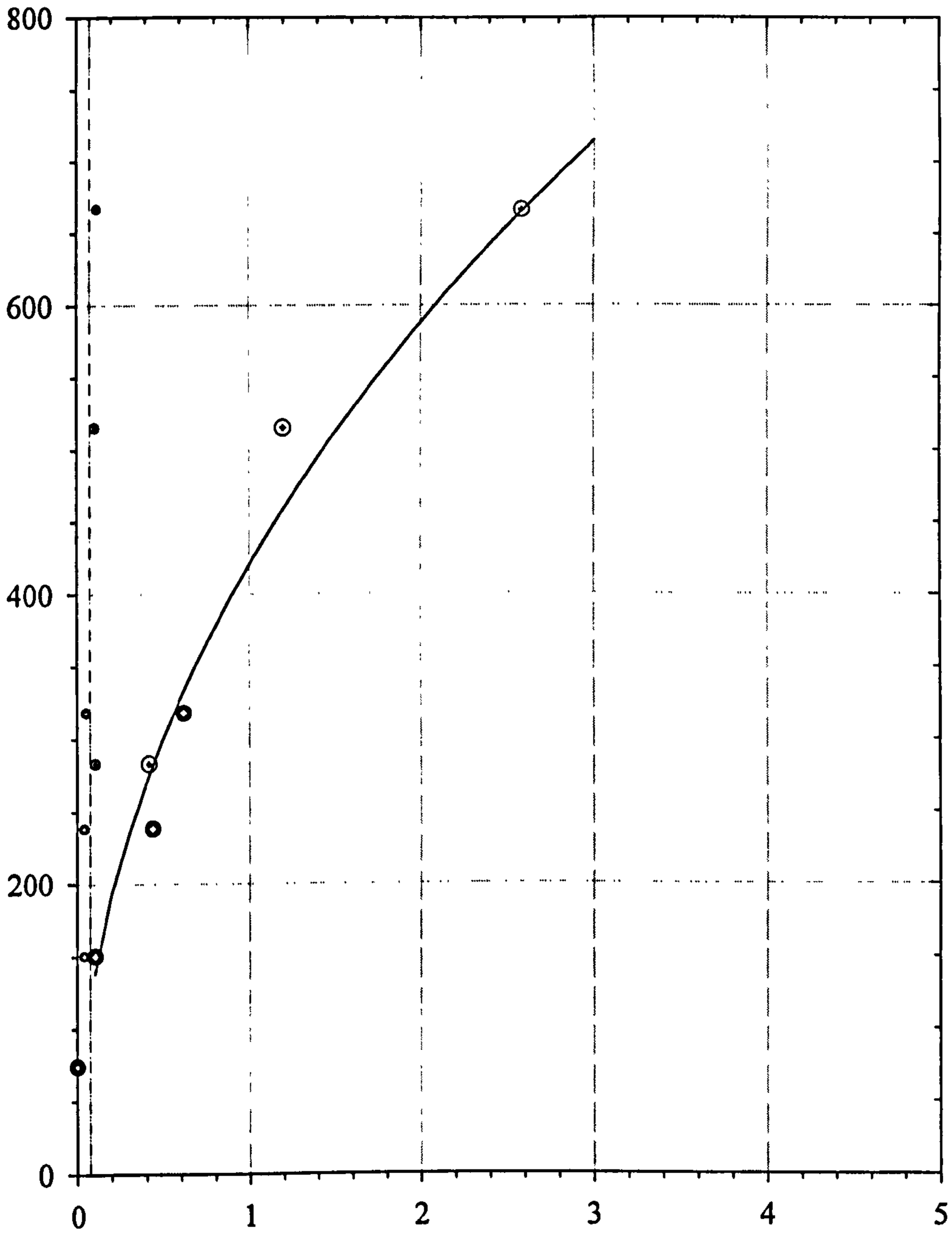

Figure 3.40. Mode II R-Curves : Size Effects, $a_o/W=0.1$

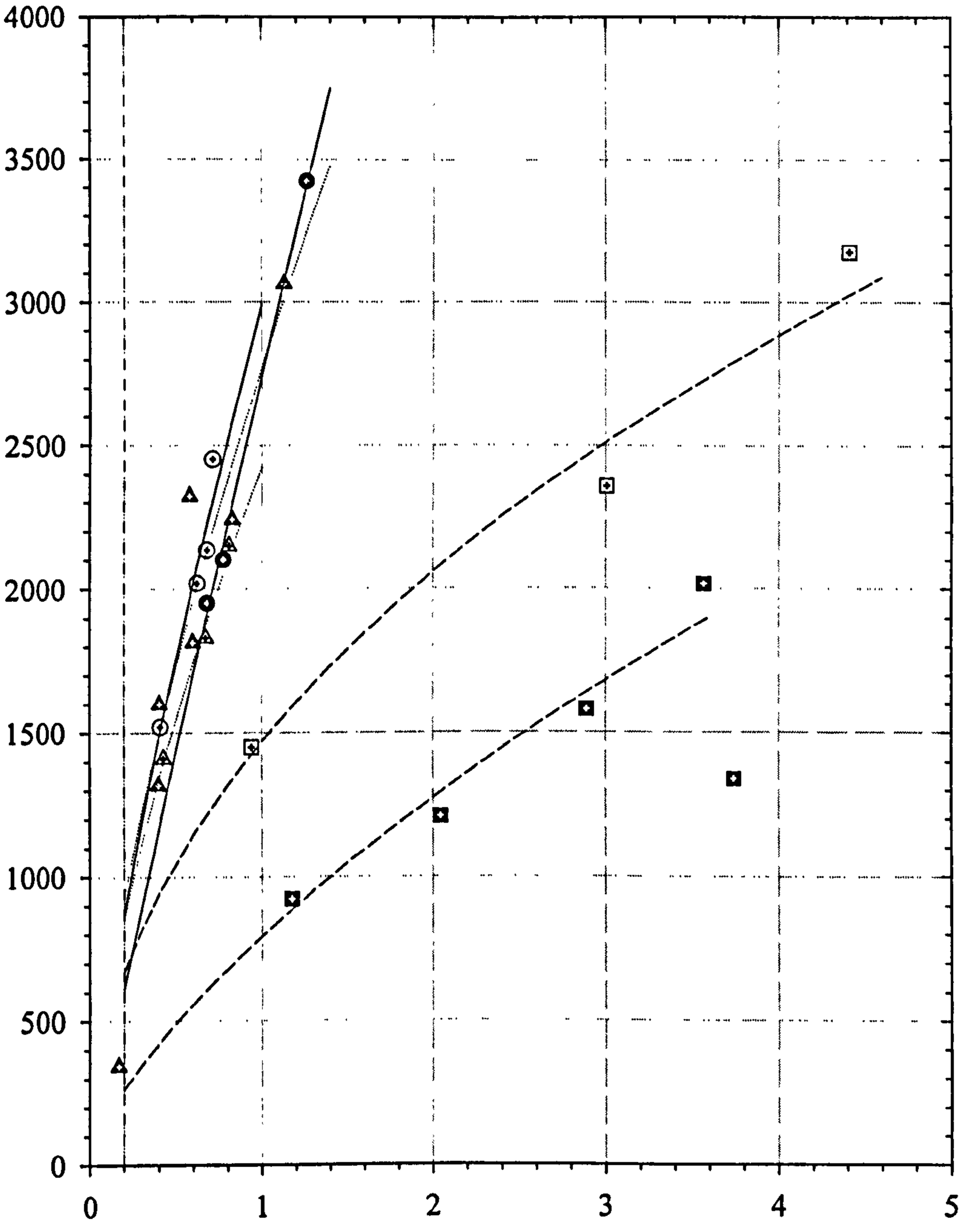

Figure 3.41. Comparison of Mode I R-Curves : $a_o/W = 0.5$ and 0.7

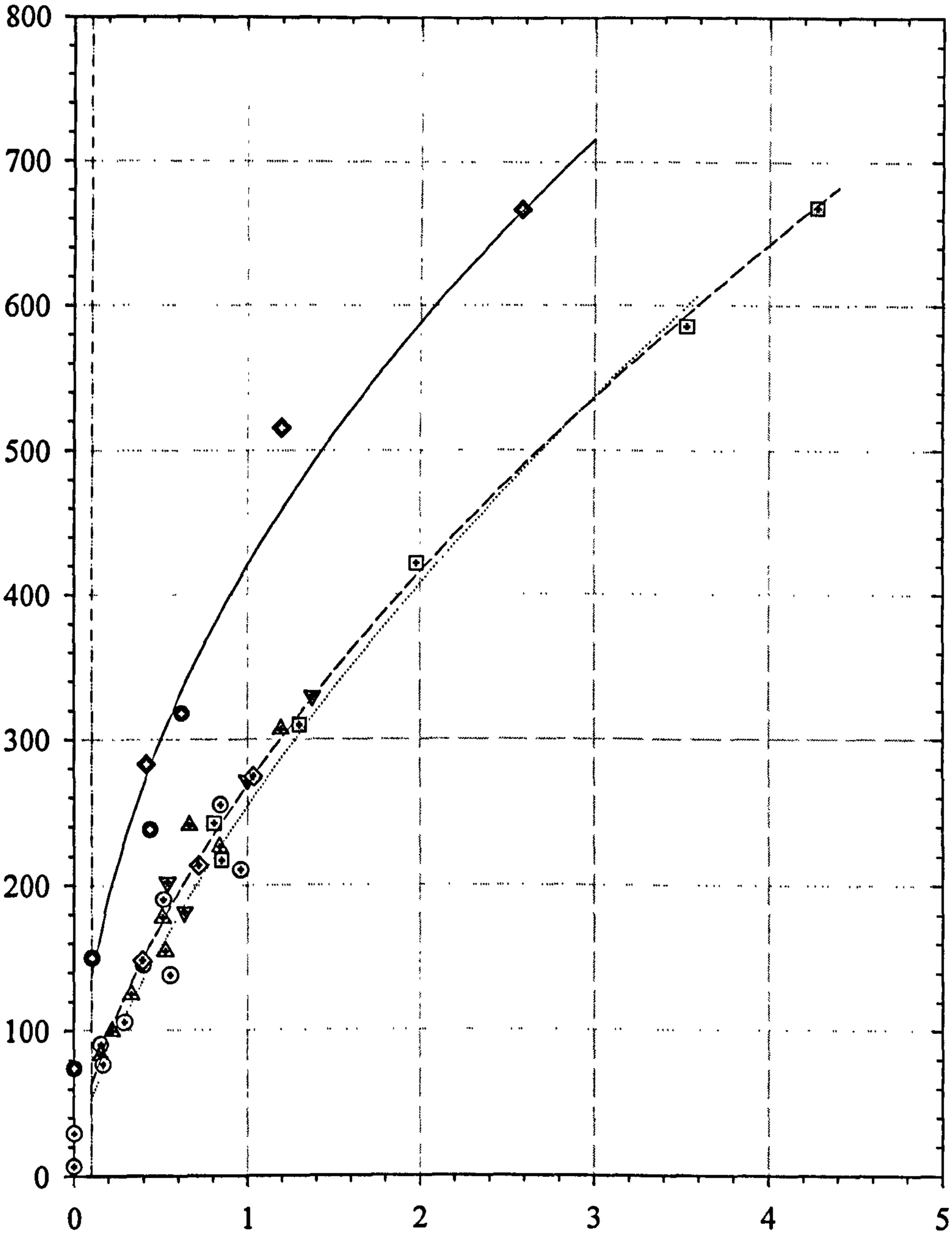

Figure 3.42. Comparison of Mode II R-Curves : a_o/W = 0.1, 0.5 and 0.7

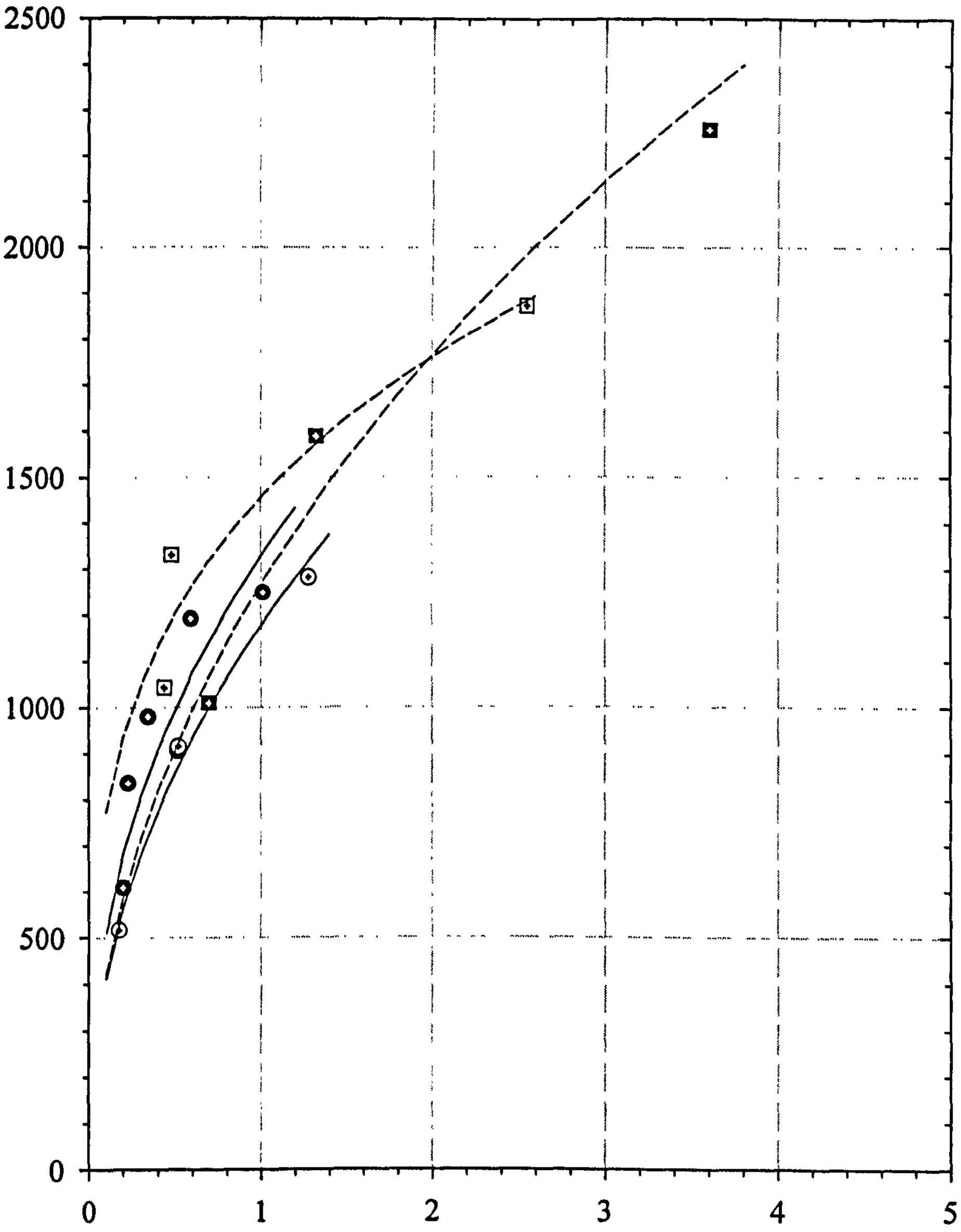

Figure 3.43. Comparison of Mixed Mode I/II R-Curves : $a_o/W = 0.5$ and 0.7 ($\alpha = 45.0°$)

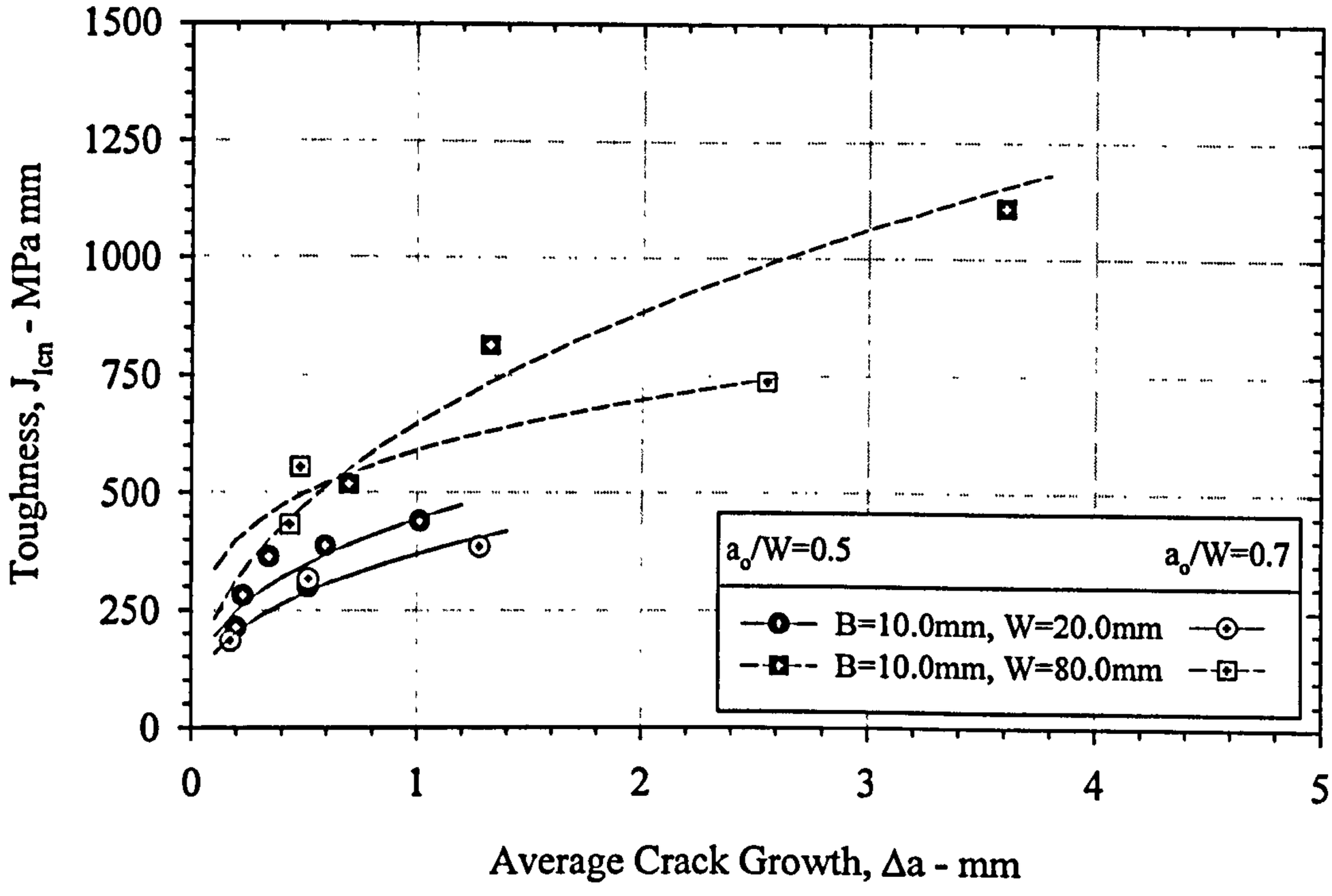

Figure 3.44a. Comparison of Local Mode I, Mixed Mode I/II (α=45.0°) R-Curves
a_o/W = 0.5 and 0.7

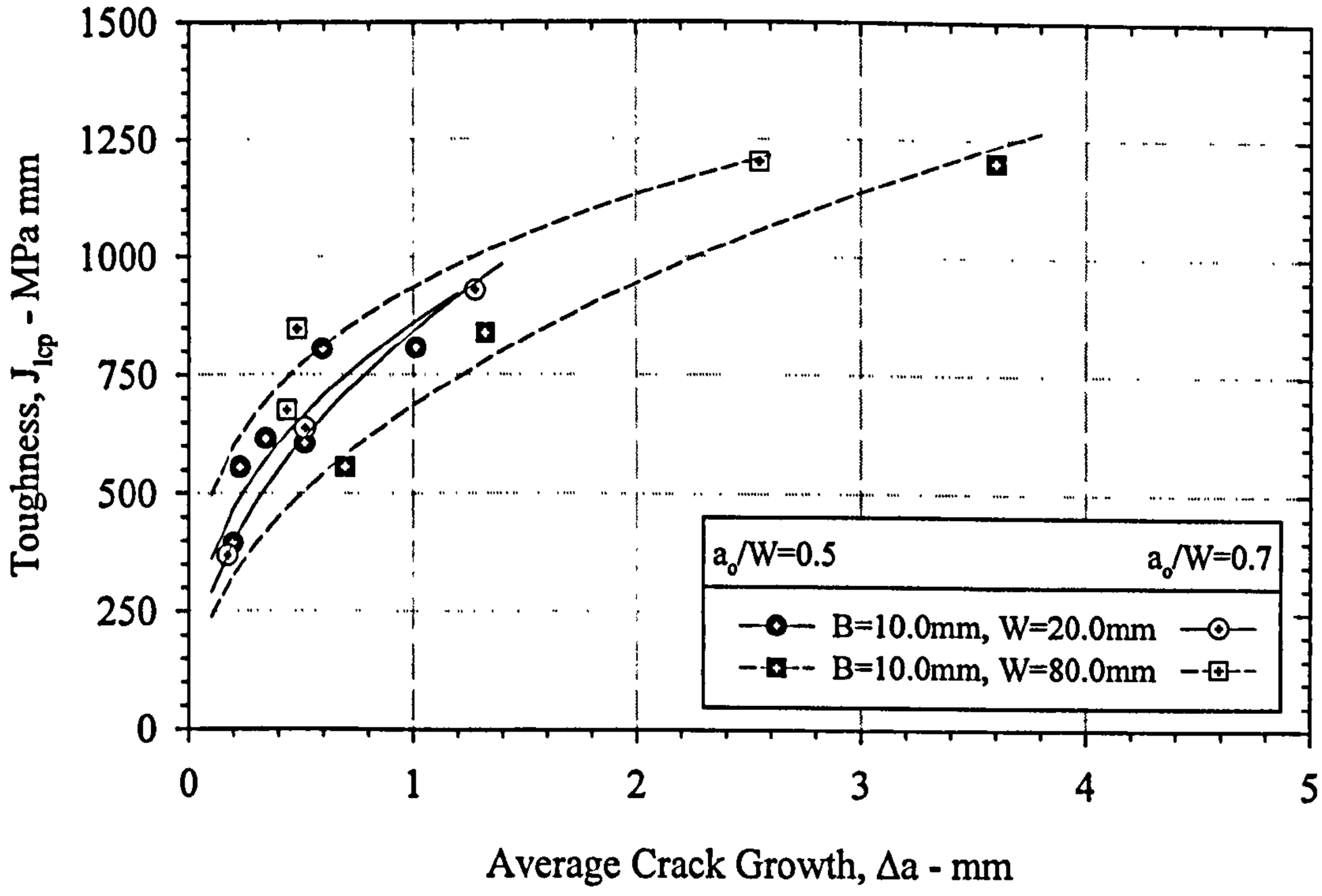

Figure 3.44b. Comparison of Local Mode II, Mixed Mode I/II (α=45.0°) R-Curves
a_o/W = 0.5 and 0.7

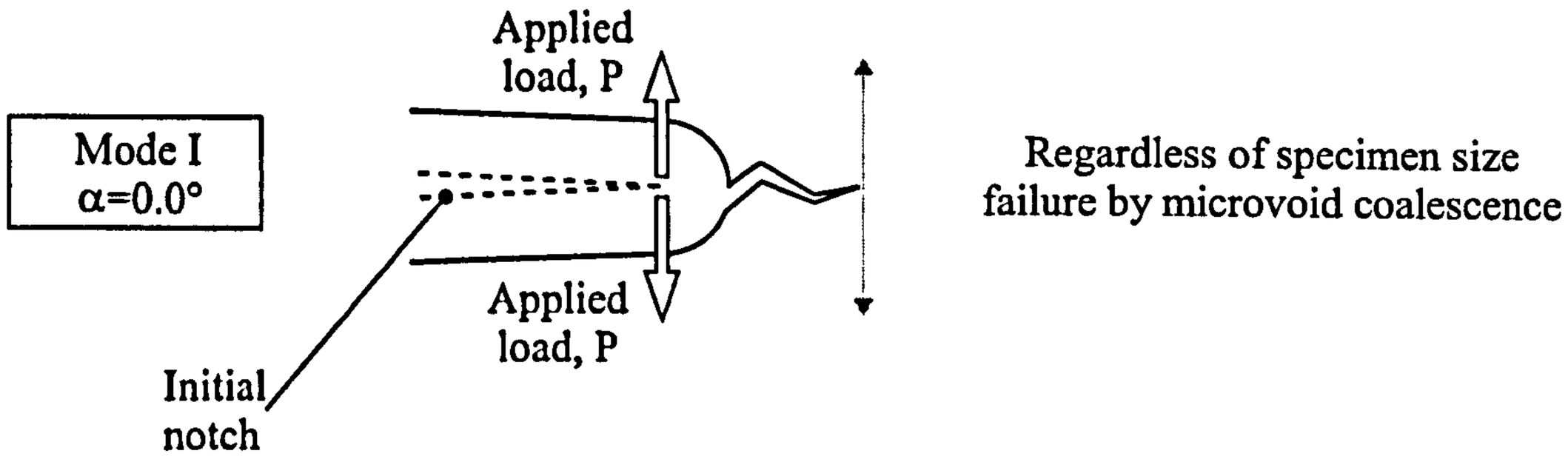

Figure 3.45a. Blunting and Crack Growth Characteristics of Mixed Mode Loading (schematic illustration)

Mode I
α=0.0°

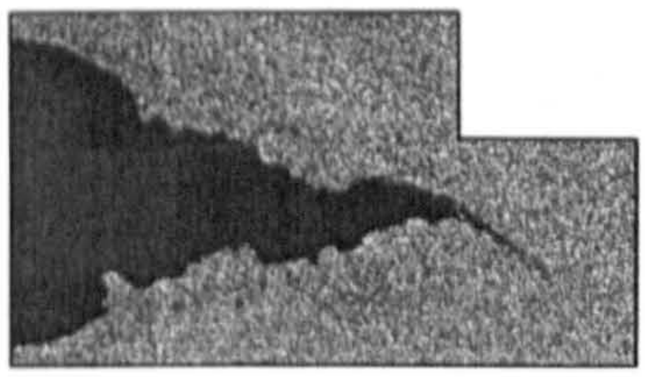

Regardless of specimen size
failure by microvoid coalescence

B=10mm, W=20mm
failure by shear localisation

B=20mm, W=80mm
failure by microvoid coalescence

Mixed Mode
α=22.5°

Mixed Mode
α=45.0°

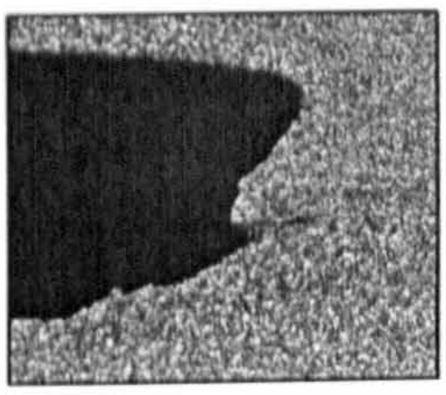

B=10mm, W=20mm
failure by shear localisation

Mixed Mode
α=67.5°

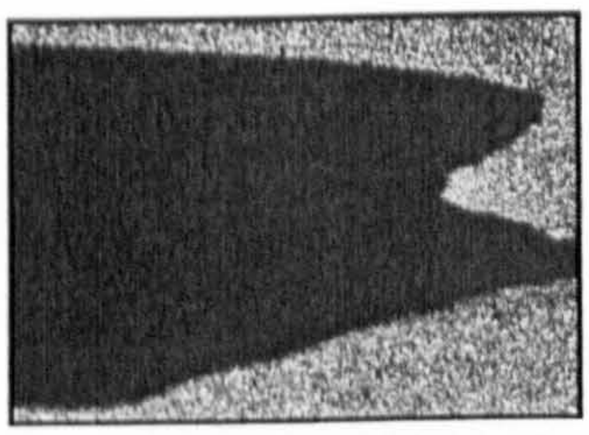

B=10mm, W=20mm
failure by shear localisation

Mode II
α=90.0°

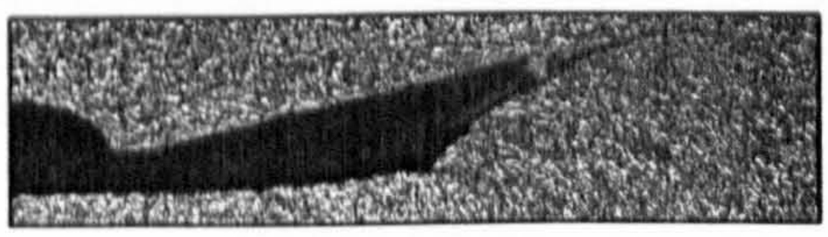

B=10mm, W=20mm
failure by shear localisation

Figure 3.45b. Blunting and Crack Growth Characteristics of Mixed Mode Loading

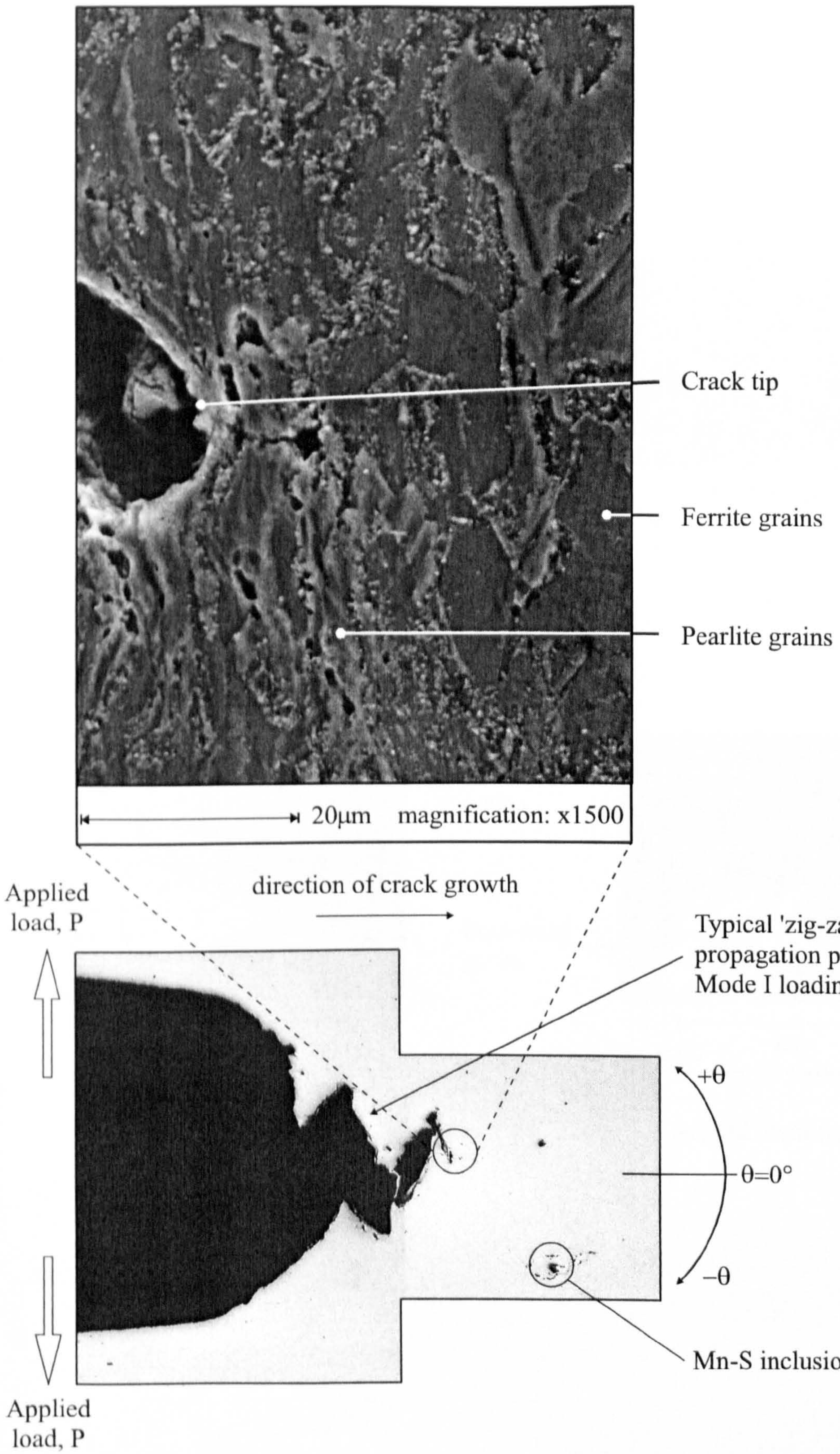

Figure 3.46. Mode I : Nucleation of Microvoids within Pearlite Grains and Along Grain Boundaries

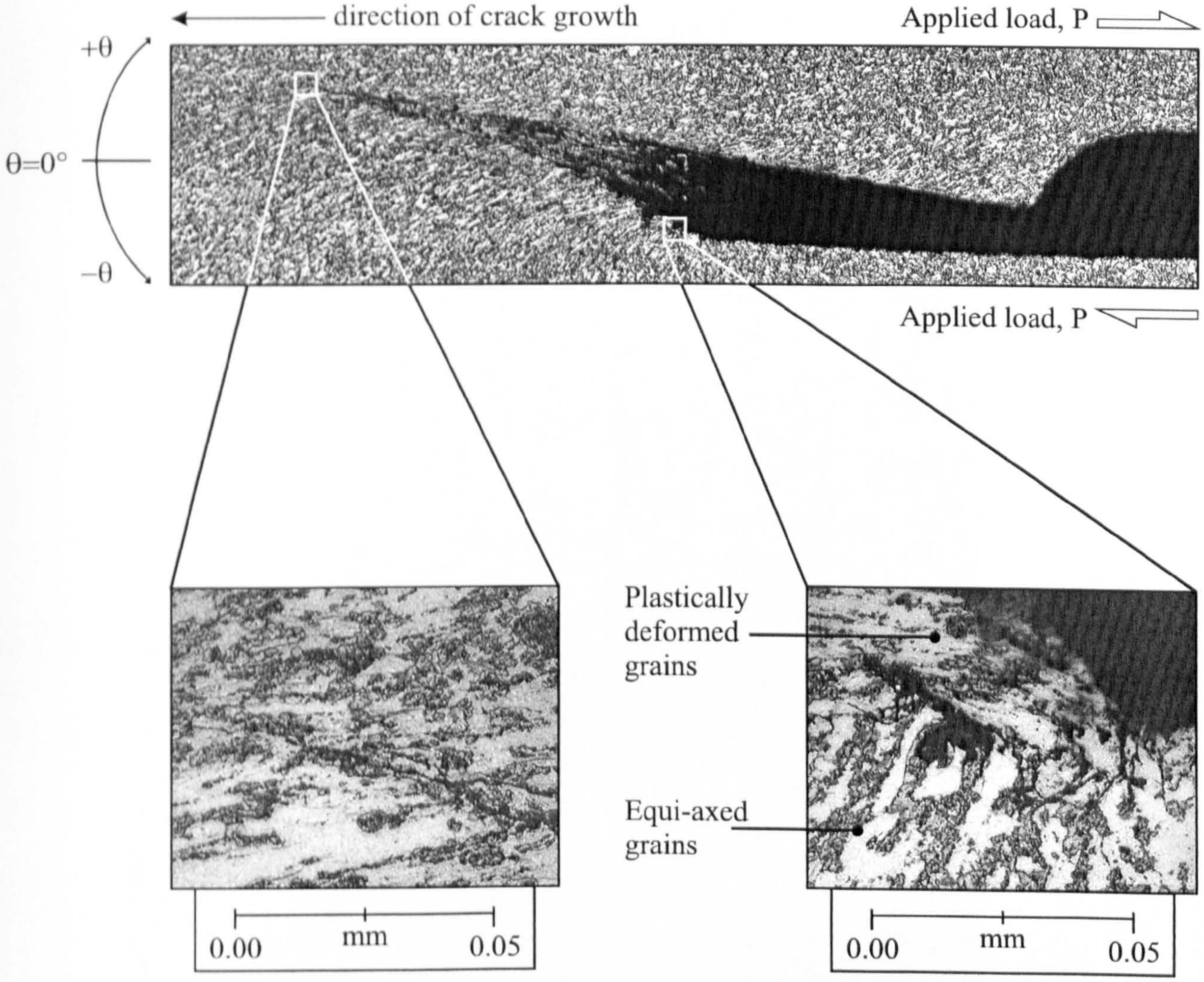

Crack tip propagating through pearlite colonies

Second blunting region

Figure 3.47. Mode II : Crack Growth Characteristics

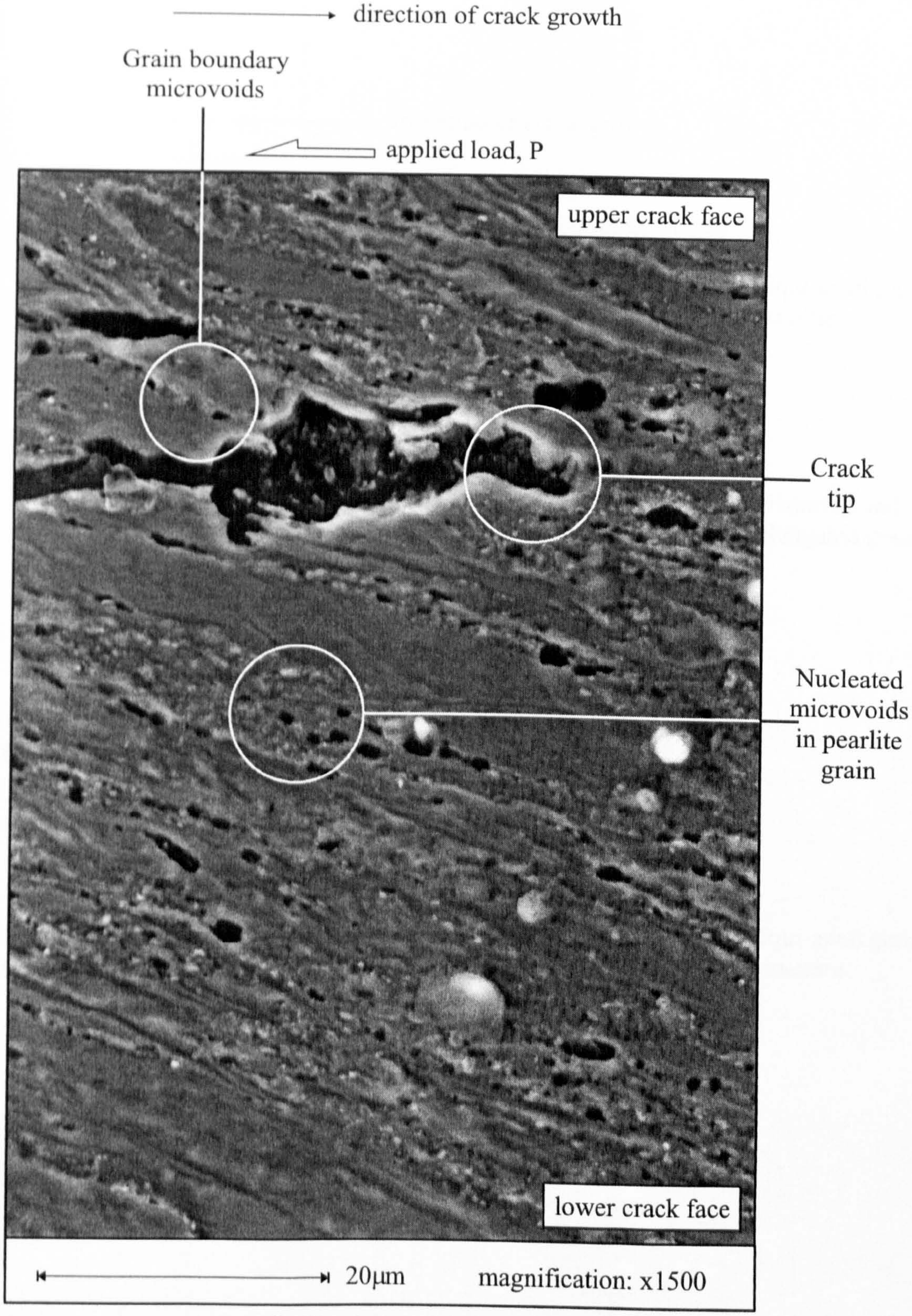

Figure 3.48. Microvoid Nucleation in Mode II Loading

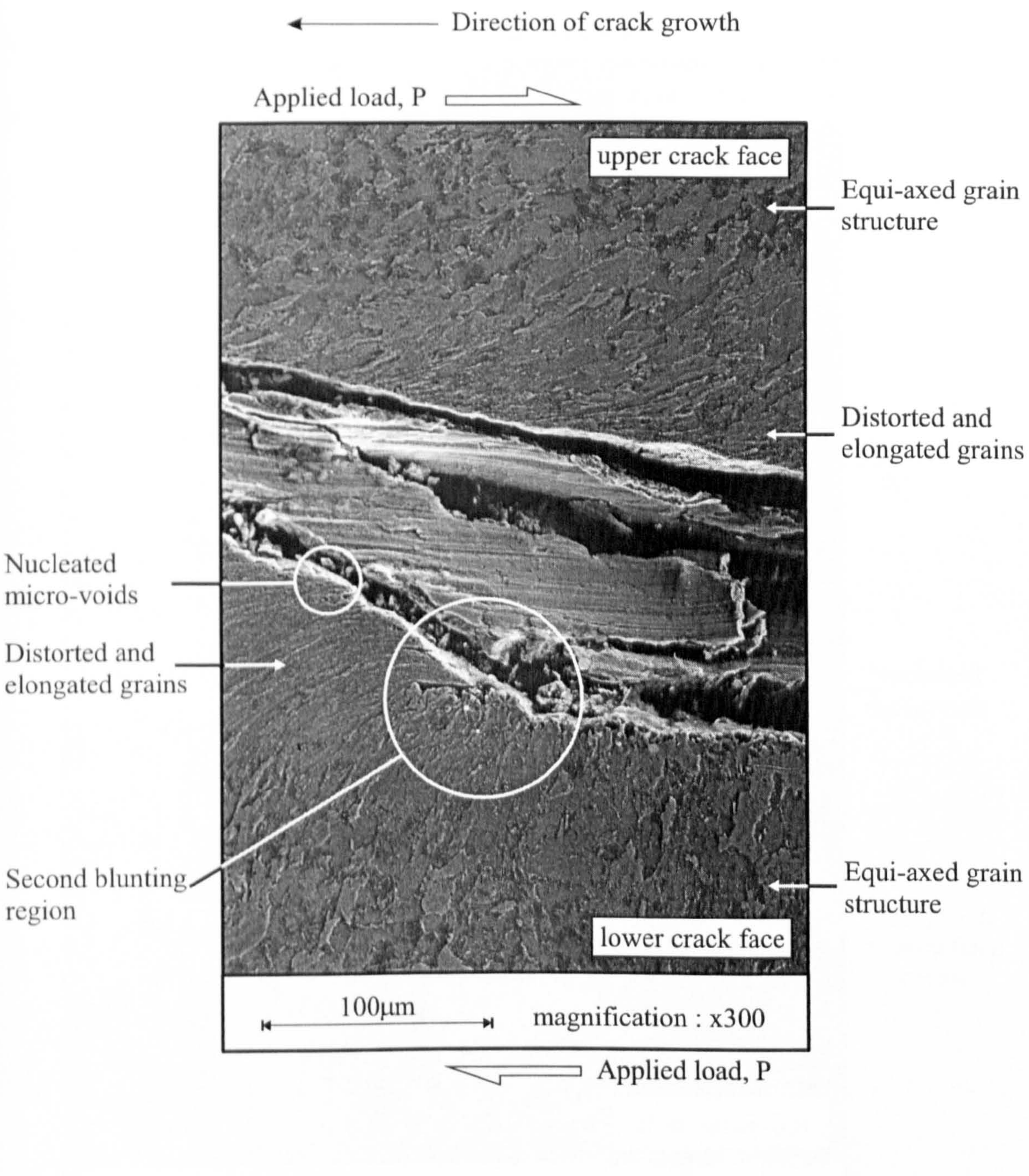

Figure 3.49a. Mode II : Plastic Deformation along the Upper and Lower Crack Flanks in the Vicinity of the Second Blunting Region

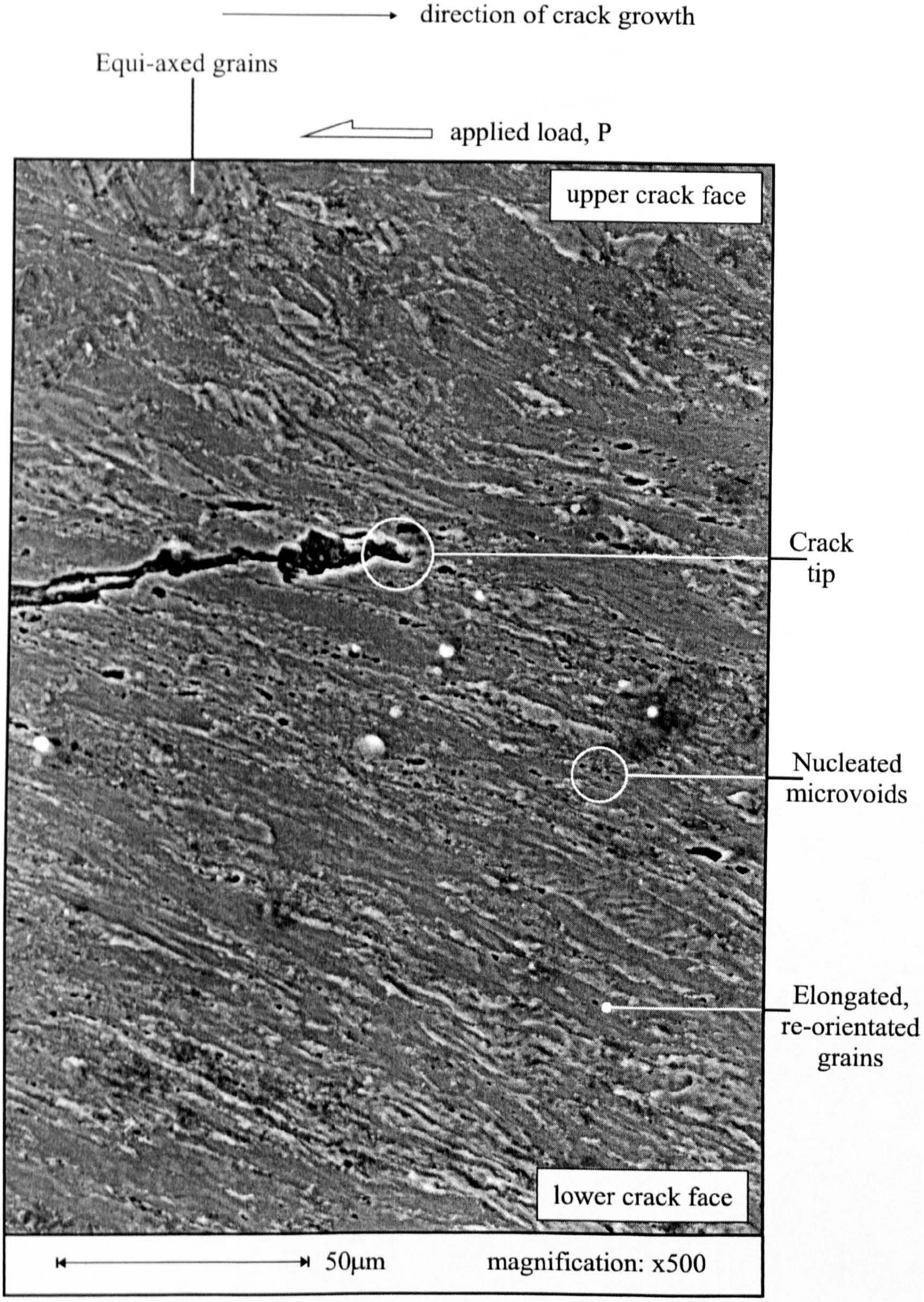

Figure 3.49b. Microstructure Deformation and Microvoid Formation in Mode II Loading

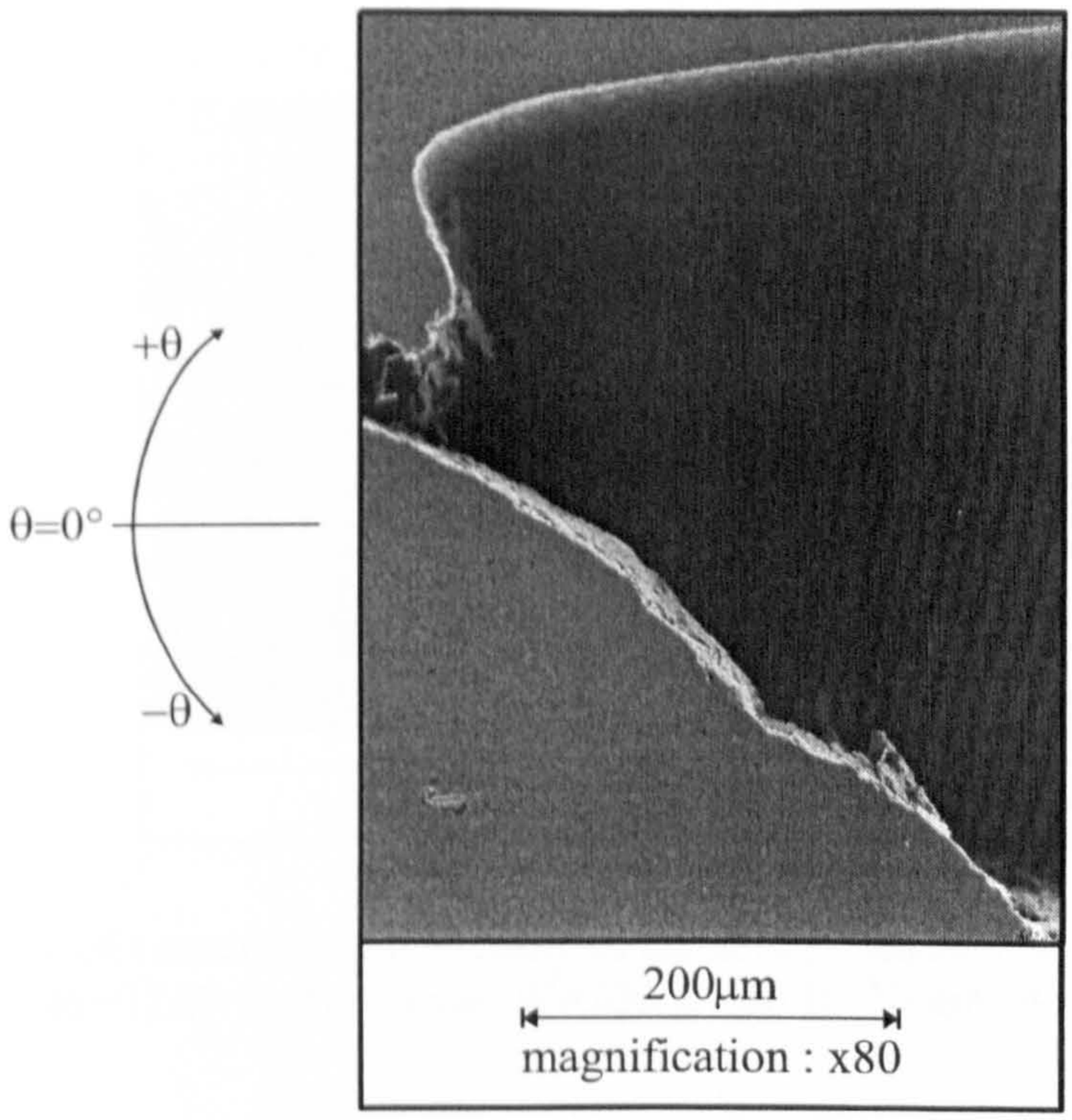

Figure 3.50a. Mixed Mode I/II (α=22.5°) Shear Crack Propagation (SEN specimen, B=10mm, W=20mm, a_o/W=0.5)

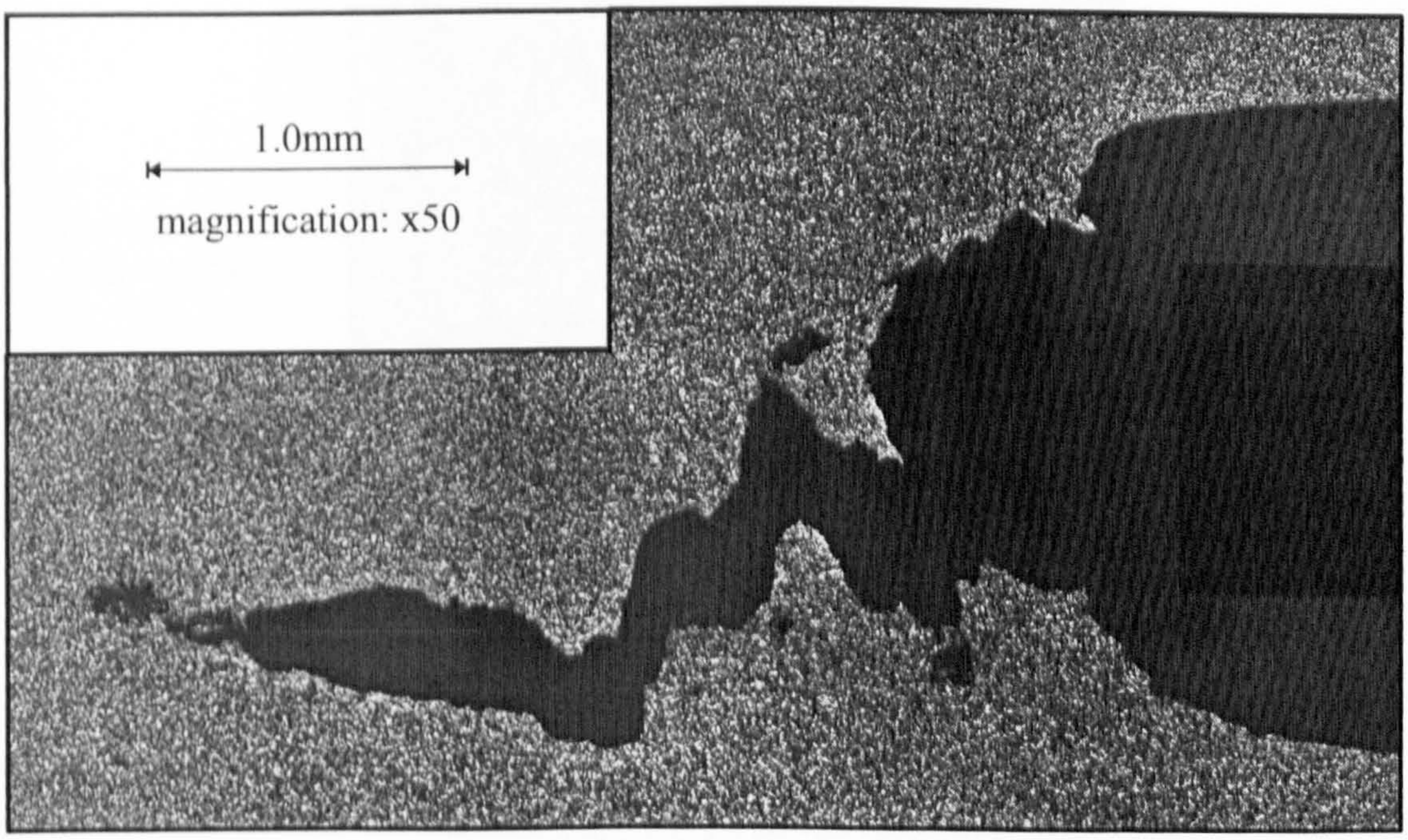

Figure 3.50b. Mixed Mode I/II (α=22.5°) Loading : Crack Propagation via Microvoid Coalescence (SEN specimen, B=10mm, W=80mm, a_o/W=0.5)

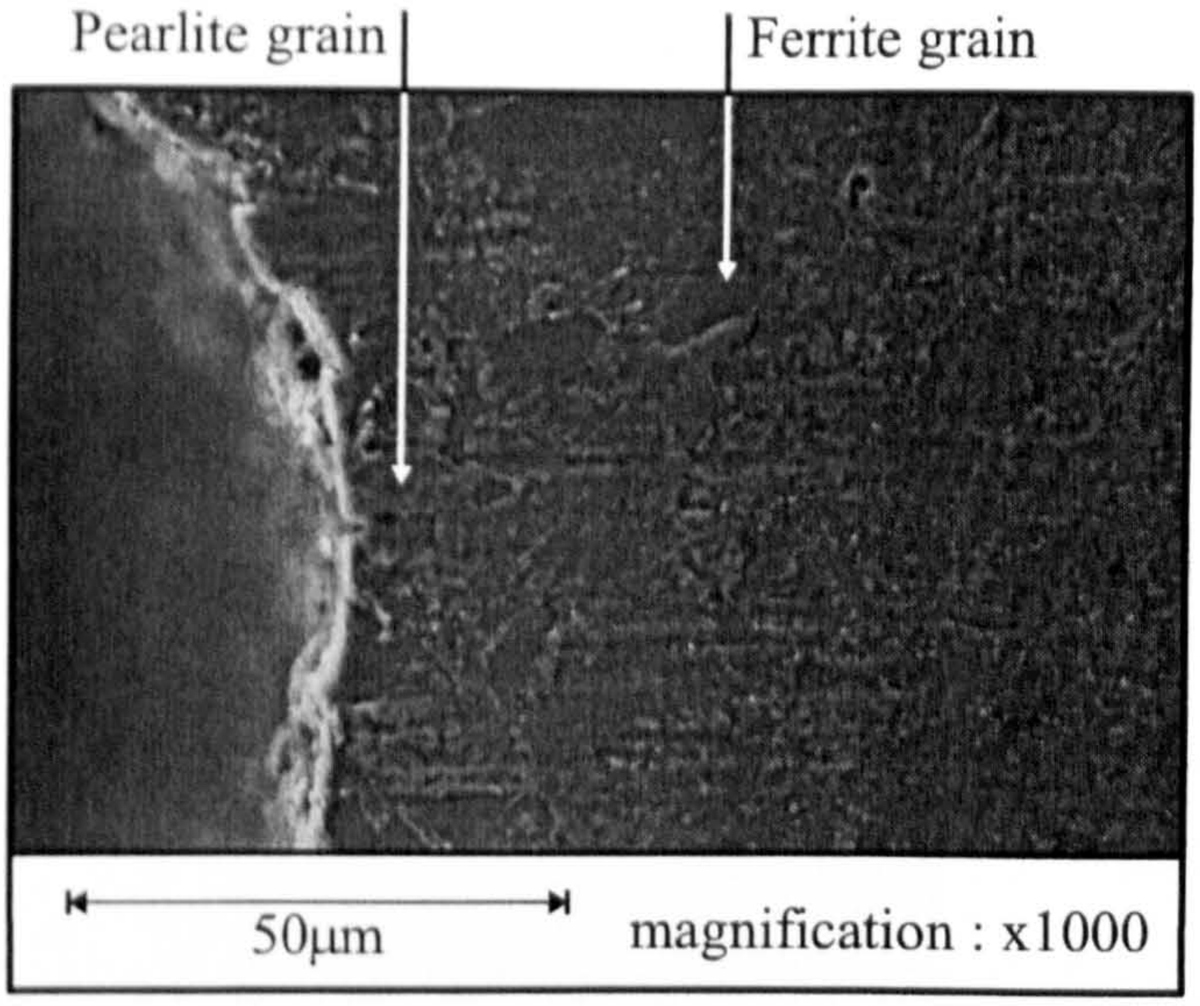

Figure 3.51. Deformation in the Vicinity of the Sharpened Region of the Blunted Notch (α=22.5° for B=10mm, W=20mm and B=20mm, W=80mm)

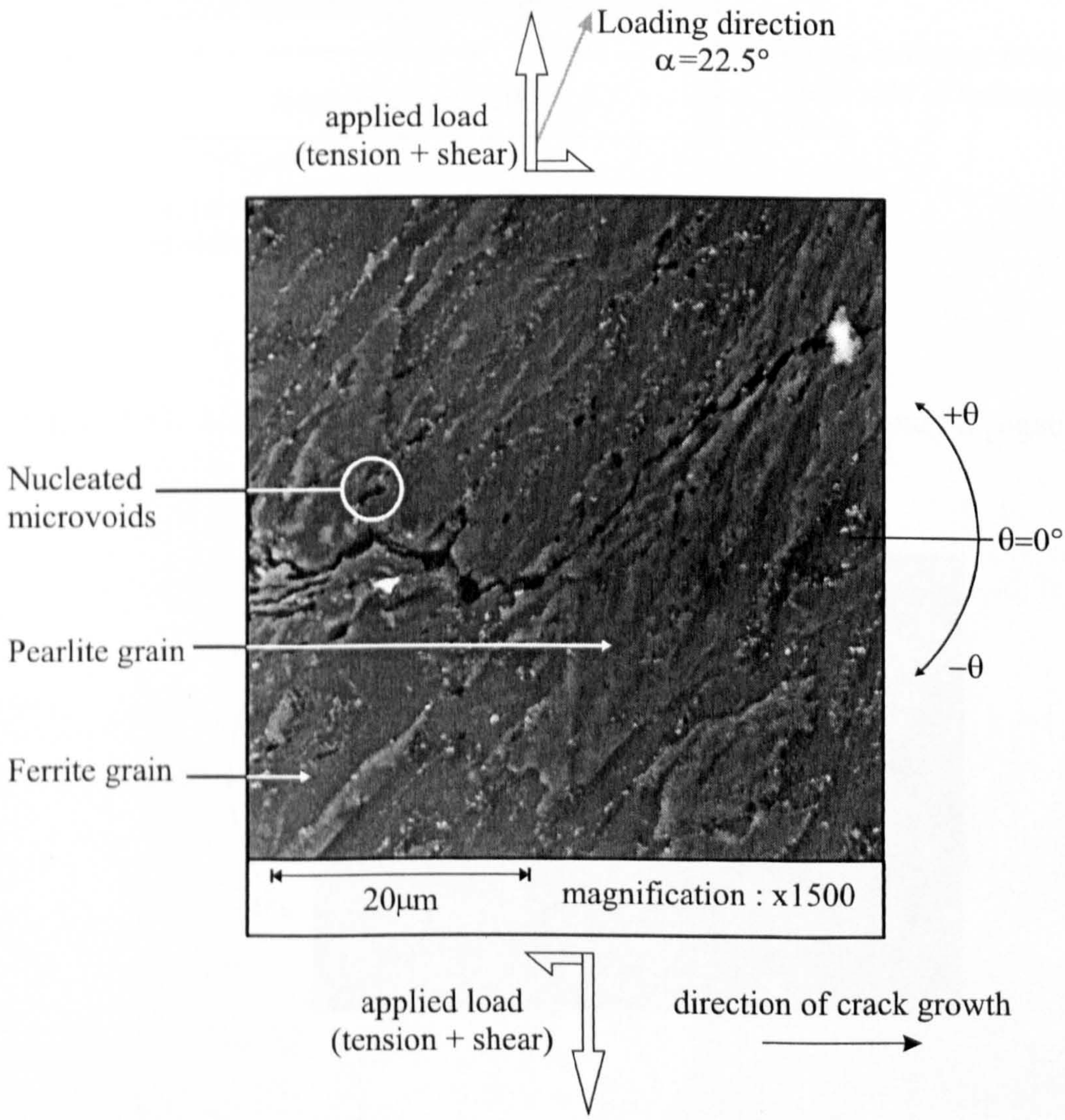

Figure 3.52. Crack Propagation Path and Microvoid Formation for Mixed Mode I/II Loading (α=22.5° for B=10mm, W=20mm)

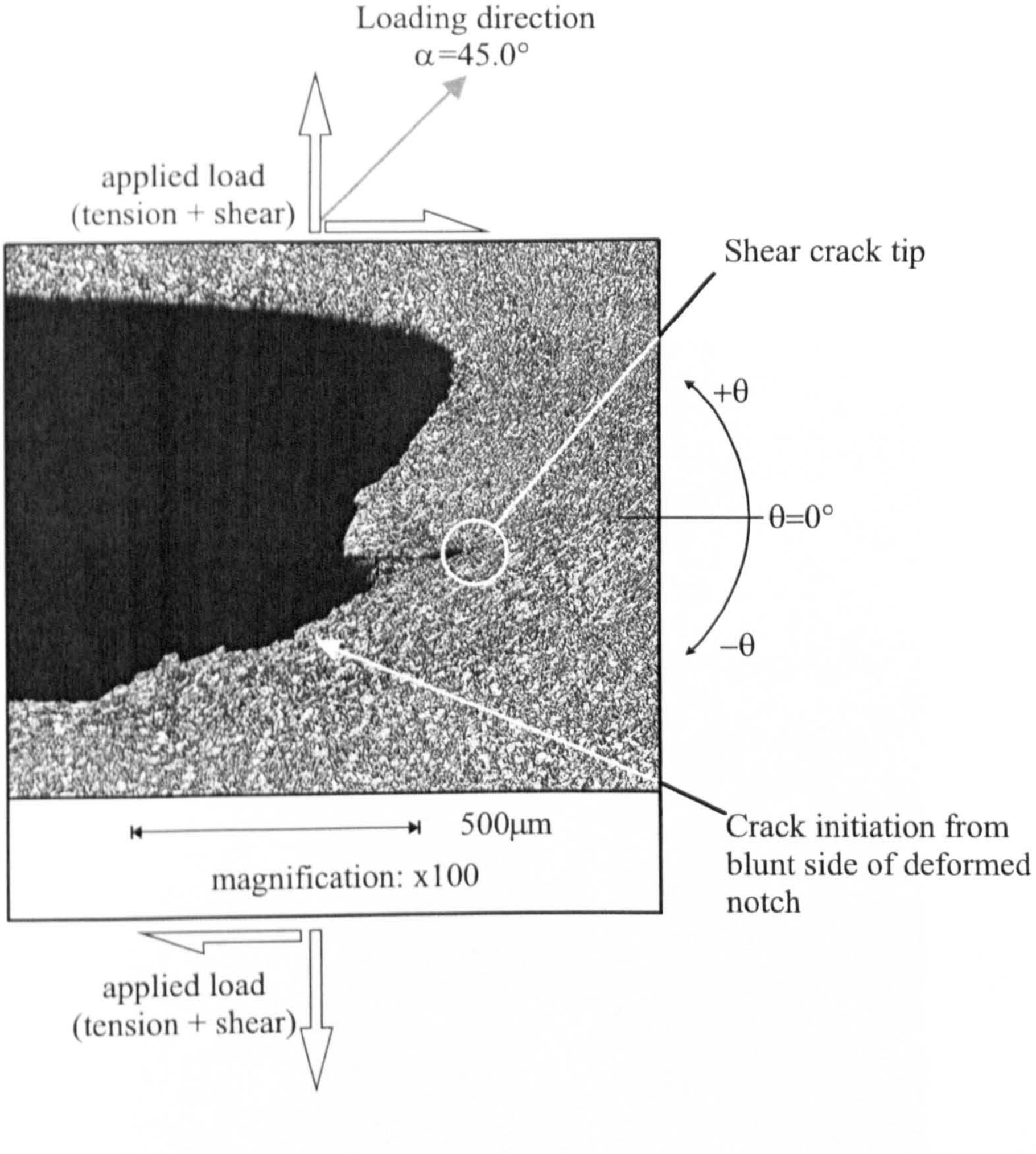

Figure 3.53. Mixed Mode I/II (α=45.0°) Shear Crack Initiation and Propagation

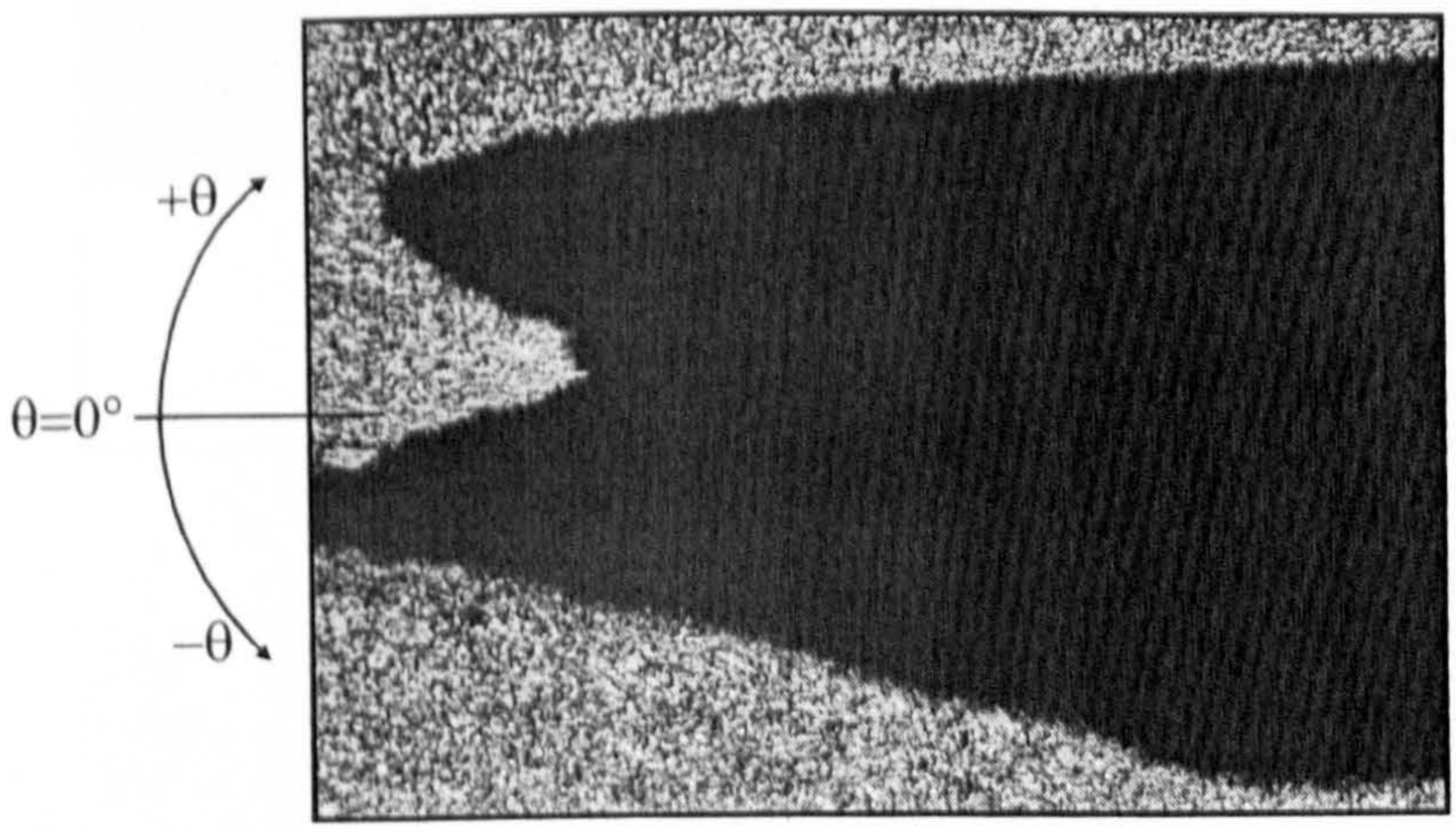

Figure 3.54. Mixed Mode I/II (α=67.5°) Crack Profile

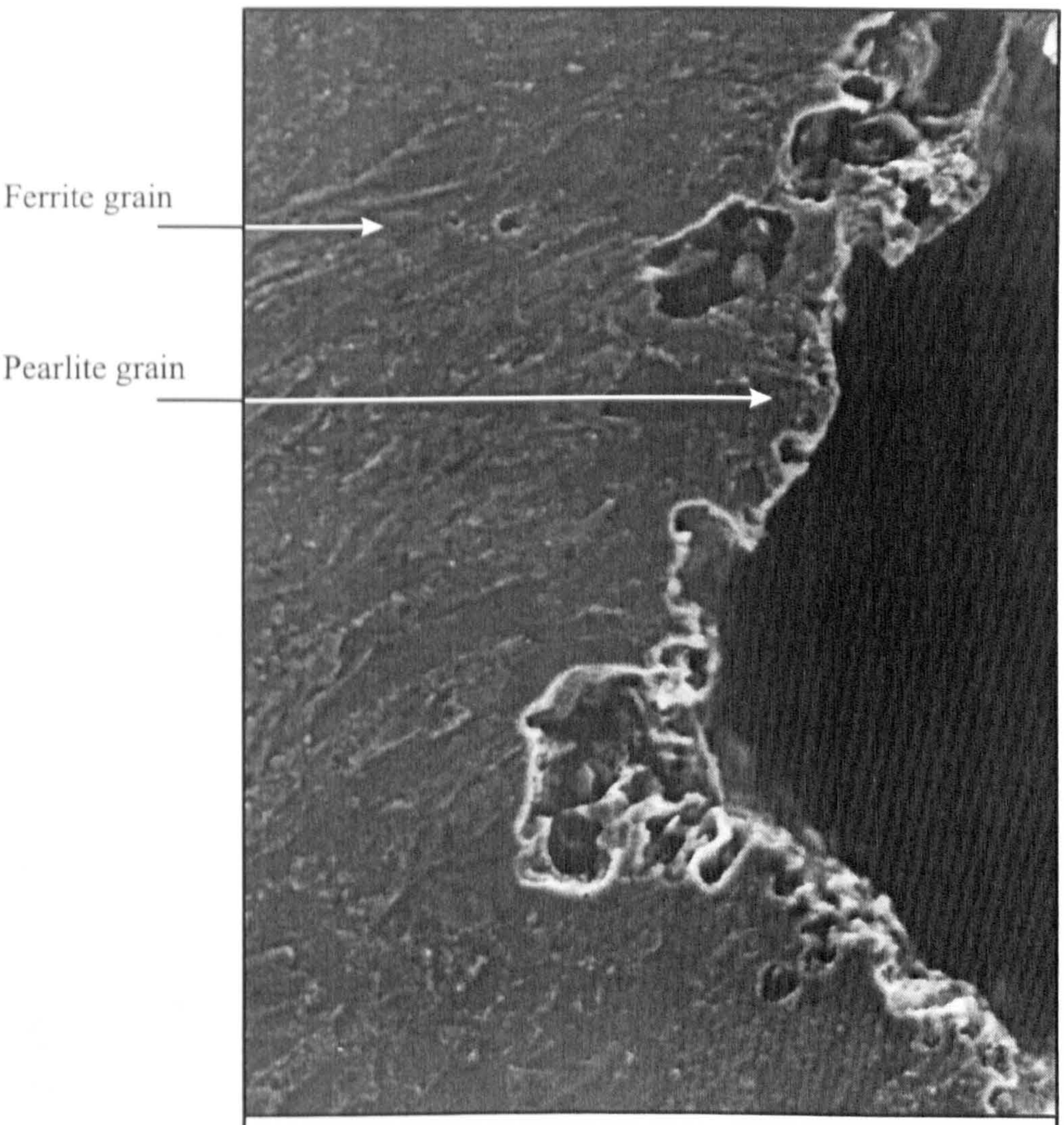

Figure 3.55. Microcracking and Deformation in the Vicinity of the Sharpened Region of the Blunted Notch (α=67.5°)

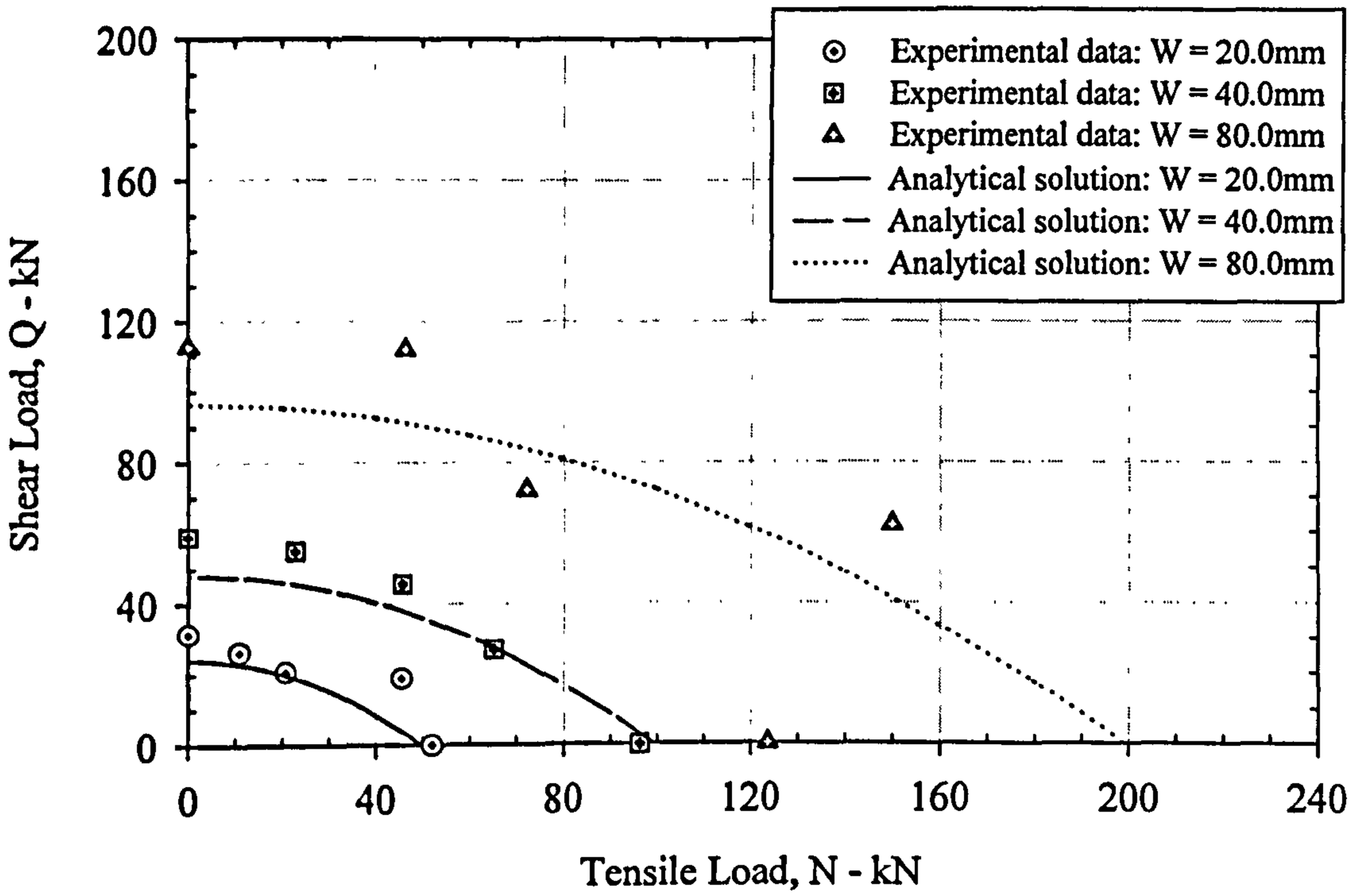

Figure 3.56a. Mixed Mode I/II Experimental Limit Loads, $a_o/W=0.5$
(Effect of specimen width for constant thickness, B=10.0mm)

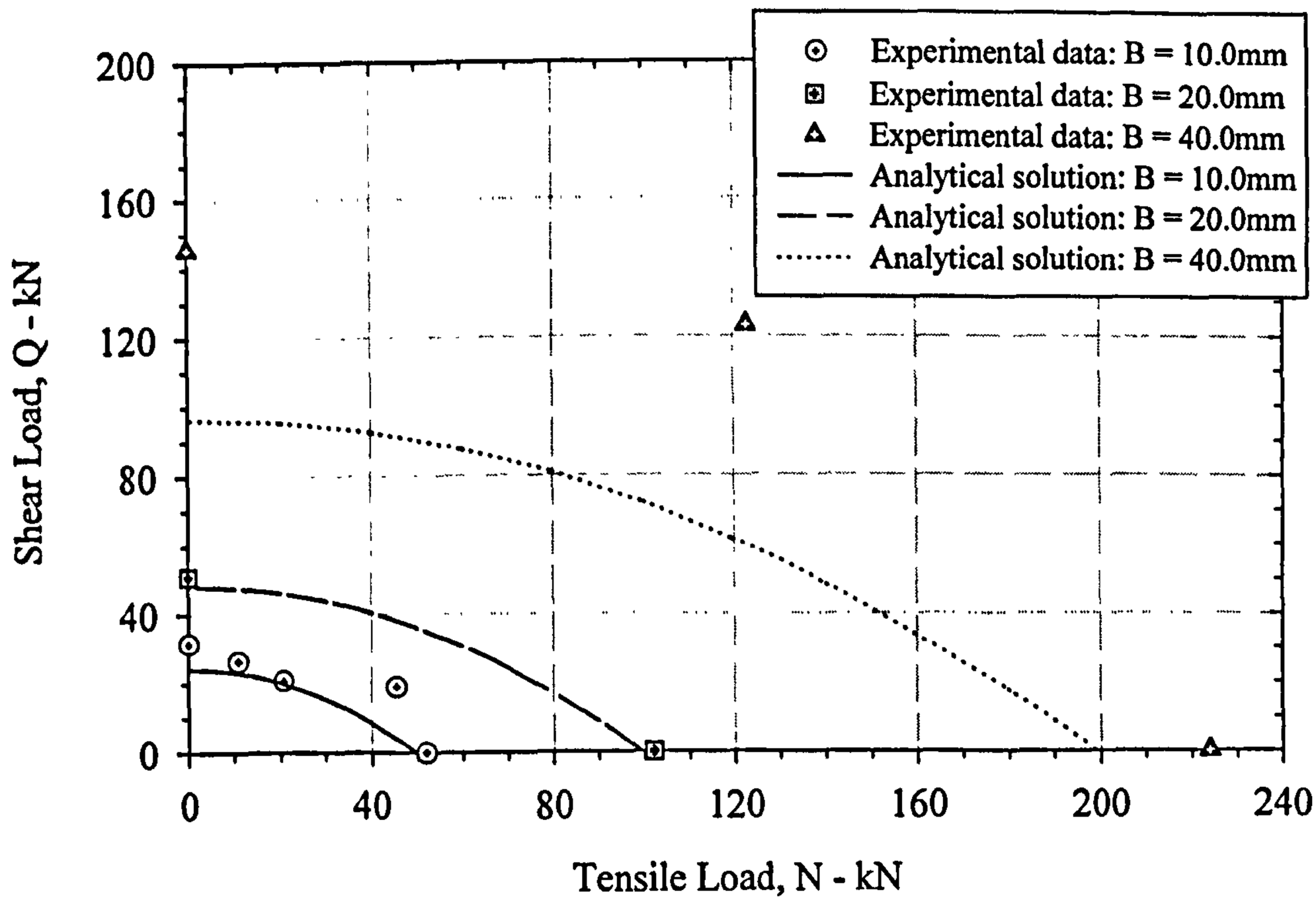

Figure 3.56b. Mixed Mode I/II Experimental Limit Loads, $a_o/W=0.5$
(Effect of specimen thickness for constant width, W=20.0mm)

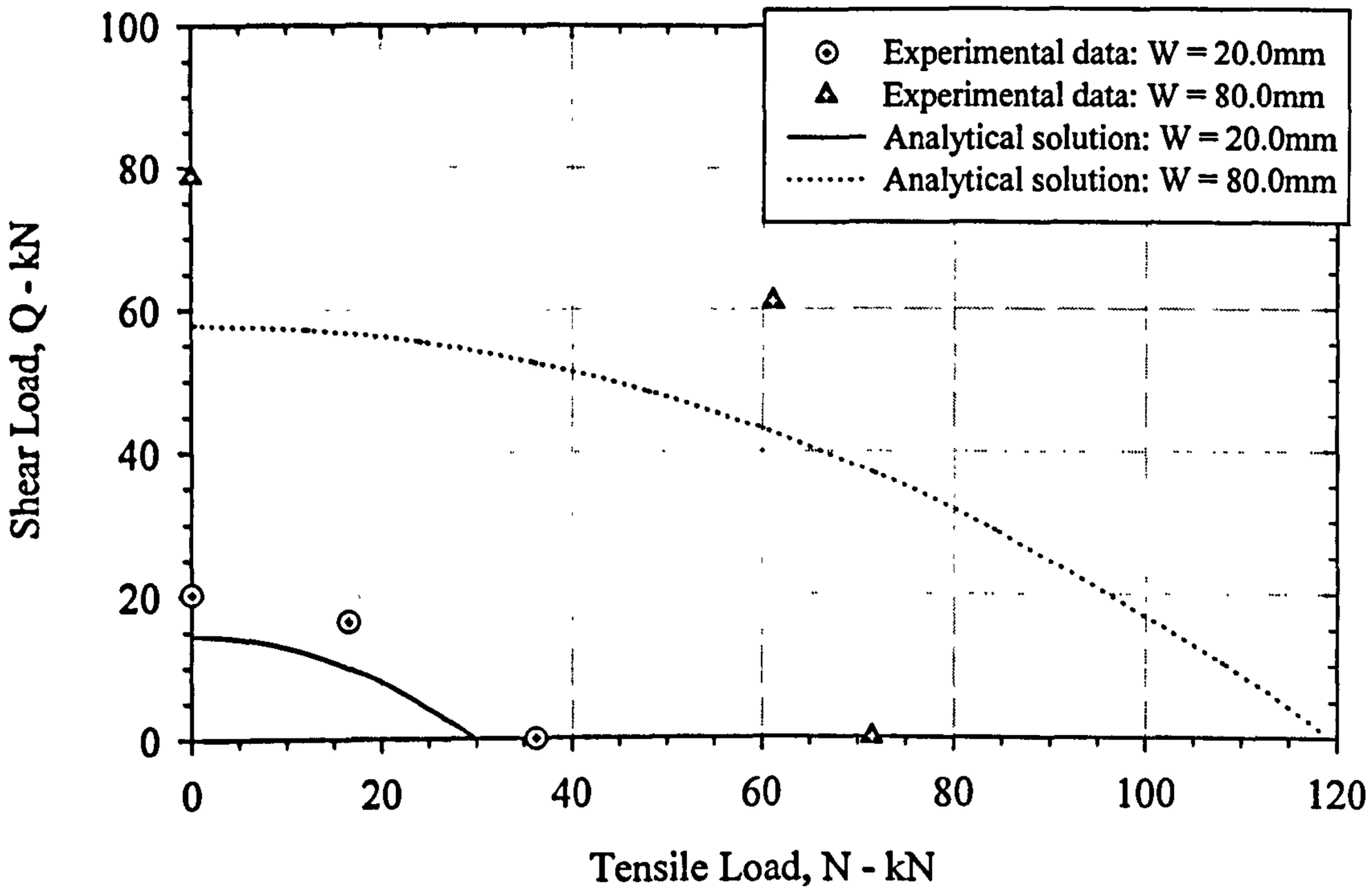

Figure 3.57a. Mixed Mode I/II Experimental Limit Loads, $a_o/W=0.7$
(Effects of specimen width for constant thickness, B=10.0mm)

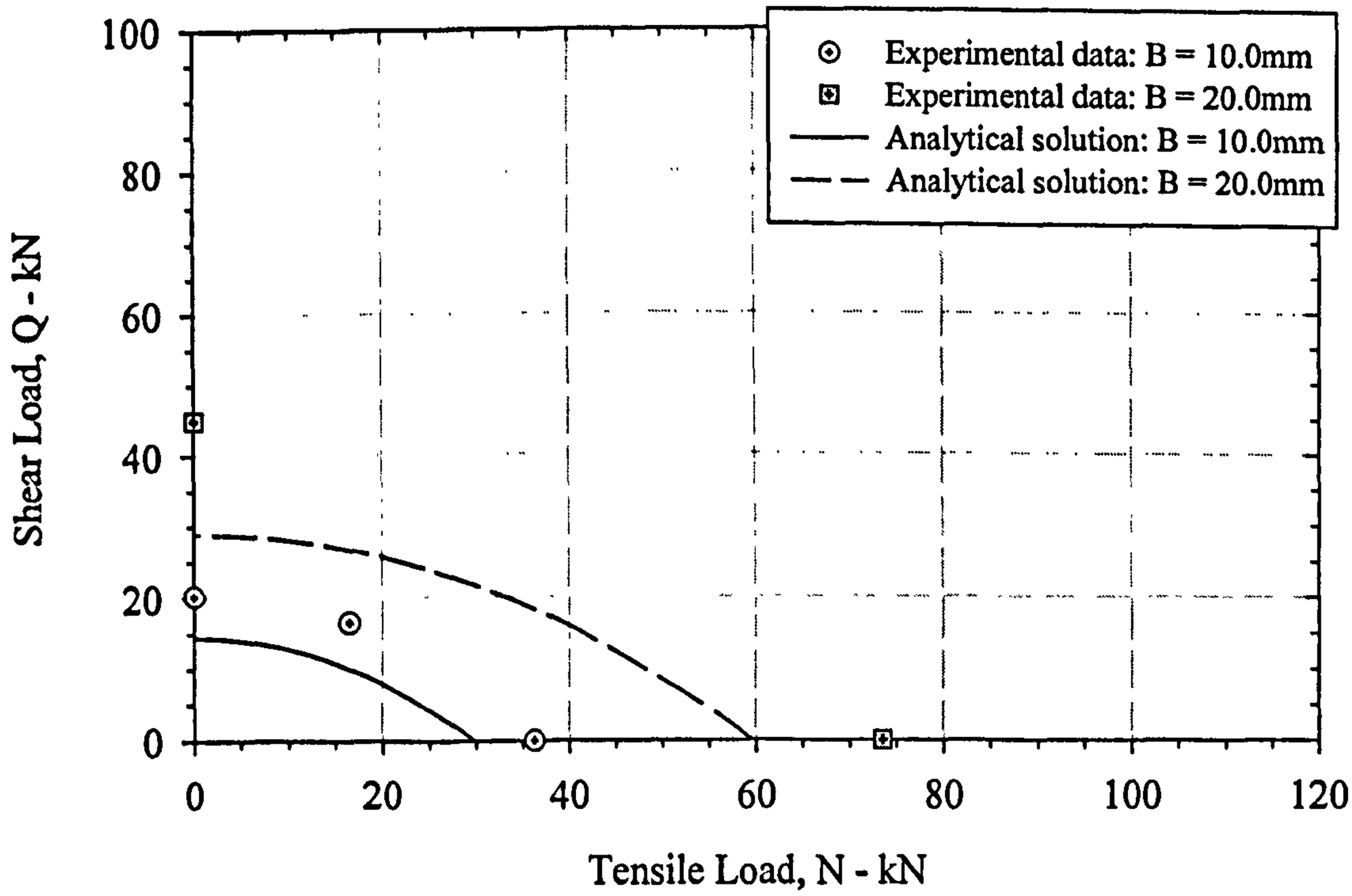

Figure 3.57b. Mixed Mode I/II Experimental Limit Loads, $a_o/W=0.7$
(Effect of specimen thickness for constant width, W=20.0mm)

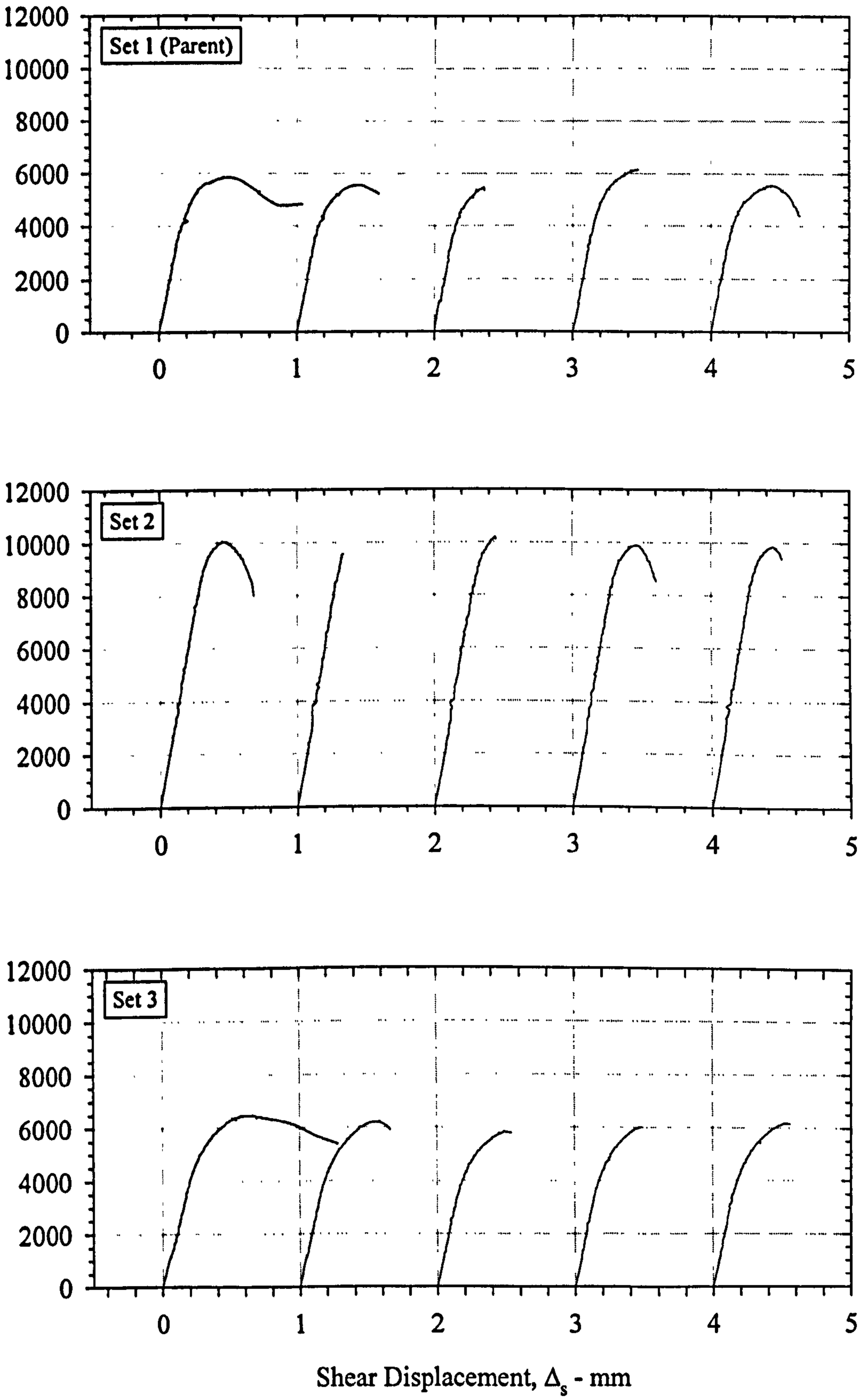

Figure 3.58. Shear Load vs. Shear Displacement Curves

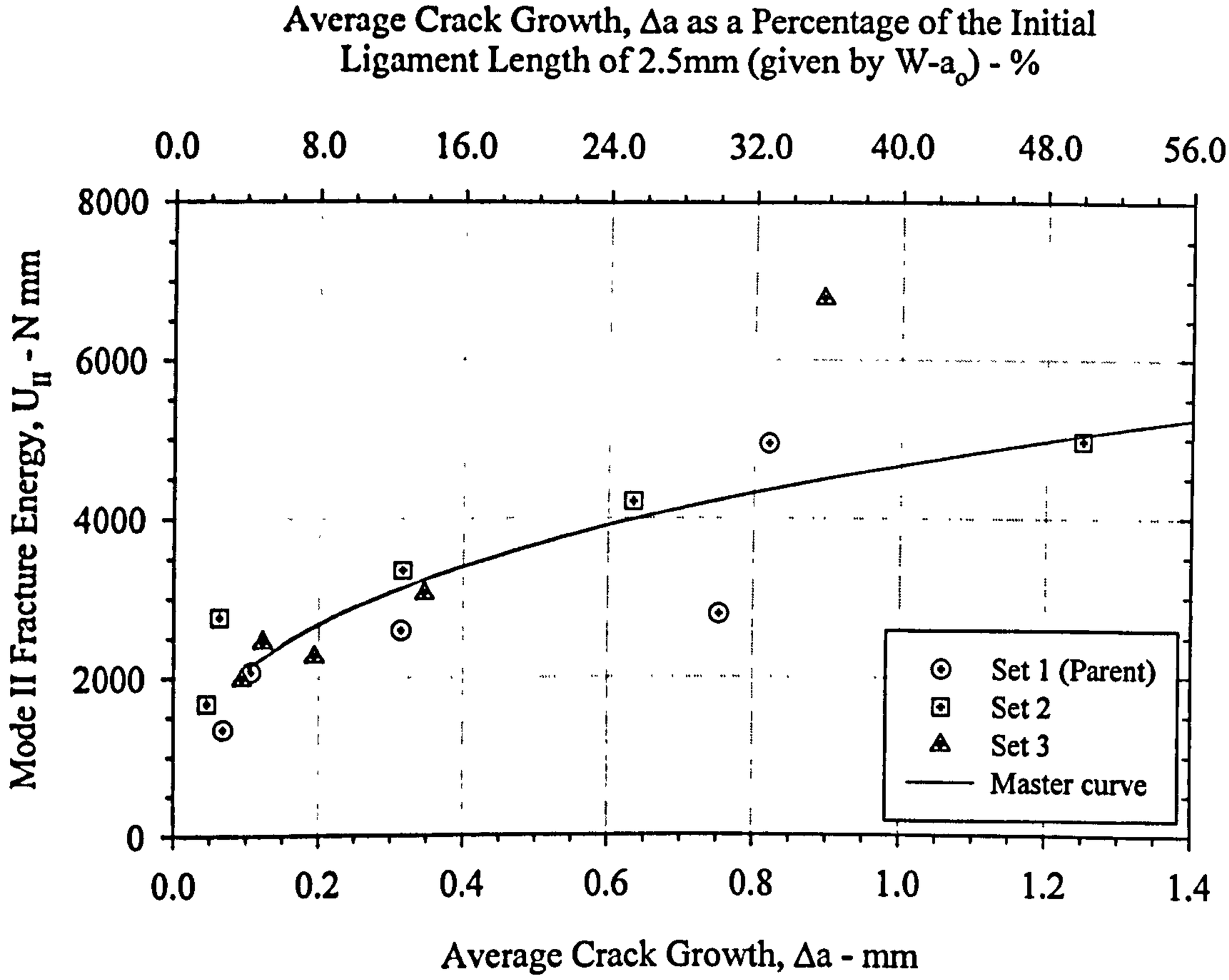

Figure 3.59. Mode II R-Curves : Effect of Heat Treatment.

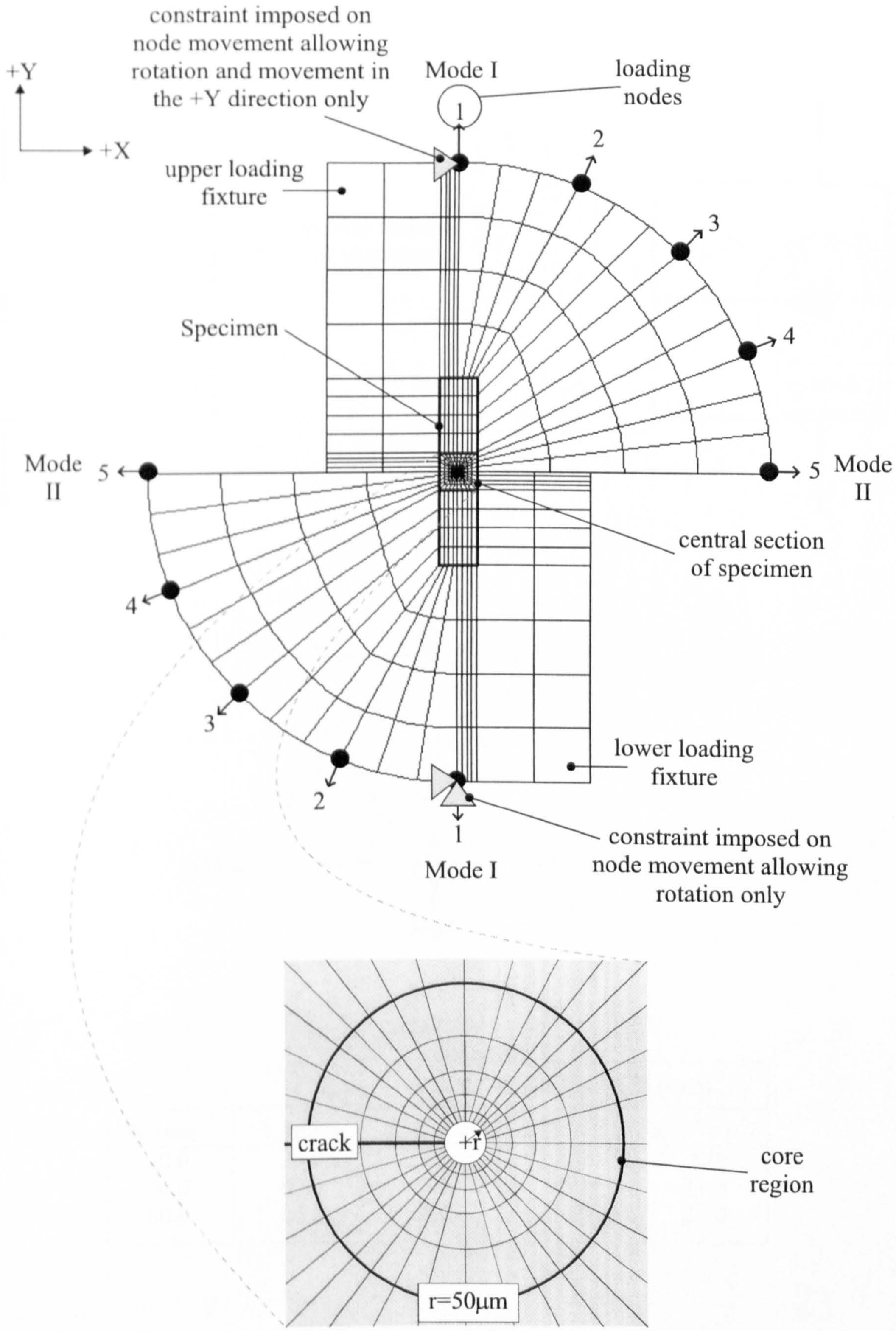

'key-hole' design of crack tip

Figure 4.1. Finite Element Mesh for Mixed Mode I/II Analyses
(for dimensions of core region, see figure 4.2)

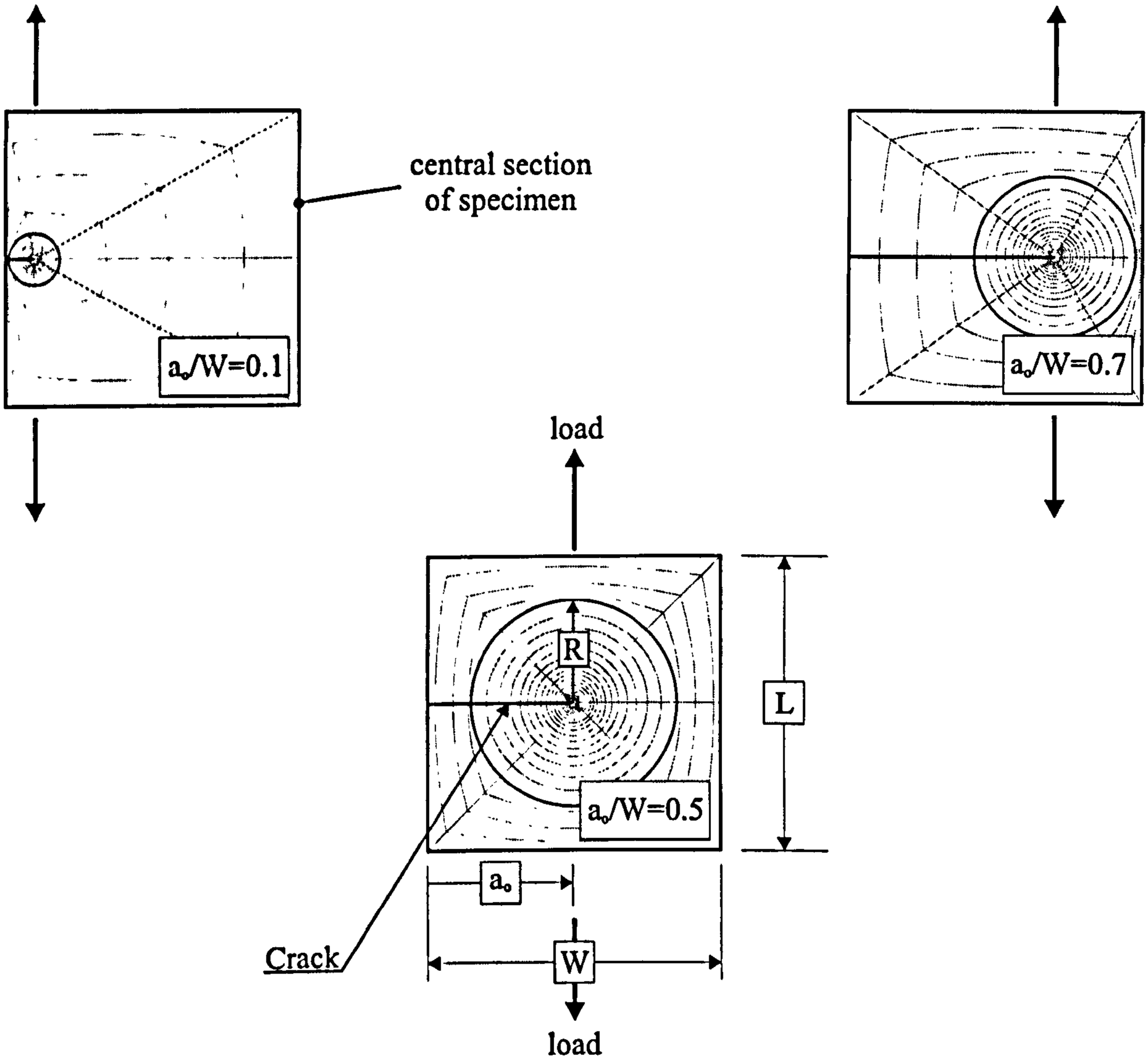

		Core region radius, R (mm)		
W (mm)	L (mm)	$a_o/W = 0.1$	$a_o/W = 0.5$	$a_o/W = 0.7$
20.0	20.0	1.5	8.0	5.0
40.0	40.0	3.5	14.0	11.0
80.0	80.0	7.0	34.0	22.0

Figure 4.2. Finite Element Mesh Design for Core Region

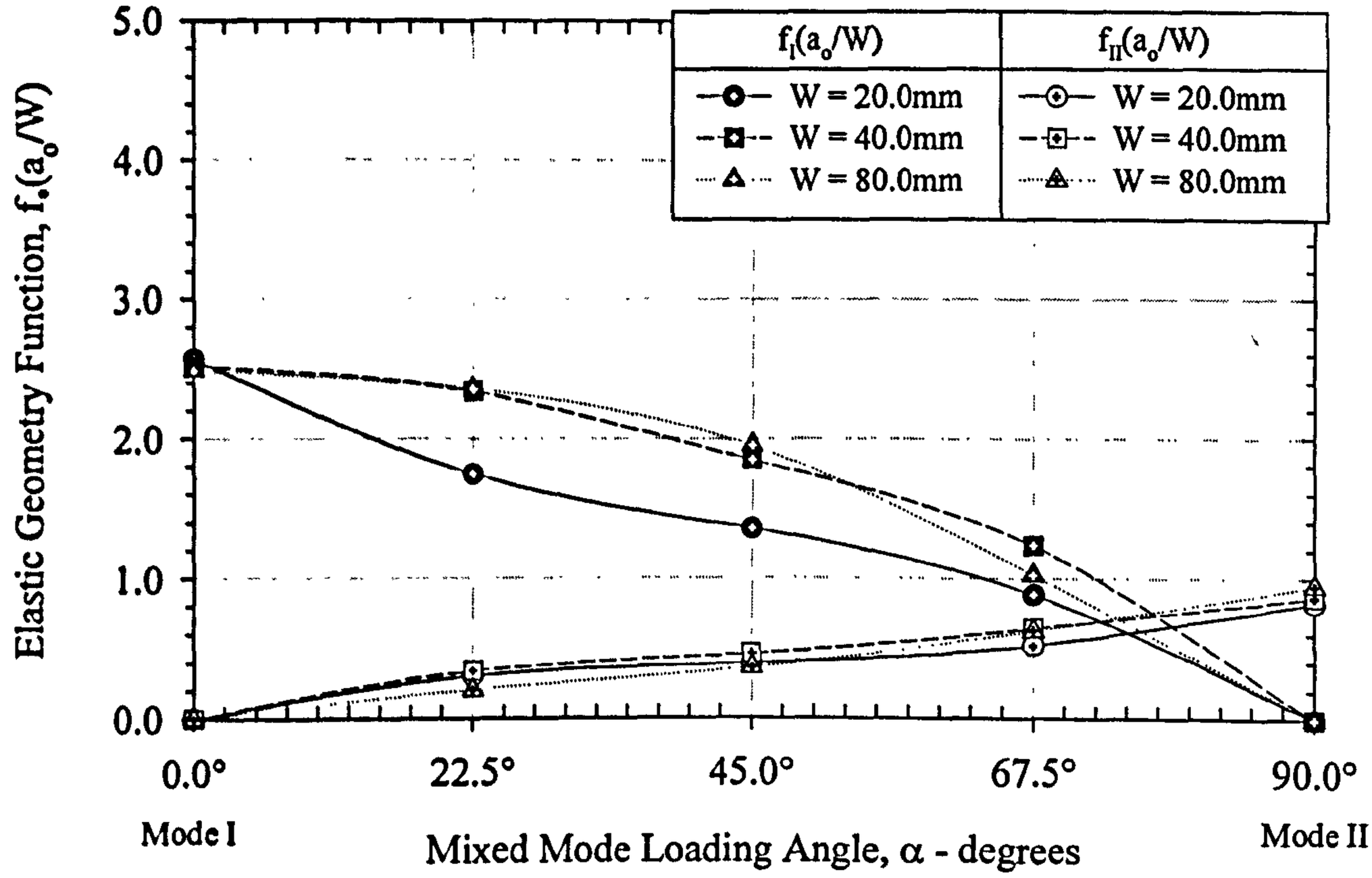

Figure 4.3. Mixed Mode Linear Elastic Geometry Functions, $a_o/W = 0.1$
(plane strain analyses)

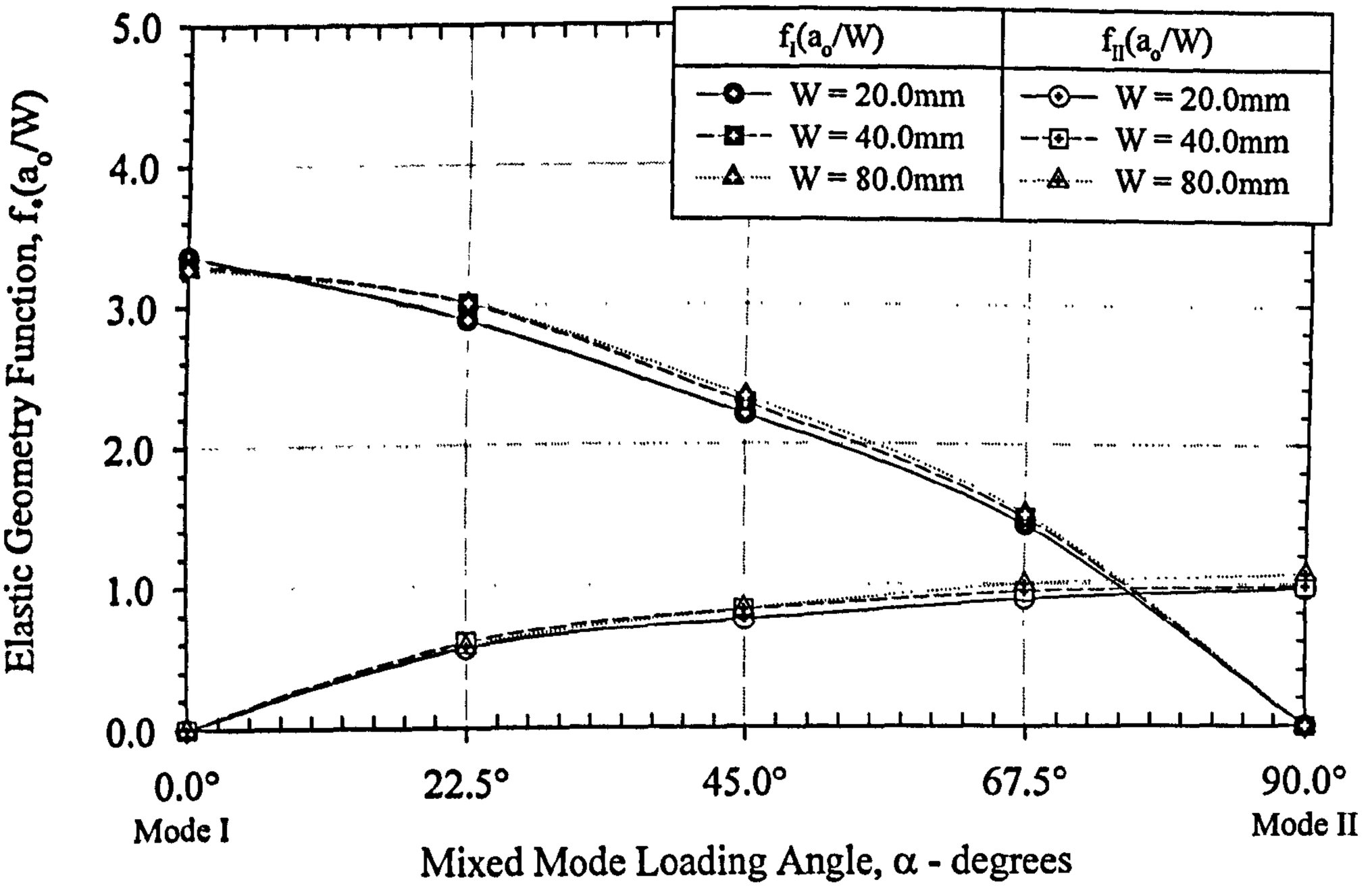

Figure 4.4. Mixed Mode Linear Elastic Geometry Functions, $a_o/W = 0.5$
(plane strain analyses)

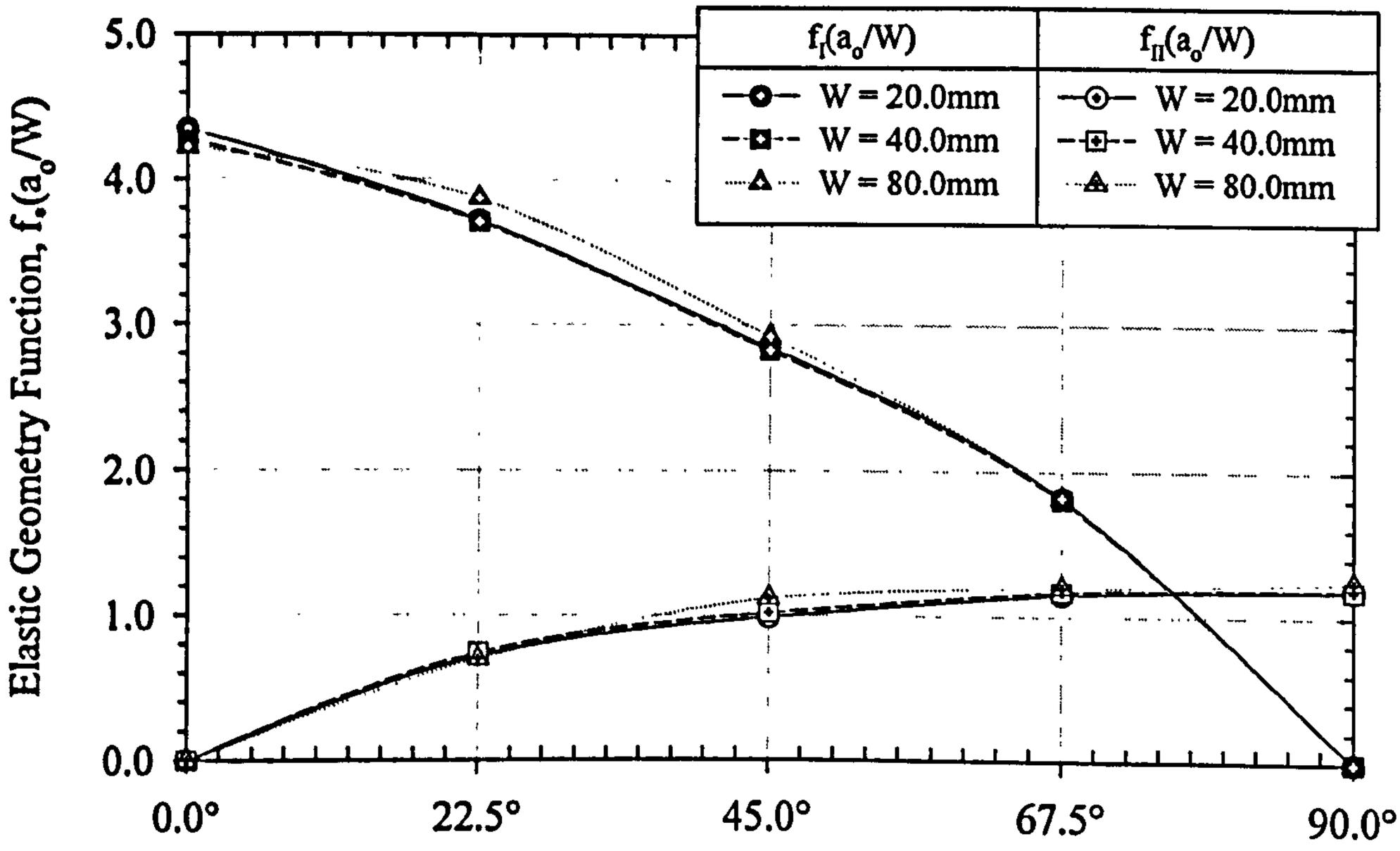

Figure 4.5. Mixed Mode Linear Elastic Geometry Functions, $a_o/W = 0.7$
(plane strain analyses)

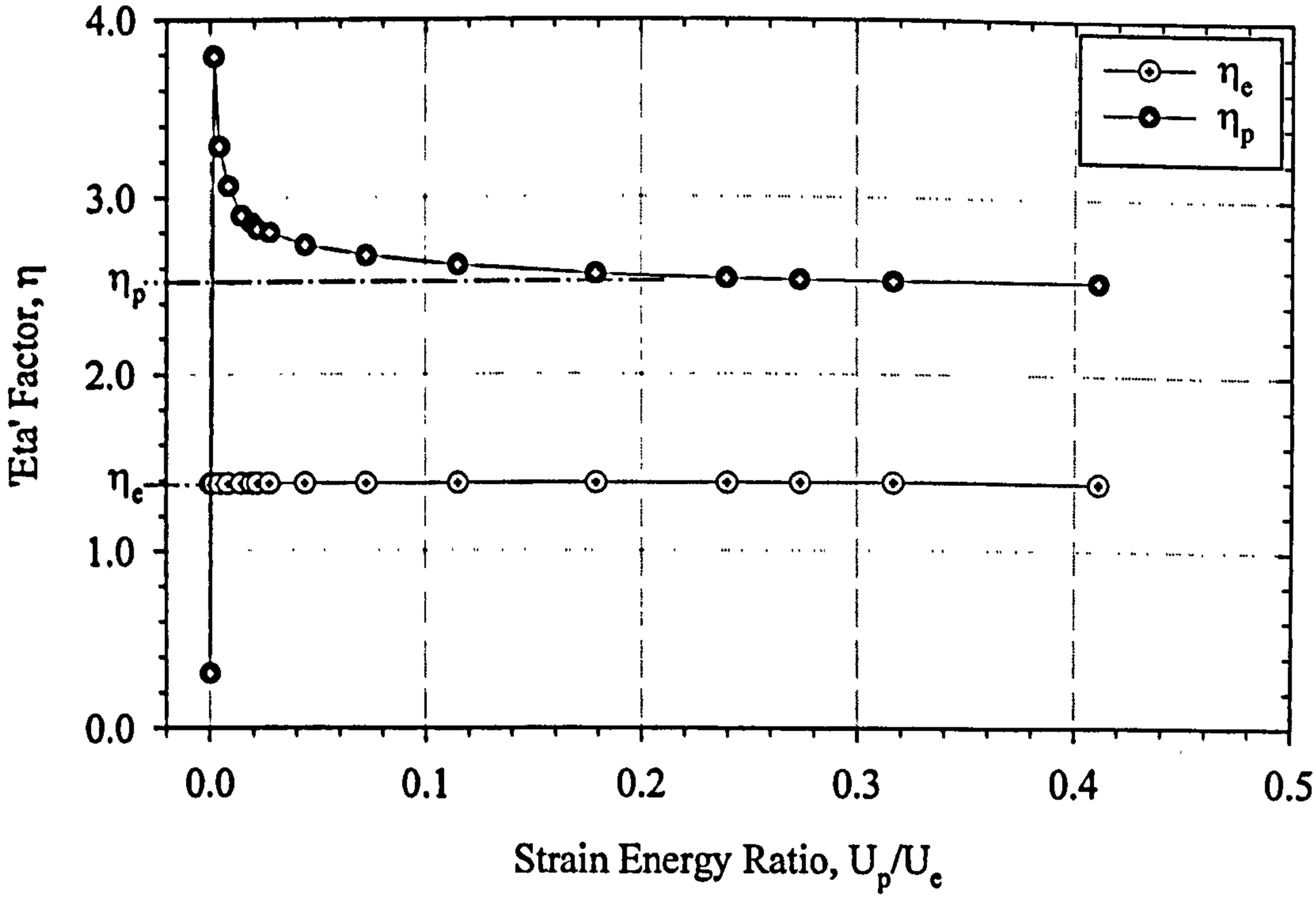

Figure 4.6. 'Eta' Factor Development with Increasing Plasticity for Mode I Loading
(plane strain analyses, W = 40.0mm, $a_o/W = 0.5$)

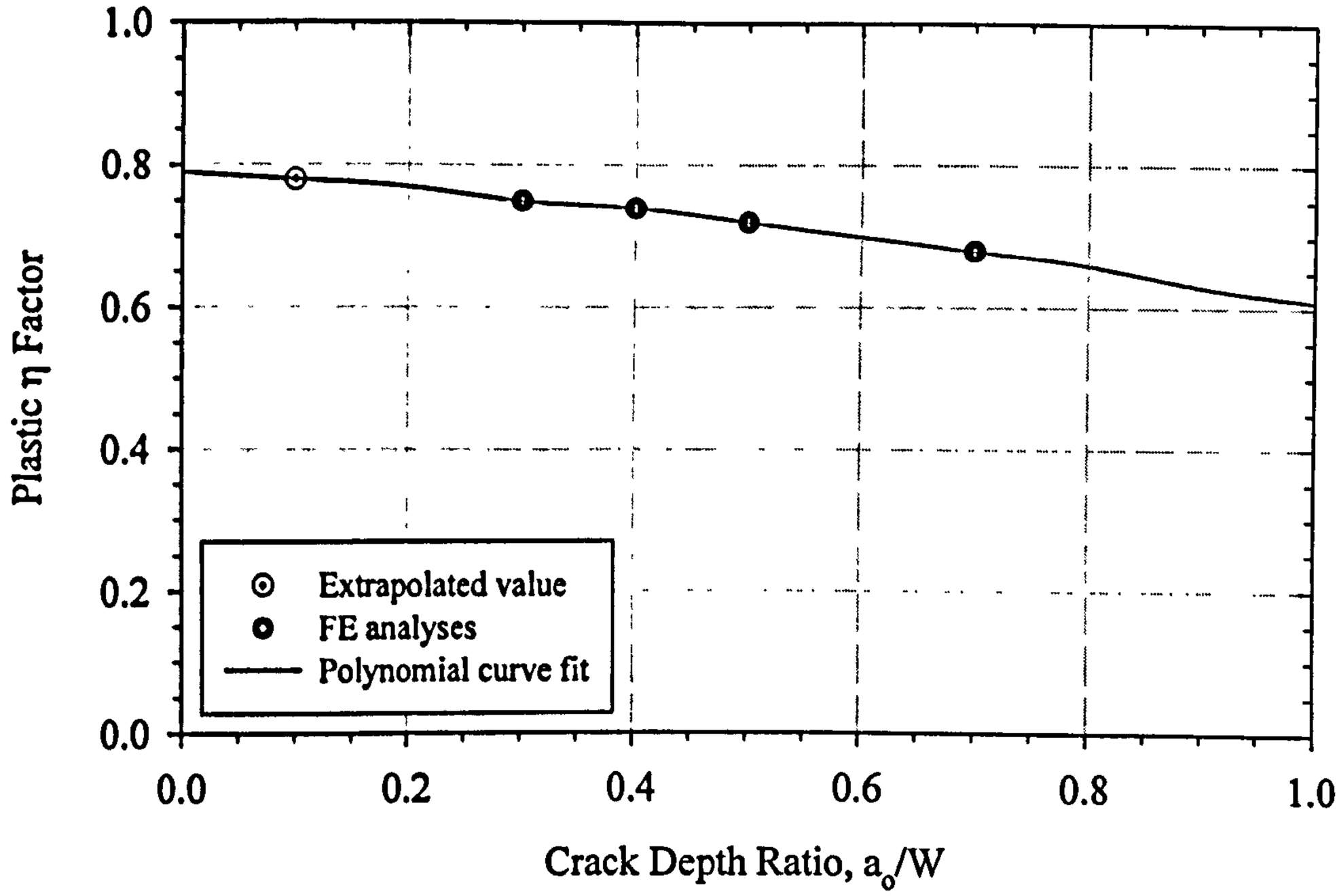

Figure 4.7. Procedure For Calculating η_p Factors for $a_o/W=0.1$
(plane strain Mode II analyses shown for W=80mm)

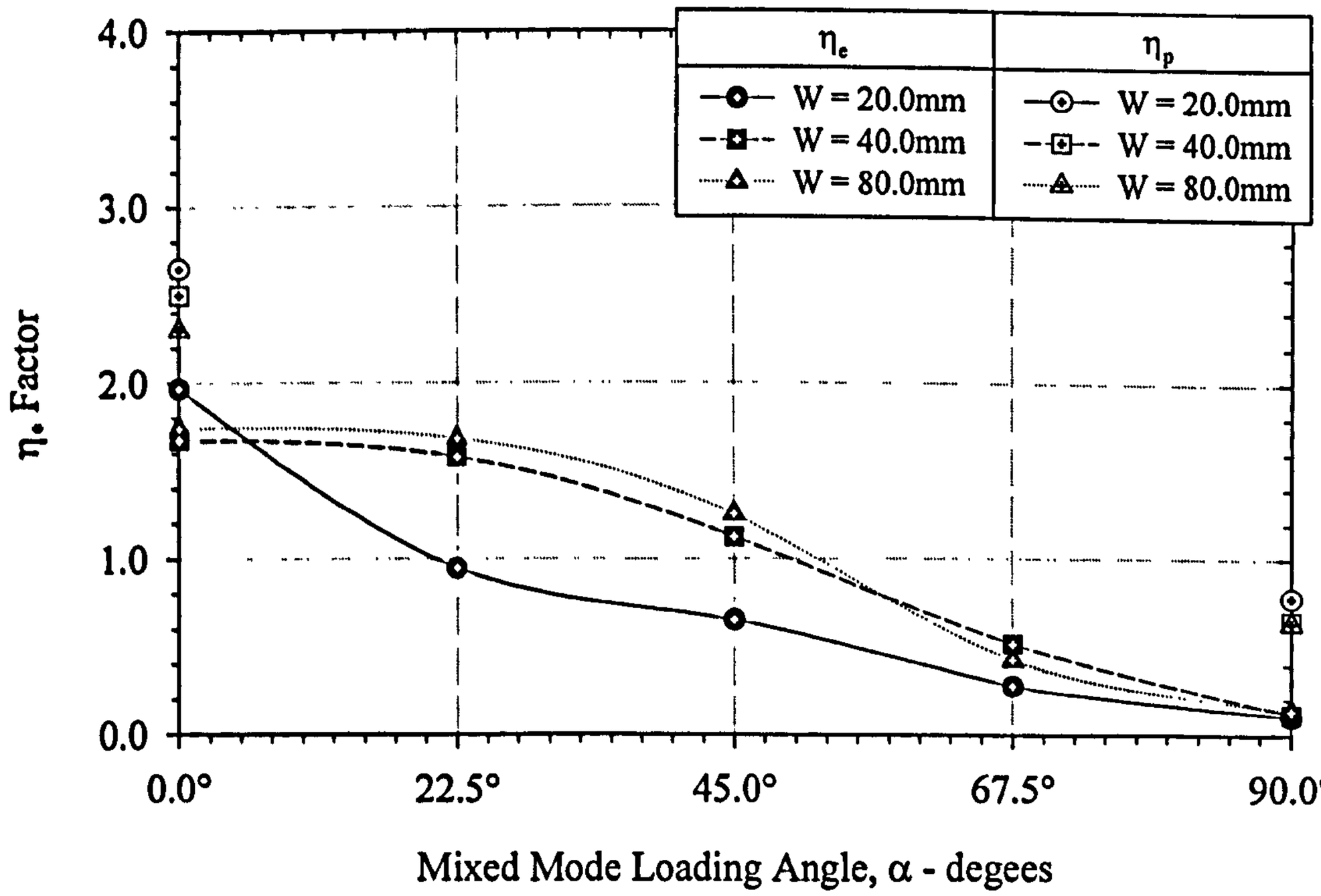

Figure 4.8. Mixed Mode Elastic and Elastic-Plastic η Factors, $a_o/W = 0.1$
(plane strain analyses)

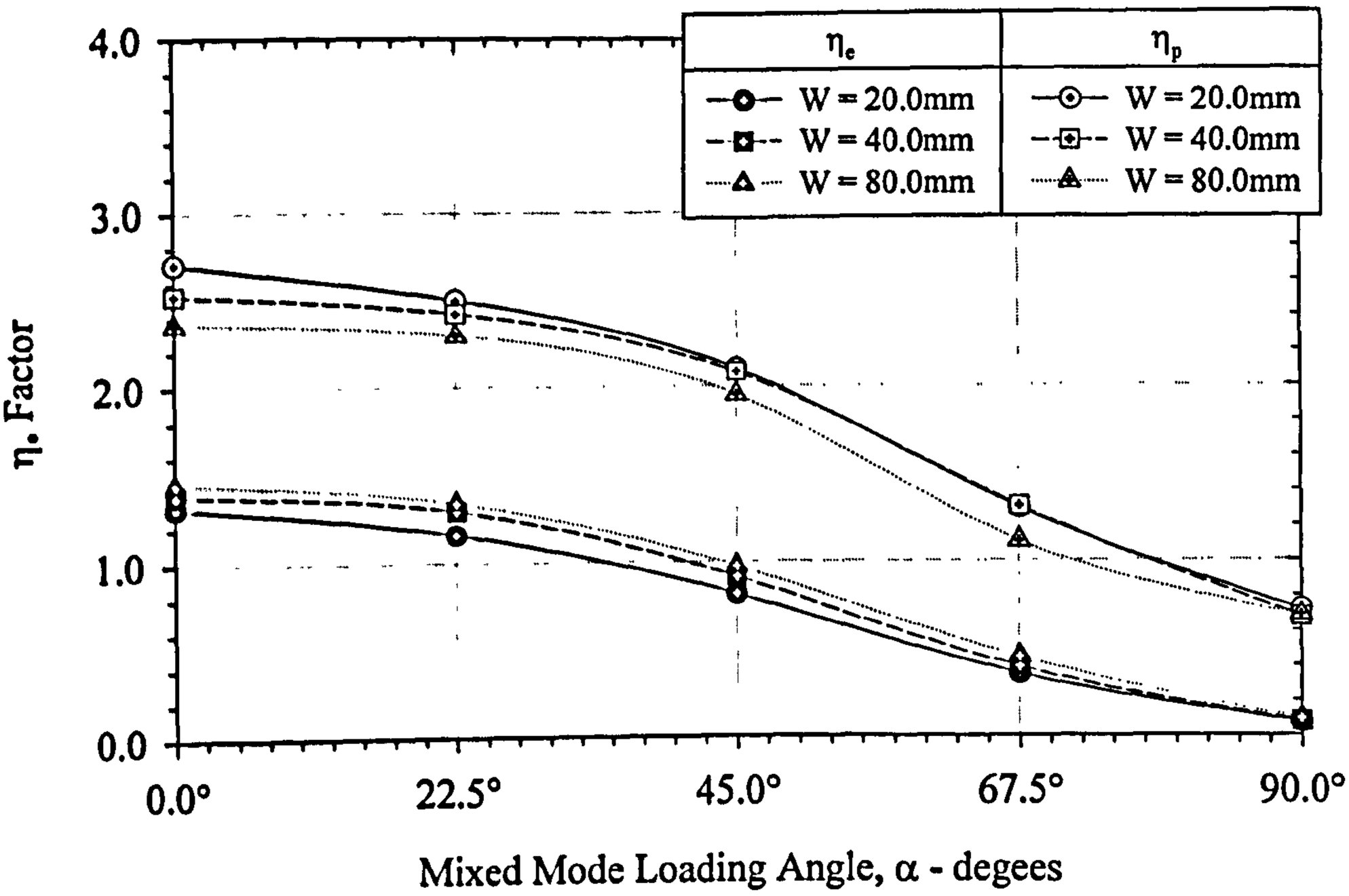

Figure 4.9. Mixed Mode Elastic and Elastic-Plastic η Factors, $a_o/W = 0.5$ (plane strain analyses)

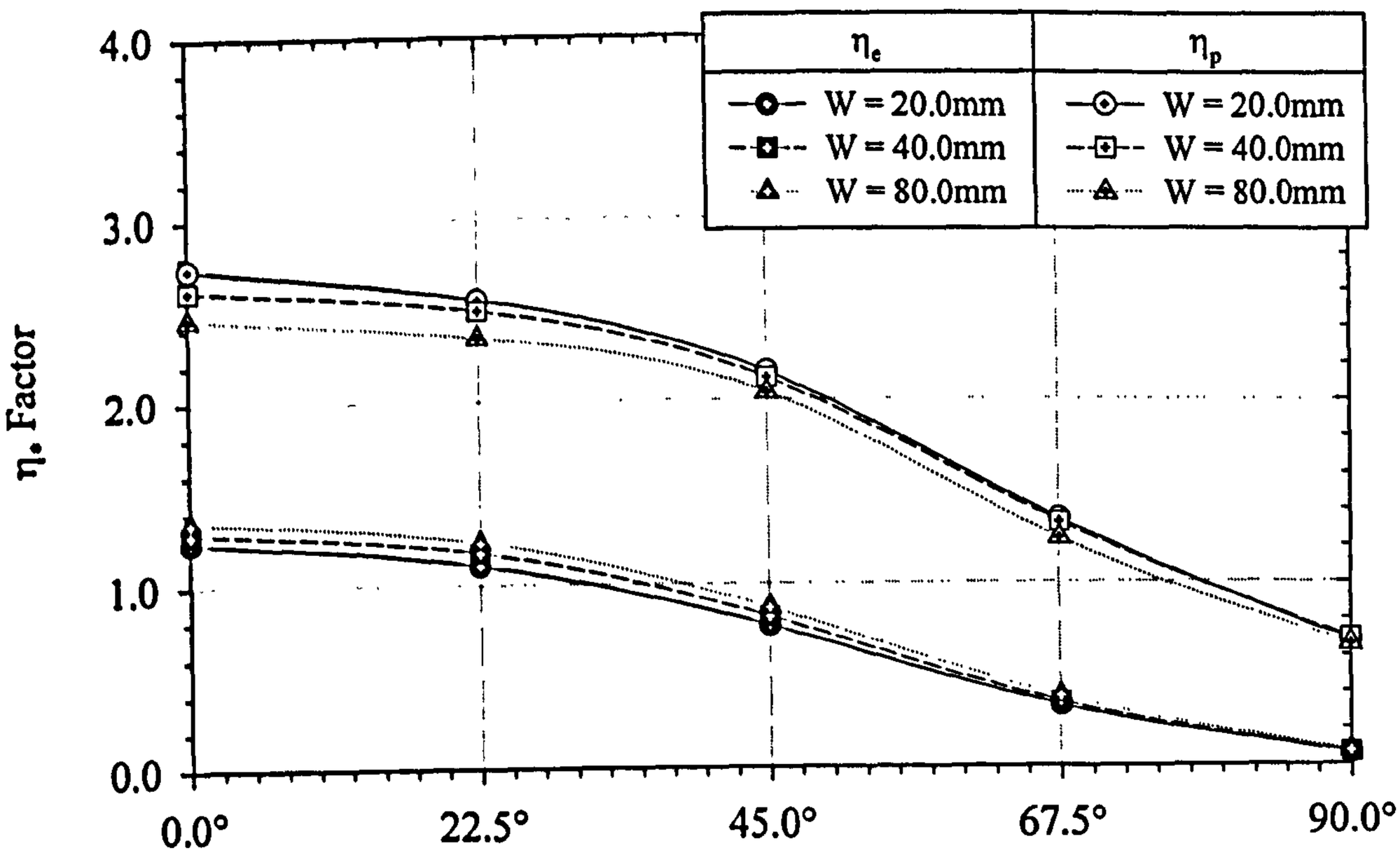

Figure 4.10. Mixed Mode Elastic and Elastic-Plastic η Factors, $a_o/W = 0.7$ (plane strain analyses)

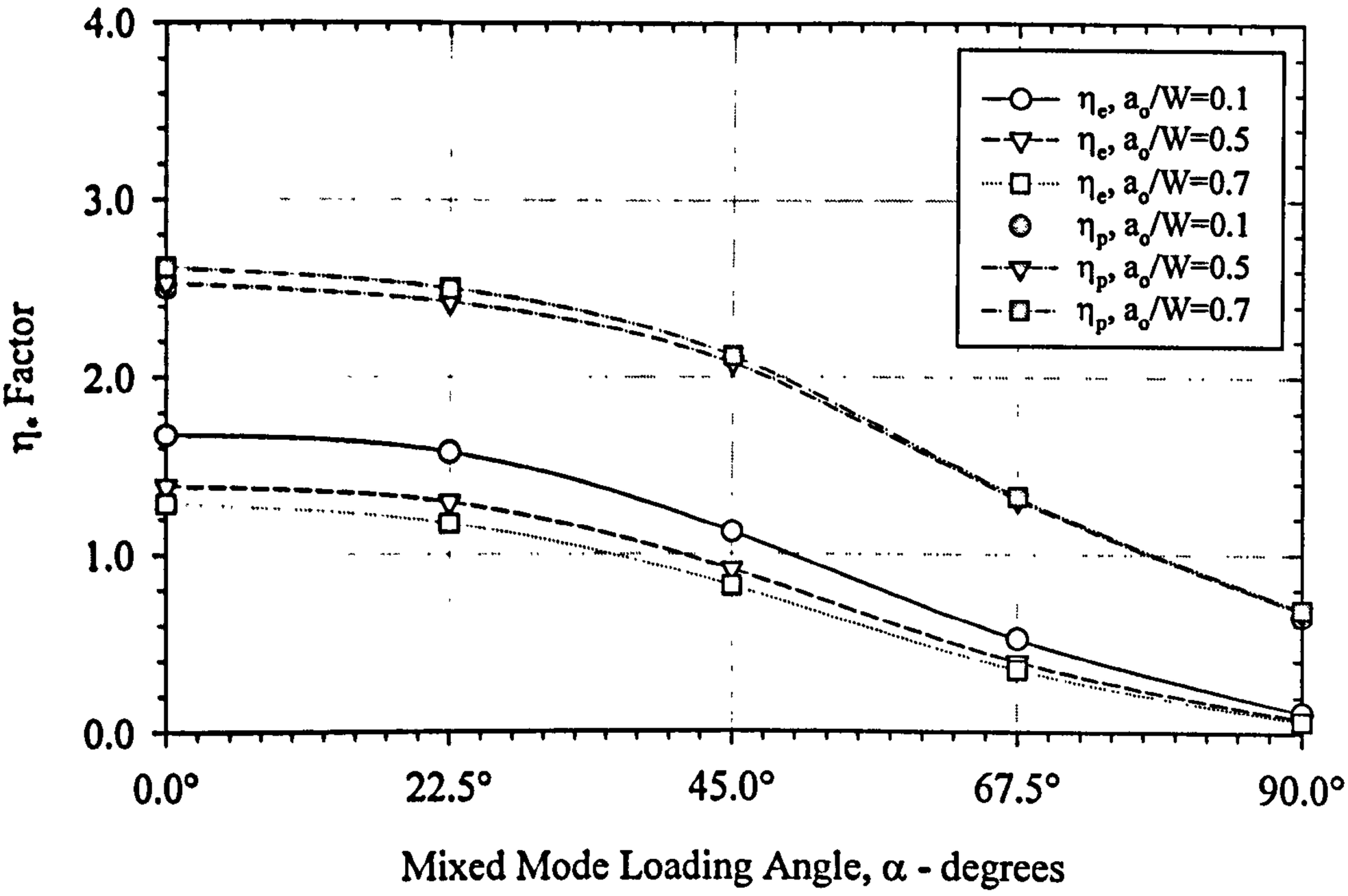

Figure 4.11. Comparison of Mixed Mode η Factors for Different a_o/W Ratios (Specimen width, W=40mm)

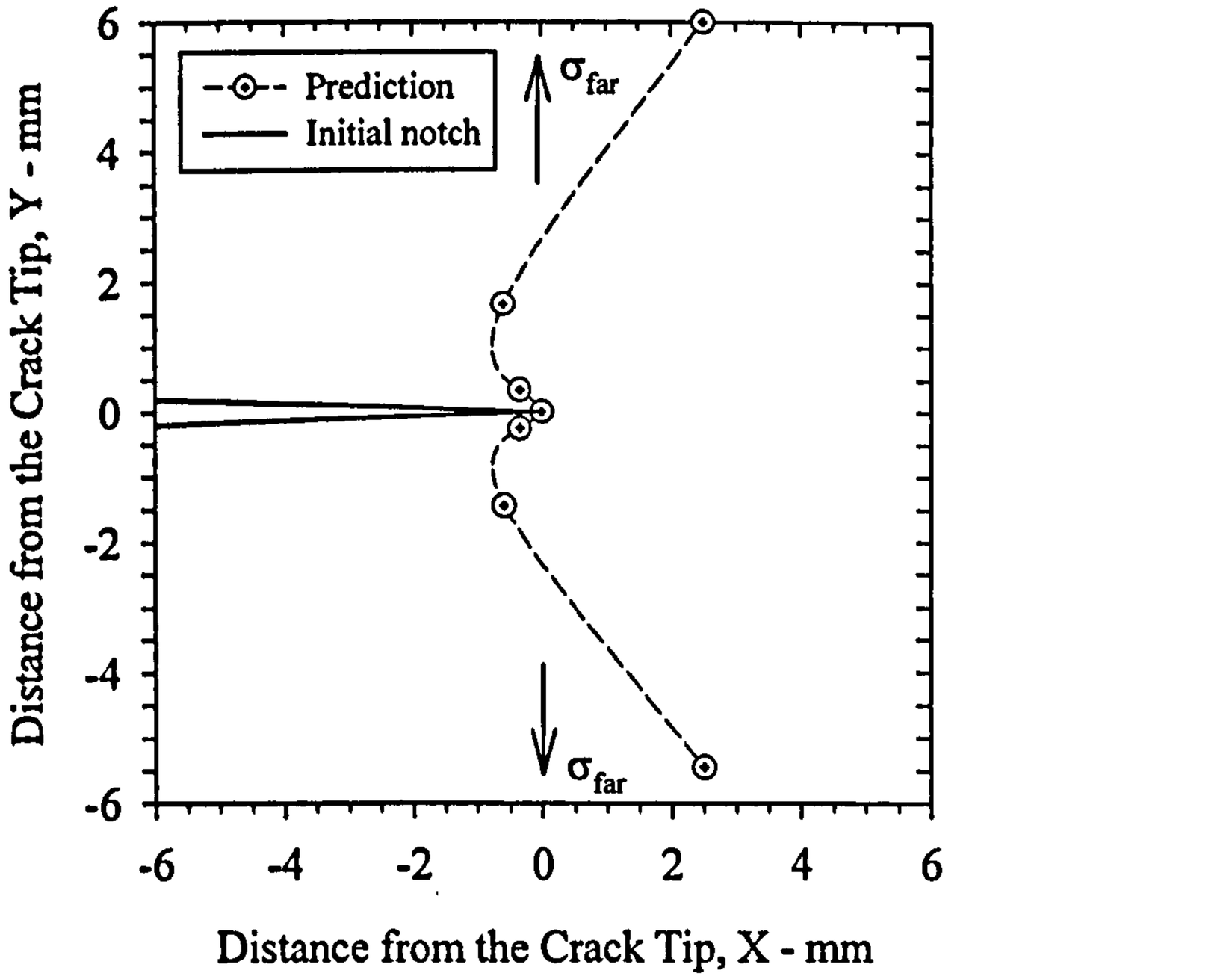

Figure 4.12. Mode I Loading : Crack Propagation Direction Predicted via the Direction of Maximum Equivalent Plastic Strain for Incremented Load Steps

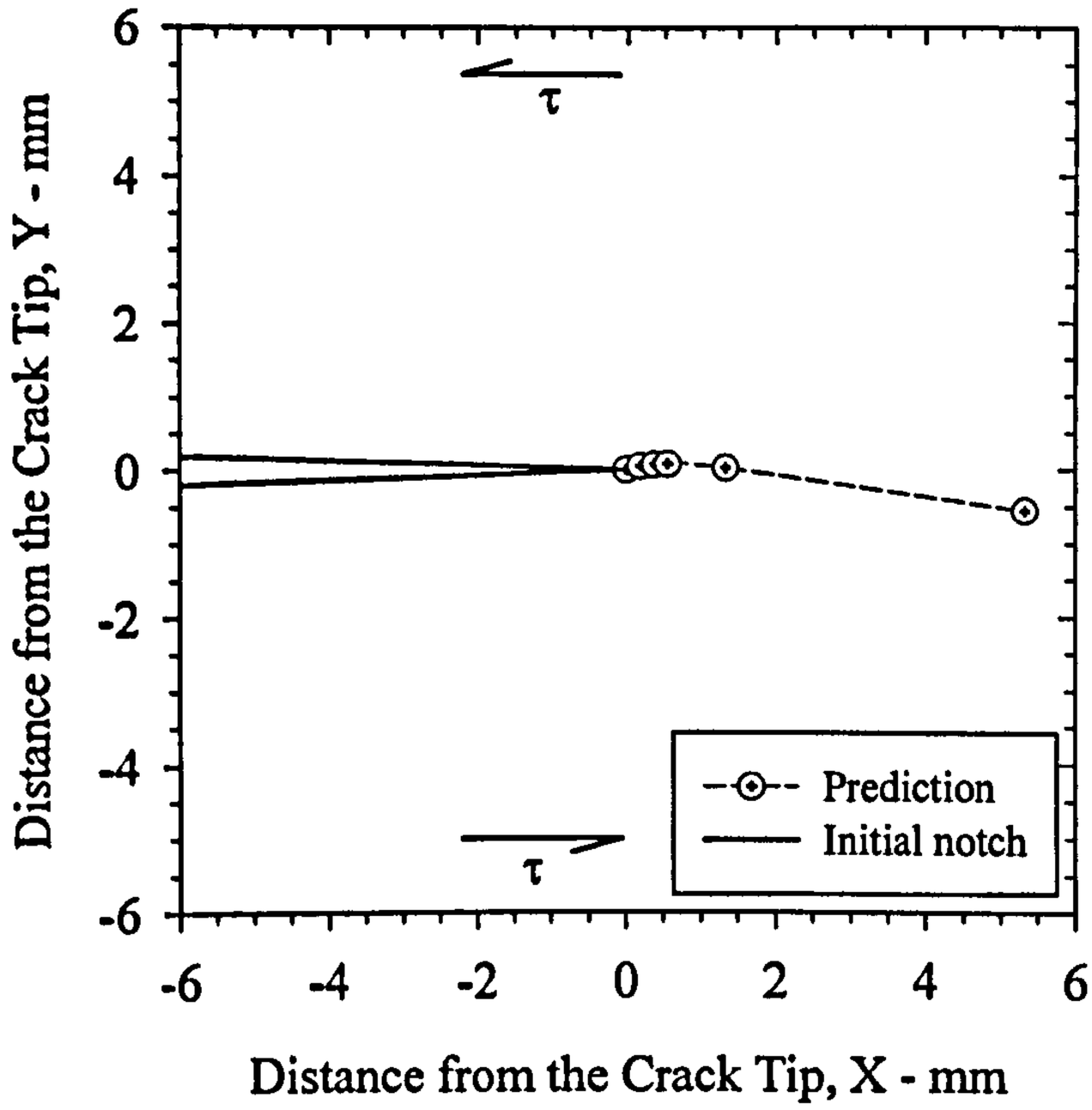

Figure 4.13. Mode II Loading : Crack Propagation Direction Predicted via the Direction of Maximum Equivalent Plastic Strain for Incremented Load Steps

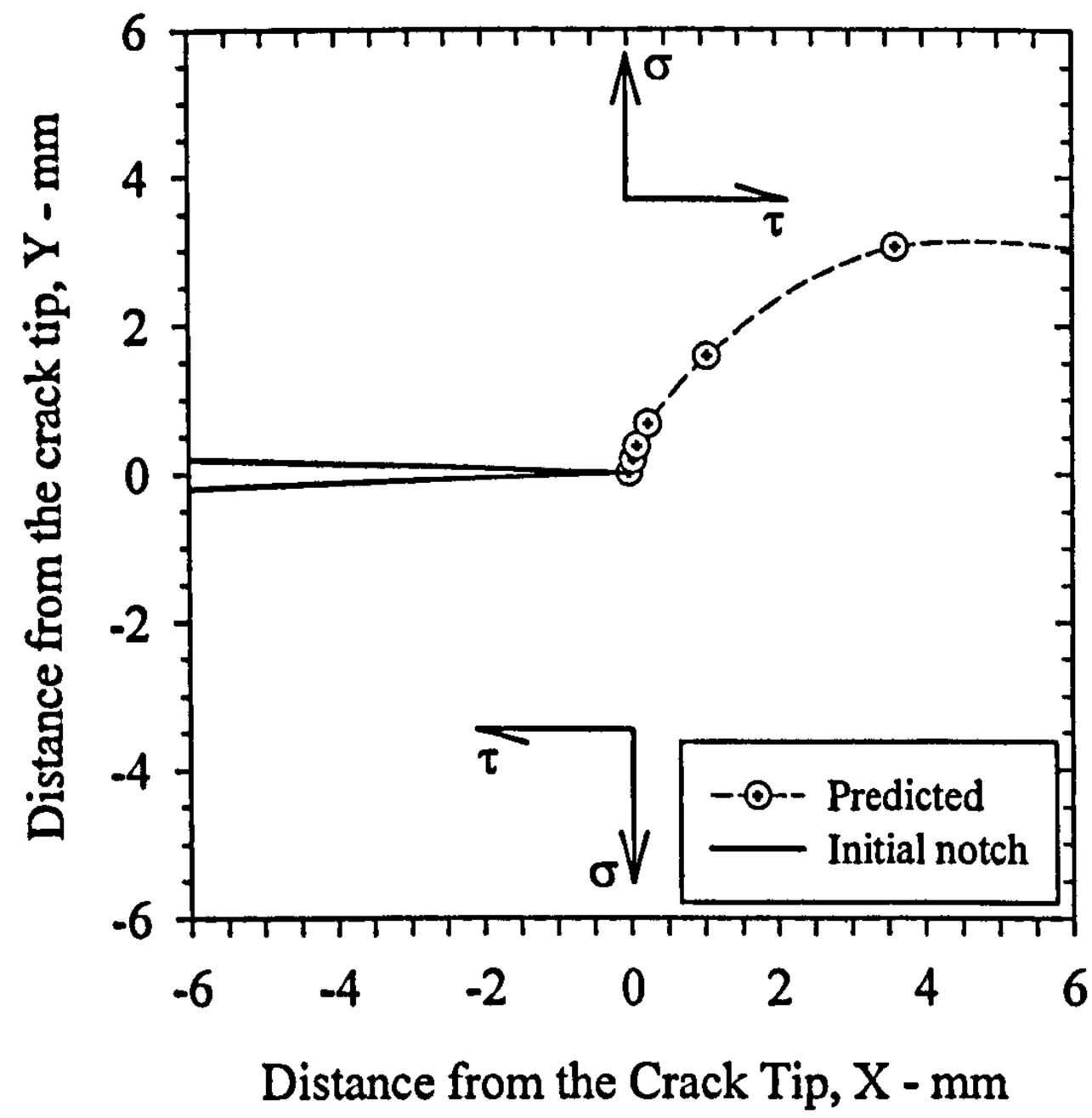

Figure 4.14. Mixed Mode (α=45.0°) : Crack Propagation Direction Predicted via the Direction of Maximum Equivalent Plastic Strain for Incremented Load Steps

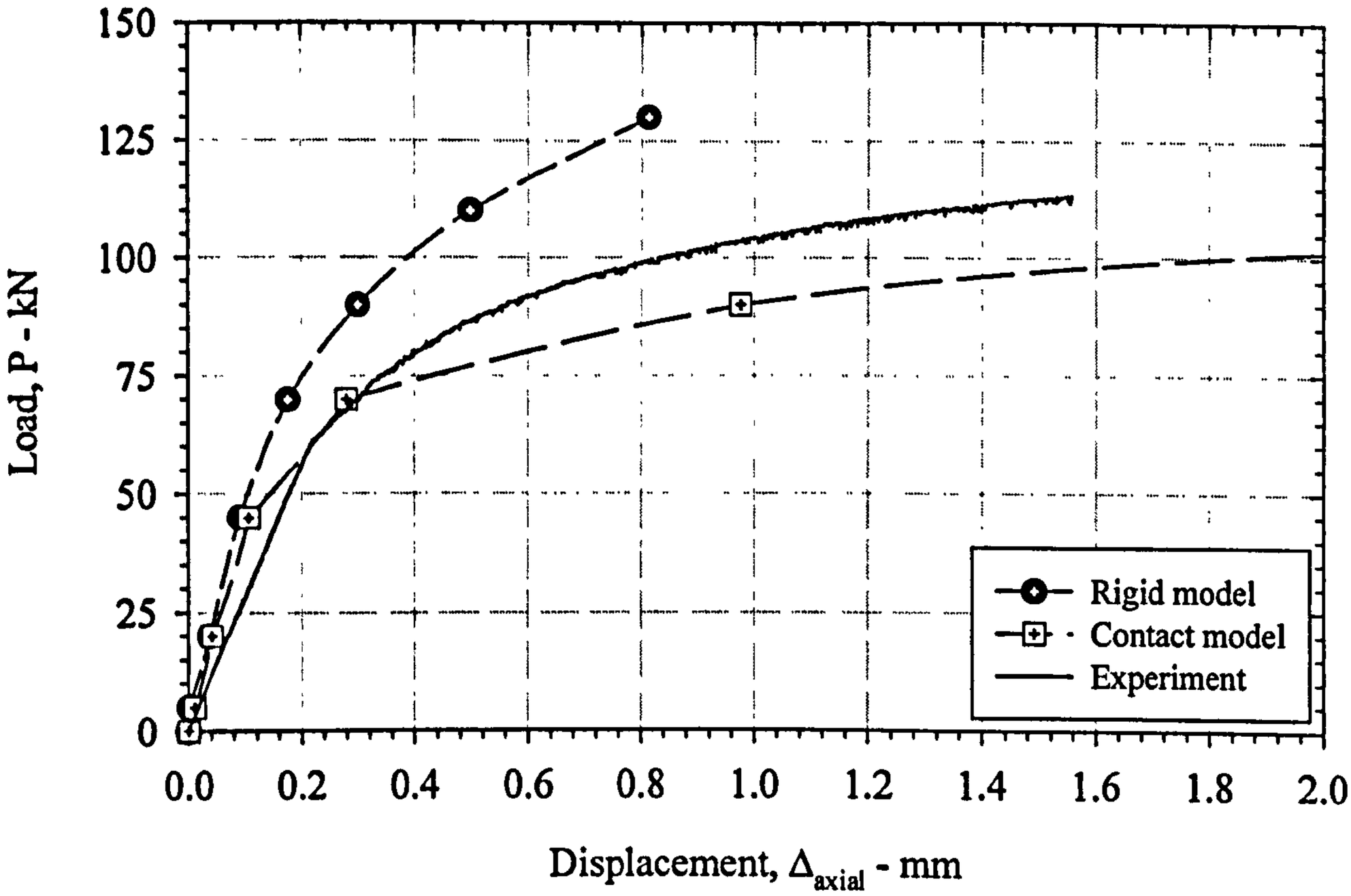

Figure 4.15a. FE : Comparison of Mode I Load vs. Displacement Curves
(Laboratory data for B=20mm, W=20mm, a_o/W=0.5 included)

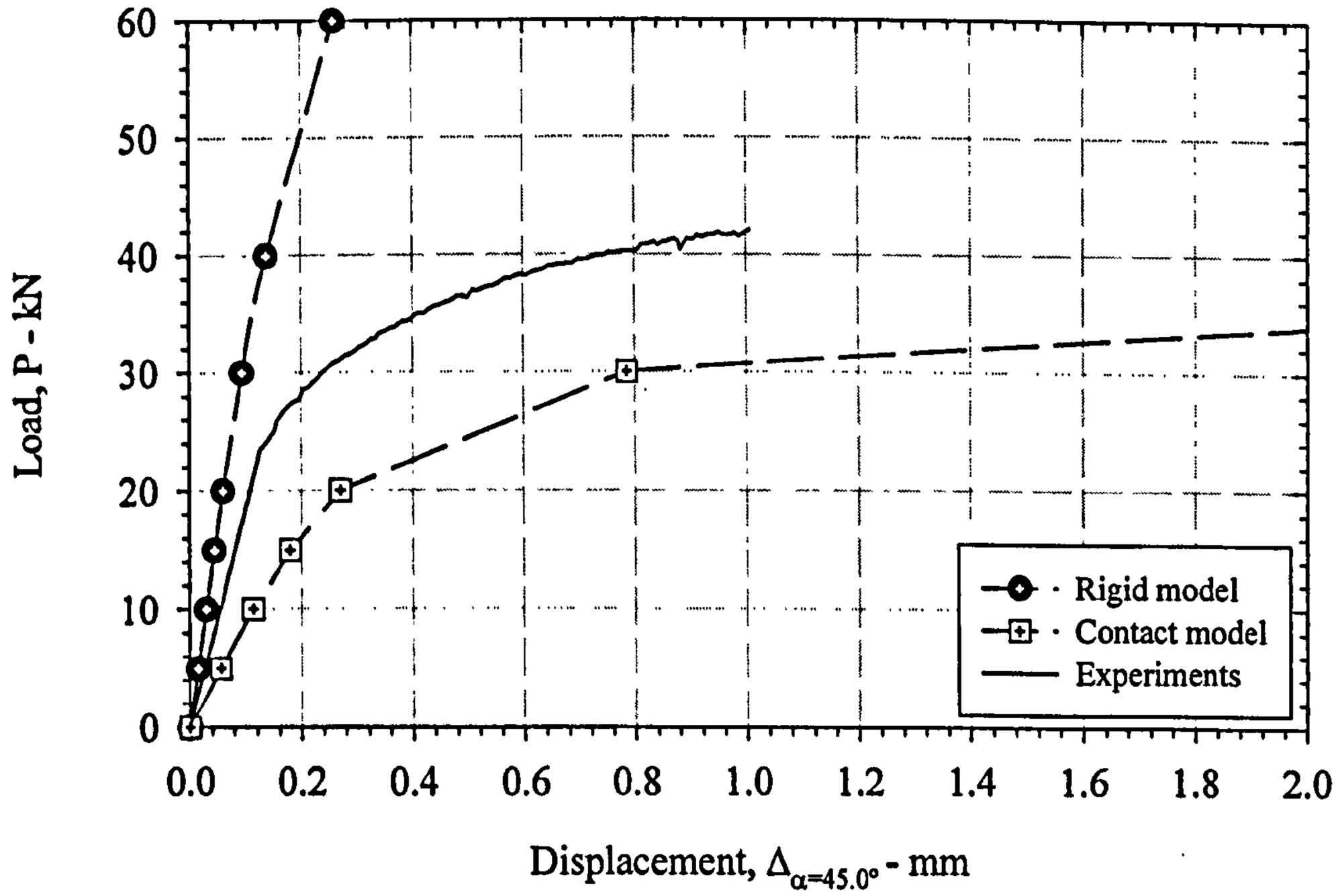

Figure 4.15b. FE : Comparison of Mixed Mode (α=45.0°) Load vs. Displacement Curves
(Laboratory data for B=10mm, W=20mm, a_o/W=0.5 included)

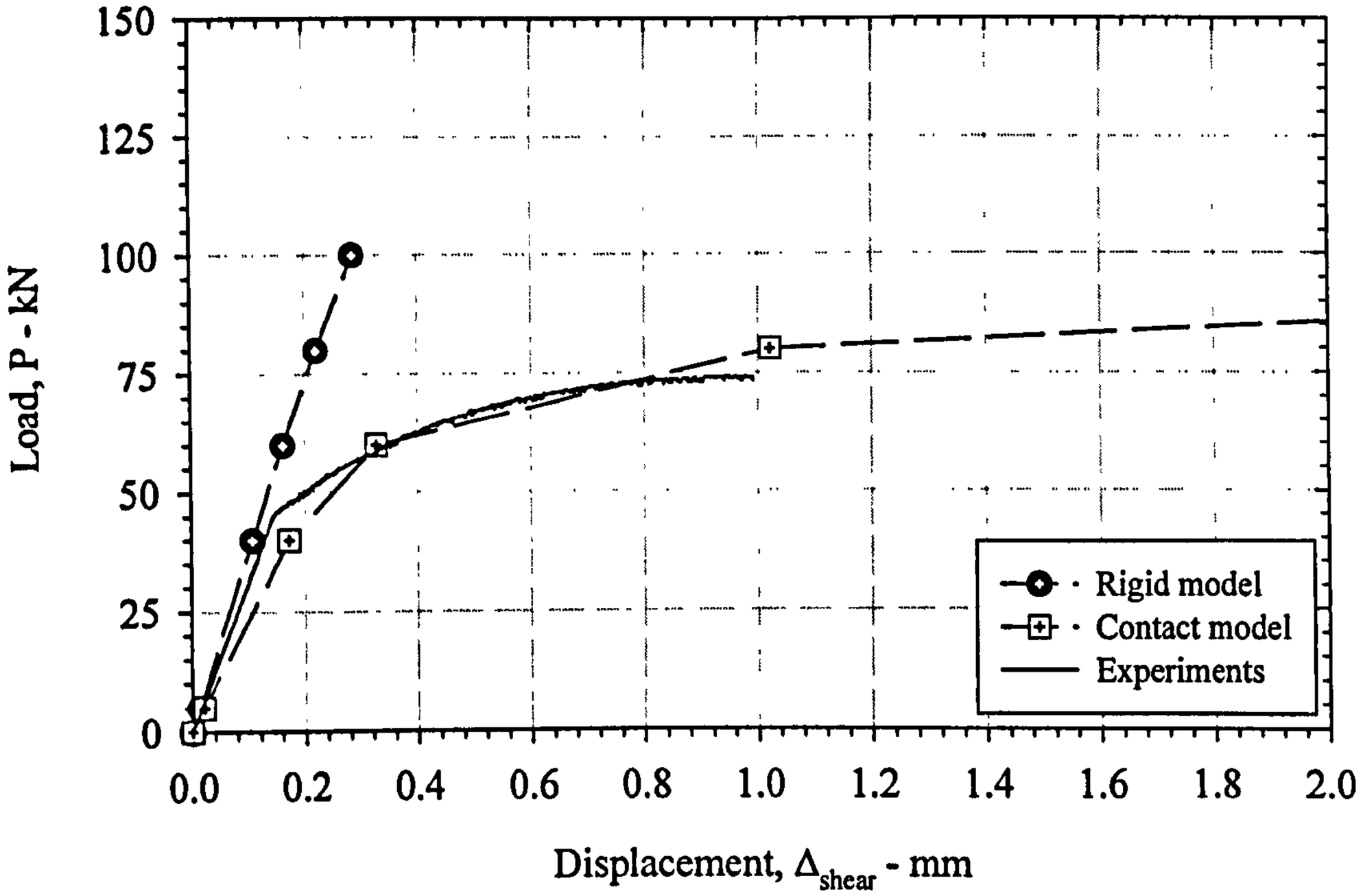

Figure 4.15c. FE : Comparison of Mode II Load vs. Displacement Curves
(Laboratory data for B=20mm, W=20mm, a_o/W=0.5 included)

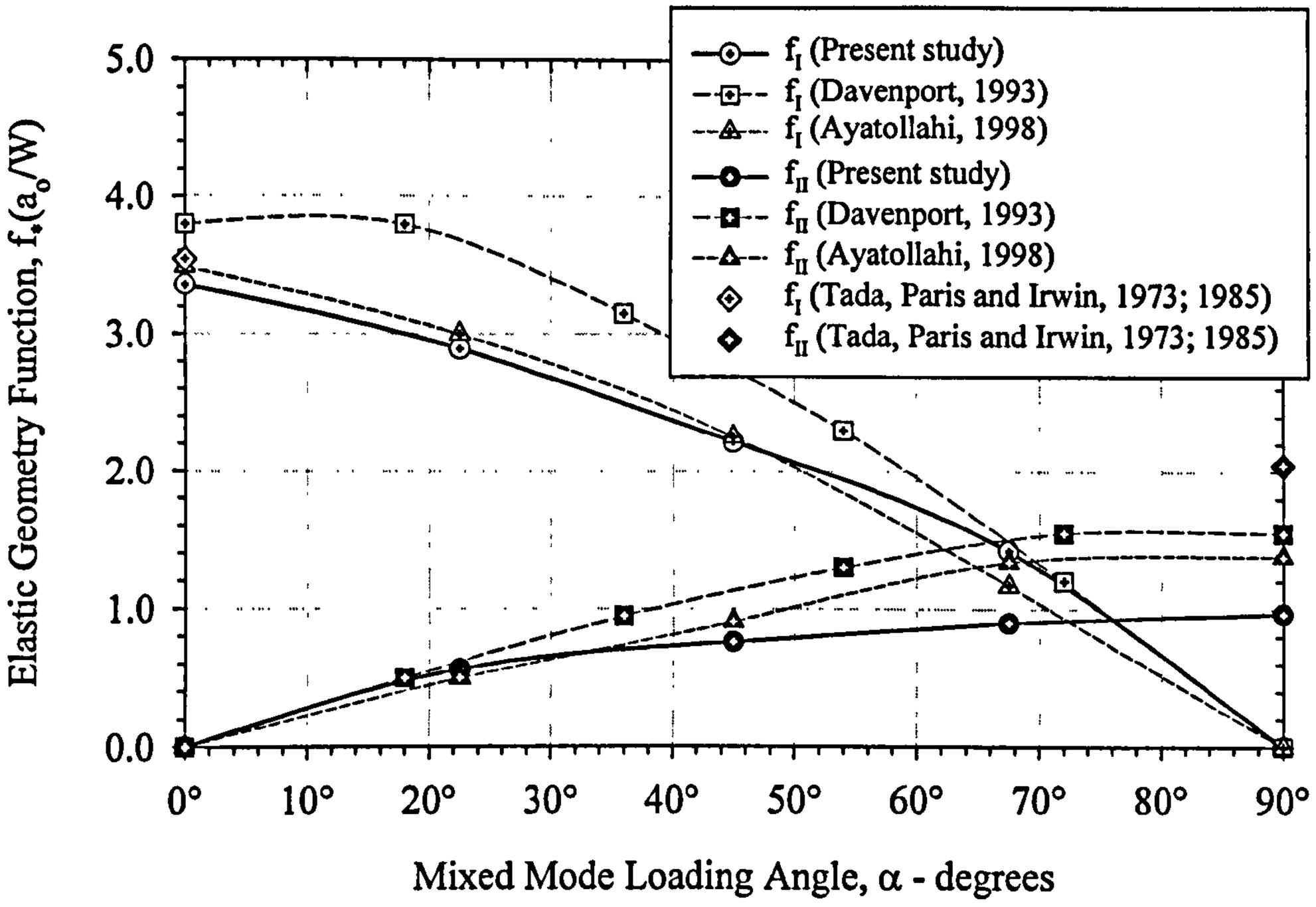

Figure 4.16. Comparison of Mixed Mode Elastic Geometry Functions (W=20mm, a_o/W=0.5)

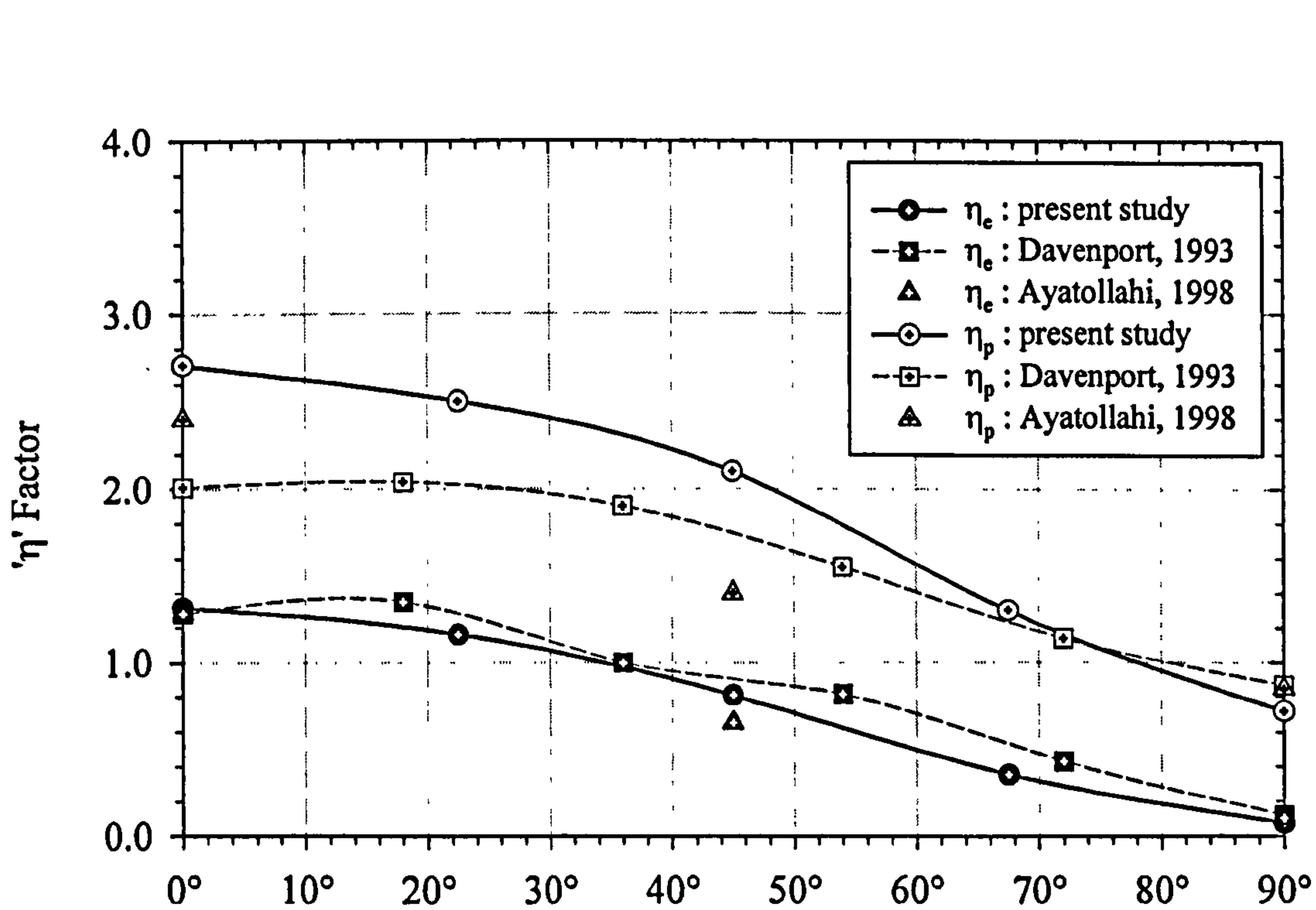

Figure 4.17. FE : Comparison of η Factors (W=20mm, a_o/W=0.5)

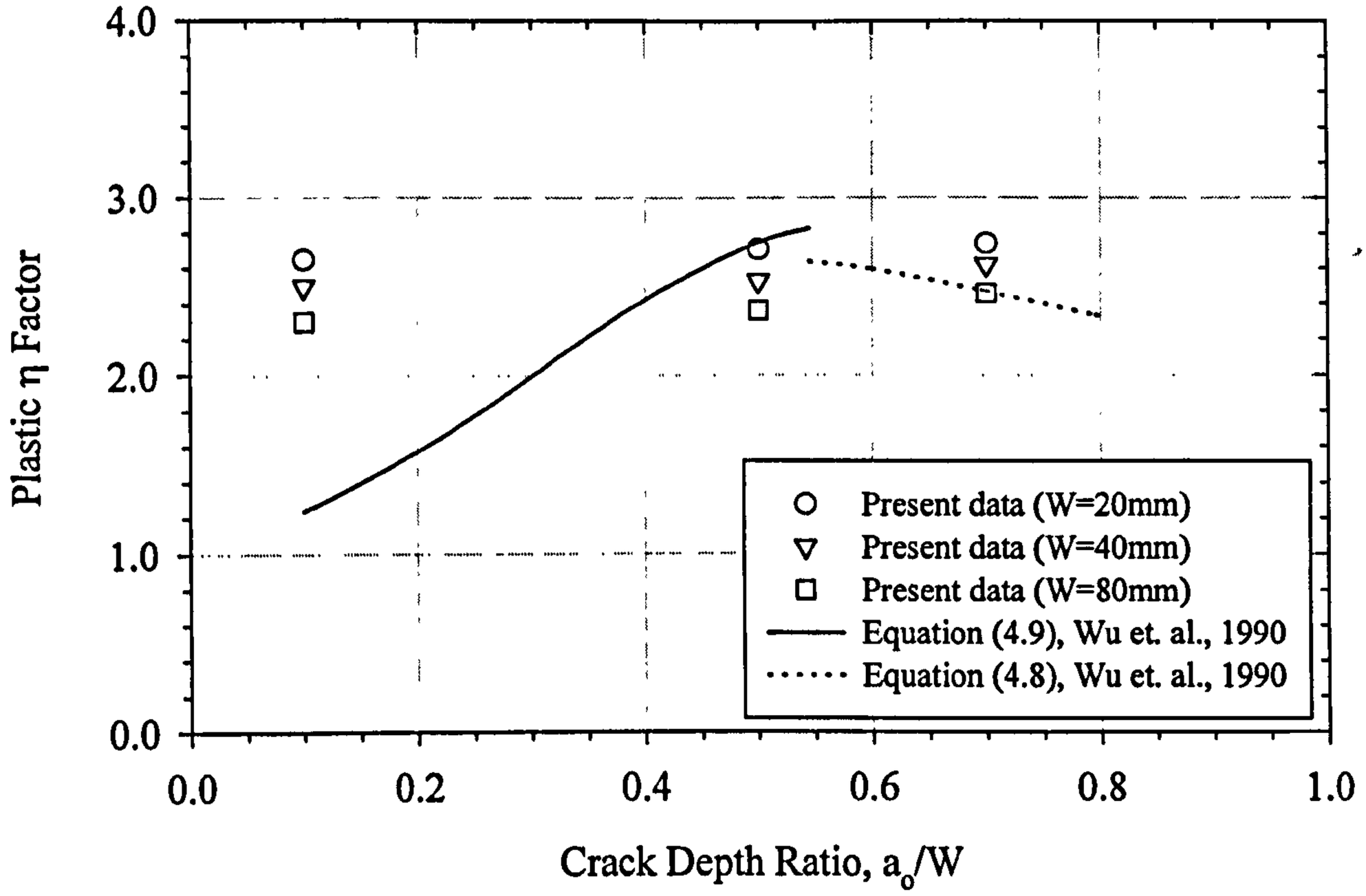

Figure 4.18. Comparison of Plastic η Factors for Different a_o/W Ratios in Mode I Loading

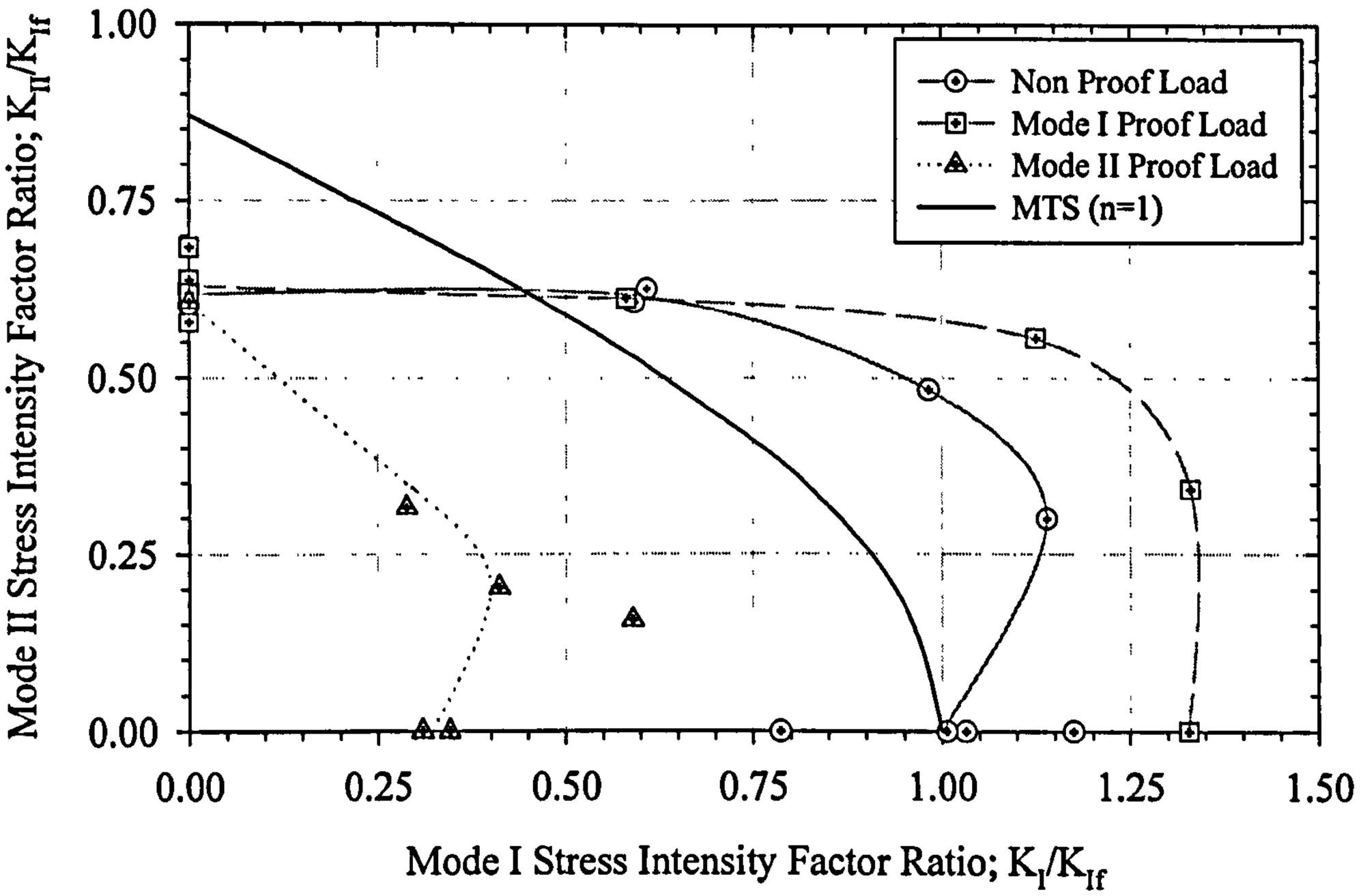

Figure 5.1. Non, Mode I and Mode II Proof Load, Mixed Mode Fracture Toughness
(comparisons with MTS criterion, Erdogan and Sih, 1963)

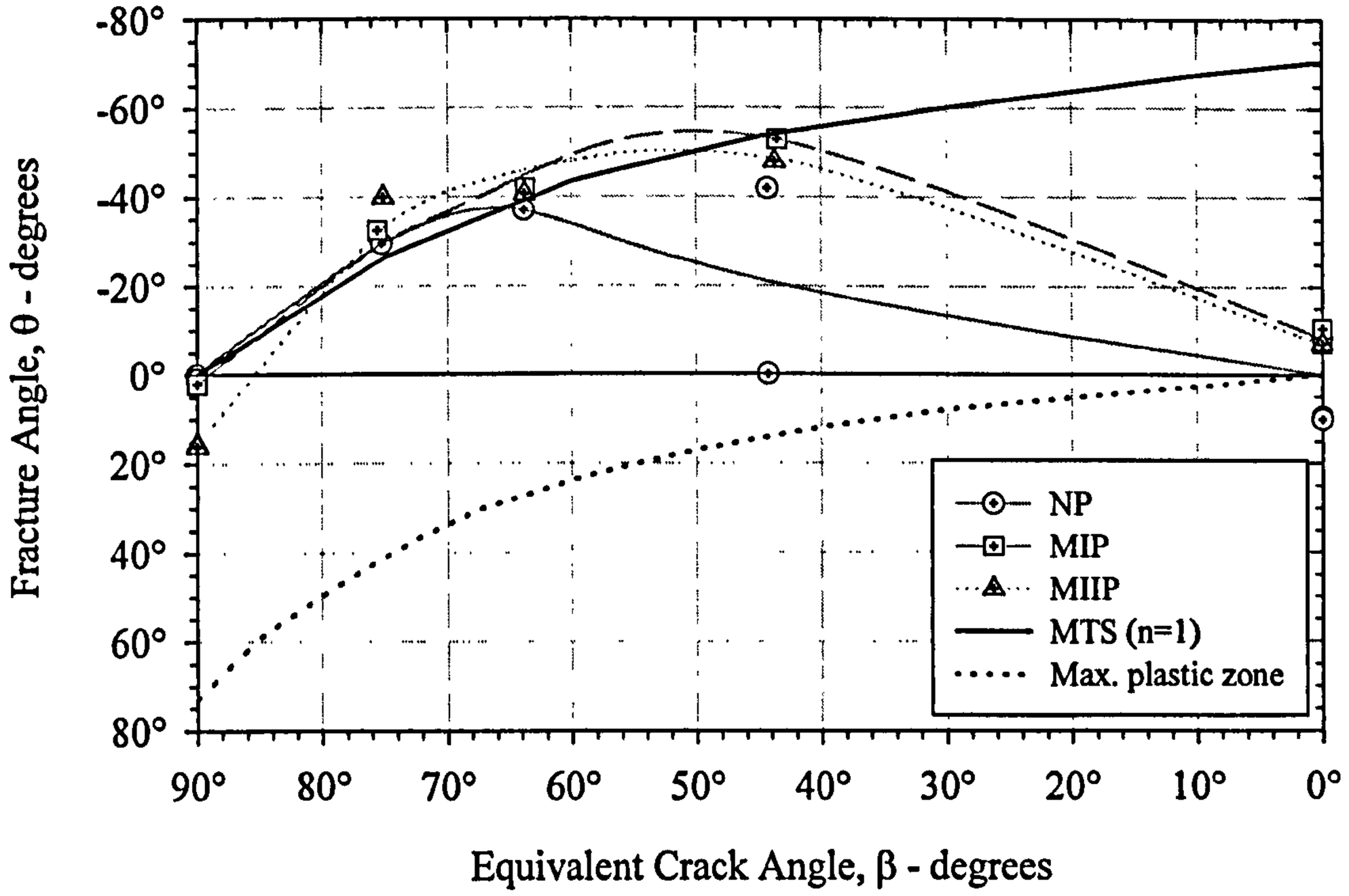

Figure 5.2. Non, Mode I and Mode II Proof Load, Mixed Mode Fracture Angles
(comparisons with MTS criterion and the maximum extent of the plastic zone)

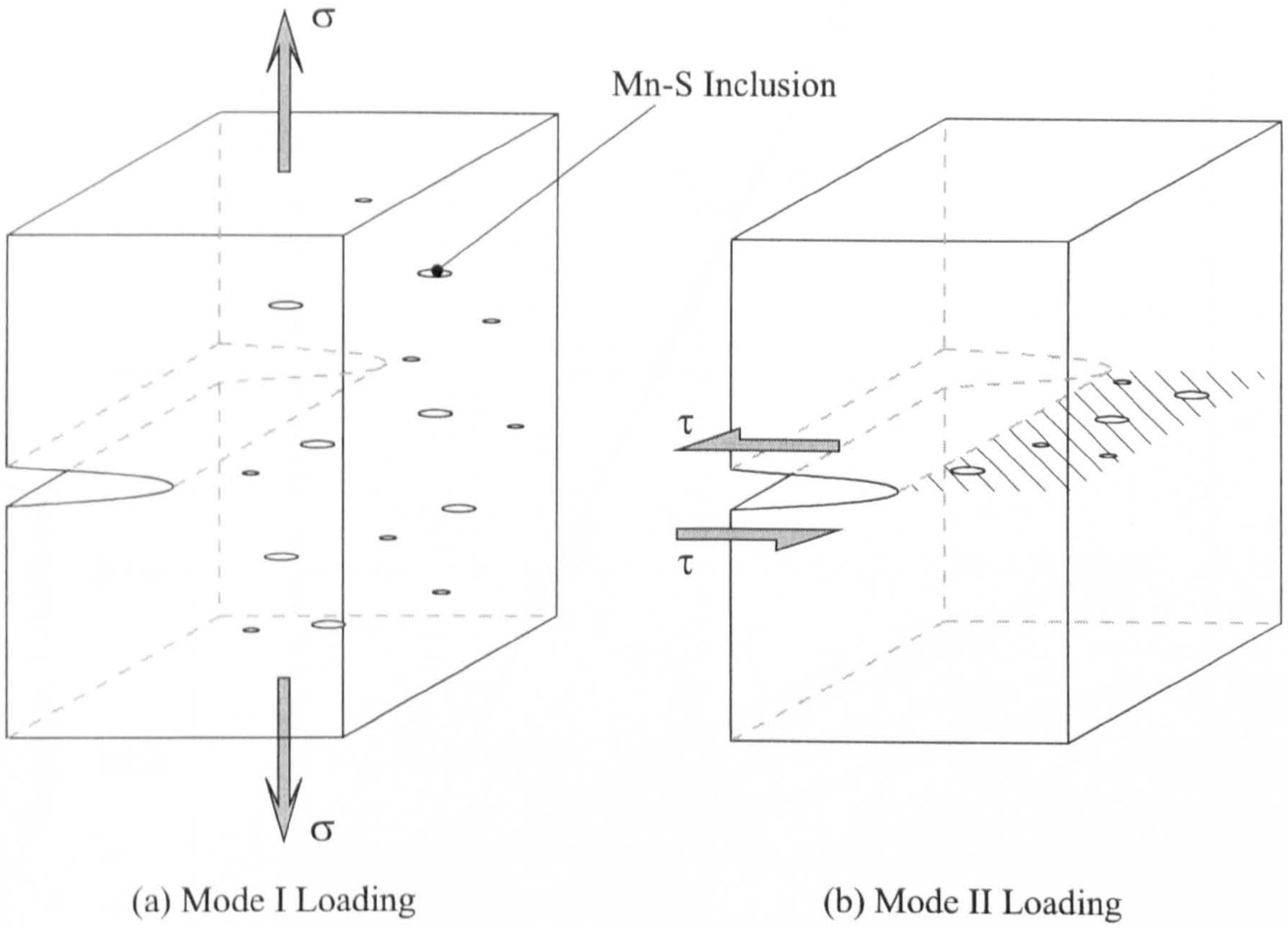

(a) Mode I Loading

(b) Mode II Loading

Figure 5.3. Effect of Mn-S Inclusion Distribution on Mode I and Mode II Loading

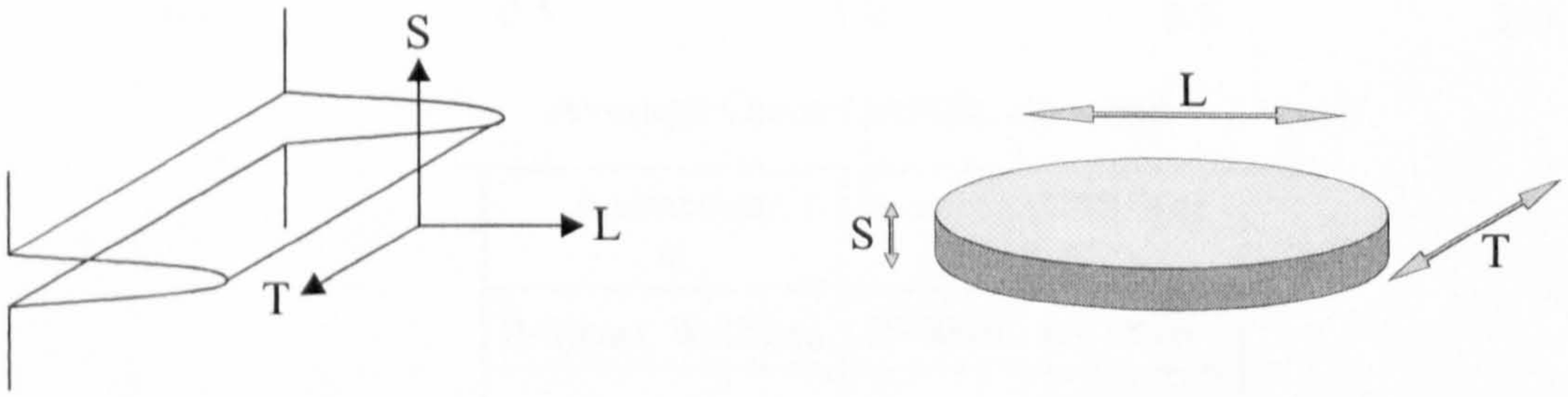

Figure 5.4. Relationship Between Crack Orientation and Mn-S Inclusion Orientation

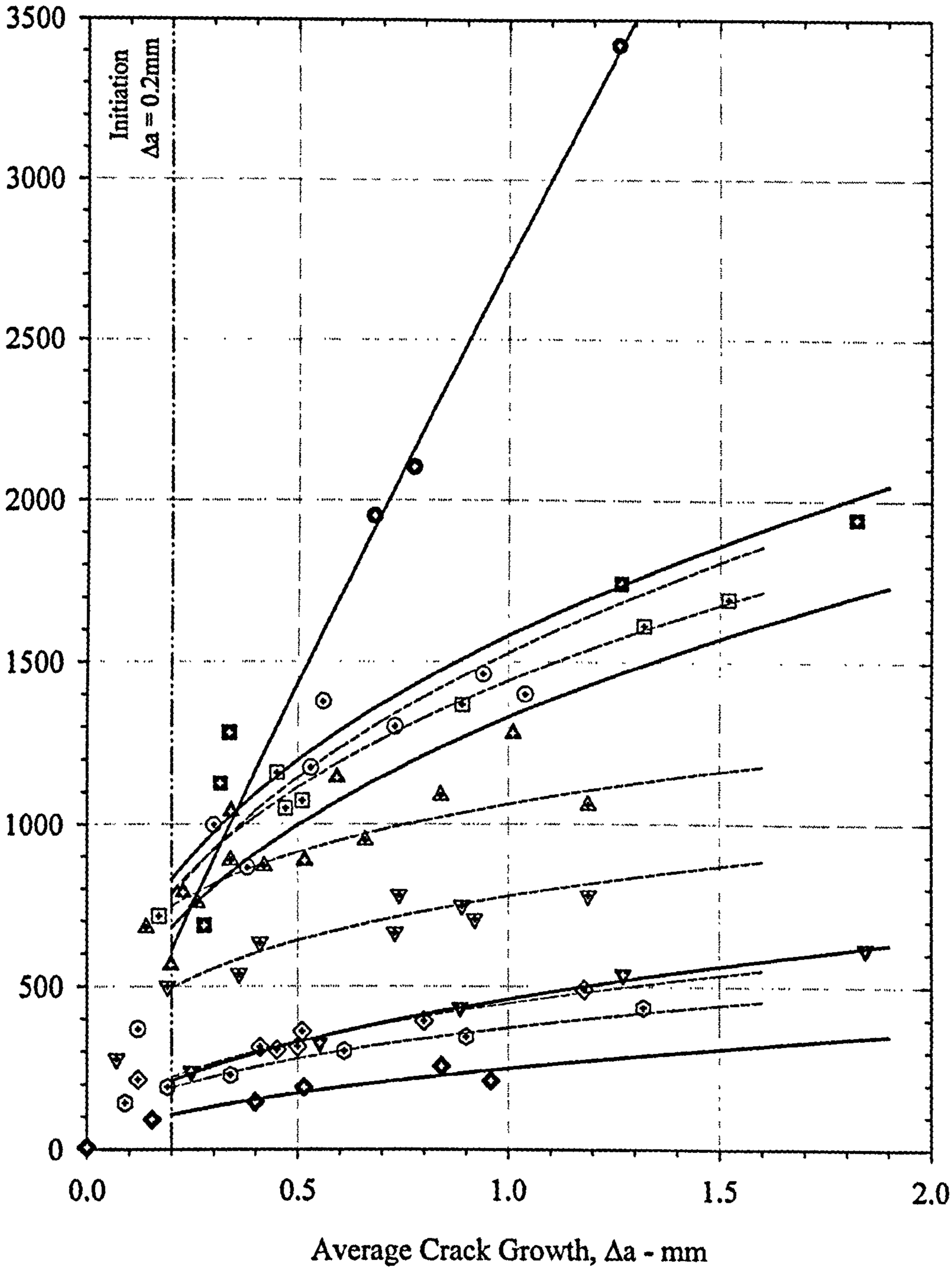

Present data α	Davenport (1993) data α
B=10mm, W=20mm	B=20mm, W=20mm
Mode I	Mode I
22.5°	18.0°
45.0°	36.0°
67.5°	54.0°
Mode II	72.0°
	Mode II

Figure 5.5. Comparison of Mixed Mode R-Curves, $a_o/W=0.5$

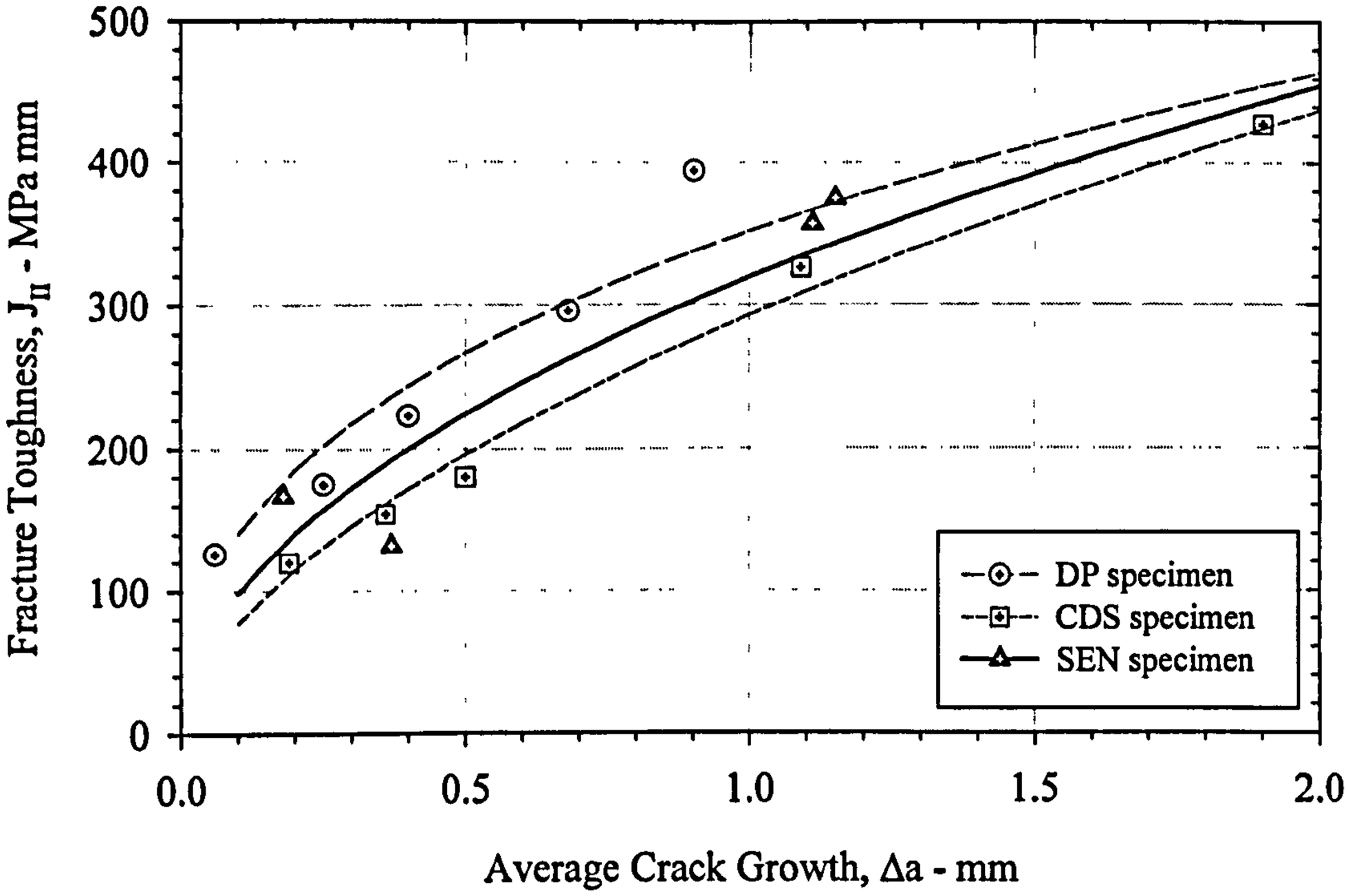

Figure 5.6. Comparison of Mode II Geometry Effects in Side Grooved Specimens (DP and CDS data obtained from Green and Miles, 1983)

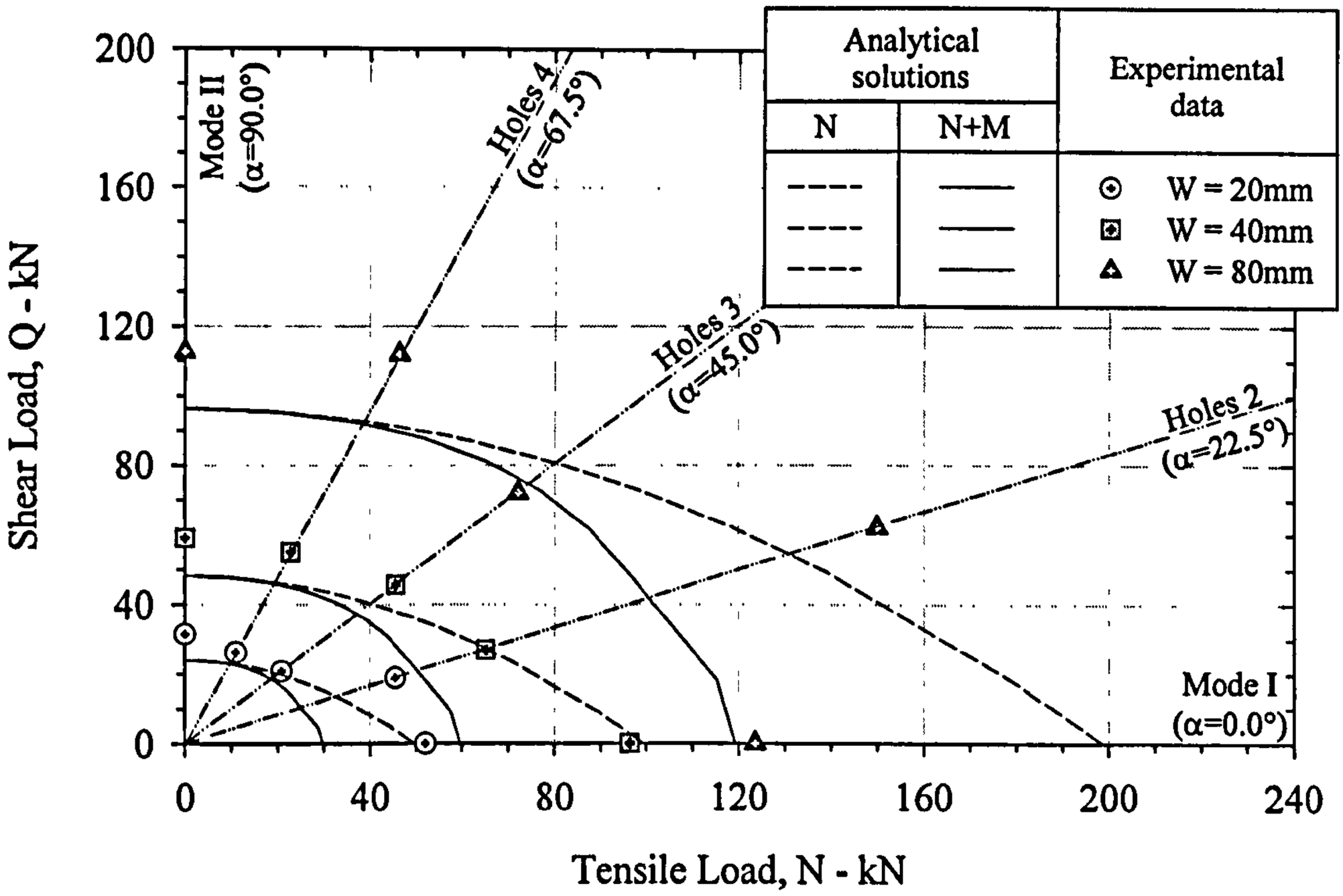

Figure 5.7a. Effect of Bend Loading (M) on Mixed Mode I/II Limit Loads, $a_o/W=0.5$
(Effect of specimen width for constant thickness, B=10mm)

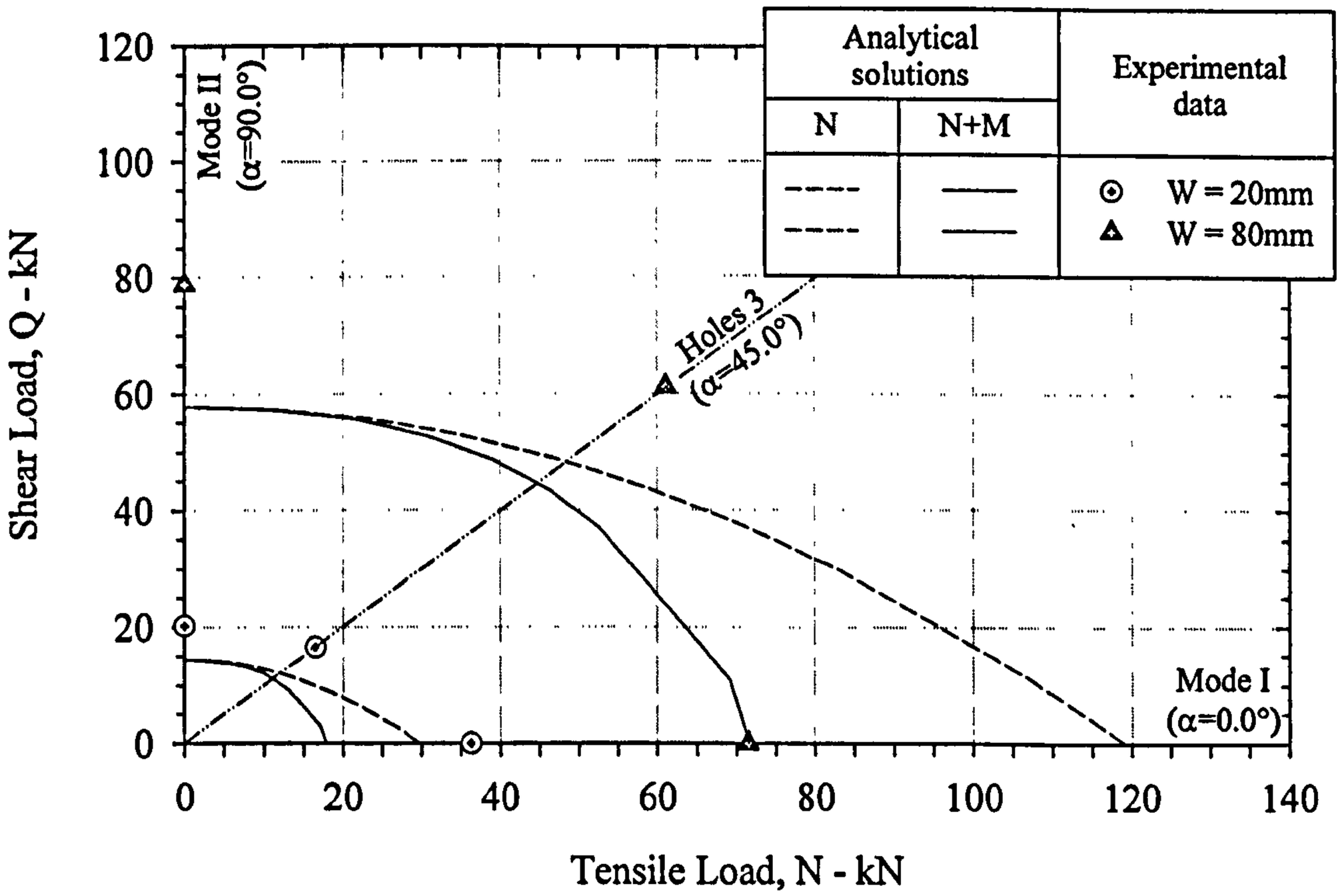

Figure 5.7b. Effect of Bend Loading (M) on Mixed Mode I/II Limit Loads, $a_o/W=0.7$
(Effect of specimen width for constant thickness, B=10mm)

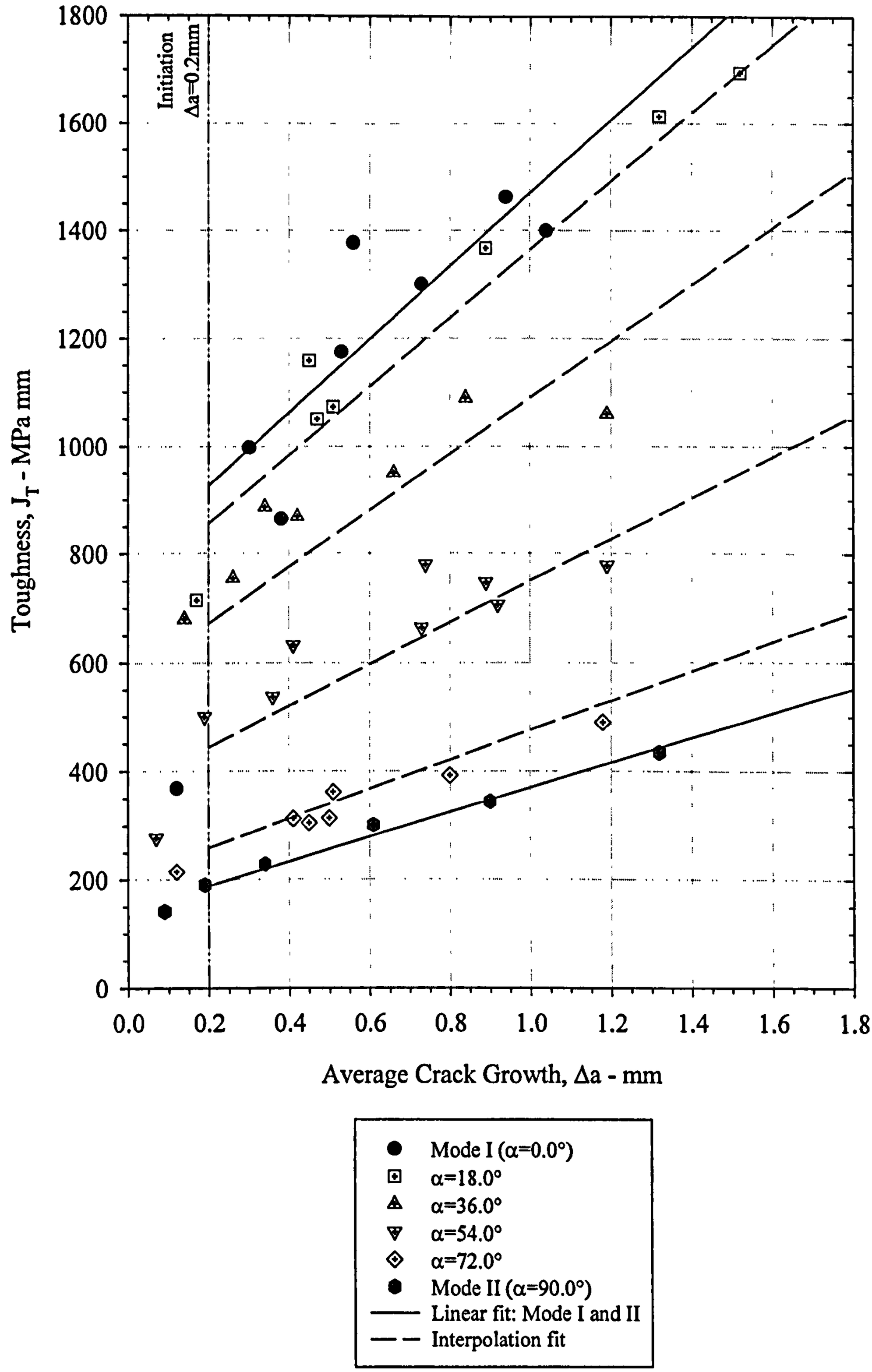

Figure 5.8. Interpolation Fit to A508 Experimental Data after Davenport (1993)
(SEN specimens, B=20mm, W=20mm, a_o/W=0.5)

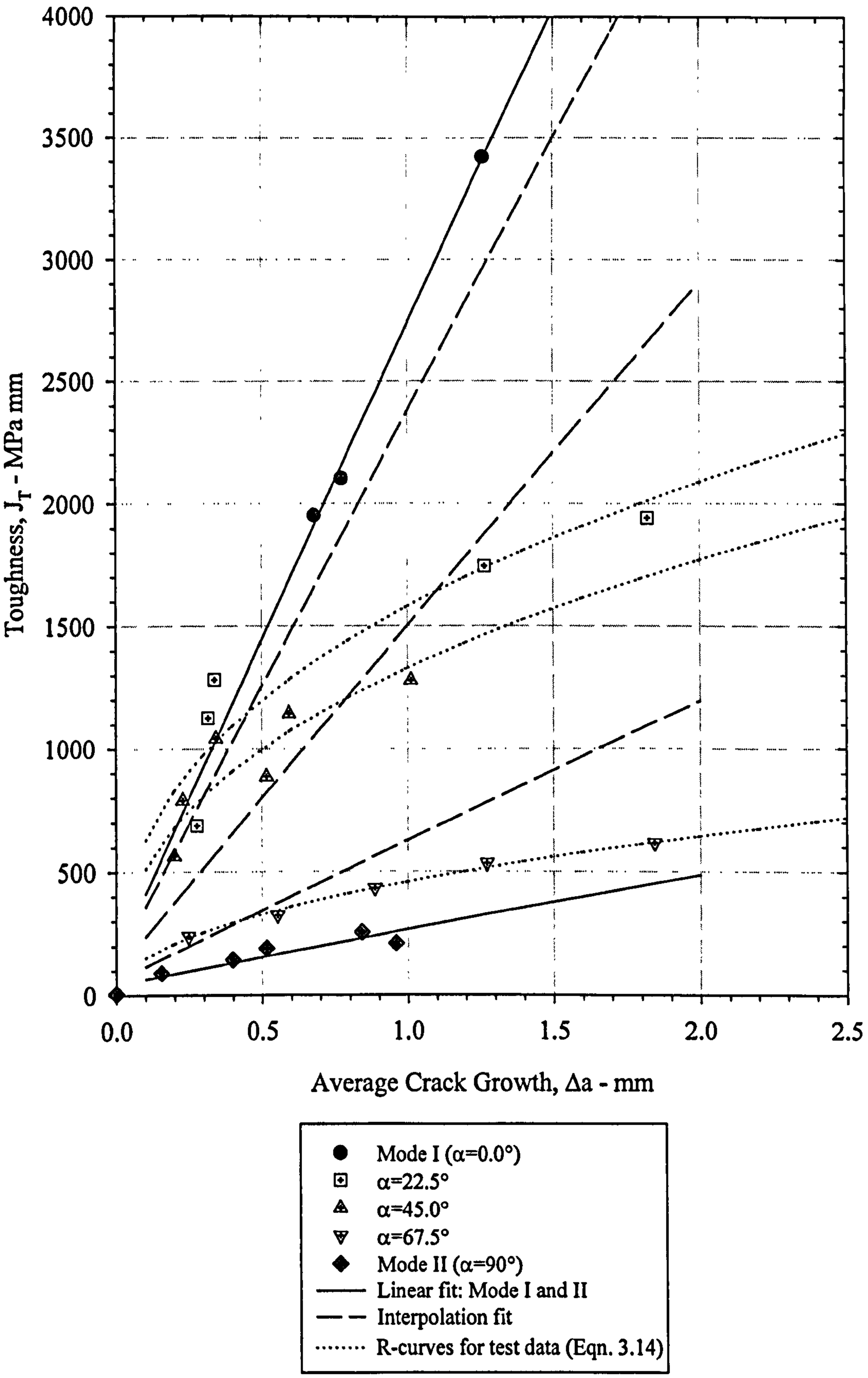

Figure 5.9. Mixed Mode R-Curves Generated using Davenport's (1993) Interpolation Model (SEN specimens, B=10mm, W=20mm, a_o/W=0.5)

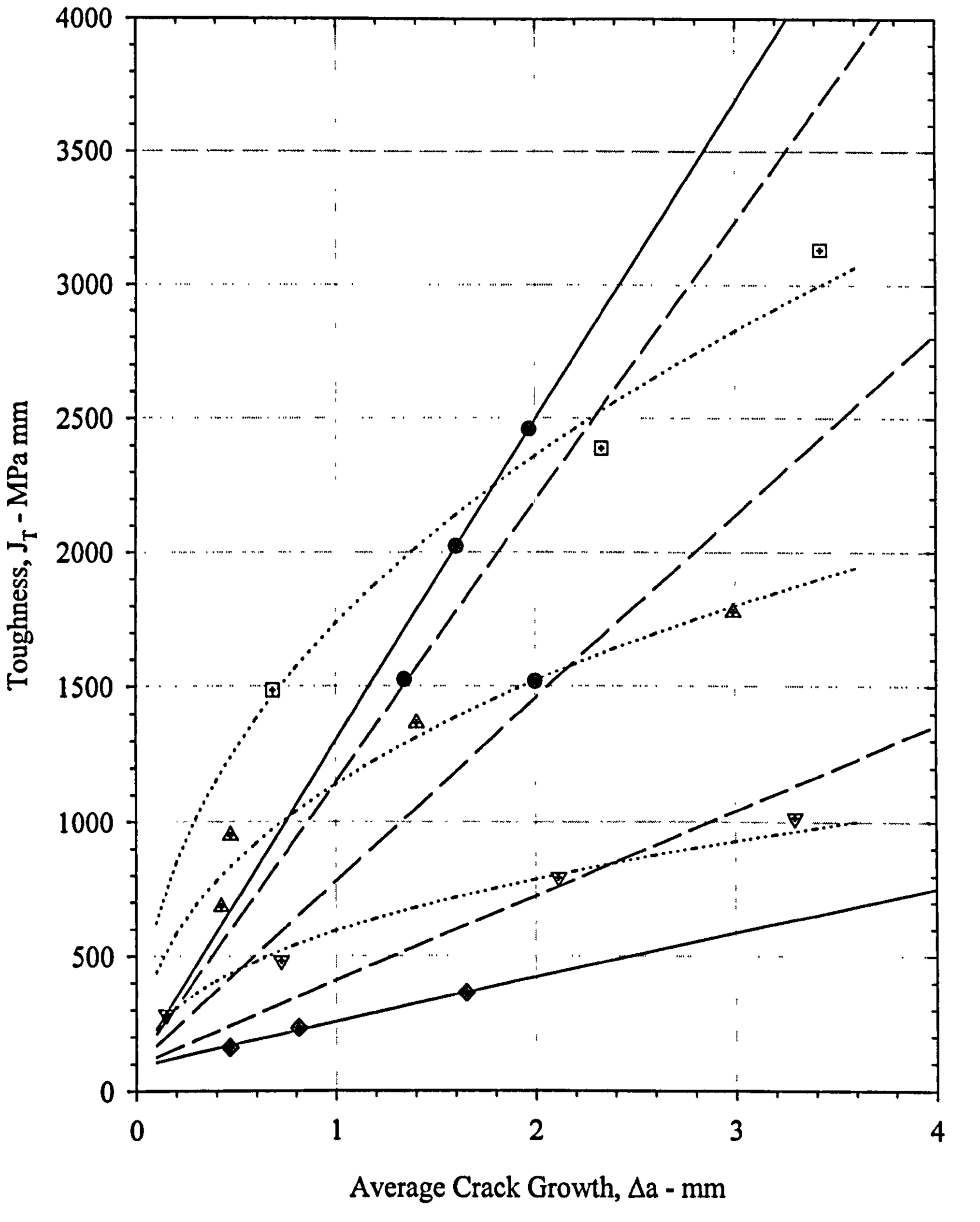

Figure 5.10. Mixed Mode R-Curves Generated using Davenport's (1993) Interpolation Model (SEN specimens, B=10mm, W=40mm, a_o/W=0.5)

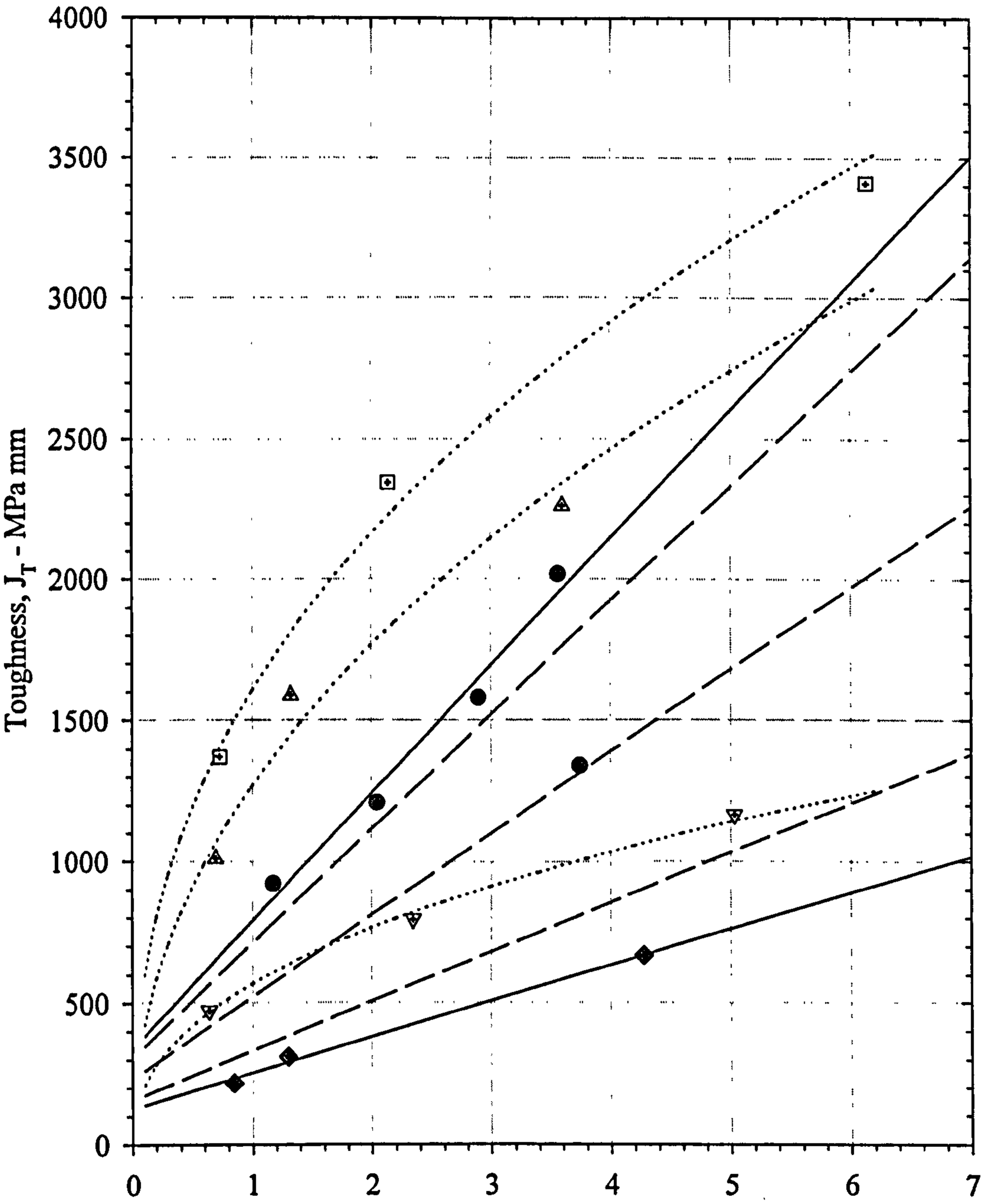

Figure 5.11. Mixed Mode R-Curves Generated using Davenport's (1993) Interpolation Model (SEN specimens, B=10mm, W=80mm, a_o/W=0.5)

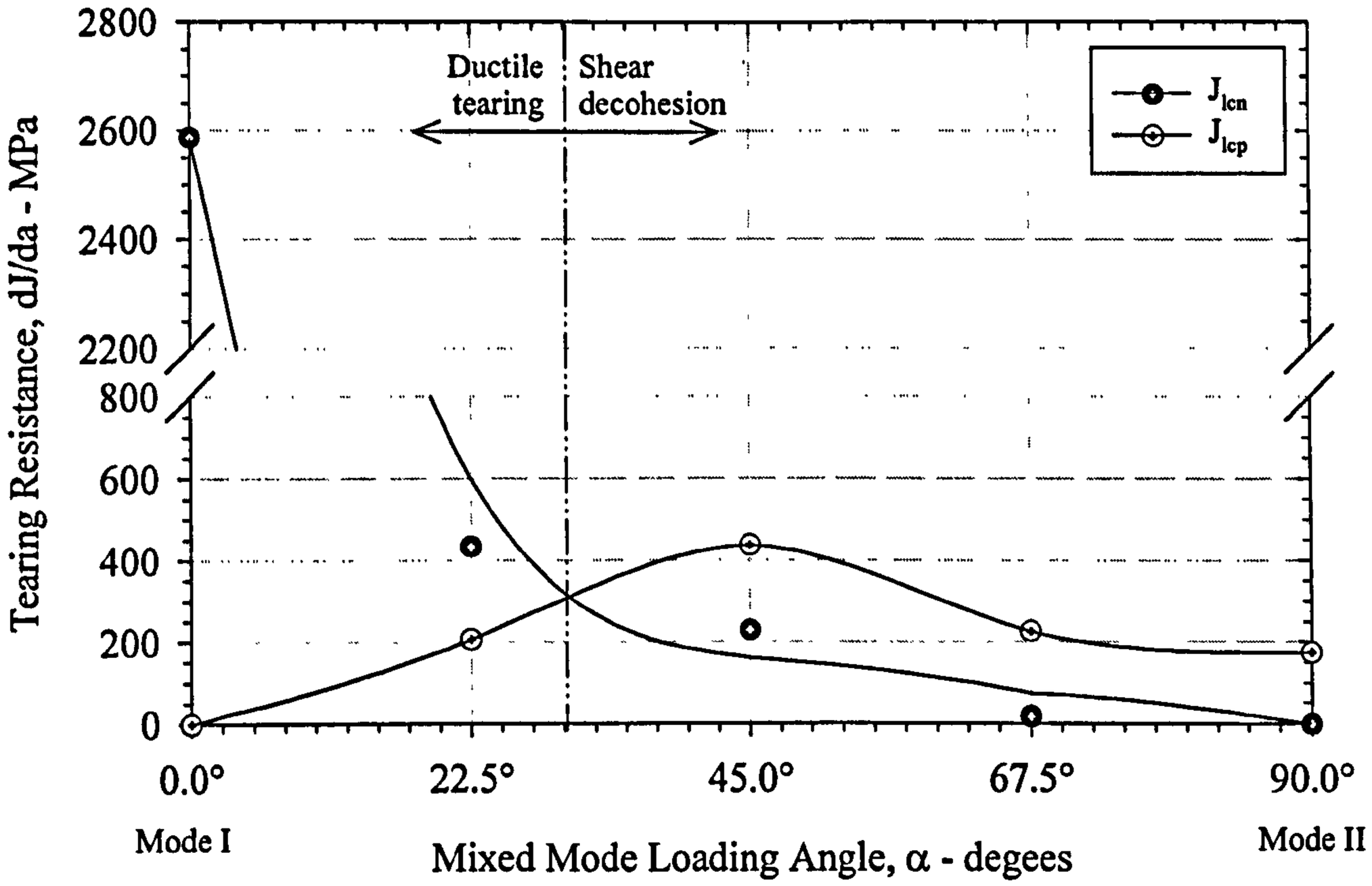

Figure 5.12. Change in Failure Mechanism During Mixed Mode Loading
(B=10mm, W=20mm, a_o/W=0.5)

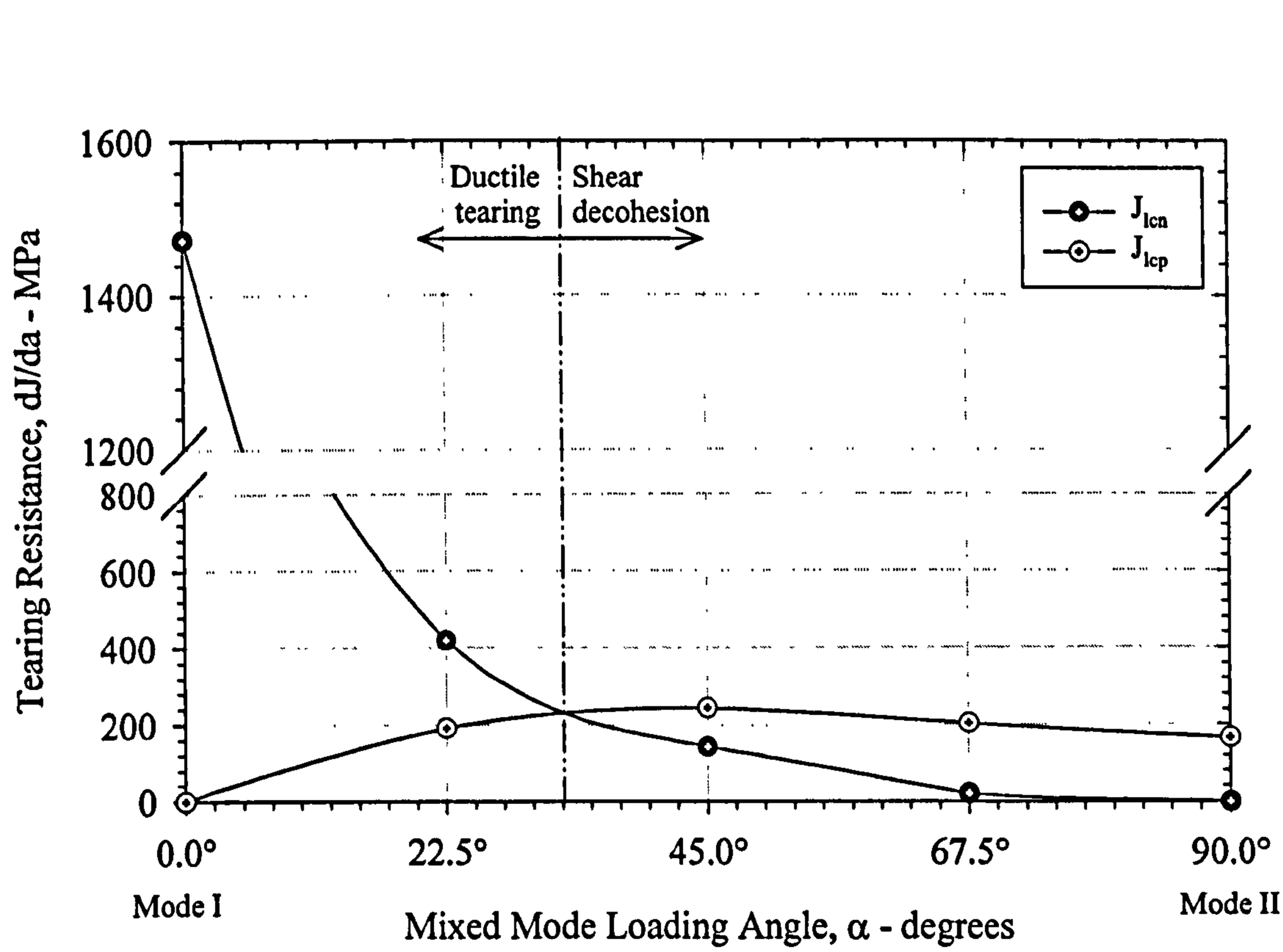

Figure 5.13. Change in Failure Mechanism During Mixed Mode Loading
(B=10mm, W=40mm, a_o/W=0.5)

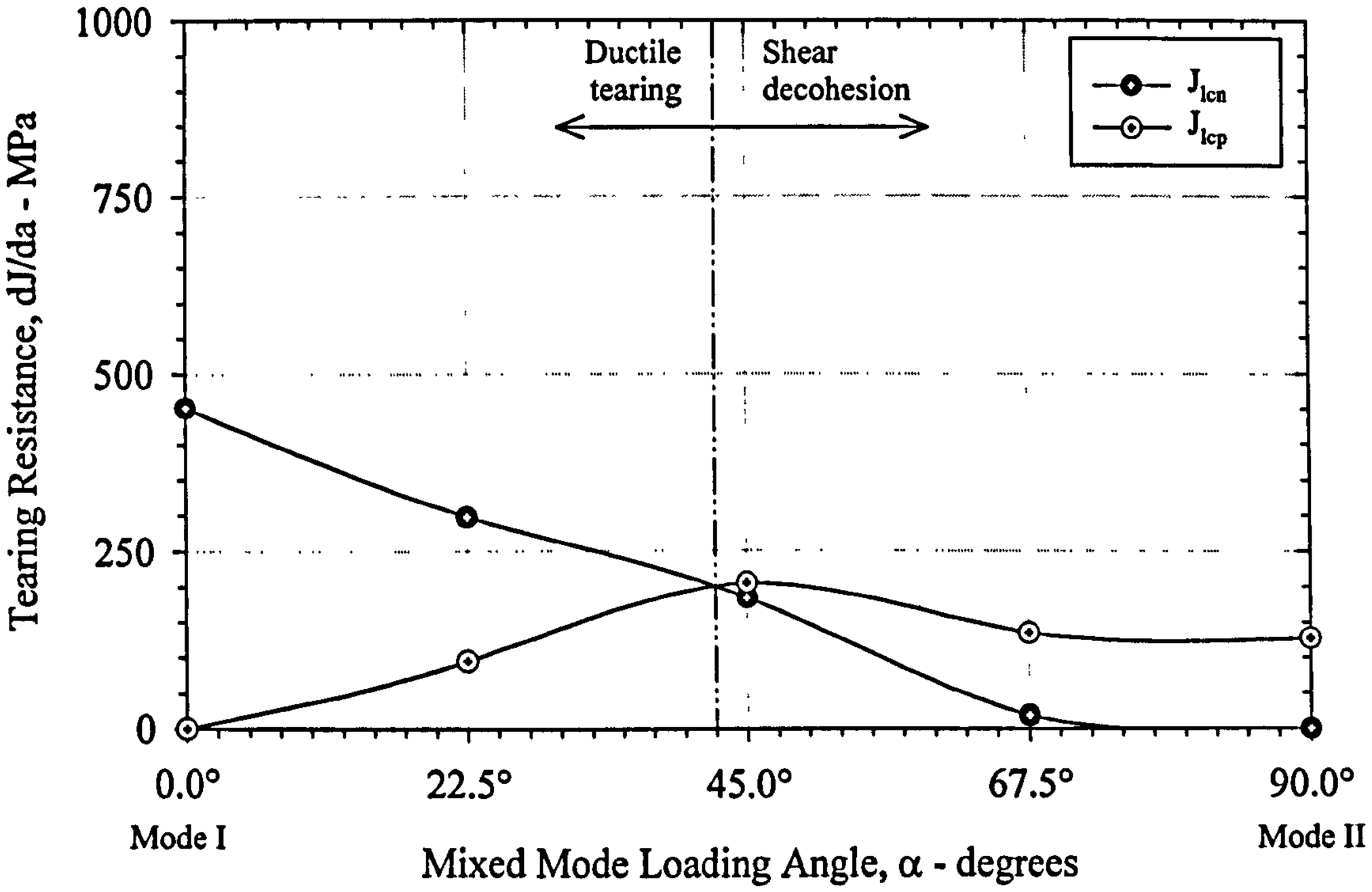

Figure 5.14. Change in Failure Mechanism During Mixed Mode Loading
(B=10mm, W=80mm, a_o/W=0.5)

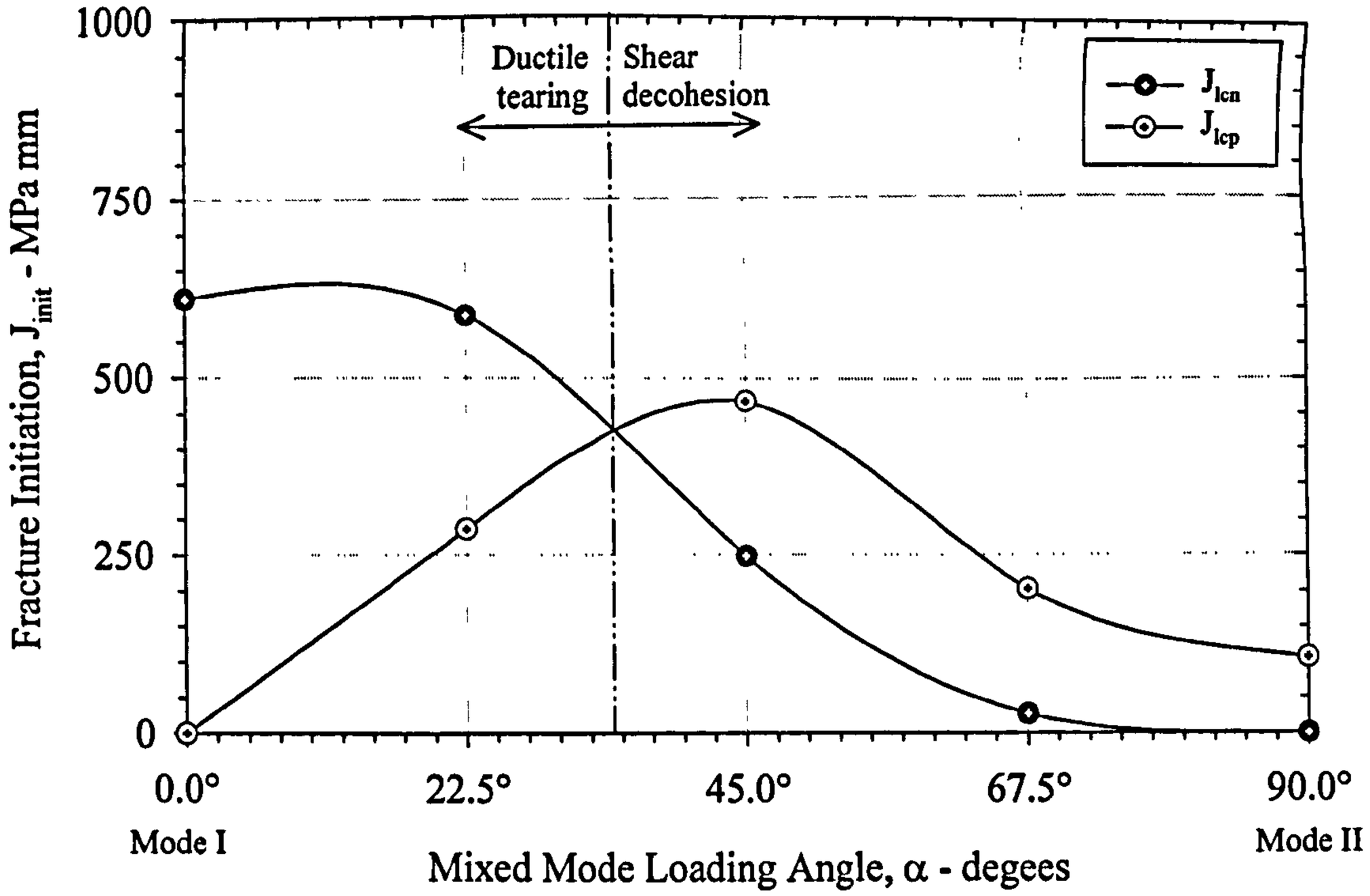

Figure 5.15. Change in Failure Mechanism During Mixed Mode Loading
(J_{init} at Δa=0.2mm, B=10mm, W=20mm, a_o/W=0.5)

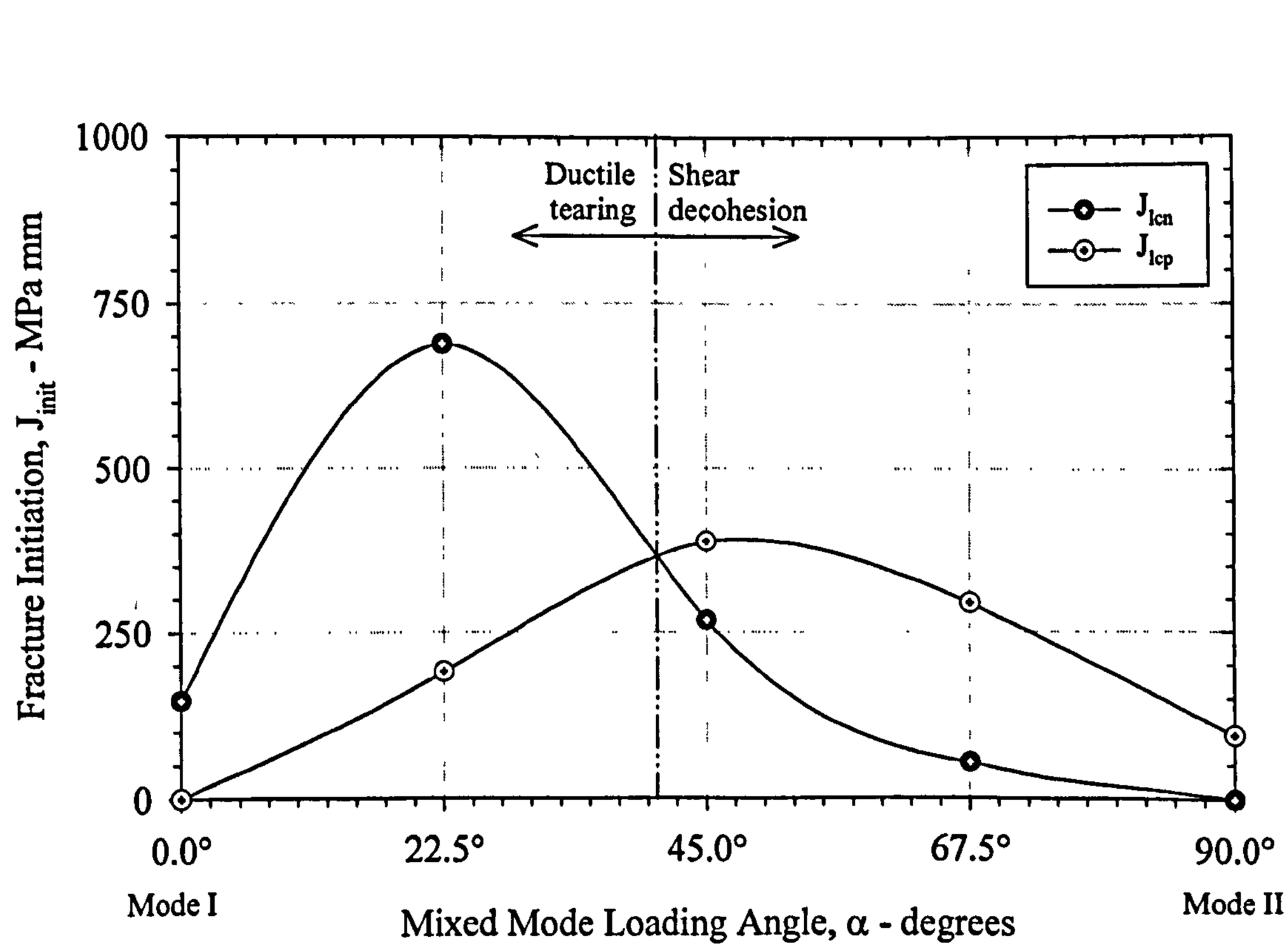

Figure 5.16. Change in Failure Mechanism During Mixed Mode Loading
(J_{init} at Δa=0.2mm, B=10mm, W=40mm, a_o/W=0.5)

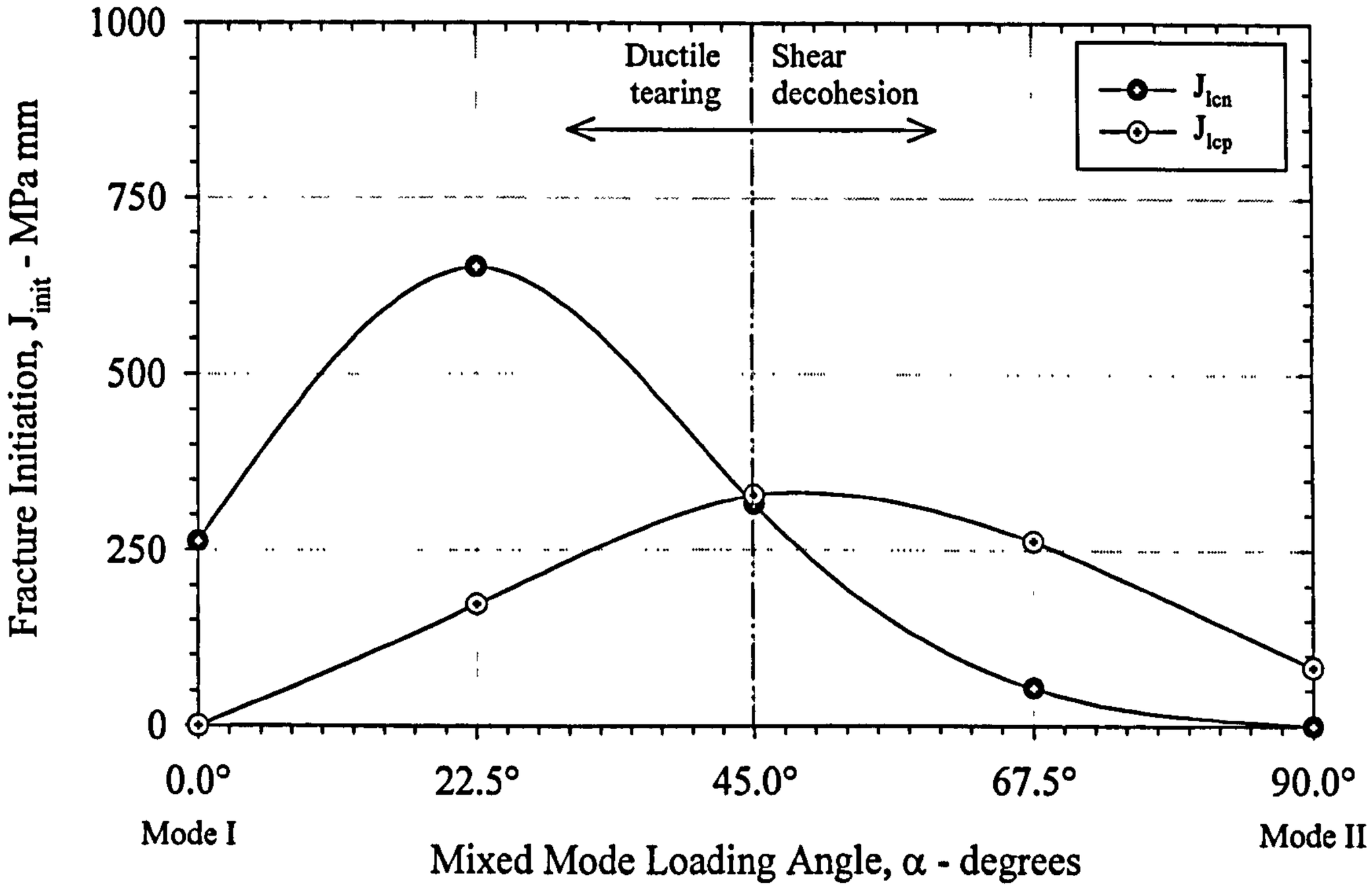

Figure 5.17. Change in Failure Mechanism During Mixed Mode Loading
(J_{init} at Δa=0.2mm, B=10mm, W=80mm, a_o/W=0.5)